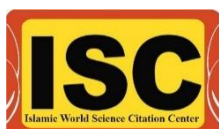مجموعه مقالات

بیست و دومین کنگره بین المللی شیمی ایران

Proceeding of
22nd Iranian Chemistry Congress

۲۴-۲۶اردیبهشت ۱۴۰۳

(13-15 May 2024)

سازمان پژوهش‌های علمی و صنعتی ایران

(Iranian Research Organization for Science and Technology)

ISC

03231-97589

IROST

بسم الله الرحمن الرحيم

22nd Iranian Chemistry Congress

Tehran - Iranian Research Organization for Science and Technology (IROST)

IROST

Iranian Chemical Society

Important Dates:

- Extended Abstract Submission Start date
  Monday, October 23, 2023

- Extended Abstract Submission Deadline
  Sunday, February 4, 2024

- Announcement of the accepted abstracts
- Registration opens
  Tuesday, March 5, 2024

- Final payment date and registration
  Monday, April 8, 2024

- Announcement of the congress program
  Thursday, May 9, 2024

- Congress date
  Monday, May 13 - Wednesday, May 15, 2024

Topics:

- **Physical Chemistry**
- **Analytical Chemistry**
- **Organic Chemistry**
- **Inorganic Chemistry**
- **Applied Chemistry**
- **Pharmaceutical, Phyto and Biochemistry**

Website: https://icc22.conf.irost.ir
Tel: 09302934895
Email: icc22@irost.ir
Address: Iranian Research Organization for Science and Technology (IROST)., Sh. Ehsani Rad St., Enqelab St., Ahmadabad Mostoufi Rd., Azadegan Highway, Tehran, Iran.

بیست و دومین کنگره بین المللی شیمی ایران
۲۴-۲۶ اردیبهشت ۱۴۰۳

ساختار سازمانی کنفرانس / Organizational Structure

❖ رئیس کنفرانس: دکتر حسن زمانیان (معاون محترم وزیر علوم، تحقیقات و فناوری و رئیس محترم سازمان پژوهش‌های علمی و صنعتی ایران)

❖ دبیر کنفرانس: دکتر فرج الله مهنازاده

❖ دبیران علمی کنفرانس:

○ دکتر راضیه حبیب پور (کمیته علمی شیمی فیزیک)

○ دکتر یاسمین بیده (کمیته علمی شیمی آلی)

○ دکتر نسرین اروج زاده (کمیته علمی شیمی معدنی)

○ دکتر ذاکر بحرینی (کمیته علمی شیمی کاربردی)

○ دکتر سید حیدر محمودی نجفی (کمیته علمی شیمی دارویی، فیتوشیمی و بیوشیمی)

○ دکتر محمد عابدی (کمیته علمی شیمی تجزیه)

❖ دبیر اجرایی کنفرانس: دکتر اسلام کاشی

محورهای کنگره / Congress Topics

Physical Chemistry

Chemical Thermodynamics/ Chemical Kinetics/ Solids and Surface Chemistry/ Computational and Theoretical Physical Chemistry/ Quantum Mechanics/ Statistical Mechanics

Inorganic Chemistry

Synthesis & Characterization of Inorganic Compounds/ Kinetic and Mechanism of Inorganic Reactions/ Organometallic Compounds/ Inorganic Catalysts/ Porous materials (zeolite, mesoporous, macroporous, and metal-organic framework)/ Inorganic Polymers/ Inorganic Nanostructures/ Inorganic Biochemistry

Organic Chemistry

Synthesis and characterization of novel organic compounds/ Organic synthesis methodology/ Stereochemistry of organic compounds/ Polymer chemistry/ Chemistry of heterocycles/ Green chemistry/ Photochemistry/ Organic and polymer nanostructures/ Organic catalysis

Applied Chemistry

Environmental chemistry/ Dye and textile chemistry/ New energies/ Chemistry of minerals/ Oil, gas and petrochemistry/ Wood and paper/ Chemistry of building materials/ Food chemistry/ Cosmetics

Analytical Chemistry

Electroanalytical Chemistry/ Analytical Spectroscopy/ Chromatography and Separation Methods/ Chemometrics/ Environmental Analytical Chemistry/ Analytical Chemistry and Standards/ Analytical Nanochemistry/ Sensors and Biosensors

Medicinal Chemistry, Phytochemistry and Biochemistry

Drug Design and discovery/ Drug Synthesis and Formulation/ Drug Analysis and Metabolism/ Drug Delivery and Controlled Release Systems/ Vaccines Chemistry/ Pharmaceutical Nanotechnology/ Extraction, Separation and Purification Technologies of Natural Compounds/ Synthesis and Characterization of Natural Compounds/ Chemistry of Medicinal Plants/ Protein Chemistry and Proteomics/ Enzymes and Biocatalysts

شیمی تجزیه

الکتروشیمی/ اسپکتروسکوپی تجزیه ای/ روش های کروماتوگرافی و جداسازی/ کمومتریکس/ شیمی تجزیه محیط زیست/ شیمی تجزیه و استانداردها/ نانوشیمی تجزیه‌ای/ حسگرها و زیست حسگرها

شیمی معدنی

سنتز و شناسایی ترکیبات معدنی/ سینتیک و مکانیسم واکنش های معدنی/ ترکیبات آلی فلزی/ کاتالیست‌های معدنی/ مواد متخلخل(زئولیت، مزو حفره، ماکرو حفره و چارچوب فلزی- آلی)/ پلیمرهای معدنی/ بیوشیمی معدنی/ نانو ساختارهای معدنی

شیمی فیزیک

ترمودینامیک شیمیایی/ سنتیک شیمیایی/ شیمی سطح و حالت جامد/ شیمی فیزیک نظری و محاسباتی/ مکانیک کوانتومی/ مکانیک آماری/ شیمی کاربردی/ فناوری محیط زیست/ فناوری رنگ و نساجی/ فناوری انرژی های نو/ شیمی مواد معدنی/ نفت، گاز و پتروشیمی/ چوب و کاغذ/ شیمی مواد ساختمانی/ صنایع غذایی/ شیمی و فناوری مواد آرایشی و بهداشتی

شیمی آلی

سنتز و شناسایی ترکیبات آلی جدید/ روش‌های نوین سنتز ترکیبات آلی/ شیمی فضایی ترکیبات آلی/ شیمی پلیمر/ شیمی هتروسیکل‌ها/ شیمی سبز/ فوتو شیمی/ نانو ساختارهای آلی و پلیمری/ کاتالیست‌های آلی

شیمی دارویی، فیتوشیمی و بیوشیمی

طراحی و کشف مواد دارویی/ سنتز و فرمولاسیون مواد دارویی/ آنالیز و متابولیسم مواد دارویی/ سامانه های دارورسانی و رهش آهسته/ شیمی واکسن ها/ نانوفناوری مواد دارویی فناوری های استخراج، جداسازی و خالص سازی ترکیبات طبیعی/ سنتز و شناسایی ترکیبات طبیعی/ شیمی داروهای گیاهی/ شیمی پروتئین و پروتئومیکس/ آنزیم‌ها و بیو کاتالیست‌ها

اعضای کمیته علمی / Scientific Committee

Physical Chemistry:

Dr. Razieh Habibpour/ Iranian Research Organization for Science and Technology (IROST)

Dr. Mohsen Oftadeh/ Payame Noor University, Isfahan, Iran

Dr. Seifollah Jalili/ K. N. Toosi University of Technology, Tehran, Iran

Dr. Reza Islampour/ Kharazmi University, Tehran, IranDr. Hassan Sabzyan

Dr. Hassan Sabzyan/ University of Isfahan, Isfahan, Iran

Dr. Mohammad Reza Housaindokht/ Ferdowsi University of Mashhad, Mashhad, Iran

Dr. Afshan Mohajeri/ Shiraz University, Shiraz, Iran

Dr. Ali Reza Berenji/ University of Gonabad, Gonabad, Iran

Dr. Aziz Habibi-Yangjeh/ University of Mohaghegh Ardabili, Ardabil, Iran

Dr. Alireza Salabat/ Arak University, Arak, Iran

Dr. Maryam Dehestani/ Shahid Bahonar University of Kerman, Kerman, Iran

Dr. Jafar Azamat/ Farhangian University, Tabriz, Iran

Dr. Leila Karami/ Kharazmi University

Dr. Farzad Molani/ Korea University

Dr. Amin Ahmadpour/ Petrochemical Research and Technology Company (NPC-RT)

Dr. Payam Barzegar/ Managing Director of Petrochemical Special Economic Zone

Inorganic Chemistry

Dr. Nasrin Oroujzadeh/ Iranian Research Organization for Science and Technology (IROST)

Dr. Reza Tayebi/ Hakim Sabzevari University

Dr. Valiollah Mirkhani/ University of Isfahan

Dr. Majid Moghadam/ University of Isfahan

Dr. Vladimir Kitaev/ Wilfrid Laurier University, Canada

Dr. Bahram Ghanbari/ Sharif University of Technology

Dr. Hamid Golchoubian/ University of Mazandaran

Dr. Maryam Ranjbar/ Iranian Research Organization for Science and Technology

Dr. Alireza Salehirad/ Iranian Research Organization for Science and Technology

Dr. Davood Sadeghi Fateh/ Iranian Research Organization for Science and Technology

Dr. Bahram Yadollahi/ University of Isfahan

Dr. Sirous Jamali/ Sharif University of Technology

Dr. Azadeh Tajarodi/ Iran University of Science and Technology (IUST)

Dr. Naser Safari/ Shahid Beheshti University

Dr. Alireza Mahjoub/ Tarbiat Modares University

Dr. Alireza Badiee/ University of Tehran

Dr. Alireza Abbasi/ University of Tehran

Dr. Zahra Shariatinia/ AmirKabir University of Technology

Dr. Majid Masetri Farahani/ Kharazmi University

Dr. Alireza Farrokhi Lashidani/ University of Birjand

Dr. Niloufar Akbarzadeh/ University of Sistan & Baluchestan

Dr. Behzad Soltani/ Azarbaijan Shahid Madani University

Dr. Mojgan Zendehdel/ Arak University

اعضای کمیته علمی / Scientific Committee

Applied Chemistry

Dr. Zaker Bahreini/ Iranian Research Organization for Science and Technology (IROST)

Dr. Said Belalaie/ K. N. Toosi University of Technology

Dr. Abdolhamid Bamoniri/ University of Kashan

Dr. Hedayatollah Ghourchian/ University of Tehran

Dr. Mansoor Zahedi/ Shahid Beheshti University

Dr. Ali Kargeri/ Amirkabir University of Technology

Dr. Majid Montazer/ Amirkabir University of Technology

Dr. Hasan Arabi/ Iran Polymer and Petrochemical Institute

Dr. Salman Taheri/ Chemistry & Chemical Engineering Research Center of Iran

Dr. Shohreh Rouhani/ Institute for color Science and Technology

Dr. Razieh Jafari/ Institute for color Science and Technology

Dr. Mohammad Abedi/ Iranian Research Organization for Science and Technology

Dr. Alireza Ashori/ Iranian Research Organization for Science and Technology

Dr. seyed Hydar Mahmoodi Najafi/ Iranian Research Organization for Science and Technology

Dr. Anvar Shalmashi/ Iranian Research Organization for Science and Technology

Dr. Islam Kashi/ Iranian Research Organization for Science and Technology

Dr. Alireza Basiri/ Iranian Research Organization for Science and Technology

Dr. Farajolah Mohanazadeh/ Iranian Research Organization for Science and Technology

Dr. Yasemin Bideh/ Iranian Research Organization for Science and Technology

Dr. Majid Javanmard Dakheli / Iranian Research Organization for Science and Technology

Organic Chemistry

Dr. Yasamin Bide/ Iranian Research Organization for Science and Technology (IROST)

Dr. Issa Yavari/ Tarbiat Modares University

Dr. Babak Karimi/ Institute for Advanced Studies in Basic Sciences

Dr. Ghodsi Mohammadi Ziarani/ Alzahra University

Dr. Iraj Mohammadpour-Baltork/ University of Isfahan

Dr. Ramin Ghorbani-vaghei/ Bu-Ali Sina University

Dr. Sadegh Rostamnia/ Iran University of Science and Technology (IUST)

Dr. Ali Hossein Rezayan/ University of Tehran

Dr. Nader Noroozi Pesyan/ Urmia University

Dr. Reza Ranjbar-karimi/ Vali-e-Asr University of Rafsanjan

Dr. Abbas Ali Esmaeili/ Ferdowsi University of Mashhad

Dr. Hadi Adibi/ Kermanshah University of Medical Sciences

Dr. Hamid Beyzaei/ Zabol University

Dr. Reza Najjar/ University of Tabriz

Dr. Abbas Ali Jafari/ Yazd University

Dr. Mojtaba Mahyari/ Malek Ashtar University of Technology

Dr. Farnaz Jafarpour/ University of Isfahan

Dr. Hamid Sadeghi Abandansari/ Royan Institute

Dr. Siyavash Kazemi Movahed/ Isfahan University of Technology (IUT)

Analytical Chemistry

Dr. Mohammad Abedi/ Iranian Research Organization for Science and Technology (IROST)

Dr. Nahid Pourreza/ Shahid Chamran University, Ahvaz

Dr. Habib Bagheri/ Sharif University of Technology

Dr. Ali Asghar Ensafi/ Isfahan University of Technology

Dr. Yadollah Yamini/ Tarbiat Modarres University

Dr. Maryam Rajabi/ Semnan University

Dr. Abdolraouf Samadi/ Mazandaran University

Dr. Amir Abbas Matin/ Azarbaijan Shahid Madani University

Dr. Esmaeil Shams/ University of Isfahan

Dr. Fahimeh Jalali/ Razi University

Dr. Mahboube Shirani/ University of Jiroft

Dr. Lida Fotouhi/ Alzahra University

Dr. Alireza Ghiasvand/ Lorestan University

Dr. Jahanbakhsh Ghasemi/ Tehran University

Dr. Javad Tashkhurian/ Shiraz University

Dr. Hossein Salar Amoli/ Amirkabir University of Technology

Dr. Farhad Raoufi/ Shahid Beheshti University

Dr. Sayed Ahmad Mozaffari/ Iranian Research Organization for Science and Technology

Dr. Ali Mohammad-khah/ University of Guilan

Dr. Mohammad Ali Kiani/ Chemistry and Chemical Engineering Research Center of Iran

Medicinal Chemistry, Phytochemistry and Biochemistry

Dr. S. Heydar Mahmoudi Najafi/ Iranian Research Organization for Science and Technology (IROST)

Dr. Farajollah Mohnnazadeh/ Iranian Research Organization for Science and Technology (IROST)

Dr. Anvar Shalmashi/ Iranian Research Organization for Science and Technology (IROST)

Dr. Zeinolabedin Bashirisadr/ Iranian Research Organization for Science and Technology (IROST)

Dr. Peyman Salehi/ Shahid Beheshti University

Dr. Abolghasem Jouyban/ Tabriz University of Medical Sciences

Dr. Mohammad Ghaffarzadeh/ Chemistry and Chemical Engineering Research Center of Iran (CCERCI)

Dr. Saeed Balalaie/ K.N. Toosi University of Technology

Dr. Saeed Mirdamadi/ Iranian Research Organization for Science and Technology (IROST)

Dr. Zahra Amini-Bayat/ Iranian Research Organization for Science and Technology (IROST)

Dr. Maliheh Safavi/ Iranian Research Organization for Science and Technology (IROST)

Dr. Nahid Bakhtiari/ Iranian Research Organization for Science and Technology (IROST)

Dr. Hamideh Ofoghi/ Iranian Research Organization for Science and Technology (IROST)

Dr. Geita Saadatnia/ Iranian Research Organization for Science and Technology (IROST)

حامیان کنگره / Sponsors

Keynote Speakers / سخنرانان کلیدی

The Importance of Nonstoichiometric Ratio of Reactants in Organic Synthesis
Dr. Mohammad Ali Zolfigol
Minister of Science, Research and Technology
22nd Iranian Chemistry Congress (ICC22)
Iranian Research Organization for Science and Technology (IROST)
13-15 May 2024

Immobolization of Enzymes on Inorganic Materials: Biocatalytic Activities
Dr. Majid Moghadam
University of Isfahan
22nd Iranian Chemistry Congress (ICC22)
Iranian Research Organization for Science and Technology (IROST)
13-15 May 2024

Water-oxidation Reaction in the Presence of Manganese Compounds
Dr. Mohammad Mahdi Najafpour
Institute for Advanced Studies in Basic Sciences, Zanjan
22nd Iranian Chemistry Congress (ICC22)
Iranian Research Organization for Science and Technology (IROST)
13-15 May 2024

Chemistry and Economic Complexity
Dr. Peyman Salehi
Deputy Minister of Science, Research and Technology
22nd Iranian Chemistry Congress (ICC22)
Iranian Research Organization for Science and Technology (IROST)
13-15 May 2024

One-Pot synthesis and assessment of the anti-corrosion effect of mercaptobenzimidazole
Dr. Abdolhamid Bamoniri
University of Kashan
22nd Iranian Chemistry Congress (ICC22)
Iranian Research Organization for Science and Technology (IROST)
13-15 May 2024

Novel Environmental Optimization Methodology Proposed for Propylene/Propane Separation
Dr. Abolghasem Kazemi
Shiraz University of Technology
22nd Iranian Chemistry Congress (ICC22)
Iranian Research Organization for Science and Technology (IROST)
13-15 May 2024

Novel Complexes of Ce(IV) & Zn(II) with Pyridine-based Ligands as Chemotherapeutic Agents
Dr. Samad Khaksar
University of Georgia,Tbilisi
22nd Iranian Chemistry Congress (ICC22)
Iranian Research Organization for Science and Technology (IROST)
13-15 May 2024

Why Early Diagnosis of Sepsis? Sepsis Biomarker Detection Methods
Dr. Ali Hossein Rezayan
University of Tehran
22nd Iranian Chemistry Congress (ICC22)
Iranian Research Organization for Science and Technology (IROST)
13-15 May 2024

Utilizing Platinum Complexes to Detecting Toxic Heavy Metal Ions
Dr. Mohsen Golbon Haghighi
Shahid Beheshti University
22nd Iranian Chemistry Congress (ICC22)
Iranian Research Organization for Science and Technology (IROST)
13-15 May 2024

Keynote Speakers / سخنرانان کلیدی

Heterobimetallic Complexes: Structural Characterization, and Cytotoxic Investigations

Dr. Hamid Reza Shahsavari
Institute for Advanced Studies in Basic Sciences, Zanjan

22nd Iranian Chemistry Congress (ICC22)
Iranian Research Organization for Science and Technology (IROST)
13-15 May 2024

Drug Detection Using Polyoxometalate-based Frameworks

Dr. Masoud Mirzaei
Ferdowsi University of Mashhad

22nd Iranian Chemistry Congress (ICC22)
Iranian Research Organization for Science and Technology (IROST)
13-15 May 2024

Novel Mesoporous Carbon Materials with Multi-functional Properties

Dr. Babak Karimi
Institute for Advanced Studies in Basic Sciences, Zanjan

22nd Iranian Chemistry Congress (ICC22)
Iranian Research Organization for Science and Technology (IROST)
13-15 May 2024

Designing of Novel Post-Transformation Reaction and Their Applications in Organic Synthesis

Dr. Saeed Balalaie
K.N.Toosi University of Technology

22nd Iranian Chemistry Congress (ICC22)
Iranian Research Organization for Science and Technology (IROST)
13-15 May 2024

Turning a Dream into Reality in the Catalyst Industry in Iran

Dr. Mehran Rezaei
Iran University of Science & Technology

22nd Iranian Chemistry Congress (ICC22)
Iranian Research Organization for Science and Technology (IROST)
13-15 May 2024

Challenges of Heterogeneous Photocatalysts as Promising Materials for Addressing Environmental and Energy Crises

Dr. Aziz Habibi-Yangjeh
University of Mohaghegh Ardabili

22nd Iranian Chemistry Congress (ICC22)
Iranian Research Organization for Science and Technology (IROST)
13-15 May 2024

A Perspective on Electro-organic Synthesis

Dr. Issa Yavari
University of Tarbiat Modares

22nd Iranian Chemistry Congress (ICC22)
Iranian Research Organization for Science and Technology (IROST)
13-15 May 2024

World Class Innovation: Requirements and Experiences

Dr. Hamid Rajaei
Head of Product Development, Technology and Innovation
Nouri Petrochemical Company

22nd Iranian Chemistry Congress (ICC22)
Iranian Research Organization for Science and Technology (IROST)
13-15 May 2024

Metal-Organic Frameworks based on Thiazole: Crystal Structure and Application

Dr. Azadeh Tadjarodi
Iran University of Science and Technology (IUST)

22nd Iranian Chemistry Congress (ICC22)
Iranian Research Organization for Science and Technology (IROST)
13-15 May 2024

Keynote Speakers / سخنرانان کلیدی

Preparation of Boron Nitride Doped with Carbon Impurity for Producing Single Photon

Dr. Mehdi Janbazi
Nuclear Science and Technology Research Institute

22nd Iranian Chemistry Congress (ICC22)
Iranian Research Organization for Science and Technology (IROST)
13-15 May 2024

Bimetallic NiCo MOFs Decorated on Carbon Felt as a Binder-less Anode Electrode for Ethanol Fuel Cell

Dr. Mir Ghasem Hosseini
University of Tabriz

22nd Iranian Chemistry Congress (ICC22)
Iranian Research Organization for Science and Technology (IROST)
13-15 May 2024

Computational and Quantum Chemistry: Unraveling Molecular Insights

Dr. Zahra Jamshidi
Sharif University of Technology

22nd Iranian Chemistry Congress (ICC22)
Iranian Research Organization for Science and Technology (IROST)
13-15 May 2024

Revolutionizing Electrocatalytic Water Splitting: Unveiling the Extraordinary Potential of Novel NiBi-LDH for Overall Activity

Dr. Mahboubeh Tasviri
Shahid Beheshti University

22nd Iranian Chemistry Congress (ICC22)
Iranian Research Organization for Science and Technology (IROST)
13-15 May 2024

Heavy Aldehyde Production from Olefin by Catalysts of Rhodium Complex Phosphite

Dr. Mahmoud Hashemi Hezaveh
National Petrochemical Industries Research and Technology Company

22nd Iranian Chemistry Congress (ICC22)
Iranian Research Organization for Science and Technology (IROST)
13-15 May 2024

Schiff Base Complexes as Homogeneous and Heterogeneous Catalysts in Oxidation Reactions

Dr. Hadi Kargar
Ardakan University

22nd Iranian Chemistry Congress (ICC22)
Iranian Research Organization for Science and Technology (IROST)
13-15 May 2024

Synthesis of New Hydrogel Composite Based on Modification of Natural Polymers Using Electron Beam Irradiation

Dr. Shayessteh Dadfarnia
Yazd University

22nd Iranian Chemistry Congress (ICC22)
Iranian Research Organization for Science and Technology (IROST)
13-15 May 2024

Amino Acid Based Derivatives of Pyromellitic Diimides: Photo and Electrochromic Features

Dr. Mohammad Reza Zamanloo
University of Mohaghegh Ardabili

22nd Iranian Chemistry Congress (ICC22)
Iranian Research Organization for Science and Technology (IROST)
13-15 May 2024

Monitoring Intramolecular Proton Transfer with Ion Mobility-Mass Spectrometry and In-source Ion Activation

Dr. Younes Valadbeigi
Imam Khomeini International University

22nd Iranian Chemistry Congress (ICC22)
Iranian Research Organization for Science and Technology (IROST)
13-15 May 2024

Keynote Speakers / سخنرانان کلیدی

From Arylamines to Strongly Polarized Multiple Azahelicences: A Fascinating Journey

Dr. Mohammad Bagher Teimouri
Kharazmi University

22nd Iranian Chemistry Congress (ICC22)

Iranian Research Organization for Science and Technology (IROST)
13-15 May 2024

Optical Trapping for Concentration of Micro and Nanoparticles

Dr. Nader Shokoufi
Chemistry & Chemical Engineering Research Center of Iran

22nd Iranian Chemistry Congress (ICC22)

Iranian Research Organization for Science and Technology (IROST)
13-15 May 2024

Pore Channels Engineering of Porous Materials as Innovation Hub for (Photo)-Catalysis Purposes

Dr. Sadegh Rostamnia
Iran University of Science and Technology (IUST)

22nd Iranian Chemistry Congress (ICC22)

Iranian Research Organization for Science and Technology (IROST)
13-15 May 2024

Design and Construction of a Hand-Held Detector

Dr. Seyed Alireza Ghorashi
Institute of Materials and Energy

22nd Iranian Chemistry Congress (ICC22)

Iranian Research Organization for Science and Technology (IROST)
13-15 May 2024

Economical Benefits or Human Health!? What Is Happening in Food Production World Based on the Analytical Chemistry Viewpoint?

Dr. Mahboube Shirani
University of Jiroft

22nd Iranian Chemistry Congress (ICC22)

Iranian Research Organization for Science and Technology (IROST)
13-15 May 2024

معرفی ظرفیت های پارک علم و فناوری بین المللی جمهوری اسلامی ایران

دکتر علیرضا زراسوندی
رئیس پارک علم و فناوری بین‌المللی جمهوری اسلامی ایران

22nd Iranian Chemistry Congress (ICC22)

Iranian Research Organization for Science and Technology (IROST)
13-15 May 2024

Novel Metal Complexes of VitaminB3-based Phosphoramides; Safe, Effective, and Body-friendly Anticancer Agents

Dr. Nasrin Oroujzadeh
Iranian Research Organization for Science and Technology (IROST)

22nd Iranian Chemistry Congress (ICC22)

Iranian Research Organization for Science and Technology (IROST)
13-15 May 2024

Synthesis and characterization of graphene oxide- silver nanowires composites for EMI shielding

Dr. Miroslav Huskic
National institute of chemistry, Slovenia

22nd Iranian Chemistry Congress (ICC22)

Iranian Research Organization for Science and Technology (IROST)
13-15 May 2024

نقش شرکت پژوهش و فناوری پتروشیمی در دانش بنیان نمودن صنعت پتروشیمی با محوریت توسعه و تجاری سازی فناوری های مورد نیاز

دکتر مجید دفتری
مدیر عامل شرکت پژوهش و فناوری پتروشیمی

22nd Iranian Chemistry Congress (ICC22)

Iranian Research Organization for Science and Technology (IROST)
13-15 May 2024

سخنرانان کلیدی / Keynote Speakers

Formulation of a New Natural Fungicide containing Carum carvi Essential Oil

Dr. Hossein Dehghan
Shahed University

22nd Iranian Chemistry Congress (ICC22)

Iranian Research Organization for Science and Technology (IROST)
13-15 May 2024

آشنایی با فرایند تدوین استانداردهای پژوهش محور برای فراورده های شیمیایی فاقد استاندارد ملی یا بین المللی

دکتر فضه آریانسب
پژوهشکده شیمی و پتروشیمی پژوهشگاه استاندارد

22nd Iranian Chemistry Congress (ICC22)

Iranian Research Organization for Science and Technology (IROST)
13-15 May 2024

Completing the Value Chain of Chemicals, Food Security, and Sustainable Development in the Chemical Industry

Naser Rezakhani
Director of Process Engineering Research Group, Iranian Institute of R&D in Chemical Industries

22nd Iranian Chemistry Congress (ICC22)

Iranian Research Organization for Science and Technology (IROST)
13-15 May 2024

معرفی و تبیین طرح تحول همکاری نیروهای مسلح با دانشگاه ها و مراکز تحقیقاتی

وحید صالحلو
حوزه علوم تحقیقات و فناوری موسسه آموزشی و تحقیقاتی صنایع دفاعی

22nd Iranian Chemistry Congress (ICC22)

Iranian Research Organization for Science and Technology (IROST)
13-15 May 2024

کارگاه‌ها / Workshops

دکتر لیلا توحیدی فر
محقق پسادکتری
دانشگاه تحصیلات تکمیلی علوم پایه زنجان

کارگاه:
سامانه های دارورسانی هدفمند بر پایه نانو به روش شبیه سازی دینامیک مولکولی با نرم افزار گرومکس

- دارورسانی هدفمند و انواع سامانه های دارو رسانی
- شبیه سازی دینامیک مولکولی و اهمیت آن
- نرم افزار "گرومکس" و ویژگی های آن
- به دست آوردن ساختار اولیه مولکول ها
- میدان نیرو و ساخت فایل توپولوژی
- حداقل سازی انرژی و فرآیند به تعادل رسانی سامانه مورد نظر
- اجرای شبیه سازی و تجزیه و تحلیل نتایج

۲۶-۲۴ اردیبهشت ۱۴۰۳، تهران- سازمان پژوهش های علمی و صنعتی ایران

مهندس آرزو مرشدی
مدیر تولید شرکت دانش بنیان طیف سنج

کارگاه:
طیف سنجی رامان و کاربرد آن در شیمی

- معرفی روش
- ساختار دستگاهی
- کاربرد در شیمی
- روش های نوین طیف سنجی رامان

۲۶-۲۴ اردیبهشت ۱۴۰۳، تهران- سازمان پژوهش های علمی و صنعتی ایران

برنامه کنگره / Congress Program

مکان	عنوان برنامه	زمان	شماره
صبح دوشنبه ۱۴۰۳/۲/۲۴ (مراسم افتتاحیه و سخنرانی)			
ساختمان امام رضا (ع)	پذیرش- ثبت نام	۸:۰۰ — ۹:۰۰	۱
سالن خوارزمی	تلاوت قرآن مجید و سرود ملی	۹:۰۰ — ۹:۱۵	۲
سالن خوارزمی	پخش کلیپ معرفی سازمان	۹:۱۵- ۹:۳۰	۳
سالن خوارزمی	خوش آمدگویی آقای دکتر حسن زمانیان (معاون محترم وزیر و رئیس سازمان پژوهش های علمی و صنعتی ایران)	۹:۳۰ — ۹:۴۵	۴
سالن خوارزمی	خوش آمدگویی دبیر انجمن شیمی ایران	۹:۴۵- ۱۰:۰۰	۵
سالن خوارزمی	تجلیل از دانشمندان برتر علوم شیمی	۱۰:۰۰- ۱۰:۴۵	۶
سالن خوارزمی	سخنرانی آقای دکتر محمدعلی زلفی گل (وزیر محترم علوم، تحقیقات و فناوری)	۱۰:۴۵- ۱۱:۳۰	۷
سالن خوارزمی	سخنرانی آقای دکتر پیمان صالحی (معاون محترم پژوهشی وزارت علوم، تحقیقات و فناوری)	۱۱:۳۰- ۱۲:۰۰	۸
سالن خوارزمی	نهار و نماز	۱۲:۰۰- ۱۳:۳۰	۹

مکان	عنوان برنامه	زمان	شماره
عصر دوشنبه ۱۴۰۳/۲/۲۴			
سالن خوارزمی	Synthesis and characterization of graphene oxide- silver nanowires composites for EMI shielding (Dr. Miroslav Huskick)	۱۳:۳۰-۱۴	۱۱
سالن ابوریحان	World Class Innovation: Requirements and Experiences (Dr. Hamid Rajaei)		۱۲
سالن خوارزمی	Synthesis of new hydrogel composite based on modification of natural polymers using electron beam irradiation and investigation of their analytical application (Dr. Shayessteh Dadfarnia)	۱۴-۱۴:۳۰	۱۳
سالن ابوریحان	Sustainable Utilization of Agricultural Waste: Extraction of Bioactive Compounds and Their Encapsulation in Lipid-Based Nano/Microcarriers (Dr. Samad Nejad-Ebrahimi)		۱۴
ساختمان امام رضا (ع)	پذیرایی و بازدید از پوستر و نمایشگاه	۱۴:۳۰-۱۵	۱۵
سالن خوارزمی	نقش شرکت پژوهش و فناوری پتروشیمی در دانش بنیان نمودن صنعت پتروشیمی با محوریت توسعه و تجاری سازی فناوری های مورد نیاز (دکتر دفتری)	۱۵-۱۵:۳۰	۱۶
سالن ابوریحان	Pore Channels Engineering of Porous Materials as Innovation Hub for (Photo)-Catalysis Purposes (Dr. Sadegh Rostamnia)		۱۷
سالن خوارزمی	معرفی ظرفیت های پارک علم و فناوری بین المللی جمهوری اسلامی ایران (دکتر علیرضا زراسوندی)	۱۵:۳۰-۱۶	۱۸
سالن ابوریحان	Design and Construction of a Hand-Held Detector (Dr. Seyed Alireza Ghorashi)		۱۹

مکان	عنوان برنامه	زمان	شماره
صبح سه شنبه ۱۴۰۳/۲/۲۵			
سالن خوارزمی	Challenges of Heterogeneous Photocatalysts as Promising Materials for Addressing Environmental and Energy Crises (Dr. Aziz Habibi-Yangjeh)	۹:۰۰–۹:۳۰	۲۰
سالن ابوریحان	One-Pot synthesis and assessment of the anti-corrosion effect of mercaptobenzimidazole in an environment with hydrochloric acid (Mehdi Kanani)		۲۱
سالن خوارزمی	Immobolization of enzymes on inorganic materials and investigation of their biocatalytic activities (Dr. Majid Moghadam)	۹:۳۰–۱۰	۲۲
سالن ابوریحان	Why early diagnosis of sepsis? Sepsis biomarker detection methods (Dr. Ali Hossein Rezayan)		۲۳
سالن خوارزمی	Designing of Novel Post-Transformation Reaction and Their Applications in Organic Synthesis (Dr. Saeed Balalaie)	۱۰–۱۰:۳۰	۲۴
سالن ابوریحان	Heterobimetallic complexes: structural characterization, and cytotoxic investigations (Dr. Hamid Reza Shahsavari)		۲۵
ساختمان امام رضا (ع)	پذیرایی و بازدید از پوستر و نمایشگاه	۱۰:۳۰–۱۱	۲۶
سالن خوارزمی	A Perspective on Electro-organic Synthesis (Dr. Issa Yavari)	۱۱–۱۱:۳۰	۲۷
سالن ابوریحان	Water-oxidation reaction in the presence of manganese compounds (Dr. Mohamad Mahdi Najaf Pour)		۲۸
سالن خوارزمی	Novel mesoporous carbon materials with multi-functional properties (Dr. Babak Karimi)	۱۱:۳۰–۱۲	۲۹
سالن ابوریحان	Economical Benefits or Human Health!? What Is Happening in Food Production World Based on the Analytical Chemistry Viewpoint? (Dr. Mahboube Shirani)		۳۰
	نهار و نماز	۱۲–۱۳:۳۰	۳۱

مکان	عنوان برنامه	زمان	شماره
عصر سه شنبه ۱۴۰۳/۲/۲۵			
سالن خوارزمی	Monitoring Intramolecular Proton Transfer with Ion Mobility-Mass Spectrometry and In-source Ion Activation (Dr. Younes Valadbeigi)	۱۳:۳۰–۱۴	۳۲
سالن ابوریحان	Formulation of a New Natural Fungicide containing Carum carvi Essential Oil Against Fusarium Oxysporum, a Tomato Pathogenic Fungus (Dr. Hossein Dehghan)		۳۳
سالن خوارزمی	Activity Investigation of Schiff Base Complexes as Homogeneous and Heterogeneous Catalysts in Oxidation Reactions (Dr. Hadi Kargar)	۱۴–۱۴:۳۰	۳۴
سالن ابوریحان	From arylamines to strongly polarized multiple azahelicences:a fascinating journey (Dr. Mohammad Bagher Teimouri)		۳۵
ساختمان امام رضا (ع)	پذیرایی و بازدید از پوستر و نمایشگاه	۱۴:۳۰–۱۵	۳۶
سالن خوارزمی	Optical Trapping for Concentration of Micro and Nanoparticles (Dr. Nader Shokoufi)	۱۵–۱۵:۳۰	۳۷
سالن ابوریحان	Utilizing Platinum Complexes to Detecting Toxic Heavy Metal Ions (Dr. Mohsen Golbon Haghighi)		۳۸
سالن خوارزمی	Drug Detection Using Polyoxometalate-Based Frameworks (Dr. Masoud Mirzaei)	۱۵:۳۰–۱۶	۳۹
سالن ابوریحان	Revolutionizing Electrocatalytic Water Splitting: Unveiling the Extraordinary Potential of Novel NiBi-LDH for Overall Activity (Dr. Mahboubeh Tasviri)		۴۰

شماره	زمان	عنوان برنامه	مکان
		صبح چهارشنبه ۱۴۰۳/۲/۲۶	
۴۱	۹:۰۰–۹:۳۰	Novel complexes of Ce (IV) and Zn (II) with pyridine-based ligands as Chemotherapeutic Agents (Dr. Samad Khaksar)	سالن خوارزمی
۴۲		Amino acid-based derivatives of pyromellitic diimides: photo and electrochromic features (Dr. Mohammad Reza Zamanloo)	سالن ابوریحان
۴۳	۹:۳۰–۱۰	Bimetallic NiCo MOFs Decorated on Carbon Felt as a Binder-less Anode Electrode for Ethanol Fuel Cell (Dr. Mir Ghasem Hosseini)	سالن خوارزمی
۴۴		Computational and Quantum Chemistry: Unraveling Molecular Insights (Dr. Zahra Jamshidi)	سالن ابوریحان
۴۵	۱۰–۱۰:۳۰	Preparation of Boron Nitride Doped with Carbon Impurity for Producing Single Photon (Dr. Mehdi Janbazi)	سالن خوارزمی
۴۶		Novel Metal Complexes of VitaminB3- based Phosphoramides; Safe, Effective, and Body-friendly Anticancer Agents (Dr. Nasrin Oroujzadeh)	سالن ابوریحان
۴۷	۱۰:۳۰–۱۱	پذیرایی و بازدید از پوستر و نمایشگاه	ساختمان امام رضا (ع)
۴۸	۱۱–۱۱:۳۰	Metal-Organic Frameworks based on Thiazole: Crystal Structure and Application (Dr. Azadeh Tadjarodi)	سالن خوارزمی
۴۹		Heavy aldehyde industrial production from olefin by high active and selective catalyst of Rhodium complex phosphite (Dr. Mahmoud Hashemi Hezaveh)	سالن ابوریحان
۵۰	۱۱:۳۰–۱۲	Turning a Dream into Reality in the Catalyst Industry in Iran (Dr. Mehran Rezaei)	سالن خوارزمی
۵۱		A Novel Environmental Optimization Methodology Proposed for Propylene/Propane Separation: Aiming the Cleanest Feasible Distillation System (Dr. Abolghasem Kazemi)	سالن ابوریحان
۵۲	۱۲–۱۳:۳۰	نهار و نماز	

شماره	زمان	عنوان برنامه	مکان
		عصر چهارشنبه ۱۴۰۳/۲/۲۶	
۵۳	۱۴–۱۴:۳۰	تکمیل زنجیره ارزش مواد شیمیایی، امنیت غذایی و توسعه پایدار در صنایع شیمیایی (مهندس ناصر رضاخانی)	سالن خوارزمی
۵۴	۱۴:۳۰–۱۵:۳۰	اختتامیه (میزگرد، جمع بندی و صدور بیانیه، تقدیر و تشکر از عوامل اجرایی و ...)	سالن خوارزمی

رویداد تجاری سازی یافته های پژوهشی در حوزه صنایع شیمیایی

مکان	عنوان سخنرانی	زمان	شماره
	سه شنبه ۱۴۰۳/۲/۲۵		
سالن فارابی	تعاملات بین المللی پارک های فناوری (دکتر ایوب فرهادی، معاون فناوری و نوآوری پارک علم و فناوری بین المللی جمهوری اسلامی ایران)	۹:۰۰ — ۹:۳۰	۱
سالن فارابی	آشنایی با خدمات و ظرفیت های صندوق های پژوهش و فناوری در مسیر تامین مالی (دکتر غلامرضا شمشیری، مدیر عامل صندوق توسعه فناوری های پیشرفته صنعتی و حسین حاجی بابایی، مدیر اعتبارات و ارزیابی صندوق توسعه فناوری های پیشرفته صنعتی)	۹:۳۰– ۱۱:۰۰	۲
سالن فارابی	از پژوهش تا تجاری سازی (مسیرها و فرآیندها) (سید سعید اشراقی، رئیس گروه ارزش گذاری و مستند سازی دانش فنی سازمان پژوهش‌های علمی و صنعتی ایران)	۱۱:۰۰– ۱۱:۳۰	۳
سالن فارابی	تجاری سازی یافته های پژوهشی (محسن دیندار، رئیس مرکز رشد واحدهای فناوری پارک علم و فناوری بین المللی جمهوری اسلامی ایران)	۱۱:۳۰ – ۱۲:۰۰	۴
	نهار و نماز	۱۲:۰۰ – ۱۳:۳۰	۵
سالن فارابی	روش های تجاری سازی در شرکت پژوهش و فناوری پتروشیمی، چالش ها و تسهیل گری ها (حسین رسولی، مدیر تجاری سازی و توسعه بازار شرکت پژوهش و فناوری پتروشیمی)	۱۳:۳۰ – ۱۴:۰۰	۶
سالن فارابی	آشنایی با فرایند ارزیابی و اعتبار سنجی محصولات و فرایندهای دارای نوآوری (دکتر فریبا رضوانی، استادیار گروه زیست فناوری صنعتی و محیط زیست)	۱۴:۰۰ – ۱۵:۰۰	۷
سالن فارابی	سنتز نوآوری: نگرشی جدید بر تجاری سازی (محمد یاسر خسروی، رئیس اداره فناوری و نوآوری پارک علم و فناوری بین المللی جمهوری اسلامی ایران)	۱۵:۰۰–۱۶:۰۰	۸
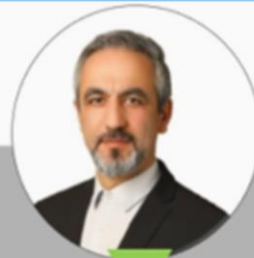
فهرست محتوا / Table of Contents

Title	Page

Title	Page

Title	Page

Title	Page

Title	Page

Title	Page

Title	Page

Title	Page

Title	Page

Title	Page

Title	Page

Title	Page

Title	Page

Title	Page

Title	Page

Title	Page

Title	Page

Title	Page

Title	Page

Title	Page

Title	Page

Title	Page

Title	Page

Modified Sessile Drop Method for Experimental Investigation of Dynamic Wettability Alteration of Oil-Wet Carbonate Surfaces in Contact with Seawater

Armin Rezaei [a], Seyyed Mobeen Fatemi*[b], Ebrahim Biniaz Delijani [c]

Corresponding Author E-mail: Fatemi@sharif.edu

[a] Faculty of Petroleum and Chemical Engineering, Science and Research Branch, Islamic Azad University, Tehran, Iran.

[b] Department of Chemical and Petroleum Engineering, Sharif University of Technology, Tehran, Iran.

[c] Faculty of Petroleum and Chemical Engineering, Science and Research Branch, Islamic Azad University, Tehran, Iran.

Abstract: Polished oil-wet calcite surfaces were used as representative of carbonate oil reservoirs. For different oil drops at different times and either on top or bottom of the surface are used. Although all drops confirmed the dynamic wettability alteration by seawater, the alteration degree depends on the considered oil drop.
Keywords: Wettability; Contact angle; Sessile Drop; Carbonate Rock

Introduction

Seawater injection into oil reservoirs is one of the main methods of water based enhanced oil recovery (EOR). The wettability of the rock surface of oil reservoirs is one of the important parameters in the performance of this EOR process [1]. Contact angle measurement is used to determine the wettability of surfaces in the rock-fluid-fluid system [2]. Youssef et al. measured the contact angle on carbonate rocks in the presence of formation water and seawater, and showed that with the decrease of fluid salinity, wettability tends towards water-wet [3]. In most researches, the measurement of the contact angle has been done in the presence of fluids represnting the initial wettability i.e., formation water. It is possible that initial wettability of the surface rock alters in contact with the injected fluid such as seawater as it disturbes the long term equilibrium between rock, formation water and oil. This research has tried to measure the degree of wettability alteration of an oil-wet calcite rock in the presence of the seawater using a modified sessile drop technique.

Experimental Section

Fluids: The seawater was prepared based on the information of the Persian Gulf brine and the used oil is from the Bangistan reservoir of Koupal oil field. The specifications of fluids are given in Table 1. The density and viscosity of oil have been measured at 25°C.

Table1: Characteristics of fluids used in this study

Fluid (seawater)		Oil	
salt	Gr/lit		
NaCl	28.40	Vicosity (mPa.s)	17
$CaCl_2.2H_2O$	1.83	Density (gr/cm3)	0.873

$MgCl_2.6H_2O$	13.73	Toatal acid number (mg KOH/g oil)	0.14
KCl	0.80	SARA test (weight percent)	Saturates	63.96
Na_2SO_4	4.49		Aromatics	25.33
$NaHCO_3$	0.10		Resins	9.06
TDS	41.60		Asphaltenes	1.65

Rock: To measure the contact angle, colorless calcite crystal has been chosen as representative of carbonate reservoirs rock. Calcite substrates were prepared in dimensions of 5 x 3 x 0.1 cm. To prepare smooth and polished surfaces, these surfaces were polished with sandpaper. To remove contamination from the surfaces, the substrates were placed in toluene for 24 hours, then washed with acetone and distilled water and dried at room temperature. To create an oil-wet surface as initial wettability, these substrates were placed in crude oil in an oven at 80°C for 24 hours, then washed with kerosene and dried at room temperature.

Contact angle measurement: The contact angle setup for the sessile drop method is shown in Fig.1. To check the wettability changes, the contact angle was measured by the sessile drop method. In this method, a set up consisting of a chamber, a chamber base, a digital microscope, a microscope base, a syringe and a light source is used to prepare high-resolution images. To create an oil drop under the calcite substrate in the chamber, a hole is built for the passage of the syringe needle through which the oil drop can be injected under the calcite substrate from the bottom of the chamber. First, the chamber with a volume of 150 ml is placed on the base of the chamber, and the calcite substrate inside the chamber is placed on the sides of the chamber, and drop No. 1 is injected from above on the substrate, then the entire chamber is saturated with seawater. Now drop No. 2 is injected under the substrate from the bottom.

22nd **Iranian Chemistry Congress (ICC22)**
Iranian Research Organization for Science and Technology (IROST)
13-15 May 2024

03231-97589

IROST

After injection, the oil-rock-brine system interacts until they reach stability and equilibrium. Equilibrium is achieved when the angle between the oil droplet and the calcite contact surface does not change. Usually, this equilibration takes about 72 hours so that the angle between the drop of oil and the contact surface of the rock does not change. To record these changes, pictures of the oil drop in the oil-rock-brine system are taken with a digital microscope from the first moment to the next 72 hours at appropriate time intervals. Checking the images and measuring the contact angle has been done with the help of drop shape analysis software. After 72 hours, drop No. 3 is injected also under the substrate from the bottom of the chamber. Photography and analysis were done another 72 hours, then the calcite substrate was taken out from the contact angle chamber and dried in the oven at 120°C for 15 minutes and the chamber was emptied, washed and prepared for drop No. 4. The calcite substrate is placed in the contact angle measuring chamber and drop No. 4 is placed similar to the first drop and the chamber is then saturated with sea-water again. For this drop, also 72 hours are given to reach equilibrium. Analysis of droplet No. 1 and 2 are performed to investigate the effect of diffusion mechanism on wettability alteration in porous media, while in the case of droplets No. 3 and 4 since the surface was in direct contact with the seawater, it is more representative of wettability aletartion under dispersion mechanism in the porous media. All the experiments were repeated 3 times to check the repeatability of the results and average values are reported.
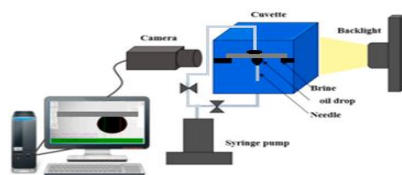
Fig.1: Contact angle setup

Results and Discussion

Fig.2 shows the contact angle measurement results. The results show that the initial contact angle for drops No. 1 and 2 is equal to 180° and 136°, respectively, and their ultimate contact angle under final equilibrium condition is equal to 150°. It can be concluded that the final equilibrium contact angle for the upper and lower drops is equal under the same conditions. In the case of drop No. 3, which was injected after 72 hours, the initial and equilibrium contact angle is equal to 90° and 132°, respectively. The comparison of drops No. 2 and 3 shows that due to the direct contact of the calcite surface with sea water, the value of the contact angle has decreased and the wettability of the surface has tended to be less

oil-wet. This change in wettability can be due to the formation of a water film on the surface of calcite, which has led to a change in the size of the contact angle concerning drop No. 2. In the case of drop No. 4, which was injected after reaching the equilibrium of drop No. 3, the initial contact angle and equilibrium contact angle were recorded as 180° and 155°, respectively. Comparison of drops No. 1 and 4 shows that there is no significant change in contact angle and wettability. This could be due to the fact that before the injection of drop No. 4, the calcite substrate was placed in oven at 120°C for 15 minutes and the formed water film has disappeared, so the calcite bed is the same as the bed of drop No. 1.
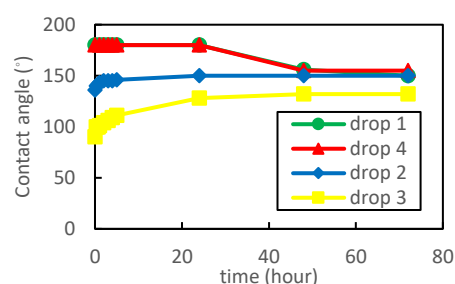
Fig.2: Contact angle changes versus time

Conclusions

In this research, contact angle measurements were performed for the crude oil drop on the smooth surface of calcite in the presence of sea water. The results showed that due to the contact of the calcite bed with sea-water over time, a water film is formed on the surface of the stone, which causes the initial wettability of calcite to be less oil-wet. This result shows that the initial wettability may change under the influence of fluids with which the rock is in contact. Therefore, it is suggested that in measuring the contact angle, in addition to the initial wettability, the contact of the surface with fluids over time should be taken into account because it affects the final results and degree of wettability alteration.

References

[1] Chen, Y., Xie, Q., Sari, A., Brady, P. V., & Saeedi, A. (2018). Oil/water/rock wettability: Influencing factors and implications for low salinity water flooding in carbonate reservoirs. https://doi.org/10.1016/j.fuel.2017.10.031.

[2] Hendraningrat, L., Engeset, B., Suwarno, S., & Torstæer, O. (2012). Improved oil recovery by nanofluids flooding: An experimental study. https://doi.org/10.2118/163335-ms.

[3] Yousef, A. A., Al-Saleh, S., Al-Kaabi, A., & Al-Jawfi, M. (2011). Laboratory investigation of the impact of injection-water salinity and ionic content on oil recovery from carbonate reservoirs. https://doi.org/10.2118/137634-PA.

Pore Polarity Engineering of Metal-Organic Frameworks to Enhance CO₂ Adsorption Capacity and Selectivity Using Hydrogen Bonds

Maryam Lalehchini[a], Ali Mohajeri [*b], Mir Mohammad Alavi Nikje[*a]

Corresponding Author E-mail: Mohajeria@ripi.ir, Alavi@sci.ikiu.ac.ir

[a] Department of Chemistry, Faculty of Science, Imam Khomeini International University (IKIU), P.O. Box 288, Qazvin, Iran.

[b] Gas Research Division, Research Institute of Petroleum Industry (RIPI), West Boulevard, Azadi Sports Complex, P.O. Box 14665-1998, Tehran, Iran.

Abstract: CO₂ emission is a significant factor in global temperature rise; among advanced CO₂ adsorbents, Metal-Organic Frameworks (MOFs) are a promising candidate for CO₂ adsorption. Among MOFs, MIL-101(Cr), exhibits attractive features for CO₂ adsorption. In this study, to enhance the polarity of pores, monoethanolamine via post-synthetic modification (PSM) of MIL-101(Cr) was introduced and the effect of pore polarity engineering on CO₂ adsorption capacity and CO₂: CH₄ selectivity was investigated.

Keywords: MOFs, MIL-101(Cr), Pore polarity engineering, CO₂ adsorption

Introduction

CO₂ emissions are a crucial contributor to the increase in global temperatures [1]. MOFs are candidates for CO₂ adsorption alongside zeolites and carbons due to their high selectivity, ease of regeneration, reusability, and tunability, making them a promising alternative to advanced porous materials[2]. MIL-101(Cr), a well-known MOF with high hydrothermal and chemical stability, has become a popular porous material for modern energy and scientific applications [3]. Recent research on post-synthetic modification of MIL-101(Cr) has shown that functionalization with diamines like DETA, TEPA, TAEA, ED, TEDA, and PEI increases CO₂ adsorption selectivity [4]. In this study, MIL-101(Cr) was functionalized using monoethanolamine (MIL-101(Cr)-OH) to enhance its CO₂ adsorption capacity and selectivity by increasing the polarity of pores. We also focused on determining and optimizing the pore polarity by various concentrations of monoethanolamine loading to investigate pore polarity engineering.

Experimental Section

MIL-101(Cr)-OH synthesis: MIL-101(Cr) modified using monoethanolamine (MIL-101(Cr)-OH) was synthesized using a wet impregnation technique. First, to remove water molecules from MIL-101(Cr) (activation), 0.5 grams of MIL-101(Cr) was kept at 130°C under vacuum for 24 hours. Following activation of MIL-101(Cr), approximately 3 mmol.g⁻¹ of coordinatively unsaturated sites (CUS) Cr (III) sites became available. Then, as shown in Figure 1, four molar concentrations of monoethanolamine (25, 50, 75, 100% mole) were used to modify MIL-101(Cr). After 24 hours of stirring, the mixtures were filtered and washed multiple times with methanol. Finally, the nanoadsorbents were dried at 50°C under a vacuum for 24 hours.
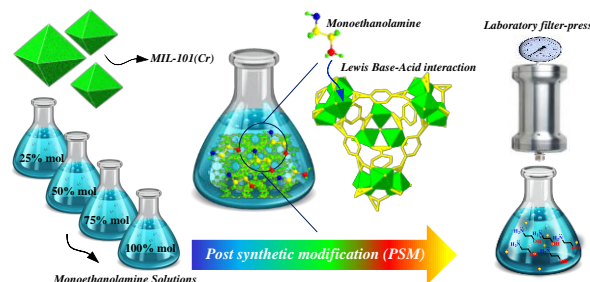
Fig 1: PSM of MIL-101(Cr) using Monoethanolamine

Results and Discussion

To investigate PSM of the nanoadsorbents, they were characterized using PXRD, XPS, IR spectroscopy, and BET surface areas. Additionally, the effect of pore polarity engineering on CO₂ adsorption capacity and selectivity was optimized by varying the concentration of monoethanolamine loading. As shown Fig 2 PXRD patterns reavel that MIL-101(Cr) maintains its crystalline structure after loading with monoethanolamine.
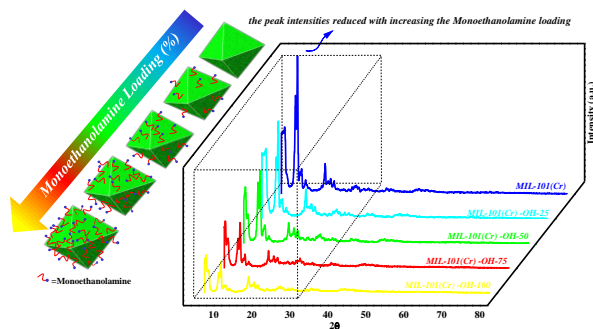
Fig.2: PXRD patterns of MIL-101(Cr)-OH nanoadsorbents

As seen in Fig 2, the PXRD peak intensities decrease with increasing concentrations of the monoethanolamine solutions. Furthermore, the PXRD peaks shift after

loading, possibly due to the formation of Cr-N bonds as evidenced by XPS (Figure 3-a). The C-N stretching band at 1080 cm^{-1}, as shown in the FTIR data in Figure 3-b, confirms the successful loading of monoethanolamine into the MIL-101(Cr)-alkanolamine nanoadsorbents structure.
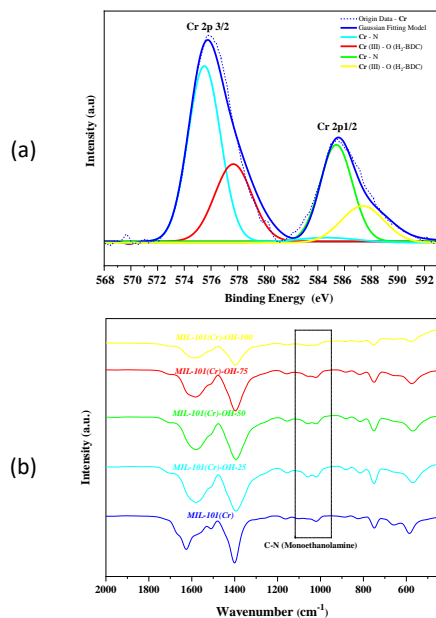
Fig.3: (a) XPS and (b) FT-IR of MIL-101(Cr)-OH.

A shown in Figure 4-a and Table 1, despite porosity and internal pore volume decreasing from the structural changes induced by modification, the CO_2 uptake unexpectedly surpassed that of the unmodified MIL-101(Cr).

Table1: physical properties of MIL-101(Cr)-OH nanoadsorbents

Nanoadsorbents	BET surface area (m²/g)	Pore Volume (cm³/g)
MIL-101(Cr)	3240	1.5
MIL-101(Cr)-OH-25	3030	1.44
MIL-101(Cr)-OH-50	2925	1.37
MIL-101(Cr)-OH-75	2767	1.30
MIL-101(Cr)-OH-100	2603	1.22

The MIL-101(Cr)-OH nanoadsorbents enhance CO_2 adsorption capacity due to electrostatic interactions and hydrogen bonding. The boosted adsorption capacity, greater than would be predicted based only on porosity differences, strongly suggests surface chemistry modifications play an even more important role relative to structural parameters (porosity) in facilitating CO_2 capture by these MIL-101(Cr)- OH nanosorbents. As seen in Figure 4-a,b, the maximum CO_2 adsorption capacity and CO_2:CH_4 selectivity was revealed in the MIL-101(Cr)-OH-50 nanoadsorbent. These results further indicate that excessive modification will lead to a decrease in adsorptive properties. Therefore, modification should be carried out to an appropriate extent to increase adsorption and selectivity. The lower adsorption capacities of MIL-101(Cr)-OH-75 and 100 seem to be because the positive effect of increased pore polarity is lowered, in part, by the decreased porosity due to the excess of modifying species.
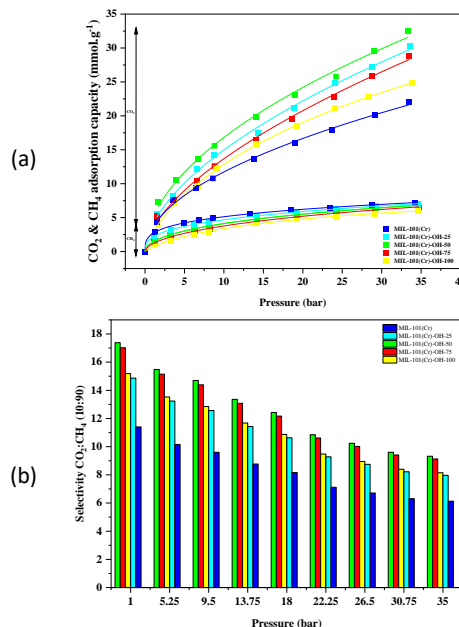
Fig.4: (a) CO_2 adsorption capacity and (b) CO_2: CH_4 selectivity of MIL-101(Cr)-OH.

According to these results, pore polarity engineering plays a key role in CO_2 adsorption capacity.

Conclusions

This study demonstrated that controlled surface modification can be employed to design and synthesize adsorbers for specific purposes. The use of monoethanolamine increases surface polarity and enhances carbon dioxide adsorption and CO_2:CH_4 selectivity. Consequently, the term "pore polrity engineering" has been chosen for this purpose.

References

[1] E.S. Kikkinides, R. Yang, S. Cho, Concentration and recovery of carbon dioxide from flue gas by pressure swing adsorption, Industrial & Engineering Chemistry Research, 32 (1993) 2714-2720.
[2] Z. Hu, Y. Wang, B.B. Shah, D. Zhao, CO_2 capture in metal–organic framework adsorbents: an engineering perspective, Advanced Sustainable Systems, 3 (2019) 1800080.
[3] N. Li, J. Xu, R. Feng, T.-L. Hu, X.-H. Bu, Governing metal–organic frameworks towards high stability, Chemical Communications, 52 (2016) 8501-8513.
[4] T.K. Vo, P.V. Vu, V.C. Nguyen, J. Kim, Construction of OH sites within MIL-101 (Cr)-NH_2 framework for enhanced CO_2 adsorption and CO_2/N_2 selectivity, Korean Journal of Chemical Engineering, 38 (2021) 1676-1685.

Investigating the Effect of Emulsifier on the Stability of Silicone Antifoam Emulsion

Saeed Iranpour[*], Mehdi Rouzbahani, Masumeh Sajadian

Corresponding Author E-mail: iranpour@ut.ac.ir

University of Tehran, Faculty of Engineering, ACECR, Farayand Chemical Research Group.

Abstract: Silicone antifoam emulsions are widely used in various industries to control foam formation during the manufacturing process. Foam can be a problem in many industrial processes, reducing efficiency, increasing costs, and even product defects. Silicone antifoam emulsions offer an effective solution to this problem, providing excellent foam control properties across a wide range of applications. The stability of silicone antifoam emulsions is influenced by various factors such as emulsifier type and concentration. By carefully considering these factors during formulation, processing, and storage, it is possible to develop highly stable silicone antifoam emulsions that effectively control foam in diverse industrial applications. This study investigated the effects of multiple emulsifiers on the stability of silicone antifoam emulsions. Using the foam system based on an anionic surfactant, functional tests of antifoams were performed. The results showed that the use of an emulsifier improves the stability of silicone antifoam emulsion. However, the improvement of emulsion stability performance is more observed in Span 60 than in the other emulsifiers.

Keywords: Antifoam; Silicone Antifoam; Emulsion; Emulsifier; Stability.

Introduction

Different classifications have been made for antifoam materials. In most cases, these compounds are classified as silicone and non-silicone antifoams, or water-soluble and oil-soluble antifoams. Silicone emulsion antifoam is one of the most important and widely used antifoams [1]. Emulsion stability, including antifoam emulsion, is one of the important challenges of these compounds [2]. Various factors such as emulsifier type and concentration, silicone oil viscosity, pH and ionic strength, temperature and shear stress, and storage conditions. play a role in emulsion stability. Emulsifying substances play a role as one of the factors affecting the stability of emulsions. The percentage of emulsifiers for silicone antifoam emulsion typically ranges from 1% to 5% of the total formulation. When selecting emulsifiers for silicone antifoam emulsions, it is essential to consider their compatibility with silicone oils, their emulsifying properties, HLB value, regulatory compliance, and application-specific requirements to ensure the stability and effectiveness of the antifoam emulsion. Considering that the best amount of HLB for preparing antifoam is reported to be 1 to 3, choosing an emulsifier based on HLB is a suitable method for preparing antifoam emulsions. [3]. The purpose of this research was to investigate the effect of emulsifiers on the stability of silicone antifoam emulsions. Due to the foam problems caused by the surfactant sodium lauryl sulfate (SLS), this substance has been used as a foaming agent.

Experimental Section

By choosing 4 types of emulsifiers, sorbitan monooleate (Span 80), sorbitan monostearate (Span 60), glycerol monostearate (GMS) and oleic acid, carboxymethyl cellulose (CMC) additive, polydimethylsiloxane (PDMS-1000) and water, according to table (1), several antifoam emulsions were prepared.

The stability of the emulsions was assessed through visual observation of phase separation, creaming, or coalescence over time. Furthermore, the defoaming performance of each emulsion formulation was evaluated using a standard foam test method to correlate stability with defoaming efficacy.

To test the performance of antifoams, 1% SLS solution was used to create foam. Based on this method, 50 ml of water was added in a 100 ml graduated cylinder and then 3 cc of 1% SLS solution was added as a foaming agent. It was stirred uniformly by adding the same amount of anti-foam material and placing the cap on each of the cylinders. Then, the performance of antifoams in removing foam was compared.

Results and Discussion

Table (1) shows the formulation of silicone antifoam emulsion and its stability and performance as an antifoam. The results show that Span 60 and GMS emulsifiers have the best performance in emulsion stability. By using oleic acid and Span 80 emulsion, an unstable emulsion was created. The comparison between the stable emulsions obtained from Span 60 and GMS

22nd Iranian Chemistry Congress (ICC22)
Iranian Research Organization for Science and Technology (IROST)
13-15 May 2024

03231-97589

IROST

showed that the emulsion obtained from Span 80 is more stable.

Since the main purpose of preparing antifoam is to eliminate foam, in addition to stability, these emulsions must also perform well as antifoam.

Some samples did not show proper performance as antifoam despite their good stability. The high viscosity of the emulsion (samples 3, 5, and 6), despite the stability of the emulsion, can be considered as one of the causes of the inefficiency of these emulsions as antifoam.

The performance test results of the prepared antifoams showed that among the stable antifoams, samples 1, 2, and 4 had good performance compared to other antifoams.

As the results of this research showed, in addition to the important role of emulsifiers in emulsion stability, the choice of emulsifier type, compatibility with formulation components, and its usage rate are of great importance.

Some samples, despite good stability, did not perform well as antifoam. The high viscosity of these compounds can be one of the reasons for the ineffectiveness of these emulsions as antifoam.

The use of emulsifiers in the formulation of antifoams can be practical research in this field, taking into account things such as low toxicity, economic considerations, ease of access, and compatibility with the consumption environment.

References

[1] Garrett, P. R., (2014), *The Science of Defoaming, Theory, Experiment and Applications*, CRC Press.

[2] Garrett, P. R., (2015), Defoaming: Antifoams and mechanical methods *Current Opinion in Colloid & Interface Science 20.2: 81-91.*

[3] Jong-Duk Kim. (2010.). The Effects of HLB Value of the Surfactants Added in the *Silicon Oil Emulsion Antifoamer on the Antifoaming Ability,* Journal of the Korean Applied Science and Technology,

Table1: Formulation of silicone antifoam emulsion

No	PDMS (gr)	Emulsifier (gr)	Water (gr)	CMC (gr)	*Stability
1	10	GMS (1)	83	2	++
2	10	GMS (2)	83	2	++
3	10	GMS (3)	83	2	++
4	10	Span60(1)	83	2	+++
5	10	Span60(2)	83	2	+++
6	10	Span60(3)	83	2	+++
7	10	Oleic acid(1)	83	2	-
8	10	Oleic acid(2)	83	2	-
9	10	Oleic acid(3)	83	2	-
10	10	Span80(1)	83	2	+
11	10	Span80(1)	83	2	+
12	10	Span80(1)	83	2	+
13	10	-	83	2	-

*Emulsion Stability: Good stability (+++), Stable (++), Relatively stable (+), unstable (-)

Conclusions

The findings of this research showed that the presence of an emulsifier is one of the important factors in the stability of silicone antifoam emulsions. As the results of this research showed, in addition to the important role of emulsifiers in emulsion stability, choosing the type of emulsifier, compatibility with formulation components and the amount of use of these compounds are also of great importance. Since the main purpose of preparing antifoam is to remove foam, these emulsions should also have a good performance as antifoam.

22nd Iranian Chemistry Congress (ICC22)
Iranian Research Organization for Science and Technology (IROST)
13-15 May 2024

03231-97589

IROST

Preparation of nanocomposite hydrogels based on bio-polymers@TA/Cu MOF bio-nanoparticles: pH-responsive and Antibacterial carrier for potential targeted anticancer drug delivery

Roghayeh Fathi, Reza Mohammadi[*]

Corresponding Author E-mail: r.mohammadi@tabrizu.ac.ir

Polymer Research Laboratory, Department of Organic and Biochemistry, Faculty of Chemistry, University of Tabriz, Tabriz, Iran.

Abstract: This work reports the preparation of new pH-responsive drug delivery systems of based on the TA/Cu MOF nanoparticles by a green, simple and inexpensive method that are important for the treatment of cancer. First, the Zingiber officinale extract was obtained and used for biosynthesis of TA/Cu MOF. They were added in the formulation of hybrid hydrogel toward the synthesis of nanocomposite hydrogels.
Keywords: Nanocomposite hydrogels; MOF; Drug delivery

Introduction

Nanocomposite hydrogels (NHs) are 3D molecular networks formed by physically or covalently crosslinking polymer with nanoparticles or nanostructures [1,2]. Fixing and loading the drugs in suitable carriers are a well-developed approach for their targeted delivery. New drug delivery systems based on biohybrid nanocomposites (natural polymeric matrix and inorganic materials as dispersed phase) were developed in recent years. Biocompatibility, biodegradation, inert, facility of preparation, appropriate mechanical strength, and ability to load high amounts of various drugs in these nanocomposites make them ideal as excellent drug delivery systems [3]. MOFs are porous inorganic–organic hybrid crystalline materials with low density, made up of metal nodes (metal ions or clusters) and organic linkers (bipodal or multipodal organic ligands). They are considered to be highly promising for therapeutic applications due to the regulation and release of antibacterial agents through various mechanisms [4]. The main goal of the present study is to design novel stimuli-responsive hydrogels that can simultaneously respond to environmental pH. First, Zingiber officinale plant extract was obtained for the green synthesis of MOF due to its antioxidant properties and biocompatibility. They were added in the formulation of hybrid hydrogel of Hyaluronic Acid and Chitosan toward the biosynthesis of nanocomposite hydrogels. Then, designed systems were considered for pH-controlled sustained drug release of doxorubicin (DOX) as a model anticancer drug. The obtained result showed that these new drug delivery systems could be used as potential carriers for targeted cancer therapy.

Experimental Section

Materials: Zingiber officinale plant (Tabriz-Iran), Chitosan (Mw = 110 kDa and DD = 84%), Hyaluronic Acid, Doxorubicin, Tannic acid, $CuSO_4.5H_2O$, NaOH.

Method:
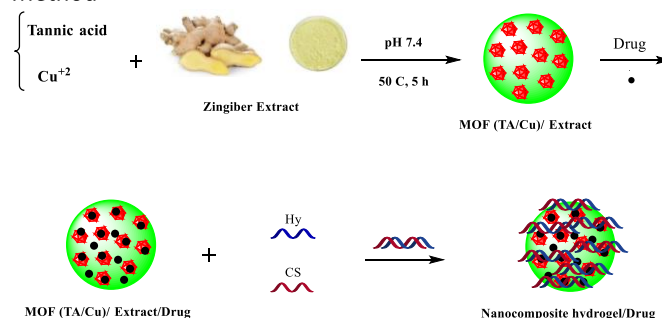
Results and Discussion

The chemical structure and morphology of the TA/Cu MOF bio-NPs@Hy@CS synthesised nanocomposite hydrogels were characterized by FT-IR, XRD, SEM and EDS analyses. The amount of drug released depends on the pH of the release medium. At pH 7.4, during 120 h almost 88% of the encapsulated DOX was released. However, the released rate dropped at pH 1.2 and 6.8 significantly (under 40% for DOX). The low release rate of hydrogel in acidic media compared to pH 7.4, is related to the low solubility of Hy in acidic media. The reason for the increase in drug release at alkaline pH is due to the deprotonation of Hyaluronic Acid acidic groups. In an alkaline environment (pH 7.4), Hy chains are separated from each other due to electrostatic repulsion, releasing the drug from the hydrogel (Fig. 1).

22nd Iranian Chemistry Congress (ICC22)
Iranian Research Organization for Science and Technology (IROST)
13-15 May 2024

03231-97589
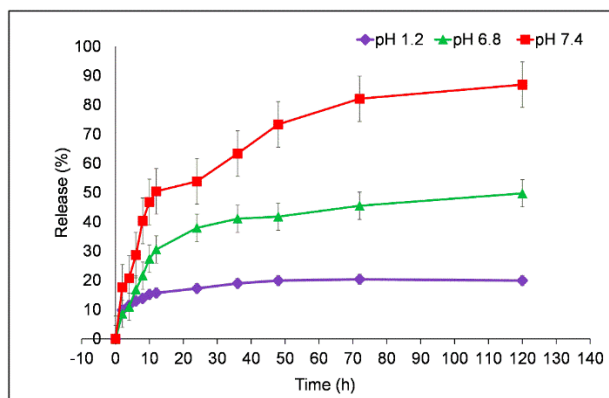
Fig. 1: Cumulative DOX release profiles from nanocomposite hydrogels at pH 1.2, 6.8 and 7.4 at 37 °C for 120 h.

Conclusions

in this study, TA/Cu MOF bio-NPs@Hy@CS nanocomposite hydrogel was synthesized using a green, simple, environmentally friendly and inexpensive method. To end this, MOF bio-NPs were synthesized by green chemistry using Zingiber officinale extract, which is eco-friendly, cost-efficient, and non-toxic. The loading and release of the drug from the prepared nanocomposite hydrogel at pH 1.2, 6.8 and 7.4 were investigated and compared. The structure of the prepared nanocomposite hydrogel was studied and confirmed by different techniques such as IR, XRD, SEM, and EDS. Investigating the antibacterial activity of TA/Cu MOF bio-NPs and final nanocomposite hydrogel showed their high ability to inactivate E. coli and S. aureus bacteria. Alternatively, the nanocomposite hydrogel has a greater ability to inhibit both bacteria compared to TA/Cu MOF bio-NPs. The designed nanocomposite hydrogel also showed a great pH-responsive delivery due to the presence of pH-sensitive CS and Hy biopolymers. Also, in-vitro cytotoxicity results exhibited that the prepared DOX-loaded nanocomposite hydrogel has higher toxicity against CRC cells, while the blank nanocomposite has a cytocompatibility nature. Therefore, the obtained results in this study showed that synthesized nanocomposite hydrogel with a high DOX loading capacity as well as its pH-dependent release profile (low release rate at pH 1.2 and 6.8 and controlled release rate at pH 7.4), can be a promising drug carrier for the treatment of cancerous tissues.

References

[1] Zhao, H., Liu, M., Zhang, Y., Yin, J., and Pei, R. (2020). Nanocomposite hydrogels for tissue engineering applications. Nanoscale 12 (28), 14976–14995. doi:10.1039/d0nr03785k.

[2] Merino, S., Martin, C., Kostarelos, K., Prato, M., and Vazquez, E. (2015). Nanocomposite hydrogels: 3D polymer-nanoparticle synergies for on-demand drug delivery. ACS Nano 9 (5), 4686–4697. doi:10.1021/acsnano.5b01433.

[3] Mallakpour S, Hatami M (2019) Fabrication and characterization of pH-sensitive bio-nanocomposite beads havening folic acid intercalated LDH and chitosan: drug release and mechanism evaluation. Int J Biol Macromol 122:157–167. doi.org/10.1016/j.ijbiomac.2018.10.166

[4] Au-Duong, A.-N., Lee, C.-K., 2017. Iodine-loaded metal organic framework as growth triggered antimicrobial agent. Mater. Sci. Eng. C 76, 477–482.

Green Synthesis of pH-responsive nanocomposite hydrogels based on bio-polymers@Fe/Cu LDH bio-nanoparticles: Antibacterial carrier for potential targeted anticancer drug delivery

Roghayeh Fathi, Reza Mohammadi*

Corresponding Author E-mail: r.mohammadi@tabrizu.ac.ir

Polymer Research Laboratory, Department of Organic and Biochemistry, Faculty of Chemistry, University of Tabriz, Tabriz, Iran.

Abstract: This study reports the development of new pH-responsive drug delivery systems for the treatment of cancer. First, the plant extract was obtained and then used for the biosynthesis of LDH nanoparticles. They were added in the formulation of hybrid hydrogel of Pectin and Chitosan toward the synthesis of nanocomposite hydrogels.
Keywords: Nanocomposite hydrogels; Plant extract; LDH; Drug delivery

Introduction

Nowadays, natural polymers, especially hydrogel nanocomposites based on polysaccharides, are one of the most important DDSs for cancer treatment due to their availability, biocompatibility, non-toxicity, high stability, biodegradability, low inflammatory reactions, cost-effectiveness, and controlled drug release profile. Therefore, many recent efforts have been directed toward developing hybrid hydrogels that can respond to external stimuli such as a magnetic field, pH, temperature, and ultrasound in order to achieve an effective and efficient anticancer drug carrier employing hydrogels [1]. Among the used nanocarriers in drug delivery systems, are double-layered hydroxides (LDH) with interchangeable anions in pseudo-brucite cationic interlayers due to low toxicity to targeted cells, biocompatibility, high stability, excellent drug protection against unwanted anaemia damage, dissolution depends on pH and developed cellular uptake behaviour compared to general drug carriers has been received much attention in cellular drug delivery of anionic drugs and other bioactive molecules [2, 3]. Among the various biological sources, plant extracts are safe, easily available, biocompatible, and provide good control over morphology and resistance. Curcuma longa is a plant determined by various pharmacological properties, such as antiviral, antibacterial, and antifungal activity [4,5]. Herein, the main goal of the present study is to design novel stimuli-responsive hydrogels that can simultaneously respond to environmental pH and temperature. First, Curcuma longa plant extract was obtained for the green synthesis of Fe/Cu LDH due to its antioxidant properties and biocompatibility. They were added in the formulation of hybrid hydrogel of Pectin and Chitosan toward the biosynthesis of nanocomposite hydrogels. Then, designed systems were considered for pH-controlled sustained drug release of doxorubicin (DOX) as a model anticancer drug. The obtained result showed that these new drug delivery systems could be used as potential carriers for targeted cancer therapy.

Experimental Section

Materials: Curcuma longa plant (Tabriz-Iran), CS (Mw = 110 kDa and DD = 84%), PT (Mw > 100 kD), DOX, $Fe(NO_3)_3 \cdot 9H_2O$, $Cu(NO_3)_2 \cdot 3H_2O$, NaOH. Method:
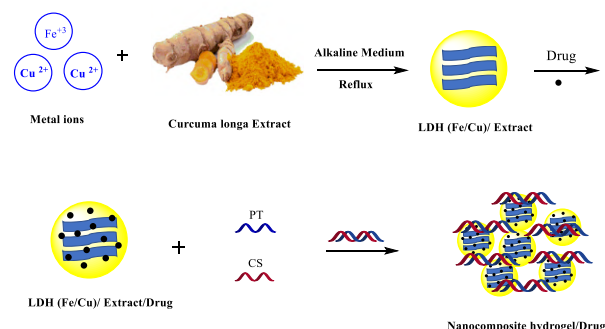
Results and Discussion

The chemical structure and morphology of the synthesised nanocomposite hydrogels were characterized by FT-IR, XRD, SEM and EDS analyses. The surface morphology of nanocomposite hydrogels was characterized using the SEM technique. Figure 1 clearly shows the formation of LDH nanoparticles on the plant extract, which were synthesized and completely dispersed on the plant extract. After the coating of CS and PT, the SEM image of the LDH bio-NPs@PT@CS also revealed the increase in particle size which confirmed the formation of nanocomposite hydrogel (Fig. 1). The amount of drug released depends on the pH of the release medium. At pH 7.4, during 96 h almost 91% of the encapsulated DOX was released. However, the released rate dropped at pH 1.2 significantly (under 38% for DOX). The low release rate of hydrogel in acidic media compared to pH 7.4, is related to the low solubility of pectin in acidic media. The reason for the increase in drug release at

22nd Iranian Chemistry Congress (ICC22)
Iranian Research Organization for Science and Technology (IROST)
13-15 May 2024

03231-97589

alkaline pH is the presence of pectinase enzyme and also due to the deprotonation of pectin acidic groups. In an alkaline environment (pH 7.4), pectin chains are separated from each other due to electrostatic repulsion, releasing the drug from the hydrogel (Fig. 2).
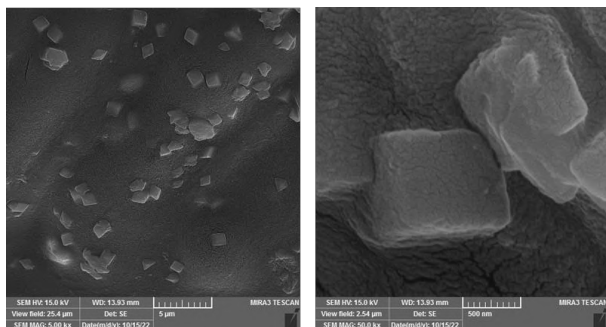
Fig. 1: SEM micrographs
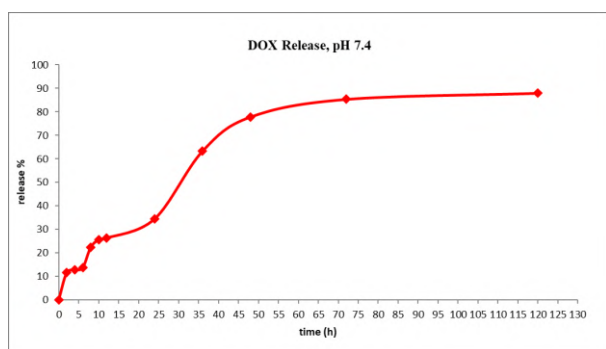
Fig.2: Release profile of DOX

Conclusions

In summary, in this work, Fe/Cu LDH bio-NPs@PT@CS nanocomposite hydrogel was synthesized using a green and simple method. To end this, LDH bio-NPs were synthesized by green chemistry using Curcuma longa extract, which is eco-friendly, cost-efficient, and non-toxic. The loading and release of the DOX from the prepared nanocomposite hydrogel at pH 1.2 and 7.4 were investigated and compared. The structure of the prepared nanocomposite hydrogel was studied and confirmed by different techniques such as IR, XRD, SEM, and EDS. Investigating the antibacterial activity of LDH bio-NPs and synthesized nanocomposite hydrogel showed their high ability to inactivate E. coli and S. aureus bacteria. Alternatively, the nanocomposite hydrogel has a greater ability to inhibit both bacteria compared to LDH bio-NPs. The designed nanocomposite hydrogel also showed a great pH-responsive delivery due to the presence of pH-sensitive CS and PT biopolymers. Also, in-vitro cytotoxicity results exhibited that the prepared DOX-loaded nanocomposite hydrogel has higher toxicity against CRC cells, while the blank nanocomposite has a cytocompatibility nature. Therefore, the obtained results in this study showed that synthesized nanocomposite hydrogel with a high DOX loading capacity as well as its pH-dependent release profile (low release rate at pH 1.2 and controlled release rate at pH 7.4), can be a promising drug carrier for the treatment of cancerous tissues.

References

[1] S.-Y. Wang, H.-Z. Hu, X.-C. Qing, Z.-C. Zhang, Z.-W. Shao, Recent advances of drug delivery nanocarriers in osteosarcoma treatment, Journal of Cancer 11(1) (2020) 69.

[2] Xu T, Xu X, Gu Y, Fang L, Cao F (2018) Functional intercalated nanocomposites with chitosan-glutathione-glycylsarcosine and layered double hydroxides for topical ocular drug delivery. Int J Nanomed 13:917–937.

[3] Gu Y, Xu C, Wang Y, Zhou X, Fang L, Cao F (2019) Multifunctional nanocomposites based on liposomes and layered double hydroxides conjugated with glycylsarcosine for efcient topical drug delivery to the posterior segment of the eye. Mol Pharm 16:2845–2857.

[4] M. Oves, M.A. Rauf, M. Aslam, H.A. Qari, H. Sonbol, I. Ahmad, G.S. Zaman, M. Saeed, Green synthesis of silver nanoparticles by Conocarpus lancifolius plant extract and their antimicrobial and anticancer activities, Saudi J. Biol. Sci. 29 (1) (2022) 460–471.

[5]. Li S, Yuan W, Deng G, Wang P, Yang P, Aggarwal BB. Chemical composition and product quality control of turmeric (Curcuma longa L.). Pharm Crop 2011;2:28-54

Electrochemical Determination of Pyrogallol as an Important Anti-Oxidant using a Modified Glassy Carbon Electrode with Poly (L-Cys)/AuNPs film

Mohammad Vazan, Javad Tashkhourian[*]

Corresponding Author E-mail: Tashkhourian@shirazu.ac.ir

Chemistry Department, Shiraz University, Shiraz, Iran.

Abstract: A modified glassy carbon electrode with poly (L-Cys)/Au nanoparticles film was used to determine the pyrogallol (PG) via electrocatalytic oxidation. The developed sensor efficiently minimized the PG oxidation potential and exhibited a wide linear response to varying PG concentrations (0.50 - 300 µM). It also showed a low detection limit (0.04 µM) and high sensitivity (1.54×10^{-6} A $M^{-1}cm^{-2}$), according to the differential pulse voltammetry measurements. Overall, the enhanced performance highlights its suitability for reliable PG determination in food samples.

Keywords: Pyrogallol; Poly (L-Cysteine); Gold nanoparticles; Electropolymerization; Electrochemical Sensor

Introduction

Pyrogallol (PG) is a polyphenolic compound found in various foods, beverages, and industrial uses, acting as both an antioxidant and a free-radical scavenger. Analytical methods, such as chemiluminescence, fluorescence, HPLC, UV-Vis spectrometry, mass spectrometry, and electrochemical techniques, can be used to detect PG in foods. This study presents a highly sensitive voltammetric sensor for PG determination using a modified glassy carbon electrode (GCE) with a poly L-cysteine and gold nanoparticles (L-Cys/AuNPs) film. Electrochemical methods include cyclic voltammetry (CV), differential pulse voltammetry (DPV) and Electrochemical Impedance spectroscopy (EIS) were used to evaluate the sensor performance and optimize parameters such as the pH, electrolyte, pulse amplitude, scan rate, and step increment. The DPV calibration curve showed linearity (0.5–300.0 µM) with a low detection limit (0.04 µM) and sensitivity (1.54×10^{-6} A M^{-1} cm^{-2}). This sensor demonstrated high sensitivity, reproducibility (relative standard deviation of 2.7% for repeatability and 2.5% for reproducibility), and stability, facilitated by a straightforward fabrication process.

Experimental Section

Before surface modification, the GCE was polished with 0.05 µm alumina slurry and sonicated in a 1:1 acetone-deionized water mixture. Electrochemical polymerization of 2.0 mM L-cysteine in phosphate buffer solution (0.10 M, pH 7.0) occurred via CV technique between -1.0 and 2.0 V for 10 cycles at 100 mV s⁻¹. Gold nanoparticle electrodeposition onto the poly(L-Cys) film followed, with three potential scans from 0.40 to 1.0 V at 25 mV s⁻¹, using a solution of 0.10 M KNO_3 and 3.0 mM $HAuCl_4$. The modified GCE was rinsed with deionized water and air-dried.

Results and Discussion

The modified GCE was characterized using non-destructive techniques (Fig. 1), specifically scanning electron microscopy (SEM) and energy-dispersive X-ray spectroscopy (EDX).

Element	W%	A%
C	83.25	92.71
N	4.21	4.02
O	3.11	2.60
S	0.07	0.03
Au	9.36	0.64
	100.0	100.0
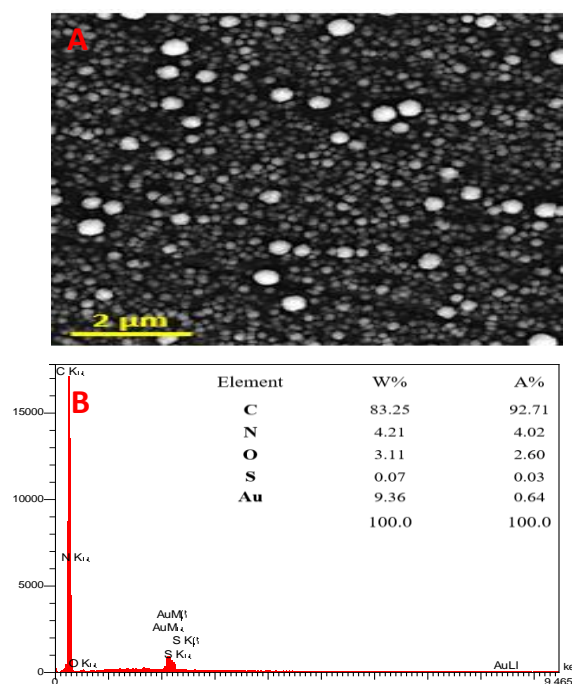
Fig. 1: (A) SEM image, and (B) Elemental spectrum and composition (wt%) of poly (L-Cys)/AuNPs/GCE.

The electrochemical response of pyrogallol (0.50 mM) in a 0.10 M phosphate buffer solution (pH 7.0) was evaluated using cyclic voltammetry at modified and unmodified GCEs (Fig. 2). The results showed a significant enhancement in the electrochemical conductivity of the modified electrodes, as indicated by a decrease in the peak potential and an increase in the peak currents, compared to the unmodified GCE. The improvement in

22nd Iranian Chemistry Congress (ICC22)
Iranian Research Organization for Science and Technology (IROST)
13-15 May 2024

03231-97589

the electrochemical performance can be attributed to the increased surface area resulting from the electropolymerization of L-cysteine and the synergistic effect between the AuNPs, which enables the low-potential measurement of pyrogallol.
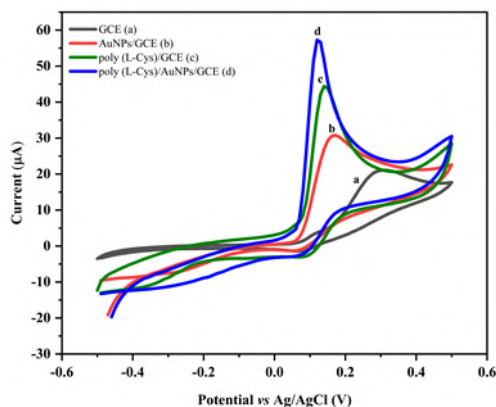
Fig. 2: CVs of 0.50 mM PG in PBS (0.10 M, pH 7.0) obtained at modified and unmodified electrodes at a scan rate of 50 mV s^{-1}.

A DPV calibration curve was obtained for pyrogallol using a phosphatebuffered solution (0.50 mM, pH 7.0) with a concentration range of 0.50-300.0 µM (Fig. 1B) with limit of detection (LOD) 0.04 µM. The resulting curve shows a linear relationship between the anodic current response and PG concentration, which can be represented by the following equation:

$$\log Ip \ (\mu A) = (0.749 \pm 0.02)[PG] \ (\mu M) + (0.360 \pm 0.03)$$
$$R^2 = 0.992 \ (LOD = 0.04 \ \mu M)$$
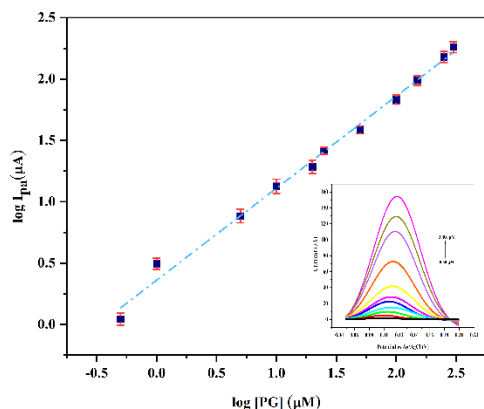
Fig.3: DVP responses for different concentrations of pyrogallol (0.50 – 300.0 µM) at poly (L-Cys)/AuNPs/GCE (PBS of 0.10 M, pH 7.0).

The ability of the developed sensor to determine the PG in tomato samples was tested. The recovery percentage was calculated by comparing the DPV results in the absence and presence of specific amounts of analyte; the results are shown in Table 1.

Table1: Application of DPV for the determination of pyrogallol in tomato juice.

Spiked (µM)	Found (µM)	Recovery (%)
0	2.81	---
25	24.15	96.6
50	52.22	104.4

After calculating the concentration of pyrogallol in the tomato solution (2.81 µM), it was determined that the tomatoes contain 0.36 mg of pyrogallol per 10 g of fruit.

Conclusions

A novel electrochemical sensor for pyrogallol determination was developed using electrochemical surface modification techniques. The developed sensor exhibited excellent analytical characteristics, including high sensitivity and selectivity, with an LOD of 0.04 µM and a sensitivity of 1.54×10^{-6} A M^{-1} cm^{-2}. The sensor also exhibited a good linear response over the concentration range, of 0.50 to 300 µM. Notably, the fabrication process was significantly simplified compared with that of other nanomaterial-based sensors, making the developed sensor a promising tool for determining PG in tomato samples.

References

[1] Rajkumar, C., & Kim, H. (2022). An amperometric electrochemical sensor based on hierarchical dual-microporous structure polypyrrole nanoparticles for determination of pyrogallol in the aquatic environmental samples. *Microchemical Journal*, *183*, 108038.

[2] Dutschke, J., & Suchowski, M. (2021). Simultaneous determination of selected catechins and pyrogallol in deer intoxications by HPLC-MS/MS. *Journal of Chromatography B*, *1180*, 122886.

[3] Ziyatdinova, G., Guss, E., & Yakupova, E. (2021). Electrochemical sensors based on the electropolymerized natural phenolic antioxidants and their analytical application. *Sensors*, *21*(24), 8385.

A Novel Zn(II) Complex of N–Nicotinyl-N', N"-bis (Piperidinyl) phosphoric triamide, and Investigating its anticancer activity

Nasrin Oroujzadeh[*a], Mahnaz Hadizadeh[b], Zahra Baradaran[a]
Corresponding Author E-mail: n_oroujzadeh@irost.ir
[a] Department of Chemical Technologies, Iranian Research Organization for Science and Technology (IROST), Tehran, Iran.
[b]Department of Biotechnology, Iranian Research Organization for Science and Technology (IROST), Tehran, Iran.

Abstract: A new Zn(II) complex (**CZ**) containing Phosphoramide ligand (**L**) with a formula of $ZnCl_2(L)_2$(**CZ**) successfully synthesized which **L**= $3\text{-}NC_5H_4CONHPO(NC_5H_{10})_2$. UV-Vis, ^{31}PNMR, FT-IR, SEM, Mass, CHN, and Molar conductivity methods were utilized to characterize **CZ**. Cytotoxic activity was investigated against two cancer cell lines (MDA-MB-231, MCF-7) and one normal cell line (MCF10A) and showed better and more selective anticancer activity compared to Cisplatin.

Keywords: Zinc (II) Complex; Phosphoramide; Anticancer; Cisplatin

Introduction

Phosphoric triamides are a type of organic compound that are widely used in various fields, including as anticancer prodrugs, cholinesterase and butyrylcholinesterase inhibitors [1], [2]. These compounds contain pyridine rings and precursors like Nicotinamide (Vitamin B3), which may contribute to their considerable biological and pharmacological effects. Recent research has shown that Nicotinamide may play a role in both cancer prevention and therapy [3]. In the realm of pharmacology and, biology, transition metals - specifically zinc - have gained significant attention due to their many applications as antibacterial, antifungal, anti-cancer, antiviral, and antioxidants [4]. The integration of Phosphoramide ligands into metal complexes has greatly expanded the range of structural diversity, leading to significant advancements in the fields of biology and pharmacology [2]. Here, we synthesized a novel Zn(II) complex of N–nicotinyl-N',N"-bis (Piperidinyl) phosphoric triamide ligand (Fig.1) and for characterizations of the synthesized complex UV-Vis, FT-IR, SEM, Atomic Absorption(AAS), and ^{31}PNMR spectroscopies besides Mass spectrometry, CHN, and Molar conductivity methods were utilized and its anticancer activities against two cancer cell lines (MDA-MB-231, MCF-7) and one normal cell line (MCF10A) were studied and compered with a generally used anticancer drug, Cisplatin, using MTT-Assay method.

Experimental Section

The ligand, N–nicotinyl-N', N"-bis (Piperidinyl) phosphoric triamide was synthesized according to our previously reported procedures [5]. The complex was synthesized by adding a solution of 1 mmol Zinc(II) chloride in ethanol to a solution of 2 mmol of the ligand in hot ethanol and stirring for 2 days. The resulting precipitate was filtered and washed by ethanol. The cytotoxic activity of the (**CZ**) and (**L**) was determined using the MTT assay [6] on two human breast cancer cell lines (MDA-MB-231 and, MCF-7), and one normal cell line (MCF10A). IC$_{50}$ was calculated as the concentration of complex needed for 50% inhibition of cell viability in 48h. Cisplatin was used as a positive control.
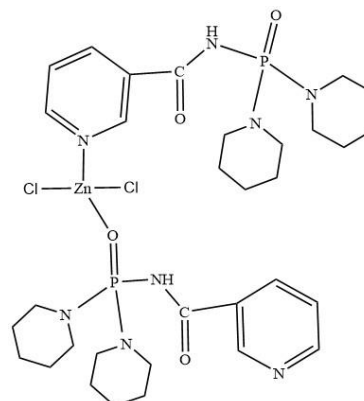
Fig.1: Our suggested structure for the Zn(II) complex (**CZ**)

Results and Discussion

Table 1 compares the FT-IR data of our synthesized complex (**CZ**) and its ligand (**L**). The complex's data shows an increased frequency of the pyridine rings and a positive shift of the C=O vibration. The UV-Vis spectra confirm the existence of the corresponding ligand in the complex structure.

Table 1: FT-IR and ^{31}PNMR data of compounds

Comp.	v(P=O)	v(C=O)	v(N$_{py(Ring)}$)	δ (P$_{NMR}$)
L	1186	1683	1589	9.90
CZ	1174	1700	1608	10.99

The singlet peak observed in the ^{31}PNMR spectra of (**CZ**) and its ligand (**L**) showed significant differences of δ(^{31}P) (Table 1). The CHN, Mass, and AAS results confirmed the formation of the complex. Molar Conductivity examinations revealed that the chlorine ions are coordinated with the Zinc metal and has entered the coordination sphere. The molar conductivity indicated that our complex is non-electrolyte [7].

22nd Iranian Chemistry Congress (ICC22)
Iranian Research Organization for Science and Technology (IROST)
13-15 May 2024

03231-97589

For Cytotoxic tests the cells were treated with different concentrations of **(CZ)** and **(L)** (0–400 µg/ml) for 48 h. Figs. 2 shows the plots of cell viability of the a breast cancer cell lines MDA-MB-231 versus the concentration of **(CZ)** and its **(L)**. The results showed that the percentage of cytotoxicity seen in the MTT assay for both compounds tested increased obviously in a dose-dependent manner with the increase of the concentration.
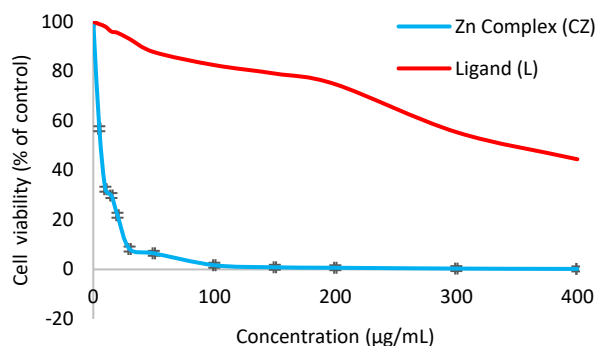
Fig 2. The plots of cell viability vs. the concentration of Zn Complex and its Ligand against MDA-MB-231 cells.

After 48 h incubation at the highest tested concentration (400 µg/ml), **(CZ)** inhibited MCF-7 and MDA-MB-231 cells by 99.8%, also, its Ligand **(L)**, inhibited MCF-7 and MDA-MB-231 cells by about 55% at 400 µg/ml, this was significantly different from their effect on MCF10A normal cells. MCF10A cells maintain viability above 58% for **(CZ)** and above 81% for its Ligand **(L)** even at high concentration (400 µg/ml) of these compounds.

Table 2. IC$_{50}$ values µM (µg/ml) of **(CZ)**, **(L)**, and the reference Cisplatin against MDA-MB-231, MCF-7, and MCF10A cell lines

Compound	IC$_{50}$ µM (µg / mL)		
	MDA-MB-231	MCF-7	MCF10A
(L)	997 µM (335 µg/ml)	1034 (347)	>1100 (>400)
(CZ)	8.56 (6.92)	9.85 (7.96)	>495 (>400)
Cisplatin	90 (27)	136 (41)	43 (13)

To further evaluate the anticancer activity of the **(CZ)**, IC$_{50}$ values of the **(CZ)**, **(L)** and Cisplatin as the positive control against all three cell lines were calculated, and the results are shown in Table 2. The calculated IC$_{50}$ values are obviously at a higher level for MCF10A than those of the two cancer cell lines, indicating that this complex, have strong anticancer activities while lower toxicity to the normal cells. The comparison of the inhibition activity for **(CZ)** with Cisplatin also demonstrates that this complex, as promising anticancer alternative drug, could be have fewer side effects than generally used anticancer drugs such as Cisplatin by exactly controlling the intake dose.
After determining the IC$_{50}$ values, the Selectivity Index (SI) was calculated and presented in Table 3, indicating the cytotoxic effects of the complexes on MDA-MB-231 and

MCF-7 cells. For **(CZ)** the SI value of >57.83 was recorded for the MDA-MB-231 cell line, while the SI value of >50.25 was recorded for the MCF-7 cell line type at 48 hours. Interestingly, these values were more than 120 and 156 times higher than the positive control, Cisplatin, and also more than 85 and 54.5 times higher than a registered breast cancer drug, Doxorubicin respectively for MDA-MB-231 and MCF-7 cells [8]. This result is far superior to the approved and commonly used drugs in the field of breast cancer treatment like Cisplatin and Doxorubicin.

Table 3. Selective index of Zn(II) complex, comparing to some anticancer drugs on MCF10A, MCF-7, and MDA-MB-231 cells.

Compound	Selective index (SI) MCF10A/MCF-7	Selective index (SI) MCF10A/MDA-MB-231	Ref.
(L)	>1.06	>1.10	Present Study
(CZ)	>50.25	>57.83	Present Study
Cisplatin	0.32	0.48	Present Study
Doxorubicin	0.92	0.68	[8]

Conclusions

The study shows that this complex have a strong effect on cancer cell lines while having a low effect on normal cell lines and IC$_{50}$ values reveald strong in-vitro antiproliferative activity with Zn(II) complex showing greater cytotoxicity than Cisplatin with surprisingly lower effect on normal cells.

References

[1] K. Gholivand *et al.*, *Curr. Med. Chem.*, 2023.

[2] S. Nikpour, N. Dorosti, F. Afshar, and M. Kubicki, *Appl. Organomet. Chem.*, vol. 34, no. 8, p. e5724, 2020.

[3] I. P. Nikas, S. A. Paschou, and H. S. Ryu, *Biomolecules*, vol. 10, no. 3, p. 477, 2020.

[4] D. Sudha, et al., *J. Coord. Chem.*, vol. 74, no. 16, pp. 2701–2719, 2021.

[5] N. Oroujzadeh and K. Gholivand, *J. Iran. Chem. Soc.*, vol. 13, no. 5, pp. 847–857, 2016.

[6] T. Hayon, A. Dvilansky, O. Shpilberg, and I. Nathan, *Leuk. Lymphoma*, vol. 44, no. 11, pp. 1957–1962, 2003.

[7] M. Sunita, et al., *Coord. Chem. Rev*, vol. 7, pp. 81–122, 1971.

[8] N. A. Razak *et al.*, *Sci. Rep.*, vol. 9, no. 1, p. 1514, 2019.

22nd Iranian Chemistry Congress (ICC22)
Iranian Research Organization for Science and Technology (IROST)
13-15 May 2024

03231-97589

IROST

Practical One-pot Synthesis of Hydroquinolines using TiO₂ nano-photocatalyst from Nitroarenes or Aminoarenes

Javad Samadi, Majid Mirzaei, Foad Kazemi*

Corresponding Author E-mail: Kazemi_f@iasbs.ac.ir

Department of Chemistry, Institute for Advanced Studies in Basic Sciences (IASBS), Zanjan, Iran.

Abstract: Due to the great importance of hydroquinoline compounds and their existence in the structure of natural products and their application in pharmacology, it has always been of interest to researchers and organic and pharmaceutical chemists. In this project, we tried to synthesize these valuable compounds in one-pot and mild conditions by using various Nitro and aniline compounds in two ways of reduction–oxidation of the aforementioned.

Keywords: Photocatalytic; Tetrahydroquinoline; flow reactor; One-pot

Introduction

Tetrahydroquinoline compounds are organic compounds that are the semi-hydrogenated derivatives of quinoline. They are commonly used in medicinal chemistry, and their substituted derivatives have been found to be bioactive. [1]. Additionally, Tetrahydroquinoline derivatives have been synthesized and evaluated for their antimicrobial and anticancer properties, making them important structures for synthesizing biologically active compounds [2]. given the substantial impact of hydroquinolines in medical sciences and the chemical industry, the development and optimization of synthesis processes for hydroquinolines using photocatalysts represent a crucial step[3-5].

Experimental Section

Two photocatalytic experiments were conducted in different ways. The first experiment was carried out on a small scale using a batch system in a 50 ml Erlenmeyer flask, while the second experiment was conducted on a larger scale using a flow reactor in a 500 ml Erlenmeyer flask. Based on the optimal conditions, a photocatalyst consisting of TiO2 nanoparticles, a certain volume of solvent, and a specific concentration of nitroarene and arylamine compounds was converted into a suspension mixture. This mixture was then irradiated with violet LED light having a wavelength of 400 nm.

Results and Discussion

Several tetrahydroquinoline compounds were synthesized using arylamines from the oxidation route and nitroarenes from the reduction route. This was done in a one-pot manner, yielding good to excellent results. Furthermore, these compounds were produced on a gram scale using a flow reactor. Figure 1 displays an example of these products.
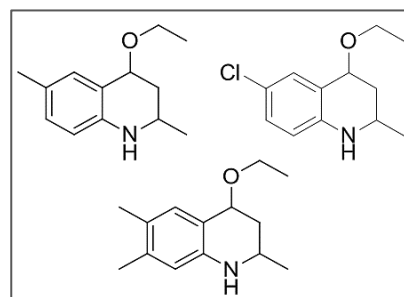
Fig.1: some examples of synthesized Tetrahydroquinoline products
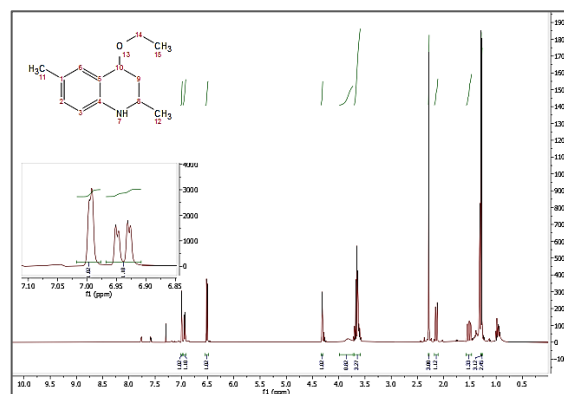
Fig.2: ¹H NMR of 4-ethoxy-2,6-dimethyl-1,2,3,4-Tetrahydroquinoline (400 MHz, CDCl₃)

22nd Iranian Chemistry Congress (ICC22)
Iranian Research Organization for Science and Technology (IROST)
13-15 May 2024

03231-97589
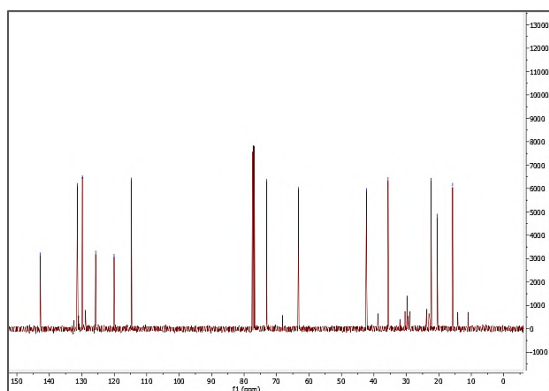
Fig.3: ^{13}C NMR of 4-ethoxy-2,6-dimethyl-1,2,3,4-tetrahydroquinoline (400 MHz, CDCl$_3$)
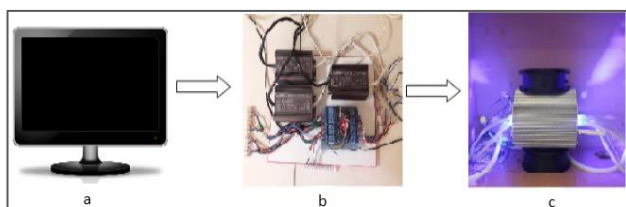
Fig.4: General schematic of the Photoreactor. a) computerized, b) digital control unit (DCU), c) Reactor shield with cooling fans

Table1: Style1 (Font: Calibri 9)

Substrate	Time(h)	Yields[a] (%)	Products
	14	88	
	11	68	
	18	63	

[a] Isolated yields.

Conclusions

An efficient and mild one-pot photocatalytic method has been reported for the synthesis of a wide range of hydroquinoline compounds using the flow and batch method. Different types of arylamine and nitroarene compounds were reacted to produce the target products. One of the highlights of this work is the use of a flow photoreactor that can be easily programmed through a computer. The flow rate, radiation intensity, temperature, and irradiation time can be adjusted using this reactor. The tetrahydroquinoline products obtained on a gram scale show the scalability and operation of this system.

References

[1] Liu, Jiayong, et al. "Design, synthesis, and biological evaluation of tetrahydroquinoline amphiphiles as membrane-targeting antimicrobials against pathogenic bacteria and fungi." European Journal of Medicinal Chemistry 243 (2022): 114734.

[2] Fathy, Usama, et al. "Facile synthesis and in vitro anticancer evaluation of a new series of tetrahydroquinoline." Heliyon 7.10 (2021).

[3] Sherborne, Grant J., et al. "Visible Light-Mediated Cyclisation Reaction for the Synthesis of Highly-Substituted Tetrahydroquinolines and Quinolines." Angewandte Chemie 135.2 (2023): e202207829.

[4] Wang, Kai-Kai, et al. "Divergent Synthesis of Highly Substituted Tetrahydroquinolines and Cyclopentenes via Lewis Base Catalyzed Switchable [4+ 2] and [3+ 2] Annulations of MBH-Carbonates with Activated Olefins." The Journal of Organic Chemistry 88.9 (2023): 5982-5996.

[5] Heidari, Aida, Kazem D. Safa, and Reza Teimuri-Mofrad. "Chlorophyll b-modified TiO2 nanoparticles for visible-light-induced photocatalytic synthesis of new tetrahydroquinoline derivatives." Molecular Catalysis 547 (2023): 113338.

Photoinduced electron transfer using TiO₂-TEOA-NC self-assembled triad

Javad Samadi, Mahshid Bagheri Natanzi, Foad Kazemi*

Corresponding Author E-mail: Kazemi_f@iasbs.ac.ir

Department of Chemistry, Institute for Advanced Studies in Basic Sciences (IASBS), Zanjan, Iran.

Abstract: The triad TiO₂-TEOA-NC (LMCT/EDA) complex system was self-assembled and used as a heterosupramolecular nano device in fast practical reduction of nitro compounds under visible light irradiation. The increased charge separation in the triad system was demonstrated by photocurrent and electrochemical impedance spectroscopy (EIS) under visible light irradiation.

Keywords: heterosupramolecular; self-assembled; triad; visible light; TiO₂-TEOA-NC

Introduction

One of the ways to increase the separation of photogenerated charge carriers and to reduce back electron transfer is to increase the distance between charges. Therefore, the design of dyads, triads, etc. molecular systems will be very fruitful in this field. In the same vein, we present here a triad heterosupramolecular system of complex (LMCT/EDA) that spontaneously assembles under visible light irradiation. This heterosupramolecular system has a high electron transfer rate and efficiency due to the distance it creates between charge carriers, which is unique in its turn [1] [2] [3].

Experimental Section

Three photocatalytic experiments were conducted. The first experiment was carried out on a small scale (1 mmol) using TiO₂-TEOA LMCT system in water solution, while the second experiment was conducted on a large scale (5 mmol) using TiO₂-TEOA LMCT complex system in the same conditions. The third experiment involved the synthesis of anilides using the superramolecular triad system. The optimum conditions for all reactions were as follows: Based on the optimal conditions, TiO₂-P25 nanoparticles, a certain volume of water solvent, a 1-5 mmol concentration of nitroarenes and a small amount of tert-butanol were converted into a 10 ml round bottom balloon. This mixture was then irradiated with violet LED light (50 w) having a wavelength of 400 nm.

Results and Discussion

In the same direction, Scheme 2 illustrates the creation of the TiO₂-TEOA LMCT complex through exposure to light and its constituents. Following the addition of nitrobenzene, the triad heterosoparamolecular system is generated in situ under light irradiation. Following the excitation, photo-induced electron transfer to the nitro compound increases the charge separation of the system. This was proven by observing an increase in the electron density of the triad compared to TiO₂-TEOA in the photocurrent analysis.
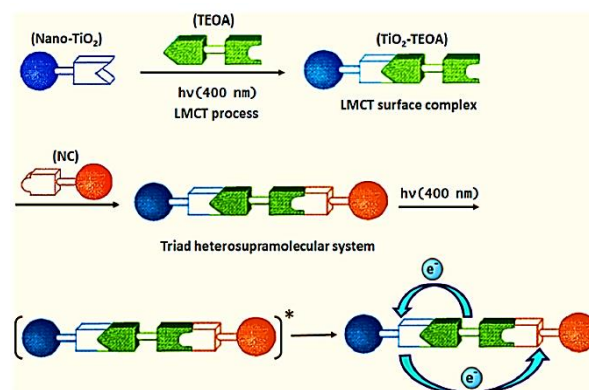
Fig.1: Schematic illustration of the formation steps of the self-assembled triad heterosupramolecular system.

we report for the first time the large scale and fast selective photoinduced reduction of nitro compounds using a TiO₂-TEOA LMCT surface complex in water at room temperature and in air. This is the first report of the reduction of nitro compounds on a large scale (1–5 mmol substrate) under photocatalytic conditions. We found that only the nitro group was chemoselectively reduced to the amino group, and aminobenzenes with reducible groups were obtained with exceptionally high selectivity and conversion without the use of precious metals or high-pressure gaseous reducing reagents. Since the nitro compounds are economical starting materials for the preparation of amines and the subsequent use of the resulting amines in reductive amination, this is very interesting because it does not require prior separation of the amines. Hence, according to the points made and due to the importance of amide derivatives such as formanilides as fundamental intermediates in organic chemistry, we report on the photocatalytic performance of this system in the one-pot synthesis of aromatic amides from nitroarenes under visible light irradiation.

22nd Iranian Chemistry Congress (ICC22)
Iranian Research Organization for Science and Technology (IROST)
13-15 May 2024

03231-97589

ISC
Islamic World Science Citation Center
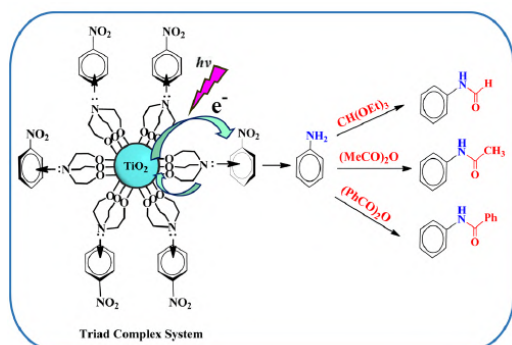
Fig.2: One-pot N-formylation, N-acylation and N-arylation of photocatalytic generated amines using a triad TiO_2-TEOA-NC system under visible light irradiation.
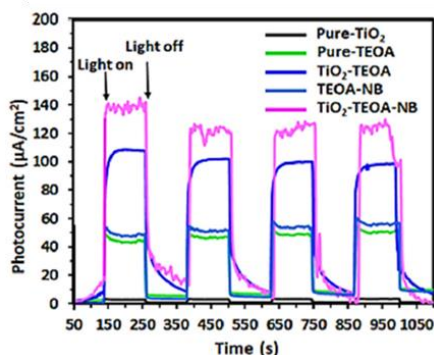
Fig.3: photocurrent measurements of pure TiO_2, pure TEOA, the TiO_2-TEOA surface complex, the TEOA-NB complex, and the TiO_2-TEOA-NB triad;
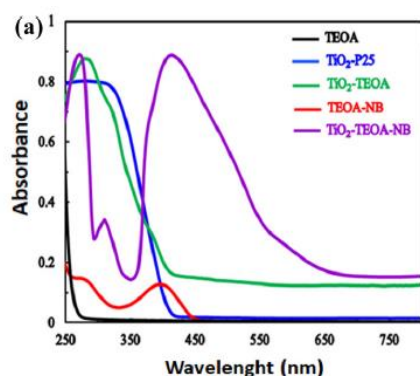
Fig.4: UV/vis diffuse-reflectance spectra (DRS) of TEOA, TiO_2-P25, the chemically adsorbed TiO_2-TEOA complex, the TEOA-NB, complex and the TiO_2-TEOA-NB triad.
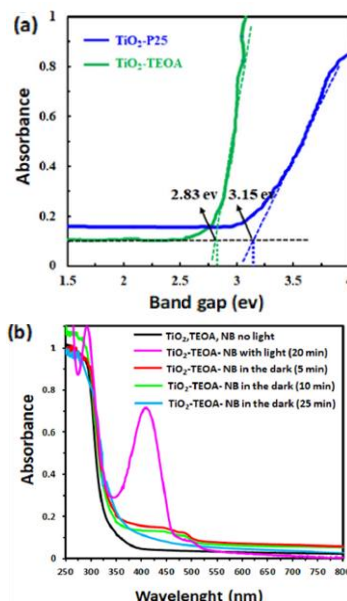
Fig.5: (a) Band gap of TiO_2-P25 and TiO_2-TEOA according to the diffuse reflectance spectra. (b) UV-vis absorption spectra of TiO_2, TEOA, NB (in the dark), TiO_2-TEOA-NB (after 20 minutes of light exposure), TiO_2-TEOA-NB (after 5 minutes in the dark), TiO_2-TEOA-NB (after 10 minutes in the dark), and TiO_2-TEOA-NB (after 25 minutes in the dark).

Conclusions

we report on a novel heterosupramolecular triad system based on nano-TiO_2, TEOA and NC (nitro compound), which self-assembles under visible light irradiation. In traditional systems, the reaction components require diffusion or encounter. In this system, the reaction components have already been loaded by light and do not need to diffuse during the reaction. This system acts as a nano device. Upon excitation of the triad in an aqueous solution, electron transfer occurs from the conduction band of TiO_2 to the nitro compound (NC). Subsequently, the luminescence of the excited state of the triad system is quenched by this electron transfer to the NC unit.

References

[1] J. B. Kelber, N. A. Panjwani, D. Wu, R. Gómez-Bombarelli, B. W. Lovett, J. J. Morton, H. L. Anderson, *Chemical Science* **2015**, *6*, 6468-6481.

[2] R. Ballardini, V. Balzani, M. Clemente-León, A. Credi, M. T. Gandolfi, E. Ishow, J. Perkins, J. F. Stoddart, H.-R. Tseng, S. Wenger, *Journal of the American Chemical Society* **2002**, *124*, 12786-12795.

[3] G. Will, G. Boschloo, R. Hoyle, S. N. Rao, D. Fitzmaurice, *The Journal of Physical Chemistry B* **1998**, *102*, 10272-10278.

22nd Iranian Chemistry Congress (ICC22)
Iranian Research Organization for Science and Technology (IROST)
13-15 May 2024

03231-97589

IROST

The structural, stability and electronic properties of Li₂CoAl Full Heusler alloy form DFT

Sima Mahmoudi [a,b], Mir Maqsood Golzan [a], Ebrahim Nemati-Kande [* b]

Corresponding Author E-mail: e.nemati@urmia.ac.ir

[a] Department of Physics, Faculty of Sciences, Urmia University, Urmia, Iran.

[b] Department of Physical Chemistry, Chemistry Faculty, Urmia University, Urmia, Iran.

Abstract: In this study, the electronic properties of Li₂CoAl Full Heusler are investigated using density functional theory methods. The GGA approximation has been used to calculate the correlation exchange potential. The results show that this alloy is dynamically stable. The calculated band structure shows that this compound has inter-metallic properties.

Keywords: Full Heusler; density functional theory; dynamically stable.

Introduction

Heusler discovered the first alloy of the Heusler type, Cu₂MnAl, in 1903 [1]. However, since they are made up of non-ferromagnetic materials, their interesting ferromagnetism has kept them a scientific wonder for a long time. They have become intriguing materials for a variety of outstanding functional applications in the twenty-first century, including thin-film growth, spintronic (giant magnetoresistance) technologies, thermoelectric and other energy conversion systems, and novel characteristics [2]. Due to their potential applications of ternary complexes, the Li atom in the form of half-Heusler compounds was used in the creation of the thermoelectric devices, spintronics, optoelectronics, and other technologies [3].

Methodology

In this project, quantum espresso package based on the denisty functional theory is used to calculate electronic properties. In this computation, the generalized gradient approximation (GGA) of the Perdew, Burke and Ernzerhof (PBE) functional was implemented. Also, Thermo-pw package was used to calculate network dynamics and to calculate phonon scattering curves and phonon density of states.

The kinetic energy cut-off of the wave function was set at 100 Ry and a 300 Ry cutoff energy was used for the charge density expansioncut-off kinetic energy. Also, the lattice structures were optimized with the energy uncertainty of 1×10^{-10} Ry.The first Brillouin zone was modeled using a $24\times24\times24$ k-point mesh. For calculation of the phonon dispersion curves and the density of phonon states, we employed a q-point mesh of $16\times16\times16$ using Thermo-pw code.

Results and Discussion

Full Heusler alloys, which have the X₂YZ chemical formula, exhibit an L2₁ crystal structure with a space group of Fm$\bar{3}$m (225). The X, Y, and Z elements occupy the Wyckoff positions of (0, 0, 0), (1/2, 1/2, 1/2), (1/4, 1/4, 1/4), and (3/4, 3/4, 3/4), respectively. If the positions of the X and Y elements are exchanged in the Full Heusler composition, the resulting compound is known as an inverse Heusler composition. Inverse Heusler compounds have the space group of F$\bar{4}$3m and XA structure (216). The crystal structures of the relaxed Li₂CoAl Heusler compounds were visualized in Fig. 1.
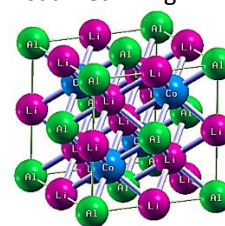
Fig.1: The relaxed inverse Heusler structures of a Li₂CoAl

To investigate the dynamical stability of Li₂CoAl Heusler alloys, we calculated phonon scattering curves and phonon density of states. Since Heusler alloys have four atoms per unit cell, each wave vector has twelve phonon modes, including three phonon modes, three acoustic modes, and nine optical modes. Fig. 2 shows the phonon scattering curve and phonon density curve of Li₂CoAl Heusler alloy.The phonon spectra obtained for the Li₂CoAl Heusler alloy in all directions exhibit a positive phonon frequency in the Brillouin zone, indicating that these compounds are dynamically stable in the inverse Heusler structure

22nd Iranian Chemistry Congress (ICC22)
Iranian Research Organization for Science and Technology (IROST)
13-15 May 2024

03231-97589

IROST
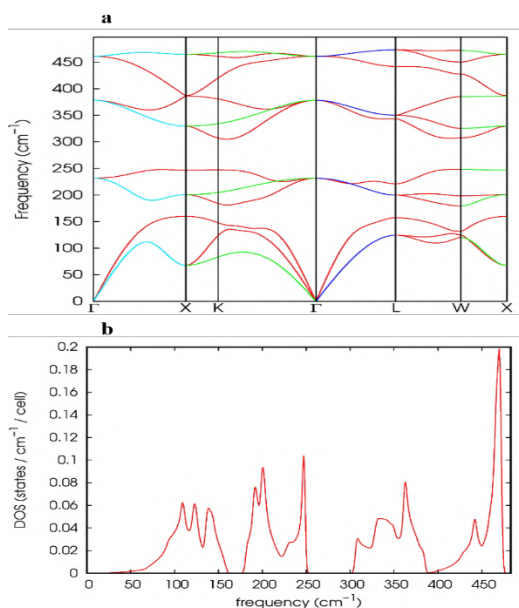
Fig.2: a calculated phonon dispersion curve and **b** phonon density of states of Li$_2$CoAl Full Heusler alloy.

References
[1] Dogan, E.K. and S.E. Gulebaglan, *Lattice dynamics and electronic properties of Heusler alloys Li2AlX (X= Ga, In): A comparison study.* Chinese Journal of Chemical Physics, 2021. **34**(2): p. 173-178.
[2] Tavares, S., K. Yang, and M.A. Meyers, *Heusler alloys: Past, properties, new alloys, and prospects.* Progress in Materials Science, 2022: p. 101017.
[3] Kalarasse, L., B. Bennecer, and F. Kalarasse, *Elastic and electronic properties of the alkali pnictide compounds Li3Sb, Li3Bi, Li2NaSb and Li2NaBi.* Computational materials science, 2011. **50**(10): p. 2880-2885.

After that, the electronic band structure of the intermetallic Li$_2$CoAl alloy along with the high symmetry directions in the energy range of -8 eV to 8 eV was calculated using the GGA approximation, which is shown in Figure 3. For the band structure calculation, high-symmetry points ($\Gamma \to X \to K \to \Gamma \to L \to W \to X$) are considered while the Fermi energy level is set to be 0.0 eV. As seen in the band structure figure, the valence bands and conduction bands overlap. This overlap of bands indicates that the Li$_2$CoAl alloy has conductive properties.
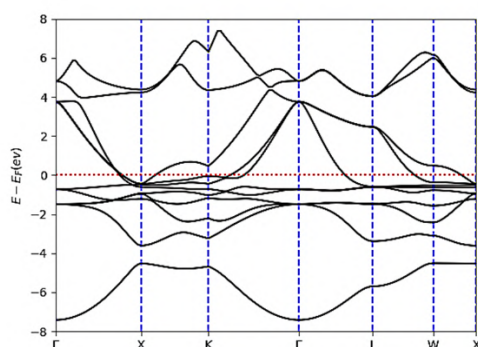
Fig.3: Electronic band structure of the Li$_2$CoAl Full Heusler alloy.

Conclusions
According to the obtained results, Li$_2$CoAl Full Heusler alloy is dynamically stable and the band structure shows that this composition has conductive properties.

22nd Iranian Chemistry Congress (ICC22)
Iranian Research Organization for Science and Technology (IROST)
13-15 May 2024

03231-97589

IROST

The structural, stability and electronic properties of Li$_2$CoB Full Heusler alloy form DFT

Sima Mahmoudi [a,b], Ebrahim Nemati-Kande * [b], Mir Maqsood Golzan [a]

Corresponding Author E-mail: e.nemati@urmia.ac.ir

[a] Department of Physics, Faculty of Sciences, Urmia University, Urmia, Iran.

[b] Department of Physical Chemistry, Chemistry Faculty, Urmia University, Urmia, Iran.

Abstract: In this work, density functional theory methods are applied to analyses electrical properties of Li$_2$CoB Full Heusler. The correlation exchange potential has been computed using the GGA approximation. The outcomes demonstrate the dynamic stability of this alloy. The intermetallic features of this chemical are demonstrated by the estimated band structure.

Keywords: Full Heusler; density functional theory; dynamically stability.

Introduction

In recent years, Heusler compounds have been the subject of theoretical investigation as they have a wide range of potential applications. Heusler alloys are used in magnetic electronic devices such as magnetic sensors and huge magnetic resistance (TMR). Additionally, Heusler alloys have generated a lot of interest as a promising option for thermoelectric (TE) materials in the future. These materials will be crucial to the development of environmentally friendly technologies because they will convert heat loss into electrical energy and emit fewer greenhouse gase.Thermoelectric materials can be used in refrigeration devices for cooling applications as well as power generation devices. Furthermore, Heusler alloys have a high Curie temperature (Tc), which means that they may be able to maintain their half-metallic nature even at ambient temperature. [1-3]

Computational

In this research, electronic characteristics are calculated using the quantum espresso package, which is based on the denisty functional theory. The Perdew, Burke, and Ernzerhof (PBE) functional's generalised gradient approximation (GGA) was used in this computation. Thermo-pw software was also utilised to compute phonon density of states, phonon scattering curves, and network dynamics.

The wave function's kinetic energy cut-off was set at 100 Ry, while the charge density expansion cut-off kinetic energy was set at 300 Ry. Furthermore, lattice structures were optimised with a 1×10^{-10} Ry energy uncertainty.The 24×24×24 k-point mesh was used to model the first Brillouin zone. We used the Thermo-pw algorithm to calculate the density of phonon states and the phonon dispersion curves using a 16×16×16 q-point grid.

Results and Discussion

The X$_2$YZ chemical formula full Heusler alloys have an L2$_1$ crystal structure with a space group of (225). The Wyckoff positions of the X, Y, and Z elements are (0, 0, 0), (1/2, 1/2, 1/2), (1/4, 1/4, 1/4), and (3/4, 3/4, 3/4), in that order. An inverted Heusler composition is created when the placements of the X and Y elements in the Full Heusler composition are switched. The XA structure and space group of inverse Heusler compounds are 216. Fig 1 showed the crystal structures of the relaxed Li$_2$CoB Heusler compounds
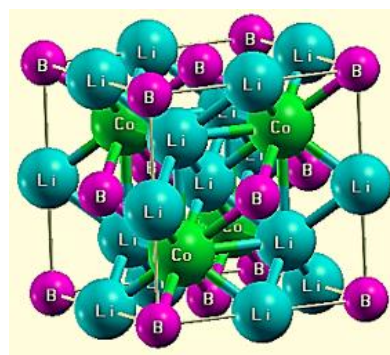
Fig.1: The relaxed inverse Heusler structures of a Li$_2$CoB

In order to examine the dynamic stability of Li2CoB Heusler alloys, we computed phonon density of states and phonon scattering curves. Heusler alloys feature twelve phonon modes per wave vector, consisting of three phonon modes, three acoustic modes, and nine optical modes because each unit cell of the alloy has four atoms. The phonon density and phonon scattering curves for the Li$_2$CoB Heusler alloy are displayed in Fig 2.Positive phonon frequencies are seen in the Brillouin zone of the phonon spectra obtained for the Li$_2$CoB Heusler alloy in all directions, suggesting that these compounds are dynamically stable in the inverse Heusler structure.

22nd Iranian Chemistry Congress (ICC22)
Iranian Research Organization for Science and
Technology (IROST)
13-15 May 2024

03231-97589

IROST
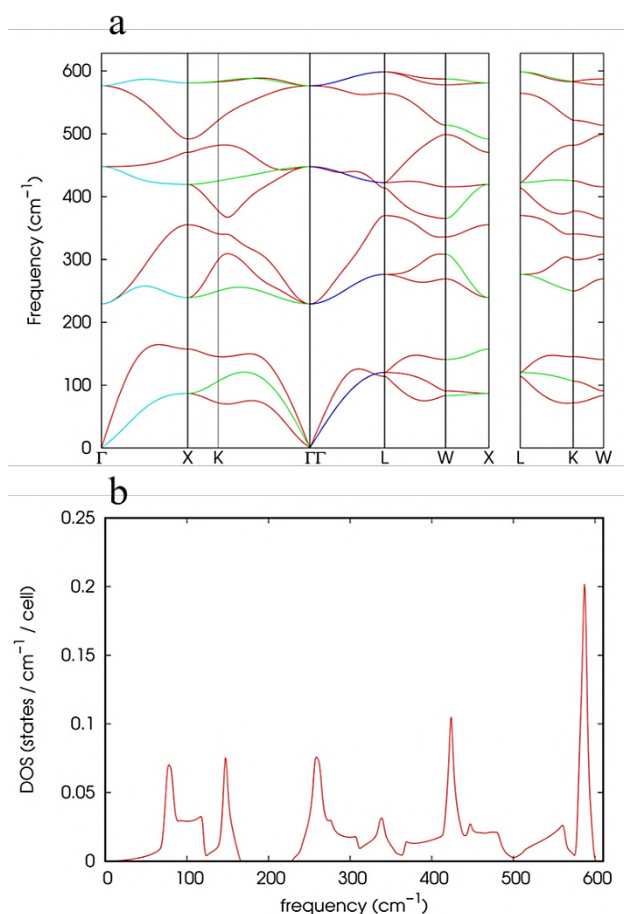
Fig.2: a calculated phonon dispersion curve and **b** phonon density of states of Li₂CoB Full Heusler alloy.

Following that, the GGA approximation was used to compute the electronic band structure of the intermetallic Li₂CoB alloy as well as the high symmetry directions in the energy range of -10 eV to 10 eV. The results are displayed in Fig 3. High-symmetry points (Γ→X→K→Γ→L→W→X) are taken into account for the band structure computation, and the Fermi energy level is placed at 0.0 eV. As can be seen in the band structure figure, Co and B atoms contribute the most near the Fermi level. The conduction and valence bands overlap near the Fermi surface, so the Li₂CoB alloy is metallic in nature.
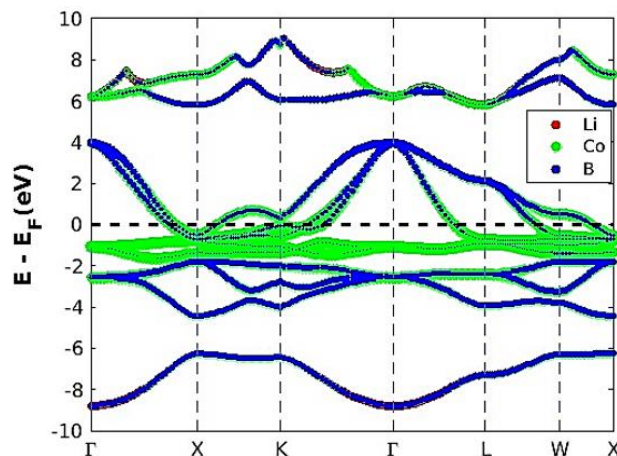
Fig.3: Electronic band structure of the Li₂CoB Full Heusler alloy.

Conclusions

The obtained results indicate the dynamic stability of Li₂CoB Full Heusler alloy and the conductive qualities of this composition as indicated by the band structure..

References

[1] Bouadi, A., et al., *A new semiconducting full Heusler Li2BeX (X= Si, Ge and Sn): first-principles phonon and Boltzmann calculations.* Physica Scripta, 2022. **97**(10): p. 105710.

[2] Bhat, T.M., M. Nabi, and D.C. Gupta, *Structural, elastic, thermodynamic and thermoelectric properties of Fe2TiSn Heusler alloy: high pressure study.* Results in Physics, 2019. **12**: p. 15-20.

[3] Pakizeh, E., J. Jalilian, and M. Mohammadi, *Electronic, optical and thermoelectric properties of Fe 2 ZrP compound determined via first-principles calculations.* RSC advances, 2019. **9**(44): p. 25900-25911.

22nd Iranian Chemistry Congress (ICC22)
Iranian Research Organization for Science and Technology (IROST)
13-15 May 2024

03231-97589

IROST

Oxidative addition of MeI to a new Pt(II) complex: kinetic and theoretical elucidation

Sana Yarahmadi, Hamid R. Shahsavari *

Corresponding Author E-mail: shahsavari@iasbs.ac.ir

Department of Chemistry, Faculty of Chemistry, Institute for Advanced Studies in Basic Sciences (IASBS), Zanjan, Iran.

Abstract: Oxidative addition (OA) of MeI to Pt(II) complex [PtAr$_2$(bpyNO)], **1**, Ar = p-MeC$_6$H$_4$, bpyNO = 5-methyl-[2,2'-bipyrimidine]-1-N-oxide, afforded the new Pt(IV) complexes [PtAr$_2$MeI(bpyNO)], **2**, as a mixture of $trans$ and cis isomers. This reaction was kinetically explored using UV-Vis spectroscopy. The OA process took place through a classical S$_N$2 attack of the Pt(II) center on the MeI reagent, according to the kinetic data.

Keywords: Platinum, Oxidative addition, Kinetic, Theoretical calculations.

Introduction

The oxidative addition (OA) reaction plays a vital role in industry, and it is one of the most critical reactions in the organometallic research area. Since platinum contains a wide range of stable complexes in organometallic chemistry, the OA in square-planar Pt(II) compounds has been further investigated in recent years [1]. The kinetics of Pt(II) complexes containing N^N [2], N^O (1,10-phenanthroline N-oxide), [3] and rollover C^N cyclometalated ligands (2,2'-bipyridine N-oxide) [4] with different reagents such as MeI, EtI, PhCH$_2$Br, $etc.$ were studied. Additionally, the mechanisms of the OA reactions on these platinum complexes were explored.

Experimental Section

A new Pt(II) complex [PtAr$_2$(bpyNO)], **1**, Ar = p-MeC$_6$H$_4$, bpyNO = 5-methyl-[2,2'-bipyrimidine]-1-N-oxide, was synthesized by the reaction of [PtAr$_2$(SMe$_2$)$_2$], **A**, and bpyNO, **B**, for 6 hours at room temperature. The dark red precipitate was cleaned with n-hexane and separated (Scheme 1).

An excess amount of MeI reagent was added to Pt(II) complex **1** to give a mixture of Pt(IV) complexes [PtAr$_2$MeI(bpyNO)], **2**, as $trans$ and cis isomers. For this purpose, 24 hours of stirring the reaction mixture were followed, and the yellow precipitate was washed with n-hexane and vacuum dried.
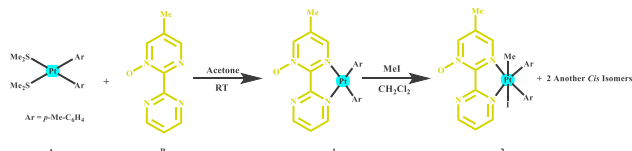
Scheme 1: Synthetic route for the preparation of the Pt(II) and Pt(IV) complexes.

Results and Discussion

Using NMR spectroscopy, all the complexes were identified. The aliphatic region of ^{1}H NMR and ^{195}Pt{^{1}H} NMR spectra of **2** are shown in Figure 1.
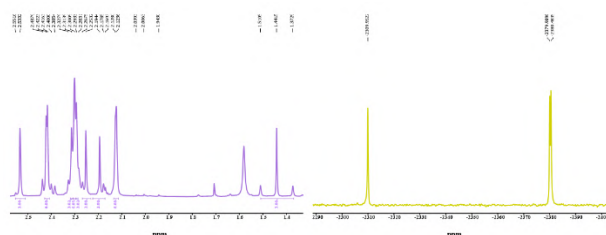
Fig. 1: Aliphatic region of ^{1}H NMR (left) and ^{195}Pt{^{1}H} NMR (right) spectra of **2** in CDCl$_3$.

The kinetic of this reaction was studied using UV-Vis spectroscopy at different temperatures, and a S$_N$2 mechanism was suggested (Figure 2). The reaction followed second-order kinetics: rate = k_2[**1**][MeI]. The activation parameters have been determined, and large negative values for ΔS‡ were obtained.
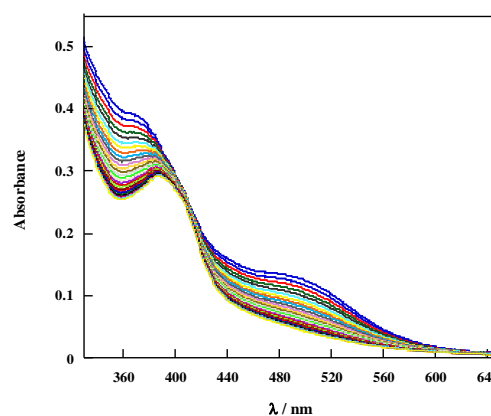
Fig. 2: The changes in the UV-Visible spectrum of **1** with MeI in CH$_2$Cl$_2$ at 25 °C.

The results were also supported by theoretical calculations. The computational investigations were used to determine the geometry of the species involved in the suggested mechanism and energy barriers (Fig. 3).

22ⁿᵈ Iranian Chemistry Congress (ICC22)
Iranian Research Organization for Science and
Technology (IROST)
13-15 May 2024

03231-97589

IROST
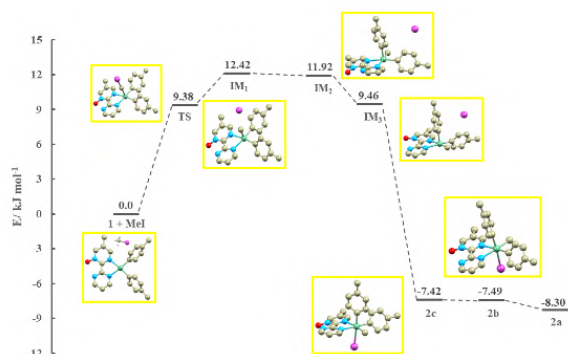
Fig. 3: Energy profile for OA of MeI to **1**, giving **2(a-c)** in CH_2Cl_2. DFT-optimized geometrical structures of **1**, the transition state, TS, and the intermediates are also shown.

Conclusions

In the current study, it has been reported on the synthesis and characterization of Pt(II) and Pt(IV) complexes containing a N^N donor ligand. The Pt(IV) complexes [PtAr₂MeI(bpyNO)], **2** (as a mixture of *trans* (**2a**) and *cis* (**2b** and **2c**) isomers), are produced. The OA reaction of methyl iodide with **1** follows second-order kinetics, which is corroborated by DFT calculations. A substantial negative value for the activation entropy, $\Delta S^{\neq}$, is compatible with an S_N2-type mechanism.

References

[1] Labinger, J. A. (2015). Tutorial on oxidative addition. *Organometallics*, *34*(20), 4784-4795.

[2] Aseman, M. D., Rashidi, M., Nabavizadeh, S. M., & Puddephatt, R. J. (2013). Secondary kinetic isotope effects in oxidative addition of benzyl bromide to dimethylplatinum (II) complexes. *Organometallics*, *32*(9), 2593-2598.

[3] Moustafa, M. E., Boyle, P. D., & Puddephatt, R. J. (2014). Carbon–hydrogen versus nitrogen–oxygen bond activation in reactions of N-oxide derivatives of 2, 2'-bipyridine and 1, 10-phenanthroline with a dimethylplatinum (II) complex. *Organometallics*, *33*(19), 5402-5413

[4] Nikravesh, M., Abbasi, A., & Shahsavari, H. R. (2021). Oxidative Addition of a Hypervalent Iodine Compound to Cycloplatinated (II) Complexes for the CO Bond Construction: Effect of Cyclometalated Ligands. *Inorganic Chemistry*, *60*(24), 18822-18831.

Safe treatment of triethylaluminium waste: Extraction and characterization of aluminum hydroxide as a byproduct

M. Bani Jamali, F. Tavakoli*, M. Dehghani, M. Babaei

Corresponding Author E-mail: F.tavakoli@npc-rt.ir, F.tavakoli27@gmail.com

Petrochemical Research & Technology Company, PO box 38671413113, Arak, Iran.

Abstract: This study discloses a hydrolysis method for safely treating triethylaluminium waste in a safe condition. whereby, we investigated the remaining solid and released gas during the hydrolysis via H_2O. The precipitate was characterized by using FT-IR, XRD, TGA-DSC, FESEM, and BET techniques. Based on the obtained results, it was revealed that the precipitate is a pure aluminum hydroxide. This method provided a simple, quick, and safe way to treat TEAL waste without the explosion hazards and environmental problems.

Keywords: Triethylaluminium, TEAL waste, safe treatment, hydrolysis, aluminum hydroxide.

Introduction

Today the use of triethylaluminium (TEAL) has been significantly enhanced as a highly efficient catalyst and co-catalyst in in petrochemical industry, especially for the production of polyolefins [1]. TEAL also plays the crucial role of reducing agent or precursor in the production of organic and organic-metallic compounds, especially organoaluminium compounds [2]. Whereas, TEAL is susceptible to air, water, and even humidity. If it is exposed to air or reacts with water may catch fire or explode. Besides, due to its easy ignition, it is eligible to be used as a rocket engine ignitor [3]. Notwithstanding the above special properties of TEAL, using TEAL is particularly challenging, so it can be accompanied by high dangers. To date, the TEAL waste is still a big issue for the industry, due to its high activity, flammability, harsh maintenance conditions, and storage risks. The TEAL that was used in this work, was proudly, produced by our team in Petrochemical Research & Technology Company/Arak Center. Indeed, TEAL waste is a serious threat to human health and the environment. In this study, we tried to introduce a method for the safe treatment of TEAL waste by using hydrolysis in the presence of the least amount of water. As well as, we investigated and characterized the precipitates obtained during the treatment process as a useable and beneficial byproduct.

Experimental Section

The hydrolysis of TEAL waste was carried out in a glass reactor equipped with a dropping funnel, a stirrer, and two gas outlets connected to a nitrogen tube and gas sampling bag. The hydrolysis reaction was performed under two different rates and at four TEAl: H_2O ratios of 500: 25, 500: 50, 500: 150, and 500: 800. This reaction was done without the need for the glove box and hydrocarbonic solvent. Nevertheless, if the concentration of TEAL waste is more than 10% it is necessary to dilute it whit white oil, and it can be prevented from intense reacting with air and water. The final suspension was centrifuged and the precipitates were collected and dried in ambient conditions.

Results and Discussion

The precipitate was characterized using FT-IR, XRD, TGA-DSC, FESEM, and BET techniques. The X-ray pattern displayed the characteristic peaks similar to pure aluminum hydroxide at 2θ of 18.4°, 20.3°, 27.8°, 40.6° and 53.2° corresponds to (001), (110), (111), (201), and (202) planes respectively [4]. As shown, the precipitate is highly crystalline in nature and matched by the bayerite polymorph of Al $(OH)_3$. Also, the morphological investigations using FESEM, it was revealed that the crystal structure is very regular and the particles have an average diameter about of 161 nm. The results of X-Ray diffraction and FESEM analysis were implied in full agreement with pure Al $(OH)_3$ in terms of crystalline structure and surface morphology analysis. TGA-DSC showed a reduced total sample mass of 56.21 % and an intense endothermic peak at 270.08°C as the transformation of Al $(OH)_3$ to AlO (OH) (boehmite) with the absorbed energy of 491.97 J/g. At the temperature of 540.74°C was the phase change of boehmite to γ-Al_2O_3 with an absorbed energy of 23.65 J/g. Then, at the temperature above 720°C there was no mass reduction, which meant it formed a stable phase of Al_2O_3 [5].The results of TGA-DSC revealed once more that the precipitate is pure aluminum hydroxide. On the other hand, the gaseous products were studied by GC chromatography analysis; it was found that it is ethane gas with high purity (over 98%). With regard to the results obtained from precipitate and exhaust gas, it seems that these results are completely consistent with the chemically

22nd Iranian Chemistry Congress (ICC22)
Iranian Research Organization for Science and
Technology (IROST)
13-15 May 2024

03231-97589

IROST

balanced equation. Additionally, for investigation of the extracted water from not producing harmful waste standpoint the TDS and COD analysis were done. In the case of the 25:500 ratio, the amount of remaining water is minimized and there is no environmental concern. Therefore, it is clear that this study is a step forward in the safe treatment of TEAL waste in petrochemical industries and any industries that use this important, critical, and sensitive material.
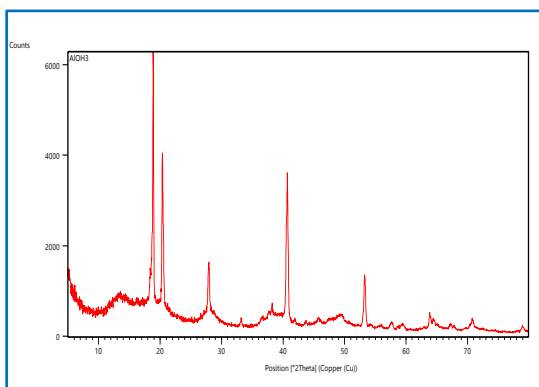
Fig.1. The XRD pattern of precipitate
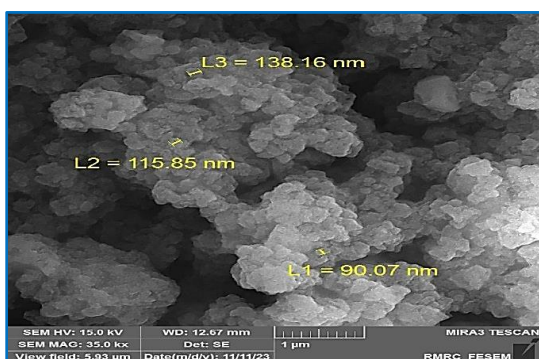
Fig.2. The FESEM image of precipitate
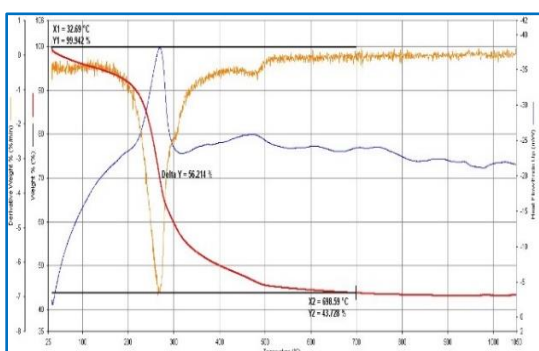
Fig.3. The TGA/DTA diagram of precipitate
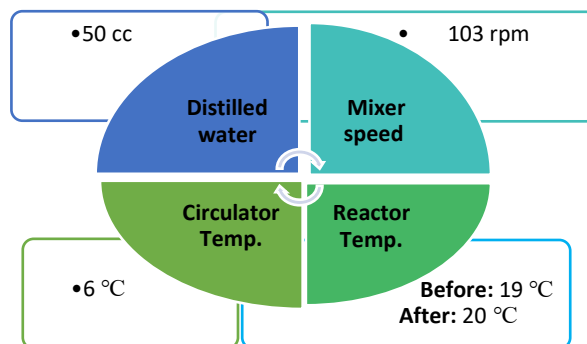
Fig.4: The hydrolysis reaction conditions

Conclusions

This study introduced a safe treatment method which is a simple, quick, and precise way to treat TEAL waste without the explosion hazards and environmental problems. As a result, it has been found that the remaining precipitate is a pure and beneficial byproduct, which can be recycled, marketed, and sold. It is noteworthy that the precipitates can easily be separated and used without the need for special washing. It is known that this method follows green chemistry because produces a useable and beneficial byproduct from discarded TEAL without considerable wastewater.

References

[1] Cotton, F. A., Wilkinson, G., Murillo, C. A., Bochmann, M. (1999). Advanced inorganic chemistry. John Wiley & Sons.

[2] Anderson, A. R. (1963). Aluminum, organometallic compounds. In A. Standen (Ed.) (2nd ed.). Encyclopedia of chemical technology, 2, 26e41. New York: John Wiley & Sons.

[3] Sato, Y., Okada, K., Akiyoshi, M., Tokudome, K., & Matsunaga, T. (2011). Reaction hazards of triethyl aluminium under closed conditions. Journal of Loss Prevention in the Process Industries, 24(5), 656-661.

[4] Su, S.Q., Yang, J., Ma, H.W., Jiang. (2011). Preparation of ultrafine aluminium hydroxide from coal fly ash by alkali dissolution process. Integrated Ferroelectrics, 128(1), 155-162.

[5] Liu, S., Chen, C., Liu, Q., Zhuo, Y., Yuan, D., Dai, Z. (2015). Two-dimensional porous γ-AlOOH and γ-Al_2O_3 nanosheets: hydrothermal synthesis, formation mechanism and catalytic performance. RSC Advances, 5(88), 71728-71734.

DNA/BSA binding study of a new cyclopalladated (II) complex

Sedigheh Abedanzadeh*, Mina Navidi

Corresponding Author E-mail: abedanzadeh@khu.ac.ir

Faculty of Chemistry, Kharazmi University, Tehran 15719-14911, Iran.

Abstract: In the current study, a new CN-cyclometalated Pd (II) complex derived from 2-phenylpyridine was synthesized. According to the important role of bioactive fragments in the structure of potential antitumor metal-based agents, an approach was designed to prepare a cyclometalated Pd (II) complex bearing a biological active ligand. After identification, the interaction of complex with DNA and protein BSA, as the important biological targets, were evaluated via UV-Vis and fluorescence spectroscopic methods.

Keywords: Organopalladium (II) Complex; anticancer; DNA-binding; Protein-binding.

Introduction

Cancer has the highest percentage of mortality rates in the world. Among the popular anticancer drugs, clinically approved Cisplatin with formula *cis*-[Pt(NH$_3$)$_2$Cl$_2$] has gained great attention and still been used world widely in treating a range of cancer types including testicular, ovarian, bladder, head and neck, lung and cervical cancer. However, there are problems associated with the use of Cisplatin, including severe side effects due to the absence of selectivity toward cancer cells and acquired cancer cell resistance. [1]

Due to the many similarities between the coordination chemistry of Pt(II) and Pd(II), there is considerable interest in studying Pd(II) complexes as anticancer drugs. The ligand-exchange rates of Pd(II) complexes are faster than those of their Pt(II) analogues, and they have better solubility than Pt(II) complexes. Therefore, Pd(II) complexes seems to be promising candidates as chemotherapeutic drugs which should be biologically studied. [2]

Chelating ligands gives high thermodynamic stability and kinetic inertness to Pd(II) complexes helping them to maintain their structural integrity in contact with different attacks in biological media until reaching the main target. Owing to their promising physicochemical characteristics and variable structural properties, cyclometalated complexes have gained widespread popularity in biological applications. [2]

Using bioactive fragments in the coordination sphere of metal-based agents, is promising to design a new antitumor agent. α- Amino acids are biologically fundamental compounds with particular significance due to their critical roles in living systems including neurotransmitters, transport, synthesis, and applications, such as biochemical probes, alternate enzyme substrates, and enzyme inhibitors. α-Amino acids induce invaluable and versatile coordination chemistry according to their structural and spatial characteristics. According to their versatile physicochemical properties, they have been considered in interdisciplinary research fields reflected in their diverse applications. [3]

In this research, a new cyclometalated Pd (II) complex was synthesized and characterized through FTIR and NMR spectroscopies, bearing an amino acid as a biological active ligand. Afterwards, the DNA and protein BSA-binding properties of CN-cyclopalladated (II) complex bearing amino acid have been investigated through UV-Vis and fluorescence spectroscopic methods.

Experimental Section

Synthesis: To the solution of the dimeric CN-cyclopalladated (II) complex of 2-phenypyridine (0.040 g, 0.062 mmol) in MeOH (60 mL), 0.124 mmol amino acid was added and the solution was refluxed for 4 hours at 70 °C.

Binding study: CT-DNA and protein BSA stock solutions were prepared using Deionized water. Buffer solution containing 5 mM Tris-HCl and 50 mM NaCl, was adjusted to pH 7.2. The DNA concentration per nucleotide was determined by the UV absorbance at 260 nm using ε = 6600 M^{-1} cm^{-1}.

Results and Discussion

Synthesis: From the bridge cleavage reaction of a dinuclear cyclometalated Pd (II) complex with amino acid, new cyclometalated Pd (II) complex was synthesized and characterized through FTIR and NMR spectroscopies.

Binding study: The electronic absorption spectra of the cyclometalated Pd (II) complex in the absence and presence of CT-DNA are shown in Fig. 1 which evidently indicated π-π* and n-π* transitions types. The UV-Vis absorption spectra were significantly affected by increasing the DNA content, confirming the DNA-binding of complex and formation of the new complex adduct with double-helical CT-DNA. Keeping the concentration of

22nd Iranian Chemistry Congress (ICC22)
Iranian Research Organization for Science and Technology (IROST)
03231-97589
13-15 May 2024

IROST

complex constant, the absorption maxima of complex exhibited significant hypochromism by increasing DNA content, and no obvious absorption band shift phenomenon was observed. The results suggests that the complex is likely bound to DNA via groove binding mode.
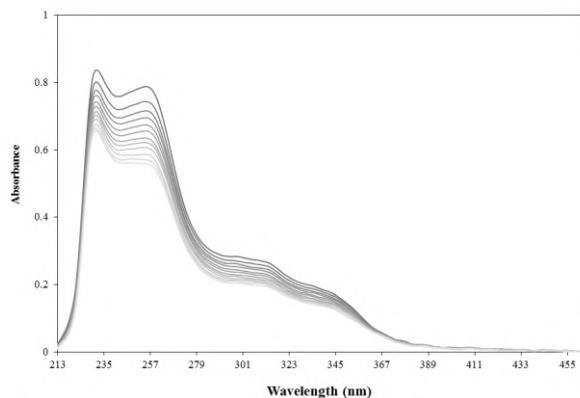
Fig.1: Electronic absorption spectrum of cyclometalated Pd (II) complex (50×10^{-6} M) in buffer solution (5 mM Tris-HCl/50 mM NaCl at pH 7.2) via increasing amounts of DNA ($0\text{-}10\times10^{-6}$ M).

As can be observed in Figure 3, a strong absorption peak at 220-240 nm and a weak absorption peak at 278 nm are attributed to the $\pi\rightarrow\pi^*$ transitions originating from the polypeptide content and the aromatic amino acids (tryptophan, tyrosine, and phenylalanine) in the backbone structure of BSA, respectively. By increasing the amounts of cyclometalated Pd (II) complex, the main BSA skeleton absorption decreased with subtle changes of the maximum absorption to longer wavelengths which indicates that the interaction of the cyclometalated Pd (II) complex with BSA may cause some conformational changes in the structure of BSA. The intensity of the BSA absorption peak at 278 nm also gradually decreased. However, no significant shift in the maximum wavelength was observed.
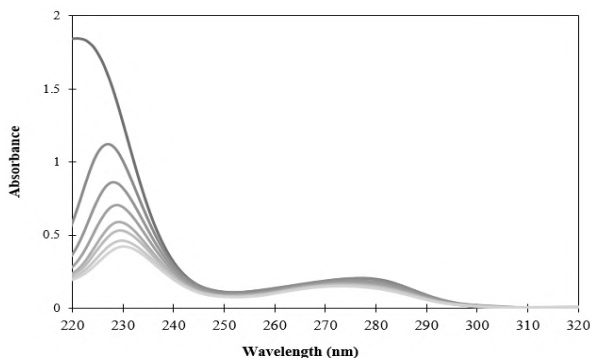
Fig.2: Electronic absorption spectrum of BSA (5×10^{-6} M) in buffer solution (5 mM Tris-HCl/50 mM NaCl at pH 7.2) with increasing amounts of cyclometalated Pd (II) complex (0-10×10^{-6} M)

Conclusions

A new organometallic Pd (II) complex was successfully synthesized bearing 2-phenylpyridine as a common CN-cyclomelating ligand along with amino acid in probably NO-chelating binding mode. ^{1}HNMR spectroscopy and FTIR technique, were used for characterization of synthesized cyclometalated Pd (II) complex. The interaction ability of cyclometalated Pd (II) complex with DNA and protein BSA as the main biomacromolecular targets were monitored by UV-Vis and fluorescence spectroscopies. Based on the results, cyclometalated Pd (II) complex bound to DNA via groove binding mechanism. In addition, the observations revealed that the microenvironment polarity around the amino acid residues of BSA has been affected through the interaction with cyclometalated Pd (II) complex. This work illustrates that cyclometalated Pd (II) complex bearing amino acid can be a promising candidate as chemotherapy drug which needs to be studied further.

References

[1] Hartinger, C. G., & Dyson, P. J. (2009). Bioorganometallic chemistry—from teaching paradigms to medicinal applications. Chemical Society Reviews, 38(2), 391-401.

[2] Scattolin, T., Voloshkin, V. A., Visentin, F., & Nolan, S. P. (2021). A critical review of palladium organometallic anticancer agents. Cell Reports Physical Science, 2(6).

[3] Abedanzadeh, S., Karami, K., Rahimi, M., Edalati, M., Abedanzadeh, M., mohammad Tamaddon, A., ... & Lyczko, K. (2020). Potent cyclometallated Pd (II) antitumor complexes bearing α-amino acids: synthesis, structural characterization, DNA/BSA binding, cytotoxicity and molecular dynamics simulation. Dalton Transactions, 49(42), 14891-14907.

Investigation of the CO_2 reduction reaction employing Cr single metal catalyst embedded onto g-C_3N_4 (heptazine).

Azadeh Masiha [a], Adel Reisi-Vanani[*,a,b]

Corresponding Author E-mail : areisi@kashanu.ac.ir; azadeh.masiha@gmail.com

[a] Department of Physical Chemistry, University of Kashan, Kashan, Iran.

[b] Institute of Nano Science and Nano Technology, University of Kashan, Kashan, Iran.

Abstract: The study explores mechanisms of CO_2 hydrogenation (Route A and B) with Cr single-atom catalyst on g-C_3N_4 using DFT-D2 calculations. In Route A, H atom separation is the rate-determining step with barrier energy of 1.64 eV, while in Route B, it's formic acid formation with barrier energy about 2.73 eV. Chromium enhances this reaction in Route A, providing insights for designing g-C_3N_4-based catalysts for CO_2 reduction and elimination.

Keywords: Graphitic carbon nitride; g-C_3N_4; CO_2 reduction reaction.

Introduction

Global warming was increased by greenhouse gases emission, particularly CO_2, and efforts has been started to adjust climate changes by CO_2 deletion. Traditional methods like carbon capture and storage (CCS) have limitations, leading to the development of carbon capture and utilization technology (CCU) [1, 2]. This study focuses on Cr/g-C_3N_4 single atom catalyst for CO_2 reduction to formic acid using DFT calculations, showing Cr/g-C_3N_4 performance and offering insights for converting CO_2 into valuable fuels.

Computational methods

The study employed spin-polarized DFT calculations with the DMol^3 module [3], utilizing the PBE functional for exchange and correlation energies within the generalized gradient approximation. The DNP basis set and DFT-D2 method corrected dispersive interactions. Simulations used a 2×2 g-C_3N_4 supercell with a 5×5×1 Monkhorst-Pack k-point mesh. Transition state locations were determined using LST/QST methods [4], confirmed by frequency calculations. Metal atom binding energy (E_b) on g-C_3N_4, adsorption energy (E_{ads}), and activation energy (E_a) for each step were calculated.

Results and Discussion

1) Adsorption of CO_2 and H_2 on the Cr/g-C_3N_4

The primary focus is CO_2 hydrogenation on Cr/g-C_3N_4 surface, investigating stable adsorption sites for CO_2 and H_2. Adsorption energies and Hirshfeld charges were calculated for individual H_2, CO_2, and co-adsorbed molecules. Results show slight stability of CO_2 and H_2 adsored on the Cr/g-C_3N_4. The co-adsorption energies on Cr/g-C_3N_4 surpass those of the previous two modes, providing a foundation for further assessing CO_2 hydrogenation into formic acid.

Table1: Adsorption energy (E_{ads} (eV)) and Hirshfeld charge of H_2 and CO_2 onto Cr/g-C_3N_4

Surface	Adsorbate	Eads (eV)	charge
Cr/g-C_3N_4	H_2	-0.19	0.010
	CO_2	-0.30	0.046
	$H_2 + CO_2$	-0.45	0.004

2) CO_2 hydrogenation onto Cr/g-C_3N_4 and without nitrogen participation (Route A) and with nitrogen participation (Route B)

The study evaluates CO_2 hydrogenation to formic acid via co-adsorption of CO_2 and H_2 in two paths: (A) without, and (B) with nitrogen atom participation in Cr/g-C_3N_4 . Focus is on the formate intermediate. For this pathway, the optimized structures of the initial state (IS), intermediate (IM), transition states (TS) and final state (FS) are shown in Fig. 1. The H_2 molecule bond length increases, leading to the formation of a non-stable formate (HCOO*) intermediate in TS1, with an energy barrier of 1.64 eV and an imaginary frequency of 1242.27 cm^{-1}. In the subsequent step, the second hydrogen atom attaches to the formate's oxygen, forming HCOOH on Cr/g-C_3N_4. Releasing HCOOH from the substrate requires about 0.30 eV, indicating the formate intermediate formation as the rate-determining step with an energy barrier of 1.64 eV.

Fig. 2 depicts the CO_2 hydrogenation on Cr/g-C_3N_4. Initially, CO_2 approaches Cr metal with one H atom moving towards Cr and the other to the nearest N atom. The distance between hydrogen atoms increases to 1.0 Å with a barrier energy of 0.72 eV and imaginary frequency of –928.88 cm^{-1}. TS2 transitions to IM1, fully splitting H_2, and forming HCOOH on Cr/g-C_3N_4. The carbon atom of CO_2 approaches the H atom on Cr in TS2 with a barrier energy of 0.41 eV and imaginary frequency of –180.81 cm^{-1}, creating formate intermediate (IM2). The H atom on N

22nd Iranian Chemistry Congress (ICC22)
Iranian Research Organization for Science and Technology (IROST)
13-15 May 2024

03231-97589

ISC

IROST

approaches oxygen of HCOO in the next step, with a barrier energy of 2.73 eV and imaginary frequency of -979.02 cm^{-1}. Formic acid is formed on Cr/g-C$_3$N$_4$, requiring -0.23 eV for HCOOH release. The rate-determining step is formic acid formation.
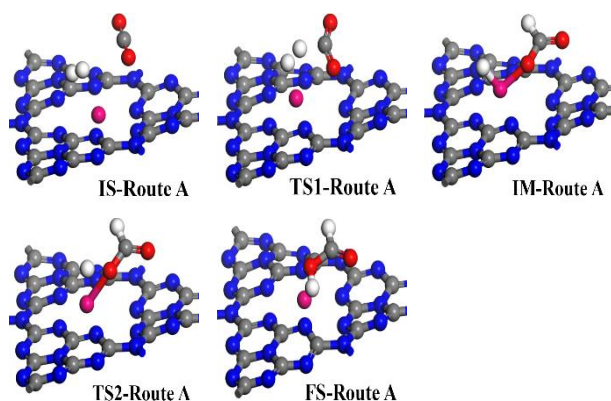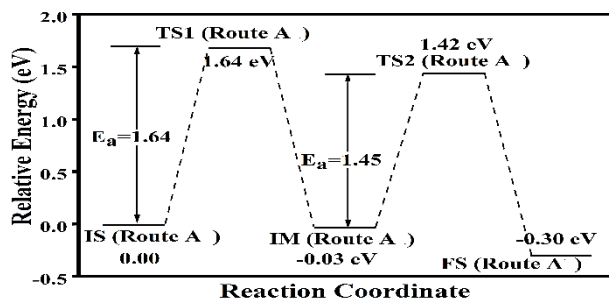
Fig.1: Schematic reaction path of CO$_2$ hydrogenation to formic acid that shows IS, TSs, IM, and FS geometries for Cr/g-C$_3$N$_4$ surface through co-adsorbed CO$_2$ and H$_2$ molecules (Route A)
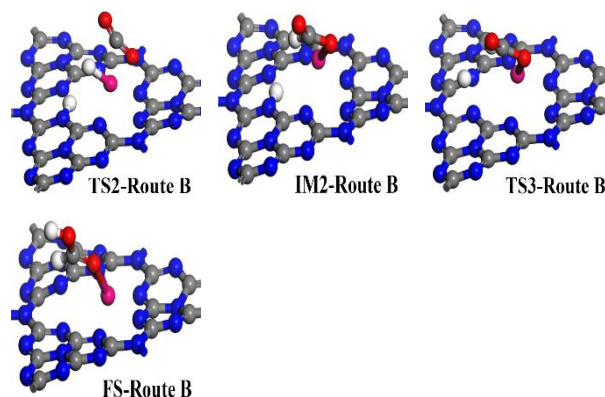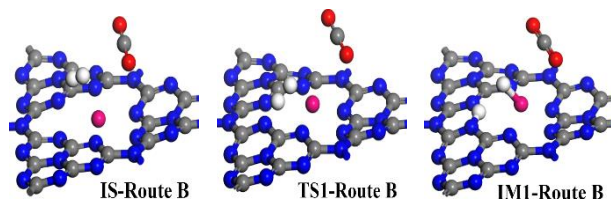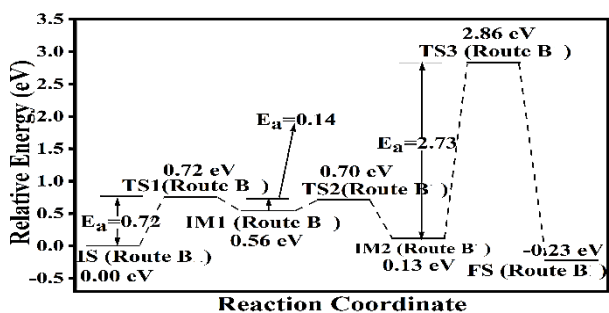
Fig.2: Schematic reaction path of CO$_2$ hydrogenation to formic acid through co-adsorbed CO$_2$ and H$_2$ gases in presence of substrate nitrogen, which shows initial state, transition states and final state geometry on Cr/g-C$_3$N$_4$ surface. (Route B)

Conclusions

This DFT study investigates CO$_2$ conversion to formic acid on Cr/g-C$_3$N$_4$ surfaces as a single-atom catalyst. Two proposed mechanisms, with and without N atom participation, demonstrate that N atom involvement facilitates formic acid formation. These findings provide guidance for designing g-C$_3$N$_4$-based catalysts for CO$_2$ reduction and chemical production.

References

[1] Park, J.H., et al. (2022). Review of recent technologies for transforming carbon dioxide to carbon materials. Chemical Engineering Journal, 427, 130980. https://doi.org/10.1016/j.cej.2021.130980.

[2] Sanz-Cobena, A., et al. (2017). Strategies for greenhouse gas emissions mitigation in Mediterranean agriculture: A review. Agriculture, ecosystems & environment, 238, 5-24. https://doi.org/10.1016/j.agee.2016.09.038.

[3] Darvishnejad, M.H. and A. Reisi-Vanani. (2020). Multiple CO$_2$ capture in pristine and Sr-decorated graphyne: A DFT-D3 and AIMD study. Computational Materials Science, 176, 109539.

https://doi.org/10.1016/j.commatsci.2020.109539.

[4] Govind, N., et al. (2003). A generalized synchronous transit method for transition state location. Computational materials science, **28**(2), 250-258. https://doi.org/10.1016/S0927-0256(03)00111-3.

Dye Removal by Mixed Matrix Membrane Fabricated by Hydrogel and Covalent-Organic Framework

Fahimeh Soltani, Simin Asadabadi*

Corresponding Author E-mail: s.asadabadi@basu.ac.ir

Department of Applied Chemistry, Faculty of Chemistry and Petroleum Sciences, Bu-Ali Sina University, Hamedan, Iran.

Abstract: The aim of this research work was to remove Methyl Violet 2B from aqueous solution by synthesis of polyethersulfone/graphene oxide-chitosan containing thin-film layer of covalent-organic framework. In this regard, mixed matrix membrane containing graphene oxide and chitosan were fabricated and by forming thin-film composite, 98% dye rejection was obtained.

Keywords: Mixed matrix membrane; Water treatment; Thin-film composite; Polyethersulfone; Graphene oxide; Chitosan; Dye Removal; Covalent-organic framework

Introduction

Freshwater resources serve as a crucial foundation for human life and social development. The dramatic global industrialization and rapid growth of the world's population have exacerbated consumption of freshwater and the discharge of large quantities of wastewater, resulting in an increasingly serious problem of freshwater scarcity. Membrane technology, featuring high separation performance and relatively low cost stands out among several technologies as an essential process for efficient recovery of freshwater [1].

Incorporation of hydrogel compatible nanoparticle such as graphene oxide (GO) nanosheets in hydrogel polymeric network not only lead to mechanical reinforcement, but also due to presence of a large surface area with abundant oxygen containing reactive groups, could increase hydrogel adsorption capacity. Blending some bio-based nanocomposite hydrogels with polymers was utilized to prepare composite membranes with improved separation properties in treatment of heavy metals and dyes wastewater. Chitosan (CS) is a linear cationic polysaccharide, the second most nature accessible biopolymer that produced commercially by deacetylation of chitin. CS-based hydrogels applicability in composite membranes for the elimination of dyes from different effluents is related to existence of multiple amino (NH_2) and hydroxyl (OH) reactive functional groups. The combination of CS-based hydrogels with suitable substances such as such as GO nanomaterials have found remarkable attention in order to improved their adsorption performances and mechanical resistance [2].

Covalent organic frameworks (COFs) are a class of crystalline porous 2D or 3D polymer networks linked by covalent bonds. Their structural merits, such as pre-designable structures, tunable functionalities and tunable pore sizes typically in the range of 0.7–5.0 nm, offer them great application potential in separation [3]. The aim of this study was to study the effect of GO-CH hydrogels and thin layer of COF on the polyethersulfone substrate in order to examine the dye removal and flux.

Experimental Section

At first, a mixture containing defined amount of PES, PVP and GO-CH were mixed thoroughly in DMac solvent. Then, the membrane (M_2) were fabricated using a non-solvent induced phase separation method employing a hand-casting knife. Finally, the thin-film composite was obtained using monomers of COF (M_3). For controlling, two membranes of PES (M_0), PES+PVP (M_1) were fabricated too. The membranes were placed into the cross-flow setup and rejection of methyl violet 2B (MV 2B) was monitored as the performance of the membranes at pressure of 4 bar. The rejection percent was calculated according the following equation [4]:

$$Re\% = \frac{C_0 - C_{res}}{C_0} \times 100\% \tag{1}$$

in which, C_0 and C_{res} were initial and residual concentration of MV 2B, respectively.

In addition, for examine the performance of membranes, pure water flux was calculated by the following equation:

$$Flux = \frac{m}{A\Delta t} \tag{2}$$

where, m was the mass of permeate, A was the effective surface area and Δt was the time for collecting permeate.

Results and Discussion

The morphology of the synthesized membrane was evaluated with FE-SEM images taken from the cross section and surface of membrane and the results are shown in Fig. 1.
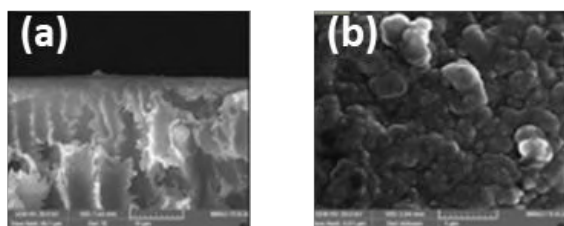
Fig.1: FE-SEM images (a) cross-section, (b) surface of the fabricated membrane M_3

It can be seen in Fig. 1 that the membrane has an asymmetric structure consists of an upper dense layer with small finger holes and a spongy porous. The GO sheets can be detected on the surface of the membrane.

Fig. 2 presents MV 2B rejection by M_0, M_1, M_2 and M_3 membranes. The two first ones were not able to romve dye molecules from aqueous solution effectively. However, dye was rejected by M_2 about 81.06% due to intercations between molecules of MV 2B and GO-CS functional groups. The presence of COF layer on the top surface of M_2 caused to rejection of 98.22%. This thin-film decresed the pore size and the rejection inclined.
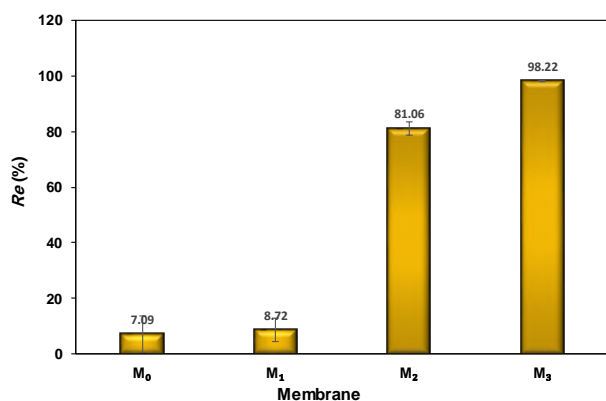
Fig.2: MV 2B rejection by prepared membranes

As can be seen in Fig. 3, the M_0 had a little pure water flux, and its value increased when PVP was added to the polymer solution. It was due to the pore formation. By adding GO-CS (M_2), the flux suprisingly inclined because of hydrophilic nature of GO-CS [2]. However, the presence of COF (M_3) caused a slight decrease in the flux since an uniform layer was created on the top layer of membrane.
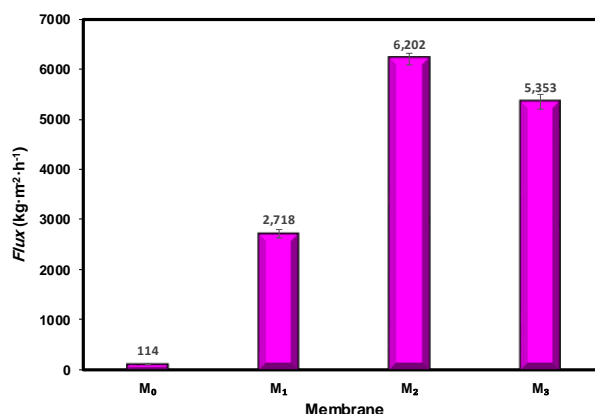
Fig.3: Flux for M_0, M_1, M_2 and M_3 membranes

Conclusions

Modifing polyethersulfone substrate by graphene oxide-chitosan (GO-CS) had significant effect on the dye rejection and flux. It was due to the interaction between dye molecules and GO-CS composite. The performance was better when a thin film of covalent-organic framework was fabricated on the surface of the membranes and the dye removal reached 98.22%.

References

[1] Feng, H., Yuan, K., Liu, Y., Luo, B., Wu, Q., Bao, X., Wang, W., Ma, J. (2023). Recent advances in covalent organic framework-based membranes for water purification: Insights into separation mechanisms and applications. Chem. Eng. J. 474, 145580. https://doi.org/10.1016/j.cej.2023.145580.

[2] Amiri, S., Asghari, A., Vatanpour, V., Rajabi, M. (2021) Fabrication of chitosan-aminopropylsilane graphene oxide nanocomposite hydrogel embedded PES membrane for improved filtration performance and lead separation. J. Environ. Manage. 294, 112918. https://doi.org/10.1016/j.jenvman.2021.112918.

[3] Lin, X., Chen, L., Chen, C., Rao, J., Chen, J., He, Y. (2022). Carboxylated-covalent organic frameworks and chitosan assembled membranes for precise and efficient dye separation, J. Memb. Sci. 663, 121075. https://doi.org/10.1016/j.memsci.2022.121075.

[4] Liu, Q., Basel, N., Li, L., Xu, N., Dong, Q., Fan, L., Wang, Q., Ding, A., Wang, T. (2022). Interfacial polymerization of a covalent organic framework layer on titanium dioxide@ graphene oxide/polyacrylonitrile mixed-matrix membranes for high-performance dye separation. J. Memb. Sci. 647, 120296. https://doi.org/10.1016/j.memsci.2022.120296.

Luminescence Depletion Imaging of SrAl$_2$O$_4$:Eu^{2+}, Dy^{3+} by Solid State Laser in Dark Field Microscopy

Fateme Dehnavi [a], Nader Shokoufi [*b]

Corresponding Author E-mail: n.shokoufi@ccerci.ac.ir

[a] Ph.D. student of Analytical Chemistry.

[b] Associate Professor of Analytical Chemistry.

Analytical Instrumentation & Spectroscopy Laboratory at CCERCI

Abstract: We used the depletion of sample luminescence emission by laser and dark field imaging for chemical analysis. The combination of spectroscopic, microscopic, and imaging methods enables sample observation and analysis. The purpose of this project is to implement the suppression of luminescence emission using a laser. It is also considered to develop the mentioned method for microscopic applications and chemical analysis.

Keywords: Depletion of Luminescence Emission; Dark Field Microscopy

Introduction

The depletion of luminescence emission using a technique used in stimulated emission depletion (STED) microscopy to achieve super-resolution imaging. STED microscopy involves exciting a diffraction-limited volume and then suppressing fluorescence in its outer parts by depletion (Gonzalez Pisfil et al., 2022). Additionally, the application of the STED method to scintillator plates has shown promise in reducing the pixel size of soft X-ray cameras (Ejima et al., 2020). Luminescence depletion imaging using luminescent quantum dots has also been demonstrated to achieve subdiffraction spatial resolution, with significant depletion of the luminescence signal and improved resolution compared to diffraction-limited imaging (Lesoine et al., 2013). Laser-diode-stimulated emission depletion has been utilized to achieve subdiffraction resolution in far-field fluorescence microscopy, enabling the resolution of neighboring individual molecules(Westphal, Blanca, Dyba, Kastrup, & Hell, 2003).

In this work, we use the quenching of SrAl$_2$O$_4$:Eu^{2+}, Dy^{3+} (SAOED) phosphors luminescence emission with a laser and with the help of dark field imaging for chemical analysis. The combination of spectroscopic, microscopic, and imaging methods enables SAOED observation and analysis.

The purpose of this project is to implement the suppression of luminescence emission using a laser. It is also considered to develop the mentioned method for microscopic applications and chemical analysis.

A dark field microscope is an optical instrument used for observing tiny structures at high magnification. It utilizes oblique off-axial illumination to provide contrast and enhance the visibility of specimens. The microscope includes an illumination system, an objective lens unit, an optical fiber bundle, and an observation system. It can achieve bright-field illumination, low-angle dark-field illumination, and wide-angle incoming dark-field illumination through different optical path systems.

Experimental Section

We designed a luminescence emission depletion detection and imaging system (Figure 1). In this system, a flashlight is used as an excitation source, along with a dedicated dark background condenser or a standard central stop, which is placed on the bright background condenser and closes the direct light path. It allows only one side light loop to pass, and a laser diode with a continuous Gaussian wave beam at 532 nm wavelength was used as the probe beam. After passing through an aperture, the excitation beam hits the sample. These two excitation and probe beams are aligned so that the beams overlap at the focal point. In a dark field microscope, the condenser is designed to form a hollow cone of light, the objective lens is placed in the hollow and dark part of this cone, and the light travels around the objective lens, but does not enter the cone-shaped region. When there is no sample on the microscope stage, the entire field of view appears dark. However, when a sample that emits luminescence is placed on the microscope stage, it appears bright against a dark background.

The sample tablet preparation process is as follows: approximately 0.5 to 1 mg of solid sample was compressed under a pressure of 10,000 psi and then tablets were formed in a vacuum environment.

22nd Iranian Chemistry Congress (ICC22)
Iranian Research Organization for Science and Technology (IROST)
03231-97589
13-15 May 2024

IROST
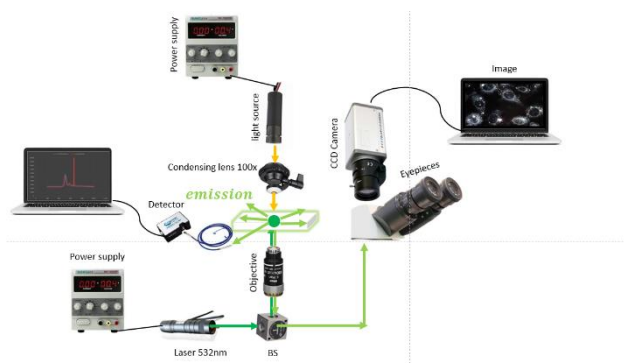
Fig.1: A schematic diagram of the designed microscope

Results and Discussion

Morphological studies: Scanning Electron Microscopy (SEM) and EDX measurements, the images of which are shown in Figure 2.
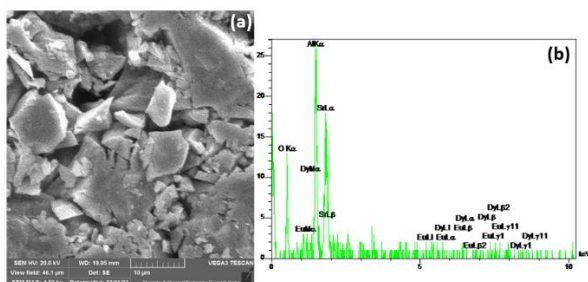
Fig.2: The SEM images (a) and EDX (b) of the commercial $SrAl_2O_4$:Eu^{2+}:Dy^{3+} particles

We prepared SAOED powder in the form of sample tablets. After irradiating the 532 nm laser beam, the depletion of the luminescence emission is observed. (Figure 3)
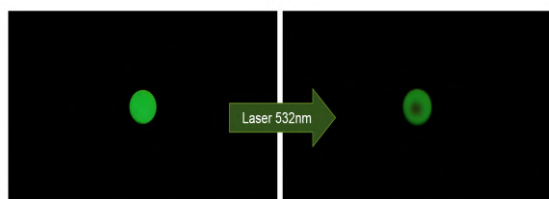
Fig.3: Sample tablets in dark room

Figure 4 shows the dark field microscope images of the excited sample and the depletion of emission using the 532 laser.
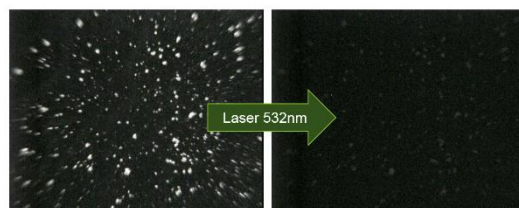
Fig.4: Dark field microscopic image of the sample (Objective Lens (100x))

Conclusions

The project aims to implement a method for suppressing luminescence emission using a laser and apply it to microscopic applications and chemical analysis. This method involves the depletion of sample luminescence emission with laser and the use of dark field imaging for chemical analysis. The combination of spectroscopic, microscopic, and imaging methods allows for sample observation and analysis. By integrating these techniques, the project aims to provide an efficient approach to studying and analyzing samples at a microscopic level.

References

[1] Ejima, T., Wakayama, T., Shinozaki, N., Shoji, M., Hatayama, G., & Higashiguchi, T. (2020). Demonstration of stimulated emission depletion phenomenon in luminescence of solid-state scintillator excited by soft X-rays. *Scientific Reports, 10*(1), 5391. doi:10.1038/s41598-020-62100-0

[2] Gonzalez Pisfil, M., Nadelson, I., Bergner, B., Rottmeier, S., Thomae, A. W., & Dietzel, S. (2022). Stimulated emission depletion microscopy with a single depletion laser using five fluorochromes and fluorescence lifetime phasor separation. *Scientific Reports, 12*(1), 14027. doi:10.1038/s41598-022-17825-5

[3] Lesoine, M., Bhattacharjee, U., Guo, Y., Vela, J., Petrich, J., & Smith, E. (2013). Subdiffraction, Luminescence-Depletion Imaging of Isolated, Giant, CdSe/CdS Nanocrystal Quantum Dots. *The Journal of Physical Chemistry C*. doi:10.1021/jp312231k

[4] Westphal, V., Blanca, C. M., Dyba, M., Kastrup, L., & Hell, S. W. (2003). Laser-diode-stimulated emission depletion microscopy. *Applied Physics Letters, 82*(18), 3125-3127. doi:10.1063/1.1571656

Tautomerism and Intramolecular Hydrogen Bond Investigation in 1,3-di(2-pyridinyl)-1,3-propanedione; Parameters Affecting the Strength of Hydrogen Bonds

Arezoo Moradi, A. R. Nekoei*

Corresponding Author E-mail: nekoei@sutech.ac.ir

Department of Chemistry, Shiraz University of Technology, Shiraz, Iran.

Abstract: Due to significance of intramolecular hydrogen bonds, key parameters for estimating strength of these bonds and the influence of substituent groups on their strength have been examined in DPPD β-diketone compound by DFT, Atoms in Molecules (AIM), and Natural Bond Orbital (NBO) analysis, besides the spectroscopic experimental data.

Keywords: Tautomeric analyses; Intramolecular hydrogen bond; β-diketone; Density Functional Theory

Introduction

Research has shown that intramolecular hydrogen bonds (IHBs) significantly affect the physical and chemical properties of various materials and have been extensively studied as a fundamental structural feature in chemistry [1]. These HBs occur in diverse organic and biological molecules, including hormones, coenzymes, proteins, and β-diketones. In particular, β-diketones have garnered special attention due to their involvement in IHB interaction [2]. The strength of hydrogen bonds and the keto-enol equilibrium state in these molecules are affected by several factors, such as temperature, solvent polarity, and the nature of substituent groups at alpha and beta positions [3]. The cis-enol form of these molecules is stabilized by formation of an IHB [4].

Method Section

Using GaussView 6.0 software, the potential keto and enol structures for DPPD were designed. Subsequently, these structures were fully optimized using Gaussian 09 software at B3LYP, B97D, M062X, and CBS levels of theory with 6-31G(d,p), 6-311G(d,p), and 6-311++G(d,p) basis sets. For further analysis, Atoms in Molecules (AIM) calculations were performed to examine the charge density and its Laplacian at the critical points of the HBs and the chelated ring, utilizing AIM2000 software. Moreover, the Espinosa model was used, which includes the relationship $E_{HB} = 1/2\ V(r)$, to predict the HB strength and to determine the correlation between the electron potential density at the critical points and the HB energy.

Results and Discussion

All possible tautomers, including 4 cis-enol, 4 trans-enol, and 3 keto tautomers, for the DPPD compound were investigated using several different theoretical levels. By comparing the results of different methods with that of CBS, it was determined that the B3LYP/6-311++G(d,p) level of theory is the most appropriate for further calculations.

Results indicate that the cis-enol forms are the most stable, in all calculation methods. The structure and relative stability of these forms at the B3LYP/6-311++G(d,p) level are shown in Figure 1.
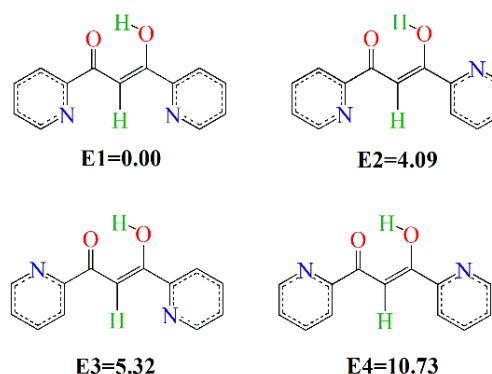
Fig.1: Cis-enol conformers of the DPPD, besides their calculated relative energies (all in kcal/mol)

Stability order of the enols at all computational levels is *E1>E2>E3>E4*. According to the investigations, presence of IHB, π-electron delocalization, and steric repulsion are the most important parameters affecting the stability.

The structural parameters, including O···H and O···O bond distance, and, O-H bond length and O-H-O bond angle (see Table 1), were utilized to investigate the IHBs strength. A comparison of these parameters indicates that trend of the IHB strength in the enolic forms of DPPD compound is as follows:

$$S_{HB}: E3>E1>E4>E2$$

22nd Iranian Chemistry Congress (ICC22)
Iranian Research Organization for Science and Technology (IROST)
13-15 May 2024

03231-97589

Table 1: Some IHB related parameters for the cis-enol forms of DPPD at B3LYP/6-311++G(d,p) level

Parameter	E1	E2	E3	E4
RO–H (Å)	1.004	1.001	1.008	1.004
RO···O (Å)	2.528	2.546	2.519	2.536
RO···H (Å)	1.613	1.637	1.598	1.622
Q (Å)	0.141	0.128	0.153	0.141
νOH (cm^{-1})	3033	3101	2968	3041
LP(O)$\leftrightarrow\sigma^*$(O-H)	29.2	26.1	31.5	28.2
E_{HB} (Schuster)[a]	17.46	4.82	18.08	5.68
E_{HB} (AIM)[a]	19.42	17.92	20.32	18.81

a: E_{HB} in kcal/mol

Using Schuster method, which involves calculating the energy difference between the chelated cis-enol form and the open (trans) form for each of the enol configurations, is a common approach to evaluating the IHB energy. However, the results (Table 1) exhibit a high degree of inconsistency between the E_{IHB} of Schuster method with the aboved mentioned trend from structural parameters. This discrepancy can be attributed to the presence of an additional IHB of N···H type in the trans forms of E2 and E4 structures. Furthermore, the repulsion between hydroxyl and pyridine hydrogens in the trans form of E1 and E3 structures contributes to errors.

Another way to calculate the IHB energy is to use data from AIM theory. Based on the E_{IHB} obtained by this method (Table 1), the trend of hydrogen bond strength is *E3>E1>E4>E2*, which is exactly consistent with the results obtained from structural parameters. This arrangement is also in perfect agreement with the values of Gilli's Q parameter, the amount of charge transfer between NBOs involved in H-bonding, and the values of OH stretching vibration frequencies, all in Table 1.

The IHB strength of DPPD was compared with that of several similar β-diketones, which have different functional groups at the β position and the results were analyzed. For instance, theoretical and experimental parameters related to the IHB strength for DPPD, acetoacetate (AA), and dibenzoylmethane (DBM) are summarized in Table 2. Comparison of these parameters demonstrates effect of substitution on IHB strength. According to the theoretical data in this table at B3LYP/6-311++G(d,p) level, the following trend in the IHB strength is observed: *DBM>DPPD>AA*. This result clearly indicates that replacing pyridine group with phenyl and methyl groups, at β-position of these compounds, respectively, decreases and increases their IHB strength. These theoretical findings are corroborated by proton chemical shifts observed in ^{1}H-NMR experiments. Additionally, the results of AIM analysis also support the previous conclusions drawn from the comparison of other theoretical and experimental parameters.

Conclusions

In this study, stability, strength, affective parameters, and substitution influence on the IHB in the enolic forms of DPPD compound were investigated using different QM computational methods. The results showed that calculation of the IHB energy via AIM and structural parameters, also results from NBO analyses, can well predict the strength of IHB in full agreement with the experimental results including proton chemical shifts (δOH). Also, the substitution of pyridine group for phenyl and methyl groups decreases and increases the strength of IHB, respectively.

Table 2: IHB related parameters of example β-diketones

Parameter	DPPD	DBM	AA
δOH (ppm)	15.84	16.8	15.40
RO···O (Å)	2.528	2.502	2.544
RO···H (Å)	1.613	1.574	1.633
RO–H (Å)	1.004	1.010	1.003
θOHO (°)	149.2	150.4	148.6
Q (Å)	0.141	0.133	0.147
ρBCP (a.u.)	0.0601	0.0663	0.0573
E_{HB} (Schuster)[a]	17.46	16.15	15.87
E_{HB} (AIM)[a]	19.42	22.11	18.11

a: E_{HB} in kcal/mol

References

[1] Giricheva, N. I., Girichev, G. V., Lapshina, S. B., & Kuzmina, N. I. (2000). Molecular structure of dipivaloylmethane and the intramolecular hydrogen bond problem. Journal of Structural Chemistry, 41(1), 48-54.

[2] Wetz, F., Routaboul, C., Lavabre, D., Garrigues, J. C., Rico-Lattes, I., Pernet, I., & Denis, A. (2004). Photochemical Behavior of a New Long-chain UV Absorber Drived from 4-tert-Butyl-4'-Methoxydibenzoylmethane. Photochemistry and photobiology, 80(2), 316-321.

[3] Belova, N. V., Oberhammer, H., Trang, N. H., & Girichev, G. V. (2014). Tautomeric properties and gas-phase structure of acetylacetone. The Journal of organic chemistry, 79(12), 5412-5419.

[4] Afzali, R., Vakili, M., Nekoei, A. R., & Tayyari, S. F. (2014). Intramolecular hydrogen bonding and vibrational assignment of 1,1,1-trifluoro-5,5-dimethyl-2,4-hexanedione. Journal of Molecular Structure, 1076, 262-271.

Investigating the effect of soapwort extract (*Saponaria officinalis*) on the reduction of chlorpyrifos pesticide residues in pistachio product

Bahareh Ranjbarmohammadi, Mahdi Moridi Farimani, Vahideh Mahdavi

Corresponding Author E-mail: Baharehma40@gmail.com

[a] Department of Phytochemistry, Medicinal Plants and Drugs Research Institute, Shahid Beheshti University.

[b] Iranian Research Institute of Plant Protection, Agricultural Research, Education and Extension Organization (AREEO).

Abstract: the treatment of pistachios contaminated with chlorpyrifos was done by soapwort root extract. The pesticide residues in pistachios were quantified by the QuEChERS extraction method followed by GC-ECD. According to the results, the treatment of dry and fresh pistachios with 10% extract concentration and 15 minutes time reduced chlorpyrifos residues by 81% and 74.2%, respectively.

Keywords: Pistachio; Residue reduction; Chlorpyrifos; QuECHERS; GC-ECD

Introduction

In the last decade, the pistachio industry has emerged as a highly competitive market, bringing substantial profits to leading producers [1]. A significant threat to pistachio crops is the common pistachio psyllid, which feeds on sap and weakens trees, diminishing both the yield and quality of pistachios. This results in financial losses for farmers [2]. To combat this pest, various insecticides have been employed, such as Amitraz and Chlorpyrifos [3]. However, there is a growing concern over the residue of organophosphate pesticides like chlorpyrifos in pistachios, as they can accumulate in the fruit and lead to severe health issues including neurological and developmental disorders, cancer, and organ damage [4]. To reduce pesticide residues, methods like washing, peeling, cooking, and drying especially under sunlight are effective. Washing is typically the initial step in processing agricultural goods for both home and commercial uses [5]. One of the different methods in the field of removing or reducing pesticide residues is the use of washing with plant extracts. During two studies, it was shown that washing strawberries with *Tamarindus indica* extract and washing tomatoes with *Albizi amara* extract reduced the chlorpyrifos residue by about 64%. [6,7]. In general, the presence of saponin compounds as surfactants in the mentioned plant extracts is an important factor in the removal of pesticides [7]. *Saponaria officinalis* is a medicinal and ornamental plant commonly known as "Soapwort". The root of this plant can have up to 21% saponin content, which is very interesting compared to other natural sources [8]. In this study, pistachio washing with soapwort extract was considered as a supplementary washing step during the industrial processing of this product to test its ability to remove chlorpyrifos pesticide residue with contact and non-systemic effect.

Experimental Section

Water-methanol extract (70:30) was prepared from 200.00 gr of soapwort roots and after concentration, solid extract was obtained by freeze drying process. Pistachios contaminated with chlorpyrifos, including two samples of fresh pistachio and dry pistachio, were washed with aqueous solutions of 2%, 5%, 10% extract, and tap water as the control group, by immersion method. In order to achieve the maximum reduction effect, the parameters of extract to sample ratio, time and temperature were also checked and their optimal values were determined. Extraction and recovery of pesticide from pistachio samples was done according to QuECHERS method and the measurement of chlorpyrifos residue was done by gas chromatography equipped with electron capture detector. In order to validate the analytical method, after drawing the calibration curves of solvent and matrix, the values of LOD, LOQ, matrix effect, RSD% and recovery% were determined. In the end, to confirm the results, dried pistachios were washed with 10% extract in a ratio of 2:1 for different times and analyzed using UHPLC-MS/MS.

Results and Discussion

The analytical method for the detection of chlorpyrifos in pistachios was confirmed by creating calibration curves in acetonitrile and pistachio matrix, which showed a matrix effect of 25%. The limit of detection (LOD) and quantitation (LOQ) were determined to be 0.005 mg/kg and 0.01 mg/kg, respectively. Repetition of the method over three days yielded an absolute recovery rate of 92-99% and a relative standard deviation of 0.44-1.99%. Washing pistachios with a ratio of extract to sample of 2:1 for 15 minutes maximized the reduction of chlorpyrifos. At the same time, the higher concentration of the extract further reduced the residual level. Temperature changes had no significant effect on the reduction of residue in dry pistachio, but it had an effect in fresh pistachio, so that washing with water at higher temperatures was more effective, while washing with extract at higher temperatures had the opposite result. Finally, analysis of dried pistachios treated with the extract by UHPLC-MS/MS confirmed these findings, as shown in Figure 3.

22nd Iranian Chemistry Congress (ICC22)
Iranian Research Organization for Science and Technology (IROST)
13-15 May 2024

03231-97589

IROST
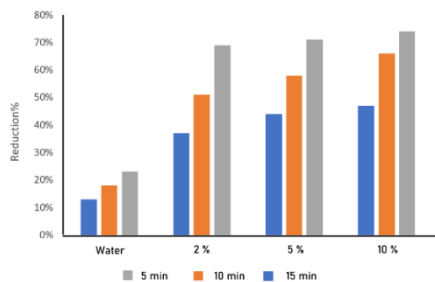
Fig.1: Reduction of chlorpyrifos residue based on extract concentration in fresh pistachios. (GC-ECD analysis results)
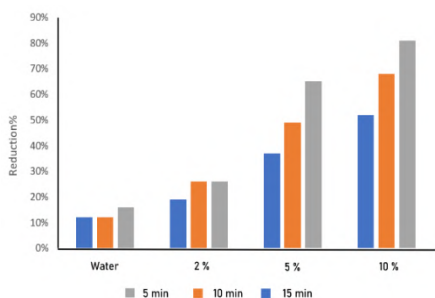
Fig.2: Reduction of Chlorpyrifos residue based on extract concentration in dry pistachios. (GC-ECD analysis results)
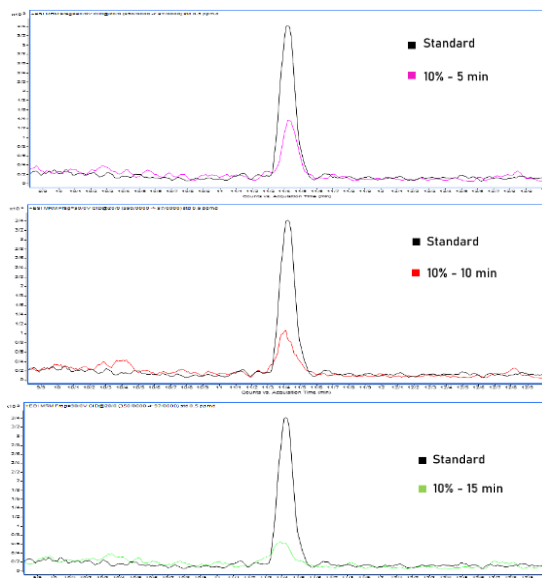
Fig.3: Comparative chromatograms obtained from the analysis of dried pistachios treated with optimal conditions by UHPLC-MS/MS.

Conclusions

Chlorpyrifos, a non-systemic pesticide with a non-polar nature, does not wash off easily from agricultural products with just water. However, adding compounds with soapy characteristics can enhance the washing process. Soapwort plant extract, rich in saponin compounds, is effective in removing pesticide residues due to its surfactant properties. In pistachio processing, which includes a two-stage water wash after peeling, soapwort extract can be integrated seamlessly. This Research has shown that soapwort root extract significantly reduces chlorpyrifos levels in both green-skinned and peeled pistachios. This reduction is especially important in the edible pistachio kernel. Also, the efficiency of this extract in removing pesticides from the green shell of fresh pistachios suggests it could work similarly for other shell-protected produce. Reducing the chlorpyrifos residue is crucial for the export of strategic products like pistachios, dried fruits, saffron, and raisins, and using soapwort extract could be beneficial for maintaining international trade standards.

References

[1] https://www.statista.com

[2] بصیرت ، امامی . (۱۳۹۶). دستورالعمل کنترل پسیل معمولی پسته . سازمان تحقیقات ، آموزش و ترویج کشاورزی ، موسسه تحقیقات علوم باغبانی ، تهران

[3] Eslami H, Dolatabadi M. (2020). Effects of Pesticides Used in Controlling Pistachio Psyllid on Human Health, and Control Strategies. Pistachio and Health Journal/ Vol. 3, No. 2, 1-4. DOI: 10.22123/phj.2021.268566.1077

[4] Eslami H. (2020). Chlorpyrifos for Pistachio Pest Control and its Effects on Human Health. Pistachio and Health Journal/ Vol. 3, No. 4, 1-3.

[5] Kaushik, G., S. Satya, and S. N. Naik. (2009). Food processing a tool to pesticide residue dissipation – A review. Food Research International 42 (1):26–40.

[6] Renuka V., Indira Ramachandran A.(2022). Removal of pesticides from strawberries using plant extracts and assessed by gas chromatography-triple quadrupole mass spectrometry. International Journal of Environmental Analytical Chemistry, 6720-6731, 102(18).

[7] Venkatachalapathy R, Anoop Chandra I, Das S, Vajiha Aafrin B, Lalitha Priya U, Peter M, Karthikeyan S, Sukumar M. (2020). Effective removal of organophosphorus pesticide residue in tomatoes using natural extracts. Journal of Food process Engineering , 43(2).

[8] Chandra, Satish, Rawat, Dharmendra S., Bhatt, Arun. (2021). Phytochemistry and pharmacological activities of Saponaria officinalis L. : A review. Notulae Scientia Biologicae, 13(1).

22nd Iranian Chemistry Congress (ICC22)
Iranian Research Organization for Science and Technology (IROST)
13-15 May 2024

03231-97589

A facile synthesis of 3-(4-methoxyphenyl)-7-propyl-5H-thiazolo[3,2-a]pyrimidin-5-one in urea/choline chloride (DES) as a green solvent: Antioxidant activity evaluation

Fatemeh Kalhorzadeh[a,b], Ashraf Sadat Shahvelayati [a,b*], Shiva Khalil moghadam[b]

Corresponding Author E-mail: avelayati@yahoo.com

[a] Department of Chemistry, College of Basic Sciences, Yadegar-e- Imam Khomeini (RAH) Shahre Rey Branch, Islamic Azad University, Tehran, Iran.
[b] Research Center for New Technologies in Chemistry and Related Sciences, Yadegar-e-Imam Khomeini (RAH) Shahre Rey Branch, Islamic Azad University, Tehran, Iran.

Abstract: A Stable thiazolopyrimidine obtained in excellent yields from reaction between 4-propylthiouracil and α-bromoketones in deep utectic solvent (DES). A mixture of urea and choline chloride (DES) was used as a green media. This product was characterized by FT-IR, 1H NMR and 13C NMR spectroscopy. In continue, Anti-oxidant activity was assessed by using an assay based on the inhibition of DPPH (1-diphenyl-2-picrylhydrazyl) radicals using Butylated hydroxytoluene as standard. Results were recorded as IC50 which is the concentration of antioxidant that reduces the free radical of DPPH about 50%. The thiazolopyrimidine derivative shows a moderate antioxidant effect with an IC50 of 5 mg/mL compared to BHT as a positive control (0.01 mg/mL).

Keywords: Nitrogen-containing heterocycles; Antioxidants; Deep eutactic solvent (DES) ; Green chemistry

Introduction:

Thiazoles are one of the major scaffolds in heterocyclic chemistry, showing various pharmacological activities like antimicrobial or anti-inflammatory.[2] Numerous natural products containing this heterocycle have been isolated and exhibit significant biological activities. Among aromatic heterocycles, thiazoles occupy a prominent position in the drug discovery process.[3] For example, the thiazolium ring is the chemically active center in the coenzyme derived from vitamin B1 (thiamin). The classical method for the synthesis of thiazoles is the Hantzsch process, in which a α-haloketone is condensed with a thioamide. This method gives excellent yields for simple thiazoles. As part of our current studies on the development of new routes in thiazole derivatives synthesis, we describe an efficient synthesis of functionalized thiazolidines from reaction of 4-propylthiouracil with α-bromoketone in a eutectic urea/choline chloride solvent at 70oC, the thiazolopyrimidine product was formed in good yields, and the Hantzsch reaction was complete in this solvent [1] (Scheme 1).

Reactive oxygen species (ROS) in the form of free radicals induce damage of biological macromolecules under oxidative stress and contribute to the pathogenesis of many health problems such as cancer, inflammation, atherosclerosis, cardiovascular and neurodegenerative diseases. The antioxidants prevent the oxidation of biological substrates, lowering oxidative stress, DNA mutations, malignant changes and thus, block the loss of cell function [4]. In this study, a newly synthesized derivative was screened for radical scavenging properties using DPPH assay.
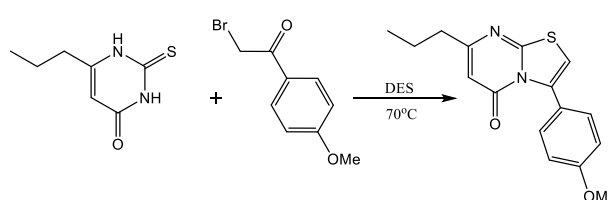
Scheme 1: preparation of 3-(4-methoxyphenyl)-7-propyl-5H-thiazolo[3,2-a]pyrimidin-5-one

Results and Discussion

In this method, 4-methoxyphenyl-7-propyl-5H-thiazolopyrimidine was synthesized as a new pyrimidine derivative by deep eutectic solvent (DES) at 70 degrees Celsius for 1 hour. This new structure was successfully confirmed by IR, ^{1}HNMR and ^{13}CNMR.

The power of synthesized Sample as an antioxidant was determined by the radical trapping of DPPH. The new sample display moderate radical trapping of DPPH (IC50 value of 5 mg/mL) relative to BHT (IC50 value of 0.01 mg/mL) The radical scavenging of DPPH at different concentrations of synthesized compound and BHT as a control is shown in Figure 1

Spectra Data of the product:

Pale yellow powder, m.p.147°C; yield: 0.24 g (80 %). IR (KBr): 3120, 1656, 1560, 1532 cm^{-1}. ^{1}H NMR: δ = 0.85 (3 H, t, ^3J 7.2, Me), 1.52 (2 H, sextet, ^3J 7.2, CH$_2$), 2.34 (2 H, t, ^3J 7.2, Me), 3.91 (3 H, s, OMe), 5.12 (1 H, s, CH), 6.03 (1 H, s, CH), 6.97 (2 H, d, ^3J 6.8, 2 CH), 8.04 (2H, d, ^3J 6.8, 2 CH) ppm. ^{13}C NMR: δ =13.6 (Me), 20.9 (CH$_2$), 37.3 (CH$_2$), 55.5 (OMe), 108.0 (CH), 113.9 (2CH), 125.4

22nd Iranian Chemistry Congress (ICC22)
Iranian Research Organization for Science and Technology (IROST)
13-15 May 2024

03231-97589

IROST

(C), 128.8 (CH), 130.9 (2CH), 159.4 (C), 163.9 (C), 165.4 (C), 169.0 (C), 191.3 (C=O) ppm. EI-MS: *m/z* (%) = 300 (M+, 2.5), 286 (10), 135 (100), 107 (35), 92 (40),77 (70). Anal. Calcd for $C_{16}H_{16}N_2O_2S$ (300.3): C, 63.98; H, 5.37; N, 9.33; S, 10.67. Found: C, 63.28; H, 6.07; N, 8.93; S, 10.17.

Fig.1: In vitro antioxidant activity
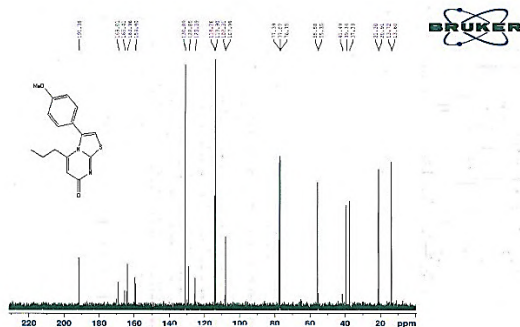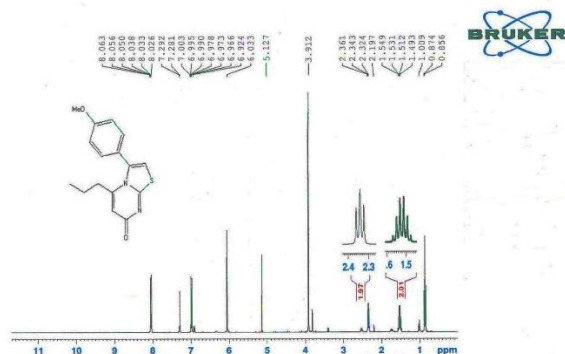
^{13}CNMR of 3-(4-methoxyphenyl)-7-propyl-5H-thiazolo[3,2-a]pyrimidin-5-one
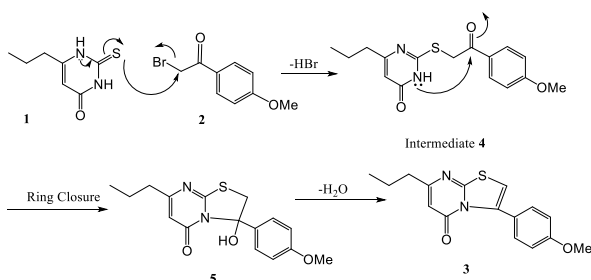
Proposed mechanism of preparation of 3-(4-methoxyphenyl)-7-propyl-5H-thiazolo[3,2-a]pyrimidin-5-one

Conclusions

We describe an efficient synthesis of functionalized thiazolopyrimidine from reaction of 4-propylthiouracil with *α*-bromoketone in a eutectic urea/choline chloride solvent. As a final point, this new sample was evaluated as an antioxidant by the radical trapping of DPPH. Results showed that new sample is a moderate antioxidant when compared to BHT as a positive control.

References:

[1] Azizi, N., Gholibeglo, E., Babapour, M., Ghafuri, H., & Bolourtchian, S. M. (2012). Deep eutectic solvent promoted highly efficient synthesis of N, N'-diarylamidines and formamides. *Comptes Rendus. Chimie*, *15*(9), 768-773.

[2] Gulcin, İ. (2020). Antioxidants and antioxidant methods: An updated overview. *Archives of toxicology*, *94*(3), 651-715.

[3] Kumar S, L., Servesh, A., Kumar Sriwastav, Y., Balasubramanian, S., Tabassum, S., & Govindaraju, S. (2023). A Bird's-Eye View on Deep Eutectic Solvent-Mediated Multicomponent Synthesis of N-Heterocycles. *ChemistrySelect*, *8*(16), e202301054.

[4] Mihailović, N., Marković, V., Matić, I.Z., Stanisavljević, N.S., Jovanović, Ž.S., Trifunović, S. and Joksović, L., 2017. Synthesis and antioxidant activity of 1, 3, 4-oxadiazoles and their diacylhydrazine precursors derived from phenolic acids. RSC advances, 7(14), pp.8550-8560.

Instrumentation and Analysis of 1D & 2D array sensors using labview for chemical analysis

Nader Shokoufi*, Hossein Heidari

Corresponding Author E-mail: n.shokoufi@ccerci.ac.ir

Analytical Instrumentation & Spectroscopy Laboratory,Chemistry & Chemical Engineering Research Center of Iran, Tehran.

Abstract: Instrumental analysis companionship with different field of transducer electronic, software, optics, Laboratory virtual Instrument Engineering workbench (LabVIEW) is a graphical programming software that has evolved into a powerful tool for engineers, scientists, and programming enthusiasts. In comparison to text-based programming languages, LabVIEW offers significant advantages such as rapid programming, ease of use, flexibility, and simulation capability. This article aims to explore the features and benefits of LabVIEW and its diverse applications across various fields. Specifically, we will delve into utilizing LabVIEW for measuring airborne particles employing lasers and array sensors. The target audience for this article includes individuals interested in graphical programming, developers of control and measurement systems, as well as students and professors specializing in chemistry and chemical engineering. By leveraging this software, users can:
- Perform and oversee images and data acquired from spectroscopic, electrochemical, and other devices in real-time and concurrently manage multiple projects.
- Gain proficiency in using LabVIEW for measuring airborne particles with lasers and array sensors. In this article, to measure airborne particles using laser systems, array sensors, telescope, and peripheral hardware, measurements are made using LabVIEW.
Keywords: Virtual Analytical Chemistry; Labview; Linear; Area; Array Sensore

Introduction:

Laboratory virtual Instrument Engineering workbench (LabVIEW) programming language is a graphical language, often called "G" for short. It is a type of visual programming, where programs are created using icons and diagrams instead of writing text code. The G language provides powerful data structures such as arrays, clusters, and matrices. LabVIEW has become a powerful tool for engineers, scientists and programming enthusiasts due to its high speed, simplicity and intuitive user interface. Compared to text programming languages, this software offers significant advantages such as high speed in programming, ease of use, flexibility and simulation capability[1].

With its intuitive user interface and user-friendly nature, LabVIEW has garnered popularity among a diverse range of users. Some notable advantages of this software include: [2]

1. Rapid programming speed: Tasks that may take weeks or months to script in other languages can be completed in hours using LabVIEW.[3]
2. Simplicity and aesthetic appeal: LabVIEW's graphical user interface simplifies programming, making it accessible and engaging for users at all levels, including beginners. [3] [4]
3. Versatility: LabVIEW is applicable across a broad spectrum of domains, encompassing measurement and control, signal processing, simulation, and training.

4. Simulation capabilities: LabVIEW facilitates the simulation of ideas and systems, allowing users to test and refine their concepts before actual implementation.[5]
5. Extensive function libraries: LabVIEW provides a comprehensive array of functions and executable subroutines, streamlining the programming process.
6. Advanced data visualization: Leveraging its robust graphical capabilities, LabVIEW enables the visualization of data through graphs, charts, and other formats.[6]

These advantages make the use of neodymium helium lasers and LabVIEW software well-suited for various fields, such as:

Air pollution monitoring: This method can be used to monitor airborne particles in various environments, including large cities, industrial areas, and factories.

Scientific research: This method can be used to study the effects of airborne particles on human health and the environment.

Air quality control: This method can be used to control air quality in industrial settings and inside buildings.

Experimental:

In this experiment, a laser: helium-neon with a wavelength of 632.8 nanometers, telescope model: 70070 with a focal distance of 700 mm, diameter of 70

22nd Iranian Chemistry Congress (ICC22)
Iranian Research Organization for Science and Technology (IROST)
13-15 May 2024

03231-97589

IROST

mm. Mirrors: Concave and flat, and labview software connected to the computer is used.
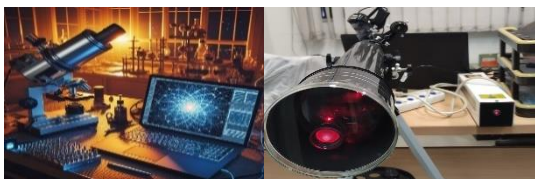
Fig.1 : Schematic view of the device setup

Results and Discussion

The results obtained by the Labview software from the setup of the created device show the intensity of the laser at the time of return and after hitting the mirror, which shows that this data is obtained by the 3D images of the Labview and the data stored in Excel with the software. Python and MATLAB are compared and are compatible with lab view images.
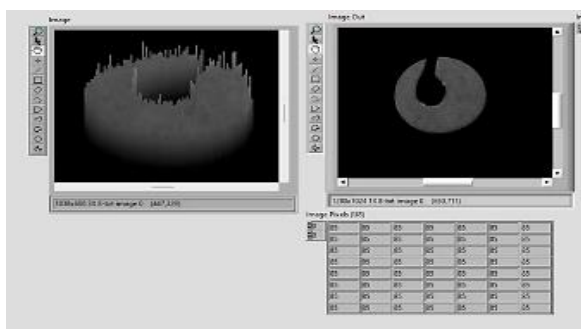
Fig.2: Simultaneously capture real-time 3D images and data from the image using LabVIEW software.
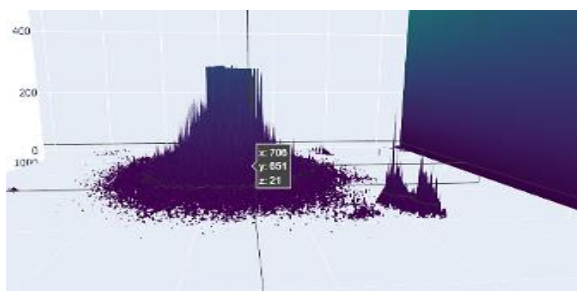
Fig.3 3D image of Python software through labview output data

Conclusion

This simple and cost-effective setup along with a simple monitoring software for its operator can be used to measure airborne particles in laboratory environments, measure airborne particles in cities or in isolated room environments.

Suggestions for future research

- Advantages of using neodymium helium lasers compared to other methods of measuring airborne particles
- Challenges facing using this method
- Solutions to overcome these challenges

References:

[1] Klinger, T., *Image Processing with LabVIEW™ and IMAQ™ Vision*. June 11, 2003: Prentice Hall PTR.

[2] Shokoufi, N., *Electronic Principles of Instrumental Analysis.* Poya science, 2022 .

[3] Madasamy,T., *Virtual electrochemical nitric oxide analyzer using copper, zinc superoxide dismutase immobilized on carbon nanotubes in polypyrrole matrix.* Talanta, 2012. 100: p. 168-174.

[4] Qin, J., Dhakal, S., Advances in Raman spectroscopy and imaging techniques for quality and safety inspection of horticultural products. Postharvest Biology and Technology, 2019. 149: p. 101-117.

[5] Barriada, Truscott J.B., and Achterberg E.P., Automation of a flow injection system for the determination of dissolved silver at picomolar concentrations in seawater with inductively coupled plasma mass spectrometry. Journal of Analytical Methods in Chemistry, 2003. 25: p. 93-100.

[6] Wrobel, P., *LabVIEW control software for scanning micro-beam X-ray fluorescence spectrometer.* Talanta, 2012. 93: p. 186-192.

Statistical Optimization of Hollow Fiber Liquid Phase Microextraction for Simultaneous Preconcentration and Determination of Bupivacaine and Dibucaine in the Postmortem Femoral Venous Blood

Ameneh Dorri [a], Fariba Safa [*a], Shahab Shariati [a], Fatemeh Shariati [b], Hassan Kefayati [a],

Corresponding Author E-mail : Safa@iaurasht.ac.ir

[a] Department of Chemistry, Rasht Branch, Islamic Azad University, Rasht, Iran.

[b] Department of Environment, Lahijan Branch, Islamic Azad University, Lahijan, Iran.

Abstract: This study presents a hollow-fiber Liquid-Phase microextraction (HF-LPME) for preconcentration of bupivacaine and dibucaine. Optimal conditions predicted by a Box-Behnken design were 89 minutes, pH=11.0, and ionic strength of 3.0 mol L^{-1}. The eco-friendly method offers good sensitivity and efficiency using a small amount a chlorine-free organic solvent.

Keywords: Hollow fiber liquid phase microextraction; GC-MS; Bupivacaine; Dibucaine; Box-Behnken design

Introduction

Bupivacaine and dibucaine are local anesthetics used for treating local pain [1]. Bupivacaine may cause muscle twitching and irregular heartbeats as potential side effects, while dibucaine can also cause skin sensitivity, burning, itching, and rarely, serious complications like cardiac arrhythmias [2]. In the research, a sensitive and reliable extraction method based on the combination of the two-phase hollow fiber liquid-phase microextraction (HF-LPME) [3] and response surface modeling (Box-Behnken design) is presented for preconcentration of bupivacaine and dibucaine, before determination by gas chromatography-mass spectrometry (GC- MS) [4].

Experimental Section

HF-LPME of bupivacaine and dibucaine was conducted using the polypropylene hollow fiber pieces (length of 8.8 cm, I.D.=600 µm, thickness of 200 µm, and pore size of 0.2 µm) filled by 1-octanol as the acceptor phase. A gas chromatograph (Agilent 7890A) coupled with a mass selective detector(Agilent 5975C) (GC−MS, Santa Clara, California, USA) was employed for determination of analytes. The experimental space was determined using the one factor at a time (OVAT) approach by examining the effects of pH, ionic strength, and the extraction time on the peak areas (as responses). Box-Behnken design experiments were conducted at the variables levels of 30, 60, and 90 min for the extraction time, 7, 9, and 11 for pH, and 1, 2, and 3 mol L^{-1} for ionic strength.

Results and Discussion

The chromatographic peak areas of bupivacaine and dibucaine as the response were satisfactorily fitted to a quadratic response surface model (R^2=0.9834 and F=46.00 for bupivacaine and R^2=0.9731 and F=28.15 for dibucaine). Using the models, optimum conditions of operation were predicted as the extraction time of 88.9 min, pH=11, and ionic strength of 2.1 mol L^{-1}. Conducting triplicate tests under the optimal conditions proved good prediction power of the generated response models for bupivacaine and dibucaine extraction. The calibration curves after extraction were linear in a range of 1-1000 µg L^{-1}. Table 1 lists the Limit of detection (LOD), the limit of quantification (LOQ), linear dynamic range (LDR), relative standard deviation (RSD), correlation coefficient (R^2), preconcentration factor (PF), extraction recovery (ER), and enrichment factor (EF). The method resulted in the high-efficiency range of 94.5%-101.0% for HF-LPME of bupivacaine and dibucaine in the femoral venous blood (FVB) samples, and the close correlation observed between the added and found values demonstrates the efficacy of the investigated technique for quantifying bupivacaine and dibucaine in real biological samples. Moreover, the method showed good precision and accuracy. The results of this study suggested the proposed method as an efficient and environmentally friendly analytical method which consumes less than 30 µL of the organic solvent for extraction of bupivacaine and dibucaine in the FVB samples.

Chromatograms of spiked samples (200.0 µg L^{-1}) versus blank and corresponding mass spectrum of bupivacaine and dibucaine after HF-LPME at optimum conditions were shown in Figs. 1. The chromatograms revealed distinct peaks corresponding to bupivacaine and dibucaine after HF-LPME under optimum conditions. These peaks were further confirmed by the corresponding mass spectra, which exhibited

22nd Iranian Chemistry Congress (ICC22)
Iranian Research Organization for Science and Technology (IROST)
13-15 May 2024

03231-97589

IROST

Table1: Figures of merit of the two-phase HF-LPME procedure of bupivacaine and dibucaine

	Bupivacaine	Dibucaine
LOD ($\mu g\ L^{-1}$)	0.4	0.4
LOQ ($\mu g\ L^{-1}$)	1.4	1.5
LDR ($\mu g\ L^{-1}$)	1.4-1000	1.5-1000
RSD *	0.82	1.72
R^2	0.9990	0.9998
PF	266.2	238.9
ER (%)	22.2	19.9
EF	266.2	245.1

* (n=3)

characteristic fragmentation patterns of bupivacaine and dibucaine. In addition, the proposed method had a suitable extraction capability compared to the similar works as a green chemometrics approach [5-7].

Conclusions

In the study, a Box-Behnken experimental design was utilized to optimize the two-phase HF-LPME of bupivacaine and dibucaine as local anesthetics. Findings of the study predicted the optimum extraction conditions at 89 min, pH=11.0, and 3.0 mol L^{-1} ionic strength. Solution pH showed the most significant effect on the peak area. The chromatographic peak areas of bupivacaine and dibucaine were satisfactorily fitted to a
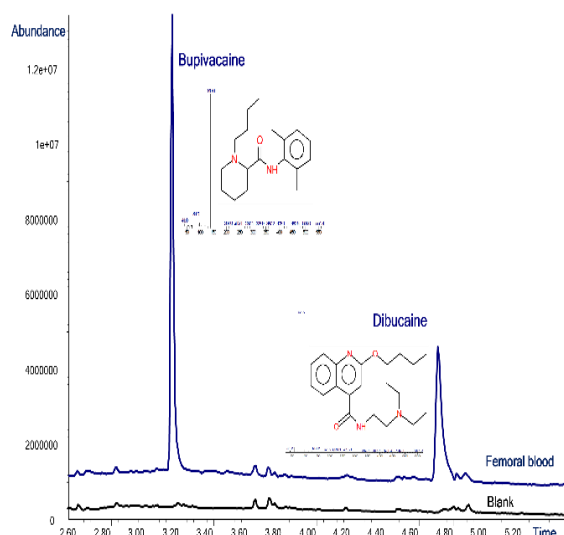
Fig. 1: Chromatograms of spiked samples (200.0 $\mu g\ L^{-1}$) versus blank) and corresponding mass spectra of bupivacaine and dibucaine after HF-LPME at optimum conditions.

and the predicted values. Repetition of the experiments under optimal conditions further validated the accuracy

quadratic response surface model, indicating a high degree of correlation between the experimental data and reliability of the developed method. Overall, the study confirms that the proposed method is sensitive, efficient, and simple for a one-step preconcentration and trace determination of bupivacaine and dibucaine in femoral venous blood samples, utilizing a small amount (25 μL) of a natural chlorine-free organic solvent.

References

[1] A. J. Trevor, Katzung & Trevor's Pharmacology: Examination & Board Review, New York, 16, McGraw-Hill, 2024.

[2] L. E. Mather and G. T. Tucker, When Regional Anesthesia Met Pharmacokinetics, Anesthesiology, 2022, 136, 588-593. https://doi.org/10.1097/ALN.0000000000004143

[3] F. Safa, A. Alizadeh, Magnetic Nanocomposite of TiO2 as Efficient Adsorbent for Direct Green 26 Dye: Multivariate Optimization, Kinetic and Equilibrium Isotherms. International Journal of Environmental Research, 2022, 107, 1-16. https://link.springer.com/article/10.1007/s41742-022-00467-w.

[4] E. Bozorgzadeh, S. Shariati, A. Esmaeilnejad, Central Composite Design for Optimizing Hollow Fiber Liquid Phase Microextraction of Carbamazepine from Aqueous and Biological Samples, Journal of Analytical Chemistry, 75, 2020, 154-160. https://doi.org/10.1134/S1061934820020033.

[5] S. Y. Liang, F. Shi, Y. G. Zhao, and H. W. Wang, Determination of Local Anesthetic Drugs in Human Plasma Using Magnetic Solid-Phase Extraction Coupled with High-Performance Liquid Chromatography, Molecules, 2022, 27, 1-13. https://doi.org/10.3390/molecules27175509

[6] M. K. Halim, O. M. Badran, A. E. F. Abbas, Sustainable chemometric methods boosted by Latin hypercube technique for quantifying the recently FDA-approved combination of bupivacaine and meloxicam in the presence of bupivacaine carcinogenic impurity: Comprehensive greenness, blueness, and whiteness assessments, Microchemical Journal, 200, 2024, 110276. https://doi.org/10.1016/j.microc.2024.110276

[7] F. Li, Wang, Z. Zhu, B. Xu, Z. Liu, Development and Application of a Rapid Screening SPE-LC-QTOF Method for the Quantification of 14 Anesthetics in Aquatic Products, Food Analytical Methods, 16, 2023, 633-649. https://link.springer.com/article/10.1007/s12161-022-02420-1.

Determination of Brucine in Stomach Content using Hollow Fiber Liquid-Phase Microextraction Coupled with Gas Chromatography-Mass Spectrometry: Optimization by Box-Behnken Experimental Design

Shahab Shariati [a], Fariba Safa [*a], Nosratollah Mahmoodi [b], Fatemeh Shariati [c], Hassan Kefayati [a], Ameneh Dorri [d]

Corresponding Author E-mail: shahabshariati@gmail.com

[a] Department of Chemistry, Rasht Branch, Islamic Azad University, Rasht, Iran
[b] Department of Chemistry, Guilan University, Rasht, Iran
[c] Department of Environment, Lahijan Branch, Islamic Azad University, Lahijan, Iran
[d] Legal Medicine Research Center, Legal Medicine Organization, Tehran, Iran

Abstract: A sensitive, efficient, and green hollow-fiber liquid-phase microextraction method followed by gas chromatography-mass spectrometry, was developed for preconcentration and determination of brucine. Optimization by the response surface methodology resulted in a linear dynamic range of 0.74-1000 μg L^{-1} and the limits of detection and quantification of 0.22, and 0.74 μg L^{-1} respectively.

Keywords: Two-phase hollow fiber liquid phase microextraction; GC-MS; Brucine; response surface methodology

Introduction

Brucine found alongside strychnine in the *Nux Vomica* plant, has promising anti-tumor effects, especially on liver and breast cancer [1], and is used in traditional Chinese medicine for inflammation and pain relief, as well as in Ayurvedic and homeopathic treatments [2]. Brucine is also used to denature alcohol, with a high bitterness threshold of 69%. Poisoning by brucine presents symptoms like muscle spasms, seizures, rhabdomyolysis, and acute kidney injury [3] and its mechanism of action as a glycine receptor antagonist mirrors strychnine's, with a potentially lethal dose in adults of around 1 gram [4]. In this study, a robust method was developed for efficient isolation and determination of brucine. In the method, a combination of the two-phase hollow fiber liquid-phase microextraction (HF-LPME) and a Box-Behnken design (BBD) was utilized for preconcentration of brucine in complicated matrices. Determination of the extracted brucine was done using gas chromatography-mass spectrometry (GC-MS) based on the principal ions appeared that at m/z 394, 395, 379, 392, 120, 197, 203 [5].

Experimental Section

HF-LPME of brucine was performed using polypropylene hollow fiber pieces (9.0 cm length, 600 μm inner diameter, 200 μm thickness, and 0.2 μm pore size) filled with 1-octanol as the acceptor phase. A gas chromatograph (Agilent 7890A) coupled with a mass selective detector (Agilent 5975C) was used for analyte determination. At first, the OVAT approach was used to investigate the effects of solution pH, ionic strength, and extraction time on peak areas (as responses). Box-Behnken design experiments were then conducted at the determined experimental space (extraction times of 30, 60, and 90 min, pH values of 7, 9, and 11, and ionic strengths of 1, 2, and 3 mol L^{-1}). Brucine determination was carried out using a GC-MS instrument. Chromatographic separations were conducted in full scan mode, using an HP-5 MS capillary column and highly pure helium (99.9999 %) as the carrier gas (flow rate of 2.5 mL min^{-1} and inlet split ratio of 1:5). The initial column temperature was set at 270°C for 1 min which was increased to 290°C with a ramp of 20°C min^{-1}. The inlet and auxiliary temperatures were set to 270 °C and 290°C, respectively.

Results and Discussion

The chromatographic peak areas of brucine as the response were satisfactorily fitted to a quadratic response surface model with R^2=0.9834 and F=77.84 which predicted the optimum conditions as the extraction time of 89.4 min, pH=10.8, and ionic strength of 2.5 mol L^{-1}. Based on the results, all the main factors, the two-factor interactions, and-second order terms of pH and ionic strength significantly affected the response. The calibration curve was linear in the range of 1-500 μg L^{-1} (R^2=0.9995), and limits of detection and quantitation were obtained as 0.2 and 0.7 μg L^{-1}, respectively. The method resulted in the high efficiency for HF-LPME of brucine in the postmortem stomach content samples. The results of this study suggested the proposed method as an efficient and environmentally friendly analytical method consuming less than 40 μL of the organic solvent for extraction of brucine from the stomach content. Limit of detection (LOD), limit of quantification (LOQ), linear dynamic range (LDR), relative standard deviation (RSD), and enrichment factor (EF) for brucine are presented in Table 1. (The enhancement factor was calculated by

22nd Iranian Chemistry Congress (ICC22)
Iranian Research Organization for Science and Technology (IROST)
13-15 May 2024

03231-97589

IROST

Table 1: Figures of merit for the two-phase HF-LPME of brucine

Figures of merit	values
LOD ($\mu g\ L^{-1}$)	0.22
LOQ ($\mu g\ L^{-1}$)	0.74
LDR ($\mu g\ L^{-1}$)	0.74-500
EF	313
Equation	y = 90273x + 12751
R^2	0.9995

dividing the slope of the calibration curve after extraction by the slope of the curve plotted for direct injection) [6]. The method demonstrated reasonably acceptable detection and quantification limits compared to another reported method [7]. The samples were extracted during triplicate experiments under optimized conditions, and the concentration of brucine in the extracted samples demonstrated satisfactory accuracy, achieving a recovery rate of 94%. The chromatograms and spectra obtained for spiked stomach content samples (100.0 $\mu g\ L^{-1}$) compared to blank are shown in Fig. 1. The chromatogram revealed a distinct peak corresponding to brucine (retention time of 13.005) after HF-LPME under optimum conditions. Further confirmation of the peak by the corresponding fragmentation patterns in the mass spectrum of brucine validated the successful extraction and detection of the analyte.

Conclusions

In this study, a two-phase HF-LPME method followed by GC-MS analysis was developed for preconcentration and trace determination of brucine in postmortem stomach content. Box-Behnken experimental design predicted the optimum extraction conditions focusing on the variables of extraction time, solution pH, and ionic strength. Based on the findings, the optimum extraction conditions were predicted at 89.4 min, pH=10.8, and ionic strength of 2.5 mol L^{-1}. All the studied factors significantly affected the peak area. Overall, the study suggests the method for the sensitive, efficient, simple, and single-step preconcentration of brucine in the stomach samples, utilizing a small amount (less than 40 µL) of a natural chlorine-free organic solvent.

Fig.1: Chromatogram and spectra of spiked stomach content (100.0 $\mu g\ L^{-1}$) versus blank and corresponding mass spectrum of brucine after HF-LPME at optimum conditions.

References

[1] J. Rao, T. Peng, N. Li, Y. Wang, C. Yan, K. Wang, and F. Qiu, Nephrotoxicity induced by natural compounds from herbal medicines, a challenge for clinical application, Critical Reviews in Toxicology, 2022, 9, 757-778. https://doi.org/10.1080/10408444.2023.2168178.

[2] Z.-G. Feng, X. D. Cai-Rang, X. Y. Tan, C. Y. Li, S. Y. Zeng, Y. Liu, and Y. Zhang, Processing methods and the underlying detoxification mechanisms for toxic medicinal materials used by ethnic minorities in China: A review, Journal of Ethnopharmacology, 2023, 305, 116126. https://doi.org/10.1016/j.jep.2022.116126

[3] L. Lu, R. Huang, Y. Wu, J. M. Jin, H. Z. Chen, L. J. Zhang, and X. Luan, Brucine: A Review of Phytochemistry, Pharmacology, and Toxicology, Front Pharmacol, 2020, 11, 377. https://doi.org/10.3389/fphar.2020.00377.

[4] E. Bozorgzadeh, S. Shariati, and A. Esmaeilnejad, Central Composite Design for Optimizing Hollow Fiber Liquid Phase Microextraction of Carbamazepine from Aqueous and Biological Samples," Journal of Analytical Chemistry, 2020, 75, 154-160. http://www.springer.com/chemistry/analytical+chemistry/journal/10809.

[5] A. C. Moffat, M. D. Osselton, B. Widdop, and J. Watts, Clarke's analysis of drugs and poisons. Pharmaceutical Press London, 2011.

[6] M. Darvishi, S. Shariati, F. Safa, A. Islamnezhad, Surface blocking of Azolla modified copper electrode for trace determination of phthalic acid esters as the molecular barricades by DPV, 11, 52, 32630-32646, 2021. https://doi.org/10.1039/d1ra04714k.

[7] R. Jain, R. Mani, T. Archna, N. Shishir, P. Singh, A simple, cost-effective and rapid method for simultaneous determination of Strychnos nux-vomica alkaloids in blood and Ayurvedic medicines based on ultrasound-assisted DLLME–TLC-image analysis, Journal of Chromatographic Science, Volume 58, Issue 5, May/June 2020, Pages 477–484. https://doi.org/10.1093/chromsci/bmaa007.

Formation of unexpected product in the reaction of 5-methoxycarbonylmethylydene-1-3-thiazolidine-4-one with phenethylcarbamodithioic acid

Parisa Nazari, Farough Nasiri*

Corresponding Author E-mail: nasiri@uma.ac.ir

Department of Applied Chemistry, Faculty of Science, University of Mohaghegh Ardebili, Ardabil, Iran.

Abstract: We have successfully rapid synthesis of new derivative of 5-methoxycarbonylmethylydene-1,3-thiazolidin-4-one **2** from the reaction between *N,N'*-disubstituted thiourea and dimethyl acetylenedicarboxylate. In the following , we investigated the reaction between **2** and phenethyl carbamodi thioic acid **3**. Contrary to expectation, instead of product (2*E*,5*E*)-3-isobutyl-2-(isobutylimino)-3'-phenethyl-2'-thioxo-2,2',3,3'-tetrahydro-4*H*,4'*H*-[5,5'-bithiazolylidene]-4,4'-dione **5**, the product (*E*)-5-(1,3-diisobutyl-5-oxo-2-thioxoimidazolidin-4-ylidene)-3-phenethyl-2-thioxothiazolidin-4-one **4** was obtained. Through extensive spectroscopic analysis, including ^{1}H NMR, ^{13}C NMR, and HMBC, we identify the product and elucidate the structure.

Keywords: *N,N'*-disubstituted thiourea derivatives; dithiocarbamates; Rhodanine-2-Thioxo-4-imidazolidinone.

Introduction

1,3-Thiazolidin-4-one compounds are central components of great importance in the field of medicinal and organic chemistry. They are an essential part of the structure of many synthetic pharmaceutical products characterized by a broad spectrum of properties, such as antibacterial, anti-HIV, anti-inflammatory, antifungal and anticancer [1-2]. The structural elucidation of these compounds, which are derived from the condensation of substituted thioureas and acetylenedicarboxylate, has been the subject of debate. While earlier studies suggested a 6-membered structure, recent single-crystal X-ray analysis has definitively resolved this ambiguity in favor of a 5-membered thiazolidinone structure [3]. A notable subgroup of rhodanines are the 2,2-dithioxo-[5,5] bithiazolidinylidene-4,4-diones, known as birhodanines, for which a one-pot synthesis method for asymmetric birhodanines has been reported [4]. In order to obtain new heterocyclic systems based on rhodanine, we have successfully synthesized new derivatives of 5-alkoxycarbonylmethylydene-1,3-thiazolidin-4-one by the rapid reaction of thioureas with dialkyl acetylenedicarboxylates at room temperature without the need for catalysts. Moreover, a catalyst-free reaction of these derivatives and dithiocarbamates in ethanol led to the synthesis of new rhodanine-based color hybrid derivatives in high yields within a short time frame of 30-60 minutes.

Experimental Section

For the synthesis of 5-methoxycarbonylmethylidene-3,1-thiazolidin-4-one **2**, dimethylacetylenedicarboxylate (1.1mmol) was added to 1,3-diisobutylthiourea **1** (1mmol) in ethanol at room temperature (Fig. 1). After completion of the reaction (30 s), a white precipitate was

formed, which was detected by TLC. The isolated solid was purified by crystallization from a mixture of *n*-hexane and ethanol.
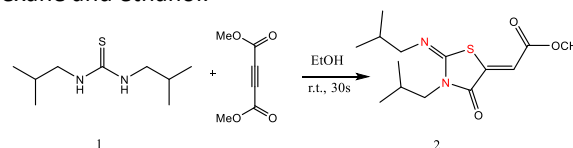
Fig.1: Synthesis of methyl (*Z*)-2-((*E*)-3-isobutyl-2-(isobutylimino)-4-oxothiazolidin-5-ylidene)acetate.

In a separate procedure, a mixture of carbon disulfide and primary amines was stirred in ethanol for 2 minutes. Then 5-alkoxycarbonylmethylidene-1,3-thiazolidin-4-one **2** was added to the reaction mixture at room temperature. The reaction lasted 25 minutes, during which time the color changed from white to orange. Then the orange precipitate was filtered, washed with a mixture of ethanol and hot *n*-hexane and dried under vacuum (Fig. 2).
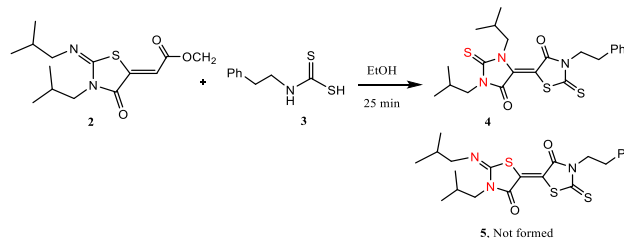
Fig.2: Synthesis of (*E*)-5-(1,3-diisobutyl-5-oxo-2-thioxoimidazolidin-4-ylidene)-3-phenethyl-2 thioxothiazo lidin-4-one **4**.

Results and Discussion

It was originally assumed that the reaction between 5-methoxycarbonylmethylyden-1-3-thiazolidine-4-one **2** and phenethylcarbamodithioic acid **3** follows a straight forward path and leads to the formation of **5**. However,

22nd Iranian Chemistry Congress (ICC22)
Iranian Research Organization for Science and
Technology (IROST)
13-15 May 2024

03231-97589

experimental observations have shown the formation of unexpected compound **4**, which led to further investigation of the underlying mechanisms.

The structures of compound **4** was deduced from their IR, ^{1}H NMR, ^{13}C NMR, and HMBC spectra. The ^{1}H NMR spectrum of **4** exhibited two doublets at 0.82 ($^3J_{HH}$ = 14.4 Hz) and 0.94 ($^3J_{HH}$ = 6.6 Hz) ppm of methyl groups. The methine protons of two isobutyl groups appears as a multiplet at 1.92 and 2.25 ppm, respectively. The methylene protons of phenylethyl and isobutyl group appear in the region of 2.92 (t, $^3J_{HH}$ = 7.5 Hz), 3.68 (d, $^3J_{HH}$ = 7.5 Hz), 4.35 (t, $^3J_{HH}$ = 7.8 Hz), and 4.75 (d, $^3J_{HH}$ = 7.8 Hz) ppm, respectively. Aromatic protons appear as multiplet at 7.22–7.31 ppm. The ^{13}C NMR spectrum of **4** showed eighteen distinct signals in agreement with the proposed structure. Also, the HMBC spectrum shows that there is a connection between the hydrogen atoms of the methylene group of isobutyl and the thiocarbonyl group.

The presence of a peak at about 180 ppm in the ^{13}C NMR spectrum of the product ruled out the expected structure of **5**. Because a signal higher than 170 ppm is not expected for the expected structure **5**.
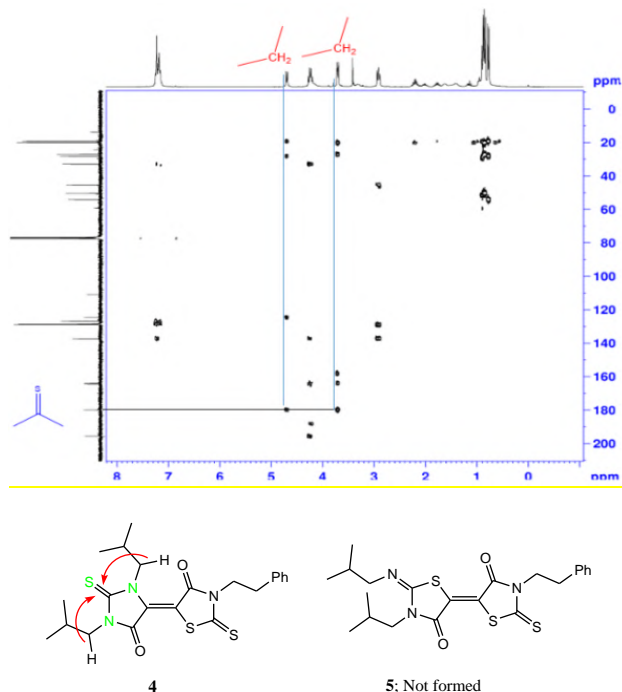
Fig 4: HMBC spectra of compound **4**.

A useful technique to more precisely identify the structure was the decoupled HMBC experiment to measure the coupling constant at **3** bonds. The HMBC spectrum of **4** shows that there is a bond between the hydrogen atoms of the methylene group and the thiocarbonyl group (see Figure 4).

A plausible mechanism for generation of (*E*)-5-(1,3-diisobutyl-5-oxo-2-thioxoimidazolidin-4-ylidene)-3-phenethyl-2-thioxothiazolidin-4-one **4** is presented in Fig. 5.
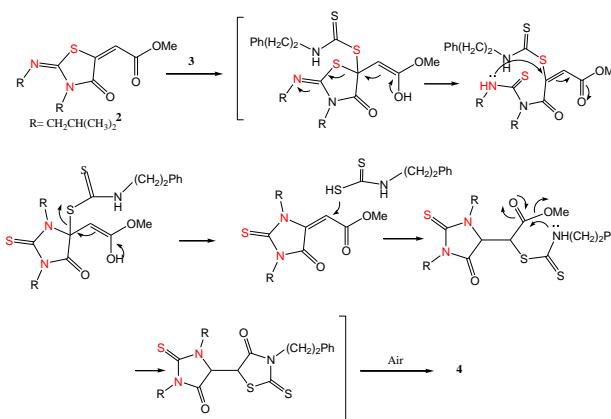
Fig.5: Proposed mechanism for the formation of **4**.

Conclusions

New rhodanine-2-thioxo-4-imidazolidinone scaffold **4** was obtained from the reaction between 5-methoxycarbonylmethylydene-1,3-thiazolidin-4-one **2** and phenethylcarbamodithioic acid **3** under catalyst-free conditions at room temperature, in high yield.

References

[1] K. Omar, A. Geronikaki, P. Zoumpoulakis, C. Camoutsis, M. Sokovic, A. Ciric, and J. Glamo clija, (2010). Novel 4-Thiazolidinone Derivatives as Potential Antifungal and Antibacterial Drugs, Bioorganic & Medicinal Chemistry 18, no. 1 426–32.

[2] M. T. Chhabria, S. Patel, P. Modi, and P. S. Brahmkshatriya, (2016). Thiazole: A Review on Chemistry, Synthesis and Therapeutic Importance of Its Derivatives, Current Topics in Medicinal Chemistry 16, no. 26, 2841–62.

[3] Lown, J. W. Ma, J. C, N. Can, (1967). Addition reactions of acetylenic esters with substituted thioureas, J. Chem, 45, 93.

[4] Nasiri N, Nazari P, (2018). One-pot solvent-free three-component reaction between primaryamines, carbondisulfide, and 5-alkylidene rhodanines (a convenient synthesis of asymmetric birhodanines), J, Molecular Diversity, 9816-5.

Advanced oxidation of the pharmaceutical pollutant ciprofloxacin with activated persulfate radical on ferrite spinels

Mahshid Mahmuodi[a], Seyed Mahdi Moosavi[*B]

Corresponding Author E-mail: mousavi.smahdi@kashanu.ac.ir

[a] Department of Physical Chemistry, Faculty of Chemistry, University of Kashan, Kashan, Iran

[b] Department of Applied Chemistry, Faculty of Chemistry, University of Kashan, Kashan, Iran

Abstract: Currently, a large number of different drugs are used to treat animal and human diseases. Due to widespread use and improper disposal, they eventually pollute surface and underground waters. Advanced oxidation processes (AOP) can be useful in the treatment of emerging pollutants. Spinels are a group of mixed metal oxides, which are a suitable option for radical activation in advanced oxidation processes due to their favorable structure and morphology. In this research, the removal of ciprofloxacin antibiotic by advanced oxidation process based on persulfate radical activated by spinel ferrite catalysts prepared by co-precipitation method was studied and the effect of different precipitating agents in the preparation of spinels on their catalytic performance was investigated. The results showed that cobalt ferrite spinel performed better than nickel ferrite spinel and manganese ferrite. Besides, the XRD results showed that the catalysts prepared with urea precipitating agent had a more regular crystal structure than other precipitating agents.

Keywords: persulfate; spinel; ciprofloxacin; advanced oxidation process

Introduction

With the development of industries, a wide variety of organic pollutants such as dyes, drugs, etc. are discharged into the environment. Most of these pollutants, even in trace amounts, are very toxic and carcinogenic. Currently, a large number of drugs are used to treat diseases, which, due to their widespread use and improper disposal, eventually appear in sewage and contaminate surface and underground water. Ciprofloxacin is a relatively new fluoroquinolone antibiotic. Ciprofloxacin, like most drugs, has low biodegradability and is difficult to remove through conventional wastewater treatment processes. The most efficient method in removing pharmaceutical pollutants is photocatalysis and advanced oxidation purification methods [1,2]. In the advanced oxidation method, hydroxyl or superoxide radicals are used for pollutant oxidation. In advanced oxidation methods, it is very efficient to use metals or metal oxides to activate oxidants and produce radicals. In some studies, spinel nanostructures have been used as catalysts for the activation of persulfate and the removal of pharmaceutical pollutants in the aqueous environment [3,4]. In this research, an attempt is made to develop a suitable and cost-effective catalyst with the ability to activate persulfate in the degradation of ciprofloxacin in aqueous environment by preparing a nanocatalyst with a spinel structure based on ferrite.

Experimental Section

In this experimental study, ferrite spinels with chemical structure (M = Ni, Co, Mn) MFe_2O_4 were prepared by coprecipitation method with different precipitation agents. To prepare spinels wit NaOH and NH_3 precipitant, first the required amount of metal precursors (their nitrate salts) was dissolved in a specified amount of distilled water at 75°C (the total concentration of metal ions is 0.1M).Then the precipitating alkaline solution (37% NH_3 or 0.1 M NaOH) was added drop by drop to the metal solution. When the solution becomes alkaline, metal deposits are formed and the solution becomes cloudy. The suspension was kept at the same temperature for 2 hours with gentle stirring. In the co-precipitation method with urea, after preparing the metal precursor solution in distilled water (the total concentration of metal ions is equal to 0.1 M), an additional amount of urea is added to it, and the temperature of the solution is increased to 75°C during intense stirring. He had reflux for 5 hours. The resulting catalysts were dried in the oven and calcined for 7 hours at a temperature of 650°C.

Next, the performance of prepared spinels in the catalytic oxidation of the medicinal pollutant ciprofloxacin was investigated in the presence of persulfate oxidant. Catalytic oxidation experiments were carried out in 100ml of drug solution with a concentration of 1ppm. In each experiment, 0.1 g of prepared spinels was added to this solution and after 30 minutes, potassium persulfate was added to it.The suspension was stirred for 2 hours. At the specified time, a sample was taken from the solution and the catalyst particles were separated by centrifugation.The concentration of the remaining drug in the separated solution was measured by UV-visible spectrophotometer at the maximum wavelength of the drug (275nm). Using

22nd Iranian Chemistry Congress (ICC22)
Iranian Research Organization for Science and Technology (IROST)
13-15 May 2024

03231-97589

IROST

the following relationship, the percent of drug removal %R was obtained. In this relation, C_0 and C_t are drug concentrations at any time and at the initial time, respectively.

$$R\% = \frac{C_0 - C_t}{C_0} \times 100$$

Results and Discussion

The XRD pattern of prepared spinels is shown in Figure 1. In the prepared samples, all the peaks that appear correspond to the spinel phase (space group fd₃m). According to these XRD patterns, the spinels prepared with urea precipitation agent had a more homogeneous crystal structure. The average size of the particles was calculated using the Scherer and Peak equation with the highest intensity ($2\theta = 35.5°$), and this size was approximately 29nm.
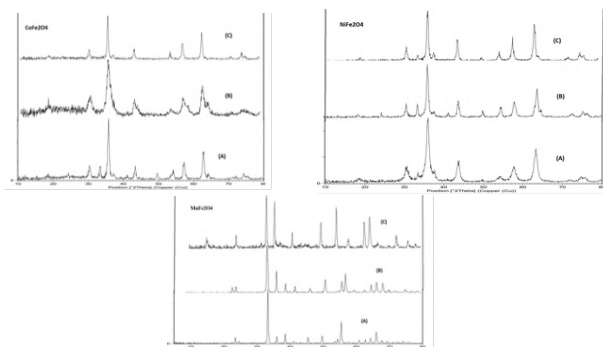
Fig.1: XRD spectrum of spinels prepared in the presence of precipitating agent: a) urea b) NH_3 c) NaOH

In Figure2, the performance of $CoFe_2O_4$, $NiFe_2O_4$, $MnFe_2O_4$ spinels is shown in the form of changes in drug removal percentage over time. According to this figure, $CoFe_2O_4$ spinel prepared with NaOH precipitating agent had the lowest efficiency (R% = 53). But $CoFe_2O_4$ spinel prepared with urea precipitant has performed better and has removed up to 80% of the drug.
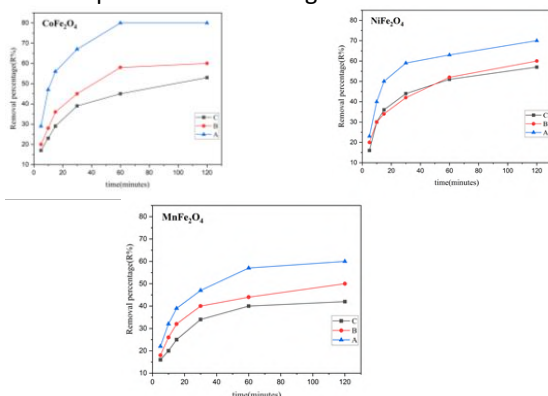
Fig.2: Catalytic performance of $CoFe_2O_4$, NiFe2O4, MnFe2O4 spinels prepared with precipitant: A) urea, B) NH_3, C) NaOH

As can be seen in the figure, the performance of $NiFe_2O_4$ and $MnFe_2O_4$ catalysts is lower than that of $CoFe_2O_4$ spinels. However, spinel prepared in the presence of urea precipitating agent showed a higher efficiency. The more regular crystal structure of spinel prepared in the presence of urea precipitation agent has an important effect on its catalytic performance.

Conclusions

Medicines have different effects in human life. In this study, the efficiency of ciprofloxacin drug removal by advanced oxidation process based on sulfate radicals activated by $CoFe_2O_4$, $NiFe_2O_4$, $MnFe_2O_4$ spinels catalysts was investigated by co-precipitation method in laboratory conditions. And the effect of the precipitating agent on the structure of spinel and their performance in the removal of ciprofloxacin was noted. According to the results obtained from the XRD patterns, it can be said that the synthesis of spinels by co-precipitation method with urea precipitating agent forms a more suitable structure and crystals of spinel. Also, according to the results obtained from the catalytic performance tests of each of the spinels in the removal of Ciprofloxacin drug, it can be concluded that the cobalt ferrite spinel prepared with urea had a better performance than other spinels. According to the results, using spinel as a catalyst in the advanced oxidation process with low cost and high efficiency can be a suitable method to remove drugs.

References

[1]. Tsitonaki, A., Petri, B., Crimi, M., Mosbaek, H. A. N. S., Siegrist, R. L., & Bjerg, P. L. (2010). Critical Reviews in Environmental Science and Technology, 40(1), 55-91.

[2]. Feng, Y., Liu, J., Wu, D., Zhou, Z., Deng, Y., Zhang, T., & Shih, K. (2015). Chemical Engineering Journal, 280, 514-524.

[3]. Robinson, I., Junqua, G., Van Coillie, R., & Thomas, O. (2007). Analytical and bioanalytical chemistry, 387(4), 1143-1151.

[4]. Comninellis, C., Kapalka, A., Malato, S., Parsons, S. A., Poulios, I., & Mantzavinos, D. (2008). Journal of Chemical Technology & Biotechnology, 83(6), 769-776.

22nd Iranian Chemistry Congress (ICC22)
Iranian Research Organization for Science and Technology (IROST)
13-15 May 2024

03231-97589

IROST

Bi-inhibition of carbazochrome compound on alpha-adrenergic and hyaluronidase enzymes in wounds to stop bleeding and speed up healing and skin rejuvenation

Yegane shadfar, hafezeh salehabadi

Corresponding Author E-mail: hsalehabadi2903@gmail.com

Department of Medicinal Chemistry, School of Pharmacy, Zanjan University of Medical Sciences, Zanjan, Iran.

Abstract: The effect of carbazochrome, a capillary stabilizing hemostatic drug, on endothelial barrier dysfunction from vasoactive substances has been investigated, but the enzymes that prevent bleeding remain unknown. This research investigated the effects of carbazochrome on enzymes related to bleeding and wound healing and showed interesting results.

Keywords: carbazochrome; hemostatic drug; molecular docking

Introduction

Bleeding control is a major surgical problem. Excessive bleeding not only increases anesthesia time but also increases morbidity and mortality. Postoperative bleeding may compromise a good technical result in any surgical procedure. The problem is minimized if a systemic hemostatic agent can be administered to the patient preoperatively. There are several in vivo reports of the success of carbazochrome as a hemostatic agent (1). On the other hand, hyaluronidase is the most important enzyme found in the interstitial matrix and effectively breaks down hyaluronic acid. Hyaluronic acid binds to water molecules that help maintain the moisture and elasticity of the skin (2). The level of hyaluronic acid in the skin decreases significantly with age and environmental damage, which can lead to skin dehydration and wrinkles.(3) that we decided to investigate the interaction of carbazochrome with important enzymes in stopping bleeding and wound healing and skin rejuvenation with molecular binding.

Experimental Section

The crystal structure of alpha-adrenergic enzyme codes (PDB: 6KUX (G protein-coupled receptor)) and 6KUY (alpha2A) and hyaluronidase enzyme (PDB: 2PE4) were obtained from the protein database (www.rcsb.org). After validation, carbazochrome was investigated by docking studies.

Results and Discussion

Three enzymes were selected by limiting the acceptable binding energy and having an appropriate orientation in the active pocket.

Table 1. The binding energy of interaction between carbazochrome and selected enzymes' active site was obtained from docking studies.

NO	Enzyme (PDB code)	carbazochrome structure	Mean binding energy
1	6KUX (alpha adrenergic)		-5.34
2	6KUY (alpha adrenergic)		-5.32
3	2PE4 (hyaluronidase)		-5.05
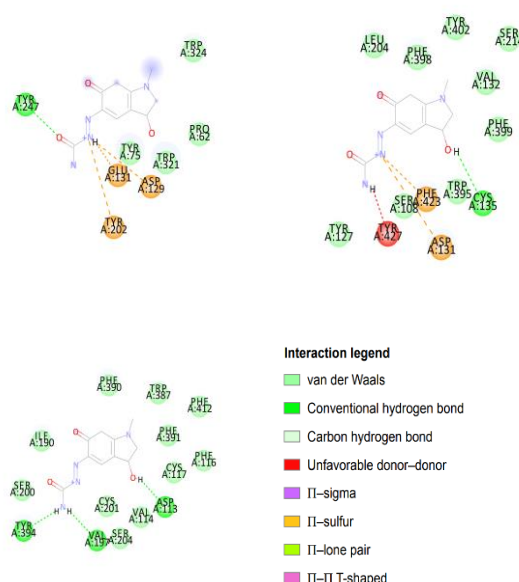
Fig. 1: Two-dimensional structures are shown above with ligand and ionic bonds with orange color and hydrogen bonding with green.

22nd Iranian Chemistry Congress (ICC22)
Iranian Research Organization for Science and Technology (IROST)
13-15 May 2024

03231-97589

Conclusions

Carbazochrome interacts with platelet surface α-adrenergic receptors, activates the IP3/DAG PLC pathway, and increases calcium levels. High calcium ions activate myosin light chain kinase via calmodulin and facilitate myosin cross-bridges. Endothelial cells change the shape of platelets and release factors such as serotonin and von Willebrand factor. Platelet activator, which is produced by platelets, increases the aggregation and adhesion of platelets through vasoactive factors and causes the formation of blood clots and prevents bleeding, and by inhibiting hyaluronidase and protecting skin hyaluronan, the speed of recovery Increases wound healing and rejuvenation.

References

[1] Dykes ER, Anderson R. Carbazochrome salicylate as a systemic hemostatic agent in plastic operations: a clinical evaluation. JAMA. 1961 Sep 9;177(10):716-7.

[2] Maurizio Cavallini, Riccardo Gazzola, Marco Metalla, Luca Vaienti, The Role of Hyaluronidase in the Treatment of Complications From Hyaluronic Acid Dermal Fillers, Aesthetic Surgery Journal, Volume 33, Issue 8, November 2013,Pages1167–1174,
https://doi.org/10.1177/1090820X13511970

[3] Bravo, B., Correia, P., Gonçalves Junior, J. E., Sant'Anna, B., & Kerob, D. (2022). Benefits of topical hyaluronic acid for skin quality and signs of skin aging: From literature review to clinical evidence. Dermatologic therapy, 35(12), e15903.

Fabrication of some visible-light-induced photocatalysts based on oxygen vacancy-rich CeO$_2$ towards wastewater detoxification

Meysam Habibi*, Aziz Habibi-Yangjeh

Corresponding Author E-mail: m.habibi@uma.ac.ir.

a Department of Chemistry, Faculty of Science, University of Mohaghegh Ardabili, Ardabil, Iran.

Abstract: Recently, the utilization of antibiotics has greatly increased, causing tremendous water pollution. In this presentation, the activity of some novel photocatalysts fabricated using oxygen vacancy-rich CeO$_2$ (denoted as CeO$_{2-x}$) was evaluated against degradation of antibiotics upon visible-light exposure.

Keywords: Antibiotics detoxification; CeO$_{2-x}$-based photocatalysts; Heterogeneous photocatalyst; Wastewater pollutants.

Introduction

In the last century, with the increase in infectious diseases, the utilization of antibiotics has tremendously increased. Despite the advantages of antibiotics for the humans and animals treatments, the changes that occur in the nature cycles owing to the presence of antibiotics cannot be ignored. Tetracycline hydrochloride (TCH), as an antibiotic, is widely used to deal with infectious diseases. The entry of effluents containing TCH into water resources can lead to many problems such as the destruction of aquatic life and the pollution of water for agricultural and drinking purposes. Therefore, elimination of antibiotics, especially TCH, has become a high priority research field. Heterogeneous photocatalysis using solar energy is a promising technology for detoxification of water resources contaminated with organic compounds, namely antibiotics, organic dyes, pesticides, perconal care compounds, etc. [1-3].

Cerium oxide (CeO$_2$) has some attractive characteristics, including high stability, facile synthesis methods, and environmentally friendly. To increase the amount of solar energy utilization by this semiconductor, the creation of oxygen vacancy is a promising technology. Hence, in this presentation, the photocatalytic activity of some recently developed photocatalysts based on oxygen vacancy-rich CeO$_2$ (denoted as CeO$_{2-x}$) will be compared, including CeO$_{2-x}$/Ag/AgFeO$_2$, CeO$_{2-x}$/Ag$_4$V$_2$O$_7$, and CeO$_{2-x}$/Cu$_3$BiS$_3$ nanocomposites upon visible-light illumination [4-6].

Experimental Section

The sythesis routes for preparation of CeO$_{2-x}$/AgFeO$_2$/Ag, CeO$_{2-x}$/Ag$_4$V$_2$O$_7$, and CeO$_{2-x}$/Cu$_3$BiS$_3$ nanocomposite have been reported elsewhere [4-6].

Results and Discussion

The XRD analyses were employed to prove the formation of nanomaterials and identify their crystal phases [4-6]. The energy gap of each photocatalyst tremendously affects on its ability for absorbing illuminated light. As shown in Table 1, band gap of CeO$_{2-x}$ was reduced compared to CeO$_2$, and CeO$_{2-x}$ nanoparticle can be easily excited upon visible light and produce electron-hole pairs. Furthermore, the energy gap of CeO$_{2-x}$/Ag/AgFeO$_2$, CeO$_{2-x}$/Ag$_4$V$_2$O$_7$, and CeO$_{2-x}$/Cu$_3$BiS$_3$ nanocomposites are significantly less than that of CeO$_{2-x}$, so they can help to produce more electron-hole pairs. Figures 1(a-c) show the results of FE-SEM analyses. As evident, the prepared photocatalysts have been grown in the spherical form and this morphology can increase the contact surface of the photocatalyst with the pollutants. On the other hand, since the surface area is an important factor in increasing the photocatalytic activity, with the creation of oxygen vacancies in CeO$_2$, the surface area has increased significantly. Figure 2 shows the rate constants of the optimal photocatalysts. The rate constant for TCH degradation by optimum CeO$_{2-x}$/Ag/AgFeO$_2$ (20%), CeO$_{2-x}$/Ag$_4$V$_2$O$_7$ (20%), and CeO$_{2-x}$/Cu$_3$BiS$_3$ (30%) photocatalysts were 55.7, 41.9, and 28.0 times faster than CeO$_2$, respectively. In addition, the CeO$_{2-x}$/AgFeO$_2$/Ag (20%), CeO$_{2-x}$/Ag$_4$V$_2$O$_7$ (20%), and CeO$_{2-x}$/Cu$_3$BiS$_3$ (30%) nanocomposites displayed 10.2, 7.69, and 5.13 times superior performance than CeO$_{2-x}$ in the detoxification of TCH, respectively [4-6].

22nd Iranian Chemistry Congress (ICC22)
Iranian Research Organization for Science and Technology (IROST)
03231-97589
13-15 May 2024

ISC Islamic World Science Citation Center

IROST
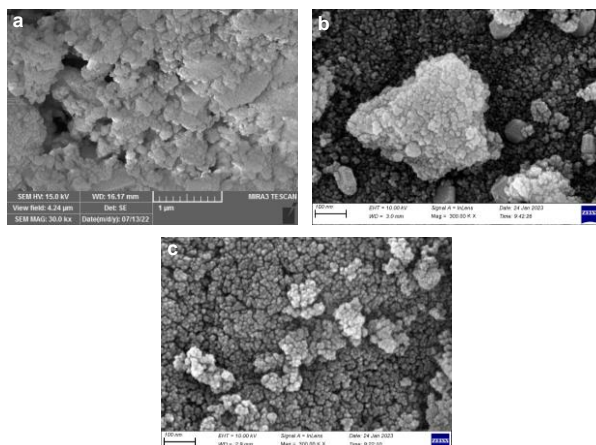
Fig.1: FE-SEM images of (a) $CeO_{2-x}/Ag/AgFeO_2$ (20%), (b) $CeO_{2-x}/Ag_4V_2O_7$ (20%), and (c) CeO_{2-x}/Cu_3BiS_3 (30%) photocatalysts.
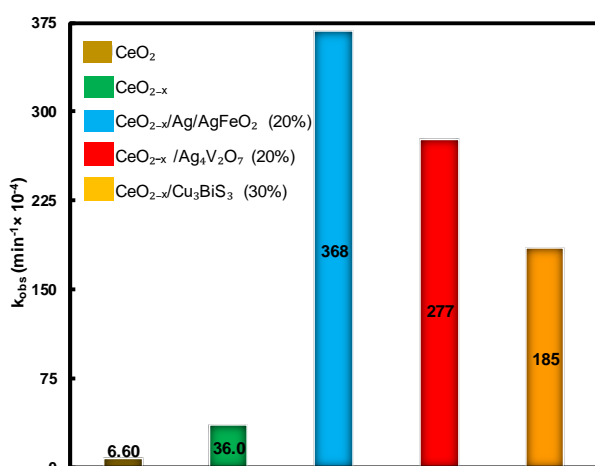
Fig.2: The TCH detoxification rate constants of the specified photocatalysts.

Table1: Energy gap values related to the specified photocatalysts.

Photocatalyst	Energy gap (eV)	Ref.
CeO_2	3.10	[4]
CeO_{2-x}	2.69	[4]
$CeO_{2-x}/Ag/AgFeO_2$ (20%)	1.89	[4]
$CeO_{2-x}/Ag_4V_2O_7$ (20%)	1.31	[5]
CeO_{2-x}/Cu_3BiS_3 (30%)	1.30	[5]

Conclusions

All in all, oxygen vacancy creation in CeO_2 improved the light absorption and reduced the energy gap, so that the TCH degradation by CeO_{2-x} was much better than CeO_2. In addition, the integration of CeO_{2-x} with $Ag/AgFeO_2$, $Ag_4V_2O_7$, and Cu_3BiS_3 counterparts improved the photocatalytic reaction rate to a superior extent. Therefore, the developing heterojunctions and creation of oxygen vacancies are efficacious in TCH degradation via heterogeneous catalytic technology upon visible-light exposure.

References

[1] Habibi-Yangjeh, A., Pournemati, K., 2024. A review on emerging homojunction photocatalysts with impressive performances for wastewater detoxification. Critical Reviews in Environmental Science and Technology, 54, 290-320. https://doi.org/10.1080/10643389.2023.2239125.

[2] Hemmati-Eslamlu, P., Habibi-Yangjeh, A., 2023. A review on impressive Z-and S-scheme photocatalysts composed of g-C_3N_4 for detoxification of antibiotics. FlatChem, 43, 100597. https://doi.org/10.1016/j.flatc.2023.100597.

[3] Seifikar, F., Habibi-Yangjeh, A., 2024. Floating photocatalysts as promising materials for environmental detoxification and energy production: A review. Chemosphere (2024): https://doi.org/10.1016/j.chemosphere.2024.141686.

[4] Habibi, M., Habibi-Yangjeh, A., & Khataee, A. (2023). S-scheme $CeO_{2-x}/AgFeO_2/Ag$ photocatalysts with impressive activity in degradation of different antibiotics under visible light. Surfaces and Interfaces, 39, 102937. https://doi.org/10.1016/j.surfin.2023.102937.

[5] Zohari-Moafi, M., Habibi, M., Habibi-Yangjeh, A., & Akinay, Y. (2024). Binary $CeO_{2-x}/Ag_4V_2O_7$ photocatalysts: Impressive performances in detoxification of organic and inorganic pollutants. Molecular Catalysis, 556, 113920. https://doi.org/10.1016/j.mcat.2024.113920.

[6] Habibi, M., Habibi-Yangjeh, A., Akinay, Y., & Khataee, A. (2023). Oxygen vacancy-rich CeO_2 decorated with Cu_3BiS_3 nanoparticles: Outstanding visible-light photocatalytic performance towards tetracycline degradation. Chemosphere, 340, 139828. https://doi.org/10.1016/j.chemosphere.2023.139828.

Synthesis and investigation of the efficiency of the MIL (88) electrode as a cathode in the electrofenton process to remove the antibiotic erythromycin from contaminated water

Parisa Yousefzadeh Taheri, Mahmoud Zarei[*]

Corresponding Author E-mail: mzarei@tabrizu.ac.ir

Department of Applied Chemistry, Faculty of Chemistry, University of Tabriz, Tabriz, Iran.

Abstract: In this paper,MIL(88)Fe is synthesized.Then,MIL(88)Fe cathode is fabricated as a new and useful electrode. To prepare this electrode MIL(88)Fe powder is covered on a suitable substrate. Then,It is used to remove Erythromycin antibiotic from waste water using Electro fenton process.

Keywords: Electro fenton; Metal organic frameworks; Gas diffusion electrode; Erythromycin

Introduction

Pharmaceutical compounds enter urban water and sewage systems through several sources, including the pharmaceutical industry, health and treatment sectors, and related treatment facilities[1] . Advanced oxidation is the preferred solution for the degradation of organic compounds in wastewater. Advanced oxidation can degrade the vast majority of pollutants, including micropollutants and organic molecules. Electrochemical oxidation (ECO) is considered a clean, versatile and effective advanced oxidation technology for removing pollutants from industrial wastewater due to its simple operation without producing toxic compounds and producing strong oxidants including hydroxyl radicals[2]. Electrochemical Advanced Oxidation Processes (EAOPs) are powerful and efficient tools for water treatment[3].

Electrochemical processes do not require chemical additions, in fact electrons are the only reactants that stimulate the removal of pollutants. One of the fundamental challenges for wider applications is the need to reduce the energy consumption and costs of electrochemical treatment[4].In recent years, a new advanced electro-oxidation technology of Electro-Fenton process is getting a rapid development[2]. The basic principle of Electro-Fenton process is based on the generation of H2O2 in-situ at the cathode by reducing O2, and then H2O2 could react with Fe2+ to generate ·OH radicals with much stronger oxidation capability to degrade macromolecular organic substances and convert them into small molecular substances or inorganic substances such as H2O and CO[6].

For the past decade, MOF-based electrodes are attracting significant research attention due to the possibilities of tuning its branches and metal centers to make it electrically conductive[7].

Experimental Section

Materials

Metal-organic framework, Poly tetra flouro ethylene 60%(PTFE), n-methyl2- pyrrolidone(nmp(Merck),N-butanol(Merck), sodium hydroxide 99%(Merck),N.N-dimethyl formamide(DMF),Terephtalic acid,FeCl₃.6H₂O(Merck)

Synthesis of MIL(88)Fe

Firt,NaOH(2M)solution is prepared.Then,1.76ml NaOH(2M) is added to 22ml DMF and mixed on stirrer to obtain a homogeneous solution.Then,1.88g FeCl₃.6H₂O and 0.7285g terephtalic acid is added to the solution.Then,it is dried 12h at 100°C in oven.Then,resulting suspension is dried on filter paper for 3 nights.Then the resulting powder is washed in 80ml for 20h on stirrer.Finally,resulting sediment is dried and turned into MIL(88)Fe powder.

Fabrication of MIL(88)Fe cathode

To prepare this electrode, 0.1 g of synthesized MIL(88)Fe powder is mixed with 0.4g of 6% PTFE,16ml nmp and 3% volumetric nbutanol.The resulting solution is placed in an ultrasonic bath for 6 min to obtain a uniform solution.
After heating and evaporation of this solution, a dough-like material is formed which is drawn as a thin layer on the carbon layer. The resulting sheet is then heated for 30 min at 35°C in the inert medium (N2 gas) inside the furnace to calcination. The resulting sheet is cut into circular plates with a diameter of 25mm.

Results and Discussion

Fig1.(a) shows SEM image of the synthesized MIL(88)Fe that has hexagonal cylindrical morphology,and its crystallinity is determind using this property.
Fig1.(b) shows SEM image of the synthesized MIL(88)Fe electrode. As can be seen in this picture,the surfaceis rough and porous which increases the surface area, the current density and oxygen diffusion rate. This will lead to

22nd Iranian Chemistry Congress (ICC22)
Iranian Research Organization for Science and Technology (IROST)
13-15 May 2024

03231-97589

a higher mass transfer rate, resulting in increased production of H2O2 at the electrode's surface. The SEM image (a) reported in this research work is consistent with those reported in literature[5].The SEM image(b) reported in this research work is consistent with those reported in literature[6].
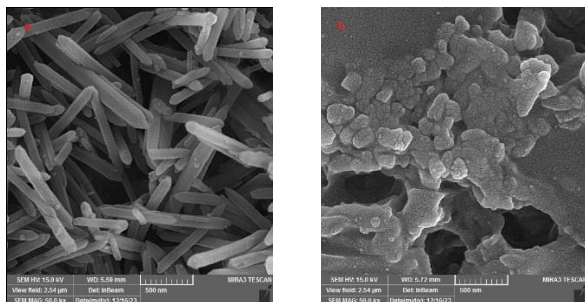
Fig.1: SEM images of a)MIL(88)Fe powder,b)MIL(88)Fe cathode

Conclusions

In the present work, the EF process for the removal of erythromycin from contaminated water was investigated using a cathode electrode made of MIL(88)Fe. As there is Fe in cathode structure there is no need to add iron to the EF process which results in the formation of ferrous sediments. Replacing porous MOF materials with common carbon materials and types of polymers, the high strength of the electrode.

The final MIL(88)Fe and MIL(88)Fe electrode structure was studied using SEM images.

References

[1] Ahmadpour N, Nowrouzi M, Avargani VM, Sayadi MH, Zendehboudi S. Design and optimization of TiO2-based photocatalysts for efficient removal of pharmaceutical pollutants in water: Recent developments and challenges. Journal of Water Process Engineering. 2024;57:104597.

[2] Amali S, Zarei M, Ebratkhahan M, Khataee A. Preparation of Fe@ Fe2O3/3D graphene composite cathode for electrochemical removal of sulfasalazine. Chemosphere. 2021;273:128581.

[3] Mehrkhah R, Park SY, Lee JH, Kim SY, Lee BH. A comparative study of advanced oxidation-based hybrid technologies for industrial wastewater treatment: An engineering perspective. Chemical Engineering Science. 2023:119675.

[4] Wei J, Liu Y, Wu X. A cyclone reactor of electrochemical advanced oxidation processes using PbO2 anode and H2O2 electrosynthesis cathode. Water Research. 2023;245:120629.

[5] Wei J, Liu Y, Wu X. Electrochemical advanced oxidation processes using PbO2 anode and H2O2 electrosynthesis cathode for wastewater treatment. Process Safety and Environmental Protection. 2023;178:444-55.

[6] Ramasubramanian B, Chinglenthoiba C, Huiqing X, Xiping N, Hui HK, Valiyaveettil S, Ramakrishna S, Chellappan V. Sustainable Fe-MOF@ carbon nanocomposite electrode for supercapacitor. Surfaces and Interfaces. 2022;34:102397.

[7] Lin Y-S, Lin K-S. Characterization of the size and porous temperature sensitivity of Pluronic F127–Coated MIL–88B (Fe) for drug release. Microporous and Mesoporous Materials. 2021;328:111456.

22nd Iranian Chemistry Congress (ICC22)
Iranian Research Organization for Science and Technology (IROST)
13-15 May 2024

03231-97589

Bio synthesis and antibacterial activity of silver nanoparticles using the extract of leaves of *Crataegus azarolus* L. harvested from Deylaman - Guilan

Parniya Hemmati [a], Shahab Ojani [*b]

Corresponding Author E-mail: Shahab_ojani@yahoo.com

[a] Department of Chemistry, Imam Khomeini international university, Qazvin, Iran.

[b] Department of Chemistry, Karaj Branch, Islamic Azad University, Karaj, Iran.

Abstract: Researchers use bio-nanotechnology techniques as eco-friendly and cost-effective routes to fabricate nanoparticles and nanomaterials. In the present project, the Bio synthesis and antibacterial activity of silver nanoparticles using the extract of leaves of *Crataegus azarolus* L. harvested from Deylaman – Guilan has been reported.

Keywords *Crataegus azarolus* L.; Green synthesis; Silver nanoparticles.

Introduction

Nanotechnology suggests characterizing and using material in nanometer size in diverse fields consisting of chemistry, biology, medicine, physics, etc. which have caught the eyes of many in recent years. Nano-medicine works at the same extent around 100 nanometers or less than structures within living cells and biological molecule's function. Nano-medicines can have a notable role in developing alternate and more efficient strategies for the diagnosis and treatment of malignancies, neurodegenerative and infectious disorders such as Alzheimer's disease. Hence, in a nanoscale, the nanomaterials, due to having a high ratio of surface-to-volume, display unique physicochemical impacts that are not common in their bulk parent materials. The synthesis of metallic nanoparticles (NPs) has attracted outstanding appeal because of their unique properties. Therefore, a variety of metals like magnesium, copper, zinc, gold, silver, titanium have been evaluated and among them, the silver nanoparticles (SNPs) have demonstrated a broad size distribution and morphologies with highly reactive specimens [1-2]. Crataegus species (Rosaceae), known as "Hawthorn" comprise approximately 280 species which are native to Mediterranean region, North Africa, Europe and Central Asia. The genus name Crataegus is derived from a Greek word Kratos meaning hardness of wood. Crataegus species have been traditionally used for treating cardiovascular diseases including congestive heart failure, angina, hypertension, peripheral vascular disease, hyperlipidaemia and diabetes mellitus. [3]. Crataegus species possess immense medicinal applications therefore, in this project, we characterized the bio synthesis and antibacterial activity of silver nanoparticles using the extract of leaves of *Crataegus azarolus* L. harvested from Deylaman – Guilan.

Experimental Section

In this project, 20 gram of powder of leaves of *Crataegus azarolus* L. (C. azarolus) was mixed with hydroalcoholic exposed to microwave irradiation at 100 W in microwave (model GE 280 S) oven with regular at intervals 10 minute irradiation during 5 minutes. After extracting, the solvent was removed under the vacuum at temperature below 45^{0C} and the extract were freeze dried. Then, 0.1 g of dried extract of *Crataegus azarolus* L. leaves is added into 50 ml deionized water and then stirred for 1 h in a magnetic stirrer at room temperature. Coarse filtering is employed prior to centrifuging the extract at 4000 rpm for 30 min to remove the heavy biomaterials in it. Clear C. azarolus leaves extract is mixed immediately into a 0.1 mM $AgNO_3$ solution of equal volume. The color change involved in the formation of (Ag-NPs). Green synthesis of (Ag-NPs) was characterized by UV-Vis, FT-IR, XRD and TEM. Then, the antibacterial activity of the synthesized (Ag-NPs) was tested using both gram positive as well as gram negative bacteria i.e. *Staphylococcus aureus* (ATCC 25923) and *Escherichia coli* (ATCC 25922), respectively.

Results and Discussion

UV-Vis characterization

The production of Ag-NPs was confirmed by the absorption spectrum of λ max at 440 nm. The UV-Vis results are given in (Fig 1).

22nd Iranian Chemistry Congress (ICC22)
Iranian Research Organization for Science and Technology (IROST)
13-15 May 2024

03231-97589

IROST
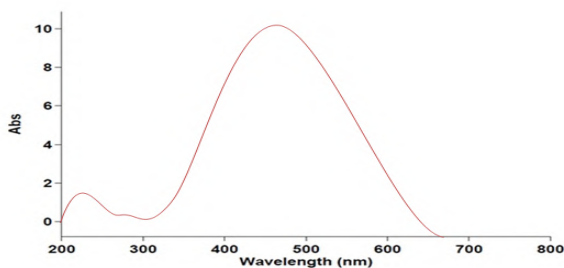
Fig.1: UV–Visible spectrum of synthesized Ag-NPs

Fig.4: TEM images indicating of (Ag-NPs) obtained using C. azarolus

FT-IR analysis

Biomolecules that are associated with (Ag-NPs) are detected via FT-IR. The FT-IR results are given in (Fig 2). The presence of of various functional groups such as NH_2, OH, C=O, etc was confirmed via FT-IR, which played vital roles as reducing and capping agents of (Ag-NPs) synthesis. These functional groups were also responsible for the stabilization of nanoparticles.
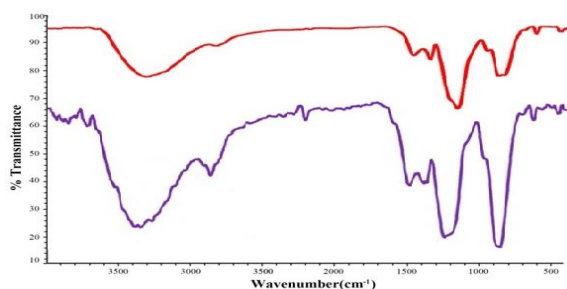
Fig.2: FT-IR spectra of (Ag-NPs) obtained using C. azarolus

XRD results

The XRD indicate that the Ag-NPs are face centered cubic, and crystalline in nature. The XRD results are given in (Fig 3).
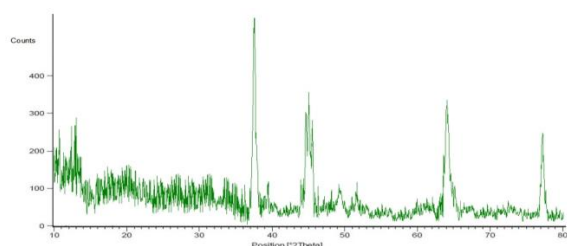
Fig.3: XRD pattern of (Ag-NPs) obtained using C. azarolus

TEM studies

The particle size of the Ag-NPs was studied by TEM and showed the presence of Ag-NPs in the size range 40 nm. (Fig 4).

Antibacterial activity

The synthesized Ag-NPs using C. azarolus exhibited good antibacterial potential against gram positive and gram negative bacterial strains. The antibacterial activity results are given in (Table 1).

Table1: Antibacterial activity of synthesized Ag-NPs using C. azarolus

No.	Bacteria	MIC (ug/ml)	MBC (ug/ml)
1	*Staphylococcus aureus*	6.25	12.5
2	*Escherichia coli*	3.12	6.25

Conclusions

Thus, this method can be used for rapid and ecofriendly bio-synthesis of stable Ag nanoparticles of size range 40 nm possessing antibacterial activity suggesting their possible application in medical industry.

References

[1] Yassin, M. T., Mostafa, A.A.-F., Al-Askar, A. A. & Al-Otibi, F. O. (2022). Facile green synthesis of silver nanoparticles using aqueous leaf extract of *Origanum majorana* with potential bioactivity against multidrug resistant bacterial strains. Crystals, 12(5), 603. https://doi.org/10.3390/cryst12050603.

[2] Öztürk Küp, F., Coskuncay, S., & Duman, F., (2020). Biosynthesis of silver nanoparticles using leaf extract of *Aesculus hippocastanum* (horse chestnut): Evaluation of their antibacterial, antioxidant and drug release system activities. Materials Science & Engineering C-Materials for Biological Applications, 107. https://doi.org/10.1016/j.msec.2019.110207.

[3] Bahri-Sahloul, R., S, Ammar, R. B., Fredj, S., Saguem, S., Grec, F., Trotin, F. H., Skhiri. (2009). Polyphenol contents and antioxidant activities of extracts from flowers of two *Crataegus azarolus* L. varieties. Pakistan Journal of Biological Sciences, 12(9): 660-8. https://doi.org/10.3923/pjbs.2009.660.668.

Chitosan-Based Hydrogels for Heavy Metal Removal from Wastewater

Sarah Fathali Bigloo, Goldasthe Zarei*, Farrokh Roya Nikmaram, Jamshid Najafpour, Faezeh Khalilian

Corresponding Author E-mail: goldasthe@yahoo.com, g.zarei@aiusr.ac.ir

Department of Chemistry, Yadegar-e-Imam Khomeini (RAH) Shahre Rey Branch, Islamic Azad University, Tehran, Iran.

Abstract: This study investigates the synthesis and optimization of chitosan-based hydrogels for the efficient removal of heavy metals from wastewater. The research focuses on enhancing the properties of these hydrogels to achieve desirable characteristics for metal ion removal. Experimental parameters such as reaction temperature, time, and raw material composition are optimized. The synthesized hydrogels are then evaluated for their effectiveness in heavy metal removal, considering factors like contact time, removal efficiency, and reusability

Keywords: Removal of Heavy Metals; Hydrogels, Chitosan.

Introduction

Water pollution from various organic and inorganic contaminants is one of the greatest challenges of the modern era. These pollutants pose serious threats to human health and the survival of plants and animals. Various physical, chemical, and biological methods have been employed for the purification and reuse of polluted water resources. Among these processes, surface adsorption is one of the most recognized and commonly used methods. Chitosan possesses a free amino group that, due to the removal of the acetyl group from the chitin structure, renders it more useful and efficient. Chitosan is a biodegradable and non-toxic polymer with a high molecular weight, being the most abundant biopolymer after cellulose and lignin. This material is one of the renewable polymer substances used extensively in pharmaceutical and medical industries for enzyme deactivation. Chitosan finds applications in wastewater purification in chemical and food industries, as well as in food formulations, serving as a binding agent, gel former, thickener, and stabilizer. Due to the biocompatibility and biodegradability of chitosan and its derivatives; it is widely utilized in the production of medical materials, enzymes, and cell immobilization, particularly for drug release. As chitosan easily dissolves in acidic solutions, cross-linking of chitosan in a network form represents the sole method for preparing chitosan hydrogels. [1-3].

Experimental Section

In this method, chitosan diacetyl is added to a 90% solution in a 1% (v/v) aqueous acetic acid solution, and it is stirred with a magnetic stirrer for 20 minutes until completely dissolved. Then, the cross-linking agent, dissolved in 2 milliliters of absolute ethanol, is gradually added to the chitosan solution, and the mixture is stirred for two hours at room temperature until the hydrogel is formed. Subsequently, the hydrogel is washed with distilled water to remove acetic acid and alcohol.

Results and Discussion

In this research, functional groups were covalently bonded to chitosan, resulting in the preparation of chitosan hydrogel. These functional groups act as ligands for metals, and by controlling synthesis parameters such as reaction temperature, reaction time, type, and quantity of raw materials; we aim to enhance the properties of synthesized hydrogels to produce hydrogels with desired characteristics.

Conclusions

The study involved the synthesis of chitosan-based hydrogels using various methods, with optimization of synthesis conditions. Subsequently, these hydrogels were employed for the removal of heavy metals from wastewater. Effective factors such as contact time, removal efficiency for metal ions, and reusability were investigated.

References

[1] Tao, X.; Wang, S.; Li, Z.; Zhou, S. (2021)Green synthesis of network nanostructured calcium alginate hydrogel and its removal performance of Cd2+ and Cu2+ ions. Mater. Chem. Phys., 258, 123931.

[2] Lü, T.; Ma, R.; Ke, K.; Zhang, D.; Qi, D.; Zhao, H. (2021). Synthesis of gallic acid functionalized magnetic hydrogel beads for enhanced synergistic reduction and adsorption of aqueous chromium. Chem. Eng. J., 408, 127327.

[3] Xu, X.; Ouyang, X. K.; Yang, L. Y.(2021).Adsorption of Pb(II) from aqueous solutions using crosslinked carboxylated chitosan/carboxylated nanocellulose hydrogel beads. J. Mol. Liq., 322, 114523.

Advanced Magnetic P₂W₁₆Ni₂O₆₂/Cr-MIL-101/CuFe₂O₄ Nanoadsorbent as a highly efficient adsorbent for the elimination of Cationic dyes from aqueous solutions

SSeyedeh Simin dakhilpour [*a], Afsoon jarrah [b], Gholamhassan Imanzadeh [a], Mohammad reza zamanlou [a], Ali Mortazavi [a]

Corresponding Author E-mail: Ssn.dakhilpour@yahoo.com

[a] Department of Chemistry, Faculty of Sciences, University of Mohaghegh Ardabili, Ardabil, Iran.

[b] Digestive Disease Research Center, Ardabil University of Medical Sciences, Ardabil, Iran.

Abstract: A novel magnetic nanoadsorbent P₂W₁₆Ni₂O₆₂/Cr-MIL-101/CuFe₂O₄ was synthesized and effectively employed to eliminate Methylene Blue, Malachite Green and Crystal Violet dyes from waste water. Several investigations were conducted such as VSM, FTIR, SEM, EDX, XRD, and BET analysis. The optimal values for the highest removal were pH of 10, Contact time of 4 min to 10 min, dye concentration of 50 mg/L, and nano adsorbent mass of 0.03 g/L. These optimal values resulted in a removal efficiency of 100%.

Keywords: Cr-MIL-101, Metal-organic framework, Magnetic nanocomposite, Dyes pollutant.

Introduction

Organic dyes have been used enormously in numerous fields, before-mentioned as coloring the product of textiles, paper, rubber, leather, printing, plastic, etc. which causes serious threat to human health and environment [1]. Polymeric resins, biomaterials, activated carbon, clay minerals, metal organic frameworks (MOF), zeolites and industrial solid wastes are used to remove pollutant [2]. Porosity of the MOFs has been the most common factor according to the size of the dyes e.g. linear dyes like methylene blue, Crystal Violet, Malachite Green and other organic dye for their adsorption [3]. Planar aromatic rings present in the skeleton of the MOF are added advantage to interact the dye molecules through π–π or C–H···π interactions with pollutants [4]. In this project, a magnetic P₂W₁₆Ni₂O₆₂/Cr-MIL-101/CuFe₂O₄ nanocomposite was fabricated with hydrothermal method and its chemical properties and physical structure were characterized. The adsorption of Crystal Violet, Methylene Blue and Malachite Green organic dyes onto P₂W₁₆Ni₂O₆₂/Cr-MIL-101/CuFe₂O₄ and the influences of the adsorbent dose, primary dye concentration, temperature, and pH on the adsorption system were checked.

Experimental Section

To evaluate the adsorption capability of the P₂W₁₆Ni₂O₆₂/Cr-MIL-101/CuFe₂O₄ for the removal of dyes from contaminated waters, three organic dyes MB, MG, and CV with different charges and sizes were used. Their adsorption was specified using the characteristic UV-Vis adsorption band. The results demonstrate that the adsorption peaks of MB, MG, and CV at 664, 614, and 588 nm completely disappeared within 4, 10, and 10 min with an adsorption efficiency of 100%, respectively. Two models, namely the pseudo-first-order (PFO) and pseudo-second-order (PSO) models, were utilized. Freundlich and Langmuir, Temkin, and Dubinin-Radushkevich isotherm

models were employed to investigate the adsorption behavior of dyes on the P₂W₁₆Ni₂O₆₂/Cr-MIL-101/CuFe₂O₄ nanocomposite and was carried out at different temperatures to determine the thermodynamic parameters, including the Gibbs free energy changes (ΔG^0). Individual and collective consequences of the diverse factors, such as pH (A, 2–10), temperature (B, 298–358 K), adsorbent dosage (C, 10–40 mg), and concentration (D, 25–200 mg/L) values with three levels (-1, 0, 1) carried out in Box-Behnken Design. 29 samples using Design-Expert 11 software were statistically analyzed for statistical investigations such as analysis of variance (ANOVA), 3D surface plots, and fit statistics.

Results and Discussion
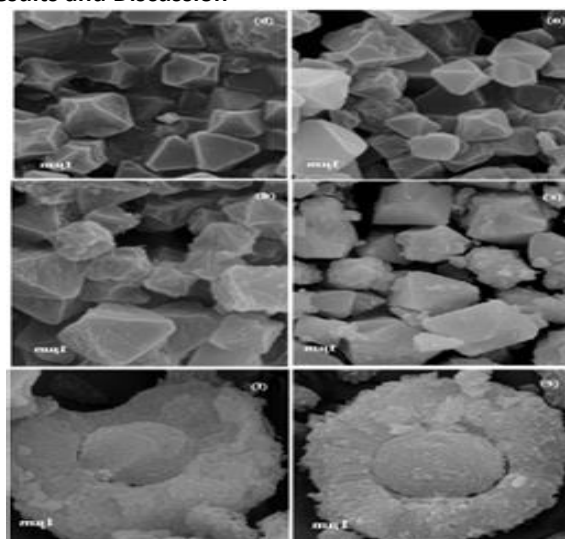
The SEM of Cr-MIL101 (a, b), P₂W₁₆Ni₂O₆₂/Cr-MIL101 (c, d), and P₂W₁₆Ni₂O₆₂/Cr-MIL101 (e, f).

22nd **Iranian Chemistry Congress (ICC22)**
Iranian Research Organization for Science and Technology (IROST)
13-15 May 2024

03231-97589
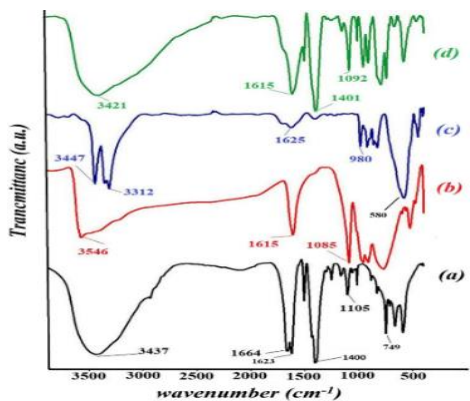
FT-IR spectra of the as-fabricated (a) Cr-MIL101, (b) $P_2W_{16}Ni_2O_{62}$, (c) $CuFe_2O_4$, (d $P_2W_{16}Ni_2O_{62}$/Cr-MIL101

XRD patterns of MIL-101(Cr), $CuFe_2O_4$ $P_2W_{16}Ni_2O_{62}$ and $P_2W_{16}Ni_2O_{62}$/Cr-MIL101/ $CuFe_2O_4$

BET isotherms and (B) pore-size dispersion of P2W16Ni2O62 /Cr-MIL-101/ CuFe2O4 (a) Cr-MIL-101 (b) P2W16Ni2O62 /Cr-MIL-101, and (c) $P_2W_{16}Ni_2O_{62}$/Cr-MIL101/ CuFe2O4

Magnetization curves of CuFO (a) and $P_2W_{16}Ni_2O_{62}$ /Cr-MIL-101/CuFO (b). The inset shows the use of an external magnetic field
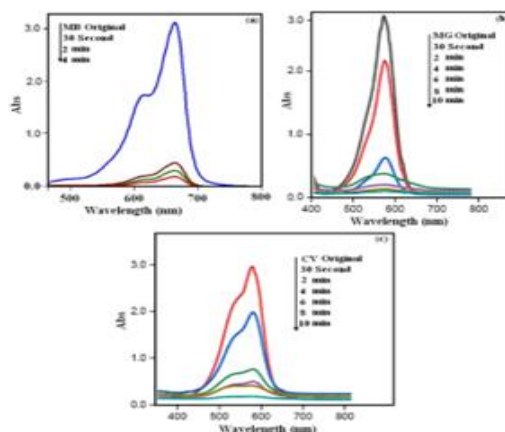
UV-vis spectra of the adsorption of three dyes over $P_2W_{16}Ni_2O_{62}$ /Cr-MIL-101/CuFO: (a) MB, (b) MG and (c) CV. Adsorbent dosage = 30 mg, [dye]$_0$ = 50 mg L^{-1}, 50 mL, T = 25 °C.

The influence of MB, MG and CV concentration (a), adsorbent dosage (b), reaction temperature (c), and pH (d) on the elimination of MB, MG and CV dyes via the P2W16Ni2O62/Cr-MIL-101/CuFO adsorbent. Conditions: C0 (MB) = 50 mg L-1, adsorbent dose = 30 mg, pH = 6 and temp = 25 °C. The adsorption time for MB = 4min, MG and CV was 10 min.

(a)Reusability cycles for removal of MB, MG and CV dyes on the P2W16Ni2O62/Cr-MIL-101/CuFO (b) SEM images, (c) FT-IR Spectroscopy of the fresh and recovered nanoadsorbent after three runs.

Conclusions

Effective factors affecting the adsorption capacity such as primary pH, temperature, initial dye concentration, and adsorbent amount of the solution were investigated. Also, the adsorption kinetics and isotherm experiments demonstrated that the adsorption processes of MB, MG, and CV dyes follow the PSO and Langmuir isotherm. The recyclability test showed that the $P_2W_{16}Ni_2O_{62}$/Cr-MIL-101/CuFO nanocomposite could be used up to three times

without a significant reduction in adsorption efficiency, thus, the $P_2W_{16}Ni_2O_{62}$/Cr-MIL-101/CuFO sample can potentially be utilized as an adsorbent for treating industrial effluents containing cationic dyes.

References

[1]. N.I. Gumerova, A. Rompel, Synthesis, structures and applications of electron-rich polyoxometalates, Nat. Rev. Chem. 2 (2018), 0112.

[2]. M.A. Rezvani, S.A. Mirsadri. Appl. Organomet. Chem., 34, e5585 (2020).

[3]. X.-J. Dui, W.-B. Yang, X.-Y. Wu, X. Kuang, J.-Z. Liao, R. Yu, C.-Z. Lu, Two novel POM-based inorganic–organic hybrid compounds: synthesis, structures, magnetic properties, photodegradation and selective absorption of organic dyes, Dalton Trans. 44 (2015) 9496–9505.

[4]. Wenjing Bao a, Tingting Huang b, Chongze Wanga, Shuyan Maa, Hailing Guo a, Yuan Pan a, Yunqi Liu a,Chenguang Liu a, Daofeng Sun c, Yukun Lu, Controlled synthesis of efficient NiWS active phases derived from lacunary polyoxometalate and the application in hydrodesulfurization, Journal of Catalysis 413 (2022) 374–387.

22nd Iranian Chemistry Congress (ICC22)
Iranian Research Organization for Science and Technology (IROST)
13-15 May 2024

03231-97589

Investigation of Free, Esterified and Bound Phenolic Acids of *Stachys byzantine*

Saeed Mollaei*[a], Fatemeh Jodari*[a], Mostafa Ebadi[b]

Corresponding Author E-mail: s.mollaei@azaruniv.ac.ir

[a] Phytochemical Laboratory, Department of Chemistry, Faculty of Sciences, Azarbaijan Shahid Madani University, Tabriz, Iran.
[b] Department of Biology, Faculty of Basic Sciences, Azarbaijan Shahid Madani University, Tabriz, Iran.

Abstract: *Stachys byzantine*, Lamiaceae family, has many biological properties. In this study, the free, esterified, and bound phenolic acids of *Stachys byzantine* were analyzed. The results indicated that the main phenolic acids in free extract were rosmarinic acid, para-coumaric acid, ferulic acid, and salicylic acid. The analysis of esterified extract revealed that para-coumaric acid, caffeic acid, gallic acid, ferulic acid, and salicylic acid were the main phenolic acids. Caffeic acid, salicylic acid, para-coumaric acid, ferulic acid and gallic acid were the main phenolic acids in bound extract. The sum of phenolic acids confirmed that, among the studied extracts, esterified extract had the highest amount of phenolic acids. So, it can be concluded that *Stachys byzantine* is a good source of esterified phenolic acids.

Keywords: Antioxidant; Caffeic acid; Rosmarinic acid; *Stachys byzantine*

Introduction

Stachys byzantine belongs to the Lamiaceae family, which is native to Turkey, Armenia and Iran. This plant is mostly used to treat rheumatic disorders, digestive problems, and also it is used as a diuretic and sedative agent in folk medicine. It also has many biological properties such as cytotoxic, antioxidant, anti-inflammatory, and antibacterial effects. The phytochemical results indicated the presence of phenols and flavonoids [1].

Phenolic compounds are the secondary metabolites distributed in plants. They are derived from pentose phosphate, shikimate, and phenylpropanoid pathways in plants. They can act as nutrient uptake, protein synthesis, enzyme activity, photosynthesis, structural components, and allelopathy. Phenols led to antibacterial effects especially against Gram positive bacteria. The structure of phenolic compounds is related to their radical-scavenging and metal-chelating activity. [2, 3].

Up to our knowledge, the free, esterified and bonded phenolic acids of *Stachys byzantine* was not studeid. So, the present work aimed to extract and isolate these phenolic acids.

Experimental Section

Plant materials

Stachys byzantine were gathered from its wild habitat in June 2022 in the Northen regions of Mazandaran province, Iran.

Extraction of free, esterified, and bound phenolic acids

For extracting the free phenolic acids, 20 ml of 80% ethanol was added to 2 g of powdered plant, and stirred for 2 hours. The sample was centrifuged (10 min, 1000 rpm). Finally, the solution was dried at 60°C. For the extraction of esterified phenolic acids, 20 ml of NaOH was added to the aqueous phase which was obtained from the previous step. The sample was kept at 25°C for 4 hours and then its pH was adjusted at pH = 2. Diethyl ether and ethyl acetate were added to the aqueous phase, and stirred for 5 minutes. The organic phase was separated, and dried at 60°C. For bound phenolic compounds extraction, 40 ml of NaOH (4 M) was added to the waste obtained from the previous step, and stirred at 25°C for 4 hours. Then, the sample was centrifuged (10 min, 10000 rpm), and the supernatant was collected, and its pH was set at 5. Finally, the sample was dried [4].

HPLC analysis

HPLC was used for the analysis of phenolic acids (free, esterified and bound). The applied column was C18 (250 mm × 0.46 mm, 5 μm). Moreover, methanol and water (0.5 mL/min) were used as mobile phase. The UV detector was adjusted at a wavelength of 254 nm. The phenolic acids was quantified using the regression equation derived from standards, and was expressed as mg per gram of dry plant (mg/g DW).

Results and Discussion

Phenolic acids are metabolites which are found inside the plant cells and can have various biological activities. Some of these activities include anti-inflammatory, anti-cancer, antimicrobial, anti-diabetes, antioxidants, etc [5, 6]. In this study, the free, esterified, and bound phenolic acids were extracted from *Stachys byzantine*, and then their amounts were quantified using HPLC. Figure 1 indicate the HPLC chromatogram of free phenolic acids extracted from *Stachys byzantine*. Also, Table 1 shows the amount of phenolic acids in free, esterified and bound extracts.

22nd Iranian Chemistry Congress (ICC22)
Iranian Research Organization for Science and Technology (IROST)
13-15 May 2024

ISC
03231-97589

IROST
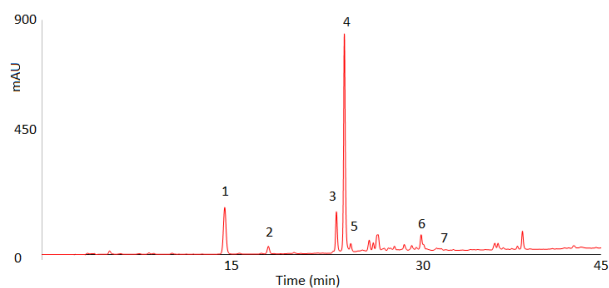
Fig.1: HPLC chromatogram of free phenolic acids extracted from *Stachys byzantine.* 1: Rosmarinic acid; 2: Caffeic acid; 3: para-Coumaric acid; 4: Ferulic acid; 5: meta-Coumaric acid; 6: Salicylic acid; 7: Cinnamic acid

As shown, the main phenolic acids in free extract were rosmarinic acid, para-coumaric acid, ferulic acid, and salicylic acid with the amounts of 129.88, 93.86, 80.24, and 17.08 mg/g dried extract, respectively. The analysis of esterified extract indicated that para-coumaric acid (360 mg/g DW), caffeic acid (135.01 mg/g DW), gallic acid (39.76 mg/g DW), ferulic acid (11.29 mg/g DW), and salicylic acid (10.60 mg/g DW) were the main phenolic acids. Caffeic acid, salicylic acid, para-coumaric acid, ferulic acid and gallic acid were the main phenolic acids in bound extract, and the amound of them were 87.27,67.20, 31.48, 15.07, and 11.48 mg/g DW, respectively. Protocatechuic acid, para-Hydroxybenzoic acid, and vanillic acid were not detected in the extracts. Also, rosmarinic acid, meta-Coumaric acid, and cinnamic acid were detected only in the free extract.

Table 1: The amount of phenolic compounds (mg/g dried extract) in extracts

Compounds	Free	Esterified	Bonded
Gallic acid	0.00	39.76	11.48
Protocatechuic acid	0.00	0.00	0.00
Rosmarinic acid	129.88	0.00	0.00
para-Hydroxybenzoic acid	0.00	0.00	0.00
Vanillic acid	0.00	0.00	0.00
Caffeic acid	4.39	135.01	87.27
para-Coumaric acid	93.86	360.55	31.48
Ferulic acid	80.24	11.29	15.07
meta-Coumaric acid	3.76	0.00	0.00
Salicylic acid	17.08	10.60	67.20
Cinnamic acid	2.55	0.00	0.00
Sum	331.81	557.31	212.52

The sum of phenolic acids confirmed that, among the studied extracts, esterified extract had the highest amount of phenolic acids (557.31 mg/g DW).

According to our results, para-coumaric acid was the major phenolic acids in esterified extract. It is found in fruits and vegetables, and can be converted into other phenolic acids such as sinapic acid, caffeic acid, and ferulic

acid. The study has indicated that it has several biological properties such as anti-cancer, anti-oxidant, analgesic, and neuroprotective [7]. According to our results, since *Stachys byzantine* had the ability to produce para-coumaric acid, it could be considered as a suitable source for the production of this compound on a commercial scale.

Conclusions

In this study, the free, esterified, and bound phenolic acids were extracted from *Stachys byzantine*, and then their amounts were quantified. The results indicated the main phenolic acids were rosmarinic acid, para-coumaric acid, caffeic acid, ferulic acid, and salicylic acid. Also, The sum of phenolic acids confirmed that, among the studied extracts, esterified extract had the highest amount of phenolic acids. So, it can be concluded that *Stachys byzantine* is a good source of esterified phenolic acids.

References

[1] Tomou, E. M., Barda, C., & Skaltsa, H. (2020). Genus Stachys: A review of traditional uses, phytochemistry and bioactivity. *Medicines*, *7*(10), 63.

[2] Al Mamari, H. H. (2021). Phenolic compounds: Classification, chemistry, and updated techniques of analysis and synthesis. Phenolic Compounds: Chemistry, Synthesis, Diversity, Non-Conventional Industrial, Pharmaceutical and Therapeutic Applications, 73-94.

[3] Rahman, M. M., Rahaman, M. S., Islam, M. R., Rahman, F., Mithi, F. M., Alqahtani, T., ... & Uddin, M. S. (2021). Role of phenolic compounds in human disease: current knowledge and future prospects. Molecules, 27(1), 233.

[4] Krygier, K., Sosulski, F., & Hogge, L. (1982). Free, esterified, and insoluble-bound phenolic acids. 1. Extraction and purification procedure. Journal of Agricultural and Food Chemistry, 30(2), 330-334.

[5] Zhang, Y., Cai, P., Cheng, G., & Zhang, Y. (2022). A brief review of phenolic compounds identified from plants: Their extraction, analysis, and biological activity. Natural Product Communications, 17(1), 1934578X211069721.

[6] Kumar, A., Khan, F., & Saikia, D. (2022). Phenolic Compounds and Their Biological and Pharmaceutical Activities. Chem. Inside Spices Herbs Res. Dev, 31, 204-234.

[7] Kaur, J., & Kaur, R. (2022). p-Coumaric acid: a naturally occurring chemical with potential therapeutic applications. Current Organic Chemistry, 26(14), 1333-1349.

A new method for immobilization and stabilization of sub–nanometric Pd colloids on single-walled carbon nanotube functionalized with TiO₂ for Stille coupling reaction

Maryam Barmaki, Nader Noroozi Pesyan, Hassan Alamgholiloo

Corresponding Author E-mail: nnp403@gmail.com

Department of Organic Chemistry, Faculty of Chemistry, Urmia University, 57159, Urmia, Iran.

Abstract: The stabilization of sub-nanometric metal particles with good distribution is discussed in the catalytic field. Herein, an efficient method for attaching and immobilizing sub-nanometric Pd colloids onto TiO_2 functionalized single-walled carbon nanotube is presented. Then the catalytic activity of Pd@TiO₂/SWCNT in the Stille coupling reaction was developed.

Keywords: Pd catalysts; SWCNT; Stille reactions

Introduction

The palladium-catalyzed cross-coupling of organostannanes with organic halides and triflates, known as Stille reaction, is one of the most important, powerful, and versatile tools for the formation of carbon–carbon bonds.[1] TiO_2 nanoparticles are common photocatalyst has been used because of unique features, involving tunable photosensitivity, nontoxic kind, chemical stability, high corrosion resistance and relatively inexpensive substance. The use of CNTs as scaffold substances can give effective properties, for example strong mechanical strength, high conductivity, huge surface areas and high adsorption ability [2]. Previous study have proven that colloidal Pd, Pd NPs, and Pd complex can greatly boost C–C bond formations.[3] We presented a smart method to immobilize sub-nanometric palladium on TiO_2 functionalized single-walled carbon and also demonstrated the catalytic activity of this nanostructure in the C-C coupling reaction.

Experimental Section

Preparation Pd@TiO₂/SWCNT

In the first step, dissolved 0.5 g of TiO_2 in 25 ml of distilled water, then prepared a SWCNT dispersion in 40 ml of distilled water and added it to the solution of the first step. Then it was stirred for 24 hours at room temperature. In the next step, added the reduced palladium to the solution and allow it to stir at room temperature for 2 hours, then dry the solution and place it in the oven for 2 hours.

General method for Stille coupling reaction

In the model reaction, a little amount of catalyst (0.01g) was added to the mixture of aryl halides, triphenyltin chloride, Na_2CO_3, polyethylene glycol-400 (PEG-400). The reaction vessel was capped and allowed to stir at room temperature for 1h.

Results and Discussion

Herein, Pd@TiO₂/SWCNT mesoporous was presented for Stille coupling reaction. TiO₂/SWCNT was prepared by grafting TiO_2 to SWCNT cavities, and then TiO₂/SWCNT was used as an organic support to stabilization colloidal Pd nanoparticles on a sub-nanometric scale(Scheme 1).
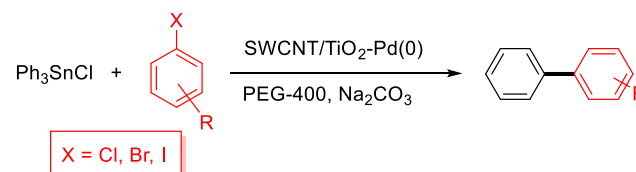
Scheme 1: Synthesis of biaryls catalyzed by SWCNT/TiO₂-Pd(0)

Structural and morphology characterization

The FT IR spectrum of nanocatalyst is shown in Fig. 1. The crystalline structure SWCNT/TiO₂-Pd(0) was analyzed using the powder XRD pattern (Fig. 2).
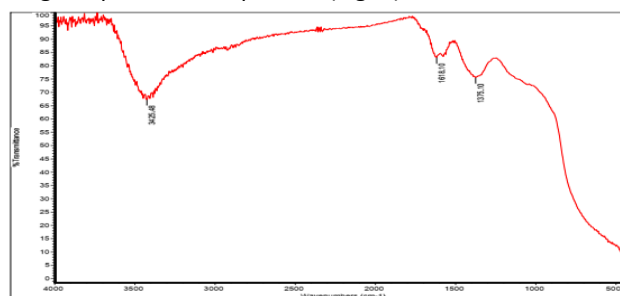
Fig. 1: FT IR spectrum of SWCNT/TiO₂-Pd(0)
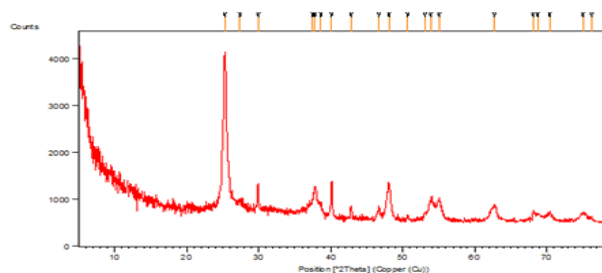
Fig.2: XRD pattern for SWCNT/TiO₂-Pd(0)

22nd Iranian Chemistry Congress (ICC22)
Iranian Research Organization for Science and
Technology (IROST)
13-15 May 2024

03231-97589

IROST

Conclusions

We indicated that TiO_2 could be an excellent compound for anchoring and stabilizing sub-nanometric Pd onto the surface of SWCNT. We also expanded an efficient protocol toward the economic synthesis of biaryls under sustainable conditions. This methodology revealed that the SWCNT/TiO_2-Pd(0) has notable advantages such as excellent stability, negligible metal leaching, large scalability, and eco-friendly nature, which could coincide with the concepts of green chemistry.

References

[1] Zhao, H., Wang, Y., Sha, J., Sheng, S., & Cai, M. (2008). MCM-41-supported bidentate phosphine palladium (0) complex as an efficient catalyst for the heterogeneous Stille reaction. Tetrahedron, 64(32), 7517-7523.

[2] Mohammed, M. K. (2020). Sol-gel synthesis of Au-doped TiO2 supported SWCNT nanohybrid with visible-light-driven photocatalytic for high degradation performance toward methylene blue dye. Optik, 223, 165607.

[3] Alamgholiloo, H., Noroozi Pesyan, N., & Rostamnia, S. (2021). A novel strategy for stabilization of sub-nanometric Pd colloids on kryptofix functionalized MCM-41: Nanoengineered material for Stille coupling transformation. Scientific Reports, 11(1), 18417.

Machine Learning-Driven Deciphering of Structure-Activity Relationships in Coronavirus Inhibitors

Marzieh sadat neiband

Corresponding Author E-mail: neiband.mrs@gmail.com

Department of chemistry, Payame Noor University, Tehran, Iran.

Abstract: This study utilizes machine learning classification models to identify critical structural features of coronavirus inhibitors.

Keywords: Coronavirus inhibitors; Structure-activity relationship; Molecular features

Introduction

The emergence and rapid spread of coronaviruses, such as SARS-CoV-2, highlight the urgent need for effective therapeutic strategies. In this fight, the development of potent inhibitors that target crucial viral processes offers a promising avenue [1]. However, the success of such inhibitors hinges on a deep understanding of the molecular properties that govern their interaction with the virus.

This study takes a computational approach to address this challenge. We leverage the power of machine learning (ML) methods to identify the critical structural features of molecules that effectively inhibit the coronavirus. By deciphering these key characteristics, we aim to pave the way for the design and development of more targeted and efficacious coronavirus inhibitors.

Results and Discussion

We employed powerful ML methods, including k-Nearest Neighbors (kNN), Support Vector Machines (SVM), and Supervised Kohonen Network (SKN) to uncover critical structural features associated with coronavirus inhibitor activity. By analyzing a dataset of 571 active and inactive molecules from the Bing database. To construct the classification models, these molecules were categorized as active or inactive based on their IC_{50} values. The predictive performance of the developed models was assessed using test data and cross-validation techniques. The statistical results of the classification models are presented in Table 1.

Table 1: statistical results of classification models for active and inactive coronavirus inhibitors

Model	Class	Precision	Sensitivity	Specificity	Non-error rate	Accuracy
		Training / Validation/ Test	Training / Validation/ Test	Training / Validation/ Test	Training / Validation/ Test	Training / Validation/ Test
SKN	Active	0.977/0.898/0.924	0.914/0.901/0.864	0.932/0.822/0.773	0.922/0.844/0.798	0.918/0.87/0.798
	Inactive	0.849/0.801/0.787	0.932/0.822/0.773	0.914/0.901/0.864		
SVM	Active	0.956/0.805/0.841	0.984/0.918/0.802	0.916/0.805/0.802	0.904/0.876/0.763	0.965/0.893/0.736
	Inactive	0.964/0.918/0.684	0.916/0.805/0.694	0.984/0.918/0.694		
KNN	Active	0.918/0.908/0.849	0.913/0.911/0.614	0.808/0.903/0.593	0.865/0.865/0.756	0.877/0.872/0.808
	Inactive	0.816/0.816/0.614	0.806/0.806/0.849	0.919/0.815/0.914		

Conclusions

Our findings indicate a direct relationship between specific structural features and inhibitory potential. Molecules with a higher number of sulfur atoms, lower molecular mass, and increased polarity exhibited a stronger ability to inhibit the coronavirus.

References

[1] Li, J., Lai, S., Gao, G. F., & Shi, W. (2021). The emergence, genomic diversity and global spread of SARS-CoV-2. *Nature*, *600*(7889), 408-418. https://doi.org/10.1038/s41586-021-04188-6

22nd Iranian Chemistry Congress (ICC22)
Iranian Research Organization for Science and Technology (IROST)
13-15 May 2024

03231-97589

ISC
Islamic World Science Citation Center

IROST

In Silico Deciphering of Angiotensin Receptor Inhibitors: Machine Learning Unveils Key Structural Features for Activity and Selectivity

Masoumeh Bakhtiari, Marzieh Sadat Neiband*

Corresponding Author E-mail: neiband.mrs@gmail.com

Department of chemistry, Payame Noor University, Tehran, Iran.

Abstract: This study employed machine learning classification approach to identify key structural features differentiating active and selective angiotensin type I & II receptor inhibitors.

Keywords: Angiotensin receptor; Target selectivity; Machine learning classification

Introduction

Angiotensin receptors (ATRs), particularly type I (AT_1R) and type II (AT_2R), regulate blood pressure and cardiovascular health [1]. Angiotensin receptors (AT_1R & AT_2R) regulate blood pressure and cardiovascular health [1]. Machine learning offers a powerful tool to identify key structural features for targeted angiotensin receptor inhibitor development.

Methodology

A dataset of 4500 ATRs molecules was classified based on activity (active/inactive) and target selectivity (AT_1R/AT_2R) using IC_{50} values. Partial Least Squares-Discriminant Analysis (PLS-DA) coupled with the Variable Importance in Projection (VIP) method identified the most significant structural features from an initial set of 450. This study utilized a variety of machine learning algorithms, namely Support Vector Machines (SVM), K-Nearest Neighbors (KNN), Counterpropagation Neural Network (CPANN), and Supervised Kohonen Networks (SKN), for the classification of ATRs based on activity and target selectivity.

Results and Discussion

All models achieved high accuracy (>80%) on test data (Table 1). KNN and SVM displayed superior performance in both activity and target selection, suggesting their potential suitability for this classification task. Identified features that significantly differentiated active from inactive molecules and those targeting AT_1R vs. AT_2R.

Table1: classification results for AT_1R and AT_2R inhibitors based on activity and selection target

Model	Precision Training/Validation/Test	Sensitivity Training/Validation/Test	Specificity Training/Validation/Test	Non-error rate Training/Validation/Test	Accuracy Training/Validation/Test
AT_1R					
SVM	0.980/0.925/0.931	0.990/0.954/0.943	0.930/0.846/0.884	0.960/0.900/0.914	0.970/0.918/0.925
CPANN	0.944/0.936/0.928	0.973/0.971/0.970	0.828/0.815/0.814	0.896/0.890/0.890	0.921/0.917/0.91
SKN	0.957/0.926/0.921	0.986/0.957/0.925	0.865/0.834/0.862	0.917/0.888/0.889	0.936/0.908/0.889
KNN	0.948/0.948/0.955	0.977/0.977/0.977	0.833/0.835/0.830	0.904/0.906/0.903	0.928/0.930/0.922
PLS-DA	0.906/0.0.889/0.907	0.941/0.937/0.945	0.830/0.819/0.819	0.878/0.874/0.885	0.907/0.892/0.896
AT_2R					
SVM	0.950/0.884/0.882	0.950/0.862/0.834	0.950/0.845/0.782	0.950/0.853/0.815	0.950/0.852/0.801
CPANN	0.924/0.874/0.878	0.913/0.854/0.835	0.855/0.843/0.789	0.878/0.846/0.810	0.875/0.874/0.810
SKN	0.923/0.889/0.886	0.913/0.874/0.865	0.887/0.845/0.724	0.897/0.856/0.792	0.896/0.855/0.792
KNN	0.889/0.886/0.881	0.876/0.876/0.852	0.819/0.817/0.809	0.855/0.855/0.834	0.855/0.851/0.825
PLS-DA	0.898/0.890/0.856	0.887/0.878/0.824	0.797/0.789/0.765	0.842/0.834/0.789	0.837/0.829/0.778
AT_1R & AT_2R					
SVM	0.985/0.965/0.948	0.982/0.964/0.956	0.889/0.867/0.854	0.977/0.914/0.876	0.986/0.956/0.933
CPANN	0.982/0.963/0.964	0.975/0.971/0.971	0.914/0.764/0.852	0.936/0.864/0.912	0.858/0.941/0.912
SKN	0.991/0.964/0.962	0.981/0.972/0.970	0.945/0.754/0.855	0.959/0.858/0.910	0.973/0.937/0.910
KNN	0.954/0.954/0.936	0.973/0.973/0.964	0.838/0.838/0.727	0.902/0.902/0.858	0.955/0.955/0.936
PLS-DA	0.967/0.967/0.934	0.941/0.941/0.962	0.806/0.806/0.872	0.866/0.866/0.875	0.923/0.923/0.921

22nd Iranian Chemistry Congress (ICC22)
Iranian Research Organization for Science and
Technology (IROST)
13-15 May 2024

03231-97589

Conclusions

This study demonstrates the utility of machine learning for classifying angiotensin receptor inhibitors. The unveiled structural features can guide the design of more effective and selective therapeutics.

References

[1] Barak, R., Goshtasbi, G., Fatehi, R., & Firouzabadi, N. (2024). Signaling pathways and genetics of brain Renin angiotensin system in psychiatric disorders: State of the art. Pharmacology Biochemistry and Behavior, 236.173706, https://doi.org/10.1016/j.pbb.2023.173706.

Aflatoxins reduction in rice flour by using ozone gas and cold plasma

Marzie Shakeri [a], Ruhollah Karami-Osboo [b], Hassan Rezadoost [*][a], Mohsen Farzaneh [a]

Corresponding Author E-mail: h_rezadoost@sbu.ac.ir

[a] Department of Phytochemistry, Medicinal Plants and Drugs Research Institute, Shahid Beheshti University, Tehran, Iran.

[b] Mycotoxins Research Laboratory, Agricultural Research Education and Extension Organization (AREEO), Iranian Research Institute of Plant Protection, Tehran, Iran.

Abstract: Mycotoxins are fungal metabolites in food. Rice, a major cereal, is prone to mycotoxins contamination. This research quantified aflatoxins in rice flour using HPLC-FLD, then applied ozone gas and cold plasma for reduction. The validated methodology showed excellent performance in selectivity, sensitivity, accuracy and precision. Results demonstrated 90% reduction with ozone gas and 82% with cold plasma.

Keywords: Aflatoxin; Rice; Cold Plasma; Ozone gas; HPLC-FLD

Introduction

Mycotoxins are the toxic secondary metabolites of some filamentous fungi, mainly *Aspergillus* spp., *Fusarium* spp. and *Penicillium* spp. Over 400 types of mycotoxins have been identified, but attention is mainly given to those with the greatest public health relevance, such as aflatoxins (AFs), ochratoxin A (OTA), fumonisins (FUMs), trichothecenes (TCs) and zearalenone (ZEA) [1]. Fungi in the genus *Aspergillus* especially *Aspergillus flavus*, *A. parasiticus*, *A. nominus* are important pathogens of many crops, produce aflatoxins (AFs) that under suitable environmental conditions, contaminate crops during harvest, storage, and processing. AFs are extremely toxic, carcinogenic, mutagenic, teratogenic, and immunosuppressive compounds, so their presence in the food chain creates potential health risks for animals and humans. The IARC classified AFs as a Group-1 agent (human carcinogens) [2]. The most relevant aflatoxins are aflatoxin B1 (AFB1), aflatoxin B2 (AFB2), aflatoxin G1 (AFG1), aflatoxin G2 (AFG2), and aflatoxin M1 (AFM1), with aflatoxin B1 being the most commonly occurring and toxic one. Food contamination by mycotoxins is dependent on the presence of fungi, the application of unsuitable agricultural practices and the conditions of harvesting, and storage. Usually, mycotoxins' contamination in rice grain is associated with fungal growth due to improper storage conditions, include temperature, humidity and rice storage time [1]. The use of ozone in the food industry has seen increased adoption in various sectors including cereals, meat processing, dairy production, and fresh agricultural products and their by-products. Ozone, consisting of three oxygen atoms, exhibits strong oxidizing properties and serves as a powerful sanitizing agent for ensuring food surface cleanliness and decontamination of storage areas to control pests and diseases. The antimicrobial action of ozone is getting popular because of residue-free products. Application of ozone in food or feed is made either in its gaseous state or aqueous form as ozonized water. The ozone application in gaseous form was reported to have higher effectiveness and practical advantages than aqueous solutions [3]. Cold plasma treatment is an emerging technology in food processing that shows great potential in enhancing food safety and prolonging shelf life. The activated chemical species generated by cold plasma exhibit rapid antimicrobial effects at room temperature without leaving behind any discernible chemical residues. These species target various sites within fungal cells, leading to disruption of cellular functions and structures, ultimately culminating in cell death. Moreover, cold plasma treatment facilitates the breakdown of mycotoxins through diverse pathways, yielding degradation products that are notably less toxic [4]. In this study, the effect of two treatment methods, ozone gas and atmospheric cold plasma, on the reduction of aflatoxins in order to find the optimal point in each method, is investigated. The investigated variables include: ozone concentration, ozonation duration, plasma flame distance from the sample surface, and plasma flame radiation duration on the sample [5].

Experimental Section

Quantitative analysis of aflatoxins, including AFB1, AFB2, AFG1 and AFG2, was carried out using high performance liquid chromatography with fluorescence detector (HPLC-FLD). Standards of aflatoxins purchased from Sigma-Aldrich and used in preparation of calibration curves for HPLC confirmation.

Methodology

Rice samples were collected from different location of Iran. In the following, each of the samples was grounded

22nd Iranian Chemistry Congress (ICC22)
Iranian Research Organization for Science and Technology (IROST)
13-15 May 2024

03231-97589

by a miller and 5 g of each sample was weighted. For extraction, samples were mixed with methanol and water solution. Then, the mixtures were placed in a shaker. In the following 1 ml from supernatant transferred into centrifuge tube and added chloroform and water to it. After that the mixture was centrifuged at 3000 rpm for 5 min and the clear phase at the bottom of tube was collected and transferred into microtube and was dried. Prior to the HPLC-FLD analysis, samples were mixed with methanol and water. Mobile phase was made of water, methanol, acetonitrile and KBr(s). Also, chromatography separation was performed on a C18 column. In the next step, we used ozone gas at room temperature, different concentration and time (table1). As well as we used cold plasma in the different the distance of the plasma flame from the sample surface and the duration of the plasma flame radiation on the sample (table2). Finally, we compared the organoleptic properties of treated samples with control.

Results and Discussion

The linearity of the standard curve was proved (R^2=0.99) using 0.4-7.2 ng/ml standard samples of aflatoxins. The results of treating rice flour samples with ozone gas and cold plasma show that ozone gas with a certain conditions was able to reduce the amount of total aflatoxin by almost 90%. Also, cold plasma has been able to reduce this amount by 82% (Fig.1). Also, according to the experiments, it was observed that the organoleptic characteristics had insignificant changes.

Table 1: The effect of time and concentration of ozone on reduction aflatoxins in the samples

Treatments	Area of Peaks in HPLC-FLD Analysis				
	AFB1	AFB2	AFG1	AFG2	AFTT
control	39661	6309	1187	2511	49668
8 cm, 15 min	24817	4659	984	2045	32505
8 cm, 30 min	18113	3174	849	1037	23173
5 cm, 15 min	19490	2830	1021	1203	24544
5 cm, 30 min	5823	1309	573	759	8464

Table 2: The effect of different the distance of the plasma flame from the sample surface and the duration of the plasma flame radiation on reduction aflatoxins in the sample

Treatments	Area of Peaks in HPLC-FLD Analysis				
	AFB1	AFB2	AFG1	AFG2	AFTT
control	51904	8155	1832	3513	65404
5 ppm, 20 min	12288	1777	1313	2663	18041
5 ppm, 40 min	9049	1089	935	1431	12504
6 ppm, 20 min	9366	1655	434	3091	14546
6 ppm, 40 min	3814	647	232	1768	6461
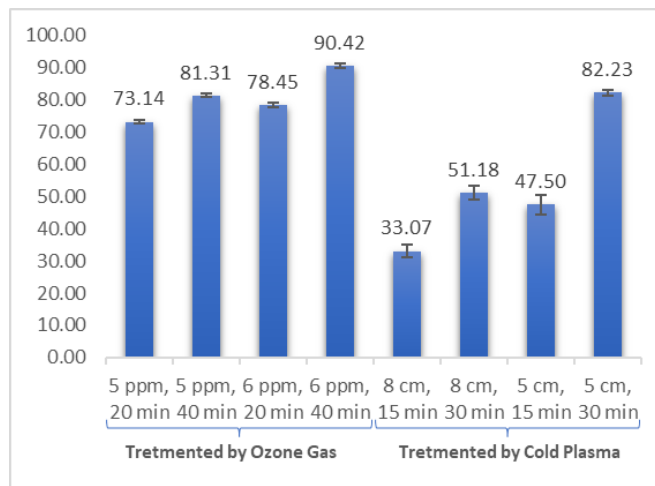
Fig.1: Percentage reduction of total aflatoxin in rice flour by ozone gas and cold plasma treatment compared to the control sample

Conclusions

According to the obtained results, ozone gas is a promising technology to efficiently degrade aflatoxins in rice flour with more than 90% reduction with 6 ppm concentration, after 40 min of treatment. Also, cold plasma treatments act rapidly against aflatoxins, require low energy input and have relatively milder impact on quality. Further our studies are required to investigate the degradation products.

References

[1] Santos, A. R., Carreiró, F., Freitas, A., Barros, S., Brites, C., Ramos, F., & Sanches Silva, A. (2022). Mycotoxins contamination in rice: Analytical methods, occurrence and detoxification strategies. *Toxins*, *14*(9), 647.

[2] Karami-Osboo, R., Mirabolfathy, M., Kamran, R., Shetab-Boushehri, M., & Sarkari, S. (2012). Aflatoxin B1 in maize harvested over 3 years in Iran. *Food Control*, *23*(1), 271-274.

[3] Sujayasree, O. J., Chaitanya, A. K., Bhoite, R., Pandiselvam, R., Kothakota, A., Gavahian, M., & Mousavi Khaneghah, A. (2022). Ozone: An advanced oxidation technology to enhance sustainable food consumption through mycotoxin degradation. *Ozone: Science & Engineering*, *44*(1), 17-37.

[4] Misra, N. N., Yadav, B., Roopesh, M. S., & Jo, C. (2019). Cold plasma for effective fungal and mycotoxin control in foods: mechanisms, inactivation effects, and applications. *Comprehensive reviews in food science and food safety*, *18*(1), 106-120.

[5] Sipos, P., Peles, F., Brassó, D. L., Béri, B., Pusztahelyi, T., Pócsi, I., & Győri, Z. (2021). Physical and chemical methods for reduction in aflatoxin content of feed and food. *Toxins*, *13*(3), 204.

22nd Iranian Chemistry Congress (ICC22)
Iranian Research Organization for Science and Technology (IROST)
13-15 May 2024

03231-97589

IROST

PAMAM and polyester dendrimers as favipiravir nanocarriers: a comparative study using DFT method

Sekineh Bazyari-Delavar[a], Farideh Badalkhani-Khamseh[b], Azadeh Ebrahim-Habibi[c,d], Nasser L. Hadipour[e]

[a] Department of Physical Chemistry, Tarbiat Modares University, Tehran, Iran.
[c] Biosensor Research Center, Endocrinology and Metabolism Molecular-Cellular Sciences Institute, Tehran University of Medical Sciences, Tehran, Iran.
[d] Endocrinology and Metabolism Research Center, Endocrinology and Metabolism Clinical Sciences Institute, Tehran University of Medical Sciences, Tehran, Iran.
[b] f.badalkhani@modares.ac.ir.
[e] hadipour@modares.ac.ir.

Abstract: The electronic sensitivity and reactivity of polyamidoamine (PAMAM) and polyester dendrimers toward favipiravir (T705) was inspected using density functional theory method. The T705 drug is adsorbed on the surface of PAMAM and polyester dendrimers with the binding energy of -27.26 and -26.80 kcal mol^{-1}, respectively, in the solvent phase. The energy gap of PAMAM and polyester dendrimers reduced by about 32% and 27%, indicating that the electrical conductance of carriers become 8.16×10^{23} and 4.41×10^{22} times higher, upon T705 adsorption. The work function (Φ) value of PAMAM and polyester is changed about 1.53 and 0.71 eV, respectively. Thus, PAMAM dendrimer is about 2.5 times stronger Φ-type sensor than polyester dendrimer. The recovery time for T705 desorption from the PAMAM and polyester surface is predicted to be 9.2×10^3 and 4.2×10^3 s, respectively, at physiological environment.

Keywords: PAMAM and polyester dendrimer; Favipiravir (T705); Density Functional Theory (DFT); Drug delivery; Nanocarriers.

Introduction

Due to the unique properties of dendrimers, these molecules are favorable for biomedical applications. Terminal groups in dendrimers can be factorized by specific and controlled therapeutic agents, which themselves have the potential to be use in targeted drug delivery. In addition, empty cavities in dendrimers are used to encapsulate hydrophobic drug molecules. Therefore, they have made a lot of interest in the field of chemistry biology and drug delivery[1]. The progress in molecular modeling provides are the basis to improve our ability to better predict and understand the biological activities and interactions of dendrimers and design of drug delivery systems[2]. Therefore, we use these methods to study in detail the interactions mechanisms of bioactive factor with drug the use of commercially available hyperbranched dendrimers. However, a comparative quantum mechanical investigation on the mechanism of interaction between PAMAM and polyester dendrimers with a drug molecule is still lacking.

Theoretical methods

Full geometry optimizations were performed using M06-2X density functional approach in conjunction with 6-31G(d,p) basis set as implemented in Gaussian 09W software package [3,4]. This functional is recommended for application in main group thermochemistry, thermochemical kinetics, noncovalent interactions, and excited states [5]. To ensure that all optimized structures are the true stationary points on the potential energy surface (PES), vibrational frequency calculations were performed using the same method and basis set.

Results and Discussion

The sensing mechanism of an adsorbent is connected to the change of its electrical conductance upon drug adsorption. The Eg is a value of kinetic stability and based on the following equation is an electronic parameter determine sensitivity of the carrier toward cargo:

$$\sigma = AT^{(3/2)} \exp(-E_g/2kT) \qquad (1)$$

Based on Eq. (1), electrical conductivity of a drug carrier increases exponentially with a decrease of Eg value, which is converted to an electrical signal in the presence of drug. Therefore, it is important to explore the change of E_g value upon drug adsorption as it alters the fluorescence emission of nanostructures and helps us to recognize the attachment of the cargo to the carrier and to trace the trajectory of drug in the body using the spectrophotometers [6].Adsorption process also affects the Fermi level of work function type (Φ-type) sensors. The Φ-type sensor applies a Kelvin oscillator instrument to calculate the values of Φ before and after adsorption process [7]. When a chemical agent is adsorbed by a Φ-type sensor, the gate voltage of adsorbent changes; therefore an electrical signal is created detecting the presence of adsorbed molecule. The Φ value is considered

22nd Iranian Chemistry Congress (ICC22)
Iranian Research Organization for Science and
Technology (IROST)
13-15 May 2024

03231-97589

as the minimum amount of energy needed to induce electron emission from the Fermi level:

$$\Phi = V_{el(+\infty)} - E_F \qquad (2)$$

where E_F is the Fermi level energy, and $V_{el(+\infty)}$ is the electron electrostatic potential energy far from the material's surface. As $V_{el(+\infty)}$ is estimated to be zero, we could write $\Phi = -E_F$. The Fermi level energy is defined as follows:

$$E_F = E_{HOMO} + ((E_{LUMO} - E_{HOMO}))/2 \qquad (3)$$
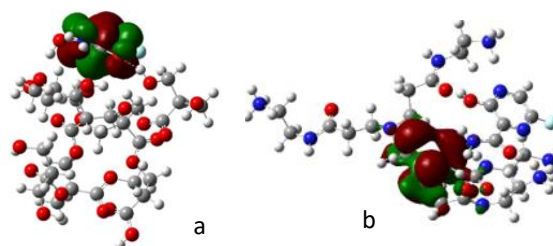
Fig.1: a) LUMO of polyester-T705 b) HOMO of PAMAM-T705

Table 1. The values of E_{HOMO}, E_{LUMO}, E_g, work function (Φ), energy of Fermi level (E_F), and quantum molecular descriptors of the most stable complexes calculated at M06-2X/6-31G (d,p) level of theory. All parameters are in eV.

Configuration		E_{HOMO}	E_{LUMO}	E_g	$\Delta E_g(\%)^a$	$\Phi(-E_F)$	μ	η	ω
T705		-8.45	-1.15	7.30		4.80	-4.80	3.65	3.16
PAMAM		-7.41	1.54	8.95		2.94	-2.94	4.48	0.96
PAMAM-T705	Gas	-7.45	-1.08	6.37	-29	4.27	-4.27	3.19	2.86
Polyester		-8.98	0.40	9.38		4.26	-4.26	4.66	1.95
Polyester-T705		-8.61	-1.37	7.24	-23	4.99	-4.99	3.62	3.44

Conclusions

The frontier molecular orbital analyses demonstrated that HOMO of PAMAM and LUMO of T705 have the main contribution in the PAMAM-T705 complex formation. The adsorption of T705 on the polyester dendrimer is affected by T705 frontier molecular orbitals, in general. The Eg of PAMAM and polyester dendrimers reduced by about 32% and 27%, indicating that the electrical conductance of carriers become 8.16×1023 and 4.41×1022 times higher, upon T705 adsorption. The Φ value of PAMAM and polyester is changed about 1.53 and 0.71 eV, respectively. Thus, PAMAM dendrimer is about 2.5 times stronger Φ-type sensor than polyester dendrimer. The recovery time of T705 from the PAMAM and polyester dendrimers is calculated to be about 9.2×103 and 4.2×103s, respectively. Therefore, PAMAM and polyester do not release T705 molecule easily at physiological environment.

References

[1] Caminade, A.-M. and C.-O. Turrin, Dendrimers for drug delivery. Journal of Materials Chemistry B, 2014, 2(26): p. 4055-4066.

[2]Nuno Martinho, Helena Florindo, Liana Silva, Steve Brocchini, Mire Zloh and Teresa Barata. Molecular Modeling to Study Dendrimers for Biomedical Applications. Molecules 2014, 19, 20424- 20467.

[3] Y. Zhao, D.G. Truhlar, Theoretical Chemistry Accounts 120 (2008) 215.

[4]M.W. Schmidt, K.K. Baldridge, J.A. Boatz, S.T. Elbert, M.S. Gordon, J.H. Jensen, S. Koseki, N. Matsunaga, K.A. Nguyen, S. Su, Journal of computational chemistry 14 (1993) 1347.

[5]S.Grimme, Wiley Interdisciplinary Reviews: Computational Molecular Science 1 (2011) 211.

[6] M.K. Hazrati, Z. Bagheri, A. Bodaghi, Physica E: Low-dimensional Systems and Nanostructures 89 (2017) 72.

[7] A. Hosseinian, E. Vessally, A. Bekhradnia, K. Nejati, G. Rahimpour, Thin Solid Films 640 (2017) 93.

22nd Iranian Chemistry Congress (ICC22)
Iranian Research Organization for Science and Technology (IROST)
13-15 May 2024

03231-97589

Co$_3$O$_4$ hollow sphere for conversion of CO$_2$ to cyclic carbonates

Nasrin Zarei, Reza khalifeh[*], Marziyeh Alaei Faradonbeh, Maryam Rajabzadeh

Corresponding Author E-mail: nasrinzarei2020@gmail.com

Department of Chemistry, Shiraz University of Technology, Shiraz, Iran.

Abstract: In this research, the hollow Co$_3$O$_4$ catalyst with a single shell structure is used as a new and efficient catalyst for CO$_2$ fixation. The performance of Co$_3$O$_4$ hollow catalyst for the chemical fixation of carbon dioxide to produce cyclic carbonates by reducing the efficiency of hollow spheres of various epoxides was investigated. At a temperature of 70°C, a pressure of 1 MPa, a catalyst loading of 1 mol% and a reaction time of 5 hours in a solvent-free reaction medium, the corresponding carbonate is produced with an efficiency of up to 97%.

Keywords: CO$_2$ Fixation; Hollow Sphere of Co$_3$O$_4$; Catalyst.

Introduction

A range of studies have explored the fixation of CO$_2$, offering potential solutions to the environmental challenges posed by this greenhouse gas. Global warming and climate change caused by greenhouse gases are among the most important issues of our time. Carbon dioxide is a greenhouse gas and its release into the atmosphere as one of the most important greenhouse gases must be controlled. This gas is significantly responsible for climate change and has a major contribution to global warming.

Recently, CO$_2$ has attracted much attention as a source of C1 in organic synthesis for chemical production due to its large-scale availability, cost-effectiveness, natural cycle recycling, non-toxicity, non-flammability and high purity.

Due to the coupling of carbon dioxide with epoxides and the production of cyclic carbonates, this matter has attracted a lot of attention. Cyclic carbonates have diverse and interesting applications such as green solvents, electrolytes in batteries, building blocks in organic synthesis, raw materials for cosmetics and intermediates. They are used in the synthesis of ethylene glycol, in pharmaceuticals and polymers. They are also found in natural products. Therefore, it is important to develop and find new production technology for the synthesis of cyclic carbonates in chemical industries. Several catalysts have been investigated for the synthesis of cyclic carbonates from CO$_2$ to epoxides. Recently, heterogeneous catalysts have been developed for CO$_2$ fixation because they can reduce processing costs compared to conventional homogeneous catalysts. However, the synthesis of a heterogeneous catalyst with good activity and high durability in mild conditions is challenging.

Experimental Section

General method for chemical fixation of carbon dioxide and air oxides: A stainless steel high-pressure batch reactor was used for cycloaddition of CO$_2$ to cyclic compounds. The reactor was loaded with epoxide (10 mmol) and tetrabutylammonium bromide (TBAB) (0.01 mmol). Then the appropriate amount of catalyst was added to the reaction mixture and the reactor was heated to the desired reaction temperature. The reactor pressure was kept constant with carbon dioxide in the range of 1MPa. After a certain period, the reactor was cooled in an ice bath and the carbon dioxide was gradually discharged. The reaction mixture was filtered to remove the catalyst, then the reaction mixture was extracted with ethyl acetate. The organic and aqueous phases were separated by ethyl acetate and water. The product was placed in the organic phase and the separation was carried out. Finally, the main product was purified and separated by thin-layer chromatography using n-hexane-ethyl acetate.

Results and Discussion

First, Co$_3$O$_4$ hollow spheres catalyst was synthesized by hydrothermal method with a hard carbon template. Then, it was detected by Feld emission scanning electron microscope (FESEM) (Fig 1).

After the successful synthesis and identification of Co$_3$O$_4$ hollow sphere, its catalytic activity was tested for the synthesis of cyclic carbonates from CO$_2$ and epoxide under solvent-free conditions. In this experiment, epoxy styrene cycloaddition with CO$_2$ was chosen as a model reaction for the best tested conditions (Scheme 1).

The effect of different parameters (pressure, temperature, amount of catalyst, amount of TBAB) was investigated. Finally, the optimum reaction conditions were temperature of 70°C, pressure of 1 MPa, 5 hours of time, 1 mol% catalyst and 10 mol% TBAB was determined (Table 1).

At the end, with the mentioned method and under the optimal conditions, the following derivatives and several other derivatives of epoxide were synthesized (Scheme 2).

22nd Iranian Chemistry Congress (ICC22)
Iranian Research Organization for Science and
Technology (IROST)
13-15 May 2024

03231-97589

IROST

Fig.1: FESEM of Co_3O_4.

a) 97%   b) 95%

c) 87%   d) 92%

Scheme 2: Several carbonylations of different epoxides.

Conclusions

In this research, the catalytic application of Co_3O_4 in the cycloaddition of CO_2 to epoxides was investigated. The study of different operational parameters showed that the reaction without solvent at a pressure of 1 MPa has the highest efficiency. Therefore, the shells of Co_3O_4 hollow spheres can catalyze the direct carbonation of epoxides with CO_2 to cyclic carbonates with an efficiency of up to 97%.

Scheme 1: Model reaction for chemical fixation of CO_2 with epoxides.

Table 1: Comparison of different conditions in the chemical fixation of carbon dioxide to epoxy styrene.

Entry	Amount of catalyst (g)	TBAB (mol %)	T (ºC)	P (MPa)	Time (h)	Yield (%)
1	0.003	-	70	1	5	75
2	0.003	10	70	5	5	99
3	0.015	10	70	3	5	98
4	0.003	10	70	1	5	97
5	0.003	10	70	1	2	87
6	0.006	5	70	1	5	92
7	0.015	5	70	1	5	95
8	0.003	10	50	1	5	92
9	0.003	10	90	1	5	98

References

[1] Meehl, G. A., & Washington, W. M. (1996). El Niño-like climate change in a model with increased atmospheric CO_2 concentrations. Nature, 382(6586), 56-60. https://doi.org/10.1038/382056a0.

[2] Zhang, S., Wang, Q., Puthiaraj, P., & Ahn, W. S. (2019). MgFeAl layered double hydroxide prepared from recycled industrial solid wastes for CO_2 fixation by cycloaddition to epoxides. Journal of CO_2 Utilization, 34, 395-403.

https://doi.org/10.1016/j.jcou.2019.07.035.

[3] Beyazay, T., Belthle, K. S., Farès, C., Preiner, M., Moran, J., Martin, W. F., & Tüysüz, H. (2023). Ambient temperature CO2 fixation to pyruvate and subsequently to citramalate over iron and nickel nanoparticles. Nature Communications, 14(1), 570. https://doi.org/10.1038/s41467-023-36088-w.

[4] Qin, N., Li, L., Wan, X., Ji, X., Chen, Y., Li, C., & Liu, Z. (2024). Increased CO2 fixation enables high carbon-yield production of 3-hydroxypropionic acid in yeast. Nature Communications, 15(1), 1591. https://doi.org/10.1038/s41467-024-45557-9.

Designing a new method for preparation of Metal-organic frameworks: synthesis, aracterization and catalytic applications

Moayad Hossaini Sadr*, Ali Pashazadeh*

Corresponding Author E-mail: hosainis@yahoo.com; a.pashazadeh20@gmail.com

Department of Chemistry, Faculty of Science, Azarbaijan Shahid madani University, Tabriz 53714-161, Iran.

Abstract: In this research, we present the development and characterization of a novel method via template condensation of macrocycle compound was coupled with 2-chloro benzimidazole derivatives in a simple reaction. The new MOF were synthesized by a reaction of Cu (II) ion with macrocyclic ligand. The synthesized compounds were fully characterized with different physico-chemical techniques like, elemental analysis (such as NMR, and FTIR spectroscopic) and electrochemical methods.

Keywords: Macrocycle; Metal-Organic Frameworks; Synthesis

Introduction

Metal-organic frameworks (MOFs) are highly crystalline subsets of microporous materials assembled by the formation of multiple coordination bonds between inorganic metal nodes and multidentate organic ligands[1,2]. Designing organic likers is a critical stage to obtain MOFs with desired functions. During the last two decades, different synthesis methods have been developed and applied to synthesize different organic linkers[3]. Many literatures has been explored reports[4] which, synthesis of macrocyclic linkers by using coordination diversity with nitrogen donors (N-donor) leads to the formation of organic linkers with very flexible properties in the synthesis of metal-organic compounds. With reference to the mentioned background, the aim of the present investigation is expand a facile and easy approach to synthesis of new linkers an imidazolate group on a flexible macrocycle based on two or more constituent materials.

Experimental Section

The macrocyclic was prepared (TAM) in a 250 mL round-bottom flask 10 mmol o-phenylene diamine dissolving in 10 ml of ethanol and mixed by slow stirring with 10 mm Phthalic acid, pyridine-2,3-dicarboxylic acid and pyridine-2,6-dicarboxylic acid with a molar ratio of 1:1 in the presence of an acid catalyst. In the next step, the macrocyclic ligandwas prepared By grafting TAM and the 2-chloro-benzimidazole derivatives (TAMBI) through an eco-friendly precipitation method. Then, the new metal-organic frameworks (MOFs) were synthesized by a reaction of Cu (II) ion with macrocyclic ligand (copper-macrocyclic organic framework(Cu-MCMOFs).

Results and Discussion

The samples were analyzed by various spectral data such as Fourier transform infrared (FT)and ^{1}HNMR techniques. The FT-IR spectrum demonstrated the tetra amid macrocyclic stretching vibrations amido and amide ring deformation and (C=N) groups in range 3452- 1440. To confirm the successful formation of structure synthesized products the NMR peaks, TAM, 2-chloro benzimidazole and TAmBI ligand was recorded. The ^{1}H NMR spectra of the precursors showed the signals of the -COOH proton and -NH$_2$, but were absent in the synthesized ligands, indicating the removal of the -COOH and -NH$_2$ protons for the formation of a macrocyclic structure. In the next step, to apply synthetic materials, the surface of the glassy carbon electrode was covered by synthetic materials and was used to examine the medicinal sample of maprotiline(MAP) drug. The electrochemical behaviour of the MAP (0.1 M PBS pH = 7.0) at Cu-MCMOFs /GCE was investigated by changing the scan rate in the range of 10–100 mVs^{-1}. From the dependence of peak currents plotted against the square root of the scan rate, it can be concluded the electrochemical oxidation process on the Cu-MCMOFs/GCE is mainly controlled by diffusion-controlled mode. The effective concentration of MAP on the anodic peak of Cu-MCMOFs /GCE was performed by using the CV technique in potential between 0 and 1 V at a scan rate of $50\,mV\,s^{-1}$ in 0.1 M PBS (pH = 7.0). In addition, for catalytic behaviour of MAP we investigated the catalytic rate constant (K_{cat}) and diffusion coefficient (D) with the chronoamperometry technique at a constant potential of 650 mV for MAP.

Conclusions

In conculation, the synthesis macrocycles compound has unique properties, such as superstructure formation with anions or electron donor guest molecules The Cu-MCMOFs/GCE presented as well as electrocatalyst with good linear relationship for determination of MAP. Besides, the modified electrode showed diverse advantages including good selectivity, acceptable reproducibility, high stability and anti-interference characteristics and can be used for real sample analysis.

22nd Iranian Chemistry Congress (ICC22)
Iranian Research Organization for Science and Technology (IROST)
13-15 May 2024

03231-97589

IROST

References

[1] Timmons, J. C., & Hubin, T. J. (2010). Preparations and applications of synthetic linked azamacrocycle ligands and complexes. Coordination Chemistry Reviews, 254(15-16), 1661-1685. https://doi.org/10.1016/j.ccr.2009.09.018

[2] Rednic, M. I., Hădade, N. D., Bogdan, E., & Grosu, I. (2015). Macrocycles embedding phenothiazine or similar nitrogen and/or sulphur containing heterocycles. Journal of Inclusion Phenomena and Macrocyclic Chemistry, 81, 263-293. https://doi.org/10.1007/s10847-014-0455-x.

[3] Luo, H., Chen, L.-X., Ge, Q.-M., Liu, M., Tao, Z., Zhou, Y.-H., & Cong, H. (2019). Applications of macrocyclic compounds for electrochemical sensors to improve selectivity and sensitivity. Journal of Inclusion Phenomena and Macrocyclic Chemistry, 95, 171-198. https://doi.org/10.1007/s10847-019-00934-6.

[4] Jo, H., Le, T.-H., Lee, H., Lee, J., Kim, M., Lee, S., . . . Yoon, H. (2023). Macrocyclic ligand-embedded graphene-in-polymer nanofiber membranes for lithium ion recovery. Chemical Engineering Journal, 452, 139274. https://doi.org/10.1016/j.cej.2022.139274.

22nd Iranian Chemistry Congress (ICC22)
Iranian Research Organization for Science and Technology (IROST)
13-15 May 2024

03231-97589

IROST

An Ultrasensitive Genosensor for Amplification-free Detection of *Clostridioides difficile*

Sepideh Ziaei Chamgordani[a], Abbas Yadegar[b], Hedayatollah Ghourchian[a]*

Corresponding Author E-mail: ghourchian@ut.ac.ir

[a] Laboratory of Bioanalysis, Institute of Biochemistry & Biophysics, University of Tehran, Tehran, Iran.

[b] Foodborne and Waterborne Diseases Research Center, Research Institute for Gastroenterology and Liver Diseases, Shahid Beheshti University of Medical Sciences, Tehran, Iran.

Abstract: *Clostridioides difficile* (*C. difficile*) is a food-born pathogen. An amplification-free electrochemical genosensor was developed for its detection, utilizing a gold nanoparticle-reduced graphene oxide nanocomposite (GNP-rGO)-coated glassy carbon electrode. This ultrasensitive genosensor displayed a low detection limit of 0.4 fM with a linear range of 0.4–478 fM, and significant specificity.

Keywords: *Clostridioides difficile*; Electrochemical genosensor; Nanocomposite

Introduction

C. difficile, is a gram-positive, spore-forming bacterium responsible for antibiotic-associated diarrhea and pseudomembranous colitis [1]. Electrochemical biosensors have been identified as an effective tool for detecting C. difficile biomarkers, especially its toxins TcdA and TcdB, in clinical samples due to their numerous benefits, such as high sensitivity, exceptional limit of detection, ease of use, and cost-effectiveness [2]. Furthermore, recent research has shown that modifying the electrode surface with graphene and metal composite materials can significantly enhance the sensitivity of electrochemical detection methods [3].

Experimental Section

GNP-rGO nanocomposite was deposited onto a glassy carbon electrode (GCE) by simple drop casting and allowed to dry naturally in ambient conditions. Subsequently, a thiolated oligonucleotide probe was immobilized onto the GNP-rGO-modified electrode surface through overnight incubation at 4 °C. To minimize non-specific binding events, the prepared GCE/GNP-rGO/probe was treated with mercaptohexanol (MCH). Finally, the resulting genosensor, GCE/GNP-rGO/probe/MCH, was ready for hybridization with its target sequence (coding gene of the TcdB toxin). An intercalator was employed as the indicator for electrochemical detection, and its oxidation peak was recorded using differential pulse voltammetry (DPV).

Results and Discussion

The abovementioned genosensor showed a low detection limit of 0.4 fM with a wide linear range of 0.4–478 fM (Fig.1). This sensitivity is because of the high conductivity of the GNP-rGO nanocomposite.
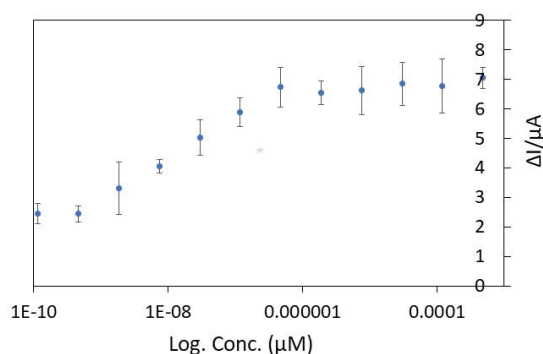
Fig.1: Calibration curve of genosensor against the different concentrations of the target gene.

As seen in Fig.2, this genosensor demonstrated notable sensitivity towards complementary target sequences with varying degrees of mismatch, including single mismatches (1MM), double mismatches (2MM), and triple mismatches (3MM). Additionally, it showed ignorable responses against non-complementary sequence (NC).
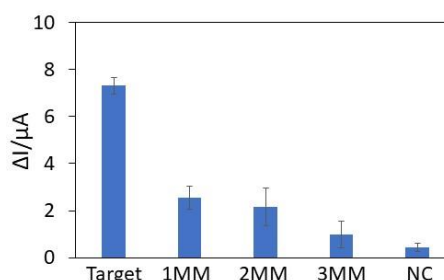
Fig.2: Results of the specificity assay of the genosensor against 1, 2, and 3 mismatched target sequences, and non-complementary sequence.

Conclusions

The study demonstrates the successful development of an electrochemical genosensor modified with a

22ⁿᵈ Iranian Chemistry Congress (ICC22)
Iranian Research Organization for Science and Technology (IROST)
13-15 May 2024

03231-97589

monolayer of GNP-rGO nanocomposite for ultrasensitive detection of the target gene without the need for prior gene amplification. The genosensor exhibits satisfactory specificity, indicating its potential for accurate and efficient detection of *C. difficile* in clinical samples.

References

[1] H. Motamedi, et al. (2021), A worldwide systematic review and meta-analysis of bacteria related to antibiotic-associated diarrhea in hospitalized patients. PloS one, 16(12)-e0260667.
https://doi.org/10.1371/journal.pone.0260667

[2] H.O. Kaya, et al. (2021), Pathogen detection with electrochemical biosensors: Advantages, challenges, and future perspectives. Journal of Electroanalytical Chemistry, 882-114989.
https://doi.org/10.1016/j.jelechem.2021.114989

[3] Y. Chen, et al. (2020), Nucleic acid amplification free biosensors for pathogen detection. Biosensors and Bioelectronics. 153-112049.
https://doi.org/10.1016/j.bios.2020.112049

Adventures in Electrochemistry: Bubble Film- Mediated Electrochemical Sensing and Deposition

Nikoo Fahemi,[a] Shayan Angizi,[c] Amir Hatamie [a,b*]

Ccorresponding Author E-mail: E-mail: *amir.hatami@iasbs.ac.ir*

[a] Department of Chemistry, Institute for Advanced Studies in Basic Sciences, Zanjan-Iran.
[b] Department of Chemistry and Molecular Biology, University of Gothenburg, Gothenburg-Sweden.
[c] Department of Chemical Engineering, McMaster University. Hamilton- Canada.

Abstract: We describe a novel electrochemical cell design with a bubble wall with thickness of about ~27 μm (Bubble or stable surfactant film) which serves as the tinny solution or medium for microelectroanalysis of nitrites on hand, without electrochemical cell, and microelectrodepsotion metallic film without template in microscale zone.

Keywords: Microelectroanalysis, Nitrite sensing, Bubble; Electrochemical deposition.

Introduction

We describe a novel electrochemical cell design with a thickness of about ~27 μm that comprises a carbon fiber electrode (10 μm diameter) placed through a bubble wall (or stable surfactant film) which serves as the solution. To create a durable surfactant film, we employed a solution infused with non-ionic Triton-X100 surfactants. For electroanalysis, a modified carbon microelectrode with graphene oxide nanosheet (GO, as a sensing electrode) was placed through a soap bubble wall along with a 1 mm diameter silver wire as the reference electrode. [1]

Using this strategy, the proposed sensing system has successfully detected NO2- both on the hand and dissolved in Triton-X100 surfactants film [2-3]. This technique holds particular significance in criminal investigations, as the presence of NO2- ions on the hand is indicative of gunshot residue and can aid in identifying suspects. Therefore, this method enables rapid analysis with a low limit of detection of 28 μM and proves functionality for on-site sensing.

To perform electrodeposition in a bubble wall, different ions such as silver and palladium ions were dissolved within the bubble film. A bare carbon microelectrode was placed inside the bubble wall, and the suitable cathodic potential was applied. The deposited metallic film was analyzed by scanning electron microscopy (SEM) and energy-dispersive X-ray spectroscopy. The images obtained from the analysis revealed that the thickness of the bubble wall or electrochemical cell imposes limitations on the electrodeposition area at the microscale level. Furthermore, the lifespan of the bubble wall [3] played a crucial role in controlling the duration and thickness of the deposited film from nanoscale to microscale.

Experimental Section
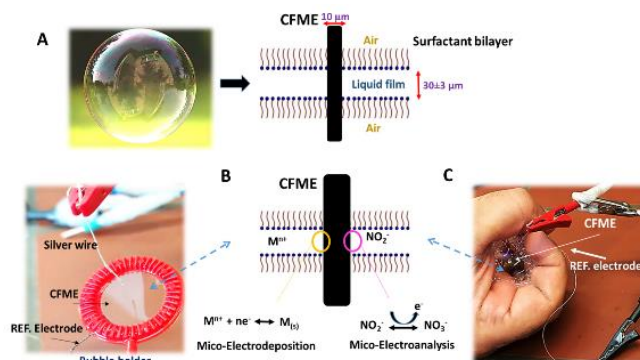
Fig. 1. (A) Schematic of the bubble wall structure and images of the experimental setups, microscale template free electrochemical deposition of metallic ions (B) and microelctroanalysis of nitrite (NO2-) oxidation on a hand (C), within tinny layer of soap bubble wall.

Results and Discussion

Estimation of bubble wall thickness and volume using spectrophotometric analysis

The Beer-Lambert law equation, $A=\varepsilon bc$, relates the absorbance of a solution (in this case, the bubble wall) to the molar absorptivity (ε), the path length of light through the sample (b) in centimeters, and the concentration of the substance (Phenol red). After obtaining the molar absorptivity coefficient (ε) of organic color compound (phenol red), we determined the thickness of the bubble wall using the Beer-Lambert law equation and estimating b, which represents the bubble wall thickness.

22nd Iranian Chemistry Congress (ICC22)
Iranian Research Organization for Science and Technology (IROST)
13-15 May 2024

03231-97589

IROST

Microsensor fabrication
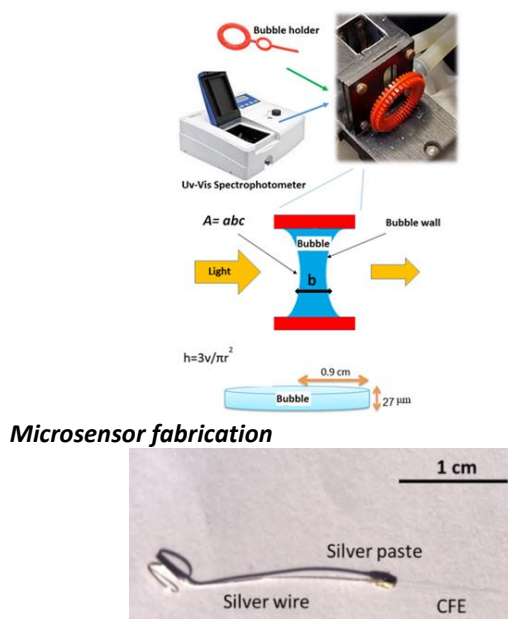
Fig. 2. A microscale carbon fiber electrodes (MCFEs) with a diameter of 10 μm were fabricated by connecting a 1 cm carbon fiber (CF) to a silver wire (as a connection wire) using silver paste.

The bubble wall thickness determines electrodeposition zone
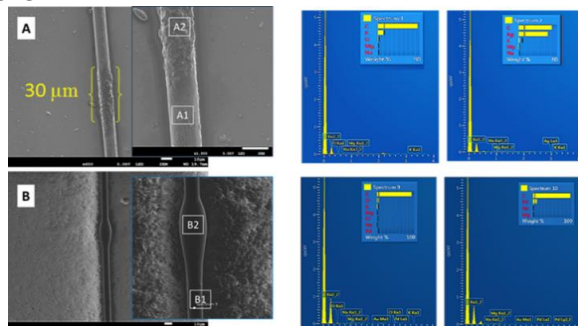
Fig. 3. Top-view SEM images of MCFE coated with a thin layer of Ag film (above) and with Pd film (below) at various magnifications, along with the corresponding EDX analysis.

Micro-electroanalysis of nitrite within and fingers !
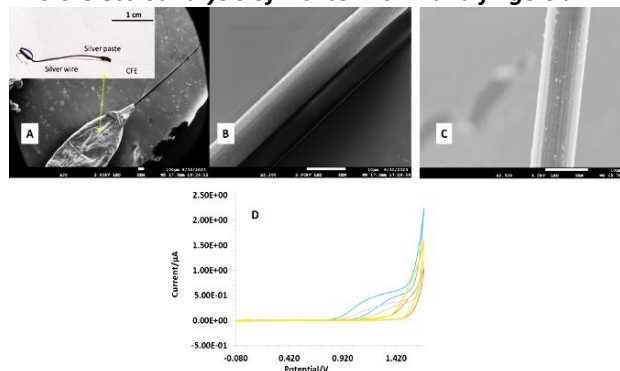
Fig. 4. (a-b) SEM images of the CFE and (c) modified CFE with GO. The inset in a shows the optical image of the

ultramicroelectrode associated with SEM. (d) CV curves in 200 μM nitrite,1.0 M TX-100 and electrolyte with a scan rate of 0.1 Vs−1 in solution and bubble wall: (Green) bare MCFE, (Red) MCFE@GO electrode in the absence of nitrite, (Blue) bare MCFE, (Black) MCFE@GO electrode in the presence of 200 μM nitrite.
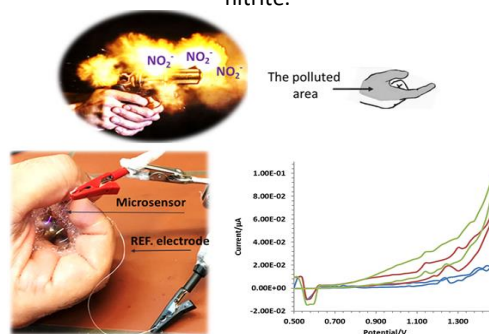
Fig. 5. Schematic and principle of nitrite Ion detection Using the modified ultramicroelectrode (CFE@GO) within the formed bubble wall, showed on the left. On the right, a simulation of microelectroanalysis for different concentrations of nitrite ions within bubble wall and on hand (Control in blue, 100 μM in red, and 300 μM in green).

Conclusions

In summary, we have developed innovative applications for a bubble wall as a thin layer of water using microscale electrochemistry. Initially, we successfully determined the thickness and volume of the bubble (electrochemical reaction media) using UV-Vis spectroscopy. Subsequently, we utilized the bubble to conduct electrochemical deposition within a microscale zone. The thickness of the bubble wall, containing metal ions, precisely controlled the deposition area of metallic films (Ag and Pd films) on the electrode surface. Importantly, the length of the deposition area correlated with the estimated thickness of the bubble wall. In the second part, we demonstrated the ability of a surfactant solution to dissolve nitrite ions, which our microelectrode could detect at micromolar levels within a matter of seconds on hands as Nitrite ion plays a pivotal role in criminal investigations.

References

1. Zhang, X., Hatamie, A., & Ewing, A. G. (2020). Nanoelectrochemical analysis inside a single living cell. Current Opinion in Electrochemistry, 22, 94-101.

2. Braide-Azikiwe, Dandisonba Chinwe Bamidele, Katherine B. Holt, David E. Williams, and Daren J. Caruana. "Soap film electrochemistry." Electrochemistry communications 11, no. 6 (2009): 1226-1229.

3. Vannoy, Kathryn J., Nicole E. Tarolla, Philip J. Kauffmann, Rebecca B. Clark, and Jeffrey E. Dick. "Detecting Methamphetamine in Aerosols by Electroanalysis in a Soap Bubble Wall." Analytical Chemistry 94, no. 16 (2022): 6311-6317.

Fe₃O₄@SiO₂@2-Aminothiophenol-Cu: a novel magnetically reusable nanostructured catalyst for the efficient synthesis of 2,3-dihydroquinazolin-4(1H)-ones

Mahsa Hassanzadeh, Nader Noroozi Pesyan*, Khadijeh Ojaghi Aghbash

Corresponding Author E-mail: nnp403@gmail.com

Department of Organic Chemistry, Faculty of Chemistry, Urmia University, 57159, Urmia, Iran.

Abstract: Fe₃O₄@SiO₂@2-Aminothiophenol-Cu demonstrates its capability as a reusable and heterogeneous catalyst in the efficient synthesis of various 2,3-dihydroquinazolin-4(1H)-one derivatives through the two-component condensation of 2-aminobenzamide and an aldehyde. This reaction offers simplicity, environmental friendliness, and cost-effectiveness. The catalyst can be easily separated and recycled by employing magnetic decantation with the assistance of an external magnet. The characterization of the catalyst was performed using FESEM, EDS, TGA, VSM, and X-ray diffraction techniques.

Keywords: Fe₃O₄@SiO₂@2-Aminothiophenol-Cu; nanocatalyst; 2,3-dihydroquinazolin-4(1H)-one

Introduction

The latest research literature provides compelling evidence that a diverse range of compounds incorporating the structural units of 2,3-dihydroquinazolin-4(1H)-one display noteworthy biological activities. These activities encompass a wide spectrum including antitumor, anticancer, antibiotic, antibacterial, antidefibrillatory properties, and etc [1].

The results indicate that in order to achieve chemical stability, magnetic nanoparticles (NPs) necessitate the presence of coating species such as silica, surfactant polymers, and nonpolymeric organic stabilizers [2]. Among these coating species, the silica shell has garnered significant interest due to its distinctive magnetic responsiveness, straightforward preparation, inertness, low cytotoxicity, chemical stability, ability to control particle size, and surface modificability [3].

we became concerned in the synthesis, characterization and catalytic application of : Fe₃O₄@SiO₂@2-Aminothiophenol-Cu as a new magnetically recyclable solid basic nanocatalyst for the efficient synthesis of 2, 3-dihydroquinazolin-4 (1H)-ones.

Experimental Section

Preparation of magnetic Fe₃O₄ nanoparticles

A mixture of FeCl₃.6H₂O (3.5gr) and FeCl₂.4H₂O (1.16 g) was dissolved in 100 mL of deionized water in a threenecked flask (139mL) at 80°C under nitrogen atmosphere. Subsequently, 23 mL of aqueous NH₃ solution (25%) was added into the mixture within 30 min with vigorous mechanical stirring. The resulting black precipitate was isolated by magnetic decantation, washed with double-distilled water until neutral, further washed twice with ethanol and dried at 80°C in vacuum to afford Fe₃O₄.

Preparation of Fe₃O₄@SiO₂

For preparation Fe₃O₄@SiO₂, 2 g of Fe₃O₄ NPs were dispersed in a mixture of deionized water (40 mL), ethanol (160 mL), and 25% ammonia (6 mL) under sonication. Subsequently, 5 mL tetraethyl or thosilicate (TEOS) was added slowly and dropwise to the mixture reaction under reflux for 12 h. Ultimately, the Fe₃O₄@SiO₂ was separated by an external magnet, then washed with ethanol several times, and then dried under vacuum.

Preparation of Fe₃O₄@SiO₂ magnetic nanoparticles (MNPs) functionalized with 3-chloropropyl trimethoxysilane (Fe₃O₄@SiO₂@(CH₂)₃-Cl)

In a round-bottomed flask (250 mL) equipped with a magnetic stirrer, Fe₃O₄@SiO₂ (2 g), 8 mL of 3-chloro propyltrimethoxysilane (CPTMS) and n-hexane (66 mL) was added and was refluxed under a nitrogen atmosphere for 30 hrs, then washed with n-hexane several times and gathered using an external magnet.

Preparation of Fe₃O₄@SiO₂‑2‑aminothiophenol

In a round-bottom flask, a mixture of MNPs@(CH₂)₃Cl (2 g) with 2-aminothiophenol (2 g) with Et₃N (4 mL) in EtOH (100 mL) was refluxed and the resulting cooking was separated from the EtOH by magnet. For 12 h, it was dried at 70 °C.

Preparation of Fe₃O₄@SiO₂‑2‑aminothiophenol-Cu

The precipitate from the previous step was mixed with the solution of 3 g of CuCl₂·6H₂O (1.5g) in ethanol (120 mL) and was refluxed for 20 h and dried at a temperature of 60 °C. The final MNPs–Cu catalyst was synthesized.

22nd Iranian Chemistry Congress (ICC22)
Iranian Research Organization for Science and Technology (IROST)
13-15 May 2024

03231-97589

IROST

General method of synthesis of 2,3-dihydroquinazolin-4(1H)-one

A mixture of the aldehyde (1.0 mmol), 2-aminobenzamide (1.0 mmol), and Fe₃O₄@SiO₂‑2‑aminothiophol–Cu (50.0 mg) in ethanol (5.0 mL) was stirred at ambient condition. The reaction process was investigated by thin-layer chromatography (TLC) with n-hexane: ethyl acetate (7:3). After completion of the reaction, the magnetic nanocomposite was separated by an external magnet and the crude product was purified by EtOH recrystallization to obtain the desired products. Finally, the ^{1}H and ^{13}C-NMR spectroscopy were used to identify the products and then comparison to the reported scientific findings.

Results and Discussion

In this work, the Fe₃O₄ NPs were fabricated via a co-precipitation method and then coated with a silica layer by Stober process. After that, the 2-aminothiophol were grown on the surface of the Fe₃O₄@SiO₂ for copper deposition (Fig. 1)
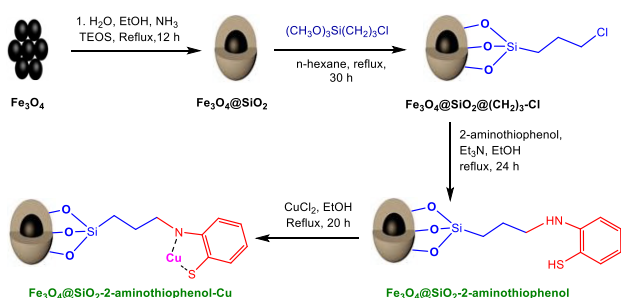
Schame 1: Schematic illustration of Fe₃O₄@SiO₂-2-aminotiophenol-Cu nanocomposite

Cu complex supported on Fe₃O₄@SiO₂ NPs was completely analyzed by SEM, EDS, TGA, XRD, and FT-IR techniques.

EDX spectra of the Fe₃O₄@SiO₂-2-aminotiophenol-Cu complex are presented in Figure 1. It can be seen from Fig. 1 (**a**), C, O, Si, Fe, N, S and Cu element have been detected in functionalized Fe₃O₄@SiO₂.

The SEM images of Fe₃O₄@SiO₂-2-aminotiophenol-Cu (b) in Figure 1 confirm that samples have spherical and regular morphology.

After synthesis and confirmation of the catalyst framework by different analyzes, we were concentrated on finding an eco-friendly, efficient, and simple procedure for the synthesis of 2,3-dihydroquinazolin-4(1H)-one derivatives through the two-component condensation of 2-aminobenzamide and an aldehyde in the presence of Fe₃O₄@SiO₂-2-aminotiophenol-Cu as a recyclable, stable, and efficient mesoporous nanocatalyst.
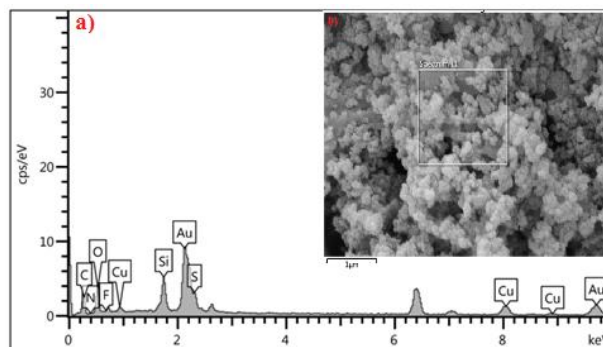
Fig.1: EDS spectrum of Fe₃O₄@SiO₂-2-aminotiophenol-Cu (a) and SEM images of Fe₃O₄@SiO₂-2-aminotiophenol-Cu (b).
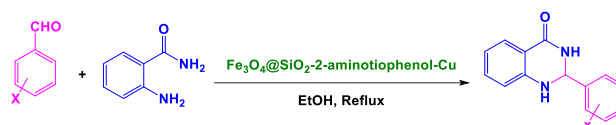
Conclusions

In the current study, we successfully designed a magnetically novel mesoporous Fe₃O₄@SiO₂-2-aminotiophenol-Cu nanocatalyst and characterized its framework by different analytical techniques, and also used it as a nanocatalyst in the clean synthesis of 2,3-dihydroquinazolin-4(1H)-one derivatives. The important advantages of this nano-catalytic system are an easy synthesis, short reaction times, reusability of the nanocatalyst and high stability, clean conditions, easy workup, excellent yields of reaction, and simple purification.

References

[1] Safari, J., & Gandomi-Ravandi, S. (2014). Application of the ultrasound in the mild synthesis of substituted 2, 3-dihydroquinazolin-4 (1H)-ones catalyzed by heterogeneous metal–MWCNTs nanocomposites. *Journal of Molecular Structure*, *1072*, 173-178.

[2] Dupont, D., Luyten, J., Bloemen, M., Verbiest, T., & Binnemans, K. (2014). Acid-stable magnetic core–shell nanoparticles for the separation of rare earths. *Industrial & Engineering Chemistry Research*, *53*(39), 15222-15229.

[3] Ghosh Chaudhuri, R., & Paria, S. (2012). Core/shell nanoparticles: classes, properties, synthesis mechanisms, characterization, and applications. *Chemical reviews*, *112*(4), 2373-2433.

Computational Study of Carvacrol and Thymol: A Comparative Insight

Fatemeh Salimi [a], Nasrin Fallah*[b]

Corresponding Author E-mail: nasrin.fallah@srbiau.ac.ir

[a] Department of Biology, Central Tehran Branch, Islamic Azad University, Tehran, Iran.

[b] Department of Chemistry, Science and Research Branch, Islamic Azad University, Tehran, Iran.

Abstract: Carvacrol (**CV**) and thymol (**TY**) are liquid phenolic monoterpenoids present in the essential oils of some plants and have a wide range of biological activities. The DFT computational data indicate that **CV** is softer than **TY**, therefore it's an appropriate ligand for the reaction with the nitrogen bases of DNA or amino acids of proteins and enzymes.

Keywords: Carvacrol; Thymol; Density Functional Theory (DFT)

Introduction

In today's medicine, there is a great tendency to use herbal medicines to reduce the side effects of all kinds of diseases, because in addition to their beneficial effects in disease control, they reduce the risk of side effects caused by the use of chemical drugs. [1].

Essential oils have great potential for the treatment of infections, especially related to antioxidant activity. Essential oils are liquid, volatile, limpid, and rarely colored; can be lipid soluble and soluble in organic solvents; and generally have densities lower than that of water. In addition to classical antioxidants, phenolic compounds are known as important antioxidants in plants. Studies show that at the molecular level, plant phenols such as flavonoids, flavonolignans, and phenolic acids can act as effective antioxidants.

Carvacrol; **CV** ($C_{10}H_{14}O$; 2-methyl-5-(1-methylethyl)phenol) and Thymol; **TY** ($C_{10}H_{14}O$; 2-isopropyl-5-methylphenol) are liquid phenolic monoterpenoid, present in essential oils of oregano (Origanum vulgare), thyme (Thymus vulgaris), pepperwort (Lepidium flavum), wild bergamot, and other plants[1].

These two isomer compounds can also be synthesized by commercial chemical and biotechnological methods [1]. These compounds possess a wide range of biological activities, including antibacterial, antifungal, antiviral, and anticarcinogenic properties[1].

This research aims to compare the structure-activity relationship of these two compounds by DFT computational method.

Experimental Section

Gaussian 09 was used for the full optimization of all the structures involved in this work at the B3LYP level of theory. All the atoms were described with a split valence Pople basis set plus diffuse functions, /6-311+G(d,p) in the gas phase [2]. Frequency calculations were also carried out at the B3LYP level of theory as used for the optimization of structures to ensure that the local minima were found. Natural bond analysis (NBO) was used at the same level of theory to analyze the electronic properties as well as the constitution of the molecular orbital (Fig. 1).

CV   **TY**
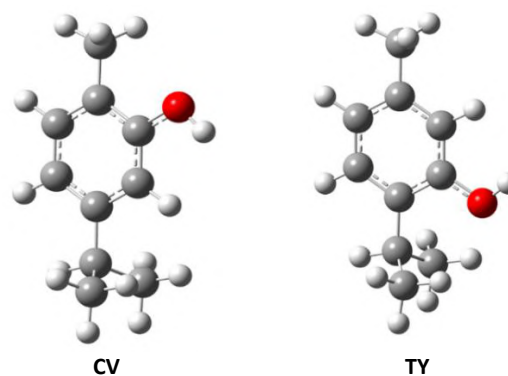
Fig.1: The optimized chemical structure of compounds

Results and Discussion

In order to better understand the reason for the biological activity and also determine the active sites in the structure of these two molecules, the optimized geometry parameter (E), dipole moment, HOMO and LUMO energy, and molecule electrostatic surface potential (MEP) were calculated. The band gap energy [Eg $(E_{HOMO} − E_{LUMO})$] was also calculated; the Eg represents the intermolecular charge transfer from an electron donor to an electron acceptor group[2,3]; hence, it can determine the stability, reactivity and chemical hardness–softness of different chemicals[2,3].

22nd Iranian Chemistry Congress (ICC22)
Iranian Research Organization for Science and
Technology (IROST)
13-15 May 2024

03231-97589

According to Table 1, **CV** has better thermodynamic stability than **TY** due to the larger total energy, and **TY** has more kinetic stability than **CV** due to the larger energy gap. **CV** is a soft molecule due to its smaller Eg(2.574 eV) and, softness (0.777 eV^{-1}), and electronegativity (χ) index (9.012 eV). The dipole moment is the most common quantity used to describe the polarity of a system and is defined as the product of charge on the atoms and the distance between the two bonded atoms[2,3]. The role of dipole moment in the efficiency of a molecule as an inhibitor has always been disputed by scientists. Some papers have suggested that a greater dipole moment value increases adsorption energy of the inhibitor, and improves the performance of the molecule. However, some researchers have noted no direct relationship between the molecule's dipole moment and inhibitor efficiency[2,3]. Therefore, **CV** can form strong electrostatic interactions or hydrogen bonds with amino acids or DNA bases, and it is predicted that its biological activity should be remarkable.

Table1: Obtained reactivity parameters of compounds from DFT calculations.

	CV	TY
Total enegy(eV)	-291705.55	-291704.30
Dipol moment($Debye$)	1.298	1.534
Energy of HOMO(eV)	-6.1036	-6.136
Energy of LUMO(eV)	-3.5294	-0.435
Eg; energy gap (eV)	2.5742	5.701
Ionization energy (I) (eV)	6.1036	6.136
Electron affinity (A) (eV)	3.5294	0.435
Hardness (η) (eV)	1.2871	2.850
chemical potential(μ) (eV)	4.8165	3.286
electronegativity(χ) (eV)	-4.8165	-3.286
Softness (σ) (eV^{-1})	0.7769	0.351
Electrophilicity index(ω) (eV)	9.0119	1.894

$$E_g = E_{LUMO} - E_{HOMO} \tag{1}$$

$$\mu = -\chi = \frac{(E_{HOMO} + E_{LUMO})}{2} = -\frac{(I + A)}{2} \tag{2}$$

$$\eta = \frac{[-E_{HOMO} - (-E_{LUMO})]}{2} = \frac{(I - A)}{2} \tag{3}$$

$$\omega = \mu^2/2\eta \tag{4}$$

$$I = -E_{HOMO} \tag{5}$$

$$A = -E_{LUMO} \tag{6}$$

The molecular electrostatic potential (MEP) maps of compounds are represented in Fig. 2. The electrophilic, nucleophilic color range of molecules falls between – 0.03 to + 0.03. The most negative site (red color) on the MEP map of two molecules is related to the lone pairs of the oxygen atoms of the hydroxyl group. Oxygen atoms of this molecule are the most reactive site to get protonated in the protonation reaction and formation of hydrogen bonds. The MEP yellow color area of both molecules shows the likelihood of intermolecular interactions such as CH- π and π- π interaction.
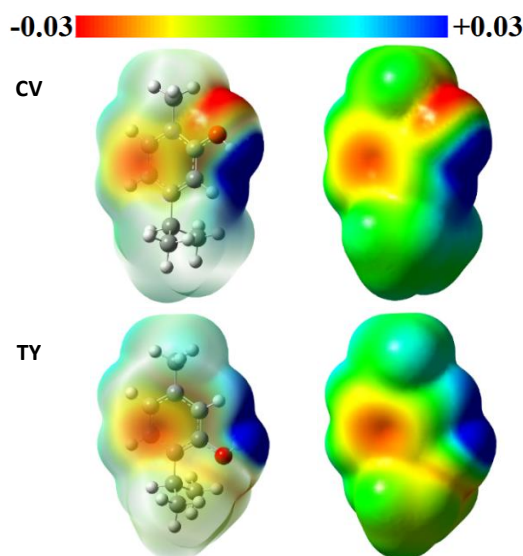
Fig.2: MEP maps of **CV** and **TY** (opaque & transparent).

Conclusions

In summary, The DFT computational data and MEP maps indicate that **CV** is softer than **TY**, therefore it's an appropriate ligand for the reaction with the nitrogen bases of DNA or amino acids of proteins and enzymes.

References

[1] Sharifi-Rad, M., Varoni, E. M., Iriti, M., Martorell, M., Setzer, W. N., del Mar Contreras, M., ... & Sharifi-Rad, J. (2018). Carvacrol and human health: A comprehensive review. *Phytotherapy Research*, *32*(9), 1675-1687

[2] Gholivand, K., Faraghi, M., Fallah, N., Babaei, A., Pirastehfar, F., Dusek, M., ... & Salimi, F. (2022). Therapeutic potential of phospho-thiadiazole derivatives as anti-glioblastoma agents: synthesis, biological assessment and computational study. *Bioorganic Chemistry*, *129*, 106123.

[3] Gholivand, K., Faraghi, M., Fallah, N., Vahabirad, M., Malekshah, R. E., Salimi, F., & Pournasir-roudbaneh, M. (2023). New phosphoramides containing 2-amino-1, 4-naphthaquinone moiety as anticancer and antibacterial agents: Experimental and theoretical evaluations. *Process Biochemistry*, *132*, 97-109.

Facile synthesis of 3,5-disubstituted isoxazoles using copper-hydroxyacetophenone thiosemicarbazone complex on silica-coated magnetite nanoparticles as an efficient heterogeneous nano catalyst

Somayeh Behrouz*, Narjes Mansouri

Corresponding Author E-mail: behrouz@sutech.ac.ir

Department of Chemistry, Shiraz University of Technology, Shiraz 71555-313, Iran

Abstract: A facile and efficient method for synthesis of 3,5-disubstituted isoxazoles via cycloaddition of terminal alkynes with *in situ* generated nitrile oxides catalyzed by $Fe_3O_4@SiO_2$-HAT-Cu(I) as a magnetically separable nano catalyst is described. The catalyst is inexpensive, reusable, chemically and thermally stable. The catalyst structure was characterized by different techniques.

Keywords: alkyne; $Fe_3O_4@SiO_2$-HAT-Cu(I); isoxazole; nitrile oxide

Introduction

Isoxazoles are an important substrates in medicinal and organic chemistry [1]. Isoxazoles exhibit different biological activities such as anticancer, analgesic, antiviral, antibacterial, and anti-inflammatory. Some famous drugs such as glisoxepide, valdecoxib, oxacillin, dicloxacillin, cloxacillin, isocarboxazid, and leflunomide contain the isoxazole core in their structures [2].

Among different synthetic strategies for preparation of isoxazoles, the cycloaddition reaction between *in situ* generated nitrile oxides and alkynes is the most extensively used approach [3,4]. To prevent the dimerization or the nucleophilic trapping of the nitrile oxides, they are *in situ* generated in the reaction media via the dehydrohalogenation of hydroximyl chlorides, the oxidation of aldoximes, and the dehydration of nitroalkanes. The thermal cycloaddition reaction between alkynes and *in situ* generated nitrile oxides in the absence of catalyst can lead to the mixtures of 3,5- and 3,4-regioisomers. However, the use of active copper (I) catalysts in this reaction promotes the formation of 3,5-disubstituted isoxazoles [3,4].

The magnetic nanoparticles (MNPs) could be easily collected from the reaction mixture using an external magnetic field [5]. Practically, catalysts based on silica-coated Fe_3O_4 MNPs are efficient alternatives to previously solid-supported heterogeneous catalysts [6]. The low cost, ease of removal by a magnet field, high surface area, reusability, stability, and ease of preparation increase the demand for design, synthesis, and application of this catalyst type in organic reactions. Herein, we report the synthesis, characterization, and application of copper-hydroxyacetophenone thio semicarbazone complex immobilized on silica-coated magnetite nanoparticles ($Fe_3O_4@SiO_2$-HAT-Cu(I)) for

synthesis of 3,5-disubstituted isoxazoles via cycloaddition reaction of *in situ* generated nitrile oxides with alkynes in H_2O/THF (1:1, V/V) at room temperature (Scheme 1).
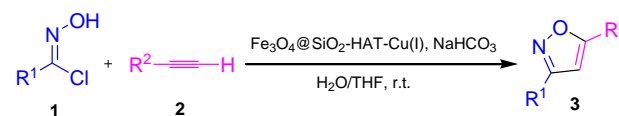
Scheme 1. Synthesis of 3,5- disubstituted isoxazoles in the presence of $Fe_3O_4@SiO_2$-HAT-Cu(I)

Experimental Section

A mixture of catalyst (0.5 mol %), appropriate hydroximyl chloride (1 mmol), alkyne (1 mmol), and $NaHCO_3$ (1.2 mmol) were stirred in H_2O/THF. After completion of the reaction (TLC monitoring), the catalyst was collected and separated from the reaction mixture using an external magnet. THF was then evaporated under vacuum. The residue was dissolved in $CHCl_3$ and washed with water. Then, the organic layer was evaporated and the crude product was purified by short column chromatography on silica gel.

Results and Discussion

After synthesis of magnetic $Fe_3O_4@SiO_2$-HAT-Cu(I), its structure was characterized using various techniques, including FE-SEM, EDS, TEM, VSM, AAS, TGA, XRD, FT-IR, DLS, and ICP-OES. Then, the catalytic potency of $Fe_3O_4@SiO_2$-HAT-Cu(I) was investigated in cycloaddition reaction of the *in situ* generated nitrile oxides from hydroximyl chlorides (**1**) with alkynes (**2**) to afford the 3,5-disubstituted isoxazoles (**3**). To optimize the reaction conditions, we chose the reaction of phenyl acetylene and N-hydroxybenzimidoyl chloride as the model substrates in the presence of catalyst at room temperature. Then, the influence of solvent type,

22nd Iranian Chemistry Congress (ICC22)
Iranian Research Organization for Science and
Technology (IROST)
13-15 May 2024

03231-97589

IROST

temperature, base and catalyst amount were examined on the model reaction to afford 3,5-diphenylisoxazole (**3a**). In this concern, various solvents including H_2O, THF, H_2O/THF, H_2O/acetone, H_2O/MeCN, H_2O/EtOH, and H_2O/dioxane were studied on the progress of the model reaction. Also, the effect of different bases including $NaHCO_3$, DBU, DABCO, DMAP, NaH, Et_3N, and MgO was examined in the model reaction. Then, the influence of different amount of catalyst and reaction temperatures ranging from 0-1 mol% and room-temperature up to reflux, respectively, were investigated on the progress of **3a** synthesis. The best result was obtained when the reaction was achieved in the presence of 0.5 mol% catalyst using $NaHCO_3$ as the reaction base in H_2O/THF at room temperature.

With optimized reaction conditions in hand, we then investigated the generality and versatility of the present method by its application to various hydroximyl chlorides and alkynes bearing different functional groups. Both aromatic and aliphatic hydroximyl chlorides and alkynes work well using the present protocol. The structures of synthesized 3,5-disubstituted isoxazole derivatives **3a-3l** are shown in Fig. 1.
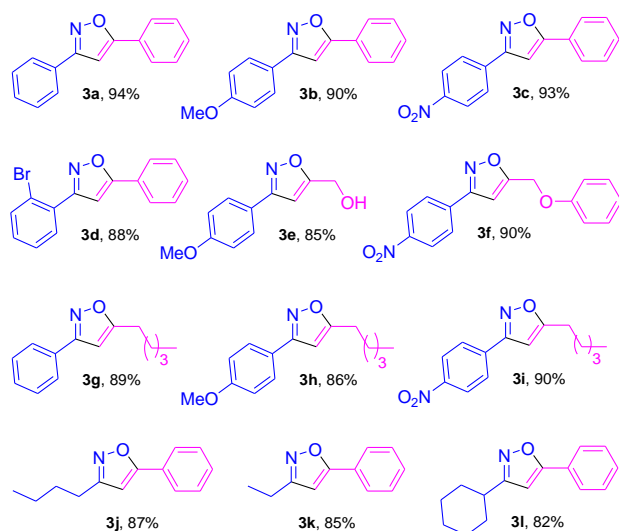
Fig.1: The structure of synthesized 3,5-disubstituted isoxazoles using Fe_3O_4@SiO_2-HAT-Cu(I)

The heterogeneous nature and reusability of Fe_3O_4@SiO_2-HAT-Cu(I) were explored over 6 reaction cycles for synthesis of **3a** under the optimized reaction conditions. After completion of each reaction cycle, the catalyst was collected from the reaction mixture by an external magnet and washed with ethanol and deionized water. Then, it was dried at 70°C in a vacuum oven. The dried catalyst was reused in the next reaction while no fresh catalyst was added to the reaction mixture. Practically, Fe_3O_4@SiO_2-HAT-Cu(I) proved to have good

reusability and recyclability even after the 6th run with negligible decrease in its reactivity. According to the ICP analysis, the ammount of copper leaching from the catalyst is 0.003% after 6 reaction runs.

Conclusions

In summary, the regioselective synthesis of 3,5-disubstituted isoxazoles in the presence of Fe_3O_4@SiO_2-HAT-Cu(I) as an efficient magnetic heterogeneous nano-catalyst is described. The cycloaddition reaction of different *in situ* generated nitrile oxides and alkynes using Fe_3O_4@SiO_2-HAT-Cu(I) in the presence of $NaHCO_3$ in H_2O/THF at room temperature affords 3,5-disubstituted isoxazoles in high yields. The catalyst can be separated from the reaction mixture by an external magnet field and reused for at least 6 reaction cycles with no considerable loss in its reactivity.

References

[1] Galenko, A. V., Khlebnikov, A. F., Novikov, M. S., Pakalnis, V. V., & Rostovskii, N. V. (2015). Recent advances in isoxazole chemistry. Russian Chemical Reviews, 84, 335-377. https://doi.org/10.1070/RCR4503

[2] Kleeman, A., Engel, J., Kutscher, B., & Reichert, D. (1999). Pharmaceutical substances, 3rd ed., Thieme, Stuttgart.

[3] Hu, F., & Szostak, M. (2015). Recent developments in the synthesis and reactivity of isoxazoles: Metal catalysis and beyond. Advanced Synthesis and Catalysis, 357, 2583-2614. https://doi.org/ 10.1002/adsc.201500319

[4] Heaney, F. (2012). Nitrile oxide/alkyne cycloadditions–A credible platform for synthesis of bioinspired molecules by metal-free molecular clicking. European Journal of Organic Chemistry, 2012, 3043-3058. https://doi.org/10.1002/ejoc.201101823

[5] Zhang, Q., Yang, X., & Guan, J. (2019). Applications of magnetic nanomaterials in heterogeneous catalysis. ACS Applied Nano Materials, 2, 4681-4697. https://doi.org/10.1021/acsanm.9b00976

[6] Veisi, H., Pirhayati, M., Mohammadi, P., Tamoradi, T., Hemmati, S., & Karmakar, B. (2023). Recent advances in the application of magnetic nanocatalysts in multicomponent reactions. RSC Advances, 13, 20530-20556. https://doi.org/10.1039/d3ra01208e

22nd Iranian Chemistry Congress (ICC22)
Iranian Research Organization for Science and Technology (IROST)
13-15 May 2024

03231-97589

IROST

Aqueous-mediated synthesis of pyrano[2,3-d]pyrimidine derivatives catalyzed by a novel morpholinium-based acidic ionic liquid

Narjes Mansouri*, Somayeh Behrouz

Corresponding Author E-mail: narjesmansouri24@gmail.com

Department of Chemistry, Shiraz University of Technology, Shiraz 71555-313, Iran.

Abstract: A green synthetic route for the preparation of pyrano[2,3-d]pyrimidine derivatives via three-component reaction between malononitrile, barbituric acid, and different aldehydes catalyzed by a new acidic ionic liquid based on morpholine has been established. The structure of the acidic ionic liquid and products was characterized using ^{1}H-NMR, ^{13}C-NMR, and FT-IR.

Keywords: acidic ionic liquid; morpholine; pyrano[2,3-d]pyrimidine; three-component reaction

Introduction

N-Heterocyclic compounds are widely found in natural and synthetic products exhibiting various applications in different areas of science especially in medicinal, chemistry, and material sciences. Among them, pyrano[2,3-d]pyrimidine derivatives are versatile substrates present in a plenty of biological active compounds with a broad range of activities such as anticancer, antiviral, antihypertensive, antibacterial, antioxidant, antimalarial, antifungal, antigenotoxic, analgesics, bronchiodilators, hepatoprotective, cardiotonic, vasodilator, sex pheromones, antiallergic, and herbicidal [1,2]. Thanks to the importance of pyrano[2,3-d]pyrimidines in drug discovery, significant research interests have been dedicated toward developing the facile and efficient synthetic approaches to access structurally diverse pyrano[2,3-d]pyrimidine derivatives [3]. The most extensively used method is the three-component reaction between malononitrile, barbituric acid, and aldehydes [3]. While the previously reported methods have their own value, however, they are associated with one or more drawbacks such as low yields, long reaction time, harsh reaction conditions, expensive catalyst, and effluent pollution. Hence, there is still a high demand for developing the new synthetic routes towards the preparation of pyrano[2,3-d]pyrimidine derivatives as important heterocyclic compounds.

Undoubtedly, ionic liquids (ILs) have played an ineradicable role in advancing the organic synthesis [4,5]. Owing to the extensive outlook of their uses in diverse field of chemical sciences especially organic chemistry, ILs have been the subject of enormous interest by many researchers [6]. Ionic liquids are generally used in organic transformations as catalysts, extractants, and green solvents. The morpholinium-based ionic liquids have gained particular attention due to their outstanding

properties and advantages. These ILs could be simply prepared via the short overall reaction and due to the low price of morpholine derivatives the final ionic liquids are inexpensive. Herein, we report the synthesis of pyrano[2,3-d]pyrimidine derivatives through the three-component reaction between malononitrile, barbituric acid, and different aldehydes in the presence of a novel morpholinium-based acidic ionic liquid in H_2O/EtOH (1:1, V/V) at room temperature (Scheme 1).

Ar= H, Cl, Me, OMe, ...
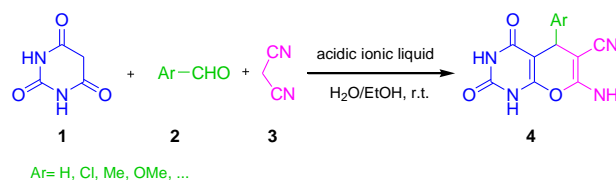
Scheme 1. Synthesis of pyrano[2,3-d]pyrimidine derivatives in the presence of acidic ionic liquid

Experimental Section

A mixture of malononitrile (1 mmol), barbituric acid (1 mmol), appropriate aldehyde (1 mmol), and acidic ionic liquid (1 mol%) were stirred in H_2O/EtOH at room temperatue. After completion of the reaction (TLC monitoring), the crude reaction mixture was filtered using a sintered glass. Then, the precipitate was washed with cold dichloromethane. Afterward, the crude precipitate was purified by recrystallization with EtOH to afford the pure product.

4c: ^{1}H NMR (DMSO-d_6, 400 MHz) δ_{ppm} = 3.36 (s, 2H, NH$_2$), 3.88 (s, 3H, OCH$_3$), 7.06 (d, J = 8.8 Hz, 2H, aryl), 8.25 (s, 1H, CH), 8.37 (d, J = 8.8 Hz, 2H, aryl), 11.19 (s, 1H, NH), 11.32 (s, 1H, NH). ^{13}C NMR (DMSO-d_6, 100 MHz) δ_{ppm} = 36.57, 56.16, 58.98, 86.82, 114.42, 116.02, 125.62, 137.97, 150.68, 155.39, 162.67, 163.90, 164.40.

22nd Iranian Chemistry Congress (ICC22)
Iranian Research Organization for Science and Technology (IROST)
13-15 May 2024

03231-97589

IROST

Results and Discussion

After synthesis of morpholinium-based acidic ionic liquid, its structure was characterized using ^{1}H-NMR, ^{13}C-NMR, and FT-IR. Then, its catalytic potency was explored in the synthesis of pyrano[2,3-d]pyrimidine derivatives **4** according to Scheme 1.
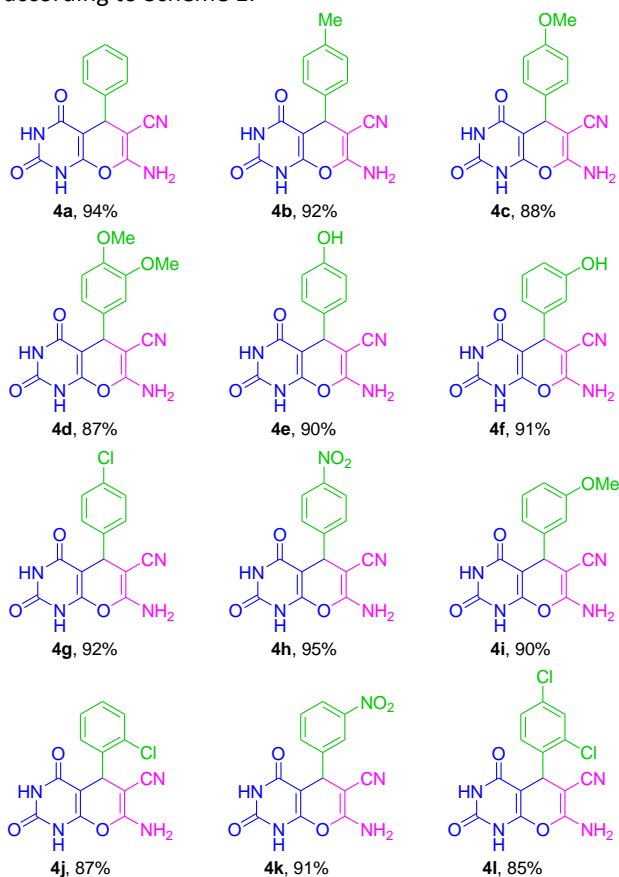
Fig.1: The structure of synthesized pyrano[2,3-d]pyrimidine derivatives using acidic ionic liquid

To gain the optimized reaction conditions, the reaction of malononitrile, barbituric acid, and benzaldehyde in the presence of acidic IL at room temperature was selected as the model reaction. Then, the influence of solvent type, temperature, and catalyst amount were examined on the model reaction to afford **4a**. In this concern, various solvents including H_2O, EtOH, H_2O/EtOH, H_2O/acetone, H_2O/THF, and H_2O/MeCN were examined on the progress of the model reaction. Then, the influence of different amount of acidic IL and reaction temperatures ranging from 0-1 mol% and room-temperature up to reflux, respectively, were investigated on the progress of **4a** synthesis. The best result was obtained when the reaction was achieved in the presence of 1 mol% acidic IL in H_2O/EtOH at room temperature. Then, we examined the versatility and scope of this approach by its application to structrally diverse aldehydes bearing electron-releasing and electron-withdrawing groups at *o*, *m*, and *p* positions of aromatic ring (Fig. 1). In general, the chemistry works well using the current procedure. When aldehydes bearing electron-withdrawing groups were used, the products were obtained in higher yields. Also, the presence of fuctional groups at *o* position led to the lower yields of product due to the steric hindrance.

Conclusions

In summary, we report the facile and green synthesis of pyrano[2,3-d]pyrimidine derivatives in the presence of morpholinium-based acidic ionic liquid as a novel and efficient catalyst. The one-pot cyclocondensation reaction of malononitrile, barbituric acid, and structurally diverse aldehydes in the presence of an acidic ionic liquid in H_2O/EtOH (1:1, V/V) at room temperature affords pyrano[2,3-d]pyrimidines in high yields under mild conditions.

References

[1] Bararjanian, M. Balalaie, S. Movassagh, B, & Amani, A. M. (2009). One-pot synthesis of pyrano[2,3-d]pyrimidinone derivatives catalyzed by L-proline in aqueous media. Journal of the Iranian Chemical Society, 6, 436-442. https://doi.org/10.1007/BF03245854

[2] AbdEl-Azim, M. H. M., Aziz, M. A., Mouneir, S. M., EL-Farargy, A. F., & Shehab, W. S. (2020). Ecofriendly synthesis of pyrano[2,3-d]pyrimidine derivatives and related heterocycles with anti-inflammatory activities. Archiv der Pharmazie, 353, e2000084. https://doi.org/10.1002/ardp.202000084

[3] Kazemi, M., Shiri, L., & Kohzadi, H. (2017). Synthesis of pyrano [2,3,d] pyrimidines under green chemistry. Journal of Materials and Environmental Sciences, 8, 3410-3422.

[4] Wasserscheid, P., & Keim, W. (2000). Ionic liquids-new "solutions" for transition metal catalyst. Angewandte Chemie International Edition, 39, 3772-3789. https://doi.org/ 10.1002/1521-3773(20001103)39: 21<3772::aid-anie3772>3.0.co;2-5

[5] Pârvulescu, V. I., & Hardacre, C. (2007). Catalysis in ionic liquids. Chemical Reviews, 107, 2615-2665. https://doi.org/10.1021/cr050948h

[6] Zuo, Y., Liu, Y., Chen, J., & Li, D. Q. (2008). The separation of cerium(IV) from nitric acid solutions containing thorium(IV) and lanthanides(III) using pure [C8mim]PF6 as extracting phase. Industrial & Engineering Chemistry Research, 47, 2349-2355. https://doi.org/ 10.1021/ie071486w

22nd Iranian Chemistry Congress (ICC22)
Iranian Research Organization for Science and Technology (IROST)
13-15 May 2024

03231-97589

IROST

Fish scale derived hydroxyapatite silica propyl bis aminoethoxy ethane cuprous complex: An efficient hybrid nano catalyst for N-arylation of N-heterocycles with aryl halides

Somayeh Behrouz*, Narjes Mansouri

Corresponding Author E-mail: behrouz@sutech.ac.ir

a Department of Chemistry, Shiraz University of Technology, Shiraz 71555-313, Iran.

Abstract: The Ullmann-type N-arylation of N-heterocycles with various aryl halides catalyzed by fish scale derived hydroxyapatite silica propyl bis aminoethoxy ethane cuprous complex (HASPBAEECC) is described. The N-aryl products were obtained in good yields and the catalyst could be reused for 5 consecutive runs with no significant decline in its reactivity.

Keywords: N-Arylation; HASPBAEECC; N-Heterocycle; Ullmann-type reaction

Introduction

The C-N bond formation is a well-known reaction in organic chemistry which provides a plenty of attractive substrates with diverse applicability in different scientific fields [1]. The N-Arylation of the N-heterocycles is an important C-N bond formation since the resulting N-aryl adducts exhibit different applications in organic and medicinal chemistry [2]. The structure of some herbicides and approved drugs containing the N-aryl N-heterocycle core is shown in Fig. 1.
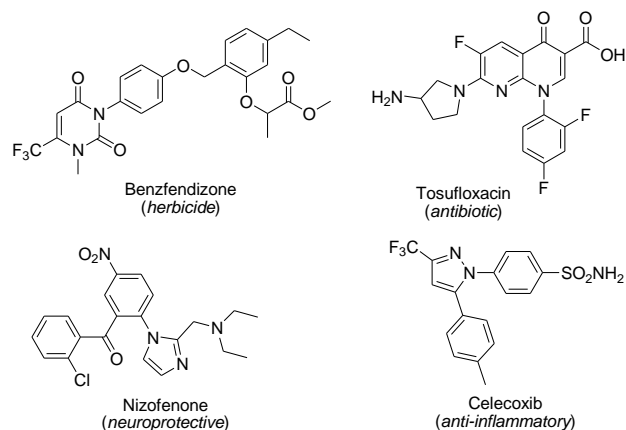
Fig.1: The structure of drugs and herbicides having N-aryl N-heterocyclic core

Up to date, several synthetic approaches have been developed for preparation of N-aryl N-heterocycles including the reaction of N-heterocycles with aryl iodonium salts [3], the N-arylation of N-heterocycles with aryl boronic acids [4], the heterocyclization of appropriate precursors [5], nucleophilic aromatic substitution (SNAr) reactions of electron-deficient aryl halides with N-heterocycles [6], and Ullmann-type reaction between N-heterocycles and aryl halides [7]. Amongst, the Ullmann-type reaction is of considerable attention due to the availability of more starting materials compared to other methods.

Herein, we report the synthesis, characterization, and application of fish scale derived hydroxyapatite silica propyl bis aminoethoxy ethane cuprous complex (HASPBAEECC) as an environmentally benign nano catalyst for Ullmann-type N-arylation of N-heterocycles with aryl halides in DMF at 110 °C (Scheme 1).
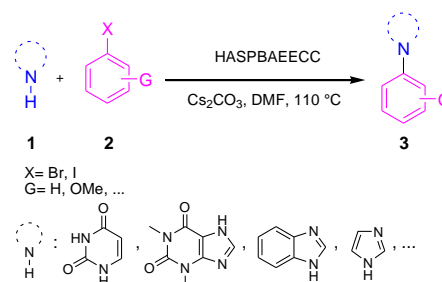
Scheme 1. Synthesis of N-aryl N-heterocycles via Ullmann-type reaction using HASPBAEECC

Experimental Section

A round bottom flask was charged with DMF (5 mL), N-heterocycle (1 mmol), Cs_2CO_3 (2 mmol), aryl halide (1.1 mmol), and HASPBAEECC (0.2 mol%). The reaction mixture was heated to 110 °C until TLC monitoring indicates no further progress of the reaction. Then, the catalyst was separated using a sintered glass and the filtrate was evaporated under reduced pressure. The remaining foam was dissolved in EtOAc and washed twice with water. Next, the organic solvent was evaporated using a rotary evaporator under a vacuum. The crude products were purified via column chromatography on silica gel to afford the desired N-aryl N-heterocycle derivatives.

Results and Discussion

Initially, HASPBAEECC was synthesized and its structure was characterized using several techniques including XRD, TGA, FE-SEM, EDS, and FT-IR. Then, its catalytic potency was explored in Ullmann-type N-arylation of N-

22nd Iranian Chemistry Congress (ICC22)
Iranian Research Organization for Science and
Technology (IROST)
13-15 May 2024

03231-97589

IROST

heterocycles with aryl halides. To identify the optimized reaction conditions, the N-arylation of imidazole with iodobenzene in the presence of HASPBAEECC was selected as the model reaction to afford product **3a**. Then, the effect of different parameters including solvent type, catalyst amount, base, and temperature was investigated on the model reaction to afford N-phenyl imidazole (**3a**). The best result was obtained when the Ullman-type reaction was carried out in the presence of 0.2 mol% catalyst using Cs_2CO_3 as the reaction base in DMF at 110 °C.

The scope and generality of the present procedure were investigated by its application to Ullmann-type N-arylation of uracil, theophylline, theobromine, imidazole, 2-phenylimidazole), benzimidazole, and indole with aryl halides including iodobenzene, 4-iodoanisole, 2-iodoanisole, and 1-bromonaphthalene (Fig. 1). As shown in Fig. 1, the N-aryl adducts **3a-3l** were obtained in good yields.
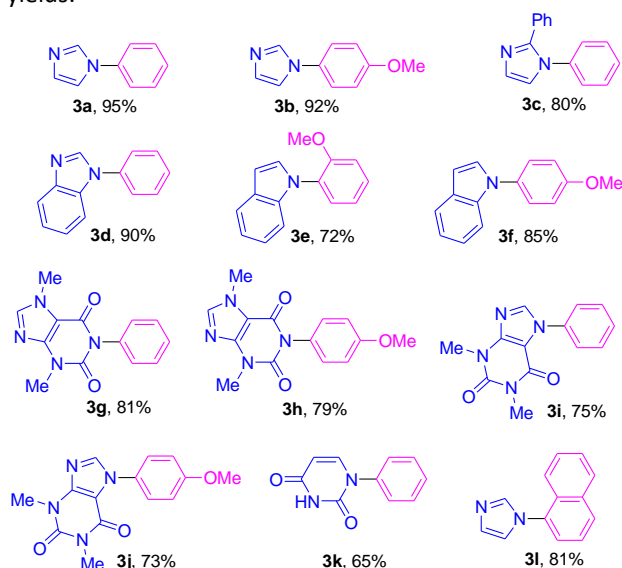
Fig.2: The structure of synthesized N-aryl N-heterocycles in the presence of HASPBAEECC

The recoverability and reusability of HASPBAEECC were studied over 5 sequential runs for synthesis of **3a** under the optimized reaction conditions. After completion of each run, the catalyst was separated from the reaction mixture using a sintered glass, washed with EtOAc and deionized water, and dried at 60°C in a vacuum oven. Then, it was reused in the next run. HASPBAEECC could be reused even after the 5th reaction cycle without considerable loss of its reactivity.

Conclusions

In conclusion, a facile and efficient method was described for the Ullmann-type N-arylation of N-heterocycles with aryl halides using HASPBAEECC in the presence of Cs_2CO_3 in DMF. The N-aryl N-heterocycle products were obtained in reasonable yields. The cheapness, heterogeneous nature, stability, facile synthesis, ease of handling, and reusability of HASPBAEECC are several advantages of this catalyst.

References

[1] Katritzky, A. R., & Rees, C. W. (1996). Comprehensive Heterocyclic Chemistry II, Elsevier, Oxford.

[2] Kleeman, A., Engel, J., Kutscher, B., & Reichert, D. (1999). Pharmaceutical substances, 3rd ed., Thieme, Stuttgart.

[3] Zhou, T., Li, T.-C., & Chen, Z.-C. (2005). Hypervalent iodine in synthesis. Part 86: Selective copper-catalyzed n-monoarylation and N1,N3-diarylation of uracil and its derivatives with diaryliodonium salts. Helvetica Chimica Acta, 88, 290-296. https://doi.org/10.1002/hlca.200590010

[4] Devarajan, N., & Suresh, P. (2016). Framework-copper-catalyzed C-N cross-coupling of arylboronic acids with imidazole: Convenient and ligand-free synthesis of N-arylimidazoles. ChemCatChem, 8, 2953-2960. https://doi.org/10.1002/cctc.201600480

[5] Hocek, M. (2003). Syntheses of purines bearing carbon substituents in positions 2, 6 or 8 by metal- or organometal-mediated C–C bond-forming reactions. European Journal of Organic Chemistry, 2003, 245-254. https://doi.org/10.1002/ejoc.200390025

[6] Gondela, A., & Walczak, K. (2005). N-Functionalization of uracil derivatives: synthesis of chiral 2-(3-methyl-5-nitro-2,4-dioxo-3,4-dihydropyrimidin-1(2H)-yl)alkanoic acids and their methyl esters. Tetrahedron: Asymmetry, 16, 2107-2112. https://doi.org/10.1016/j.tetasy.2005.05.009

[7] Zhou, Q., Du, F., Chen, Y., Fu, Y., Sun, W., Wu, Y., & Chen, G. (2019). L-(–)-Quebrachitol as a ligand for selective copper(0)-catalyzed N arylation of nitrogen-containing heterocycles. The Journal of Organic Chemistry, 84, 8160-8167. https://doi.org/10.1021/acs.joc.9b00997

22nd Iranian Chemistry Congress (ICC22)
Iranian Research Organization for Science and Technology (IROST)
13-15 May 2024

03231-97589

IROST

Short-range ^{31}P-X NMR coupling constants (X = ^{1}H and ^{13}C) in two new phosphoramides

Haniyeh Salari Jaieni and Mehrdad Pourayoubi*

Corresponding Author E-mail: pourayoubi@um.ac.ir

Department of Chemistry, Faculty of Science, Ferdowsi University of Mashhad, Mashhad, Iran.

Abstract: The syntheses and spectroscopic characterizations of two new phosphoramides, $P(O)(NHCH_2C_6H_4-2-Cl)_3$ (I) and $(4-Cl-C_6H_4O)P(O)(NHCH_2C_6H_4-2-Cl)_2$ (II) are investigated. Some topics related to the NMR coupling constants (^{31}P-^{1}H and ^{31}P-^{13}C) and chemical shifts (^{31}P, ^{1}H and ^{13}C) are addressed.

Keywords: Phosphoric Triamide; Diamidophosphoester; Phosphorus-Carbon Coupling Constant; NMR Spectroscopy

Introduction

Nuclear magnetic resonance (NMR) is one of the best techniques for the characterization of compounds ranging from small molecules to macromolecules [1–4]. NMR spin-spin coupling constants are interesting for studying, due to the application in conformational analysis and the assignments of some signals [5]. In the phosphorus chemistry (including organic groups), the usual NMR-active nuclei are ^{1}H, ^{13}C and ^{31}P, which are investigated in view point of chemical shifts, coupling constants and the fine structures arisen from couplings [3]. Here, the synthesis and spectroscopic characterization of two new phosphoramides, *i.e.* $P(O)(NHCH_2C_6H_4-2-Cl)_3$ phosphoric triamide (I) and $(4-Cl-C_6H_4O)P(O)(NHCH_2C_6H_4-2-Cl)_2$ diamidophosphoester (II) are discussed (Schemes 1 and 2).

Experimental Section

Syntheses

For the preparation of (I), to a solution of $POCl_3$ (6.9 mmol) in dry chloroform (15 ml), a solution of 2-chlorobenzylamine (20.7 mmol) and triethylamine (20.7 mmol) in the same solvent (15 ml) was added at 0 °C under stirring. After 4 hours, the mixture was transferred to a beaker and stood at room temperature (1 week) to evaporate the solvent. The residue (pale brown solid) was washed with distilled water to remove $(C_2H_5)_3NHCl$ salt. ^{1}H NMR (300.81 MHz, DMSO-d_6): δ = 7.70 – 6.73 (m, 12H), 5.44 (m, 3H), 4.38 (m, 6H). ^{13}C{^{1}H} NMR (75.65 MHz, DMSO-d_6): δ = 139.18 (d, J = 6.1 Hz), 131.98 (s), 129.30 (s), 129.10 (s), 128.44 (s), 127.32 (s), 42.37 (s). ^{31}P{^{1}H} NMR (121.76 MHz, DMSO-d_6): δ = 17.10 (s). IR (KBr, v, cm^{-1}): 3399, 3264, 3188, 2925, 1623, 1585, 1471, 1442, 1237, 1183, 1126, 1039, 888, 844, 746, 683.

For the preparation of (II), to a solution of 4-chlorophenyl dichlorophosphate (5.8 mmol) in dry chloroform (15 ml), a solution of 2-chlorobenzylamine (23.2 mmol) in the same solvent (15 ml) was added at 0 °C under stirring. After 4 hours, the mixture was transferred to a beaker and stood at room temperature (1 week) to evaporate the solvent. The resulting white precipitate was washed with distilled water to remove $[2-Cl-C_6H_4CH_2NH_3]Cl$ salt. ^{1}H NMR (300.81 MHz, DMSO-d_6): δ = 7.56 – 7.15 (m, 12H), 5.66 (dt, J = 11.4 Hz, 7.4 Hz, 2H), 4.13 (dd, J = 12.0 Hz, 7.5 Hz, 4H). ^{13}C{^{1}H} NMR (75.65 MHz, DMSO-d_6): δ = 150.76 (d, J = 6.6 Hz), 138.17 (d, J = 5.8 Hz), 132.00 (s), 129.73 (s), 129.27 (s), 128.78 (s), 128.36 (s), 127.42 (s), 122.77 (d, J = 4.8 Hz), 42.23 (s). ^{31}P{^{1}H} NMR (121.76 MHz, DMSO-d_6): δ = 13.25 (s). IR (KBr, v, cm^{-1}): 3600, 3457, 3409, 3263, 3170, 2917, 2847, 1592, 1484, 1440, 1358, 1232, 1196, 1117, 1094, 1040, 1010, 928, 828, 756, 736, 644, 600.
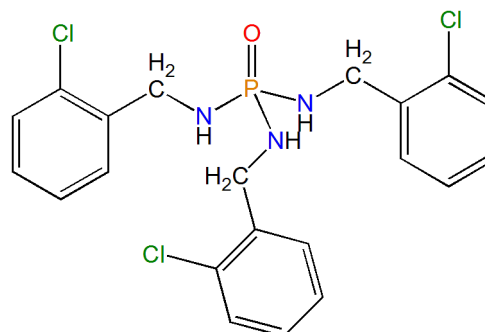
Scheme 1: Chemical structure of (I)
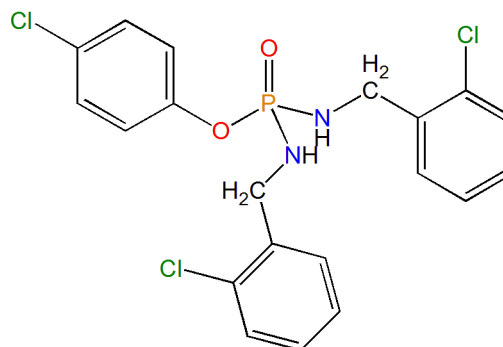
Scheme 2: Chemical structure of (II)

22nd Iranian Chemistry Congress (ICC22)
Iranian Research Organization for Science and Technology (IROST)
13-15 May 2024

03231-97589

IROST

Results and Discussion
Spectroscopic measurements

In the $^{31}P\{^1H\}$ NMR spectra, the signlets are observed at 17.10 ppm for (I) and at 13.25 ppm for (II).

The NH protons (in the ^1H NMR spectra) appear a multiplet at 5.44 ppm for (I), and a well-resolved doublet of triplets at 5.66 ppm for (II), due to geminal phosphorus-hydrogen (^2J = 11.4 Hz) and vicinal hydrogen-hydrogen couplings (^3J = 7.4 Hz).

For two compounds, the *ipso*-carbon atom of the 2-Cl-$C_6H_4CH_2NH$ moiety appears as a doublet, at 139.18 ppm (J = 6.1 Hz) for (I) (Figure 1) and at 138.17 ppm (J = 5.8 Hz) for (II) (Figure 2), due to a phosphorus-carbon coupling with a three-bond separation between nuclei.
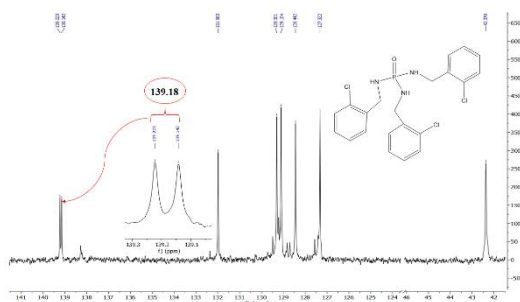
Fig. 1: $^{13}C\{^1H\}$ NMR spectrum of $P(O)(NHCH_2C_6H_4-2-Cl)_3$

The two doublets at 150.76 ppm (J = 6.6 Hz) and 122.77 ppm (J = 4.8 Hz) in the $^{13}C\{^1H\}$ NMR spectrum of (II) associate to the *ipso*- and *ortho*-carbon atoms of the 4-Cl-C_6H_4O moiety. In the IR spectrum of (I), the bands centered at 3264/3188 and 1237 cm^{-1} are assigned to the NH and P=O stretching vibrations. Similar bands for II are revelad at 3263/3170 and 1232 cm^{-1}.

Conclusions
Two new phosphoramides belonging to the phosphoric triamide and diamidophosphoester families were synthesized and characterized by spectroscopic methods. These compounds are $P(O)(NHCH_2C_6H_4-2-Cl)_3$ (I) and $(4-Cl-C_6H_4O)P(O)(NHCH_2C_6H_4-2-Cl)_2$ (II). Both two compounds show a doublet signal for the *ipso*-carbon atom of the $NHCH_2C_6H_5-2-Cl$ moiety with the three-bond separation phosphorus-carbon coupling constants of 6.1 Hz for (I) and 5.8 Hz for (II). The *ipso*- and *ortho*-carbon atoms of the 4-Cl-C_6H_4O moiety are revealed as doublets with $^2J_{PC}$ = 6.6 Hz > $^3J_{PC}$ = 4.8 Hz.
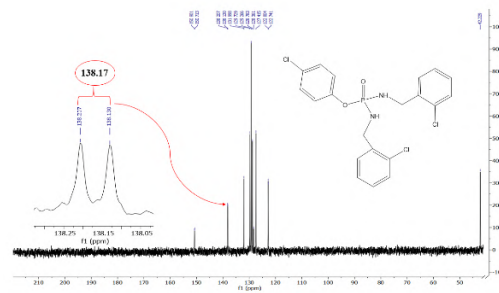
Fig. 2: $^{13}C\{^1H\}$-NMR spectrum of $(4-Cl-C_6H_4O)P(O)(NHCH_2C_6H_4-2-Cl)_2$

References
[1] Doskocz, M., Malinowska, B., Młynarz, P., Lejczak, B., & Kafarski, P. (2010). Long range phosphorus–phosphorus coupling constants in bis (phosphorylhydroxymethyl) benzene derivatives. Tetrahedron Letters, 51 (26), 3406-3411. https://doi.org/10.1016/j.tetlet.2010.04.107

[2] Kühl, O. (2008). Phosphorus-31 NMR spectroscopy: a concise introduction for the synthetic organic and organometallic chemist. Springer Science & Business Media.

[3] Lal Zakaria, N., Pourayoubi, M., Eghbali Toularoud, M., Dušek, M., & Skorepova, E. (2021). Structural differences/similarities of diastereotopic groups in three new chiral phosphoramides. Acta Crystallographica Section C: Structural Chemistry, 77 (4), 186-196. https://doi.org/10.1107/S2053229621002047

[4] Ahmadabad, F. K., Pourayoubi, M., & Bakhshi, H. (2019). Chiral phosphoric triamide-based polymers for enantioseparation. Journal of Applied Polymer Science, 136 (41), 48034. https://doi.org/10.1002/app.48034.

[5] Gholivand, K., Shariatinia, Z., & Pourayoubi, M. (2005). $^2J_{(P,C)}$ and $^3J_{(P,C)}$ coupling constants in some new phosphoramidates. Crystal structures of $CF_3C(O)N(H)P(O)[N(CH_3)(CH_2C_6H_5)]_2$ and $4-NO_2-C_6H_4N(H)P(O)[4-CH_3-NC_5H_9]_2$. Zeitschrift für anorganische und allgemeine Chemie, 631 (5), 961-967. https://doi.org/10.1002/zaac.200400517

22nd Iranian Chemistry Congress (ICC22)
Iranian Research Organization for Science and Technology (IROST)
13-15 May 2024

03231-97589

IROST

Core-shell heterostructured nickel–cobalt sulfide decorated on carbon spheres as a binder-free electrode for an enhanced energy storage system

Reza Dehghani Abdoljabbar, Hanieh Sharifpour, Saeed Shahrokhian*

Corresponding Author E-mail: shahrokhian@sharif.edu

Department of Chemistry, Sharif University of Technology, Tehran 11155–9516, Iran.

Abstract: In this study, a flexible carbon felt substrate was modified with Ni-based nitrogen-doped carbon and then decorated with $NiCo_2S_4$ nanosheets to enhance electrochemical performance. The prepared electrode exhibits highly efficient energy storage ability as well as good mechanical properties. The asymmetric supercapacitor was assembled and showed excellent energy density and long-term durability.

Keywords: Asymmetric supercapacitor - Carbon felt substrate – Nickel and Cobalt sulfide- Energy storage system

Introduction

The shortage of global energy resource is one of the most serious threats to global technological, economic, and social development. Supercapacitors (SC) as an advanced energy storage device are increasingly used as a high efficient energy storage system. Supercapacitors exhibit a high-power density suitable for a broad range of applications where high-power delivery or uptake is needed [1]. Regarding the energy storage mechanisms, two distinct families of supercapacitors can be considered. The first one is electrochemical double-layer capacitors (EDLCs) which use porous carbon electrodes with high accessible surface area. The second one is pseudocapacitor based on redox reactions that occur largely on oxide-based material surfaces. Understanding cell architecture and material capabilities is critical for SC performance. Doping heteroatoms into carbon electrodes can enhance energy density by enabling both EDLCs and pseudo-capacitances [2]. Incorporating transition metal compounds onto carbon materials is a promising strategy to tolerate high currents, offering a promising solution for high-energy and high-power energy storage. Binary nickel-cobalt sulfides, with their higher conductivity and excellent electrochemical activity, show promise for energy storage applications. Asymmetric supercapacitors (ASCs) were constructed from dissimilar electrodes and offered a feasible approach to achieve wider working potential windows [3,4].

Experimental Section

In the present work, nickel–cobalt sulfide nanosheets (NCS) as an electroactive material were chemically co-deposited on the carbon felt (CF) flexible substrate which is modified with Ni-based Nitrogen-doped carbon (NCNi). NCNi electrode was synthesized via a simple hydrothermal process on CF from $NiSO_4.6H_2O$, HMT, and glucose at a weight ratio of (2:1:1). The solution was sealed in a Teflon-lined autoclave and kept at 180°C for 24 hours in water.

Afterward, NCS was deposited onto the NCNi@CF to boost the capacitive performance of the positive electrodes. Carbon-felt flexible substrate modified with Nitrogen-doped carbon (NC@CF) was employed as the negative ones to assemble high-performance ASCs. NC@CF is obtained through a process involving the immersion of the NCNi@CF in 12 N HCl solution for 6 hours.

The ASC device was fabricated using the NCS@NCNi@CF as the positive electrode and NC@CF as the negative electrode in a 3 M KOH aqueous solution. The loading mass ratio of the positive and negative electrodes was calculated using the following equation:[5]

$$\frac{m_+}{m_-} = \frac{C_- \, \Delta V_-}{C_+ \Delta V_+} \qquad (1)$$

Results and Discussion
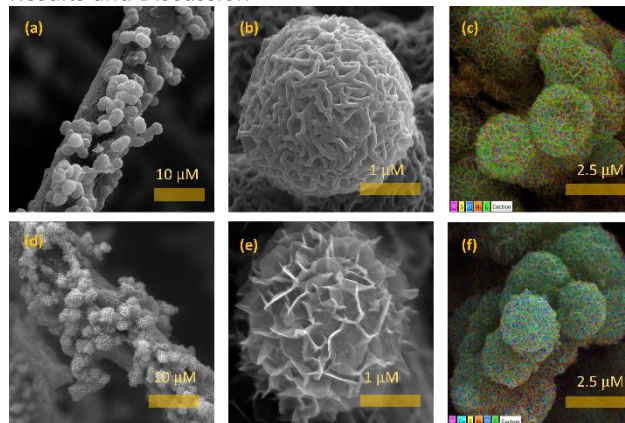
Fig.1: SEM of (a,b) NCNi spheres integrally decorated on the CF at different magnifications and (c) the corresponding EDS maps of the elements C, Ni, N, and O. (d,e) NCS NSs core/shell-like decorated binder-free NCNi/CF based electrode (f) the EDS maps of the elements Ni, Co, S, C, N, and O

22nd Iranian Chemistry Congress (ICC22)
Iranian Research Organization for Science and Technology (IROST)
13-15 May 2024

03231-97589

IROST

As seen in Fig. 1, the porous structure of CF was integrally decorated with the microstructures of flower-like NCNis to prepare binder-free electrodes. The successful formation of N-doped Ni-based carbon material was verified by EDS mapping analysis in Fig 1 (c). Receiving benefits from a porous structure, NCNi decorated CF seems to be a suitable substrate for subsequent deposition of NCS-NSs. SEM images of NCS-NSs integrally deposited onto NCNi@CF-based electrodes are given in Fig. 1(d-e). The elemental composition of the binder-free NCS@NCNi@CF electrodes was further evaluated by EDS mapping and the results are shown in Fig. 1 (f).
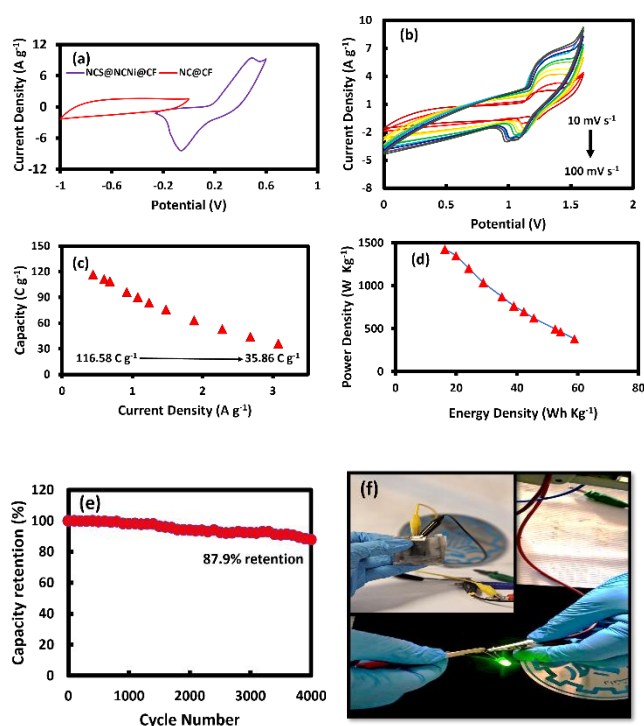
Fig.2 CV curves of NCS@NCNi@CF and NC@CF in the three-electrode system corresponding work voltage window (a), CV curves of the NCS@NCNi@CF // NC@CF (b specific capacity as a function of current density (c), Ragone plot (d), cycling performance of NCS@NCNi@CF // NC@CF (e), photograph of green LED lighted up by two ASCs in series and an inset showcasing an image of the actual device (f).

Fig. 2a exhibits the CV plots of the NCS@NCNi@CF (positive electrode) and NC@CF (negative electrode) which are recorded at a scan rate of 10 mV s^{-1} in a three-electrode system and with the potential range of (0-0.6) V and (-1 – 0) V, respectively. Owing to the ability of the NCS@NCNi@CF cathode and NC@CF anode to accumulate electric charges within the potential range of -1 V to 0.6 V, the operational voltage of the ASC is effectively established from 0 to 1.6 V. Fig. 2b depicts the CV curves of the NCS@NCNi@CF//NC@CF, charted within

a potential window of 0-1.6 V at scan rates from 10 to 100 mV.s^{-1}.

The assembled ASC cell has a specific capacity of 116.58 C g^{-1} at a current density of 0.44 A g^{-1}. Even when the current density increases to 3.08 A g^{-1}, the specific capacity is still 35.86 C g^{-1}. This specific measurement demonstrates the commendable rate capability of the ASC, as shown in Figure 2c.

Fig. 2d displayed the Ragone plot of the NCS@NCNi@CF //NC@CF. The ASC achieves a maximum energy density of 58.88 Wh kg^{-1} at 0.44 A g^{-1} with a power density of 381.94 W kg^{-1}, and retains a considerable energy density of 16.24 Wh kg^{-1} at 3 A g^{-1}, alongside a power density of 1426.78 W kg^{-1}.

The cycling stability of the NCS@NCNi@CF //NC@CF cell was meticulously examined and illustrated in Fig. 2e. Impressively, the ASC maintained excellent cycling stability, retaining 87.9% of its initial specific capacity after 4000 charge-discharge cycles.

A pair of ASCs were elegantly deployed in a series configuration to demonstrate practical application. The obtained ASC cell voltage was 3.2 V. The NCS@NCNi@CF //NC@CF cell in two parallel configurations was capable of powering a green LED for an impressive duration exceeding 20 minutes at the parallel voltage (Figure 2f).

Conclusions

In this study, we designed highly efficient NCS@NCNi@CF and NC@CF binder-free electrodes for the supercapacitor's practical application. Compared to the bare substrate, the pretreated NCS@NCNi@CF exhibited excellent electrochemical performance. Finally, the asymmetric flexible NCS@NCNi@CF//NC@CF was assembled and displayed high energy density and power density. Therefore, the new ASC device is presented with complete flexibility and stability, with potential applications in wearable electronics.

References

[1] J. Huang, Y. Xie, Adv. Funct. Mater. 2023, 2213095.

[2] P. Simon, Y. Gogotsi, Adv. Energy Mater. 2019, 9, 1902007.

[3] J. Liu, J. Wang, Adv. Sci. 2018, 5, 1700322.

[4] F. Hekmat, S. Shahrokhian, Energy Storage Materials. 2020, 20, 621-635.

[5] F. Hekmat, S. Shahrokhian, Sustainable Energy Fuels, 2022, 6, 3042.

22nd Iranian Chemistry Congress (ICC22)
Iranian Research Organization for Science and Technology (IROST)
13-15 May 2024

03231-97589

IROST

Application of Nitrogen, Sulfur co-doped carbon dots as fluorescence probes for tannic acid determination

Farhad Akhgari [a]*, Anese Farhangi [b]

Corresponding Author E-mail: Farhad.akhgari@gmail.com

[a] Faculty of Materials and Manufacturing Technologies, Malek Ashtar University of Technology,Iran.

[b] Department of Chemistry, Payame Noor University, Urmia, Iran.

Abstract: In this work, a novel, ultrasensitive and simple method for the determination of Tannic acid was proposed based on the quenching of the fluorescence intensity of Nitrogen, Sulfur co-doped fluorescent carbon dots-(N,S-CDs).The N,S-CDs were synthesized from the mixture of pomegranate juice and cysteine by one step hydrothermal method.

Keywords Nitrogen, Sulphur Co-Doped Fluorescent Carbon Dots; Quenching; Tannic Acid

Introduction

Tannic acid is a natural polyphenolic compound and consists of a central carbohydrate (glucose) and 10 galloyl groups. It is also used as additive in medicinal products, including those used for treatment of burns. Therefore, the determination of Tannic acid is of significance in food, medical and other industrial products.

In this study, we synthesized green N,S–CDs with high quantum yield through simple hydrothermal method and testified their application as sensitive probes for the detection of Tannic acid. Pomegranate juice was used as the carbon source while cysteine was used as both nitrogen and sulfur source. The as-prepared N,S-CDs showed good luminescence stability, and high solubility [2].

Experimental Section

Carbon nanoparticles were synthesized from the mixture of pomegranate juice and cysteine. In a typical procedure, 3g cysteine was dissolved in 15 mL pomegranate juice and was mixed with 5 ml deionized water. The resulting mixture was transferred into a Teflon-lined autoclave for hydrothermal treatment at 120 °C for 5 h. For collecting highly fluorescent carbon dots, the resulting red solution was centrifuged at 10000 rpm for 25 min to separate large particles. The as-prepared N,S-CDs were freeze dried and then re-dispersed in ultrapure water at the concentration of 1mg ml^{-1} for further characterization and use.

Results and Discussion

The structure and components of N,S-CDs were characterized by Fourier transformed infrared (FTIR) spectroscopy and X-ray photoelectron spectroscopy (XPS). The FT-IR spectrum (Fig. 2) exhibited characteristic absorption bands of N-H and OH stretching vibrations at 3440 cm^{-1}. The peaks at 2928 cm^{-1} and 1638 cm^{-1} were ascribed to the C-H and C=O stretching vibration, respectively. The peak at 2360cm^{-1} was attributed to C–N and S–H bond. [2]. The XPS survey spectrum exhibited three peaks at 285, 400 and 532.6 eV (Fig. 3), which were attributed to C_{1s}, N_{1s}, O_{1s}, S_{2p} respectively [2].
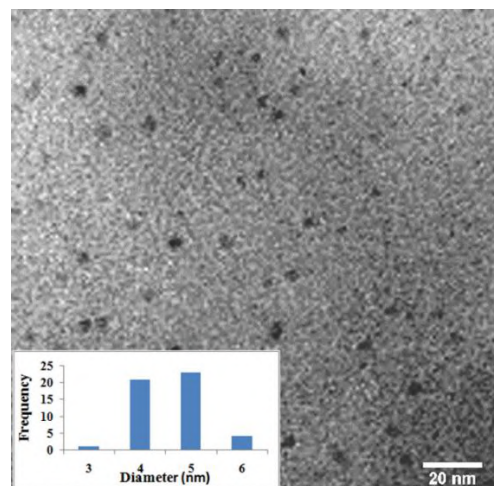
Fig.1: TEM image of N,S-CDs
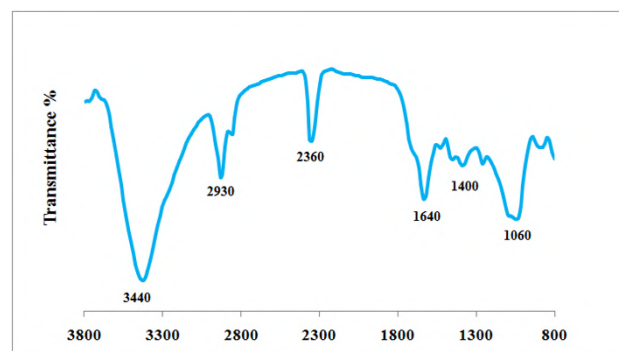
Fig. 2: The FT-IR spectrum of N,S-CDs

22nd Iranian Chemistry Congress (ICC22)
Iranian Research Organization for Science and
Technology (IROST)
03231-97589
13-15 May 2024

IROST

As shown in Fig. 4, under the optimum condition mentioned above, the fluorescence intensity of N,S-CDs was found to bdecreased with increasing the concentration of Tannic acid. The mechanism of this phenomenon could be explained by the interactions between the surface groups of N,S-CDs and cephalexin.

In the presence of Tannic acid at low concentrations, the relationship between the fluorescence quenching of N,S-CDs and the concentration of cephalexin can be described by the Stern–Volmer equation:

$F_0/F = 1+ KSV[Q]$ where F_0 and F are the fluorescence intensities in the absence and presence of Tannic acid, respectively. KSV is the Stern–Volmer constant and [Q] is the concentration of Tannic acid. As shown in the inset of Fig. 6.b, the Sterne–Volmer plot showed a linear relationship ($R^2 = 0.998$) between F_0/F and the concentration of Tannic acid over the ranges from 16 to 700 nM. The limit of detection (LOD) was estimated to be 6 nM (at a signal-to-noise ratio of 3) which was comparable with other reported values using alternative methods.

Conclusions

In this work, N,S-CDs were successfully used as a sensitive and selective florescence probe for fast detection of Tannic acid for the first time. This sensor is based on the fluorescence quenching effect of Tannic acid, which interacts with functional group of N,S-CDs. The selectivity assay reveals that this fluorescence probe has good selectivity to tannic acid over other acids, carbohydrates and metal ions. Additionally, this nanosensor has been successfully applied for the determination of spiked tannic acid in food samples. Under the optimum conditions, the calibration plot was linear in the range between 16–650 nM and with a correlation coefficient of 0.9985. The detection limit of this sensor is 6 nM. Therefore, this method can be provided excellent selectivity and sensitivity for fast, simple and accurate detection of trace Tannic acid in food samples

References

[1] Akhgari, F., Samadi, N., & Farhadi, kh. (2017). Fluorescent Carbon Dot as Nanosensor for Sensitive and Selective Detection of Cefixime Based on Inner Filter Effect. J. Fluorescence, 27(3):921-927.
https://link.springer.com/article/10.1007/s10895-017-2027-0

[2] Akhgari, F., Samadi, N., Farhadi, kh. &Akhgari, M. (2017). A green one-pot synthesis of nitrogen and sulfur co-doped carbon quantum dots for sensitive and selective detection of cephalexin,Can. J. Chem. 95: 641–648.
https://doi.org/10.1139/cjc-2016-0531

Fig.3: Result of XPS analysis of N,S-CDs
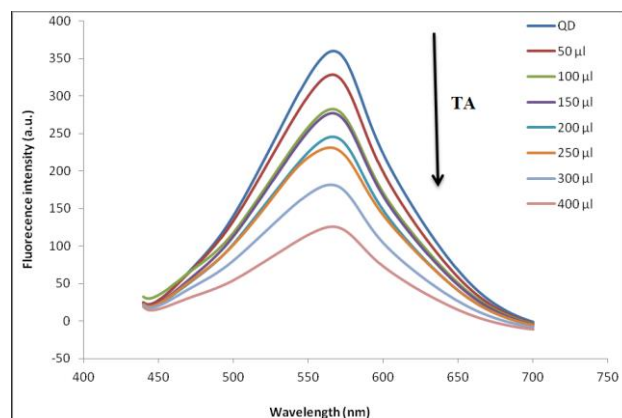
Fig.4: Variatiion of the fluorescence intensity of N,S-CDs with increasing the concentration of Tannic acid

Exploring Efficient Platinum Extraction from Choline Chloride Based Deep Eutectic Solvents with Tri-Octylamine: A Feasibility Study

Mahdi Rezaei, Seyed Mohammad Raouf Hosseini, Ali Ahmadi

Corresponding Author E-mail: m.rezaeiprocessing@gmail.com

Department of Mining Engineering, Isfahan University of Technology.

Abstract: This study investigates the feasibility of extracting platinum from a deep eutectic solvent (DES) based on choline chloride and ethylene glycol using an organic solvent extraction process with tri-octylamine (TOA) as the extractant and kerosene as the diluent. The initial platinum concentration in the DES was 217 ppm. Three experiments were conducted to evaluate the impact of various process parameters on the platinum extraction efficiency. The results showed that the highest platinum recovery of 98.02% was achieved in the third experiment, where the TOA concentration in the organic phase was 10%, the water-to-organic ratio was 1:1, the contact time was 5 minutes, and the temperature was 45°C. the kinetics of the extraction process were found to be remarkably fast, with more than 77% of the platinum being recovered within the first 5 minutes. The high extraction recoveries, even at the lower TOA concentrations, indicate the potential for process optimization to further improve the extraction efficiency and reduce operating costs. The findings highlight the promise of this approach for the selective separation and purification of platinum from complex matrices, with potential applications in the processing of petrochemical catalysts and the recovery of valuable metals from waste streams.

Keywords: Deep eutectic solvent; Solvent extraction; Tri-octylamine; Platinum

Introduction

Platinum (Pt) is a rare and valuable metal extensively used in automotive, petrochemical, and electronics industries, with global demand steadily rising due to its unique properties[1]. However, its limited supply from major mining regions like South Africa, Russia, and Canada has led to price fluctuations and the necessity for efficient extraction methods[2]. Deep eutectic solvents (DES) have emerged as a promising alternative, boasting low toxicity, biodegradability, and the capability to dissolve various compounds[3]. DES offer advantages for extracting and separating platinum, addressing sustainability concerns in industrial and environmental applications[4, 5].

The purification of DES containing platinum is a critical step for the recovery and reuse of this valuable metal[6]. Although several techniques, including membrane filtration, adsorption, and electrochemical methods, have been explored, using organic solvents for platinum extraction from DES has received less attention[7]. Solvent extraction using organic solvents, particularly trioctylamine (TOA), has emerged as a promising method due to its high selectivity, efficiency, and simplicity of operation. TOA, a tertiary amine with a long alkyl chain, is highly lipophilic and can form stable complexes with various metal ions, making it ideal for the separation and purification of valuable metals like platinum[8].

The feasibility of using TOA as an extractant for the purification of DES containing platinum has not been extensively explored[9]. This study aims to investigate the potential of using TOA-based solvent extraction for the purification of deep eutectic solutions containing platinum.

Experimental Section

In this study, trioctylamine (≥99.7%) and industrial kerosene from Merck, Germany, were utilized alongside a 500 mL platinum-charged solution derived from a deep eutectic solvent made with choline chloride and ethylene glycol, obtained from a used petrochemical catalyst. After rigorous analysis, the solution was confirmed to contain 217 ppm platinum and securely stored. Three distinct tests were meticulously designed based on existing literature, adhering to specified conditions outlined in Table 1. Platinum concentrations in both the organic and DES phases were quantified using inductively coupled plasma-optical emission spectroscopy (ICP-OES), with extraction recovery calculated as the percentage of platinum transferred from DES to organic solvent. An example of an organic solvent extraction test is presented in Figure 1.

Table1: solvent extraction tests design

	Extractant in Organic phase(wt%)	Aqu/Org	Time (min)	Temperature(°C)
1	2	3:1	5	35
2	6	2:1	15	45
3	10	1:1	5	45

22nd Iranian Chemistry Congress (ICC22)
Iranian Research Organization for Science and Technology (IROST)
13-15 May 2024

03231-97589

ISC

IROST

Fig.1: solvent extraction test during separation

Results and Discussion

The results of the three experiments conducted demonstrate the feasibility and effectiveness of using TOA-based organic solvent extraction for the purification and recovery of platinum from deep eutectic solutions.

In the first experiment, the platinum extraction recovery was 77.59%. This relatively high recovery rate suggests that TOA can effectively form stable complexes with platinum and facilitate its transfer from the DES to the organic phase.

The second experiment involved increasing the TOA concentration to 6% in the organic phase. These modifications resulted in an even higher platinum extraction recovery of 89.85%. The increased TOA concentration likely contributed to the enhanced extraction efficiency.

In the third experiment, the TOA concentration was further increased to 10% in the organic phase. This set of conditions yielded the highest platinum extraction recovery of 98.02%. The higher TOA concentration and the more favorable water-to-organic ratio appear to have been the key factors in achieving this near-complete platinum extraction.

The concentration of trioctylamine in the organic phase significantly influenced platinum recovery. As the trioctylamine concentration increased from 2% to 10%, the recovery improved proportionally. This suggests that optimizing the extractant concentration is crucial for efficient platinum extraction.

The results of these three experiments demonstrate the feasibility and effectiveness of using organic solvent extraction with TOA for the purification and recovery of platinum from deep eutectic solutions. The high extraction recoveries obtained, particularly in the third experiment, suggest that this approach could be a promising technique for the selective separation and purification of platinum from complex matrices, such as those encountered in the processing of petrochemical catalysts.

Conclusions

The results obtained across the three experiments conducted provide valuable insights into the extraction kinetics and the influence of key process parameters on the platinum recovery efficiency. The findings indicate that the extraction kinetics of platinum from the DES using TOA are remarkably fast, with a significant portion of the maximum recovery (77.59%) being achieved within the first 5 minutes of contact time. Furthermore, the results illustrated a clear relationship between trioctylamine concentration and extraction efficiency, as higher extractant concentrations correlated with improved recovery rates. While increasing the extractant concentration enhanced extraction efficiency, it also raised extraction costs, underscoring the importance of determining the optimal point to balance efficiency and cost-effectiveness in the extraction process. optimization of the process parameters, including the TOA concentration, water-to-organic ratio, and temperature, could potentially lead to even higher recovery rates and purity levels of the recovered platinum, making this approach a viable option for industrial-scale applications. Additionally, the integration of DES-based extraction with TOA-driven organic solvent extraction represents a sustainable and environmentally friendly approach for the recovery of valuable metals from waste streams.

References

[1] Heck, R.M., R.J. Farrauto, and S.T. Gulati, *Catalytic air pollution control: commercial technology*. 2016: John Wiley & Sons.

[2] Mudd, G.M., *Key trends in the resource sustainability of platinum group elements.* Ore Geology Reviews, 2012. **46**: p. 106-117.

[3] Paiva, A., et al., *Natural deep eutectic solvents– solvents for the 21st century.* ACS Sustainable Chemistry & Engineering, 2014. **2**(5): p. 1063-1071.

[4] Abbott, A.P., et al., *Novel solvent properties of choline chloride/urea mixtures.* Chemical communications, 2003(1): p. 70-71.

[5] Dai, Y., et al., *Ionic liquids and deep eutectic solvents in natural products research: mixtures of solids as extraction solvents.* Journal of natural products, 2013. **76**(11): p. 2162-2173.

[6] Souhaimi, M.K. and T. Matsuura, *Membrane distillation: principles and applications.* 2011.

[7] Yakoumis, I., et al., *Recovery of platinum group metals from spent automotive catalysts: A review.* Cleaner Engineering and Technology, 2021. **3**: p. 100112.

[8] Baba, Y., et al., *Recent advances in extraction and separation of rare-earth metals using ionic liquids.* Journal of Chemical Engineering of Japan, 2011. **44**(10): p. 679-685.

[9] Vadke, V.S., *Principles of Vegetable Oil Extraction*. 2024: CRC Press.

Investigation of Interaction of Synthesized Emulsion Mulch on Significant Physicochemical Factors of Soils

Seyedeh Bahareh Azimi

Corresponding Author E-mail: Baharazimi.env@gmail.com

Research Group of Assessment and Environment Risks, Research Center of Environment and Sustainable Development (RCESD), Department of Environment, Tehran, Iran.

Abstract: Soil is an important ecosystem component and it contain of heavy metals and hydrocarbon-based products that could affecte on health and the growth of plants. In this research study, tried to investigate intraction of soils filled with two types of mulchs for finding its effect on physicochemical factors of soils. The studied parameters were pH, EC, concentration of some cations and anions of the soil and results showed that use of these kinds of mulchs could improve significant features of soil.

Keywords: Mulch, Soil, Environmental

Introduction

Soil is one of the important and basic resources that plays a big role in providing the basic and essential needs of humans. This renewable resource is formed so slowly that it is considered a non-renewable resource [1]. In today's world, the rapid growth of the population on the one hand and the excessive pressure on the land and the inappropriate and wrong exploitation of the soil on the other hand have caused a lot of damage to this important resource and have caused more than one Third, all the lands of the world are exposed to severe erosion [2]. The increasing process of destruction of natural resources in many parts of the world is considered a serious threat to humanity. Wind erosion, as one of the manifestations of this destruction, has affected the developing and developed countries. In this study, an effort was made to investigate the effect of synthetic petroleum mulch as one of the solutions for stabilizing quicksand. To be examined and studied on the soil [3].

Material and methods

The test was carried out in an area of Kashan located between 51 degrees 42 minutes and 257 minutes north to 33 degrees 57 minutes and 128 minutes north in the north of Isfahan province. This region has a dry and desert climate.

This city is located 6 kilometers northeast of Kashan with a longitude of 51 degrees and 29 minutes and a latitude of 34 degrees and 4 minutes.

This city with an area of 6051 square kilometers is connected to Kashan and the country's main road network through two main roads. Due to the desert nature of the region, 1900 square kilometers (31% of the city's area) are located in sand dunes.

The purpose of this study was to investigate soil characteristics under the influence of emulsion mulch. The used mulches were of two types, which were introduced as A and B. In order to investigate the effect of emulsion viscosity on soil properties, samples were taken from the covered areas at different depths (specified in the results table) and at intervals of 6 and 12 months. In addition to collecting the soil sample, a separate sample was prepared from the remaining mulch on the soil surface.

Also, in order to compare the results with soils that were not affected by emulsion affinity, soil samples were taken as a control from the areas that did not receive mulch, so that at the end of the work, the effect of petroleum mulch on the soil could be compared to the control. The samples were air-dried and sent to a specialized laboratory.

work order

1- Soil texture: The soil texture was determined using the hydrometer method and the ASTM 152H standard method.

2- pH of the soil sample: The pH of the studied soil sample was measured in a 1:5 water to soil extract using a pH meter. Standard method (ASTM D-1293)

3- The electrical conductivity of the studied soil sample in the 1 to 5 water-to-soil extract was measured using the electrical conductivity meter (SM 2510 standard method)

4- The dissolved cations were measured by titration with EDTA (SM 2340C standard method) using a film photometer and flame measurement method.

5- The dissolved anions were measured by titration method with Ag NO3 (standard method EPA 9253) and (SM 2310 B).

Table1: Results of pHand EC

EC* (dS m^{-1})	pH*	sand/.	salit/.	clay/.	soil pattern	soil depth (cm)	sample
2.7	7.6	89	7	4	Sandy	0-5	A1
2.8	7.6	89	7	4	Sandy	5-15	
3.4	6.7	-	-	-	-	mulch	A2

22ⁿᵈ Iranian Chemistry Congress (ICC22)
Iranian Research Organization for Science and Technology (IROST)
13-15 May 2024

03231-97589

EC* (dS m^{-1})	pH*	sand٪	salit٪	clay٪	soil pattern	soil depth (cm)	sample
3.4	7.1	68	28	4	Sandy Loam	0-5	
3.6	7.3	68	28	4	Sandy Loam	5-15	
3.4	6.8	-	-	-	-	mulch	
3.4	7.4	91	5	4	Sandy	0-5	B1
3.7	7.6	91	5	4	Sandy	5-15	
1.27	7.4	-	-	-	-	mulch	
1.94	7.5	86	10	4	Sandy	0-5	B2
2.92	7.8	86	10	4	Sandy	5-15	
1.16	7.5	-	-	-	-	mulch	
1.97	7.6	78	17	5	Loamy Sand	0-5	C1
2.27	7.8	78	17	5	Loamy Sand	5-15	
22.5	7.7	51	45	4	Sandy Loam	0-5	Control sample 1
22.9	7.6	51	45	4	Sandy Loam	5-15	
23.7	8.2	74	22	4	Loamy Sand	0-5	Control sample 2
24.5	8.3	74	22	4	Loamy Sand	5-15	

* In the extract 1:5 water to soil

Conclusions

Among the effects of mulches on soil chemical properties, we can mention soil pH, which has different effects on soil pH based on the type of mulch. The range of pH changes in the examined samples under the influence of mulch was 6.7-6.7. The pH of the mulch on the surface of the soil was lower than the soil below. Compared to the control soil samples that show a pH range of 3.8-6.7, it can be concluded that the oil mulch coating has reduced the pH of the soil. This decrease in pH is also seen in the surface samples, which shows a relative decrease in the pH value compared to the subsoil (Table-1). The effect of mulches on soil pH depends on the type of mulch in terms of acidity or alkalinity. In general, soil pH does not change easily, which can be caused by the buffering capacity of soils due to the presence of calcium carbonate.

References

[1] Zumrawi MME, Awad M (2017) Effect of bitumen and fly ash on expansive soil properties. J Sci Engin Res 4(9):228–237

[2] Savari S, Kulkarni SD, Whitfill DL, Jamison DE (2015) Engineering design of lost circulation materials (LCMs) is more than adding a word. SPE/IADC 173018 paper presented at the SPE/IADC drill- ing conference and exhibito, London, UK

[3] Lin, A. M., Timshina, A. S., Magnuson, J. K., Bowden, J. A., & Townsend, T. G. (2023). Emerging polycyclic aromatic hydrocarbon (PAH) and trace metal leachability from reclaimed asphalt pavement (RAP). Chemosphere, 333, 138937.

22nd Iranian Chemistry Congress (ICC22)
Iranian Research Organization for Science and Technology (IROST)
13-15 May 2024

03231-97589

IROST

Effect of adding plasmonic Cu to CdS@SiO₂ to enhancing photocatalytic degradation of RhB from water

Ali Rostami, Alireza Mahjoub[*]

Corresponding Author E-mail: mahjouba@modares.ac.ir

Department of Chemistry, Faculty of Basic Sciences, Tarbiat Modares University, Tehran, Iran

Abstract: Metal nanoparticles (NPs) such as Cadmium (Cd) and Copper (Cu) can strongly absorb visible light, therefore efforts have been made to the application of plasmonic metal NPs as direct photocatalyst in organic reactions. A core-shell SiO2@CdS composite and LSPR Cu^{2+} on its surfaces with effective photocatalytic activity were successfully synthesized. The nanocomposite Characterized by FE-SEM, TEM, XRD and FT-IR. Photocatalytic activity of this nanocomposite was determined by degradation Rhodamine B (RhB) in water.

Keywords: Core-shell; CdS photocatalysts; Pollutant degradation; nanocomposite, LSPR

Introduction
that are capable of using visible-light (λ = 400–700 nm) including metal ion doping, nonmetallic element doping, and sensitization with organic dyes or small band-gap semiconductors such as CdS. CdS with band-gap energy of 2.4 eV has been frequently used to form hybrid or composite photocatalysts. Furthermore, the conduction band (CB) position of CdS semiconductor is negative enough to meet the thermodynamic requirements for many photocatalytic redox reactions. Spherical CdS photocatalysts show great photocatalytic activity toward pollutant degradation. This structures with larger surface area, more exposed active sites for catalysing a series of redox reactions and reduced diffusion length for mass/charge transfer[1,2].

In this paper, we reported the photocalytic activity of SiO2@CdS core-shell. With doping Cu with LSPR [3] properties we studied the photocalytic activity by the presence of Cu on RhB pollutant degradation.

Experimental Section
Synthesis of the SiO2 spheres [4]. SiO₂ spheres were prepared through a modified Stöber method. Typically, 9 mL of NH₃·H₂O, 24 mL of deionized water were added in 16 mL of ethanol mixing at room temperature to form a clear solution A. Next 5 mL of TEOS was added in 45 mL ethanol and mixed as well referred to as solution B. Then, the solution B was added into the solution A drop by drop with vigorous stirring. After stirring for 2 h, silica spheres were collected and washed multiple times with water and ethanol, and then dried under vacuum conditions at 80 °C for 4 h.

Synthesis of CdS@SiO₂ spheres[5]
Firstly, 300 mg of SiO2 was prepared and dispersed in 200 mL DI water. Then 4.0 mL of 1.0 M sodium citrate aqueous solution added into the SiO₂ solution. Next 1.0 mL of 1.0 M cadmium chloride aqueous solution added into the

above solution dropwise. After 1 h stirring, 4 mL of NH₃.H₂O and 4 mL of 1 M thiourea aqueous solution were slowly added sequentially to the mixture and heated in an oil bath for 3 h at 80 °C. After being dried naturally the yellow powder centrifuged and washed with water and ethanol

Synthesis of CdS@SiO₂/Cu
100 mg of the CdS was ultrasonicated and uniformly dispersed in 100 mL DI water. 1 mmol of Cu(ac)₂.H₂O added to 40 mL H₂O and stirring for 30 min. 10 mL of 0.2 mol L⁻¹ NaBH₄ were added to Cu(ac)₂.H₂O. Then, solution was added into the CdS mixture dropwise under vigorous stirring. The resulted mixture was permitted to proceed under continuous stirring for 24 h at room temperature. After the reaction, the powder was centrifuged and washed several times with EtOH and DI water, and dried at 60 °C.

Results and Discussion
The XRD pattern of as-prepared CdS nanospheres is shown in Figure 1. The diffraction peaks at 2θ values of 26.5°, 33.8, 43.9° and 52.0° , correspond to the diffraction of (111), (111), (220), and (311) lattice plane of the β-CdS crystal, respectively. The result indicates that the obtained CdS nanosphere is in a cubic phase.
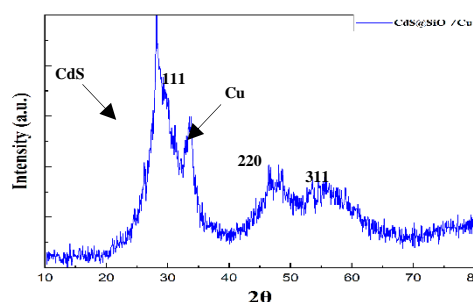
Fig.1: XRD patterns of CdS/Cu nanospheres

22nd **Iranian Chemistry Congress (ICC22)**
Iranian Research Organization for Science and
Technology (IROST)
13-15 May 2024

03231-97589

Typical FE-SEM and TEM images of CdS nanospheres are shown in Figure 2. This figure shows that uniform CdS nanospheres are obtained, and that the diameter of the CdS nanospheres is found to be 153± 15 nm.
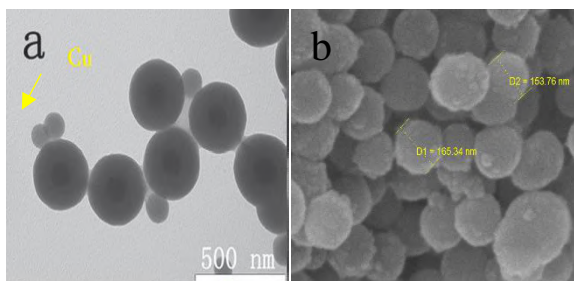
Fig.2: TEM (a) and FE-SEM images of the CdS/Cu nanosphere

FT-IR spectra of CdS@SiO2 spheres and CdS@SiO$_2$/Cu composite nanoparticles are shown in Figure 3. As depicted in Figures 3(b) and (c), the absorption bands at 1101.5 and 1105.1 cm^{-1} are ascribed to the Si–O–Si asymmetric stretching vibration. The absorption bands at 470 and 471.9 are about Cd-S and Cu.
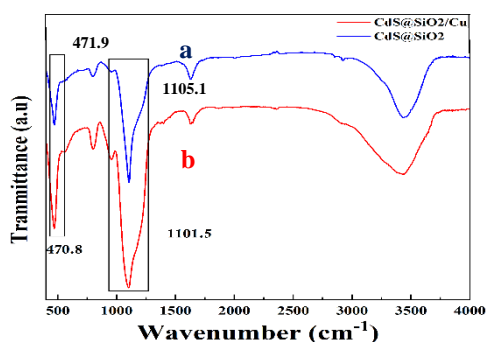
Fig.3: FT-IR spectra of CdS@SiO2 spheres (a), CdS@SiO$_2$/Cu (b)

Photocatalytic Degradation of RhB with CdS@SiO$_2$/Cu
Figure 4 shows the time-dependent UV-Vis absorption spectra of RhB aqueous solutions during photodegradation in the presence of CdS@SiO2/Cu composite. RhB solutions typically display two absorption bands at around 322 and 272 nm. After 90 min shows the 91.1% degradation of RhB by the CdS@SiO$_2$/Cu.
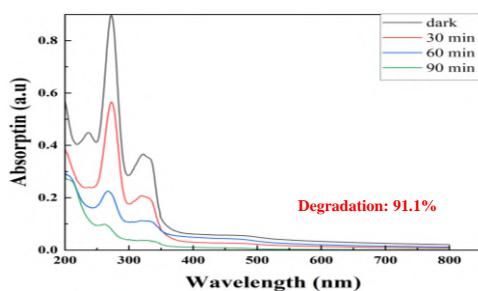
Fig.4: UV-Vis absorption spectra of RhB aqueous

Conclusions

We demonstrate a StÖber method to prepare SiO$_2$ spheres and by hydrothermal method prepare CdS@SiO$_2$ core–shell and CdS@SiO$_2$/Cu composite nanoparticles. The XRD pattern proofs the CdS spheres and the TEM and FE-SEM shows the spheres. The as-prepared CdS@SiO2/Cu composite nanoparticles show a good photocatalytic performance for RhB degradation.

References

[1] Chong, W.-K.; Ng, B.-J.; Tan, L.-L.; Chai, S.-P. Recent Advances in Nanoscale Engineering of Ternary Metal Sulfide-Based Heterostructures for Photocatalytic Water Splitting Applications. Energy Fuels 2022, 36 (8), 4250–4267.

[2] Liu, Y.; Zhang, H.; Ke, J.; Zhang, J.; Tian, W.; Xu, X.; Duan, X.; Sun, H.; O Tade, M.; Wang, S. 0D (MoS2)/2D (g-C3N4) heterojunctions in Z-scheme for enhanced photocatalytic and electrochemical hydrogen evolution. Applied Catalysis B: Environmental 2018, 228, 64–74.

[3] Shin, Y.-B.; Park, C. B.; Shin, J.; Lee, K. J.; Ahn, S.; Lee, M.; Kim, J. U. Aluminum Nanoarrays for Plasmon-Enhanced Light Harvesting. ACS Nano 2015, 9, 6206–6213.

[4] Yun, Y. Shujuan, T. Gang, F. Zhiyan, Y. Yongchao,Li. Chaowen, Y. The compatible performance of three-dimensional SiO2–ZnO amorphous photonic crystals in adjustable structural color and low infrared emissivity

[5] Qian Liang, Lijuan Liu, Zhenyu Wu, Haodong Nie, Hong Shi, Zhongyu Li and Zhenhui Kang. 2021/05/10. Polytriptycene@CdS double shell hollow spheres. Journal of Materials Chemistry A 2.

[6] Zeynab Khazaee, Ali Reza Mahjoub, Amir Hossein Cheshme Khavar. 2021. "One-pot synthesis of CuBi bimetallic alloy nanosheets-supported functionalized multiwalled carbon nanotubes as efficient photocatalyst for oxidation of fluoroquinolones." Applied Catalysis B: Environmental 2.

22nd Iranian Chemistry Congress (ICC22)
Iranian Research Organization for Science andTechnology(IROST)
13-15 May 2024

03231-97589

Phosphoramido Acid Derivatives: QSAR Study of Anti-Urease Activity and DFT Calculation

Lida Asadi

Corresponding Author E-mail: lidaasadi89@gmail.com

Department of chemistry, Omidiyeh Branch, Islamic Azad University, Omidiyeh, Iran.

Abstract: New derivatives of phosphoramido acid were synthesized and in each of these compounds, the P atom was in a tetrahedral environment. (QSAR) was used to understand the relationship between molecular structural features and inhibitory. Results demonstrated the importance of Q_H parameter in describing the anti–urease activities of phosphoramido acids including P(O)-NH$_2$ moiety.
Keywords phosphoramido acid; urease inhibitor; QSAR

Introduction

Quantitative structure–activity relationship (QSAR) equations enabled us to create correlations between the electronic and structural parameters and the inhibition potency [1-3]. The electronic and structural properties data can act as a guide to create and develop the QSAR models. So far, no model in the literature has been suggested to explain the inhibition mechanism of phosphoramido acids derivatives against Urease enzyme. Here, we explain the inhibition mechanism of Urease by theoretical QSAR models.

Experimental Section

Three novel structures of Phosphoramido acid derivatives with the formula $(C_6H_{11}NCH_3)(NHCOCF_3)P(O)(O^-)(CH_3-{}^+NH_2-C_6H_{11})$ **(1)**, $(C_6H_5)_2P(O)(O^-)({}^+NH_3-C_6H_4-NH_2)$ **(2)**, $(C_6H_5O)_2P(O)(O^-)({}^+NH_3-C_6H_4-NH_2)$ **(3)** were synthesized,(fig.1), for this a solution of amine or diamine (1 mmol) and triethylamine (2 mmol) in hydrated THF were added at 50 °C to a solution of $(R)_2P(O)Cl$ (2 mmol) in hydrated THF. After 8 h refluxing, the solvent was removed in vacuum and the resulting white powder was washed with distilled water and recrystallized at room temperature.
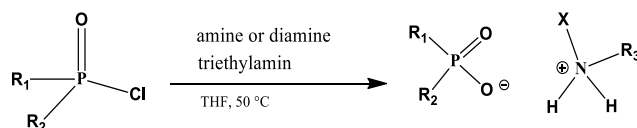
$R_1= C_6H_{11}NMe$,$R_2= F_3CONH$, $R_3=CH_3$, $X= C_6H_{11}$**(1)**
$R_1=R_2= C_6H_5$, $R_3=H$, $X=C_6H_4NH_2$**(2)**
$R_1=R_2= C_6H_5O$, $R_3=H$, $X=C_6H_4NH_2$ **(3)**

Fig.1: three novel structures of phosphoramide derivatives

addition experimental Urease activitis were carried on phosphoramide derivatives (4-10) in Table 2 the results of experimental Urease activitis of phosphoramide derivatives were reported.

The MLR method performed by the software package SPSS 16.0 was used for selection of the descriptors. The electronic and structural descriptors are obtained by the quantum chemical calculations (DFT) were performed at B3LYP/6–311+G** level and experimental studies.

Results and Discussion

The QSAR technique was used to find the effective electronic and structural parameters. The electronic and structural properties data can act as a guide to create and develop the QSAR models. where n is the number of compounds, r is the correlation coefficient, R^2 is the determination coefficient, R_{Adj}^2 is the adjusted determination coefficient, S_{reg} is the standard deviation of regression and $F_{statistic}$ is the Fisher statistic.

$$\log(1/\text{IC}_{50}) = -0.827Q_P - 0.148Q_N + 19.533Q_X - 574.774Q_H + 15.551E_{HOMO} - 30.194E_{LUMO} - 0.686\log P + 0.001Mv + 278.264$$

$$n = 16; R^2 = 0.827; R_{Adj}^2 = 0.630; S_{reg} = 0.822; r = 0.910; F_{statistic} = 4.194$$

According this Eq, the most effective variable in the interaction of Urease and phosphoramido acids derivatives was Q_H with the coefficient value of -574.774. The high interrelationship in Table 1 (r = +0.540) between Q_H and Q_P showed that the properties of derivatives affect in the inhibition of urease. It means that P=O and NH$_2$ groups interaction to Ni metals of urease enzyme (active side) were affected in inhibition of urease enzyme. This result was according to discussion in reference [4]

22nd Iranian Chemistry Congress (ICC22)
Iranian Research Organization for Science
andTechnology(IROST)
13-15 May 2024

03231-97589

Table1: Correlationmatrix for Selected variables in Urease-QSAR in final

Selected variables	Q_P	Q_N	Q_X	Q_H	E_{HOMO}	E_{LUMO}	log p
Q_P	1.000						
Q_N	-.034	1.000					
Q_X	.001	-.198	1.000				
Q_H	-.540	-.095	.526	1.000			
E_{HOMO}	-.347	.430	-.085	-.103	1.000		
E_{LUMO}	-.177	.193	.142	-.268	.646	1.000	
log p	-.383	.258	.579	.332	.534	.507	1.000
Mv	-.336	.407	-.176	-.093	.826	.468	.479

Table 2: experimental Urease activitis of phosphoramide derivatives

No.	R	X	Y	Z	R'	Experimental (IC_{50} μM) Urease
4	4-nitrophenyl	O	O	N	H2	0.063
5	Phenyl	O	O	N	H2	0.003
6	3,5-dimethylphenyl	O	O	N	H2	0.025
7	4-benzyloxyphenyl	O	O	N	H2	0.016
8	4-methyl-2-nitrophenyl	O	O	N	H2	---
9	4-benzyloxyphenyl	O	S	N	H2	16.54
10	3-methoxyphenyl	NH	O	N	H2	5.57
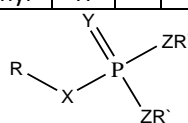
Conclusions

The electron density value at the bcp of the N−H bond confirmed the presence of the stronger hydrogen bonds in P−O···H−N with the linear N−H···O contact angle. The high interrelationship between E^2 and E_{HB} showed that electronic delocalization of $Lp(X=O, S)_i \rightarrow \sigma^*(N–H)_j$ controlled the effect of hydrogen bond energy in solid state models. Quantitative structure–activity relationship (QSAR) was used to understand the relationship between molecular structural features and inhibitory. DFT–QSAR models for enzymes demonstrated the importance of Q_H parameter in describing the anti–urease activities of phosphoramido acids including P(O)-NH2 moiety.

References

[1] W. Sippl, J. Comput.-Aided Mol. Des. **16**, 825 (2002).

[2] A. Amadasi, A. Mozzarelli, C. Meda, A. Maggi, P. Cozzini, Chem. Res. Toxicol. **22**, 52 (2009).

[3] . N.C. Wang, R. Venkatapathy, R.M. Bruce, C. Moudgal, Regul. Toxicol. Pharmacol. **59**, 215 (2011).

[4] M. Font, M. J. Dominguez, C. Sanmartin, J. Palop, S. San Francisco, O. Urrutia, F. Houdusse, J.M. Garcı´a-Mina, J. Agric. Food Chem. **56**, 8451 (2008).

Potential Application of Al and Si Doped Carbon Nanotubes for Metronidazole Detection:

A Theoretical Study

Lida Asadi*, Zohreh Saadati, Mahboobeh Salehpour

Corresponding Author E-mail: lidaasadi89@gmail.com

Department of Chemistry, Omidiyeh Branch, Islamic Azad University, Omidiyeh, Iran.

Abstract: The interaction of metronidazole (MNZ) drug with pristine, Al and Si doped single-walled carbon nanotubes (SWCNTs) was explored utilizing density functional theory (DFT)method. The calculations revealed that MNZ prefers to be adsorbed on the pristine CNT via its 5-membered ring with an $E_{adsorption}$ value of -17.88 kcal.mol^{-1}. The HOMO-LUMO energy gap (E_g) of pristine CNT increases by about 60.9% upon adsorption of MNZ

Keywords Carbon nanotubes; DFT; Metronidazole

Introduction

Metronidazole (MNZ) is a nitroimidazole antibiotic used broadly to treat giardiasis, trichomoniasis, anaerobic, and parasitic infections[1]. Long term using MNZ causes adverse effects including peripheral neuropathy, central nervous system toxicity, seizures, nausea, epigastric discomfort, and vertigo, in addition to neutropenia[2, 3]. Moreover, MNZ shows a low biodegradability and high solubility in water andthe precise detection and removal of MNZ is technically challenging[4]. Therefore, the development of a simple, rapid, and yet sensitive method for determining the MNZ in human and wildlife is necessary.

Experimental Section

All calculations in our study were performed based on density functional theory (DFT) method usingM06-2X functional in conjunction with 6-31G(d,p) valence double-zeta polarized basis set. Vibrational frequencies were computed at the same level to be confirmed that the optimized structures are the global minima on the potential energy surface and to get the zero-point energy (ZPE) corrections for thermochemical parameters.

Results and Discussion

The optimized structure of zigzag (8,0) SWCN and its molecular electrostatic potential (MEP) surfacesare represented in Fig. 1. This model is comprising of 96 C atoms and 16 H atoms are added to dangling bonds.The diameter and length of the nanotube were about 6.2 Å and 14 Å, respectively, and the average C—C bond length was 1.42 Å, which is in the range of C—C bond lengths of graphene (~1.42 Å) [44]and CNTs (~1.42-1.46 Å). The calculated vibrational frequencies are in the range of 86-3197 cm^{-1}indicating that the optimized

structure is located on a true local minimum on the potential energy surface. The HOMO and LUMO energy levels are predicted to be -4.09 and -3.45 eV, respectively, producing an E_g of 0.64 eV.
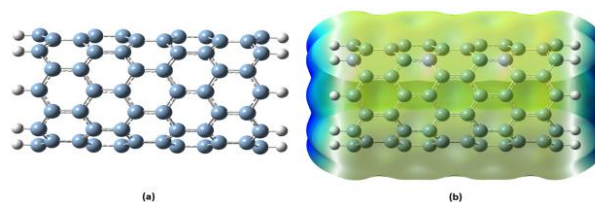
Fig.1: (a) Optimized geometry and (b) computed electrostatic potentials on the molecular surface of pristine CNT.

The mean value of Al…O and Si…O interaction distances are about 1.97and 1.76 Å, respectively. Based on NBO analysis, a charge transfer of 0.62 and 1.27|e|occurs from CNT to MNZmolecule in Al- and SiCNT-MNZ complexes, respectively. The substantialamount of transferred charge from CNT to MNZ along with the reduction in the amine group vibrational frequency going from isolated MNZ to AlCNT- and SiCNT-MNZ suggest that a π backdonation takes place from the doped CNTs to NO$_2$ group of MNZ. The π backdonation leads to the weakening of the N—O bond via transferring the electron density into the empty antibonding π orbital.The weakening of the N—O bond is confirmed by geometrical parameters in which N—O bond length increases from 1.22 Å in isolated MNZ to 1.32 and 1.43 Å in AlCNT- and SiCNT-MNZ complexes, respectively.

The BSSE corrected adsorption energies (kcal mol^{-1}), HOMO and LUMO energies (E_{HOMO} and E_{LUMO}) and band gap (E_g) in eV, are presented in Table1.

22nd Iranian Chemistry Congress (ICC22)
Iranian Research Organization for Science and
Technology (IROST)
13-15 May 2024

03231-97589

IROST

Table1: The BSSE corrected adsorption energies

System	$E_{adsorption}$	$E_{HOMO}*$	E_{LUMO}	E_{LUMO}	E_g
AlCNT	---	-5.10	-2.79	-2.79	2.31
AlCNT-MNZ	-43.94	-5.01	-2.70	-2.70	2.32
SiCNT	---	-4.25	-3.23	-3.23	1.02
SiCNT-MNZ	-49.25	-4.70	-3.30	-3.30	1.40

Conclusions

In this study, we have explored the pristine, Al and Si doped single-walled carbon nanotubes (SWCNTs) as metronidazole (MNZ) sensorsusing density functional theory (DFT) method. Adsorption of MNZ on the pristine CNT is originated from π-π stacking interactions with an $E_{adsorption}$ value of -17.88 kcal.mol^{-1}. The HOMO level of CNT stabilizes by about 0.19 eV after adsorption of MNZ, but the LUMO level destabilizes by about 0.2 eV and therefore, $E_g$increases significantly (60.9%). In the case of doped CNTs, MNZ molecule prefers to be adsorbed via its NO$_2$ group with a binding energy of about -43.94 and -49.25 kcal mol^{-1}, respectively. The electronic properties of SiCNT are more sensitive to MNZ adsorption than those of AlCNT but not pristine CNT.

References

[1] Y. Orooji, M.H. Irani-nezhad, R. Hassandoost, A. Khataee, S.R. Pouran, S.W. Joo, Cerium doped magnetite nanoparticles for highly sensitive detection of metronidazole via chemiluminescence assay, Spectrochimica Acta Part A: Molecular and Biomolecular Spectroscopy, (2020) 118272.

[2] T. Ma, C. Jin, S.A. Aslanzadeh, Quantum chemical study on the sensing properties of Pt-decorated BC3 nanotube toward metronidazole drug, International Journal of Quantum Chemistry, (2020) e26407.

[3] Y. Sun, P.J. Overby, H. Mehta, Case 271: Metronidazole-induced Encephalopathy, Radiology, 293 (2019) 473-479.

[4] Y. Gu, X. Yan, C. Li, B. Zheng, Y. Li, W. Liu, Z. Zhang, M. Yang, Biomimetic sensor based on molecularly imprinted polymer with nitroreductase-like activity for metronidazole detection, Biosensors and Bioelectronics, 77 (2016) 393-399.

22nd Iranian Chemistry Congress (ICC22)
Iranian Research Organization for Science and Technology (IROST)
13-15 May 2024

03231-97589

IROST

Synthesis and Characterization of a New Thiophosphorylated-Thiourea, (C₂H₅O)₂P(S)(NHC(S)NH(C₄H₃N₂)), and Study of the Crystal Structure

Saeed Hosseinpoor[a], Mehrdad Pourayoubi*[a], Michal Dušek[b]

Corresponding Author E-mail: pourayoubi@um.ac.ir

[a] Department of Chemistry, Faculty of Science, Ferdowsi University of Mashhad, Mashhad, Iran.

[b] Institute of Physics of the Czech Academy of Sciences, Na Slovance 2, 182 21 Prague 8, Czech Republic.

Abstract: A new thiophosphorylated-thiourea with the formula $(C_2H_5O)_2P(S)(NHC(S)NH(C_4H_3N_2))$ was synthesized, and characterized by the IR, MS, and (^{31}P, ^{13}C, ^{1}H) NMR spectroscopies. Intermolecular interactions in the crystal structure are studied by the analysis of the d_{norm}-mapped Hirshfeld surface.

Keywords: Thiophosphoramide; Thiourea; Crystal structure; Hirshfeld surface analysis

Introduction

Thiophosphoramide compounds have been utilized for a wide range of applications, from fire retardants to pesticides [1,2]. Moreover, a category of thiophosphoramides with the general formula $(R^1O)_2P(S)(NHC(S)NR^2)$ (R^1 = any organic group, NR^2 = any amine fragment), named thiophosphorylated-thiourea (TPT), have shown antimicrobial and anticancer activity [3,4]. The presence of several functional groups in these molecules allows the formation of coordination compounds and crystal structures in various ways.

In the molecular structure of the noted type of TPT, there are at least four electron donor groups, including P═S, C═S, and two oxygen atoms. Additionally, there are two nitrogen atoms: the P-bonded NH group that acts as an electron acceptor; and the NR^2 group inherited from the amine reactant used in the synthesis procedure, which can act as either an electron donor or acceptor dependent on the type of the used amine substance [5]. Therefore, with the different designs in the synthesis and the crystallization process, different properties and structural features can be expected.

Herein, a new TPT compound with the formula $(C_2H_5O)_2P(S)(NHC(S)NH(C_4H_3N_2))$, is synthesized and characterized with the IR, MS, and (^{31}P, ^{13}C, ^{1}H) NMR spectroscopies. Intermolecular interactions participating in the crystal structure are studied using the analysis of the Hirshfeld surface.

Experimental Section

A solution of O,O-diethyl chlorothiophosphate in anhydrous acetonitrile was treated under vigorous stirring with potassium thiocyanate (1:1 mole ratio) for 18 hours. The potassium chloride salt was filtered off, and the filtrate was reacted with 2-aminopyrimidine (1:1 mole ratio). After 4 hours, the solution was filtered and left for slow evaporation. After a few days, formed crystals suitable for X-ray analysis, were separated, washed with acetonitrile, and dried.

M.p.: 122 °C. IR (KBr disc, v, cm^{-1}): 3748, 3560, 3502, 3203, 2985, 2068, 1675, 1593, 1523, 1416, 1342, 1206, 1168, 1058, 953, 794, 740. MS (70 eV, EI): m/z (%) = 306 (5) [M]$^+$, 226 (27) [(M − C₄H₃N₂) − 1]$^+$, 168 (53) [O₂P(S)(NHC(S)N)]$^+$, 94 (92) [NH(C₄H₃N₂)]$^+$. ^{31}P{^{1}H} NMR (121 MHz, DMSO-d_6): δ (ppm) = 60.74 (s). ^{1}H NMR (DMSO-d_6, 301 MHz): δ (ppm) = 12.80 (d, $^2J_{H-P}$ = 12.4 Hz), 12.48 (d, $^2J_{H-P}$ = 11.2 Hz), 11.68 (s), 8.75 (d, $^3J_{H-H}$ = 5.1 Hz), 8.74 (d, $^3J_{H-H}$ = 4.8 Hz), 8.57 (d, $^3J_{H-H}$ = 5.4 Hz), 8.57 (d, $^3J_{H-H}$ = 5.1 Hz), 7.28 (m), 6.94 (t, $^3J_{H-H}$ = 5.3 Hz), 4.19 (m), 3.98 (dq, $^3J_{H-P}$ = 9.7 Hz, $^3J_{H-H}$ = 7.1 Hz), 1.31 (t, $^3J_{H-H}$ = 7.0 Hz), 1.23 (t, $^3J_{H-H}$ = 7.1 Hz). ^{13}C{^{1}H} NMR (DMSO-d_6, 75 MHz): δ (ppm) = 181.40 (d, $^2J_{C-P}$ = 8.8 Hz), 180.14 (d, $^2J_{C-P}$ = 8.7 Hz), 158.75 (s), 157.92 (s), 157.60 (s), 117.10 (s), 117.03 (s), 110.35 (s), 64.66 (d, $^2J_{C-P}$ = 5.5 Hz), 64.16 (d, $^2J_{C-P}$ = 5.8 Hz), 63.09 (d, $^2J_{C-P}$ = 5.4 Hz), 16.49 (d, $^2J_{C-P}$ = 6.6 Hz), 16.30 (d, $^2J_{C-P}$ = 7.2 Hz), 16.20 (d, $^2J_{C-P}$ = 7.3 Hz).

Results and Discussion

The synthesized product was characterized by IR, MS, ^{31}P{^{1}H} NMR, ^{1}H NMR, and ^{13}C{^{1}H} NMR spectroscopies.

In the IR spectrum, the bands at 3203/3502 cm^{-1} and 1058 cm^{-1} are assigned to the NH units and the esteric P–O–C stretch. The mass spectrum shows the molecular ion peak (m/z = 306 amu).

The ^{31}P{^{1}H} NMR spectrum shows a singlet peak at 60.74 ppm, which is evidence for the formation of the compound. The complete assignment of the ^{1}H NMR and ^{13}C{^{1}H} NMR spectra are illustrated graphically in Fig. 1. In these spectra, the appearance of a couple of peaks for chemically equivalent H and C atoms represents the existence of different stable conformers in the solution phase. Especially, every equivalent H atom, except the H atom of the P-bonded NH unit, shows a pair of similar signals with the integral ratio 2:1.

22nd Iranian Chemistry Congress (ICC22)
Iranian Research Organization for Science and Technology (IROST)
13-15 May 2024

03231-97589

Fig. 2 (*a*) The asymmetric unit of the structure. Displacement ellipsoids are drawn at the 50% probability level. (*b*) The Hirshfeld surface of a molecule in crystal structure, showing four bold red spots corresponding to the four hydrogen bonds represented.

presence of different stable conformers in the solution phase.

The most prominent interaction in the crystal structure is the NH···N hydrogen bonds, which construct dimer assembly. The dimer assemblies are linked together through some weak interactions, *e.g.*, CH···HC, S···HC, and O···C contacts.

References

[1] Nollet, L. M. L., & Rathore, H. S. (Eds.). (2010). *Handbook of pesticides: Methods of pesticide residues analysis*. CRC Press.

[2] Wilkie, C. A., & Morgan, A. B. (2009). *Fire retardancy of polymeric materials, Second edition*. CRC Press.

[3] Kataeva, O. N., Metlushka, K. E., Yamaleeva, Z. R., Ivshin, K. A., Kiiamov, A. G., Lodochnikova, O. A., Nikitina, K. A., Sadkova, D. N., Punegova, L. N., Voloshina, A. D., Lyubina, A. P., Sapunova, A. S., Sinyashin, O. G., & Alfonsov, V. A. (2019). Co-ligand induced chiral recognition of N-thiophosphorylated thioureas in crystalline Ni(II) complexes. *Cryst. Growth Des.*, *19*(7), 4044–4056. https://doi.org/10.1021/acs.cgd.9b00446

[4] Metlushka, K. E., Sadkova, D. N., Shaimardanova, L. N., Nikitina, K. A., Ivshin, K. A., Islamov, D. R., Kataeva, O. N., Alfonsov, A. V., Kataev, V. E., Voloshina, A. D., Punegova, L. N., & Alfonsov, V. A. (2016). First coordination polymers on the bases of chiral thiophosphorylated thioureas. *Inorg. Chem. Comm.*, *66*, 11–14. https://doi.org/10.1016/j.inoche.2016.01.021

[5] Pourayoubi, M., Toghraee, M., Zhu, J., Dušek, M., Bereciartua, P. J., & Eigner, V. (2014). Database analysis of hydrogen bond patterns in phosphoric triamides completed with seven new compounds: A crystallographic and 15N NMR study. *CrystEngComm*, *16*(47), 10870–10887. https://doi.org/10.1039/C4CE01793E

Fig. 1 Signals in the 1H NMR (top) and 31C{1H} NMR (bottom) spectra of the compound. The colors of the peaks match the colors of the respective atoms in the scheme represented.

The compound crystallizes at the triclinic space group P$\bar{1}$, and the asymmetric unit contains two complete molecules (Fig. 2*a*).

In the crystal structure, an intramolecular NH···N hydrogen bond is formed between one of the N atoms of the pyrimidinyl ring and the P-bonded NH group.

To analyze intermolecular interactions in the crystal structure, the d_{norm}-mapped Hirshfeld surface created with CrystalExplorer software is studied. On the Hirshfeld surface, the four most prominent red spots are related to the hydrogen-bonded dimer constructed through two equivalent NH···N interactions, between the other pyrimidinyl N atom and NH unit that are not involved in the intramolecular interaction, and two equivalent CH···S=C interactions (Fig. 2*b*). This dimer assembly propagates through some weak interactions, such as CH···HC, S···HC, and O···C contacts that appear as pale red spots on the Hirshfeld surface.

Conclusions

The title compound was synthesized and characterized by different spectroscopic methods. In the 1H NMR and 13C{1H} NMR spectra, the emergence of a couple of signals for chemically equivalent C and H atoms suggests the

Enhancement of the Internal Electric Field in BiFeO₃/ZnS Z-Scheme Heterostructure for RhB Degradation

Zahra Mohammadi, Shahrbanoo Rahman Setayesh*

Corresponding Author E-mail: setayesh@sharif.edu

Department of Chemistry, Sharif University of Technology, Tehran 11155-9516, Iran.

Abstract: We designed a novel lead-free BiFeO₃-ZnS (BFO/ZnS) heterostructure for piezocatalytic reactions. BFO/ZnS (90/10) represented superior performance in RhB oxidation, degrading 94.2% of RhB in 15 min vibration. The open circuit voltage analysis revealed that BFO/ZnS (90/10) possesses a higher internal electric field, supporting its exceptional piezocatalytic activity.

Keywords: Built-in electric field; Z-scheme heterostructure; Piezocatalysis

Introduction

Piezocatalysis, an emerging technology, utilizes the piezoelectric effect in noncentrosymmetric crystals for water purification. External mechanical stress, such as ultrasonic vibration or stirring, causes a shift in charge centers within the crystal unit cell, generating polarization charges and an internal electric field. This built-in electric field is crucial in boosting the separation of electron-hole pairs and generating reactive oxygen species through reactions with water molecules or dissolved oxygen [1].

BiFeO₃ (BFO) is a lead-free piezoelectric ceramic with a perovskite structure and R3c space group, exhibiting ferroelectric ($T_C \approx 1103$ K) and G-type antiferromagnetic ($T_N \approx 643$ K) ordering. High piezoelectric coefficient (d_{33} ~100 pm. V^{-1}) and spontaneous polarization (~100 $\mu C. cm^{-2}$) at room temperature of single phase BFO arise from its rhombohedral perovskite structure [2]. By utilizing a proper cocatalyst to construct a heterojunction structure it is possible to extend the higher internal electric field and lifespan of charge carriers, thereby enhancing the piezoelectric features of BFO. ZnS is the tetrahedral semiconductor of II-Ⅵ and III-Ⅴ types that exist in the cubic zinc blend and the hexagonal wurtzite forms. The wurtzite structure, being non-centrosymmetric, creates an internal electric field under external mechanical stress, leading to excellent piezoelectric characteristics [3].

In the present study, BFO as a lead-free piezoelectric ceramic was chosen to treat water pollutants. Due to the easy deformation of 1D materials under mechanical stress, a heterojunction structure between BFO and ZnS nanorods was synthesized to enhance piezocatalytic activity towards the RhB degradation.

Experimental Section

BFO/ZnS heterostructures were synthesized by adjusting the pH of a solution containing different weight ratios of hydrothermally synthesized BFO and ZnS to 4 using NaOH and HNO₃ (0.1 M) based on the determined isoelectric point. Boiling the mixture for 30 min facilitated electrostatic attraction, causing ZnS to attract BFO. The resulting mixture was then centrifuged, dried at 80 °C for 12 h, annealed at 280 °C for 3 h, and characterized by XRD, PL, and open circuit voltage techniques.

To test the piezocatalytic activity, each piezocatalyst (1 g L^{-1}) was added to a 50 mL solution of 10 mg L^{-1} RhB in water and then sonicated (180 W, 53 kHz). At specific intervals, 2 mL of the treated solution was removed, and the catalyst particles were filtered out. The remaining RhB concentration was measured by analyzing the absorbance at 562 nm.

Results and Discussion

As shown in XRD patterns (Fig. 1a), BFO nanoparticles had 8 distinct peaks which align well with JCPDS card No. 86-1518, confirming the successful synthesis of the rhombohedral phase of perovskite BFO with the R3c space group [4]. The characteristic diffraction peaks of ZnS match JCPDS card No. 36-1450 and the strongest intensity of the (002) peak, indicating that wurtzite ZnS is a 1D crystal [5]. Additionally, the XRD pattern of BFO/ZnS (90/10) displays a peak at 29.13°, corresponding to the (002) crystal plane of ZnS, confirming the successful formation of the BFO/ZnS heterostructure.
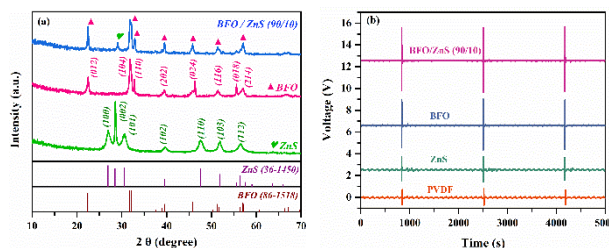
Fig.1: (a) XRD patterns, (b) Output voltage of BFO, ZnS, BFO/ZnS (90/10) nanocomposites.

The piezoelectric effect directly influences the open circuit voltage of PVDF composite films. When a 50 N compressive cyclic force at 3 Hz is applied, the BFO/ZnS (90/10) composite film generates a higher voltage of 3.0 V compared to BFO (2.3 V) and ZnS (1.12 V) composite films, due to its superior piezoelectric effect (Fig. 1b).

22nd Iranian Chemistry Congress (ICC22)
Iranian Research Organization for Science and Technology (IROST)
13-15 May 2024

03231-97589

IROST

The synthesized nanocomposites were evaluated for piezocatalytic activity using RhB degradation under ultrasonic irradiation. Fig. 2a revealed that the heterojunction structure in BFO/ZnS nanocomposites enhances piezocatalytic activity compared to pure BFO and ZnS, demonstrating a synergy effect. The addition of 5% and 10% weight of ZnS improved piezodegradation performance to 84.6% and 94.2%, respectively, but higher ZnS ratios inhibited the piezocatalytic reaction.

The linear relationship (Fig. 2b) between $\ln(C_t/C_0)$ and ultrasonic time suggests that the piezocatalytic degradation reaction of RhB follows the pseudo-first-order reaction kinetics. The apparent rate constant (k_{app}) value can be calculated from the slope of $\ln(C_0/C_t)$ against time. The results illustrated that the piezodegradation rate of RhB over BFO/ZnS (90/10) composite was ~2.5 and ~11.2 times higher than pristine BFO and ZnS, respectively.

Figure 3a depicts the possible charge transfer pathway in the BFO/ZnS (90/10) piezocatalyst based on the energy diagram. The synergistic effects can be explained as follows: Firstly, the direct Z-scheme mechanism likely enhances piezocatalytic activity. This mechanism allows for the migration of thermally excited electrons from the conduction band (CB) of BFO to the valence band (VB) of ZnS, where they recombine with holes. Additionally, residual electrons on the CB of ZnS react with dissolved O_2 to generate $O_2^{\bullet-}$, while holes in the VB of BFO oxidizes H_2O/HO^- to $^{\bullet}OH$ in the solution, effectively hindering carrier recombination. Secondly, the stronger piezoelectric response of the BFO/ZnS creates a higher built-in electric field, accelerating the separation of carriers and suppressing recombination as supported by PL spectra (Fig. 3b), thereby enhancing the piezocatalytic activity of BFO/ZnS (90/10) piezocomposites.
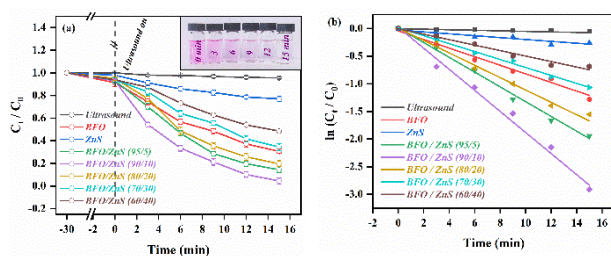
Fig.2: (a) RhB piezodegradation over as-prepared samples, (b) kinetic investigation of RhB piezodegradation process over different piezocatalysts.
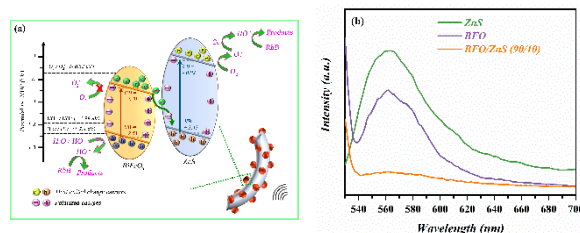
Fig.3: (a) Schematic illustration of the possible charge transfer pathway in the BFO/ZnS (90/10) piezocatalyst under ultrasonic vibration, (b) PL spectra of BFO, ZnS, BFO/ZnS (90/10) nanocomposites.

Conclusions

In summary, the novel BFO/ZnO piezocatalysts were fabricated by utilizing the isoelectric point-assistant annealing method. Open circuit voltage measurements confirmed the stronger internal electric field in BFO/ZnS with 10% ZnS loading, enhancing piezoactivity for RhB degradation. The RhB piezodegradation over the BFO/ZnS (90/10) showed outstanding results: 94.2% degradation on 15 min ultrasonic stimulation and 1 g L^{-1} catalyst dosage.

References

[1] Liang, X., Shi, X., Zou, X., Wang, Z., & Cheng, Z. (2022). Synergetic degradation of organic dyes and Cr (vi) by the piezocatalytic BZT-x BCT. New Journal of Chemistry, 46(19), 9184-9194.

[2] Xu, J., Qin, T., Chen, W., Lv, J., Zeng, X., Sun, J., ... & Zhou, J. (2021). Synergizing piezoelectric and plasmonic modulation of Ag/BiFeO₃ fibrous heterostructure toward boosted photoelectrochemical energy conversion. Nano Energy, 89, 106317.

[3] Feng, W., Yuan, J., Zhang, L., Hu, W., Wu, Z., Wang, X., ... & Zhang, S. (2020). Atomically thin ZnS nanosheets: Facile synthesis and superior piezocatalytic H₂ production from pure H₂O. Applied Catalysis B: Environmental, 277, 119250.

[4] Wang, Y., Chen, J., Wu, J., Armutlulu, A., & Xie, R. (2023). Constructing durable BiFeO₃@ SrBi₂B₂O₇ pn heterojunction for persulfate enhanced piezo-photocatalytic water purification. Separation and Purification Technology, 324, 124479.

[5] Gawai, U. P., Deshpande, U. P., & Dole, B. N. (2017). A study on the synthesis, longitudinal optical phonon–plasmon coupling and electronic structure of Al doped ZnS nanorods. RSC advances, 7(20), 12382-12390.

Preparation of a Conductive, Self-Healing and Flexible Composite Hydrogel as A Pressure Sensor for Human Motion Sensing

Nahid Salimiyan, Alireza shaabani, Roya Sedghi*

Corresponding Author E-mail: r_sedghi@sbu.ac.ir

Department of Polymer and Materials Chemistry, Faculty of Chemistry and Petroleum Sciences, Shahid Beheshti University, G.C, 1983969411, Tehran, Iran.

Abstract: Smart hydrogels are of great importance in pressure sensing wearable devices. The presented hydrogel exhibited desirable conductivity (1.12±0.05 S/m), sensitivity, and self-healing properties. These outstanding properties are demonstrated by electrical and electromechanical evaluations. The obtained results revealed these hydrogels could be a potential candidate in biomedical and electronic monitoring devices.

Keywords: Nanocomposite hydrogel, self-healing, motion sensing.

Introduction

Self-healing and smart hydrogels with decent strain-sensitivity, electrical conductivity and desired mechanical properties for pressure sensing applications and wearable smart devices have attracted a huge surge of attentions in recent decade owing to their potential capabilities for pressure sensors, health monitoring devices and biomedical applications [1]. These smart hydrogels can transform the various strains and pressures (as external stimuli) to corresponding electrical signals. Hence, the desired electrical conductivity and shape recovery as well as pressure-sensitivity are of great urgency for these smart and stimuli-responsive materials [2]. Carbon nanotubes (CNTs) are used in conductive materials and conductive nanocomposite hydrogels to a large degree, owing to considerable electrical conductivity and mechanical strength. Chitosan (CS) is a natural polycationic linear polysaccharide with decent biocompatibility, biodegradability, and non-toxicity. However, the poor solubility of pure chitosan in neutral aqueous media is a considerable limitation for practical applications of this biopolymer. Therefore, chemical functionalization of chitosan with hydrophilic functional groups to generate a water-soluble derivative of CS could be an appropriate strategy for chitosan-based hydrogel preparation. Herein, a zwitterionic derivative of chitosan with decent water solubility was prepared to form the hydrogel network in aqueous media. After bringing the CNTs into the prepared polymeric network, a decent electrical conductivity and strain-sensitivity were detected via electrical measurements. Moreover, the presence of zwitterionic moieties in the hydrogel network, endowed it with the efficient and fast self-healing property [3]. These self-healing, cost-effective and stimuli-responsive hydrogels could find widespread potential in biomedical devices, electronic skin and health-monitoring stations.

Experimental Section

Chitosan powder (Mw=200000 gr/mol) with the degree of deacetylation of 91% was added to a 2% w/v solution of acetic acid in water at 70 °C. The mixture was stirred on a magnetic hot plate for 12 h to dissolve chitosan completely. The resulted solution (2% w/v of CS in acetic acid solution) was cooled to room temperature and the zwitterionic agent ((2-(N-3-Sulfopropyl-N, N-dimethyl ammonium) ethyl methacrylate)) was added to the CS solution (1 gr). The reaction was carried out for 24 h at 50 °C. Afterwards, the obtained pale yellowish solution was dialysed against deionized water using a dialysis tube with the molecular weight cut-off of 12-14 KDa for 2 Days in a dark place. The solution was freeze-dried for 24 h to obtain a white cotton-like solid. This water-soluble derivative of chitosan (ZCS) was dissolved in deionized water to obtain a 3% w/v solution. Then, various amounts of carboxylated multi-walled carbon nanotube (MWCNT-COOH) were added to the solution to form nanocomposite hydrogels and then were dispersed completely using an ultrasonic bath. The hydrogel samples were labelled as Gel(x) where x is the amount of MWCNTs in the hydrogel samples (mg/mL) [3].

Results and Discussion

The conductive hydrogels were prepared as demonstrated in Fig.1. The electrostatic interactions between zwitterionic moieties on CS chains in the hydrogel network as well as inter/intramolecular hydrogen bonds between carboxylic acid groups on MWCNT-COOH and zwitterionic groups and hydroxyl groups on the CS chains, endowed the hydrogels with a fast and physical cross-linking. Moreover, the aforementioned interactions could lead to form a fast and efficient self-healing network.

22nd Iranian Chemistry Congress (ICC22)
Iranian Research Organization for Science and
Technology (IROST)

13-15 May 2024

03231-97589

IROST
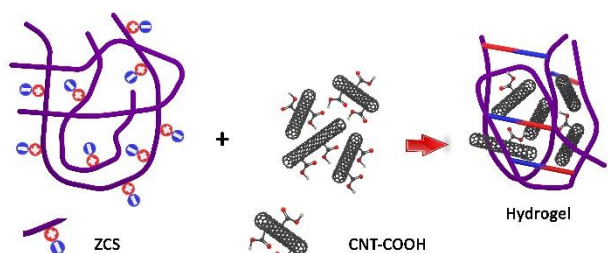
Fig.1: Schematic representation of preparation of composite hydrogels.

To evaluate the morphological properties of the samples, FESEM analysis was performed. As shown in Fig.2, the average pore size of the Gel3 sample (as an example) was $12 \pm 4\ \mu m$. Moreover, the pores was interconnected.
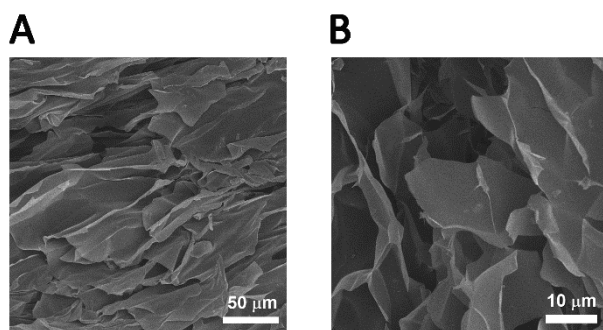
Fig.2: FESEM images of Gel3 sample with the different scale bars of 50 μm (A) and 10 μm (B).

The electrical properties and the strain sensitivity of the samples were also evaluated using a digital sourcemeter coupled with a compression machine. As shown in Fig.3, the resistance changes was evaluated in real time for Gel3 (as an optimal sample) under the various pressures. The resistance changes increased with the increase of the pressure (KPa), revealing decent strain-sensitivity property in the hydrogel network. In addition, the surface electrical conductivity was evaluated quantavely for the hydrogel samples. The measured surface conductivity was increased and then decreased with the increase of conductive filler (MWCNT-COOH) content. It could be owing to the aggregation of the MWCNT clusters in the hydrogel network in Gel4 sample, leading to a decreased conductive pathway in the polymeric network and subsequently decreased electrical conductivity [4]. The maximum obtained electrical conductivity was related to the Gel3 sample (1.12 ± 0.05 S/m). Additionally, the samples were cut into 2 pieces to evaluate the self-healing property. After setting of the samples together, the electrical conductivity of the self-healed samples were evaluated after 1 h. The electrical conductivity was decreased for all of the self-healed samples, which could be due to the decrease of the electrostatic and hydrogen bonds between MWCNT-COOH and ZCS chains [5].
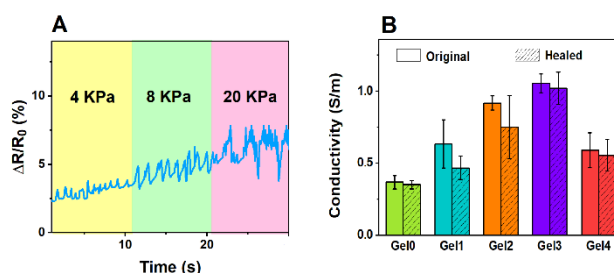
Fig.3: (A) The resistance changes of the Gel3 under various pressures. (B) The electrical conductivity of the hydrogels before and after self-healing process.

Conclusions

In this work, stimuli-responsive and self-healing composite hydrogels with desired conductivity and pressure sensitivity properties were presented. The self-healing mechanism endow the hydrogels with the fast regeneration of the conductivity without external healing agent at the room temperature. The electrical conductivity of the samples reached 1.12 ± 0.05 S/m. Moreover, owing to the cost-effective and facile preparation process, we believe that these smart hydrogels have a considerable potential application in health monitoring and motion detection systems.

References

[1] Liu, C., Xu, Z., Chandrasekaran, S., Liu, Y., & Wu, M. (2023). Self-healing, antibacterial, and conductive double network hydrogel for strain sensors. *Carbohydrate Polymers*, *303*, 120468.

[2] Zhang, W., Zhang, X., Zhao, W., & Wang, X. (2023). High-sensitivity composite dual-network hydrogel strain sensor and its application in intelligent recognition and motion monitoring. *ACS Applied Polymer Materials*, *5*(4), 2628-2638.

[3] Snyder, D., & Emrick, T. (2024). Embedding Thiols into Choline Phosphate Polymer Zwitterions. *Macromolecular Rapid Communications*, 2300690.

[4] Long, Y., Zhang, Z., Sun, K., Wang, C., Zeng, N., Gao, B., ... & Fan, R. (2023). Enhanced electromagnetic wave absorption performance of hematite@ carbon nanotubes/polyacrylamide hydrogel composites with good flexibility and biocompatibility. *Advanced Composites and Hybrid Materials*, *6*(5), 173.

[5] Shen, K., Liu, Z., Xie, R., Zhang, Y., Yang, Y., Zhao, X., ... & Cheng, Y. (2023). Nanocomposite conductive hydrogels with Robust elasticity and multifunctional responsiveness for flexible sensing and wound monitoring. *Materials Horizons*, *10*(6), 2096-2108.

Soft and Flexible Conductive Plant-Based Composite Film with Strain Sensitivity for Motion Detection

Nahid Salimiyan, Roya Sedghi*

Corresponding Author E-mail: r_sedghi@sbu.ac.ir

Department of Polymer and Materials Chemistry, Faculty of Chemistry and Petroleum Sciences, Shahid Beheshti University, G.C, 1983969411, Tehran, Iran.

Abstract: Flexible and stretchable films are of great urgency in various fields such as biomedical devices and sensors. Herein, a soft and conductive composite film was prepared through a cost-effective and facile strategy with high strain sensitivity for motion detection. The electrical conductivity of this film reached 0.9 ± 0.3 S/m.

Keywords: Conductive, Composite, Human Motion Detection.

Introduction

Flexible and stimuli-responsive composite films have attracted a huge surge of attention in recent decade owing to their widespread practical applications in biomedical systems, sensors, and electronic devices. However, preparation a mechanically robust, soft, flexible, conductive, plant-based, biodegradable, and biocompatible film with desirable stretchability and shape recovery property remains a great challenge [1]. To accomplish these functions, the conductive and flexible films require not only excellent strain sensitivity to detect the various strains with a high accuracy, but also superior mechanical properties such as ductility and strength to transfer various strains to the electronic detector. Carboxymethylcellulose (CMC) is a cost-effective, water soluble, and non-toxic derivative of cellulose which is a water-insoluble and eco-friendly biopolymer. Moreover, multi-walled carbon nanotube (MWCNT) is a conductive carbon material with excellent thermal, mechanical, and electrical properties. However, the hydrophobic nature of the MWCNTs could lead to a limited application of these nanotubes in water-based systems [2].

Herein, we prepared a soft, stretchable, mechanically robust, conductive and strain-sensitive composite film after bringing the amine-functionalized hydrophilic MWCNT (AMWCNT) into the CMC gel in aqueous medium. A certain amount of glycerol improved ductility as an appropriate plasticizer. Therefore, the dispersion capability of the AMWCNT and decent stability in CMC solution, endowed it with the effective interactions between polymer network and carbon nanomaterials. The aforementioned inter/intramolecular interactions such as hydrogen bonding and chain entanglements, could lead to improved mechanical properties and rapid shape recovery. Moreover, the effective contact areas between the nanotubes in the CMC matrix enhanced the electrical conductivity of the flexible composite films.

Experimental Section

Carboxymethyl cellulose (CMC) was dissolved in 10 mL of deionized water at 60 °C to obtain a 0.5% w/v CMC solution. Then, 0.2% w/v of glycerol was added dropwise to the CMC solution. Then, amine functionalized MWCNTs (diameter of 0.7-1.8 nm, length of 6-35 μm) were dispersed in CMC solutions using an ultrasonic bath at the frequency of 40 KHz for 30 min to obtain the dispersions of the amine functionalized MWCNTs (AMWCNTs) with the concentrations of 1,2,3, and 4 mg/mL in the CMC solutions. The obtained gels were cast on glass slides, allowing to dry at 50 °C for 0.5 h in a vacuum oven. Afterwards, the obtained films were peeled off the slides by a small amount of deionized water for wetting them. The films were stored in a vacuum oven to avoid water evapuration. The films were also labelled as F(x) where x is the AMWCNT content in the gels before drying (mg/mL) [3].

Results and Discussion

The conductive composite films were prepared as demonstrated in Fig.1. The secondary interactions between CMC polymer chains and amine functional groups on carbon nanotubes, improved the stability and compatibility of the filler and matrix in the prepared films.
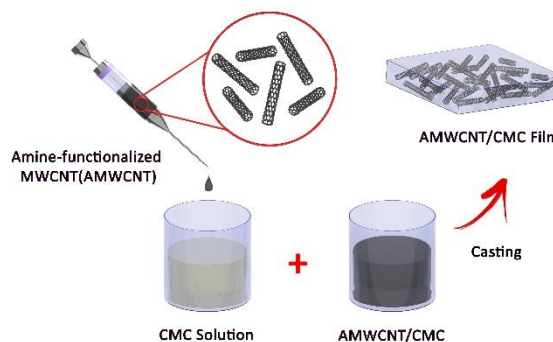
Fig.1: Schematic representation of preparation of composite CMC/AMWCNT films.

22nd Iranian Chemistry Congress (ICC22)
Iranian Research Organization for Science and Technology (IROST)
13-15 May 2024

03231-97589

IROST

For instance, the reversible inter/intramolecular hydrogen bonding between the hydroxyl and / or carboxylate groups on CMC and amine groups on MWCNTs could lead to an enhanced mechanical properties.

To investigate the morphological properties of the samples, field-emmision scanning electron microscopy (FESEM) analysis was conducted. As shown in Fig.2, the surface of the vacuum-dried composite film (F3) is rough with several grains which could be due to the agglomerated AMWCNTs in the polymeric matrix.
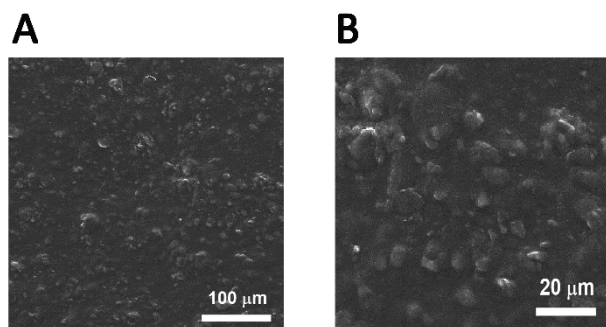
Fig.2: FESEM images of F3 sample with the different scale bars of 100 μm (A) and 20 μm (B).

The electrical properties and the strain sensitivity of the samples were also evaluated using a digital sourcemeter coupled with a tensile machine. As shown in Fig.3, the resistance changes was investigated in real time for F3 (as an optimal film) under several cycles of loading-unloading tensile stresses. The resistance changes of the film are repeatable and reliable in real time, indicating excellent strain-sensitivity properties for the sample. Furtheremore, the surface electrical conductivity of the films was measured quantiavely for the various film samples. The obtained surface conductivity was increased and then decreased with the increase of AMWCNTs concentration in the CMC matrix. It could be arising from the aggregation and intermolecular hydrogen bonds of the AMWCNTs in the CMC matrix in F4 sample, leading to a diminished conductive pathway in the CMC matrix and subsequently diminished electrical conductivity [4]. The maximum measured electrical conductivity was corresponded to the F3 sample (0.9 ± 0.3 S/m). Moreover, the samples were placed at room temperature for 1 h. Then, the electrical conductivities of these semi-dried samples were investigated. The electrical conductivities were slightly decreased for all of the semi-dried films which could be arising from the considerable water evaporation and subsequent brittleness, leading to a disturbed conductivity and decreased flexibility.
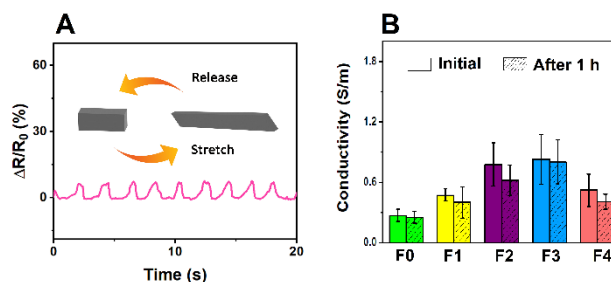
Fig.3: (A) The resistance changes of the F3 composite film under cyclic stretching. (B) The electrical conductivity of the as-prepared composite films and the same samples after 1 h.

Conclusions

In this research, conductive and stretchable composite films were prepared through a one-pot, eco-friendly and facile casting method. The electrical conductivity of the samples reached 0.9 ± 0.3 S/m. Furthermore, the film showed a repeatable and reliable resistance changes in loading-unloading tensile stress which could be arising from the superior mechanical properties and fast shape recovery capability. Owing to the cost-effective preparation strategy, the prepared bio-based film could be utilized as a multifunctional strain sensor in motion detection systems and biomedical applications.

References

[1] Zhang, Q., Wang, Q., Wang, G., Zhang, Z., Xia, S., & Gao, G. (2021). Ultrathin and highly tough hydrogel films for multifunctional strain sensors. *ACS Applied Materials & Interfaces*, *13*(42), 50411-50421.

[2] Bains, D., Singh, G., Bhinder, J., Agnihotri, P. K., & Singh, N. (2020). Ionic liquid-functionalized multiwalled carbon nanotube-based hydrophobic coatings for robust antibacterial applications. *ACS Applied Bio Materials*, *3*(4), 2092-2103.

[3] Okahashi, K., Takeuchi, M., Zhou, Y., Ono, Y., Fujisawa, S., Saito, T., & Isogai, A. (2021). Nanocellulose-containing cellulose ether composite films prepared from aqueous mixtures by casting and drying method. *Cellulose*, *28*(10), 6373-6387.

[4] Mahesh, V. (2023). Artificial neural network (ANN) based investigation on the static behaviour of piezo-magneto-thermo-elastic nanocomposite sandwich plate with CNT agglomeration and porosity. *International Journal of Non-Linear Mechanics*, *153*, 104406.

Prediction of Torque in Accelerated Sulfur Vulcanization of Radial Tire Tread Compound

Ali Nikakhtar, Jalal Abedini

Corresponding Author E-mail: anikakhtar@birjand.ac.ir.

Department of Chemistry, Faculty of Science, University of Birjand, Birjand.

Abstract: Prediction of the accelerated sulfur vulcanization is still a challenging task. One type of model used for this purpose is the phenomenological model used here. By modifying the equation of the model, it became possible to predict torque values. By fitting the model equation with the experimental data, the parameters of the model were calculated, then the dependence of the parameters on the temperature was obtained, thus the rheumatic diagrams were simulated at different temperatures and a good agreement was observed.

Keywords: Accelerated Sulfur Vulcanization.; Torque.; Curve Fitting.

Introduction

The prediction of the curing degree of rubber vulcanized with accelerated sulphur is still a challenging task, because the actual kinetic strongly dependent on several factors, such as the rubber type, carbon black content, presence of different accelerators, coadiuvants, etc.

In general, three steps are clearly distinguishable to describe well a curing process, namely induction, curing and post-curing. These steps are usually adopted for all rubber materials exhibiting double bonde in the backbone of the macromolecules. It is necessary to obtain complete kinetic, thermal, and rheological characterization of the material during reaction Hence, determination of the reaction kinetics becomes very important. Three types of approach, including curing, are: phenomenological, mechanistic, and semi-mechanistic models[2-5].

In this research, Qureshi's phenomenological model [5] was modified and the torque and rate curves obtained from the rheometer were simulated. Parameters of the equation were calculated by curve fitting of radial tire tread compound. This work was done for the curing curve at different temperatures and the relationships for the dependence of model parameters with temperature have been obtained. in the following, the torque and velocity curves were simulated in different temperatures.

Experimental Section

The tread compound, which had been composed in the production line, was randomly taken, then compound was mixed by roll mile and after one day the ODR Reomether test was taken at temperaturs 155, 165, 175 and 185 C.

Results and Discussion

Figures (1) and (2) , respectively, show the graphs of torque and speed with respect to time for temperatures of 155, 165, 175 and 185. The increase in temperature is due to the increase in the rate of formation of initial intermediates, then induction time decreases and the
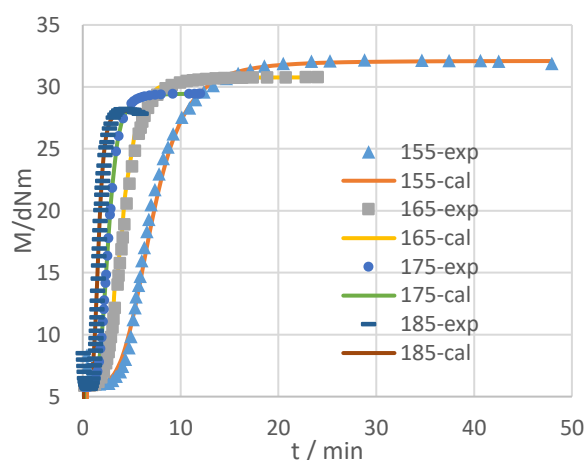
Fig.1: Rheometric crosslinking curves for all tested temperatures

rate of curing step increases. This is the reason for increasing the maximum in the rate curve and shifting it to shorter times. In the curing process of this compound, there are no chemical reactions to break crosslinks, so torque reduction is not observed in the post curing stage and the rate curve approaches zero at these times.

Equations (1) and (2) introduce the torque and its changes with respect to time, respectively.

$$M = M_{Max} - \frac{M_{Max} - M_{\circ}}{1 - (k_c t)^n} \tag{1}$$

$$dM/dt = (M_{Max} - M_{\circ}) \frac{n k_c{}^n t^{n-1}}{1 - (k_c t)^n} \tag{2}$$

In these equation M_{Max} is maximum of torque, $M_{\circ}$ is minimum of torque, k_c is a parameter same as rate constant, n is called the degree of reaction .

Eequation (1) was fitted on the experimental data by using MATLAB software. The results of these calculations are reported in Table (1) for different temperatures. In this table M_{Max} and $M_{Max} - M_{\circ}$ are obtain form experimental data. R-square values are close to one therefore, this model is suitable for simulating the curing process of this compound.

22nd Iranian Chemistry Congress (ICC22)
Iranian Research Organization for Science and
Technology (IROST)
13-15 May 2024

03231-97589

IROST

Table 1: Values of the parameters presented in equation

	kc	n	M_{max}	M_{max}-M_{min}	R-square
155	0.1456	4.48	32.1576	26.1342	0.9959
165	0.2455	4.43	30.7373	25.0423	0.9925
175	0.383	4.938	29.3137	23.4463	0.9923
185	0.5918	6.122	28.222	22.5834	0.9952

The dependence of k on temperature is similar to the rate constants of chimical reactions. therefore it is obtained by plotting $Ln(k_c)$ in terms of $\frac{1}{T}$ as a linear graph. By examining the dependence of these data on temperature, it was found that the relationship between n , $M_{max} - M_{min}$ and M_{max} on temperature is linear and the slopes and the intecepts of these lines are reported in table (2). Good values for R-Square are also seen here

, $M_{max} - M_{min}$ and M_{max}There are two parameters that have been obtained using experimental data, these two parameters decrease with the increase in temperature, because the increase in temperature also increases the speed of side reactions, so not all intermediates can produce crosslinks, and as a result, the final torque and change in Torque will decrease

Table2: intercept and slope of model

	Intercept	Slope	R-Square
Ln(kc)	78.58	-0.1225	0.9882
N	88.74	-0.1323	0.9963
M_{max}-M_{min}	19.44	-9141.84	0.9993
M_{max}	-21.53	0.0597	0.9979

By applying the dependence of these parameters on temperature, Table (2), in the model equation, simulation of rheometric data was done (Fig. (1) and (2)). A good agreement between the calculated and experimental data shows that this model can obtain suitable results for curing the compound. Because the fitting is done based on the torque equation, some deviation can be seen in figure (2) especially at times when the speed is maximum.
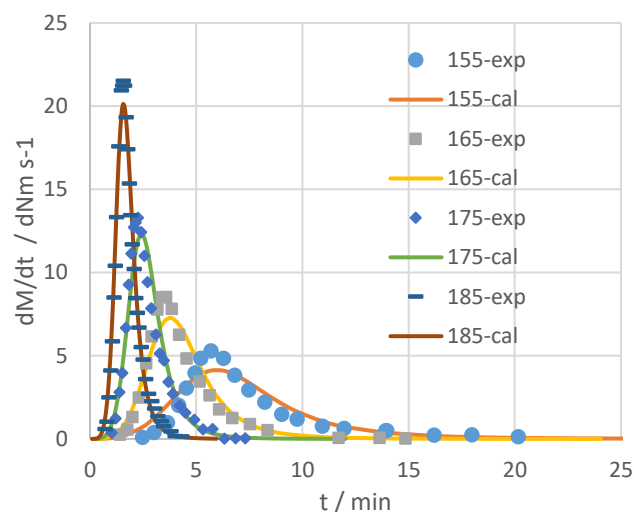
Fig.2: Crosslinking rate curves for all tested temperatures

Conclusions
Due to the importance of crosslinks, in this model the torque diagram is directly simulated and therefore information about crosslinks will be obtained. ..

References
[1] C A. Ciesielski, (1999). *An introduction to rubber technology*. Smithers Rapra publishing,.

[2] B. Oskar, J Pavličević, B Ikonić, J Lubura, D. Govedarica, P Kojić, (2021). A new approach for kinetic modeling and optimization of rubber molding, 61,879-890

[3] F. Sanainejad, A. Nikakhtar, M Kamkar (2021), simulation of rheometer results (ODR) using a mathematical function, the fifth applied chemistry seminar of the Iranian Chemical Society,

[4] G. Milani, F. Milani,(2017) Parabola-Hyperbola PH kinetic model for NR sulphur vulcanization, Polym. Test. 58, 104-115

[5] M. Rafei, M.H.R. Ghoreishy, G. Naderi,(2009). Development of an advanced computer simulation technique for the modeling, of rubber curing process, Comp Mat Sci, 2, 539-547.

Investigating the Heat Transfer and Vulcanization Reactionin Temperature Changes of the Points of a Thick Piece in the Process of Accelerated Sulfur Curing

Ali nikakhtar* [a], jalal abedinime [a], Alireza Afsari Moghadam[b], Ali Ziyatbar[c]

Corresponding Author E-mail: anikakhtar@birjand.ac.ir.

[a] Department of Chemistry, Faculty of Science, University of Birjand, Birjand, Iran.

[b] Department of Mechanical Engineering, Faculty of Engineering, University of Birjand, Birjand, Iran.

[c] Kavir Tire Company, Technology Unit.

Abstract: Temperature and curing time are among the most important factors influencing the curing of thick parts. In this research, a raw rubber compound was placed in a trapezoidal mold by heating it in a curing press, and the temperature changes of several points inside it was recorded, then the previous experiment was repeated with the cured compound inside it. In justifying the observed temperature changes, it was found that the heat effect created by the reaction in the process is a factor that should be considered in the simulation of the process.

Keywords: Heat transfer, vulcanization process, temperature changes

Introduction

Rubbers are among the materials that are used in many industries and for different purposes. Useful rubber products such as tires cannot be produced without the vulcanization process. Vulcanization is a chemical process during which the raw rubber acquires an elastic state and the physical properties of the rubber are improved. Temperature and time of cure are among the most important influencing factors in curing process [1].

The rubber curing process is an exothermic chemical reaction so a kinetic model is needed to describe the rate of reaction as a function of time and temperature [2-4]. The degree of curing (α), can be described by the relation of the heat produced up to time (Q_t) to the total heat of reaction (Q_∞) per unit volume as follows:

$$\propto = \frac{Q_t}{Q_\infty} \implies \dot{Q} = Q_\infty \frac{d\alpha}{dt}$$

The thermal conductivity coefficient of rubber is low, so different point of the piece are not at the same temperature during the curig process. Therefore, the two factors of heat transfer and heat released in the reaction determine the temperature of these points.

In this research, thermocouple wires were placed at different points of the compound, then the sample was placed in the cured press and the temperature was recorded during the curing. After the piece cooled down, this test was repeated in the same way as the previous stage for the baked rubber. The comparison of temperature changes in these two states shows the effect of heat released is in the process.

Experimental Section

The tread compound, which had been composed in the production line, was randomly taken, then compound was re-mixed in the roll mill machine and made into a sheet with a thickness of 0.5 cm, then these sheets are placed into the mold and four thermocouple wires were installed in different parts of the mold
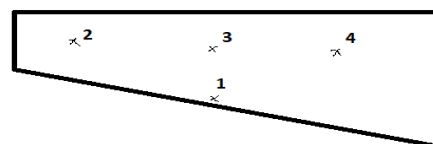
Fig.1: The cross-section of the mold and the location of the wires

Results and Discussion

Figure (2) is related to the point (1) or wire (1) and point (3) or wire (3) and show comparison of temperature changes of these points during the reaction. The following results can be mentioned about these charts:

1- On the point (1) the rate of temperature increase is high because the heat transfer coefficient of the metal is much larger than that of the compound. this trend is also observed in both steps of the test.

2- In the second step, the temperature increase becomes slower after a while compared to the first stage, and this difference can be the result of the vulcanization reaction

22nd Iranian Chemistry Congress (ICC22)
Iranian Research Organization for Science and
Technology (IROST)
13-15 May 2024

03231-97589

IROST

3-After twenty minutes, the curing press is opened. At point 1, the cure is complete, so the temperature changes after that are similar in two stages.

4-on the point (3) the temperature increase slower than point (1) because its distance from the boundaries of heat transfer is greater, In addition, after opening the curing press, the temperature continues to increase, and this increase is greater in step 1, because the reaction releases heat.
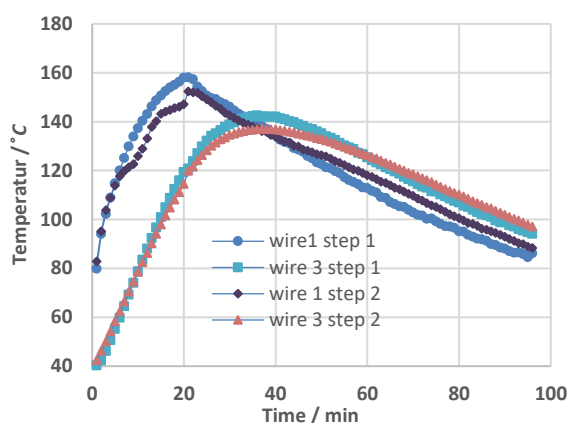
Fig.2: Temperature changes during the process for two steps and two points (1) and (3)

5- After opening the press, the temperature continues to increase because the heat transfer coefficient of the rubber is low.

Figure (3) is related to the point (2) or wire (2) and point (4) or wire (4) and show comparison of temperature changes of these points during the reaction. The following results can be mentioned about these charts:

1- The comparison of temperature changes in the thin part, point (2), and the thick part, point (4), shows that as the thickness increases, due to the low heat transfer coefficient of the rubber, the heating speed and also the cooling speed will be lower and this effect can be seen in both stages

2- At the beginning and end of the process, the temperatures are almost the same, but in the times between these two, the temperatures recorded in the first step are higher than the second step, and this is related to the heat released in the process.

3-The start time of the difference between the two graphs indicates the end time of the curing stage.
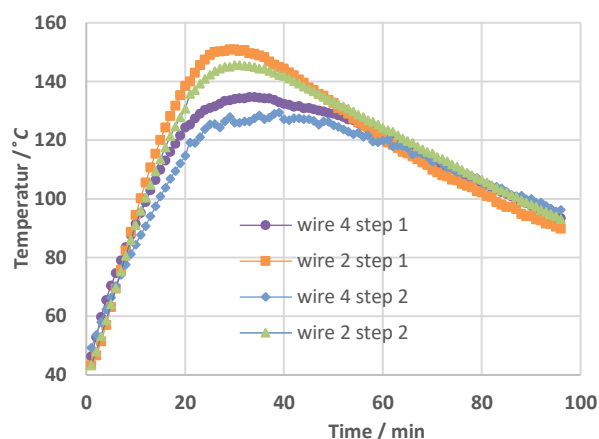
Fig.3: Temperature changes during the process for two steps and two points (2) and (4)

By entering these temperatures into the simulation equation of cooking kinetics, the progress graphs of the reaction in terms of time were obtained for each of the points, and it was found that the progress of the reaction at point 4 is the lowest and before the reaction is complete, the process stops in the cooling stage.

Conclusions

The general trend of the graphs is the same as Figure (2), which means that the main factor determining the temperature of different points is only heat transfer, but to achieve reliable results, the reaction and heat of reaction must also be considered in curing simulations.

References

[1] Ciesielski A.,(1999) *An introduction to rubber technology*. Smithers Rapra publishing.

[2] Han I. S., Chung C. B., Kang S. J., Kim S. J., Jung H. C.,(1998), A kinetic model of reversion type cure for rubber compounds, Polymer, 22, 223

[3]. Ghoreishy] M. H. R, (2016), "A state-of-the-art review on the mathematical modeling and computer simulation of rubber vulcanization process," *Iran. Polym. J. (English Ed.*, vol. 25, no. 1, pp. 89–109, Jan.

[4] Sanainejad F., Nikakhtar A., Kamkar M. (2021), simulation of rheometer results (ODR) using a mathematical function, the fifth applied chemistry seminar of the Iranian Chemical Society.

22nd Iranian Chemistry Congress (ICC22)
Iranian Research Organization for Science and Technology (IROST)
13-15 May 2024

03231-97589

IROST

Secondary Residue of Sugarcane Bagasse for Removal of Dyes from Wastewater

Asal Azarhoosh [a], Elham Askarizadeh [a], Mokhtar Heidari [b], Ensieh Ghasemi [c]

Corresponding Author E-mail: elhamaskarizadeh@gmail.com.

[a] Department of Applied Chemistry, Faculty of Pharmaceutical Chemistry, Tehran Medical Sciences, Islamic Azad University.

[b] Department of horticultural science, Agricultural sciences and natural resources, university of Khuzestan, Molla Sani, Iran.

[c] Faculty of Pharmaceutical Chemistry, Tehran Medical Sciences, Islamic Azad University, Tehran, Iran.

Abstract: In summary, modified sugarcane bagasse holds significant potential as an environmentally friendly and effective method for organic compounds removal from contaminated wastewater. Researchers continue to explore innovative approaches to address water pollution and enhance water quality. In this study, modified sugarcane bagasse (SB) was utilized as a bio-absorbent that effectively removed 80% of methyl orange (MO) from water at pH=7, within 45 minutes at ambient temperature.

Keywords: Sugarcane Bagasse; Bio-Adsorbent; Organic Compounds; Water Quality.

Introduction

The widespread global production and use of dyes, produce a large amount of wastewater containing dyes, which causes pollution and environmental problems [1]. There are many methods to treat wastewater contaminated with organic dyes, but in industry, artisans are looking for efficient and low-cost alternative methods to remove pollutants, which are natural adsorbents due to favourable conditions in terms of price, wide availability, fast kinetics and compatibility with the environment have been considered. Sugarcane and its derivatives are among the natural compounds that are used to absorb pollutants [2,3]. The main components of sugarcane bagasse are generally natural polymers, including cellulose (40-50%), hemicellulose (25-30%) and the rest contains lignin, wax, etc (14.9 to 25.4%) [4,5], but unprocessed bagasse does not naturally have a very high absorption capacity, but If reforms are applied with different methods, it will lead to an increase in its absorption capacity.

Biosorbents derived from sugarcane bagasse have functional groups such as -COOH, -OH, NH2-, -OCH3, -CONH2, and -SH, which help to absorb and bind pollutant ions [6]. To investigate other characteristics of bagasse nanoparticles, we have used physical methods such as Fourier Transform Infrared (FTIR) spectroscopy, X-ray diffraction studies (XRD), and Scanning Electron microscopy (SEM). Furthermore, UV-Visible spectroscopy was used to examine the dye adsorption.

Experimental Section

The modified sugarcane bagasse was purchased from Shushtar furfural factory. The materials were first dried at 70◦C for 24 hrs in an oven. The dried SB was milled and sieved (<250 μm). Adsorption experiments were performed by preparing a 0.3 M stock solution of methyl orange and the intended concentrations were diluted from it. The effect of different parameters was investigated respectively. Different amounts of bagasse 0.2, 1.5, and 0.1 g were added to 15 ml of diluted methyl orange solution and mixed by a magnetic stirrer at 15, 30, and 45 minutes. The pH of the mixtures was adjusted with HCL (0.5 M) and NaOH (0.5 M) at pH 3, 7 and 9. As a result, we designed 15 experiments to get the best consequence.

All experiments were performed several times and the observations were reported. After the adsorption process, the obtained solution was centrifuged at 300 rpm for 2 minutes and it was filtered with a syringe filter to separate the adsorbent. Afterward, the absorbance of methyl orange was measured by UV-Vis spectrophotometer at the maximum absorption wavelength (λmax) at 464 nm. Eventually, the concentration of methyl orange was then determined by using the equation created from the calibration curve. The adsorption capacity (qe) and percentage removal efficiency (%R) were estimated by the following Eqs. (1) and (2):

$$qe = \frac{(C_i - C_f)}{m} \times V \qquad (1)$$

$$\%R = \frac{C_i - C_f}{C_i} \times 100 \qquad (2)$$

where qe (mg/g) is the adsorption capacities of dyes, Ci and Cf (mg/g) are the concentrations at initial and time t, respectively; V (L) is the volume of the solutions; M (g) is the mass of the adsorbent used Sb and R (%) represents the removal efficiency of methyl orange dyes onto the adsorbent.

22nd **Iranian Chemistry Congress (ICC22)**
Iranian Research Organization for Science and Technology (IROST)
13-15 May 2024

03231-97589

IROST

Results and Discussion

The results showed that the initial absorption of methyl orange shown by the spectrophotometer was 0.62. After adding modified sugarcane bagasse, the adsorption of MO decreased significantly and it reached 80% adsorption in certain intervals.
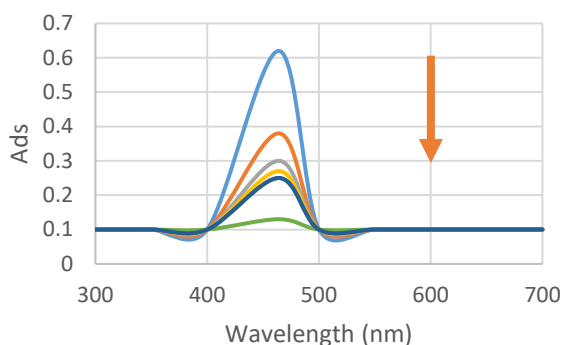
Fig.1: UV-Vis spectrum of methyl orange after adding modified SB

Conclusions

In this study, an efficient, eco-friendly, and low-cost adsorbent, which is an industrial waste, was prepared to remove organic dyes (methyl orange) from wastewater.

The study aimed to analyze the effect of various parameters such as concentration, adsorbent dose, pH, time, and temperature on adsorption. The study concluded that the most effective adsorption was achieved under the following optimal conditions: 0.2 grams of nanoparticles, a removal process of 45 minutes, and a pH level of 4 without any additional temperature (ambient temperature). As a result, this natural compound can be used as bioadsorbents of organic dyes and removal of dyes from wastewater.

References

[1] Rezende, C.A., de Lima, M.A., Maziero, P., deAzevedo, E.R., Garcia, W., Polikarpov, I., 2011. Chemical and morphological characterization of sugarcane bagasse submitted to a delignification process for enhanced enzymatic digestibility. Biotechnol Biofuels. 4, 54

[2] Zhou, Y., Zhang, L., Cheng, Z., 2015. Removal of organic pollutants from aqueous solution using agricultural wastes: A review. J. Mol. Liq. 212, 739–762. https://doi.org/10.1016/j.molliq.2015.10.023

[3] Allen, S. J., Mckay, G. Porter, J. F., 2004. Adsorption isotherm models for basic dye adsorption by peat in single and binary component systems. J. Colloid Interf. Sci. 280, 322– 333. https://doi.org/10.1016/j.jcis.2004.08.078

[4] Wyman C.E. Biomass ethanol: technical progress, opportunities, and commercial challenges. Ann. Rev. Energy Environ. 1999;24:189–226. [Google Scholar]

[5] Sun J.X., Zhao X.F.S.H., Sun R.C. Isolation and characterization of cellulose from sugarcane bagasse. Polym. Degrad. Stab. 2004;84:331–339.[Google Scholar]

[6] Aruna et al. (2021) 'A review on modified sugarcane bagasse biosorbent for removal of dyes', Chemosphere, 268, p. 129309. https://doi.org/10.1016/j.chemosphere.2020.129309

Fabrication of Temperature-Responsive Membrane (PES/GO-g-PNIPAM) for Efficient Separation and Recovery of Dyes in Wastewater Treatment

Hossein Mahdavi, Hossein Rouhbakhsh*

Corresponding Author E-mail: hosseinrouhbakhsh@ut.ac.ir

School of Chemistry, College of Science, University of Tehran, Tehran, Iran.

Abstract: Nanofiltration membranes are used in organic dye purification, allowing water recycling and product recovery. In this work, first, graphene oxide was synthesized using the improved Hammers method, then it was functionalized using vinyltriethoxysilane. In the next step, N-isopropylacrylamide monomer was polymerized on the surface of graphene oxide using a free radical process. The temperature-responsive membrane was fabricated during phase inversion process using non-solvent. The performance of the membrane was investigated at two temperatures of 25 and 65℃ and showed good results.

Keywords Temperature responsive membrane, Poly(N-isopropylacrylamide), Graphene oxide, Nanofiltration

Introduction

The many large amounts of wastewater are created daily in the homes, industrial, and agricultural sectors as a result of the growing human population. However, freshwater supplies are not renewed to meet an expanding population's demands and water use [1]. One of the industries with the highest water use is the textile sector, which uses a lot of water during the various production stages and produces up to 200-350 m3 of wastewater for every ton of finished goods [2]. Due to their persistent, carcinogenic, and low biodegradability characteristics, dyes seem to be the most worrisome contaminant among these substances. Therefore, advanced treatment processes are needed to manage textile wastewater so that dye and water can be recovered to be reused in the textile industry, which results in significant savings in water consumption. For smart controllable separation, the use of stimuli-responsive polymers has been considered in recent years. Among polymers responsive to environmental stimuli, thermoresponsive polymers have attracted more attention in recent years because temperature changes commonly occur in the natural world and can also be easily manipulated artificially. In this work, modified nanoparticles (GO-g-PNIPAM) were synthesized using free radical polymerization process[3]. Then, PES/GO-g-PNIPAM membranes were made using the non-solvent induced phase inversion (NIPS) process And the physical and chemical characteristics of the membrane were investigated.

Experimental Section

First, the synthesis of graphene oxide was conducted through the enhanced Hammers method, followed by its functionalization with vinyltriethoxysilane. Subsequently, the polymerization of N-isopropylacrylamide monomer on the graphene oxide surface was achieved via a free radical mechanism. The formation of a temperature-responsive membrane occurred during the phase inversion process utilizing a non-solvent. The physical and chemical characteristics of the produced nanosheets were assessed through FTIR, SEM, and DSC analysis, along with the evaluation of membrane flux and rejection performance using a dead-end cell. (Font: Calibri 10)

Results and Discussion

FTIR spectra of GO, GO-VTES, and GO-g-PNIPAM particles shown in (Figure.1) GO absorption peaks at 3400-3500,1727, and 1633 linked to (OH), COOH carbonyl groups, and aromatic C=C vibration. GO spectrum shows peaks at 1066 and 1400 related to (C-O vibration) and (C=O vibration). GO-VTES FT-IR spectrum displays new peaks 1130, 2938, 3160 for Si-O-C stretching and =CH2 symmetric/asymmetric vibration. C=C aromatic peak shifted from 1633 to 1610 in GO-VTES. Vinylization reaction of GO successfully done. PNIPAM grafting on graphene oxide led to new peaks 2945, 1650, 1541, 1386 for C-H groups, C=O, amide group, NH, and isopropyl group -CH(CH3)2, indicating successful grafting.The temperature-responsive behavior of GO-g-PNIPAM in the temperature range of 25 to 60 ℃ was investigated by DSC, which is shown in (Fig.1). temperature of 46 ℃, and this phase transition change corresponds to the LCST of GO-g-PNIPAM. the presence of numerous oxygenated functional groups on graphene oxide's surface makes the modified nanoparticle highly hydrophilic. This necessitates more energy to break the hydrogen bonds between water molecules and GO-g-PNIPAM, shifting the system to a hydrophobic state. Consequently, the Lower Critical Solution Temperature (LCST) has increased from 32°C to 46°C, showcasing the temperature-responsive properties of GO-g-PNIPAM. Images of FE-SEM GO and GO-G-PNIPAM are depicted in (Fig.2), displaying smooth surface of non-functionalized graphene oxide sheets without irregularities. Upon PNIPAM addition, pages' surface becomes wrinkled with disorderly edges, showing

22nd Iranian Chemistry Congress (ICC22)
Iranian Research Organization for Science and
Technology (IROST)
13-15 May 2024

03231-97589

IROST

visible polymer chains on GO sheets. Morphological change in GO suggests successful grafting of PNIPAM on its surface.
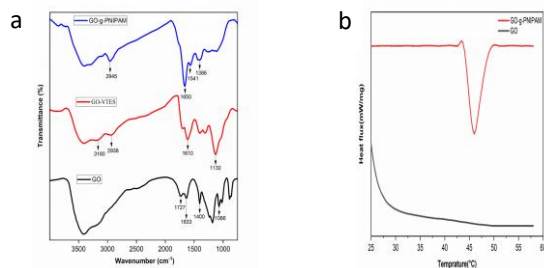
Fig.1: (a) FT-IR and (b)DSC (GO-g-PNIPAM)
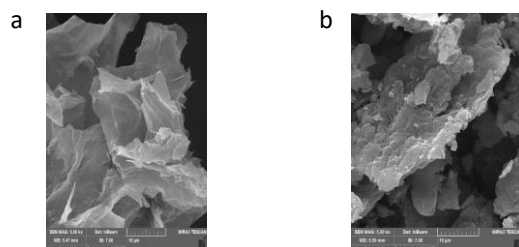
Fig.2. SEM images (a)GO and(b) GO-g-PNIPAM

The study examined water flux and dye separation of M_1(with nano addtive) and M_0 (without nanoaddtive) membranes at 25 °C and 65 °C. Water flux of M_1 increased from 67 to 95 L/(m²·h) at 25 °C compared to 65 °C due to lower water viscosity. At 25 °C, PNIPAM chains form hydrogen bonds with water, hindering water passage. However, at 65 °C, the hydrogen bonds break, making the chain hydrophobic. The M_1 membrane has larger pores due to the synergistic effect of GO-g-PNIPAM and PEG, resulting in increased water flux at high temperatures compared to M_0. The GO-g-PNIPAM nano additive alters membrane performance significantly by enhancing hydrogen bonding with dye molecules, resulting in improved dye repellency and dye removal efficiency. At 25℃ , PNIPAM chains create steric hindrance and increased hydrogen bonding with dye molecules. This leads to better separation of dye molecules from the aqueous solution, enhancing dye repellency and color removal rates. dye removal for acid blue increases from 88% to 94.6% and for direct red from 96% to 97%. When the temperature rises to 65 , PNIPAM chains establish intramolecular hydrogen bonds, causing the chain to shrink and become hydrophobic. Due to the opening of the pores at this temperature and also being hydrophobic, molecules that are smaller in size and more hydrophobic pass through the gates more easily (Fig.3).
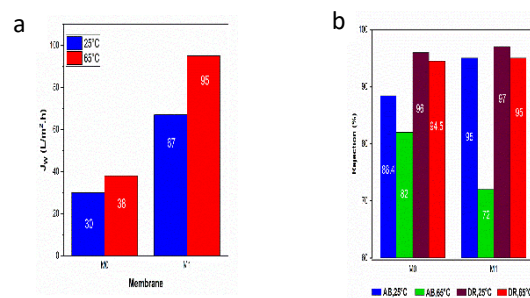
Fig.3. (a)Flux and (b) repulsion performance of membranes

Conclusions

By using phase inversion technique, a temperature-responsive membrane was created with high water flux and selectivity at 25 and 65 °C. At 25 °C, pores closed, separating Acid Blue 7 and Direct Red 23 with high efficiency, allowing water recovery. At 65 °C, pores opened, allowing Blue 7 acid to pass through due to its smaller size and hydrophobic nature compared to Direct Red 23, facilitating dye recovery. This technique's simplicity and cost-effectiveness make it promising for developing stimuli-responsive membranes in industries like textile, pharmaceutical, and petrochemicals for material separation and recovery.

References

[1] Obotey Ezugbe, E., & Rathilal, S. (2020). Membrane Technologies in Wastewater Treatment: A Review. *Membranes, 10*(5), 89.

[2] Ranganathan, K., Karunagaran, K., & Sharma, D. (2007). Recycling of wastewaters of textile dyeing industries using advanced treatment technology and cost analysis—Case studies. *Resources, Conservation and Recycling, 50*(3), 306-318.

[3] Liu, J., Wang, N., Yu, L.-J., Karton, A., Li, W., Zhang, W., et al. (2017). Bioinspired graphene membrane with temperature tunable channels for water gating and molecular separation. *Nature communications, 8*(1), 1-9.

A Ligand from Amino Acides Gapped Mn Immobilized on Multi-Walled Carbon Nanotube: A New Nanocatalyst for Coupling Reaction

Shadi Namdar, Nader Noroozi Pesyan[*]

Corresponding Author E-mail: nnp403@gmail.com ; n.noroozi@urmia.ac.ir

Department of Organic Chemistry, Faculty of Chemistry, Urmia University, 57159 Urmia, Iran.

Abstract: In this research, a Mn transition metallic complex on CNT has been designed and utilized as an effective, recoverable, and thermally stable heterogeneous nanocatalyst in the formation of the C-C bond. Also, the synthesis of amino benzyl naphthol derivatives was performed by the three-component reaction of coupling from aromatic aldehydes, type II amines, and 8-hydroxyquinoline in the presence of the CNT- A ligand from amino acides -Mn nanocatalyst under reflux conditions. Finally, the nature of catalysts was studied by using some techniques such as the Fourier transform infrared spectrum, energy-dispersive spectroscopy, hot filtration test, transmission electron microscopy, scanning electron microscopy, X-ray diffraction, inductively coupled plasma optical emission spectrometry, and N2 adsorption-desorption (BET). The synthesized heterogeneous catalysts showed perfect catalytic activity and also good recyclability in the coupling reaction. They could be reused at least for five consecutive cycles without significant loss of their catalytic activities.
Keywords: MWCNT, Nanocatalyst, Amino acid, coupling reaction

Introduction

In recent decades, green chemistry has been expanding as an important branch of chemistry [1]

A heterogeneous catalyst has emerged as a useful method to reduce waste production due to the simplicity of the process, less contamination of the product with active catalytic species, and less use of toxic solvents. The metallic nanostructure has excellent promise owing to its unique properties like a great surface area–volume ratio, great surface area, and separa tion.[2]

Considering that some carbon materials (CNT) have high potential, stability, and surface area in surface modification, they can be easily converted into an efficient material by surface modification method [3]

Nowadays, carbon-based nanomaterials have attracted a lot of attention in the production of unique and intelligent heterogeneous catalysts, Significant advances have been made with transition metal-based heterogeneous catalysts as the frontiers of green catalysis .

Our ligand, an α-amino acid, is used as a ligand. It contains a side chain indole, an α-carboxylic acid group, and an α-amino group. The hydroxyl group and indole nitrogen play a key role in the formation of the chelate ring of metal complexes. The use of $MnCL_2$ as an transation metal in connection with tryptophan is an efficient metal with good performance for nanocatalytic synthesis.[4]

[1-(α-aminobenzyl)-2-naphthol, 7] is known as an important compound and its applications in the ring-closure reactions to give naphthalene-based heterocyclic derivatives have not been thoroughly investigated.[5]

In particular, cross-coupling reactions between aromatic and aliphatic compounds have been extensively studied. This type of reaction usually occurs in the presence of a catalyst. Among the various reactions, Betti's basic synthesis (modified Mannich reaction or Mannich amino alkylation) is found to be of great importance because of the mild conditions of reaction for forming C−C and C−N bonds.[6,7]

Nanoparticle (NP) catalytic activity is a rich source for chemical processes used in both industry and academia. High interest in catalysis using nanomaterials has led to the synthesis and study of a variety of highly functional NPs including nanocarbon catalyst-integrated nanocatalysts as well as various metal nanostructures.[8]

Experimental Section

a_Preparation of CNT@S^{n}Pr-Cl:

In a 100 mL round bottom flask equipped with a stirrer, magnetic nanotube (0.5 g) dispersed in 30 mL n-hexane added 1 mL trimethoxysilyl propyl chloride was added into the dispersed solution and refluxed for 24 hrs.

b_Preparation of CNT@S^{n}Pr-ligand:

In a ۲۵ mL round bottom flask equipped with a stirrer, put CNT@S^{n}Pr-Cl (0.3 g) and ligand from amino acides (0.3 g) dispersed in 10 mL n-hexane along with 2 mL of triethylamine is refluxed for 24 hrs and then the sediment is filtered and washed with ethanol.

c_Preparation of CNT @S^{n}Pr-ligand-Mn:

In the last step, in a 100 mL round bottom flask equipped with a stirrer, an equal amount of the product (CNT@S^{n}Pr-ligand) and $MnCL_2$ (0.3 g) together with 50 mL ethanol, refluxed for 20 hrs, filtered off, washed with few mL methanol and water. After drying, nanocatalyst as a sediment was obtained.

d_Test reaction:

In a 15 mL vacuum flask equipped with a magnetic stirrer, acetic acid (4 mL) and benzaldehyde (0.09 g) were added, and the flask was placed on a heater for 30 min. Then, after adding the CNTtryptophan-Mn catalyst (0.02 g), it

22ⁿᵈ Iranian Chemistry Congress (ICC22)
Iranian Research Organization for Science and
Technology (IROST)
13-15 May 2024

03231-97589

was subjected to reflux for 30 min. Subsequently, after adding aniline (0.12 g), it was refluxed for 1 h and next, 8-hydroxyquinoline (0.14 g) was added to the reaction mixture. The progress of the reaction was controlled by TLC using a 3:1 ratio of an n-hexane-ethyl acetate solvent mixture. After the reaction was complete, the nanocatalyst was separated by centrifugation. The product was extracted by evaporating the solvent. Finally, 7-(phenyl (phenylamino)methyl)quinolin-8-ol products were obtained

with high purity. The obtained products were identified and 380 confirmed by spectroscopic techniques.

Results and Discussion

This article describes the synthesis of new nanocatalyst based on functionalized multi-walled carbon nanotube linked to trimethoxysilyl n-propyl chloride as a spacer then connected to amino acid ligand loaded Mn ion (CNT @S^{n}Pr-ligand-Mn) .Then this nanocatalyst is used for the one-pot synthesis of coupling reaction.

Conclusions

In this study, we would like to prepare a new Mn complex deposited on a tryptophan-functionalized nanostructured as an ideal green heterogeneous catalyst with easy catalyst preparation, high stability, and simple separation of the reaction mix with no loss of catalytic to synthesize 7-(phenyl(phenylamino)methyl) quinolin-8-ol and 2-(phenyl(phenylamino)methyl)94naphthalen-1-ol from aromatic aldehydes, type II, amines and 8-hydroxyquinoline and also with α-naphthol catalyzed by a new effective nanocatalyst (CNT-ligand-Mn) under reflux conditions in CH$_3$COOH solvent at 120 °C.

References

[1]Mansoori, A.; Eshghi, H.; Lari, J.(2020) Synthesis and Characterization of Betti Bases Derivatives via Green Mannich Reaction by NS-PCS and FHS as the Catalyst. Polycyclic Aromat. Compd., 40, 1470– 1478. https://doi.org/10.1080/10406638.2018.1557705.

[2] Shu, X. Z., Nguyen, S. C., He, Y., Oba, F., Zhang, Q., Canlas, C., ... & Toste, F. D. (2015). Silica-supported cationic gold (I) complexes as heterogeneous catalysts for regio-and enantioselective lactonization reactions. *Journal of the American Chemical Society*, *137*(22), 7083-7086. https://doi.org/10.1021/jacs.5b04294

[3] Şenocak, A., Khataee, A., Demirbas, E., & Doustkhah, E. (2020). Ultrasensitive detection of rutin antioxidant through a magnetic micro-mesoporous graphitized carbon wrapped Co nanoarchitecture. *Sensors and Actuators B: Chemical*, *312*, 127939. https://doi.org/10.1016/j.snb.2020.127939

[4] Ghorbani-Choghamarani, A., Mohammadi, M., Hudson, R. H., & Tamoradi, T. (2019). Boehmite@ tryptophan-Pd nanoparticles: a new catalyst for C–C bond formation. *Applied Organometallic Chemistry*, *33*(8), e4977. https://doi.org/10.1002/aoc.4977

[5] Szatmári, I., Hetényi, A., Lázár, L., & Fülöp, F. (2004). Transformation reactions of the Betti base analog aminonaphthols. *Journal of heterocyclic chemistry*, *41*(3), 367-373.https://doi.org/10.1002/jhet.5570410310

[6] Szatmári, I., & Fulop, F. (2004). Syntheses and transformations of 1-(α-aminobenzyl)-2-naphthol derivatives. *Current Organic Synthesis*, *1*(2), 155-165. https://doi.org/10.2174/1570179043485402

[7] Cardellicchio, C., Capozzi, M. A. M., & Naso, F. (2010). The Betti base: the awakening of a sleeping beauty. *Tetrahedron: Asymmetry*, *21*(5), 507-517. https://doi.org/10.1016/j.tetasy.2010.03.020

[8] Pesyan, N. N., Batmani, H., & Havasi, F. (2019). Copper supported on functionalized MCM-41 as a novel and a powerful heterogeneous nanocatalyst for the synthesis of benzothiazoles. *Polyhedron*, *158*, 248-254. https://doi.org/10.1016/j.poly.2018.11.005.

Development of a New Isotherm Model to Describe the Equilibrium Sorption of Nonionic Dyes by Semicrystalline Polymeric Fibers

Navid Rabiei

Corresponding Author E-mail: nrabiei@aut.ac.ir

Department of Textile Engineering, Amirkabir University of Technology, Tehran, Iran

Abstract: One of the most important aspects of physical chemistry of dyeing is the description as well as the explanation of the equilibrium sorption behavior of dyes by textile fibers. Because of the complex fine structure of textile fibers, having a single universal isotherm model to describe the dye sorption behavior of these substrates remains unsolved. In this work, a new isotherm model to describe the equilibrium sorption of disperse dyes by semicrystalline polymeric fibers, based on the modification of the well-known Dual-mode sorption isotherm model, is developed.

Keywords: sorption isotherm; nonionic dyes; semicrystalline polymeric fibers

Introduction

It is firmly believed that the optimum choice, use, control, and adaptation of modern dyeing technology can only be achieved through a sound understanding of basic principles [1, 2]. As a matter of fact, despite all the wonderful technology available for textile dyeing, we really understand so very little of the fundamentals. One of the most important aspects of dyeing theory is the equilibrium aspect of dye sorption by the semicrystalline polymeric substarets. Different adsorption isotherms, including Nernst, Langmuir, and Freundlich isotherms, have been employed for the description of disperse dyes equilibrium sorption data on polyester fibers, an issue showing that there is no consensus about the equilibrium behavior of sorption and therefore its mechanism by the mentioned fibers. One of the main causes of these apparently contradictory observations is attributable to the complex fine structure of textile fibers, which, based on the dominance of each of the defining characteristics of this fine structure, the equilibrium sorption behavior can be completely affected. In this research, an attempt is made to modify the dual-mode sorption isotherm model [3, 4] in such a way that it can be used as a general isotherm to describe and explain the different observed equilibrium behaviors of disperse dye sorption by polyester fibers.

Model Development

According to the dual-mode isotherm model, the disperse dye sorption is governed by two ostensibly incompatible theories of dye sorption which may well operate conjointly, perhaps separately or even synergistically [5]. According to this particular mechanistic approach, the curvature of the sorption isotherm can be attributed to Langmuir-type adsorption (i.e., dye sorption onto specific adsorption sites) which occurs in parallel with Nernst-type absorption (i.e., nonspecific site sorption). As such, the sorbed dye molecules are present within the substrate as two different physical forms, namely **adsorbed species** that were adsorbed via a Langmuir mechanism and **dissolved species** that were absorbed by a Nernst mechanism [5].

Unlike the dual-mode sorption isotherm model, in the modified model [6], three different species or populations of the sorbed dyes are considered. The first population is based on Nernst-type partitioning or Henry's law dissolution and represents dye absorption in the non-crystalline part of the fiber. The second and third populations are formulated based on Langmuir adsorption, with the difference that in the second population, adsorption is done from the dye aqueous solution, while the third population is the dyes adsorbed from the dye solution wherein the supercooled liquid polymer acts as a solvent. In other words, dye adsorption from the first population occurs on the surfaces of the internal crystallites that are in contact only with the amorphous (supercooled liquid polymer) portion of the polymeric fiber, not with the aqueous solution. Accordingly, the equation of the modified model was obtained [6] as follows:

$$[D]_f = K_p[D]_b + \frac{S_e K_e [D]_b}{1 + K_e[D]_b} + \frac{\rho_T S_i K_i K_p [D]_b}{1 + \rho_T K_i K_p [D]_b}$$

where $[D]_f$ and $[D]_b$ are the equilibrium dye concentration on fiber and in water, S_e and S_i are the saturation values (capacity terms) for the Langmuir sorption of the second and third populations respectively. K_p is the partition coefficient, and finally K_e and K_i are the Langmuir constants (affinity parameters) of the second and third populations respectively. ρ_T is the density of the amorphous polyester in the dyeing temperature.

22nd Iranian Chemistry Congress (ICC22)
Iranian Research Organization for Science and Technology (IROST)
13-15 May 2024

03231-97589

Results and Discussion

The figure below (Fig. 1) shows the experimental data of the equilibrium sorption of purified CI Disperse Red 15 on polyester microfiber (0.32d) at 95 °C, reported by Nakamura et al [4]. Due to the small values of S_e, as a first approximation to the equation of the modified model of dual-mode sorption isotherm, the second term could be eliminated from the equation. The simulated isotherms demonstrate the contribution of absorption and adsorption in the observed behavior of equilibrium sorption of dye on the fiber. These contributions could be affected by the change in the fine structure of fibers [6].
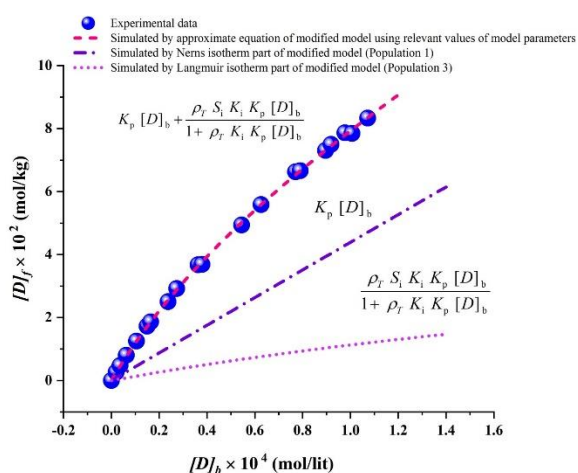
Fig.1: Sorption isotherm data described by the new isotherm model developed by modification of dual-mode isotherm.

Conclusions

The equilibrium sorption data of nonionic dyes on semicrystalline polymeric fibers are satisfactorily described by the modified model of dual-mode sorption isotherm. Using this model, it can be claimed that the standard affinity of dyes toward fibers can be calculated more accurately [6].

References

[1] Broadbent, A. D. (2001). Basic principles of textile coloration. Society of Dyers and Colourists.

[2] Burkinshaw, S. M. (2016). Physico-chemical aspects of textile coloration. Society of Dyers and Colorists.

[3] Shibusawa, T., & Chigira, Y. (1992). Dual-mode sorption of nonionic azo dyes by nylon 6. Journal of Polymer Science: Part B: Polymer Physics, 30, 563-568.

[4] Nakamura, T., Ohwaki, S., & Shibusawa, T. (1995). Dyeing properties of polyester microfibers. Textile Research Journal, 65, 113-118.

[5] Burkinshaw, SM. (2023). The roles of elevated temperature and carriers in the dyeing of polyester fibres using disperse dyes: Part 2. Analysis of conventional models of dye adsorption. Coloration Technology, Early view.

[6] Rabiei, N. Development of a new equilibrium sorption isotherm model of nonionic dyes by semicrystalline polymeric fibers. In preparation.

Monitoring the Physical Aging of Poly(Ethylene Terephthalate) Fibers Using Dye Sorption Method

Navid Rabiei

nrabiei@aut.ac.ir

Department of Textile Engineering, Amirkabir University of Technology, Tehran, Iran.

Abstract: This work is aimed to monitor the physical aging (structural relaxation) of polyester fibers in terms of changes in the number of dye molecules sorbed by aged specimens as a new method and to make some aspects of this complex phenomenon more clear which rarely considered in the literature. Specimens, aged thermally at the specified temperature and periods, are thus, conducted to the dye sorption experiments to monitor their physical aging. The results show that the method yields reliable information on physical aging of the polymer.

Keywords: Polyester fibers; Physical aging; Disperse dye sorption

Introduction

Physical aging is in fact a universal phenomenon in glassforming materials at temperatures moderately below their glass transitions resulting from the fact that they are generally out-ofequilibrium [1,2]. When a thermodynamic system is out-ofequilibrium, it spontaneously tends toward equilibrium state. In this work it is intended to detect the physical aging in stabilized polyester fibers using 'dye sorption' technique. The absorption of dye molecules from dyebath at a temperature below the glass transition of the specimens is selected as a strategy to monitor the physical aging from the outside of the polymer bulk. The kinetics of the physical aging of thermally aged specimens in the context of changes in the number of absorbed dye molecules are described and the results in terms of the concept of the free volume are explained. The KWW (Kohlrausch-Williams-Watts) stretched exponential function [3] and two additive exponential models are employed to fit the shape of kinetics of physical aging known as the relaxation function in the context of dye sorption observations to examine the non-exponential character of the relaxation.

Experimental Section

Evaluated materials were commercial polyester fabrics of poly(ethylene terephthalate) fibers (PET) produced by Polyacryl Company (Isfahan, Iran) in which warp and weft consist of 75/36 (the yarn count was 75 denier and consisting of 36 filaments) and 150/48, respectively. The selected disperse dye for this work was the commercial grade of C.I. Disperse Blue 56 named Serilene Blue RL from Yorkshire Group, UK. De-aging and relieving the stresses of the sample were achieved by the heating of fabric for 30 s at the constant temperature of 180 °C which is well above the glass transition of amorphous as well as semicrystalline PET sample. The fabric sample was then quenched in air to room temperature of 20 °C and finally was cut into rectangular specimens of the weight 0.22 g. Specimens were then kept in the refrigerator (−20 °C) until the commencement of the aging experiment. the specimens were subjected to thermal and hygrothermal aging at aging (annealing) temperature of 63 °C for a wide period of time, i.e. 1−63 days. Dye sorption experiment was conducted to the unaged and thermally aged specimens. The sorption experiments were conducted in the dyebaths contained 0.01 g/L of the dye at 63 °C for 2 h. The changes in the concentrations of dye effluents were measured by Cary 100 UV–vis. Any decrease in the concentration of dye in the dyebath was considered as the amount of dye absorbed by the specimen spectrophotometer.

Results and Discussion

Fig.1 shows the change of the number of dyemolecules, N, absorbed from dyebaths by the specimens after specified thermal aging periods.
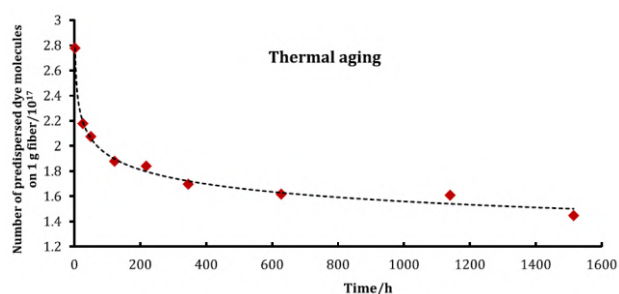
Fig.1: Number of dye molecules of commercial dye absorbed by the thermally aged specimens for specified aging periods. Dashed line is a guide for the eye.

It is clear that the plot of the amount of dye molecules absorbed by the aged specimens decreases with the increasing of the aging duration. This observation, i.e.

22nd Iranian Chemistry Congress (ICC22)
Iranian Research Organization for Science and Technology (IROST)
13-15 May 2024

03231-97589

IROST

reduction in dye sorption caused by thermal aging, can be interpreted by the help of the free volume concept.

It is recognized that free volume controls the molecular mobility of large segments of the polymer chain to a large extent, which in turn influences many of the physical and mechanical properties of polymers [4–6]. In the case of dye sorption, in fact, in a given period of time, the amount of dye molecules absorbed by the polymer has a strong dependency to the rate of dye diffusion into the matrix which is determined by the mobility of segments of polymer chains according to the free volume model [7]. On the other hand, in the context of free volume concept, it was suggested that physical aging causes densification of polymers by moving vacancies (cavities, holes or pores) constituting excess free volume to the external surface where disappear [8]. This leads to changes in the inter-chain packing. Therefore, the reduction in the amount of absorbed dye molecules seems reasonable.

In the structural relaxation studies, to show some features of relaxation behaviors, it is useful to fit some well-known decay functions which their characteristic parameters have important physical meanings to the experimentally obtained data. The KWW function can be mentioned as a reasonable choice. However, in addition to the KWW, the single exponential and the double additive exponential functions were also used as models to fit the non-dimensional relaxation data $\Phi(t)$. Fig. 2, shows the best fitting of the KWW, single exponential (Exp1), and double additive exponential (Exp2) functions to the data obtained from absorption of dye by the thermally aged samples upon different aging periods.
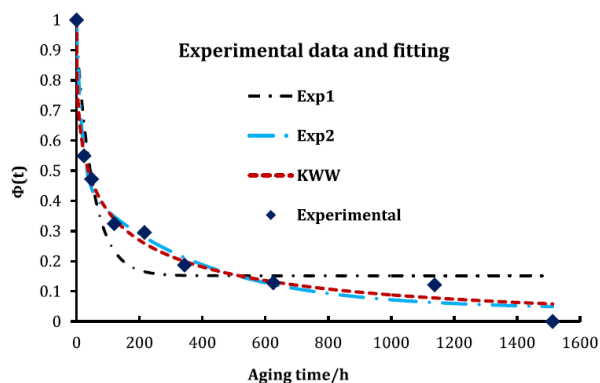
Fig.2: Non-dimensional relaxation functions for the dye sorption of thermally aged samples versus aging time. Dashed lines are the fits to the data.

molecules absorbed by the specimens with aging period at a suitable dye sorption experiment. Results of the method for monitoring the physical aging can be successfully interpreted by the use of the free volume concept and can be modeled by KWW decay function.

References

[1] D. Cangialosi, V.M. Boucher, A. Alegría, J. Colmenero, Physical aging in polymers and polymer nanocomposites: recent results and open questions, Soft Matter 9 (36) (2013) 8619.

[2] A. Shavit, J.F. Douglas, R.A. Riggleman, Evolution of collective motion in a model glass-forming liquid during physical aging, J. Chem. Phys. 138 (12) (2013) 12A528.

[3] J.C. Phillips, Stretched exponential relaxation in molecular and electronic glasses, Rep. Prog. Phys. 59 (9) (1996) 1133.

[4] L.C.E. Struik, Physical Aging in Amorphous Polymers and Other Materials, Amsterdam, Elsevier, 1978.

[5] J.M. Hutchinson, Physical aging of polymers, Prog. Polym. Sci. 20 (4) (1995) 703–760.

[6] E.A. McGonigle, J.H. Daly, S.D. Jenkins, J.J. Liggat, R.A. Pethrick, Influence of physical aging on the molecular motion and structural relaxation in poly(ethylene terephthalate) and related polyesters, Macromolecules 33 (2) (2000) 480–489.

[7] R.M. Rohner, H. Zollinger, Porosity versus segment mobility in dye diffusion kinetics- A differential treatment: dyeing of acrylic fibers, Text. Res. J. 56 (1) (1986) 1–13.

[8] A.W. Thornton, K.M. Nairn, A.J. Hill, J.M. Hill, Y. Huang, New relation between diffusion and free volume: II. Predicting vacancy diffusion, J. Membr. Sci. 338 (1–2) (2009) 38–42.

Conclusions

The process of physical aging caused by thermal aging close to the glass temperature of polymer can be conveniently followed by measuring the number of dye

Construction of a New Acidic Covalent Organic Framework and Its Application as Robust Catalyst for the Synthesis of Imidazoles

Morteza Torabi, AmirMahdi Tavassoli, Meysam Yarie, Mohammad Ali Zolfigol*

Corresponding Author E-mail: mzolfigol@yahoo.com

Department of Organic Chemistry, Faculty of Chemistry and Petroleum Sciences, Bu-Ali Sina University, Hamedan, Iran.

Abstract: Herein, we delve to synthesis of new acidic covalent organic framework *via* post modification of COF by sulfonic acid tags. The reported COF due to having acidic cites in its structure and high specific surface area, is an excellent candidate as heterogeneous catalyst for the multicomponent synthesis of imidazole derivatives.

Keywords: Catalyst; COF; Imidazole; Multicomponent reaction

Introduction

Covalent organic frameworks (COFs) are constructed by connection of different organic units into on system [1,2]. Thanks to designable, durable and crystalline building blocks of COFs, these materials have attracted the attention of most scientists [3]. Meanwhile, COFs have high surface area, adjustable pore size, outstanding thermal and chemical stability, environmental sustainability, law density, and easy functionalization at the molecular level [4,5]. In recent years several applications such as energy storage and conversion, photocatalyst, organocatalyst, electrocatalyst, gas separation, sensor, medicinal and drug delivery have been emerged for COF-based materials [6, 7]. According to literature, modified COFs by acidic sections can be unique and fantastic candidate as catalyst for chemical transformations [8]. Imidazole derivatives have been known as the main marketed drug agents such as anti-inflammatory, anticancer, carboxypeptidase inhibitors, antiaging agents, hemeoxygenase inhibitors, anticoagulants, antiviral, antifungal, and antidepressant agents [9-12].

Experimental Section

In experimental section, imidazole derivatives were synthesized by using aromatic aldehyde derivatives, benzyl, ammonium acetate and 4,4'-methylenedianiline as starting materials under solvent-free conditions at 110 $^{\circ}$C and in the presence of COF-SO$_3$H catalyst (Scheme 1).

R= H, 4-Cl, 2-Cl, 2,4-(Cl)$_2$, 4-Br, 4-OH, 3-OH, 4-F, 4-CN
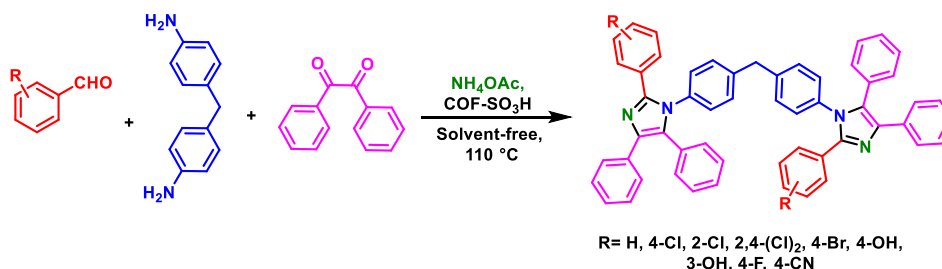
Scheme 1: synthesis of imidazole derivatives by using COF-SO$_3$H as catalyst

Results and Discussion

The synthesized COF-SO$_3$H was characterized by using FT-IR, XRD, FESEM, TEM, EDS/Mapping, TGA and BET analyses. According to XRD pattern, existence of sharp peak at 6.6 °, the catalyst has good crystalline structure (figure 1). Moreover, FESEM images show the ordered rod-like morphology (Figure 2).
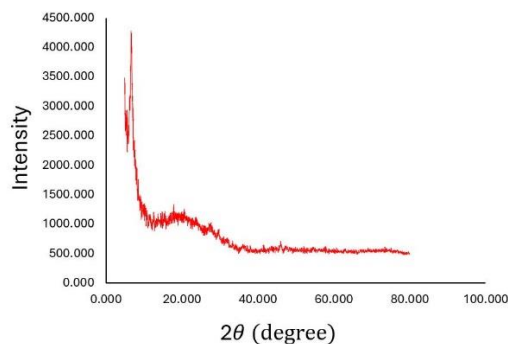
Fig.1: XRD pattern of COF-SO$_3$H

22nd Iranian Chemistry Congress (ICC22)
Iranian Research Organization for Science and Technology (IROST)
13-15 May 2024

03231-97589
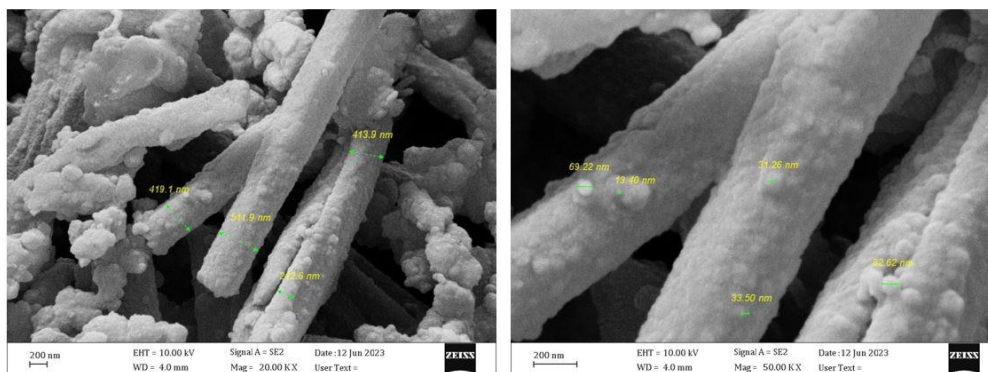
Fig.2: SEM images of COF-SO₃H

Conclusions

In conclusion, we have demonstrated the synthesis of a new acidic COF via reduction of imine moieties of COF and post modification by butane sultone. The orderd morphology, high porosity and active cites of COF-SO₃H converted it as an ideal and benefitial catalyst for multicomponent reactions. Hence, COF-SO₃H was successfully applied as heterogeneous catalyst for the synthesis of imidazoles. The generality of catalytic performance of COF-SO₃H for the preparation of variant imidazoles was investigated and most of products have good yields and short reaction times.

References

[1] Yaghi, O. M. (2016). Reticular Chemistry Construction, Properties, and Precision Reactions of Frameworks. *Journal of the American Chemical Society, 138*(48), 15507-15509.

[2] Freund, R., Canossa, S., Cohen, S. M., Yan, W., Deng, H., Guillerm, V., ... & Diercks, C. S. (2021). 25 years of reticular chemistry. *Angewandte Chemie International Edition, 60*(45), 23946-23974.

[3] Cote, A. P., Benin, A. I., Ockwig, N. W., O'Keeffe, M., Matzger, A. J., & Yaghi, O. M. (2005). Porous, crystalline, covalent organic frameworks. *science, 310*(5751), 1166-1170.

[4] Qi, S. P., Guo, R. T., Bi, Z. X., Zhang, Z. R., Li, C. F., & Pan, W. G. (2023). Recent Progress of Covalent Organic Frameworks-Based Materials in Photocatalytic Applications: A Review. *Small, 19*(48), 2303632.

[5] Diercks, C. S., Kalmutzki, M. J., & Yaghi, O. M. (2017). Covalent organic frameworks—organic chemistry beyond the molecule. *Molecules, 22*(9), 1575.

[6] Huang, L., Yang, J., Asakura, Y., Shuai, Q., & Yamauchi, Y. (2023). Nanoarchitectonics of hollow covalent organic frameworks: Synthesis and applications. *ACS nano, 17*(10), 8918-8934.

[7] Guan, X., Chen, F., Fang, Q., & Qiu, S. (2020). Design and applications of three dimensional covalent organic frameworks. *Chemical Society Reviews, 49*(5), 1357-1384.

[8] Yao, B. J., Wu, W. X., Ding, L. G., & Dong, Y. B. (2021). Sulfonic acid and ionic liquid functionalized covalent organic framework for efficient catalysis of the Biginelli reaction. *The Journal of Organic Chemistry*, *86*(3), 3024-3032.

[9] Hossain, M., & Nanda, A. K. (2018). A review on heterocyclic: synthesis and their application in medicinal chemistry of imidazole moiety. *Science, 6*(5), 83-94.

[10] Rani, N., Sharma, A., & Singh, R. (2015). Trisubstituted imidazole synthesis: A review. Mini-Review. *Org. Chem, 12*(1), 34-65.

[11] Zheng, X., Ma, Z., & Zhang, D. (2020). Synthesis of imidazole-based medicinal molecules utilizing the van leusen imidazole synthesis. *Pharmaceuticals, 13*(3), 37.

[12] Shalini, K., Sharma, P. K., & Kumar, N. (2010). Imidazole and its biological activities: A review. *Der Chemica Sinica, 1*(3), 36-47.

22nd Iranian Chemistry Congress (ICC22)
Iranian Research Organization for Science and Technology (IROST)
13-15 May 2024

03231-97589

Research Development on Biochar Functionalized Cupper-L-Histidine: Application to Aniline Synthesis

Mahrokh Farrokh, Maryam Hajjami*, Sepideh Jalali-mola, Mohammad Ali Zolfigol*

Corresponding Author E-mail: zolfi@basu.ac.ir, mhajjami@yahoo.com

Department of Organic Chemistry, Faculty of Chemistry and Petroleum Sciences, Bu-Ali Sina University, Hamedan.

Abstract: Each year, different species of catalysts are produced that play an important role in various sciences such as chemistry, medicine, and biotechnology. It would be valuable to implement the principles of green chemistry in their production. This way, we can utilize waste materials for recycling and converting them into precious compounds. In our study, we aimed to use olive pomace, food industry waste, as biomass to produce biochar nanoparticles. The surface of the biochar was coated with L-histidine ligand, and cupper metal was added for catalytic applications in the synthesis of aniline derivatives. Another notable feature of this catalyst is its reusability. It maintained significant efficiency even after multiple uses in reactions. To characterize the novel catalyst, we employed various techniques such as FT-IR, EDS, XRD, TGA, FE-SEM, and ICP. These analyses confirmed that our catalyst was well-formed [1-2].

Keywords: biochar catalysts; reduction reaction; amines derivatives, amino acids.

Introduction

Amino acids are one of the basic organic materials in structure of proteins and form about 20% of human body. They belong in one of this two branches: essential or nonessential amino acids. This class of compounds contain two functional group, amine and carboxyl group, which are the center of chemical reactions. Present of two functional group given amphoteric properties to Amino acids. As one of the significant applications of them can refer to their catalytic properties which put them in class of green catalysts. in some cases amino acids and their salts have been used as solvent and absorbent, which they are owed these properties to their functional groups [3-4].

During the recent decades use of modified nanoparticles as heterogeneous catalysts in order to synthesis of organic compounds are very common. Biochar nanoparticles are one of the newest supports to immobilization of organic moieties. They are class of porous materials which earn from pyrolysis of renewable resources, biomasses under limited oxygen condition [4] .In recent years widespread of nano-biochars properties such as catalysis, agriculture and carbon capture application have been noticed. In fact biochar is a solid rich of carbon element so in order to management of agro-food industrial waste its suitable that convert them to biochar as a biosorbents for soil and water treatment. Surface of biochars are rich of functional group which gives the many properties to them. Also the source of biochars determine the physiochemical nature of them. Use of acids, alkali, oxidizing agents and metal ions modification upgrade of biochar attribute. Reduction of nitro group to amines and anilines are one of the

basicreactions which commonly used in organic chemistry synthesis, pharmaceutical industry, explosives and fertilizers [5-7].

in this work L-histidine is used as amino acid for modification of biochar and then complexation with Cu designed it as an efficient catalyst for conversion of nitro to amine and also nitrile to amide compounds .

Experimental Section

Nitro benzenes (1 mmol), sodium tetrahydridoborate (5 mmol) and 0.04 g of catalyst added to a round-bottomed flask and heated to 90 °C. For observation of reaction procedure TLC technique (n-Hexane/Ethyl acetate: 8/2) was used. when reaction completed in order to remove catalyst it separated by filter paper and washed by hot ethylacetate, ethanol and water. then the oily product separated with decanter funnel.
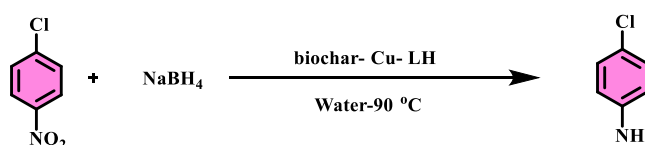
Results and Discussion

Biochar-Cu-LH as a novel heterogeneous catalyst was synthesized, characterized and applied in the synthesis of target organic molecules. The FT-IR spectrum of Biochar, L-Histidine, Biochar-LH , Biochar-Cu- LH is shown in figure 1 . The peak of 1596cm^{-1}, 3417cm^{-1} in A ; These peaks indicate the biochar substrate and B is the diagram of the corresponding amino acid that has a COOH functional group and C By adding amino acid, the peaks related to biochar have been preserved, and in the last step D, with

22nd Iranian Chemistry Congress (ICC22)
Iranian Research Organization for Science and
Technology (IROST)

03231-97589

13-15 May 2024

IROST

the addition of copper metal, in addition to maintaining the peaks of biochar and the appearance of the metal peak, the efficiency of the catalyst increased. Result of FE-SEM techniques which presented in figure 2 shows the morphology and the microstructure image from the surface of Particles of catalyst had a good homogeneity in shape and size. catalyst. images show the quasi- spherical shapes of catalyst particles, with about 50 nm in size. **Figure 1**.
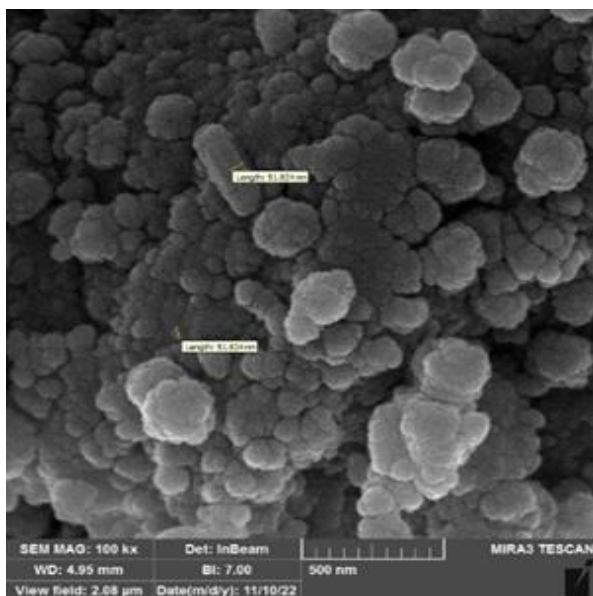
Fig 1: FE-SEM image of Biochar- Cu-LH.

Conclusions

The design of Biochar-Cu-LH as a heterogeneous catalyst was the goal pursued here. Catalyst Despite the easy synthesis and availability of materials and cheapness, the above catalyst easily performs the reduction reaction and creates amine derivatives from nitro-containing derivatives.. The obtained compounds were obtained in a relatively short time and with significant efficiency.

References

[1] Tonouchi, N., & Ito, H. (2017). Present global situation of amino acids in industry. Amino Acid Fermentation,3-14. https://doi.org/10.1007/10_2016_23.

[2] Sang Sefidi, V., & Luis, P. (2019). Advanced Amino Acid-Based Technologies for CO_2 Capture: A Review. Industrial & engineering chemistry process design and development, 58(44). https://doi.org/10.1021/acs.iecr.9b01793.

[3] Goswami, L., Kushwaha, A., Singh, A., Saha, P., Choi, Y., Maharana, M., ... & Kim, B. S. (2022). Nano-biochar as a sustainable catalyst for anaerobic digestion: a synergetic closed-loop approach. *Catalysts*, 12(2), 186.

https://doi.org/10.3390/catal12020186.

[4] Chen, W., Meng, J., Han, X., Lan, Y., & Zhang, W. (2019). Past, present, and future of biochar. *Biochar*, 1, 75-87. https://doi.org/10.1007/s42773-019-00008-3.

[5] Cortes-Clerget, M., Lee, N. R., & Lipshutz, B. H. (2019). Synthetic chemistry in water: applications to peptide synthesis and nitro-group reductions. *Nature Protocols*, 14(4), 1108-1129. https://doi.org/10.1038/s41596-019-0130-1.

[6] Sun, S., Quan, Z., & Wang, X. (2015). Selective reduction of nitro-compounds to primary amines by nickel-catalyzed hydrosilylative reduction. *RSC advances*, 5(103), 84574-84577. https://doi.org/10.1039/C5RA17731F.

[7] Moradi, P., & Hajjami, M. (2021). Magnetization of biochar nanoparticles as a novel support for fabrication of organo nickel as a selective, reusable and magnetic nanocatalyst in organic reactions. *New Journal of Chemistry*, 45(6), 2981-2994. https://doi.org/10.1039/D0NJ04990E.

22nd Iranian Chemistry Congress (ICC22)
Iranian Research Organization for Science and Technology (IROST)
13-15 May 2024

03231-97589

IROST

Fabrication of Cationic Antibiotic Affinity-Based Sulfated Alginate Nanofibers for Drug Delivery

Maryam Zare Gachi [a], Atefeh Solouk [*a], Mahdi Shafieian[a], Hamed Daemi[*b]

Co-corresponding Authors Email: H.daemi@royaninstitute.org (H.Daemi), atefeh.solouk@aut.ac.ir (A.Solouk)

[a] Department of Biomedical Engineering, Amirkabir University of Technology (Tehran Polytechnic), Tehran, Iran.

[b] Department of Cell Engineering, Cell Science Research Center, Royan Institute for Stem Cell Biology and Technology, ACECR, Tehran, Iran.

Abstract: The sulfate functional groups can effectively interact with cationic antibiotics, load high doses of drugs and release them in a sustained manner. Sulfated polymeric was selected as an excellent choice for loading of cationic antibiotics. Chemical structure, release and morphological properties of nanofibers were investigated with FTIR, UV and SEM.

Keywords: Antibiotics, Sulfated Alginate, Drug Delivery

Introduction

In general, electrospun scaffolds have been shown to gradually release the encapsulated drug over days to months depending on their composition. Various studies have investigated sulfated group interactions in the drug delivery systems of growth factors, drugs, and cells [1]. Several pharmaceutical drugs constitute small cationic molecules; therefore, the evaluation of their complexes with sodium alginate and its sulfated derivatives (SSA) is likely to provide valuable results in the development of new delivery systems [2]. The purpose of this work was to load cationic drugs in polymer nanofibers with negatively charged functional sulfate groups that can electrostatically interact with cationic biomolecules, thereby increasing the antibiotic delivery capacity of SSA (Fig. 1a).
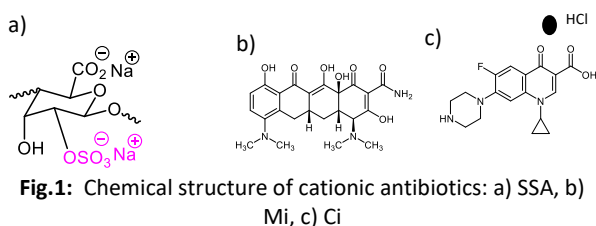
Fig.1: Chemical structure of cationic antibiotics: a) SSA, b) Mi, c) Ci

Experimental Section

To prepare the Polyvinyl alcohol (PVA)/Sodium Sulfated
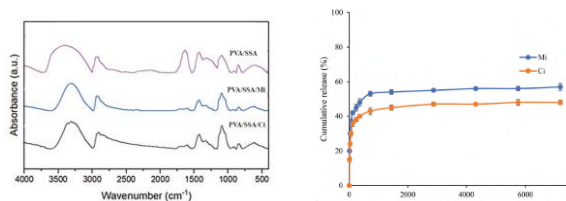
Fig. 2: a) The FTIR spectra of PVA/SSA, Mi and Ci loading, b) The *in vitro* drug release profiles of drug loading nanofibres

alginate (SSA) electrospun solution [3] loaded with the drug, PVA solution (10 wt%) and SSA (7 wt%) were obtained by dissolving separately in distilled water with stirring at 80°C and 40°C for 2 h, respectively. Then, aqueous solutions of SSA were distinctly mixed with PVA solution at a 70:30 weight ratio for 1 h. Samples were mixed with 0.01% v/v Triton X-100. Subsequently, specified drugs, including ciprofloxacin (Ci) and minocycline (Mi) (Fig. 1b, c), at a concentration of 2 mg/mL were added to the solution. The solutions were placed in a stirrer for 1 h at room temperature. After that, the best values of parameters were 1mL/h for feeding rate, 22-25 kV voltages, and 12-15 cm for the nozzle tip to the collector distance. Nanofibrous scaffolds were collected using a grounded cylindrical steel model collector for at least 2 h. Finally, after crosslinking nanofibers with Ca^{2+}, the samples prepared for characterization and release analysis.

Results and Discussion

FTIR analysis was used to confirm the structure of drug-loaded PVA/SSA. As displayed in Fig 2a, adsorption bands appearing at 1262 cm^{-1} was confirmed S=O and 3471 cm^{-1} in the SSA sample, which were assigned to a C–O–SO3 and OH groups, respectively. When SSA formed an interaction with Mi, these bands were shifted at 1268 cm^{-1} and 3411 cm^{-1}, respectively. The adsorption band appearing at 1632 cm^{-1} in SSA is attributed to the carboxylate group that was shifted to 1655 cm^{-1} in interaction. These results indicate that the sulfate and hydroxyl groups of SSA can interact with Mi. Furthermore, the FTIR spectrum revealed that Mi had a band at 1650 cm^{-1} corresponding to C=O stretching on one of the carbons related to the chelating site. This adsorption band was shifted to 1608 cm^{-1} in Complex, which confirms an interaction between Mi. Ciprofloxacin shows bands at 3042 cm^{-1} and 1279 cm^{-1} for -OH stretching and bending, respectively, 1583 cm^{-1} for aromatic C—C stretching, and 1019 cm^{-1} for -CF stretching [4, 5].

22nd Iranian Chemistry Congress (ICC22)
Iranian Research Organization for Science and
Technology (IROST)
13-15 May 2024

03231-97589

ISC

IROST

The morphological properties of the nanofibers were evaluated by SEM. As presented in Fig. 3, smooth, bead-free, and thinner nanofibers with an average fiber diameter of 140±20 nm were obtained non-modified PVA/SSA scaffolds compared with the drug-loaded samples. The average fiber diameter increased from approximately 140 to 160 and 200 nm for the non-modified and Ci- and Mi-loaded fibers, respectively. Among the used drugs, the minocycline drug with the electrical charge of +2 chemical groups has significantly increased the thickness of the fibers and beads. While, drugs containing one positive chemical group, and solution polymers with ciprofloxacin loaded has nanofibers without beads. The Mi solution had low viscosity. We believe that the viscosity of the polymer solution can be affected by the electrospinning process. Therefore, Mi loaded with an increased nanofiber diameter decreases the electrical conductivity and viscosity [6]. Furthermore, after loading the drugs into the samples, a few beads were observed in the mat because of the reduction in the viscosity of the electrospun solution and spraying droplets. It is worth mentioning that the number of beads is not sufficient to cause structural failure or a significant reduction in strength.
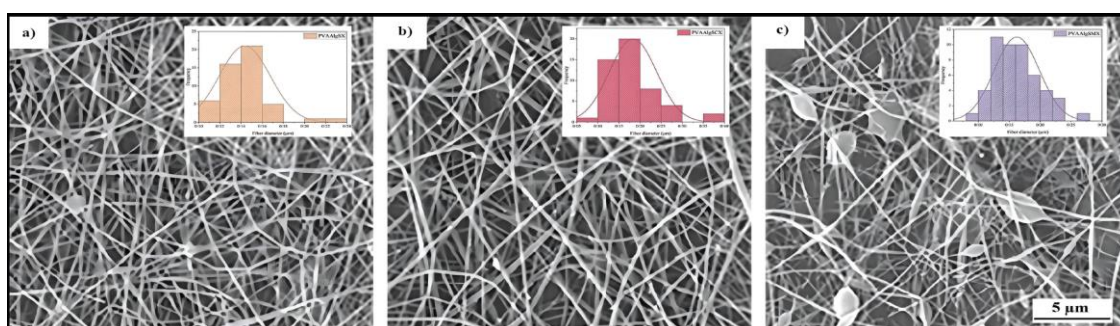
Fig.3: The SEM images of electrospun PVA/SSA nanofibers with different drug loaded, respectively: a) no drug, b) Ci, c) Mi. (10X)

The amount of drug released by the antibiotic-loaded nanofibers is shown in Fig. 2b. the absorbance of each sample was measured using a UV spectrophotometer for Ci and Mi at λ_{max} = 220 and 280 nm, respectively. The concentration of the drug in each aliquot was calculated on the basis of a calibration curve for the drug in PBS. By 5 days, Ci-loaded nanofibrous mat had a higher release rate than those loaded with Mi. Furthermore, the amount of release of drugs in nanofibers were continuous for 5 days. The burst release from the Ci-loaded nanofibrous was lower than that from the Mi-loaded nanofibrous. Interestingly, no comparable difference was observed between the release results of PVA/SSA nanofibers loaded with Mi and Ci. 54.63 ± 1.42% and 45.42 ± 1.93% of Mi and Ci were released from PVA/SSA nanofibers after 24 h and 5 days. Mi drug has more positive charges than that in Ci drug, and we think that it can be affected by loading and release profiles.

Conclusions

According to previous studies, we utilized modified alginate with a sulfated group for improving the electrospinnability alginate and increased the amount of sulfated alginate in nanofibers compared with neat alginate. In addition, we used the sulfated group for long-term release with a strong electrostatic interaction between sulfate and cationic drugs. We used two drugs to compare drug release and electrospinnability.

References

[1] Amhare, A. F., Lei, J., Deng, H., Lv, Y., Han, J., & Zhang, L. (2021). Biomedical application of chondroitin sulfate with nanoparticles in drug delivery systems: systematic review. Journal of Drug Targeting, 29(3), 259-268.

[2] Nazemi, Z., Nourbakhsh, M. S., Kiani, S., Heydari, Y., Ashtiani, M. K., Daemi, H., & Baharvand, H. (2020). Co-delivery of minocycline and paclitaxel from injectable hydrogel for treatment of spinal cord injury. Journal of controlled release, 321, 145-158.

[3] Daemi, H., Mashayekhi, M., & Modaress, M. P. (2018). Facile fabrication of sulfated alginate electrospun nanofibers. Carbohydrate polymers, 198, 481-485.

[4] Mansur, H. S., Sadahira, C. M., Souza, A. N., & Mansur, A. A. (2008). FTIR spectroscopy characterization of poly (vinyl alcohol) hydrogel with different hydrolysis degree and chemically crosslinked with glutaraldehyde. Materials Science and Engineering: C, 28(4), 539-548.

[5] Ju, T., Gaisford, S., & Williams, G. R. (2024). Ciprofloxacin-loaded electrospun nanofibres for antibacterial wound dressings. Journal of Drug Delivery Science and Technology, 91, 105264.

[6] Drew, C., Wang, X., Samuelson, L. A., & Kumar, J. (2003). The effect of viscosity and filler on electrospun fiber morphology. Journal of Macromolecular Science, Part A, 40(12), 1415-1422.

22nd Iranian Chemistry Congress (ICC22)
Iranian Research Organization for Science and Technology (IROST)
13-15 May 2024

ISC
03231-97589

IROST

Synthesis and Spectroscopic Characterization of P(O)(OC$_6$H$_5$)$_2$(NHC$_6$H$_4$-4-Cl) and P(O)(OC$_6$H$_5$)$_2$(NHC$_6$H$_4$-4-C$_2$H$_5$)

Yalda Khoshakhlagh Ostad, Mehrdad Pourayoubi*, Tahereh Sayyadi Kalateh-Bali

Corresponding Author E-mail: pourayoubi@um.ac.ir

Department of Chemistry, Faculty of Science, Ferdowsi University of Mashhad, Mashhad, Iran.

Abstract: The P(O)(OC$_6$H$_5$)$_2$(NHC$_6$H$_4$-4-Cl) (I) and P(O)(OC$_6$H$_5$)$_2$(NHC$_6$H$_4$-4-C$_2$H$_5$) (II) phosphoramides were synthesized and characterized. In the IR spectra, the bands centered at 3180 cm^{-1} for (I) and at 3172 cm^{-1} for (II) associate to the NH stretching frequencies, and the P=O stretching bands appear at 1231 and 1195 cm^{-1}, respectively. In the mass spectra, the molecular ion peaks are revealed (m/z = 359 for (I) and 353 for (II)). Phosphorus signals for (I) and (II) appear at –6.96 and –6.36 ppm, respectively.

Keywords: NMR Spectroscopy; Synthesis; Diphenyl Phosphoryl Chloride.

Introduction

Phosphoramides are commonly used as insecticides and acaricides in agriculture as well as antiviral and anticancer agents in pharmaceutical research. Some derivates are used as flame retardants in plastics and textiles [1,2]. Here, the synthesis and characterization of two (P(O)(OC$_6$H$_5$)$_2$(NHC$_6$H$_4$-4-Cl) (I) and P(O)(OC$_6$H$_5$)$_2$(NHC$_6$H$_4$-4-C$_2$H$_5$) (II), Fig. 1) phosphoramides are investigated.
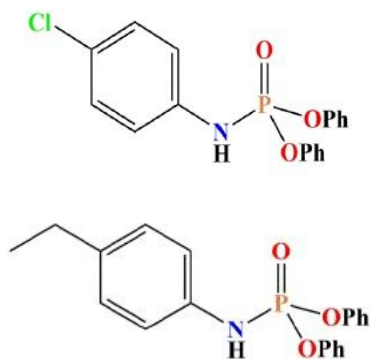
Fig. 1: Chemical structures of (I) (left) and (II) (right).

Experimental Section

For the synthesis of (I), a solution of 4-chloroaniline (2 mmol) in dry chloroform was added dropwise to a solution of diphenyl phosphoryl chloride (1 mmol) in the same solvent. After stirring for 4 hours, the reaction was stopped, the solvent was removed and the obtained solid was washed with distilled water. The crystallization solvent was chloroform and n-heptane (5:1 *v/v*). The formulation is C$_{18}$H$_{15}$ClNO$_3$P.

MW: 359.75 g/mol. **m.p:** 112 °C. **IR** (KBr disc, υ, cm^{-1}): 3180, 3147, 3057, 2948, 1592, 1231, 1179, 979, 758. **MS** (70 eV, EI: m/z (%)) = 361 (18) [M]$^+$ (^{37}Cl), 359 (93) [M]$^+$ (^{35}Cl), 126 (10) [NC$_6$H$_5$^{35}Cl]$^+$, 94 (12) [C$_6$H$_6$O]$^+$, 77 (7) [C$_6$H$_5$]$^+$. ^{31}P{^{1}H} NMR (DMSO-d_6, 121 MHz, 297.4 K, 85% H$_3$PO$_4$): δ (ppm) = –6.96 (s). ^{1}H NMR (DMSO-d_6, 301 MHz, TMS): δ (ppm) = 9.08 (d, $^2J_{H-P}$ = 10.1 Hz, 1H), 7.45 – 7.37 (m, 6H), 7.29 – 7.22 (m, 8H). ^{13}C{^{1}H} NMR (DMSO-d_6, 75 MHz, 297.9 K, TMS): δ (ppm) = 150.45 (d, $^2J_{C-P}$ = 6.4 Hz), 139.34 (s), 130.49 (s), 129.66 (s), 126.07 (s), 125.87 (s), 120.59 (d, $^3J_{C-P}$ = 4.7 Hz), 119.84 (d, $^3J_{C-P}$ = 8.2 Hz).

For the synthesis of (II), to a solution of diphenyl phosphoryl chloride (1 mmol) in dry chloroform, a solution of 4-ethyl aniline (2 mmol) in the same solvent was added under stirring. After 4 hours, the solvent was removed and the obtained solid was washed with distilled water. The crystallization solvent was chloroform and n-heptane (4:1 *v/v*). The formulation is C$_{20}$H$_{20}$NO$_3$P.

MW: 353.36 g/mol. **m.p:** 115°C. **IR** (KBr disc, υ, cm^{-1}): 3475, 3172, 2956, 1593, 1492, 1294, 1195, 992, 773. **MS** (70 eV, EI: m/z (%)) = 353 (60) [M]$^+$, 352 (89) [M – 1]$^+$, 351 (98) [M – 2]$^+$, 337 (88) [M – CH$_4$]$^+$, 93 (48) [C$_6$H$_5$O]$^+$, 29 (60) [C$_2$H$_5$]$^+$. ^{31}P{^{1}H} NMR (DMSO-d_6, 121 MHz, 297.4 K, 85% H$_3$PO$_4$): δ (ppm) = –6.36 (s). ^{1}H NMR (DMSO-d_6, 301 MHz, TMS): δ (ppm) = 8.82 (d, $^2J_{H-P}$ = 10.7 Hz, 1H), 7.44 – 7.39 (m, 4H), 7.29 – 7.16 (m, 10H), 2.54 (q, $^3J_{H-H}$ = 7.6 Hz, 2H), 1.16 (t, $^3J_{H-H}$ = 7.6 Hz, 3H). ^{13}C{^{1}H} NMR (DMSO-d_6, 75 MHz, 297.9 K, TMS): δ (ppm) = 150.62 (d, $^2J_{C-P}$ = 6.2 Hz), 137.84 (s), 137.44 (s), 130.42 (s), 128.98 (s), 125.70 (s), 120.60 (d, $^3J_{C-P}$ = 4.8 Hz), 118.32 (d, $^3J_{C-P}$ = 7.8 Hz), 27.90 (s), 16.18 (s). The mass and NMR spectra are given in Figures 2 to 5.

Results and Discussion

The N-H protons of (I) and (II) appear as doublets at 9.08 ppm ($^2J_{H-P}$ = 10.1 Hz) and 8.82 ppm ($^2J_{H-P}$ = 10.7 Hz), respectively. The fourteen hydrogen atoms of arene rings are revealed in the range of 7.22 to 7.29 ppm and 7.37 to 7.45 ppm for (I), and 7.16 to 7.29 ppm, 7.39 to

22nd Iranian Chemistry Congress (ICC22)
Iranian Research Organization for Science and
Technology (IROST)
13-15 May 2024

03231-97589

IROST

7.44 ppm for (II). In the ^{13}C{^{1}H} NMR spectra of (I) and (II), eight and ten signals are observed, related to different carbon atoms. The doublet signals at 150.45 ppm ($^2J_{C-P}$ = 6.4 Hz) for (I) and at 150.62 ppm ($^2J_{C-P}$ = 6.2 Hz) for (II) correspond to the *ipso*-carbon atoms of the C_6H_5O moieties. The melting points are 112°C (I) and 115°C (II).
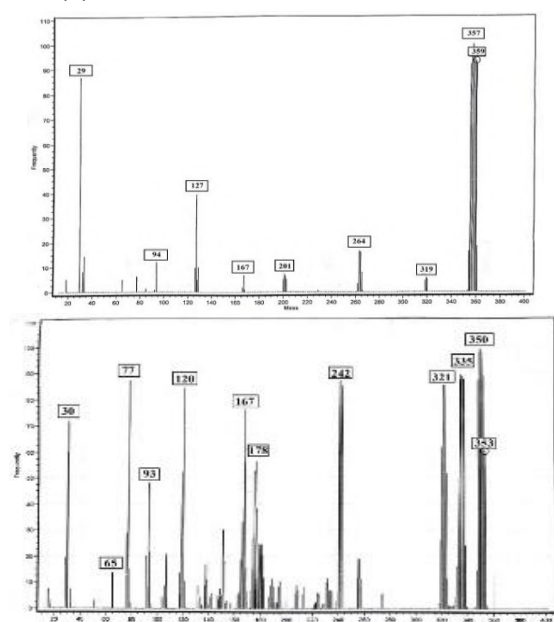
Fig. 2: Mass spectra of (I) (top) and (II) (bottom).
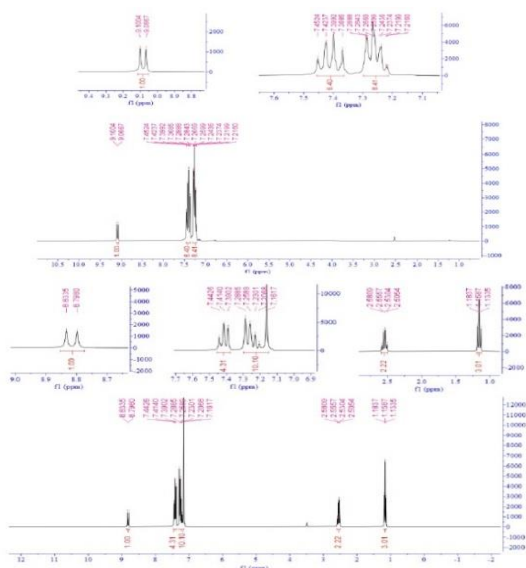
Fig. 3: ^{1}H NMR spectra of (I) (top) and (II) (bottom).
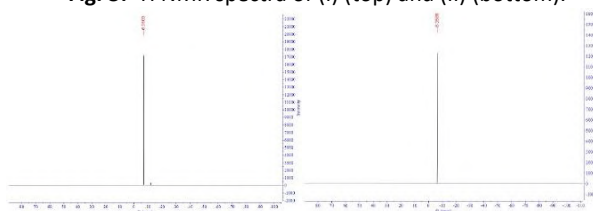
Fig. 4: ^{31}P{^{1}H} NMR spectra of (I) (left) and (II) (right).
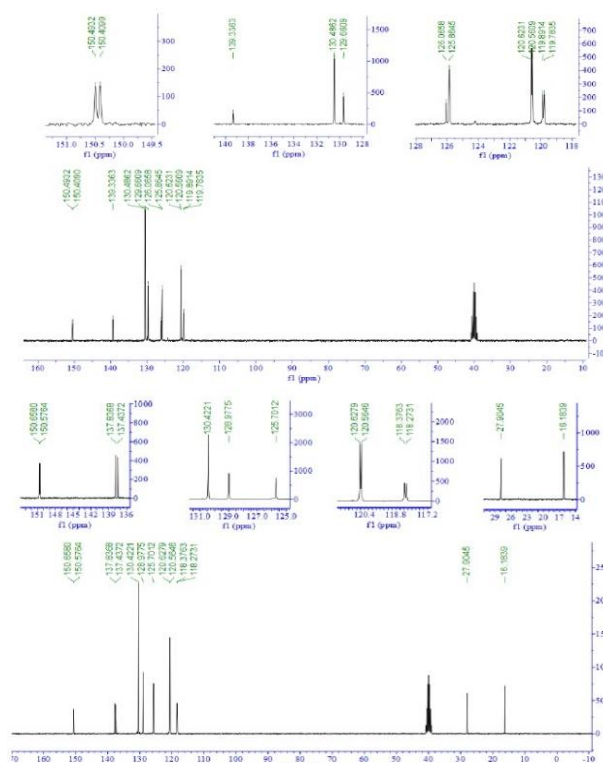
Fig. 5: ^{13}C NMR spectra of (I) (top) and (II) (bottom).

Conclusion

Two new diphenyl phosphoramides were synthesized and investigated using infrared spectroscopy, nuclear magnetic resonance, and mass spectrometry. These compounds were prepared with good yield and purity.

References

[1] Subramanyam, Ch., Venkata Ramana, K., Rasheed, S., Adam, S., & Naga Raju, C. (2012). Synthesis and Biological Activity of Novel Diphenyl N-Substituted Carbamimidoyl phosphoramidate Derivatives, Phosphorus, Sulfur, and Silicon and the Related Elements., 187(12):1419-1433.
https://doi: 10.1080/10426507.2012.745075.
[2] Li, M., Chen, Y., C., Kong, Z., K., Sun, Zh., & Qian, L., (2023). Impact of a Novel Phosphoramide Flame Retardant on the Fire Behavior and Transparency of Thermoplastic Polyurethane Elastomers, ACS Omega., 8, 18151−18164.
https://doi.org/10.1021/acsomega.3c01464.

Synthesis and application of CuO and CuAl$_2$O$_4$ hollow sphere structures as active electrode materials in supercapacitors

Ali Keshavarz [a], Javad Tashkhourian [*a], Reza Khalifah [b], Maryam Rajabzadeh [b]

Corresponding Author E-mail: Tashkhourian@shirazu.ac.ir

[a] Chemistry Department, Shiraz University, Shiraz, Iran.

[b] Chemistry Department, Shiraz University of Technology, Shiraz, Iran.

Abstract: In this study, two hollow sphere structures, CuO and CuAl$_2$O$_4$, were synthesized and their supercapacitor behavior was investigated by cyclic voltammetry and galvanostatic charge-discharge methods. The obtained capacitance was 210 and 160 F g^{-1} for CuAl$_2$O$_4$ and CuO in a three electrode system and at 1 A g^{-1} current density, respectively. Also, CuAl$_2$O$_4$ showed 24.7 Wh kg^{-1} and 700 W kg^{-1} energy and power density, in asymmetric supercapacitor respectively. After 3000 charge and discharge cycles, 78.1% of the initial capacitance of the device was maintained.

Keywords: Supercapacitor; Energy storage; Pseudocapacitor; Energy density; Power density

Introduction

The use of porous materials is very important in the field of supercapacitors, because porosity directly affects their performance and efficiency. Higher porosity leads to larger surface area, which is an important feature for high performance supercapacitors [1, 2]. Porous structures play an important role in increasing the specific surface area, pore volume, and conductivity of electrode materials, thereby effectively improving charge accumulation and double layer capacity [3]. Therefore, in order to investigate the effect of porosity on supercapacitor performance, two porous compounds CuO and CuAl$_2$O$_4$ were used. Also, the characterizatin of the synthesized compounds was done by the use of FE-SEM, HR-TEM, XRD, FT-IR, BET and XPS methods. Although, cyclic voltammetry (CV), galvanostatic charge-discharge (GCD) and electrochemical impedance spectroscopy analyzes were applyied to check the electrochemical performance.

Experimental Section

To conduct electrochemical tests, a three-electrode arrangement was set up in a 6 M KOH solution. A slurry was coated on nickel foam by combining the synthesized material (as the active component), carbon black (as a conductivity enhancer), and polytetrafluoroethylene (PTFE, as a binder) in an 8:1:1 ratio in a container. The reference electrode consisted of Ag/AgCl/KCl (3 M), with a Pt wire serving as the counter electrode.

Results and Discussion

The synthesized CuO and CuAl$_2$O$_4$ structures were characterized using non-destructive techniques (Fig. 1), specifically scanning electron microscopy (SEM) and energy-dispersive X-ray spectroscopy (EDX).
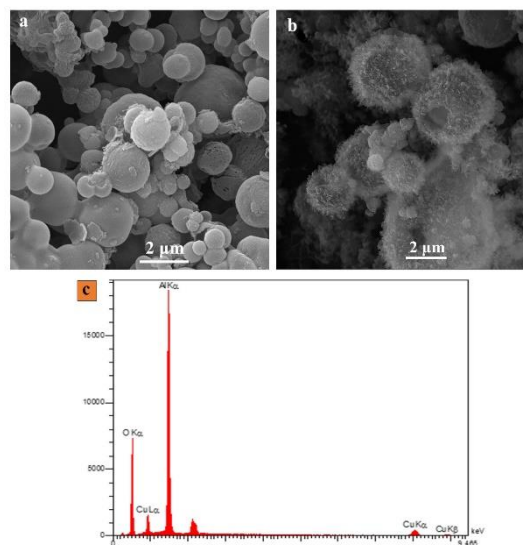
Fig. 1: (a) SEM imageof CuO, (b) SEM image of CuAl$_2$O$_4$ and (c) Elemental spectrum and composition (wt%) of CuAl$_2$O$_4$.

The electrochemical performance of CuO and CuAl$_2$O$_4$ in a 6 M KOH electrolyte was evaluated using CV and GCD methods (Fig. 2). CV curves obtained for CuO and CuAl$_2$O$_4$ at a scan rate of 5 mV s^{-1} are shown in Figure 2a. The presence of oxidation-reduction peaks in the CV diagram indicates the pseudocapacitive behavior of these electrode compounds. According to more area under the curve, the composition of CuAl$_2$O$_4$ showed a higher specific capacitance.

22nd Iranian Chemistry Congress (ICC22)
Iranian Research Organization for Science and
Technology (IROST)
13-15 May 2024

03231-97589
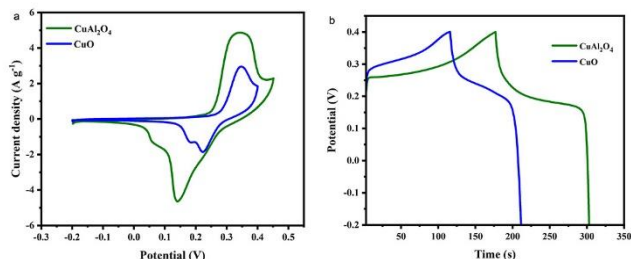
Fig. 2: (a) CV of CuO and $CuAl_2O_4$ at 5 mV s^{-1} and (b) GCD of CuO and $CuAl_2O_4$ at 1 A g^{-1} current density.

GCD curves indicated that both electrode materials show pseudocapacitive behavior. This pseudocapacitive behavior was also observed in the CV diagrams with the presence of oxidation-reduction peaks. According to the relationship related to calculating the specific capacity, the longer the discharge time, the higher the specific capacitance. Therefore, having a longer discharge time, $CuAl_2O_4$ showed better supercapacitor performance in terms of charge storage and specific capacitance (Figure 2b). To make the configuration of two asymmetric electrodes and check the electrochemical performance of the supercapacitor, $CuAl_2O_4$ compound was used as the positive electrode and activated carbon (AC) compound was used as the negative electrode. The CV diagrams of the combination of $CuAl_2O_4$ and AC with a scanning rate of 5 mV s^{-1} are presented in Figure 3a. The pseudocapacitive behavior of $CuAl_2O_4$ in the potential range of -0.2 to 0.45 V and also the capacitive behavior of activated carbon in the potential range of -0.95 to 0 V can be seen well. The GCD diagrams of the $CuAl_2O_4$ // AC asymmetric supercapacitor are presented in Figure 3b. From the GCD diagram, the pseudocapacitive behavior of the supercapacitor can be well observed. It is shown in Figure 3c that, by increasing the current density by 6 times, the specific capacitance provided is almost half of the specific capacitance provided in the current density of 1 A g^{-1}, which indicates the proper rate performance of the device. It was observed that at a current density of 3 A g^{-1}, 78.1% of its initial specific capacitance has been maintained after 3000 charge and discharge cycles (Figure 3d).

Conclusions

In this work, the supercapacitor performance of two porous CuO and $CuAl_2O_4$ structures was investigated and compared. According to the analyzes and confirmation of the synthesis of these two compounds, BET analysis showed that the $CuAl_2O_4$ compound has a much larger surface area and pore volume than CuO, which can be one of the reasons for the better performance of $CuAl_2O_4$. Besides more porosity, the presence of aluminum as an additional oxidation-reduction substrate can be another

reason for improving the performance of $CuAl_2O_4$. The calculated specific capacity of $CuAl_2O_4$ and CuO at a current density of 1 A g^{-1} is 210 and 160 F g^{-1}, respectively. Also, in the asymmetric supercapacitor made $CuAl_2O_4$ // AC, the energy and power density were 24.7 Wh kg^{-1} and 700 W kg^{-1}, respectively. The achieved cyclic stability shows reaching 78.1% of the initial capacity after 3000 charge-discharge cycles.
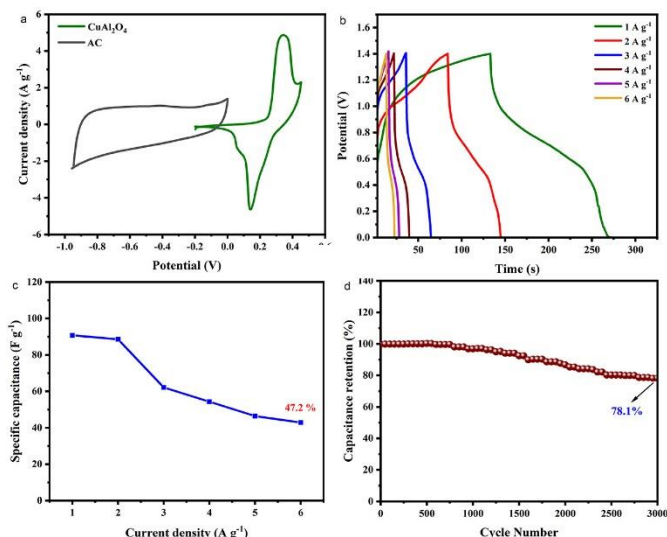
Fig.3: (a) CV of $CuAl_2O_4$ and AC (b) GCD of asymmetric device (c) Rate performance of device and (d) Cycle life of device.

References

[1] M. Sethi, H. Bantawal, U.S. Shenoy, D.K. Bhat (2019). Eco-friendly synthesis of porous graphene and its utilization as high performance supercapacitor electrode material. *Journal of Alloys and Compounds,* 799, 256–266.

[2] P. De, J. Halder, C.C. Gowd, S. Kansal, S. Priya, S. Anshu, A. Chowdhury, D. Mandal, S. Biswas (2023). Role of porosity and diffusion coefficient in porous electrode used in supercapacitors – Correlating theoretical and experimental studies, *Electrochemical Science Adv,* 3, e2100159.

[3] A. Keshavarz, J. Tashkhourian, S.F. Nami-Ana (2023). Designing an asymmetric supercapacitor based on Co(OH)2@PANI nanocomposite synthesized via a facile hydrothermal method, *Journal of Energy Storage*, 73, 108825.

The new mercury-thiophosphoramide complex: Synthesis, crystal structure and spectroscopic characterization of {[(C5H9)NH]2[(C6H10)NH]P(S)}2HgCl2

Narjess Peyman [a], Mehrdad Pourayoubi*[a], Mojtaba Keikha [a], Arie van der Lee [b]

Corresponding Author E-mail: pourayoubi@um.ac.ir

[a] Department of Chemistry, Faculty of Science, Ferdowsi University of Mashhad, Mashhad, Iran.
[b] Institut Européen des Membranes, Université de Montpellier, 34095 Montpellier, France.

Abstract: The synthesis, spectral characteristics, and X-ray crystal structure of {[(C5H9)NH]2[(C6H10)NH]P(S)}2HgCl2 were investigated. This compound crystallizes in the monoclinic space group *C2* and the asymmetric unit contains one complete molecule and one-half of a molecule. In the crystal structure, a three-dimensional assembly is mediated from N–H...Cl and C–H...S hydrogen bonds.
Keywords: Thiophosphoramide; Coordination Chemistry; Mercury

Introduction

Thiophosphoramides have been known as promising compounds with potential applications in medicine [1] and anti-inflammatory properties [2], as well as their utility in catalysis [3], pesticide activity [4], and coordination chemistry [5]. These compounds can be introduced with the general formula $P(S)(NR^1R^2)(R^3)(R^4)$, where R^1/R^2 = hydrogen or any organic group; and R^3 and R^4 = amine/amide, halogen/hydroxyl, or even alkoxy/aryloxy [6]. Thiophosphoramides offer a soft center (S atom) for the formation of coordination bonds with metals, specifically soft metals such as mercury.

Mercury with a d^{10} electronic configuration adopts a versatile coordination environment with a range of coordination numbers, from two and three [7] to higher, with a variety of coordination shapes.

In the present article, we report on the synthesis and structural/spectroscopic features of a new thiophosphoric triamide-mercury complex.

Experimental Section

For the preparation of the title complex, a solution of $HgCl_2$ (2 mmol) in acetonitrile was added dropwise to a solution of $(C_6H_{11}NH)P(S)[NHC_5H_9]_2$ (4 mmol) in methanol under stirring in a reflux condition for 24 hours. Suitable single crystals were obtained from the gradual evaporation of the solvent at room temperature. **IR** (KBr, ū, cm^{-1}): 3240, 3052, 2918, 2860, 1591, 1488, 1242, 1196, 1162, 1075, 1013, 929, 894, 799, 744, 686, 651. **1H NMR** (300.85 MHz, CDCl3, 294.5 K, TMS): δ = 1.11 – 1.98 (*m*, 52H, CH2), 3.09 (*m*, 2H, NH), (*m*, 6H, CH), 3.89 (*m*, 4H, NH). **31P{1H}** NMR (121.78 MHz, CDCl3, 303.2 K, 85% H3PO4): δ = 54.59 (*s*).
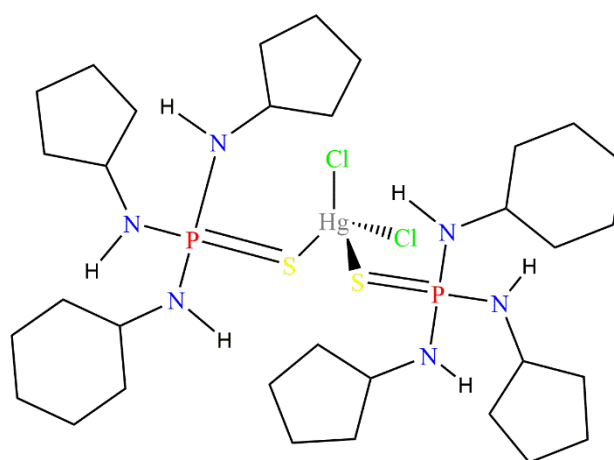
Fig. 1: Chemical structure of the title compound

Results and Discussion

The $^{31}P\{^{1}H\}$ signal (in CDCl3) is observed at 54.59 ppm. In the 1HNMR spectrum, multiplet signals are observed in the range of 1.11-1.98 ppm for the CH and CH2 protons of (C5H9) and (C6H11) fragments.

This complex crystallizes in the monoclinic space group *C2*, and the asymmetric unit contains one complete molecule and one-half of a molecule (molecules a and b, which are shown with yellow and purple colors in Fig. 2). The complete molecule of b is generated by a C2 axis at the Hg atom (which bisects the Cl47^i—Hg46—Cl47 and S48^i—Hg46—S48 angles).

The Hg atom in these molecules adopts a distorted tetrahedral S2HgCl2 geometry with bond angles ranging from 97.27(8)° (Cl3—Hg1—S25) to 135.29(8)° (S4—Hg1—S25) for yellow molecule and 102.38(10)° (Cl47^i—Hg46—Cl47) to 113.65(8)° (S48^i—Hg46—Cl47) for purple molecule. The sp^2 hybridization of the nitrogen atom is reflected in the sum of the surrounding angles (3×P–N–H), and the bond-angle sums are close to 360°.

In this compound, molecules are assembled in a three-dimensional arrangement through Cl...H–N and S...H–N interactions.

22nd Iranian Chemistry Congress (ICC22)
Iranian Research Organization for Science and Technology (IROST)
13-15 May 2024

03231-97589
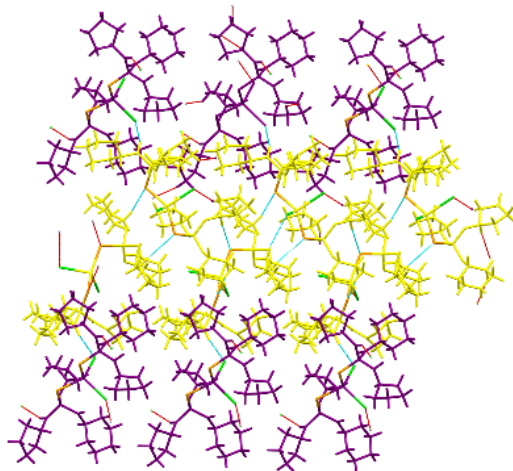
Fig. 2: Crystal stacking formed through Cl….H–N and S…H–N hydrogen bonds in the structure.

Table 1: Crystallographic data

Chemical formula	$2(C_{32}H_{60}Cl_2HgN_6P_2S_2) \cdot C_{32}H_{64}Cl_2HgN_6P_2S_2$
M_r	2783.26
Crystal system	Monoclinic
space group	$C2$
a, b, c (Å)	26.7521 (8), 12.4239 (3), 19.0467 (4)
Z	2

Conclusions

This article reports the single crystal X-ray diffraction study of a mercury(II) coordination compound with the phosphorothioic triamide ligand. The Hg atom in the complex has a distorted four-coordinate Cl_2HgS_2 environment.

References

[1]   Subramanian, E. & Trotter, J. (1969). Crystal structure of triethylenethiophosphoramide. Journal of the Chemical Society A: Inorganic, Physical, Theoretical, 2309–2312. https://doi.org/10.1039/J19690002309.

[2]   Zhang, J., Zhang, Q., Wang, Y., Li, J., Bai, Z., Zhao, Q., He, D., Wang, Z., Zhang, J. & Chen, Y. (2019). Toxicity, bioactivity, release of H_2S in vivo and pharmaco-kinetics of H_2S-donors with thiophosphamide structure. European Journal of Medicinal Chemistry, 176, 456–475. https://doi.org/10.1016/j.ejmech.2019.05.017

[3]   Zhang, W. & Shi, M. (2007). Chiral thiophosphoramide and thioamide ligands in catalytic asymmetric carbon-carbon bond-formation reactions. Synlett, 2007, 0019–0030. https://doi.org/10.1055/s-2006-956486.

[4]   Nollet, L. M. & Rathore, H. S. (2016). Handbook of pesticides: methods of pesticide residues analysis. CRC press. https://doi.org/10.1201/9781420082470.

[5]   Khorramaki, M., Abad, M., Darugar, V., Pourayoubi, M., Vakili, M., Nečas, M., Choquesillo-Lazarte, D., Andreev, P. V. & Shchegravina, E. S. (2022). Competitor hydrogen-bond acceptors in the $SP(NH)_3$-based structures: Comparison of structural features– Computational/database and experimental. Polyhedron. 228, 116157, https://doi.org/10.1016/j.poly.2022.116157

[6]   Hosseinpoor, S., Pourayoubi, M., Abrishami, M., Sobati, M., Ahmadabad, F. K., Sabbaghi, F., Nečas, M., Dušek, M., Kučeráková, M. & Kaur, M. (2023). Competing and directing interactions in new phosphoramide/thiophosphoramide structures: energy considerations and evidence for CH··· HC contacts and aliphatic-aromatic stacking. CrystEngComm, 25, 2557–2569. https://doi.org/10.1039/D3CE00204G.

[7]   Saneei, A., Pourayoubi, M., Crochet, A., Fromm & K. M. (2016). The first phosphoramide–mercury (II) complex with a $Cl_2Hg–OP[N(C)(C)]_3$ segment. Acta Crystallographica Section C: Structural Chemistry, 72, 230–233. https://doi.org/10.1107/S2053229616002394.

Assessment of the Thermal Properties and Operation Temperature for Metal-Organic Frameworks and Amine-Functionalized Metal-Organic Frameworks/Epoxy/Novolac Composites: A Comparative Study

Alireza Mirkhani Deligani[a], Omid Moini Jazani[*a], Payam Molla-Abbasi[a], Majid Moghadam[b], Saeid Asghari[b]

Corresponding author E-mail address: Alireza.mirkhani77@gmail.com

[a] Department of Chemical Engineering, Faculty of Engineering, University of Isfahan, Isfahan, Iran.

[b] Department of Chemistry, Catalysis Division, University of Isfahan, Isfahan, Iran.

Abstract: Metal-organic frameworks (MOFs) are known for their excellent physical and thermal properties. UiO-66 and UiO-66-NH2 were used to prepare a series of novel composites from epoxy resin and Novolac (EU and EUN samples, respectively). Moreover, the operating temperature of the prepared composites was calculated and compared for four sets of heating rates. Up to 10% mass loss, the mean operating temperature for using the neat epoxy, EU, and EUN composites for 20000 h, was found to be 184.17 $^\circ$C, 246.26 $^\circ$C, and 247.73 $^\circ$C, respectively.

Keywords: Epoxy composite; Metal-organic frameworks (MOFs); Operating temperature; Degradation

Introduction:

MOFs exhibited excellent properties, including high thermal and chemical stability, specific surface area, and predictable channel size. The exceptional thermal stability of MOFs compared to the traditionally used carbonaceous materials could enhance the thermal resistance of thermoset epoxy/MOF composites [1–5]. Since epoxy resin and MOFs contain several functional groups, they can have desirable, attractive forces to increase mechanical and thermal properties. Knowing decomposition and degradation knowledge can help develop a methodology to characterize the damaged composite materials in industries [6]. Despite the fact that MOFs enhance the thermal stability of the polymeric matrices, the current paper studies the effect of functional groups on the thermal stability, degradation kinetics, and thermal lifetime of epoxy/UiO-66 and epoxy/UiO-66-NH2 nanocomposites. Also, the thermal lifetime of the prepared samples was calculated and compared thoroughly.

Experimental Section :

UiO-66 was synthesized according to a procedure reported in the literature. Briefly, ZrCl4 (3.4 mmol, 795.0 mg) and TA (3.4 mmol, 565.0 mg) were mixed in 250 mL DMF at ambient temperature. The mixture was transferred into the autoclave reactor and heated to 120 $^\circ$C for 21 h. After that, the reactor was cooled to room temperature. The obtained solid was separated and washed with DMF (4 × 15 mL). The prepared white precipitate was dried in a vacuum oven at 150 $^\circ$C (yield = 40%).

The procedure for synthesizing UiO-66-NH2 was similar to that of UiO-66, while TA was replaced by ATA (3.4 mmol, 616 mg). A slightly yellow powder was obtained with a yield of 43%.

The epoxy adhesive films were prepared using a constant ratio of 0.5 Phr MOF nanoparticles (NPs) into the DGEBA matrix. The DGEBA epoxy resin was heated to 60 $^\circ$C, and 20 Phr of Novolac was added.

Results and Discussio

Also, using functionalized linkers, such as amine groups, in the preparation of MOFs, can accelerate the curing process. In this regard, UiO-66 and UiO-66-NH2 were prepared in a solvothermal reaction and used as thermally resistant fillers in the epoxy film adhesives (Fig. 1).
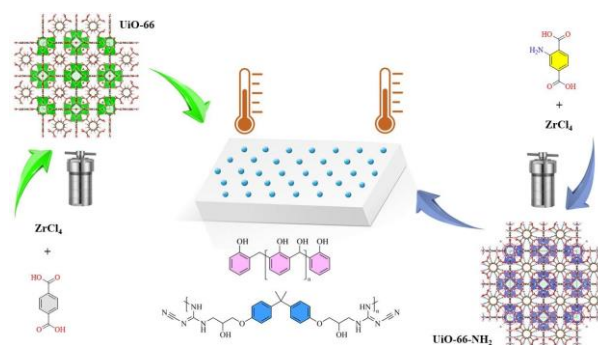
Fig.1: Schematic illustration of epoxy adhesive preparation and their kinetic behavior.

To further confirm the crystallinity of the prepared MOF, their XRD patterns were collected. (Fig.2) [7]. The intense diffraction peaks observed at 2θ = 7.4°, 8.6°, and 25.8° are

22nd Iranian Chemistry Congress (ICC22)
Iranian Research Organization for Science and Technology (IROST)
13-15 May 2024

03231-97589

IROST

attributed to the (111), (002), and (115) crystalline planes. Due to the presence of amine groups in the UiO-66-NH$_2$ structure, the lattice parameters of it were slightly different from that of UiO-66, which is responsible for the slight peak shift observed in the patterns (Fig. 2).
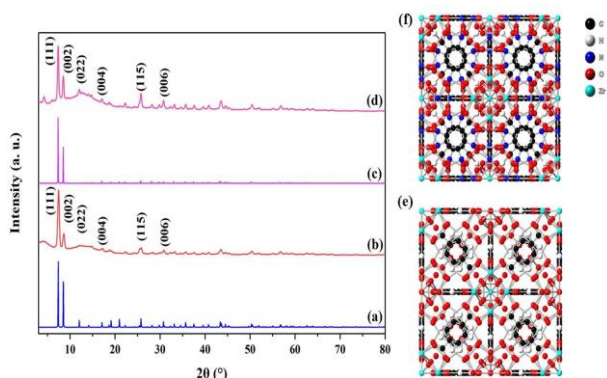
Fig. 2: XRD patterns of (a) simulated UiO-66, (b) as-synthesized UiO-66, (c) simulated UiO-66-NH$_2$, (d) as-synthesized UiO-66-NH$_2$, (e) schematic illustration of UiO-66 cubic crystals, and (f) schematic illustration of UiO-66-NH$_2$ cubic crystals.

The thermal stability of the adhesive films was studied using the TGA curves of the prepared samples. The decomposition parameters of the samples are summarized in Table 1.

Table1: Summary of therma lstability parameters

Entry	Sample	Heating rate (K. min^{-1})	$T_{5\%}$ (K)	T_p (K)	Wr (%)
		5	482.25	656.48	22.78
1	Neat epoxy	10	474.15	671.15	20.44
		15	510.15	681.15	18.31
		20	528.15	685.15	18.30
		5	471.48	678.15	19.71
2	EU	10	483.15	688.15	21.64
		15	482.85	696.15	20.66
		20	488.15	701.15	17.79
		5	525.65	681.50	21.39
3	EUN	10	584.82	688.98	21.85
		15	582.15	697.15	21.48
		20	595.15	701.15	19.14

Up to 10% of conversion (or failure) ($\alpha = 0.1$), the operating temperature for 20,000 h was calculated and summarized in Fig.3. for each heating rate.
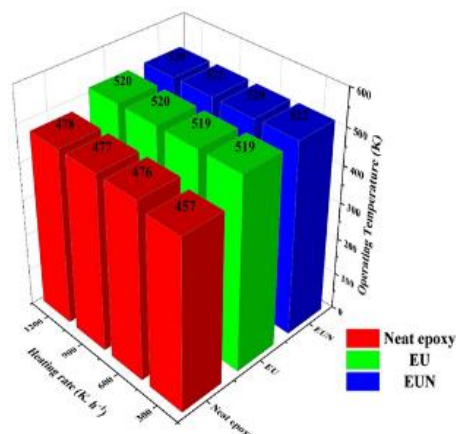
Fig. 3: Increase in the operating temperature of neat epoxy, EU, and EUN samples.

References:

[1] Wang, W., Yang, F., Yang, Y., Wang, Y. Y., & Liu, B. (2022). Rational synthesis of a stable rod MOF for ultrasensitive detection of nitenpyram and nitrofurazone in natural water systems. *Journal of Agricultural and Food Chemistry*, *70*(50), 15682-15692.

[2] Lisensky, G. C., & Yaghi, O. M. (2022). Visualizing pore packing and topology in MOFs. *Journal of Chemical Education*, *99*(5), 1998-2004.

[3] Zorainy, M. Y., Sheashea, M., Kaliaguine, S., Gobara, M., & Boffito, D. C. (2022). Facile solvothermal synthesis of a MIL-47 (V) metal–organic framework for a high-performance Epoxy/MOF coating with improved anticorrosion properties. *RSC advances*, *12*(15), 9008-9022.

[4] Liang, C., He, J., Zhang, Y., Zhang, W., Liu, C., Ma, X., ... & Gu, J. (2022). MOF-derived CoNi@ C-silver nanowires/cellulose nanofiber composite papers with excellent thermal management capability for outstanding electromagnetic interference shielding. *Composites Science and Technology*, *224*, 109445.

[5] Hou, Y., Hu, W., Gui, Z., & Hu, Y. (2017). A novel Co (Ⅱ)–based metal-organic framework with phosphorus-containing structure: Build for enhancing fire safety of epoxy. *Composites Science and Technology*, *152*, 231-242.

[6] G. Zhou, E. Mikinka, J. Golding, X. Bao, W. Sun, A. Ashby, Investigation of thermal degradation and decomposition of both pristine and damaged carbon/epoxy samples with thermal history, Compos B Eng 201 (2020) 108382.

[7] Ni, B., Sun, W., Kang, J., & Zhang, Y. (2020). Understanding the linear and second-order nonlinear optical properties of UiO-66-derived metal–organic frameworks: A comprehensive DFT study. *The Journal of Physical Chemistry C*, *124*(21), 11595-11608.

Synthesis and Characterization of Adamantane-Based Schiff Bases

Hadi Abdolmohammadi Vahid, Adeleh Moshtaghi Zonouz*

Corresponding Author E-mail: adelehmz@yahoo.com, ac.moshtaghi@azaruniv.ac.ir

Department of Chemistry, Faculty of Science, Azarbaijan Shahid Madani University, Tabriz, Iran.

Abstract: Adamantane-based Schiff bases were synthesized by condensation reaction of amantadine (1-aminoadamantane) and various aldehydes under refluxing in ethanol. The structure of obtained Schiff bases was confirmed by FT- IR, ^{1}H and ^{13}C NMR spectroscopy.

Keywords: Adamantane; Schiff base; Diamondoid; Nanodiamond

Introduction

Diamondoid are cage hydrocarbons molecules that are superimposable on the diamond lattice [1]. Diamondoids can also be described as fully hydrogen-terminated nanometer-sized diamonds. A diamond combines several very useful properties, such as extreme mechanical hardness, stability against chemical reagents, broad optical transparency, wide band gap, high radiation hardness, and high thermal conductivity. Adamantane molecule, corresponding to $C_{10}H_{16}$ formula, is the smallest Diamondoid. Derivatives of adamantane have found numerous applications in medicinal chemistry [2-4].

Schiff bases with the general structure $R_2C=NR'$ ($R' \neq H$) are found to be a versatile pharmacophore for design and development of various bioactive compounds [5]. Schiff bases show biological activities like antibacterial [6], antifungal [7], anti-HIV activity [8], antimycobacterial activity [9]. Besides biological applications, Schiff base and their metal complexes have enormous applications in analytical chemistry [10], dye industry [11], and corrosion inhibitors [12].

Schiff bases containing adamantane have also exhibited various medical application, such as antimicrobial and antibacterial activities[13-14]

In this work, we wish to combine the remarkable structure and chemical properties of adamantane with Schiff base molecule and synthesize adamantane-modified Schiff base derivatives. For this purpose substituted benzaldehydes and 1-aminoadamantane were used for the synthesize of adamantane containing schiff base derivatives.

Experimental Section

Typical procedure: A solution of 1- adamantanamine (2 mmol) in 10 ml of ethanol was refluxed with an equimolar amount of the appropriate benzaldehyde derivative. The reaction mixture was refluxed for 8– 24 h. The solvent was removed in vacuo and the pale-yellow residue was recrystallized from ethanol. The spectral data confirm the synthesis of Schiff base molecules.

2-(1-Adamantyliminomethyl)phenol (3f)

IR (KBr) ṽ = 1280,1460, 1629, 3450 cm^{-1}; ^{1}H NMR (400 MHz, CDCl$_3$): δ = 1.71-1.78 (6H, m, CH$_2$), 1.81-1.88 (6H, m, CH$_2$), 2.22 (3H, s, CH), 6.85 (1H, s, Ar-H), 6.97 (1H, s, Ar-H), 7.26 (1H, s, Ar-H), 8.35 (1H, s, CH=N), 14.56 (1H, s, Ar-OH) ppm; ^{13}C NMR (100 MHz, CDCl$_3$): δ = 28.3 (CH), 35.23 (CH$_2$), 41.89 (CH$_2$), 56.02 (C), 116.32 (C), 116.86 (CH), 117.82 (C), 130.21 (CH), 158.11 (C=N) ppm.

Results and Discussion

Schiff bases containing diamondoid adamantane-moiety were synthesized by condensation reaction of amantadine (1-aminoadamantane) with benzaldehyde derivatives under refluxing in ethanol (Table 1). The structure of obtained Schiff bases were confirmed by FT- IR , ^{1}H and ^{13}C NMR spectroscopy.

The FT-IR spectra of the Schiff bases showed characteristic peaks corresponding to the imine bond formation. Also ^{1}H NMR and ^{13}C NMR analysis confirmed the formation of adamantane-containing imines.

For example, FT-IR data of **3f** confirmed the formation of the imine bond (CH=N) by the appearance of C=N stretching band at 1629 cm^{-1}. The IR spectrum of salicylaldehyde indicates a strong band at 1663 cm^{-1} due to stretching vibration of C=O group, which was absent in resulting imine. The ^{1}H NMR spectrum of 3f shows singlet at 8.35 ppm for the resonance of imine proton (CH=N). Also, presence of signal at 158.11 ppm in the ^{13}C NMR spectra of **3f** was another reason for confirming the formation of product **3f**.

Table 1. Synthesis of adamantane-containing Schiff bases
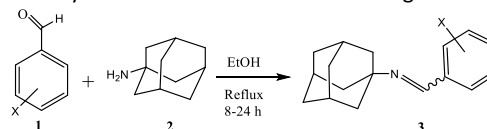
Entry	X	Product	Yield (%)	Mp (°C)
1	4-Nitro	**3a**	60	111
2	3-Nitro	**3b**	29	118
3	2-Nitro	**3c**	56	139
4	3-Methyl	**3d**	53	70
5	4-Methyl	**3e**	59	105
6	2-Hydroxy	**3f**	24	90
7	3-Hydroxy	**3g**	26	165
8	2-Chloro	**3h**	29	96

22nd Iranian Chemistry Congress (ICC22)
Iranian Research Organization for Science and Technology (IROST)
13-15 May 2024

03231-97589

Conclusions

In this work we synthesized Schiff bases incorporating diamondoid adamantane moiety from substituted benzaldehydes and 1-aminoadamantane , in a facil and convenient way.

The results of this study provide valuable insights into the structure-activity relationships of these compounds for further exploration of their biological and pharmaceutical applications.

References

[1] Mansoori, G. A. (2007) Diamondoid Molecules. *Advances in Chemical Physics*. vol. 136, pp. 207–258, 2007, doi: 10.1002/9780470175422.ch4.

[2] Wanka, L., Iqbal, K., & Schreiner, P. R. (2013) The lipophilic bullet hits the targets: medicinal chemistry of adamantane derivatives. Chem Rev, 113(5), 3516-3604.

[3] Martel-Estrada, S.-A. (2018) Recent Progress in Biomedical Applications of Nanodiamonds. Nanoscience and Nanotechnology - Asia, 8, 11-24.

[4] Tsai, L. W., Lin, Y. C., Perevedentseva, E., Lugovtsov, A., Priezzhev, A., & Cheng, C. L. (2016) Nanodiamonds for Medical Applications: Interaction with Blood in Vitro and in Vivo. Int J Mol Sci, 17(7).

[5] Raczuk, E., Dmochowska, B., Samaszko-Fiertek, J., & Madaj, J. (2022) Different Schiff Bases-Structure, Importance and Classification. Molecules, 27(3).

[6] El-Gammal, O. A., Mohamed, F. S., Rezk, G. N., & El-Bindary, A. A. (2021) Synthesis, characterization, catalytic, DNA binding and antibacterial activities of Co (II), Ni (II) and Cu (II) complexes with new Schiff base ligand. Journal of Molecular Liquids, 326, 115223.

[7] Wei, L., Zhang, J., Tan, W., et al. (2021) Antifungal activity of double Schiff bases of chitosan derivatives bearing active halogeno-benzenes. International Journal of Biological Macromolecules, 179, 292-298.

[8] Al-Masoudi, N. A., Aziz, N. M., & Mohammed, A. T. (2009) Synthesis and In vitro anti-HIV activity of some new Schiff base ligands derived from 5-Amino-4-phenyl-4 H-1, 2, 4-triazole-3-thiol and their metal complexes. Phosphorus, Sulfur, and Silicon, 184(11), 2891-2901.

[9] Meeran, I. S., Raja, T. W., Dusthakeer, V. A., Ali, M. M. N., Tajudeen, S. S., & Shabeer, T. (2022) An insight into antimycobacterial and antioxidant potentials of INH-Schiff base complexes and in silico targeting of MtKasB receptor of M. tuberculosis. New Journal of Chemistry, 46(10), 4620-4633.

[10] Kaur, P., Singh, R., Kaur, V., & Talwar, D. (2021) Anthranilic acid Schiff base as a fluorescent probe for the detection of arsenite and selenite: A detailed investigation of analytical parameters and mechanism for interaction. Analytical Sciences, 37(4), 553-560.

[11] Refat, M. S., Saad, H. A., Gobouri, A. A., Alsawat, M., Adam, A. M. A., & El-Megharbel, S. M. (2022) Charge transfer complexation between some transition metal ions with azo Schiff base donor as a smart precursor for synthesis of nano oxides: An adsorption efficiency for treatment of Congo red dye in wastewater. Journal of Molecular Liquids, 345, 117140.

[12] Saha, S. K., Murmu, M., Murmu, N. C., & Banerjee, P. (2021) Synthesis, characterization and theoretical exploration of pyrene based Schiff base molecules as corrosion inhibitor. Journal of Molecular Structure, 1245, 131098.

[13] Caliş, U., Yarim, M., Köksal, M., & Ozalp, M. (2002) Synthesis and antimicrobial activity evaluation of some new adamantane derivatives. Arzneimittelforschung, 52(10), 778-781.

[14] Zhu, J., Teng, G., Li, D., Hou, R., & Xia, Y. (2021) Synthesis and antibacterial activity of novel Schiff bases of thiosemicarbazone derivatives with adamantane moiety. Medicinal Chemistry Research, 30(8), 1534-1540.

Ultrasonic Degradation of Amylose and Effect of Concentration of Amylose on Degradation Kinetics

Ali Bahadori

Corresponding Author E-mail: a.bahadori@yahoo.com

Department of Physical Chemistry, Faculty of Chemistry, University *of Urmia*, Iran.

Abstract: Ultrasonicaton of Amylose was carried out in aqueous solution at 25°C. The effect of concentration of Amylose on degradation kinetics was studied by viscometry method. The calculated rate constants indicate that degradation rate of Amylose solutions decreases with increasing of solution concentration. The extent of degradation decreases with an increase in solution concentration.

Keywords: Ultrasonic degradation; Amylose; kinetics

Introduction

This Starch is a polysaccharide, which consists of amylose and amylopectin as constituents. Ultrasonic treatment of starch can cause the physical degradation of starch granules, a decrease in starch suspension viscosity and reduction in molecular sizes of starch polymer [1]. In this study ultrasonic degradation of Amylose was investigated. The objective was to introduce a simple kinetic model for the evaluation of degradation rate of Amylose via viscometry.

Experimental Section

Materials

Amylose (fur biochemische Zwecke), and KCl, LiBr with an average molecular weight of 74.56 and 88.85 and DMSO as a solvent were obtained from Merck without purification. Water was double distilled and filtered before use as a solvent.

Ultrasonic degradation

Solutions of 10, 20 and 30 gLit^{-1} of Amylose in aqueous solution 0.33 M of KCl were prepared. For the degradation, 25 and 50 cm^3 of Amylose solutions was placed in a cylindrical glass reactor with a diameter 10 cm and a height of 20 cm, and its temperature was controlled to 25 ± 0.1 °C by circulating thermostated water (Grant model RC 1400 G England) through the cylindrical glass and sonicated for a long time. An ultrasonic generator (Dr. Hielscher UP 200 H ultrasonic processor) with an H3 sonotrode (u = 3 mm) was used in this experiment.

Results and Discussion

Kinetic model

The rate of degradation is defined as the number of scission that occurs in one liter in unit time and we must keep in mind that a scission in a chain yields two pieces.

Thus, the rate equation of the degradation is as follows [2]:

$$R = \frac{dM}{dt} = kM^n$$

where M is the total molar concentration of the polymer, k is the rate constant and n is the order of reaction with respect to the total molar concentration of the polymer.

The plots of $\Delta\eta - \Delta\eta_o$ versus sonication time for different Amylose concentrations and molecular weights are presented in Figure1. The apparent degradation rate constants, k, defined in Eq, $\Delta\eta^{1-n} - \Delta\eta_0^{1-n} = k't$ can be estimated from the slopes of the plots in Figure1. Based on these, degradation rate constants, k, were calculated. The experimental values are shown in Table 1. It can be also seen from Table 1, the extent of degradation decreases with an increase in solution concentration.
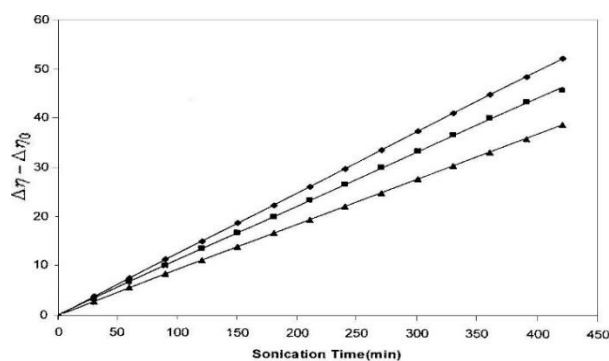
Fig.1: The plot of $\Delta\eta - \Delta\eta_o$ versus the sonication time for different concentration of Amylose aqueous solutions with ♦–10, ■–20, ▲–30 gr/Lit at 25 °C.

Table1: The effect of concentration of Amylose aqueous solution on the apparent degradation rate constants at 25 °C

Concentration (g/Lit)	$k \times 10^6 (\frac{mol}{Lmin})$
10	1.390
20	1.244
30	1.031

22nd Iranian Chemistry Congress (ICC22)
Iranian Research Organization for Science and Technology (IROST)
13-15 May 2024

03231-97589

At high concentration, entanglements influence the energy transfer processes between solvent and polymer and appears to reduce the probability of degradation accruing [3]. In quantitative terms, the extent of degradation at 10 glit^{-1} concentration is higher as compared to degradation at 30 glit^{-1} concentration. Thus observed effect of concentration are quite similar to those reported in literature for different chemical constituents [4]. The calculated values of k indicate that the rate of degradation decreases with increasing concentration. These results indicate that the extent of degradation is more pronounced in more dilute solutions. This might be due to the fact that the probability of chemical bond scission caused by efficient shearing in the polymer chain is greater in dilute solution.

Conclusions

The aim of this research was to study the effect of concentration of solution on the ultrasonic degradation of Amylose. At high concentration, entanglements influence the energy transfer processes between solvent and polymer and appears to reduce the probability of degradation accruing. In quantitative terms, the extent of degradation at 10 glit^{-1} concentration is higher as compared to degradation at 30 glit^{-1} concentration. The calculated rate constants indicate that degradation rate of Amylose solutions decreases with increasing of solution concentration.

References

[1] Seguchi, M., Higasa, T., Mori, T.(1994). "Study of wheat starch structure by sonication treatment", Cereal Chem, 71, 636–639.

[2]Taghizadeh, M.T., Asadpour, T.(2009)."Effect of molecular weight on the ultrasonic degradation of poly(vinyl-pyrrolidone)", Ultrasonics Sonochemistry, , 16, 280–286.

[3] Kanwal, F., Liggat, J. J., Pethrick, R. A.(2000) "Ultrasonic degradation of polystyrene solution", Polymer Degradation and Stability, 68, 445-449.

[4]Peters, D.(2000) "Sonolytic degradation of volatile pollutants in natural ground water: conclusions from a model study", Ultrason. Sonochem, 8, 221-226.

Influence of Thiopyridine Ancillary Ligands on the Stability and Resistance to Reductive/Elimination Reactions in the Cycloplatinated(II) Complexes

Zahra Ahmadi Khamesi, Hamid R. Shahsavari*

Corresponding Author E-mail: shahsavari@iasbs.ac.ir

Department of Chemistry, Institute for Advanced Studies in Basic Sciences (IASBS), Zanjan 45137-66731, Iran.

Abstract: Complexes [PtAr(C^N)(S)] (Ar = C_6F_5, and p–MeC_6H_4; C^N = benzoquinoline, bzq, 2-phenylpyridine, ppy, and 2-(2,4-difluorophenylpyridine), dfppy; S = dmso, and SMe_2) were reacted with various thiopyridine ligands to afford complexes [PtAr(C^N)(Spy)] (Spy = 2-pyridinethione, 2-Spy, 5-(trifluoromethyl)-2-pyridinethione, $SpyCF_3$-5, and 4-pyridinethione, 4-Spy. These complexes were thoroughly characterized using NMR spectroscopy, and their stability in solution was investigated.
Keywords: Cycloplatinated complexes; Thiol ligands; Platinum.

Introduction

Due to their remarkable versatility and widespread applications in diverse fields, cycloplatinated complexes have emerged as a subject of great interest in the study of cyclometalated complexes. Monoalkyl cycloplatinated complexes containing a labile ligand are known to display different behaviors in fundamental reactions such as oxidative addition and substitution reactions. Based on literature, reaction of the cycloplatinated(II) complexes [PtR(C^N)(S)] (S = labile ligand) with 2-Spy results in synthesis of the monodentate S-bound complex [PtR(C^N)(κ^1-S-Spy)], with NH pendant group, along with a dimeric complex [Pt(C^N)(N^S)]$_2$, which is the outcome of C–H bond reductive elimination. The monomeric form is not stable and formation of intramolecular Pt···H-N hydrogen bonding following by oxidative addition reaction in the complex [PtR(C^N)(κ^1-S-Spy), gives the Pt(IV) intermediate complex [PtRH(C^N)(N^S)], and the reductive elimination of R-H bond performs the dimeric form [1, 2]. According to previous studies on pentafluorophenyl complexes, the presence of ortho-fluorine atoms, known for their high group electronegativity, typically results in strong Pt–C bonds. As a result, these bonds tend to resist reductive/elimination processes effectively [3, 4]. The aim of this research is to examine how the stability of a mononuclear cycloplatinated(II) complex is affected by either introducing an electron-withdrawing supporting ligand (C_6F_5) or altering the position of the heteroatom on the aromatic ring of the thiolate ligand.

Experimental Section

All the reactions were carried out in common solvents in the lab without any further purification and starting complexes were prepared as reported in the literature [1, 5]. All the products were characterized using multinuclear (^{1}H, ^{19}F{^{1}H}, ^{195}Pt{^{1}H}) NMR spectroscopy with a Bruker Avance III 400 MHz spectrometer and are referenced to the peak of the residual solvent. The chemical shifts (δ) and coupling constants (J) are reported as ppm and Hz respectively. The schematic labeling of **3a** is shown in Scheme 2.

Pt(p–MeC_6H_4)(dfppy)(4-Spy)], **3a**, As depicted in Scheme 1, [Pt(p–MeC_6H_4)(dfppy)(SMe_2)], **C**, was introduced into solution of 4-Spy ligand at room temperature, and the resulting yellow solution was stirred for 24 hours. Subsequently, the solvent was evaporated under reduced pressure, and the residue was treated with n-hexane, followed by drying under an Ar atmosphere to obtain Pt(p–MeC_6H_4)(dfppy)(4-Spy)], **3a**. The remaining complexes were synthesized using the same procedure as **3a** by reacting the respective precursors with appropriate thiolate ligands. ^{1}H NMR (400MHz, Acetone d_6, 20 °C, δ): 9.19 (d, $^3J_{HH}$ = 5.7 Hz, 1H, H^9), 8.11 (d, $^3J_{HH}$ = 8.4 Hz, 1H, H^6), 7.99 (t, $^3J_{HH}$ = 8.0 Hz, 1H, H^7), 7.90 (d, $^3J_{HH}$ =6.9 Hz, 2H, $H^{1'}$), 7.74 (d, $^3J_{HH}$ = 7.0 Hz, 2H, $H^{2'}$), 7.27-7.23 (m, $^3J_{PtH}$ = 61.2 Hz, 3H, H^8, H^o), 6.71 (dd, $^3J_{FH}$ = 9.6 Hz, $^4J_{HH}$ = 2.3 Hz, 1H, H^2), 6.66 (d, $^3J_{HH}$ = 7.6 Hz, 2H, H^m), 6.56 (td, $^3J_{FH}$ = 11.7 Hz, $^4J_{HH}$ = 2.4 Hz, 1H, H^4), 2.11 (s, 3H, H^p), 2.08 (s, 1H, H^3); ^{195}Pt{^{1}H} NMR (64.25 MHz, D_2O in Acetone d_6, 20 °C, δ): -3659.8 (t, $^3J_{HPt}$ = 56 Hz, 1Pt); ^{19}F{^{1}H} NMR (376 MHz, Acetone d_6, 20 °C, δ): -111.1 (d, $^4J_{PtF}$ = 77 Hz, $^4J_{FF}$ = 8 Hz, 1F, F^3), -112.8 (d, $^4J_{PtF}$ = 67 Hz, $^4J_{FF}$ = 8 Hz, 1F, F^5).

Results and Discussion

The synthesis pathway for the cycloplatinated complexes is depicted in Scheme 1. Starting complexes [PtAr(C^N)(Spy)], Ar = C_6F_5, C^N = benzoquinoline, bzq, S = dmso, **A**; Ar = C_6F_5, C^N = 2-phenylpyridine, ppy, S = dmso, **B**; Ar = p–MeC_6H_4, C^N = 2-(2,4-difluorophenylpyridine), dfppy, S = SMe_2, **C**, which serve as platinum precursors, reacted with one equivalent of

22nd Iranian Chemistry Congress (ICC22)
Iranian Research Organization for Science and Technology (IROST)
13-15 May 2024

03231-97589

IROST

commercial available thiopyridine ligands (Spy). This reaction yields [PtAr(C^N)(Spy)] complexes (Ar = C_6F_5, C^N = bzq, Spy = 2-pyridinethione, 2-Spy, **1a**; Ar = C_6F_5, C^N = bzq, Spy = (5-(trifluoromethyl)-2-pyridinethione, SpyCF$_3$-5, **1b**; Ar = C_6F_5, C^N = ppy, Spy = 2-Spy, **2a**; Ar = C_6F_5, C^N = ppy, Spy = SpyCF$_3$-5, **2b**; and Ar = p–MeC$_6$H$_4$, C^N = dfppy, Spy = 4-pyridinethione, 4-Spy, **3a**. The characterization of all complexes was accomplished through multinuclear (^{1}H, ^{13}C{^{1}H}, ^{19}F{^{1}H}, ^{195}Pt{^{1}H}) NMR spectroscopy. To elucidate the stability of the complexes in biological environments, their stability in solution was examined. To achieve this, **3a** was dissolved in Acetone-d$_6$, and a mixture of Acetone-d$_6$/D$_2$O, and their ^{1}H NMR spectra were recorded immediately and after 24 hours. ^{1}H NMR monitoring revealed that this complex remained stable over the 96 hours period.

The DFT-optimized S_0 geometries of all complexes were theoretically calculated at the B3LYP/6-31g(d) level (using LanL2DZ for Pt) both in the gas phase and in dichloromethane solution. These calculations aimed to provide insights into the geometric parameters of these compounds and the electronic transitions occurring within the singlet states (S_0). Percentage compositions of molecular orbitals were gained using Chemissian software, and all molecular orbitals of complexes were visualized using the Chemcraft program.
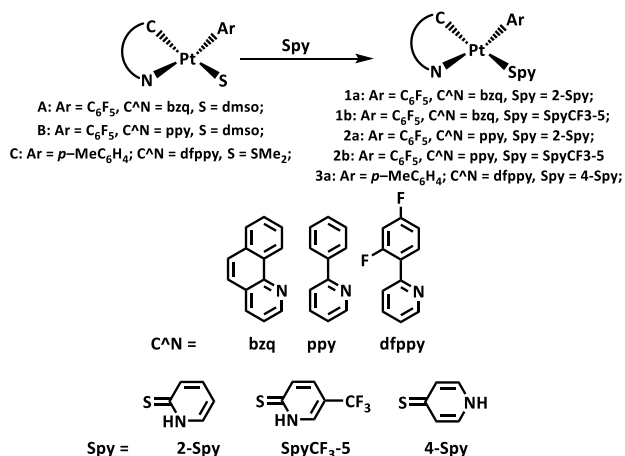
Conclusions

The investigation into the impact of C_6F_5 as a strong field ligand, characterized by its high electronegativity and resistance to reductive/elimination processes, on the stability of Pt(II) complexes was conducted. Given the demonstrated moderate cytotoxicity of several Pt(II) complexes, mononuclear cycloplatinated(II)-C_6F_5 complexes have exhibited promising potential across various domains, including biomedical chemistry and materials science. Moreover, substituting C_6F_5 by p–MeC$_6$H$_4$, and the 2-Spy ligand with the 4-Spy ligand ensures the protection of the NH pendant group against the formation of an intramolecular Pt···H–N hydrogen bond, which typically leads to oxidative addition reactions within the complex and subsequent reductive elimination of the R–H bond, resulting in the formation of the dimeric form. Consequently, altering the position of the heteroatom on the aromatic ring of the thiolate ligand ensures the stability of the monomeric form even in the absence of a strong electronegative ancillary ligand such as C_6F_5.

References

[1] M.D. Aseman, S.M. Nabavizadeh, H.R. Shahsavari, M. Rashidi, RSC Adv. 5 (2015) 22692.

[2] H.R. Shahsavari, R.B. Aghakhanpour, M. Babaghasabha, M.G. Haghighi, Nabavizadeh SM, B. Notash, New. J. Chem. 41 (2017) 3798.

[3] A. Auger, J.C. Swarts, Organometallics. 26 (2007) 102.

[4] J.R. Berenguer, E. Lalinde, M.T. Moreno, Coord. Chem. Rev. 366 (2018) 69.

[5] J. Berenguer, J. Pichel, N. Gimenez, E. Lalinde, M. Moreno, S. Pineiro-Hermida, Dalton Trans. 44 (2015) 18839.

A: Ar = C_6F_5, C^N = bzq, S = dmso;
B: Ar = C_6F_5, C^N = ppy, S = dmso;
C: Ar = p–MeC$_6$H$_4$; C^N = dfppy, S = SMe$_2$;

1a: Ar = C_6F_5, C^N = bzq, Spy = 2-Spy;
1b: Ar = C_6F_5, C^N = bzq, Spy = SpyCF3-5;
2a: Ar = C_6F_5, C^N = ppy, Spy = 2-Spy;
2b: Ar = C_6F_5, C^N = ppy, Spy = SpyCF3-5
3a: Ar = p–MeC$_6$H$_4$; C^N = dfppy, Spy = 4-Spy;

C^N =   bzq   ppy   dfppy

Spy =   2-Spy   SpyCF$_3$-5   4-Spy

Scheme 1: The synthetic route for the formation of the cyclometalated platinum(II) complexes.

Scheme 2: Numerical scheme for the ^{1}H NMR assignment of 3a.

22nd Iranian Chemistry Congress (ICC22)
Iranian Research Organization for Science and Technology (IROST)
13-15 May 2024

03231-97589

IROST

Rational synthesis of Cu(OAc)₂ embedded ferrocene-based porous organic polymer/carbon nanotube hybrid system: Catalytic application for the preparation of tetrazoles

Zahra Alishahi, Morteza Torabi, Mohammad Ali Zolfigol*, Meysam Yarie

Corresponding Author E-mail: mzolfigol@yahoo.com

Department of Organic Chemistry, Faculty of Chemistry and Petroleum Sciences, Bu-Ali Sina University, Hamedan, Iran.

Abstract: In this work, we synthesized Cu(OAc)₂ embedded ferrocene-based porous organic polymer (POP)/carbon nanotube (CNT) hybrid namely POP/CNT-Cu(OAc)₂ as highly active catalyst. This composite because of intimately construction of POP on the surface of CNT has tube-type core-shell structures. After full characterization of catalyst, it used for the preparation of tetrazole derivatives.

Keywords: Catalyst; ferrocene; POPs; carbon nanotube

Introduction

POPs as a new generation of porous materials, are assembled by organic linkers which have strong buiding blocks [1,2]. In recent years, due to irreplaceable and advantages and properties of POPs, they have many applications in several fields such as energy storage and conversion, sensors, drug delivery, catalyst, gas capture, and others [3-5]. The well-defined porosity, high specific surface area, low density, exellent thermal and physical stability, and post modification ability of POPs endow them to have fruitfully catalytic potential for organic transformations [6]. Tetrazole-containing compounds are known as one of the most important families of *N*-heterocylcle compounds. These chemicals have been used in diverse fields such as medicinal chemistry, sensors, energitic materials, catalyst and agricalture [7-9].

Experimental Section

In current study, POP/CNT-Cu(OAc)₂ was applied as robust catalyst for the preparation of tetrazoles by using oxime derivatives and sodium azide as starting materials and DMF as solvent under reflux condition (Scheme 1).

R= H, 4-Cl, 2-Cl, 2,4-(Cl)₂, 3,4-(Cl)₂, 4-CN, 4-OMe, 4-Me, 4-OH, 3-OH
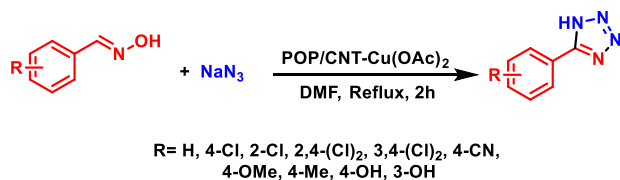
Scheme 1: Schematic preparation of tetrazoles by POP/CNT-Cu(OAc)₂ catalyst

Results and Discussion

After synthesis of POP/CNT-Cu(OAc)₂, we precisely characterized it by several instrumental techniques such as FT-IR, FE-SEM, EDS/Mapping, TGA, XRD and BET analyses. The BET surface area of POP/CNT and POP/CNT-Cu(OAc)₂ are 441 and 116 respectively. TGA analysis show the good thermal stability of POP/CNT and POP/CNT-

Cu(OAc)₂ up to 400 and 220 respectively. According to SEM and TEM results, the catalyst has tube-type core-shell morphology (Figure 1 and 2).
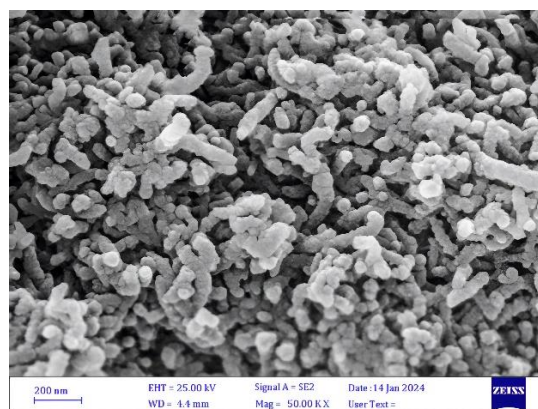
Fig.1: SEM images of POP/CNT-Cu(OAc)₂
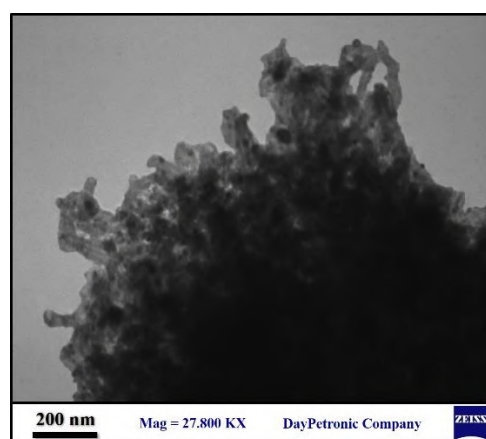
Fig.2: TEM images of POP/CNT-Cu(OAc)₂

In another study, we delve to generality of catalytic activity of POP/CNT-Cu(OAc)₂ in the preparation of tetrazole derivatives. A variety of substituted oximes with electron-withdrawing and electron-donating nature were

22nd Iranian Chemistry Congress (ICC22)
Iranian Research Organization for Science and Technology (IROST)
13-15 May 2024

03231-97589

used and all of products have high yield and short reaction times table 1.

Table 1: Synthesis of tetrazole derivatives in the presence of POP/CNT-Cu(OAc)$_2$ catalyst

1a, 90 %
M.P.: 205-207 °C

1b, 95 %
M.P.: 250-252 °C

1c, 90 %
M.P.: 240-242 °C

1d, 95 %
M.P.: 171-173 °C

1e, 85 %
M.P.: 163-165 °C

1f, 80 %
M.P.: 240-242 °C

1g, 85 %
M.P.: 232-234 °C

1h, 80 %
M.P.: 280-283 °C

1i, 88 %
M.P.: 239-241 °C

1j, 92 %
M.P.: 222-225 °C
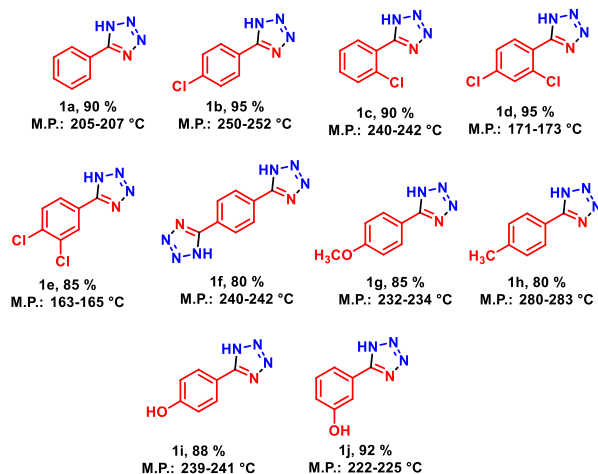
Conclusions

In summery, we introduced a Cu(OAc)$_2$ decorated POP/CNT hybrid system as heterogeneous catalyst. Due to existence of ferrocene cores in the structure of POP and its high specific surface area, POP/CNT have inherent catalytic activity. Beside it, due to synergistic effect of Cu(OAc)$_2$ nanoparticles by POP/CNT, this composite can be an active catalyst for the preparation of tetrazoles.

References

[1] Daliran, S., Oveisi, A. R., Peng, Y., López-Magano, A., Khajeh, M., Mas-Ballesté, R., ... & Garcia, H. (2022). Metal–organic framework (MOF)-, covalent-organic framework (COF)-, and porous-organic polymers (POP)-catalyzed selective C–H bond activation and functionalization reactions. Chemical Society Reviews, 51(18), 7810-7882. https://doi.org/10.1039/D1CS00976A

[2] Sarkar, C., Shit, S. C., Das, N., & Mondal, J. (2021). Presenting porous–organic–polymers as next-generation invigorating materials for nanoreactors. Chemical Communications, 57(69), 8550-8567.https://doi.org/10.1039/D1CC02616J

[3] Zhang, T., Xing, G., Chen, W., & Chen, L. (2020). Porous organic polymers: a promising platform for efficient photocatalysis. Materials Chemistry Frontiers, 4(2), 332-353. https://doi.org/10.1039/C9QM00633H

[4] Chen, W., Chen, P., Zhang, G., Xing, G., Feng, Y., Yang, Y. W., & Chen, L. (2021). Macrocycle-derived hierarchical porous organic polymers: synthesis and applications. Chemical Society Reviews, 50(20), 11684-11714. https://doi.org/10.1039/D1CS00545F

[5] Li, Z., & Yang, Y. W. (2022). Macrocycle-based porous organic polymers for separation, sensing, and catalysis. Advanced Materials, 34(6), 2107401. https://doi.org/10.1002/adma.202107401

[6] Cheng, Y. Z., Ding, X., & Han, B. H. (2021). Porous organic polymers for photocatalytic carbon dioxide reduction. ChemPhotoChem, 5(5), 406-417. https://doi.org/10.1039/C9QM00633H

[7] Ishihara, K., Kawashima, M., Shioiri, T., & Matsugi, M. (2016). Synthesis of 5-substituted 1H-tetrazoles from aldoximes using diphenyl phosphorazidate. Synlett, 27(15), 2225-2228. https://doi.org/10.1055/s-0035-1561668

[8] Kazemnejadi, M., Mahmoudi, B., Sharafi, Z., Nasseri, M. A., Allahresani, A., & Esmaeilpour, M. (2020). Copper coordinated-poly (α-amino acid) decorated on magnetite graphene oxide as an efficient heterogeneous magnetically recoverable catalyst for the selective synthesis of 5-and 1-substituted tetrazoles from various sources: A comparative study. Applied Organometallic Chemistry, 34(2), e5273. https://doi.org/10.1002/aoc.5273

[9] Herr, R. J. (2002). 5-Substituted-1H-tetrazoles as carboxylic acid isosteres: medicinal chemistry and synthetic methods. Bioorganic & medicinal chemistry, 10(11), 3379-3393. https://doi.org/10.1016/S0968-0896(02)00239-0

22nd Iranian Chemistry Congress (ICC22)
Iranian Research Organization for Science and Technology (IROST)
13-15 May 2024

03231-97589

IROST

A DFT Study on the Mononuclear Hg(II) Complex of 1,3-bis(2-cyanophenyl)triazene ligand

Akbar Bakhtiari

Corresponding Author E-mail: akbar.bakhtiari@pnu.ac.ir, bakhtiari.a1@gmail.com

Department of Chemistry, Faculty of Basic Sciences, Payame Noor University, PO Box 19395-4697, Tehran, Iran.

Abstract: The mononuclear complex [Hg(L^1)$_2$] (HL = 1,3-bis(2-cyanophenyl)triazene) is investigated using DFT at B3LYP level of theory in the gaseous state. HOMO and LUMO are ligand π and π^* orbitals. For HL^1 and [Hg(L^1)$_2$], the strongest electronic absorption band is calculated (by TDDFT method) at 350 and 380 nm, respectively.

Keywords linear bis(phenyl)triazene; Hg(II) complex; electronic structure; spectroscopic properties; TDDFT

Introduction

Meldola and Streatfeild pioneered the synthesis and analysis of the initial metal coordination complexes of triazene derivatives, with triazene molecules predominantly acting as monoanionic ligands [1-3]. These ligands display remarkable versatility in coordinating with various metal ions, with the geometry of the triazene unit influencing their binding modes. They can exhibit monodentate or bidentate coordination, forming chelate rings or bridging multiple metal centers. A range of well-characterized metal complexes involving triazenide ligands, spanning s-block, group 13, and transition metals [4-6], exists in the literature.

Building upon prior research on d^{10} and main group metal ion coordination compounds, this study focuses on the chemistry of [Hg(L^1)$_2$] (HL^1 = 1,3-bis(2-cyanophenyl)triazene) from a theoretical perspective. It delves into the coordination bonding and electronic spectroscopy of this mercury(II) complex, particularly highlighting the impact of substituents on the phenyl rings. Notably, detailed investigations into the electronic structures and chemical bonding, of these complex are limited in existing literature [7]. This paper employs density functional theory (DFT) to calculate the molecular and electronic structures, as well as electronic transition energies, of [Hg(L^1)$_2$] in the gas phase. Additionally, it discusses chemical bonding, metal-ligand orbital interactions.

Computation details

Spin-unpolarized density functional theory (DFT) calculations were conducted for free ligand and its Hg(II) complex in the free gaseous state using Gaussian 09 Revision-A.02 at the B3LYP level of theory. Molecular orbitals were visualized using GaussView 5.0.8 software. The TDDFT calculated electronic spectra were interpreted using GaussSum 3.0 software. Molecular geometry optimization was performed without symmetry constraints. A 6-311G(d,p) basis set was applied for all elements in the free neutral ligands, while for the complex, a 6-31G(d,p) basis set was used for C, H, N, and O elements. The LanL2DZ basis set was employed for the mercury atom.

Results and Discussion

The optimized molecular structures of free gaseous HL^1 is depicted in Fig. 1. The calculated values are in good agreement with those experimentally measured for HL^1 in solid state. The N(2)=N(3) and N(1)–N(2) bond lengths in the molecular structure of optimized free gaseous HL^1 are, respectively, 1.258 Å and 1.333 Å .
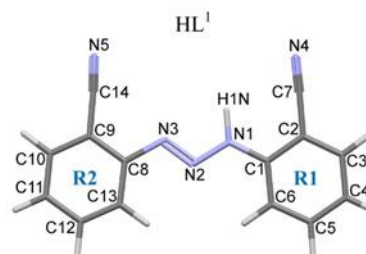
Fig. 1. Molecular structures of HL^1 optimized in free gaseous state.

The calculated bond distances are comparable with those observed for HL^1 (N=N and N–N bond lengths of 1.293(5) Å and 1.330(5) Å, respectively). Also, the calculated N–N=N bond angle (112.09°) is in accord with the respective experimental value (111.0(3)°) of HL^1. According to the DFT calculations, the optimized free gaseous molecules are planar. The angle between two mean planes crossing the aryl carbon atoms is 1.54° in gas phase. In comparison, the respective measured value is 1.80° for crystalline HL^1. Similar to those found previously for solid HL^1, the calculated C–C≡N angles for the nitrile- substitutions in molecule is almost linear.

$\sigma^*[(p_{(N\text{-triazene})})_2\text{-}d_{yz\,(Hg)}\text{-}(\pi_{(nitrile)})_2]$
L+66 (E = 9.6739 eV)
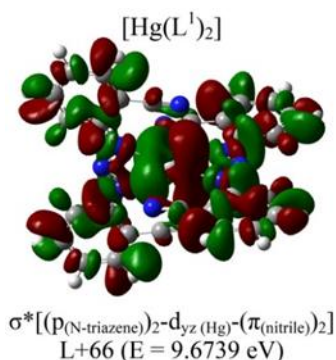
Fig. 2. Calculated isosurfaces of $\sigma^*[(p_{(N\text{-triazene})})_2\text{-}d_{yz\,(Hg)}\text{-}(\pi_{(nitrile)})_2]$ for $[Hg(L^1)_2]$

For the complex , $[Hg(L^1)_2]$ the calculated H−9 (MO 124) was found to be the bonding $\sigma[p_{(N\text{-triazene})}\text{-}s_{(Hg)}\text{-}p_{(N\text{-triazene})}]$ molecular orbital (Fig.2). Also, the respective anti-bonding $\sigma^*[p_{(N\text{-triazene})}\text{-}s_{(Hg)}\text{-}p_{(N\text{-triazene})}]$ molecular orbital is L+2 (MO 136). For the complex $[Hg\ ((L^1)_2]$, the unoccupied L+9 (Mo 143) and L+10 (Mo 144) are anti-bonding $\pi^*[\pi^*_{(triazene)}\text{-}d_{yz\,(Hg)}\text{-}\pi^*_{(nitrile)}]$ and $\pi^*[\pi^*_{(triazene)}\text{-}d_{xz\,(Hg)}\text{-}\pi^*_{(nitrile)}]$, respectively. (Fig.3)

$\pi^*[\pi^*_{(triazene)}\text{-}d_{xz\,(Hg)}\text{-}\pi^*_{(nitrile)}]$
L+10 (E = 0.5464 eV)

$\pi^*[\pi^*_{(triazene)}\text{-}d_{yz\,(Hg)}\text{-}\pi^*_{(nitrile)}]$
L+9 (E = 0.5453 eV)
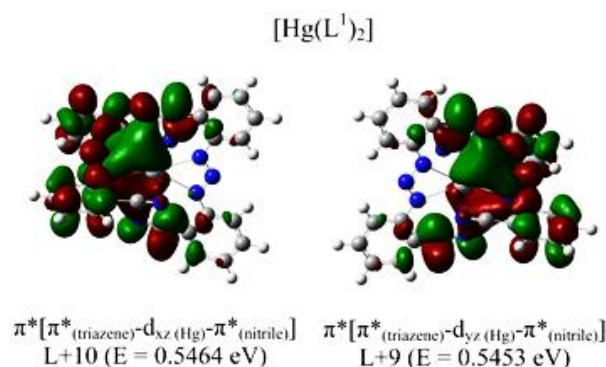
Fig. 3. The calculated $\pi^*[d_{(Hg)}\text{-}\pi^*_{(ligand)}]$ molecular orbitals for $[Hg(L^1)_2]$

It is notable that atomic $p_{(Hg)}$ orbitals are not involved in the calculated occupied molecular orbitals of the complexes. However, anti-bonding interactions between ligand group orbitals and $p_{(Hg)}$ orbitals were observed at higher energies. This founding is comparable with the results reported for mercury(II) Schiff base complexes, where natural electron configuration calculated (by natural bond orbital method, NBO) for Hg^{2+} shows low electron density on the 6p atomic orbital.

The HOMO to LUMO electronic transition in HL^1 is appeared as a very strong band at 350 nm in time-dependent DFT (TDDFT) calculated UV-Vis spectrum of the compound. TDDFT calculated electronic spectrum of $[Hg(L^1)_2]$ exhibits the strongest absorption peak at 380 nm due to ligand centered electron transitions.

Conclusions

linear ortho-substituted diphenyl-1,2,3-triazene ligands (HL^1) and the related $[Hg(L^1)_2]$ complex were studied by DFT calculations in free gaseous state. HOMO and LUMO for the compounds are calculated to be ligand π and π^* orbitals, respectively. For the calculated complex, the highest occupied metal-ligand bonding molecular orbital was found to be $\sigma[p_{(N\text{-triazene})}\text{-}dxy_{(Hg)}\text{-}p_{(N\text{-triazene})}]$ and $\sigma^*[p_{(N\text{-triazene})}\text{-}s_{(Hg)}\text{-}p_{(N\text{-triazene})}]$ is the lowest unoccupied metal-ligand anti-bonding molecular orbital.

References

[1] R. Meldola, F.W. Streatfeild, XLVI.–Researches on the constitution of azo- and diazo-derivatives. II. Diazoamido-compounds (continued), J. Chem. Soc., Trans. 51 (1887) 434–451.

[2] E. Correa-Ayala, C. Campos-Alvarado, D. Chávez, D. MoralesMorales, S. Hernández-Ortega, J.J. García, M. Flores-Álamo, V. Miranda-Soto, M. Parra-Hake, RutheniumII(p-cymene) complexes bearing ligands of the type 1-[2′-(methoxycarbonyl)phenyl]-3-[4′-X-phenyl]triazenide (X = F, Cl, Br, I): Synthesis, structure and catalytic activity, Inorg. Chim. Acta 466 (2017) 510–519.

[3] D.B. Kimball, M.M. Haley, Triazenes: A versatile tool in organic synthesis, Angew. Chem., Int. Ed. 41 (2002) 3338–3351.

[4] M. Hörner, G.M. de Oliveira, J.S. de Oliveira, W.M. Teles, C.A.L. Filgueiras, J. Beck, Stabilization of the (η4-COD)Pt-fragment (COD = η2,η2-cyclo-octa-1,5-diene) by a bistriazenide: Synthesis and X-ray structural characterization of [(η4-COD)Pt(NNN-Ph)2C6H4], a neutral 1,2-bis(phenyltriazenido)benzene complex of platinum(II), J. Organomet. Chem. 691 (2006) 251–254.

[5] A.S. Peregudov, D.N. Kravtso, G.I. Drogunova, Z.A. Starikova, A.I. Yanovsky, X-ray structure and fluxional behaviour of N,N′-di-p-fluorophenyltriazenido complex of nickel(II), J. Organomet. Chem. 597 (2000) 164–174.

[6] A.P.H. Vaniel, A.E. Mauro, A.V.G. Netto, E.T. de Almeida, P.C. Piquini, P. Zambiazi, D.F. Back, M. Hörner, Asymmetric and symmetric triazenido cyclopalladated complexes: Synthesis, structural analysis and DFT calculations, J. Mol. Struct. 1083 (2015) 311–318.

[7] M.K. Rofouei, M. Barghamadi, M. Taghdiri, J. Attar Gharamaleki, Bis[1,3-bis(2-cyanophenyl)triazenido]mercury(II), Acta Cryst. E 65 (2009) m1185–m1186.

DFT Study on Mononuclear Hg(II) Complex of 1-(2-Ethoxyphenyl)-3-(2-Cyanophenyl)triazene Ligand

Akbar Bakhtiari

Corresponding Author E-mail: akbar.bakhtiari@pnu.ac.ir, bakhtiari.a1@gmail.com

Department of Chemistry, Faculty of Basic Sciences, Payame Noor University, PO Box 19395-4697, Tehran, Iran.

Abstract: Molecular structures and electronic properties of the linear ligand 1-(2-ethoxyphenyl)-3-(2-cyanophenyl)triazene (HL^2) and its [$Hg(L^2)_2$] complex were studied by DFT at B3LYP level of theory in the free gaseous state. TDDFT predicts strong UV-Vis bands at 372 nm and 390nm for (HL^2) and its [$Hg(L^2)_2$], respectively.

Keywords linear triazene ligand; mononuclear Hg(II) complex; electronic structure; electronic transitions; DFT

Introduction

Mercury's coordination chemistry attracts attention due to its diverse applications and toxicity. Mercury(II) compounds show versatile coordination behavior, favoring soft donor atoms. The closed-shell d^{10} electronic configuration of Hg(II) makes them ideal for constructing fluorescence materials [1-6]. Recently, 1-(2-ethoxyphenyl)-3-(2-cyanophenyl)triazene) (HL^2) and the [$Hg(L^2)_2$] [7] metal complex have been synthesized and characterized.

Here, the molecular and electronic structures and electronic transitions energies of HL^2 and the related mononuclear Hg(II) complex [$Hg(L^2)_2$]) are calculated by density functional theory (DFT) method in gas phase. In addition, the chemical bonding and metal-ligand orbitals mixing in the electronic structures of the complexes are discussed. Furthermore, electronic absorption spectra of the free gaseous compounds are calculated by time-dependent DFT (TDDFT) method and discussed on the base of the electronic structures.

Computation details

Spin-unpolarized density functional (DFT) calculations were performed for free ligand and its corresponding Hg(II) complexes in the gaseous phase using Gaussian 09 Revision-A.02 at the B3LYP level of theory. Molecular orbitals were visualized with GaussView 5.0.8, and electronic spectra were interpreted using GaussSum 3.0. Molecular geometry optimization was conducted without symmetry constraints. The 6-31G(d,p) basis set was utilized for C, H, N, and O elements. The LanL2DZ basis set was employed for the mercury atom.

Results and Discussion

The optimized molecular structures of free gaseous HL^2 is depicted in Fig. 1. The calculated values are in good agreement with those experimentally measured for HL^2 in solid state.
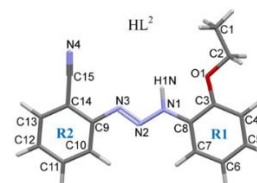
Fig. 1. Molecular structures of HL^1 optimized in free gaseous state.

The HOMO and LUMO for uncoordinated neutral ligand is π and π* orbitals, respectively, which are calculated to expand over diphenyl triazene and nitrile substitutions. For the complex, the calculated HOMO and LUMO are ligand π and π* orbitals, respectively (Fig. 2).

$\sigma[(p_{(N\text{-triazene})})_2\text{-}d_{yz\,(Hg)}\text{-}(\pi_{(nitrile)})_2]$
H-17 (E = -9.0168 eV)
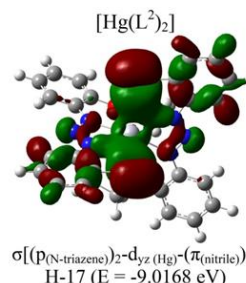
Fig. 2. Calculated isosurfaces of $\sigma*[(p_{(N\text{-triazene})})_2{-}d_{yz\,(Hg)}{-}(\pi_{(nitrile)})_2]$ for [$Hg(L^2)_2$]

For the complex, [$Hg(L^2)_2$] the calculated L+9 (Mo 155) is $\pi*[\pi*_{(triazene)}{-}d_{xz\,(Hg)}{-}\pi*_{(nitrile)}]$ while the L+10 (Mo 156) is found to be $\pi*[\pi*_{(triazene)}{-}d_{yz\,(Hg)}{-}\pi*_{(nitrile)}]$. Fig. 3 demonstrates the calculated isosurfaces for these molecular orbitals.

$\pi*[\pi*_{(triazene)}\text{-}d_{yz\,(Hg)}\text{-}\pi*_{(nitrile)}]$
L+10 (E = 0.8163 eV)

$\pi*[\pi*_{(triazene)}\text{-}d_{xz\,(Hg)}\text{-}\pi*_{(nitrile)}]$
L+9 (E = 0.7442 eV)

Fig. 3. The calculated $\pi*[d_{(Hg)}{-}\pi*_{(ligand)}]$ molecular orbitals for [$Hg(L^1)_2$]

22nd Iranian Chemistry Congress (ICC22)
Iranian Research Organization for Science and Technology (IROST)
13-15 May 2024

03231-97589
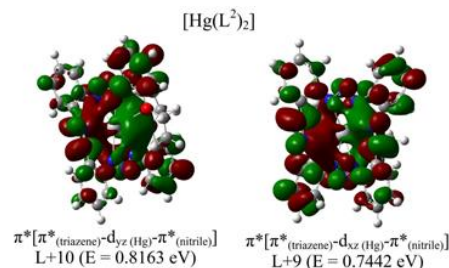
In the lowest energy region, the calculated UV-Vis spectrum of the free HL^2 exhibits a distinct very strong band at 372.02 nm (calculated f = 0.7355) due to the HOMO to LUMO, $\pi(HL^2) \rightarrow \pi^*(HL^2)$, electronic transitions (Fig.4).
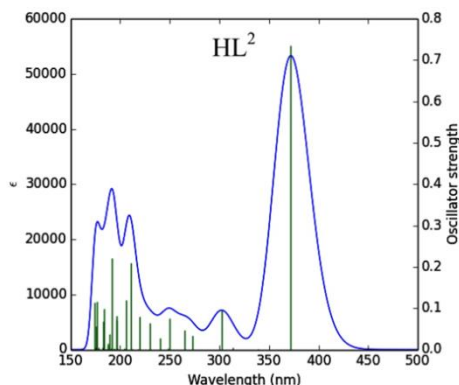
Fig. 4. TDDFT calculated electronic absorption spectrum for the optimized free gaseous HL^2. Vertical lines represent the calculated excitation energies and the oscillator strengths.

TDDFT calculated electronic spectrum of $[Hg(L^2)_2]$ exhibits the strongest absorption peak at 390 nm due to ligand centered electron transitions. Also, promotion of ligand π electrons to $\sigma^*[p_{(N\text{-triazene})} - s_{(Hg)} - p_{(N\text{-triazene})}]$ contributes to this band. Moreover, an unresolved shoulder at about 406 nm was calculated to occur, mostly due to $\pi(L) \rightarrow \sigma^*[p_{(N\text{-triazene})} - s_{(Hg)} - p_{(N\text{-triazene})}]$ electron transitions, in the electronic spectrum of $[Hg(L^2)_2]$.

Conclusions

linear ortho-substituted diphenyl-1,2,3-triazene ligand (HL^2) and the $[Hg(L^2)_2]$ complex were studied by DFT calculations in free gaseous state. the calculated HOMOs and LUMOs are ligand π/π^* orbitals.The strongest absorption band in the TDDFT calculated spectra of HL^2 appears at 372.02 nm due to the HOMO to LUMO electronic transitions. Absorption bands with contribution of metal-ligand bonding or anti-bonding molecular orbitals were found in the calculated electronic spectra of the complex.

References

[1] A. Morsali, L. Hashemi, Mercury(II) coordination polymers, in: A. Morsali, L. Hashemi, Main group metal coordination polymers: Structures and nanostructures, John Wiley & Sons, Inc., Hoboken, NJ, USA, 2017, pp. 83–100.

[2] A. Morsali, M.Y. Masoomi, Structures and properties of mercury(II) coordination polymers, Coord. Chem. Rev. 253 (2009) 1882–1905.

[3] M.K. Rofouei, J. Attar Gharamaleki, E. Fereyduni, A. Aghaei, G. Bruno, H. Amiri Rudbari, Structural and solution studies of two mercury(II) complexes with [1,3-Bis(2-ethoxy)benzene]triazene, Z. Anorg. Allg. Chem. 638 (2012) 220–223.

[4] H.-P. Zhou, J.-H. Yin, L.-X. Zheng, P. Wang, F.-Y. Hao, W.-Q. Geng, X.-P. Gan, G.-Y. Xu, J.-Y. Wu, Y.-P. Tian, X.-T. Tao, M.-H. Jiang, Y.-H. Kan, Anion-induced assembly of different mercury coordination complexes and DFT calculations to evaluate weak interactions between similar double-helical chains, Cryst. Growth Des. 9 (2009) 3789–3798.

[5] J.G. Melnick, G. Parkin, Cleaving mercury-alkyl bonds: A functional model for mercury detoxification by MerB, Science 317 (2007) 225–227.

[6] I. Onyido, A.R. Norris, E. Buncel, Biomolecule–Mercury interactions: Modalities of DNA base–mercury binding mechanisms. Remediation strategies, Chem. Rev. 104 (2004) 5911–5930.

[7] M.K. Rofouei, J. Attar Gharamaleki, M.R. Melardi, S.M. Hosseini, F. Hosseinzadeh, M. Peyman, A. Ghannadan, B. Notash, G. Bruno, H. Amiri Rudbari, Synthesis, characterization and crystal structures of Hg^{II} complexes with asymmetric ortho-functionalized 1,3-bis(aryl)triazenide ligands, Polyhedron, 44 (2012) 138–142.

In-Situ Formation of the Adsorbent Based on Octadecylamine for The Extraction of Ag+ Ions from Aqueous Solutions and Its Determination by Microinjection Fame Atomic Absorption Spectrometry

Ali Asghar Zendehdel[a], Saeed Mohammad Sorouraddin [b], Mir Ali Farajzadeh[c]

Corresponding Author E-mail: aliaznd77@gmail.com

[a] Department of Analytical Chemistry, Faculty of Chemistry, University of Tabriz, Tabriz, Iran.

[b] Engineering Faculty, Near East University, 99138 Nicosia, North Cyprus, Mersin 10, Turkey.

Abstract: In this research, a dispersive solid phase extraction procedure based on changing the solubility of octadecylamine with pH was proposed to determine Ag+ ions in different water samples. In optimal conditions, the developed method showed a linear range of 0.50–200 µg L−1. The limits of detection and quantification were 0.18 and 0.50 µg L−1, respectively. Extraction recovery was 93.6%. The relative standard deviations were less than 4%.

Keywords: Dispersive solid phase extraction; Octadecylamine; pH-induced microextraction; In-situ formation of adsorbent; Silver; Flame atomic absorption spectroscopy

Introduction

In the current era, many efforts are made to develop the methods for detecting metal ions from biological and chemical point of view, and among the various types of metal ions, silver ion is considered for identification due to its effective roles in the biology and environment and also as a valuable metal for the production of products such as mirror, photographic film [1], coin [2], electronic components and paper jewelry [3]. Because of antibacterial properties of silver ion, it is used in antibacterial clothes and water purification [4]. It is utilized in traditional Indian and Chinese medicines because of its antimicrobial properties to eliminate contaminations in food hygiene [5]. The WHO announced that about 0.1 mg L−1 of silver(I) ions does not have adverse effects on human life, and this level in drinking water does not harm human health [6]. Long time exposure to silver or its high concentrations can result in significant health problems. The purpose of this work was analysis of Ag+ ions in aqueous samples by DSPE and FAAS. Because of the presence of amino group in the ODA structure, it can also form complex with Ag+ ions. Therefore, the extraction step is performed without adding further complexing agent. The proposed procedure needs to no desorption step, which is time-consuming and requires sonication or vortexing. Easy operation, short extraction time, high extraction efficiency, and inexpensiveness can be the major advantages of the proposed procedure.

Experimental Section

First, for preparation of ODA solution, 100 mg of ODA was added to a mixture of 4 mL concentrated hydrochloric acid solution (12 M) and 36 mL deionized water. To dissolve ODA, the mixture was stirred at 300 rpm at 80 ºC for 40 min. Then for preparation of buffer solution, triethylamine solution (1.0 M) was mixed with hydrochloric acid solution (0.1 M) in the volume ratio of 1:1. In the following, 1 mL of this solution was added to 5 mL of sample solution or spiked deionized water (10 µg L−1 Ag+) was mixed with 1 mL of the prepared buffer solution in a test tube. Then, 1 mL of the prepared ODA solution was injected into it. The formed cloudy solution was vortexed for 2 min. Then the tube

was centrifuged at 7000 rpm for 7 min. The supernatant was removed and the sedimented particles were dissolved in 100 µL of nitric acid solution (5%, v/v) and injected into FAAS.

Results and Discussion

Various parameters such as the volume of ODA solution, type and amount of desorption solvent, time and speed of centrifugation, and vortexing can affect the extraction efficiency of the procedure. Therefore, their effect should be evaluated and optimized. The LR of the calibration curve was 0.50–200 µg L−1. The LOD (3 Sb/m, where m is slope of the calibration curve and Sb is standard deviation of blank measurements, n=7) was 0.18 µg L−1. The LOQ (10 Sb/m) was obtained 0.50 µg L−1. The precision of the proposed method was evaluated in the solutions containing 10 µg L−1 of Ag+ (intra-day, n=6) and in 4 consecutive days (inter-day). The results of the relative standard deviations (RSDs) were in the range of 2.7–3.9%,. The ER and EF were 93.6% and 46.8, respectively.
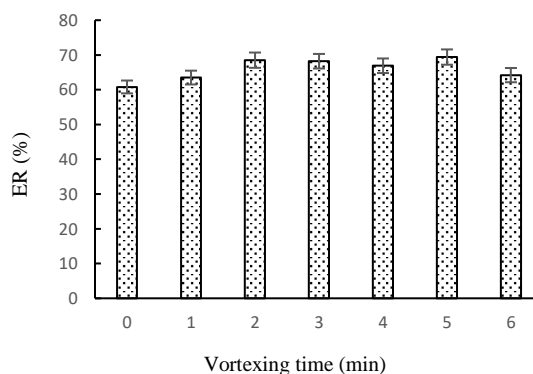
Fig.1. Study of the effect of the volume of ODA solution on ER of Ag+

22nd Iranian Chemistry Congress (ICC22)
Iranian Research Organization for Science and
Technology (IROST)
13-15 May 2024

03231-97589

IROST
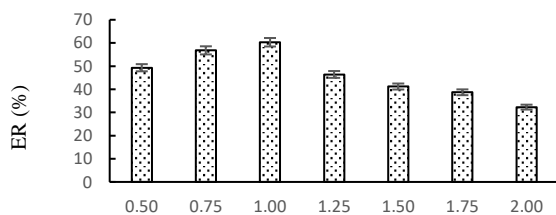
Fig. 2. Study of the effect of vortex time on ER of Ag+.
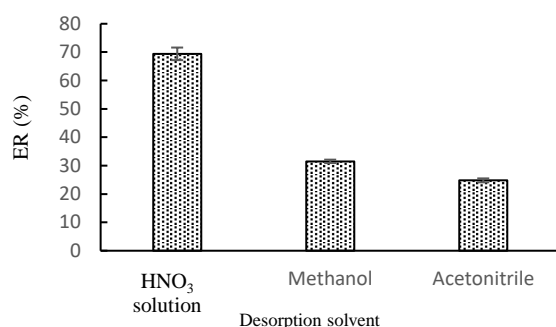
Fig. 3. Study of the nature of desorption solvent
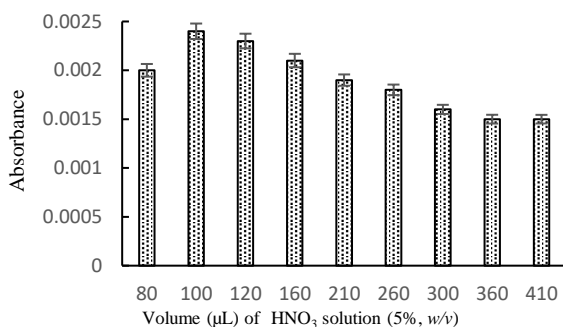
Fig. 4. Studying the volume of HNO$_3$ solution (5%, *w/v*).

Table 1 Tolerance limits of interferent/analyte ratios of coexisting ions in determination of Ag+ ions using the proposed method.

Species	Tolerance limit of interferent / Ag+ ratio
Co^{2+}	800
Cu^{2+}	600
Cd^{2+}	250
Ni^{2+}	600
Zn^{2+}	450
Pb^{2+}	350
Mg^{2+}	1300
K$^+$	1750
Ca^{2+}	2500
Na$^+$	2250
NO$_3^-$	3000
Cl$^-$	300
SO$_4^{2-}$	600

Table 2. Quantitative characteristics of the developed method for Ag(I).

Analyte	LOD [a] (µg L^{-1})	LOQ [b] (µg L^{-1})	LR [c] (µg L^{-1})	r^2 [d]	RSD% [e] Intra-day (n=6)	RSD% [e] Inter-day (n=6)	ER ± SD [f]	EF ± SD [g]
Ag(I)	0.18	0.50	0.50–200	0.993	2.7	3.9	93.6 ± 2.6	46.8 ± 1.3

Conclusions

In this study, ODA was used as adsorbent and complexing agent to extract Ag + ions from aqueous solutions. This extraction method was suggested for the first time based on the dependence of ODA solubility on pH. The results showed that the most amounts of Ag + ions were extracted in the stage of formation of ODA. Therefore, it can be concluded that the most of extracted analyte were in the inside of the particles of ODA, not on the surface of sorbent. Because of this, the diluted solution of nitric acid, which is able to dissolve the particles, had better results than methanol and Table acetonitrile, because in the case of the mentioned solvents, only the desorption of the extracted analytes from the surface of the sorbent was occurred. The use of nitric acid solution led to the easy coupling the method with FAAS. Verification of the method in the determination amount of Ag+ ions was done by analyzing a CRM and several water and wastewater samples. The approach provided satisfactory results including broad LR of the calibration curve, low LOD and LOQ, and high ER.

References

[1] A.S. Kholmogorova, M.L. Chernysh, L.K. Neudachina, I.S. Puzyrev, React. Funct. Polym. 152, 104596 (2020)

[2] M.T. Doménech-Carbó, F.D. Turo, N. Montoya, F. Catalli, A. Doménech-Carbó, C.D. Vito, Sci. Rep. 8, 10676 (2018)

[3] E.Y. Frag, N.A. El-ZaherSally, E.A. Elashery, Microchem. J. 155, 104750 (2020)

[4] N. Duran, P.D. Marcato, G.I.H. De Souza, O.L. Alves, E. Esposito, J. Biomed. Nanotech. 3, 203–208 (2007)

[5] S.P. Deshmukh, S.M. Patil, S.B. Mullani, S.D. Delekar, Mater. Sci. Eng. 97, 954–965 (2019)

[6] P.D. Howe, S. Dobson, Silver and silver compounds: environmental aspects, In: Concise International Chemical Assessment Document, 44, World Health Organi-zation, Geneva, 2002.

Development of Salt-Induced Homogeneous Liquid–Liquid Extraction Using a Deep Eutectic Solvent Performed in a Narrow-Bore Tube for the Extraction of Zn(II), Cu(II), and Cd(II) Ions from Honey Samples

Ali Asghar Zendehdel[a], Saeed Mohammad Sorouraddin [b], Mir Ali Farajzadeh[c]

Corresponding Author E-mail: aliaznd77@gmail.com
[a] Department of Analytical Chemistry, Faculty of Chemistry, University of Tabriz, Tabriz, Iran.
[b] Engineering Faculty, Near East University, Mersin, 10, 99138 Nicosia, North Cyprus, Turkey

Abstract: In this study, a sample preparation procedure based on salt-induced homogeneous liquid–liquid extraction performed in a narrow-bore tube was used for the preconcentration and extraction of Zn(II), Cu(II), and Cd(II) ions from honey samples. The linear ranges and extraction recoveries were obtained in the ranges of 1.5–100 mg kg−1 and 89.6–94.8%, respectively. The detection limits ranged from 0.35 to 0.48 mg kg−1. Low relative standard deviations (C = 10 mg L−1 , n = 6) of 3.1, 2.8, and 3.4% for Zn(II), Cu(II), and Cd(II), respectively, were obtained.

Keywords: homogeneous liquid–liquid extraction.; honey; Zinc; Cadmium; Copper; Flame atomic absorption spectroscopy

Introduction

Honey is a naturally sweet substance produced by bees through the collection and transformation of flower nectar and other plant elements.[1,2] In the present study, an improved version of homogeneous liquid–liquid microextraction (HLLME) as counter current with the aid of salt-induced phenomena was developed to extract and preconcentrate Zn (II), Cu (II), and Cd (II) ions in honey samples. The optimized procedure was used to determine the selected ions in various honey samples to evaluate efficiency of the developed method in real samples.

Experimental Section

At first, the end of a narrow tube (length and external diameter; 45.0 and 1.0 cm, respectively) was connected to a stopcock. Sodium chloride (7 g) was loaded into the tube. Then 7 g sodium chloride along with 200 mL complexing agent (8-HQ, 0.1 M) were added to 27 mL of honey working solution. Next, a mixture of 6.5 mL of ACN and 375 mL of the synthesized DES was added. The homogeneous solution was poured into the tube and passed through the tube at the flow rate of 2 mL min−1. At this stage, tiny droplets of the mixture of the DES and ACN were formed at the interface of solid sodium chloride and solution and due to their lower density compared to the aqueous phase, they were transferred to the top of the tube and collected as a separated layer. The stopcock was closed after passing 8 mL of solution. organic phase It was removed using a 2 mL syringe and injected rapidly into 5 mL deionized water It was eventually analyzed to determine the Zn (II), Cu(II) and cd (II) ions by the FAAS.

Results and Discussion

In the suggested approach, an additional solvent was employed to assist the synthesized DES in extracting the analytes Also with the aid of this solvent, the DES was gathered on the surface of the working solution. Hence, The experiments showed that only ACN and acetone produced the two-phase system by passing the solution through the tube. The results shown in Fig. 1 indicate that ACN has higher efficiency compared to acetone.

The desired ions were extracted and separated from the water based solution as it flowed through the salt particles, thanks to the salting-out effect. By this action, the aqueous solution was saturated with sodium chloride, leading to the formation of tiny droplets of organic solvents. These tiny droplets ascended within the tube and extracted the analytes in a way that resembled a continuous extraction technique. EFs of 81.0, 78.0, and 76.6 and ERs of 94.8, 91.3, and 89.6%, for Zn(II), Cu(II), and Cd(II) ions, respectively, show good performance of the proposed method. The linear ranges of calibration curves of the developed method are comparable with those of the previous methods. The LODs, LOQs, and RSDs of the proposed method are comparable with or better than those of the presented methods.
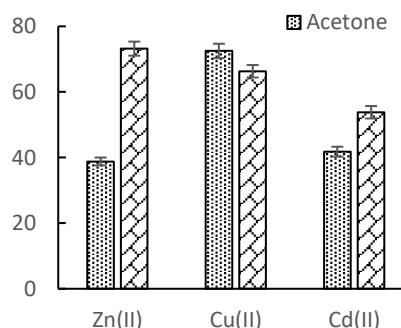
Fig.1: Optimizing the type of co-extraction solvent

158

22nd Iranian Chemistry Congress (ICC22)
Iranian Research Organization for Science and
Technology (IROST)
13-15 May 2024

03231-97589

ISC

IROST
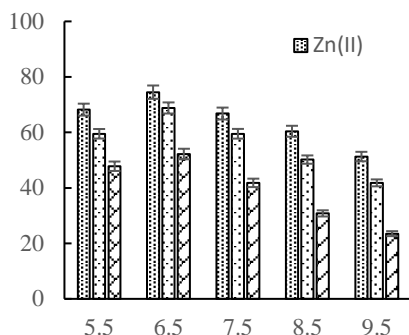
Fig. 2. Investigating the volume of CAN
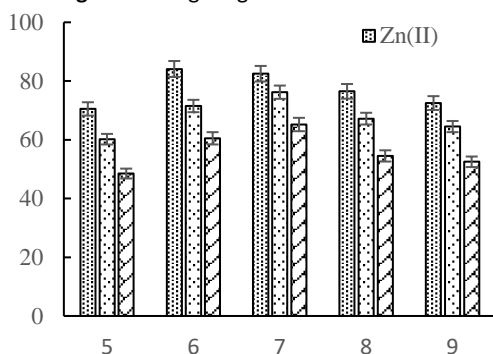
Fig.3. Investigating the amount of salt loaded into the extraction tube.
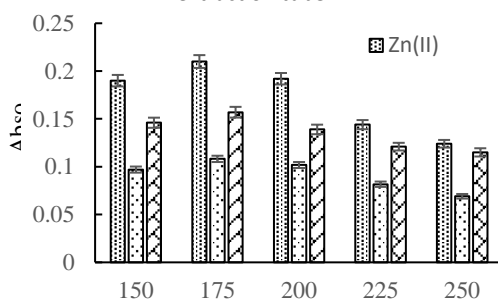
Fig.4 Investigating the volume of DES
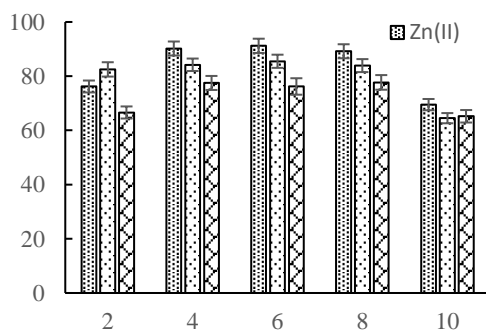
Fig. 5. Study of the effect of salt concentration in the working solution.
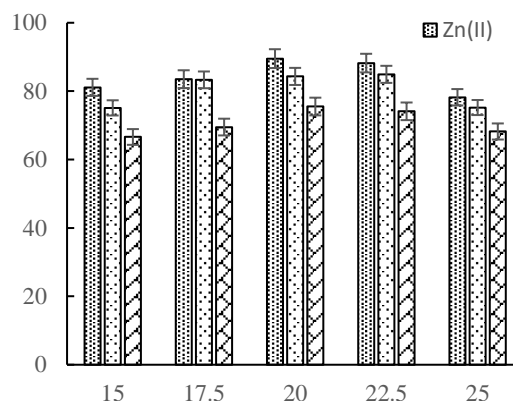
Fig. 6. The effect of pH.
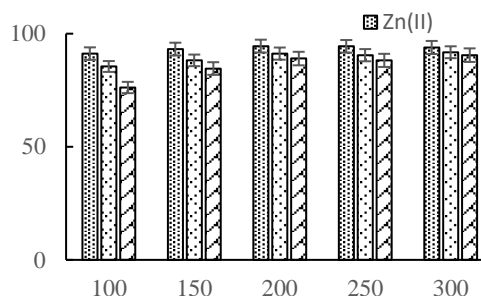
Fig.7. Investigating the volume of the complexing agent solution

Table 1: Tolerance limits of interferent/analyte ratios of coexisting ions in determination of Zn(II), Cu(II), and Cd(II) ions using the proposed method

Species	Tolerance limit of interferent / analyte ratio		
	Zn(II)	Cu(II)	Cd(II)
Ca^{2+}	2000	2000	1750
Na^+	1750	2000	1500
Fe^{3+}	2000	1750	1750
Al^{3+}	1000	2000	2000
Pt(II)	750	1000	850
Co(II)	800	800	1000
Ni(II)	800	800	600
Mg(II)	1500	2000	2000
Pb(II)	800	700	500
K^+	1250	1250	1250
SO_4^{2-}	1750	1500	1500
NO_3^-	2000	2000	2000

Table 2 Quantitative characteristics of the method for the studied heavy metal ions

Analyte	LR[a] ($\mu g\ Kg^{-1}$)	r^{2b}	LOD[c] ($\mu g\ Kg^{-1}$)	LOQ[d] ($\mu g\ Kg^{-1}$)	RSD%[e]		ER ± SD[f]	EF ± SD[g]
Zn(II)	1.5-100	0.9959	0.48	1.5	3.1	4.0	94.8 ± 2.9	17.1 ± 0.5
CCu(II)	1.0-100	0.9914	0.36	1.0	2.8	3.6	91.3 ± 2.5	16.4 ± 0.4
CCd(II)	1.0-100	0.9993	0.35	1.0	3.4	4.5	89.6 ± 3.0	16.1 ± 0.5

Conclusions

In this study, a developed mode of homogeneous liquid–liquid extraction using counter current extraction was implemented. The aim of this technique was to extract and determine Zn(II), Cu(II), and Cd(II) ions from honey samples and determine by FAAS. In the proposed method, the homogeneous honey working solution containing the analytes, ACN, and a water-immiscible DES was broken in the presence of high concentration of salt. The results demonstrated that the proposed method is fast, sensitive, and simple, as well as has high EFs and ERs. In addition, the proposed extraction method is environmentally friendly because of using DES as an extraction solvent. Consequently, it is likely that by adjusting the extraction conditions, this method can be adapted to extract the target compounds in similar sample types.Ultimately, the method was successfully utilized to accurately determine concentrations of the studied ions at the mg kg−1 level in various honey samples.

References

1 P. Pohl, Determination of metal content in honey by atomic absorption and emission spectrometries, TrAC, Trends Anal. Chem., 2009, 28, 117–128.

2 A. Srivastava, L. J. Rao and T. A Shivanandapp, A novel cytoprotective antioxidant: 4-hydroxyisophthalic acid, Food Chem., 2012, 132, 1959–1965.

3 K. A. Osman, M. A. Al-Doghairi, S. Al-Rehiayani and M. I. Helal, Mineral contents and physicochemical properties of natural honey produced in Al-Qassim region, Saudi Arabia, J. Food, Agric. Environ., 2007, 5, 142.

Introduction of Dispersed Solid Extraction Method Based on Magnetic Adsorbent with Octadecylamine to Extract Cu (II) and Cd (II) Ions from Dairy Products

Ali Asghar Zendehdel[a], Saeed Mohammad Sorouraddin [b], Mir Ali Farajzadeh[c]

Corresponding Author E-mail: aliaznd77@gmail.com

[a] Department of Analytical Chemistry, Faculty of Chemistry, University of Tabriz, Tabriz, Iran.

[b] Engineering Faculty, Near East University, Mersin, 10, 99138 Nicosia, North Cyprus, Turkey.

Abstract: In this study, a brand-new, very effective adsorbent was created for the extraction of magnetically distributed solid phase. Octadecylamine and Fe_3O_4 were co-precipitated to create the adsorbent. Finally, a flame atomic absorption device was used to study the enriched analytes. The detection limits of the above method for Cu (II) and Cd (II) were 0.85 and 0.56 µg/L, respectively, under ideal conditions. Cu (II) and Cd (II) ions had a linear range of 200-2.3 and 1.5-200 µg/L, respectively. Copper (II) and cadmium (II) showed enrichment factors of 27.0 ± 0.7 and 26.5 ± 0.8 and extraction efficiency of 96.3 ± 2.6% and 94.6 ± 2.8%, respectively.

Keywords: solid extraction method based on magnetic; octadecylamine; dairy products; Cadmium Copper; Flame atomic absorption spectroscopy

Introduction

The need for milk in the world will probably increase by 35% by 2030, which is mainly due to the growth of demand in Latin America, as well as Africa and Asia [1]. The production of dairy products In different countries, especially in developing countries, is increasing strongly and has a significant contribution to health, environment, nutrition and livelihood [2]. Complex colloidal compounds of milk [3] extracted from mammals are needed by all people [4]. Milk is a complete food and its nutrition is more important for the health of babies [5,6]. The purpose of this research is to identify the concentration of essential and toxic metals (cadmium and copper) in two samples of milk, two samples of cheese, two samples of buttermilk and one sample of yogurt purchased from different brands in the markets of Tabriz and to check whether these levels of these metals are lower. Or higher than the limit recommended by (WHO) and other regulations for human consumption.

Experimental Section

The absorbent was synthesized by simultaneous chemical deposition. Concomitant deposition is an effective method of synthesizing MNPS. To prepare it, octadecylamine was combined with hydrochloric acid and dionized water. To dissolve octadecylamine, we put a mixture of water. Then some $FeSO_4.7H_2O$ and $FeCl_3-6H_2O$ were poured into the solution. Up to Fe_3O_4 was produced. The MNPS, which had been created despite the external magnetic field, was isolated. After adding the adsorbent to the working solution and performing the adsorbent extraction process inside the solution, it was carried out by a strong magnet. Nitric acid was added as solvent and adsorbent to the adsorbent particles then the adsorbent was separated from the solution by a strong magnet. The resulting solution containing the analytes was injected into the AAS to determine the extracted values of the analytes using the highest peak.

Results and Discussion

The method's performance was evaluated in terms of reproducibility (RSDs within and between days), linear range (LR), limit of quantification (LOQ), limit of detection (LOD), coefficient of determination (r^2), ER, and EF for both cations in the working solution. r^2 values of 0.9973 and 0.9976 for Cu(II) and Cd(II), respectively.

Calibration curves for Cu(II) and Cd(II) were obtained using standard solutions with similar turbidity and linear ranges of 200–2.3 and 1.5–200 µg/L for Cu(II) and Cd(II), respectively. The limits of detection (LODs) for Cu(II) and Cd(II) were 0.85 and 0.56 µg/L, respectively, which were calculated using the standard deviation of the blank (SB) and the slope of the calibration graph. (LOQs) for Cu(II) and Cd(II) were 2.3 and 1.5 µg/L, respectively, which were calculated using 10 times the standard deviation of the blank (10SB) divided by the slope of the calibration graph (m) The enrichment factors (EFs) and extraction recoveries (ERs) for Cu(II) were 27.0 ± 0.7% and 96.3 ± 2.6%, respectively, while for Cd(II) they were 26.5 ± 0.8% and 94.6 ± 2.8%, respectively.

22nd Iranian Chemistry Congress (ICC22)
Iranian Research Organization for Science and Technology (IROST)
13-15 May 2024

03231-97589

IROST
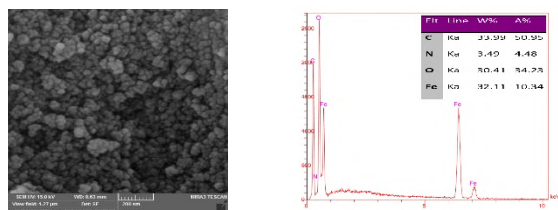
Fig.1: Image SEM nanoparticle Fe3O4 modified and EdX spectrum
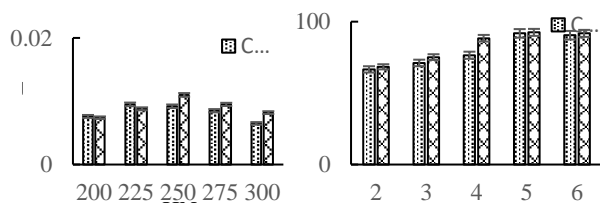
Fig.2: PRC size halal nitric acid and Vortex time

Table1: Tolerance limits of interferent/analyte ratios of coexisting ions in determination of Cu(II), and Cd(II) ions using the proposed method

Species	Tolerance limit of interferent / analyte ratio	
	Cu(II)	Cd(II)
Ca^{2+}	1750	1750
Co(II)	800	900
Ni(II)	600	900
Zn(II)	900	1000
Pb(II)	800	600
Mg(II)	1500	1500
K^+	1500	2000
Na^+	1250	1750
Fe^{3+}	1500	750
Al^{3+}	1500	2000
K^+	1250	1500
SO_4^{2-}	1500	2000
NO_3^-	2000	2000

Conclusions

In this work, MSPE research based on Magnetic adsorbent methods for extraction and preconcentration of dairy products (milk, buttermilk, cheese and yogurt) was presented. The above nanocomposite acts as a reliable and efficient absorbent. The obtained results show outstanding features in the above method, such as suitable reproducibility, low LOD, high EFs and better ERs. Low cost, simplicity and not time-consuming are the advantages of this method.

References

[1] A. T. Adesogan and G. E. Dahl, MILK Symposium Introduction: Dairy production in developing countries, J DAIRY SCI 103(11), 9677-9680 (2020)

[2] D. Grace, F. Wu, A.H. Havelaar. MILK Symposium review: Foodborne diseases from milk and milk products in developing countries—Review of causes and health and economic implications, J DAIRY SCI 103(11), 9715-9729 (2020)

[3] Lean, E. J. "Fox and Cameron's Food Science, Nutrition and Health", (7th Ed.) Edward Arnold Publishers, London, 2006, pp. 80-129

[4] Belitz, H. D., Grosch, W. and Schieberle, P. "Food Chemistry", 4th Revised and Extended ed, SpringerVerlay Berlin Heidelberg, 2009, pp. 421-428

[5] Choodamani, C., Sudhir, K. J., Chaturvedani, A. K., Sambhuti, S. S., Monika and Upendra, W. "A Review on Heavy Metals Residues in Indian Milk and Their Impact on Human Health". International Journal of Current Microbiology and Applied Sciences, 7(05), 2018, pp.1260-1268 doi: https://doi.org/10.20546/ijcmas.2018.705.152

[6] C. M. Iwegbue, S. O. Nwozo, E. K. Ossai, and G. E. Nwajei. Heavy Metal Composition of Some Imported Canned Fruit Drinks in Nigeria, J FOOD TECHNOL 3(3), 220-223 (2008)

Table2: Quantitative characteristics of the method for the studied heavy metal ions

Analyte	LR[a] (μg L^{-1})	r^{2b}	LOD[c] (μg L^{-1})	LOQ[d] (μg L^{-1})	RSD%[e]				ER ± SD[f]
					C = 10 μg L^{-1}		C = 50 μg L^{-1}		
					Intra-day	Inter-day	Intra-day	Inter-day	
Cu(II)	2.3-200	0.9973	0.85	2.3	2.9	3.6	2.6	3.4	96.3 ± 2.6
Cd(II)	1.5-200	0.9976	0.56	1.5	3.1	3.5	2.9	3.5	94.6 ± 2.8

Synthesis Of Carbon Spheres by Green Way for Catalyst Preparation of Pyridopyrimidine Compounds

Zahra Torkashvand, Milad Mohammadi Rasooll, Hassan Sepehrmansourie, Mohammad Ali Zolfigol*

Corresponding Author E-mail: zolfi@basu.ac.ir & mzolfigol@yahoo.com.

Department of Organic Chemistry, Faculty of Chemistry and Petroleum Sciences, Bu-Ali Sina University, Hamedan, Iran.

Abstract: Materials made of carbon that can be synthesised and characterised at the nano level have become a mainstay in the nanotechnology arena. A type of mesoporous carbon composites with spherical morphology on the nano scale called carbon spheres are synthesized in a green way for various applications such as energy storage and conversion, absorption, catalysis, biomedicine, and environmental applications. Therefore, it has been used as a catalyst for the phenylpyrido[2,3-d]pyrimidine derivatives preparation reaction, that they have many medical and medicinal properties such as antibacterial and antifungal.
Keywords: carbon sphere; catalyst; pyridopyrimidne

Introduction

Carbon spheres have unique properties such as high porosity, low density, excellent reactivity, thermal insulation, and high compressive strength. As a result, these properties lead to an increase in the efficiency of its applications[1]. So far, carbon spheres have been used in energy storage and conversion, absorption, catalyst, biomedicine[2-4]. The carbon spheres that were made were used as organic catalysts to make pyridopyrimidine derivatives Derivatives of pyridopyrimidine compound in the structure of substances such as niacin and some drugs such as isoniazid, bipyridine, pyridoxal, there are also coal tar and Sulfapyridine [5]. Recently, with the growing shortages of traditional energy sources and fears of greenhouse gas induced global warming, scientists and engineers are looking for a renewable, highly efficient method of creating and storing energy without disruption to the environment [6].

Experimental Section

Conducting the synthesis reaction of pyridopyrimidine derivatives using carbon spheres as organic catalyst in solvent-free conditions and at a temperature of 110°C degrees gave favorable results, which led to high reaction efficiency and short time to perform, as well as easy purification.
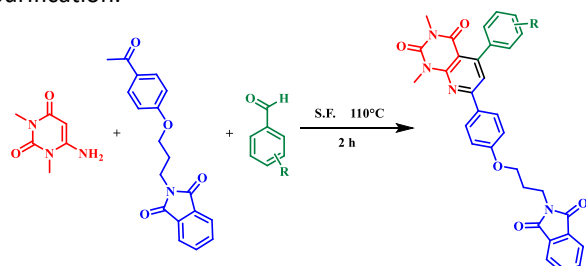
Scheme 1: Reaction of formation of pyridopyrimidine with the help of carbon spheres

Results and Discussion

The SEM analysis of the intended catalyst has confirmed the well-formed spherical structure. This assures us that the carbon spheres are formed.

Conclusions

Finally, the attempt to make pyridopyrimidine derivatives in relatively green and mild conditions using an organic catalyst called carbon spheres was successful.

References

[1] Gill, I., & Ballesteros, A. (1998). Encapsulation of biologicals within silicate, siloxane, and hybrid sol– gel polymers: an efficient and generic approach. *Journal of the American Chemical Society*, *120*(34), 8587-8598. https://doi.org/10.1021/ja9814568

[2] Liu, H. J., Cui, W. J., Jin, L. H., Wang, C. X., & Xia, Y. Y. (2009). Preparation of three-dimensional ordered mesoporous carbon sphere arrays by a two-step templating route and their application for supercapacitors. *Journal of Materials Chemistry*, *19*(22), 3661-3667. https://doi.org/10.1039/B819820A

[3] Huang, X., Kim, S., Heo, M. S., Kim, J. E., Suh, H., & Kim, I. (2013). Easy synthesis of hierarchical carbon spheres with superior capacitive performance in supercapacitors. *Langmuir*, *29*(39), 12266-12274. https://doi.org/10.1021/la4026969

[4] Wang, J., Feng, S., Song, Y., Li, W., Gao, W., Elzatahry, A. A., ... & Zhao, D. (2015). Synthesis of hierarchically porous carbon spheres with yolk-shell structure for high performance supercapacitors. *Catalysis Today*, *243*, 199-208. https://doi.org/10.1016/j.cattod.2014.08.037

[5] Saurat, T., Buron, F., Rodrigues, N., de Tauzia, M. L., Colliandre, L., Bourg, S., ... & Routier, S. (2014). Design, synthesis, and biological activity of pyridopyrimidine scaffolds as novel PI3K/mTOR dual inhibitors. *Journal of medicinal chemistry*, *57*(3), 613-631. https://doi.org/10.1021/jm401138v

[6] Liu, J., Wang, X., Gao, J., Zhang, Y., Lu, Q., & Liu, M. (2016). Hollow porous carbon spheres with hierarchical nanoarchitecture for application of the high performance supercapacitors. *Electrochimica Acta*, *211*, 183-192. https://doi.org/10.1016/j.electacta.2016.05.217

Design, Synthesis, And Biological Properties of Novel Triazine Based Ampicillin Derivatives

Alireza Karami, Ahmad Reza Massah

Corresponding Author E-mail: massahar@yahoo.com

Department of Medical Chemistry, Shareza Branch, Islamic Azad University, P.O. Box 311-86145, Shareza, Isfahan, Iran

Abstract: A few new beta lactam-ring derivatives have been synthesized under green solvent and confirmed by FT-IR and ^{1}H-NMR. The antibacterial potential of the synthesized compounds was also studied against staphylococcus aureus and Escherichia coli.

Keywords: anti-biotics; triazine; ampicillin; cyanuric chloride

Introduction

Microbial natural products, particularly those produced by filamentous Actinobacteria, have been a cornerstone of the pharmaceutical industry for more than half a century [1]. Bacterial resistance to antibiotics has been increasing in Europe over the last few years. New classes of antibiotics have not been introduced recently and thus, more resistance to old drugs is developing daily [2].

The cell wall plays a key role in the survival of bacteria and is considered as the first line of defense against pathogenic and lethal substances. Gram-positive and gram-negative bacteria have a peptidoglycan structure in their cell wall, which is composed of the connection of disaccharide units, and the glycan strands are polymerized by the glycosyltransferase enzyme. Transpeptidase plays the main role in cross-linking and cross-linking in the bacterial cell wall, which connects the two amino acid dialanine linker.[3]

Pharmaceutical substances do not cause pollution as much as other pollutants such as pesticides and herbicides. However, in the last decade, the increase in the use of drugs has led to an increase in the production of new drugs. Since pharmaceutical chemicals exist in very low concentrations, they are not considered as a threat to the environment, so the information There is not enough information about the effects of these medicinal chemicals in the hazardous environments associated with it for humans and the environment [4]

Heterocycles play an important role in synthetic drugs and biological processes. Heterocycle triazine plays an important role in the pharmacophore of antimalarial, antibacterial, and anticancer [5].

Considering the low complexity of beta-lactam drugs and the antibacterial properties of the triazine ring, in this research, we have tried to prepare hybrid derivatives of these compounds and also to investigate the antibacterial properties of these derivatives.

Experimental Section

At first, amine was added to cyanuric chloride and stirred for replacement of amine to chlorine then the same amine was added and stirred for replacement to the second chlorine with amine, and then ampicillin was added for replacement to the last chlorine with ampicillin.

Results and Discussion

The main target for this project is the synthesis of triazin ampicillin derivatives according to green chemistry and under safe solvent conditions.

Firstly, 2-amine-4,6-dichloro-phenyl-1,3,5-triazin was prepared by addition-elimination of cyanuric chloride with amine under the acetone.
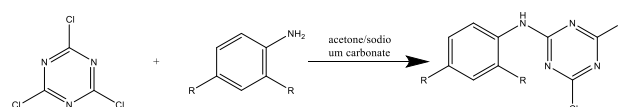
Then the same amine was added and make diamine triazine under the same reaction conditions at room temperature.
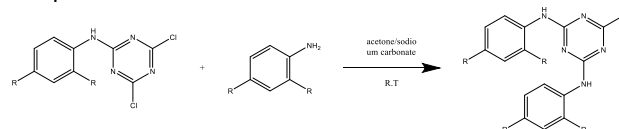
Then the last chlorine replaced with ampicillin in carbon tetrachloride.
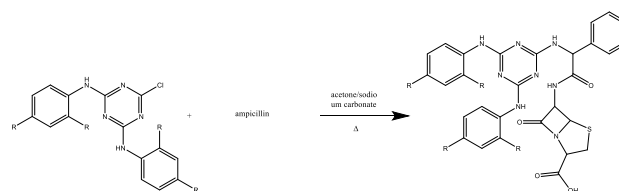
22nd Iranian Chemistry Congress (ICC22)
Iranian Research Organization for Science and
Technology (IROST)
13-15 May 2024

03231-97589

Conclusions

In this work, some new penicillin derivatives have been synthesized and charecterized by FT-IR and ^{1}H-NMR. The antibacterial potential of the synthesized compounds was also studied against.

References

[1] Joynt, R., & Seipke, R. F. (2018). A phylogenetic and evolutionary analysis of antimycin biosynthesis. Microbiology, 164(1), 28-39.

[2] Ferraz, R., Silva, D., Dias, A. R., Dias, V., Santos, M. M., Pinheiro, L., ... & Branco, L. C. (2020). Synthesis and antibacterial activity of ionic liquids and organic salts based on penicillin g and amoxicillin hydrolysate derivatives against resistant bacteria. Pharmaceutics, 12(3), 221.

[3] Shiri, Y., Khodavirdipour, A., & Kalkali, N. (2020). Re-construction of co-expression network of genes involved in bacterial cell wall synthesis and their role in penicillin resistance. Avicenna Journal of Clinical Microbiology and Infection, 7(3), 65-71.

[4] Ghamkhari, A., Mohamadi, L., Kazemzadeh, S., Zafar, M. N., Rahdar, A., & Khaksefidi, R. (2020). Synthesis and characterization of poly (styrene-block-acrylic acid) diblock copolymer modified magnetite nanocomposite for efficient removal of penicillin G. Composites Part B: Engineering, 182, 107643. nanocomposite for efficient removal of penicillin G. Composites Part B: Engineering. 2020; 182:107643.

[5] Dinari, M., Gharahi, F., & Asadi, P. (2018). Synthesis, spectroscopic characterization, antimicrobial evaluation and molecular docking study of novel triazine-quinazolinone based hybrids. *Journal of Molecular Structure*, *1156*, 43-50.

Co-Delivery System of Triple Anticancer Drugs Using Chitosan Modified Single-Walled Carbon Nanotube: Molecular Dynamics Simulation Study

Leila Tohidifar[a], Mohammad H. Kowsari[*a,b]

Corresponding Author E-mail: mhkowsari@iasbs.ac.ir

[a] Department of Chemistry, Institute for Advanced Studies in Basic Sciences (IASBS), Zanjan, 45137-66731, Iran.

[b] Centre for Research in Climate Change and Global Warming (CRCC), Institute for Advanced Studies in Basic Sciences (IASBS), Zanjan , 45137-66731, Iran.

Abstract: Molecular dynamics (MD) simulations were applied for investigation of co-loading of doxorubicin (DOX), paclitaxel (PTX), and methotrexate (MTX) drugs on/into the chitosan functionalized single-walled carbon nanotube (FSWCNT) in the various conditions. Results indicate that encapsulation process is desired strategy for effective drugs co-loading using FSWCNT, especially for encapsulated DOX molecules.

Keywords: Combinational Chemotherapy; Single-Walled Carbon Nanotube; Chitosan; Doxorubicin; Paclitaxel; Methotrexate; Molecular Dynamics Simulation

Introduction

Traditional cancer treatment with single chemotherapeutic agents possess many problems due to the complexity of cancer which involves various pathways with substantial drug resistance. Moreover, delivery of drugs to the normal and abnormal cells as well as their excretion from the body and degradation before reaching targeted tissues are another chalenges of chemotherapeutic drugs administration techniques which significantly reduce the overall therapeutic effects. To address these issues, nonobiotechnology based combinational chemotherapy has been gained ground in cancer treatment [1]. Various pH-sensitive polymers such as chitosan (CS) have been employed for drug delivery systems due to their ability for icreasing drug solubility, protect it from inactivation, and exhibit controlled release [2]. Besides, carbon nanotubes (CNTs) have been gaining attention for targeted drug delivery applications. Compared to loading on the surface, the drug encapsulation provides more advantages as drug molecules are released within the targeted tissues in a specific condition and prevent any undesirable degradation [1]. Our goal in this study is to compare the effectiveness of drug loading patterns on/into the CS functionalized single-walled carbon nanotube (FSWCNT) in the case of triple ani-cancer drugs delivery applications using molecular dynamics (MD) simulations. Toward this aim, doxorubicin (DOX), paclitaxel (PTX), and methotrexate (MTX) (three of the most influential potent agents used in fighting a wide range of cancers) were chosen to propose suitable model of a triple-drug delivery system for optimal therapeutic effects.

Computational Section

A (12,12) armchair SWCNT terminated with hydrogen atoms with a diameter of approximately 16.5 Å and 50 Å in length was designed by a modified python script named BuildCstruct. The structure of drugs DOX, PTX, and MTX were extracted from the crystal structures with PDB codes (1I1E), (1tub), and (1DDS), respectively. CS chain consisting of 15 units bounded together via beta-1,4 linkage in 3:2 ratio of GCS:NAG (degree deacetylation of 60%) was obtained using the AmberTools program. The proper structure of CS modified SWCNT consisting of two CS chains surrounding the SWCNT surface was obtained through minimization and equilibration followed by 100 ns MD production simulation. The four initial systems are distinguished by drugs location listed as follows: (1) FSWCNT with four DOX, four PTX, and four MTX molecules; (2) the FSWCNT with two DOX molecules encapsulated, and two DOX molecules and four PTX and four MTX adsorbed on the sidewall of the SWCNT; (3) the FSWCNT with two MTX molecules encapsulated, and two MTX, four DOX and four PTX molecules adsorbed on the sidewall of the SWCNT; (4) the FSWCNT with one DOX molecule and one MTX molecule encapsulated, and three DOX, three MTX and four PTX molecules adsorbed on the sidewall of the SWCNT. MD simulations were performed using GROMACS 5.0.4 package [3]. The drug molecules and SWCNT were parametrized by using the updated general AMBER force field (GAFF) and the GLYCAM 06j force field was used for CS chains. All the complexes were surrounded by TIP3P modelled water molecules, Na^+, and Cl^- ions in concentration of 0.1 M NaCl. After minimization, 400 and 2000 ps *NVT* and *NPT* equilibration processes, respectively, 200 ns production run performed in *NPT* ensemble where the temperature and pressure were controlled at 310 K and 1 bar by means of Nose-Hoover thermostat and Parrinello-Rahman barostat. The integration time step of 2 fs was adopted and a cutoff distance of 12 Å was selected.

22nd Iranian Chemistry Congress (ICC22)
Iranian Research Organization for Science and
Technology (IROST)
13-15 May 2024

03231-97589

ISC

IROST

Results and Discussion

Despite of the numerous experimental studies referring to the simultaneous loading of the anticancer drugs on the nano-carriers, the triple loading mechanism of drugs (DOX, PTX, and MTX agents) on/into the SWCNT-based carriers have been reported for the first time in this research. As mentioned above, we probed the loading process and interactions of the three drugs with CS-CNT nano-carrier at the various conditions to produce a more effective multiple-drug delivery system. To quantitatively address the details of this phenomenon, the van der Waals (vdW) and Coulomb (Coul) intermolecular interaction energies between drugs and FSWCNT are reported in Table 1.

Table 1. Average intermolecular interaction energies (kJ. mol^{-1}) between drugs and FSWCNT in all considered systems.

System	Intermolecular Interaction Energy		
	vdW	Coul	Total
FSWCNT@Sidewall	-1353.97	-140.38	-1494.35
FSWCNT@DOX Encapsulated	-2057.34	-173.48	-2230.82
FSWCNT@MTX Encapsulated	-1970.82	-117.83	-2088.65
FSWCNT@DOX, MTX Encapsulated	-1750.17	-95.28	-1845.45

Based on these data, negative values of vdW and Coul interactions can be evidence of the strong affinity of all three drugs towards the FSWCNT and their simultaneous adsorption on the nano-vector substrate in the four designed systems which the contribution of the vdW energies is predominant. Based on the available observations related to the mechanism of DOX and PTX adsorption on the SWCNTs surface and our MD simulation results, it is indicated that the planar tricyclic moiety of DOX and three separated aromatic benzene rings of PTX have the most contributions in the stable drug adsorption process through π-π stacking yet supplemented by X-π (X = C-H, N-H, and C=O) interactions. In the case of MTX molecules, it is indicated that π-π stacking interactions between their pteridine and aromatic benzene ring moieties and aromatic surface of SWCNT are the dominant forces involved in loading process. A comparison between four considered systems reveals significant differences in drugs interactions with the FSWCNT which the following encapsulation loading patterns tends to the most efficacy of drugs loading on the nano-vector substrate. Interestingly, the system consisting of two DOX molecules encapsulated has the highest intermolecular interaction energy of ~ -2230 kJ. mol^{-1} among the other systems may also plays a very important role in the drug delivery. In agreement with the energy findings, the results of dynamic analysis indicate the desired effect of drugs encapsulation strategy on the effective loading of therapeutic agents, specially encapsulation of DOX molecules. Calculated mean square displacement (MSD) (Main parameter for estimation of particles mobility) for DOX, PTX, and MTX molecules as shown in Figure 1 predicts the lowest values in the system based two DOX encapsulated molecules (red lines) in the case of all three drugs. Since the lower MSD values can be attributed to the stronger drug-FSWCNT interactions, the higher efficacy loading pattern can be predicted for DOX encapsulation process.
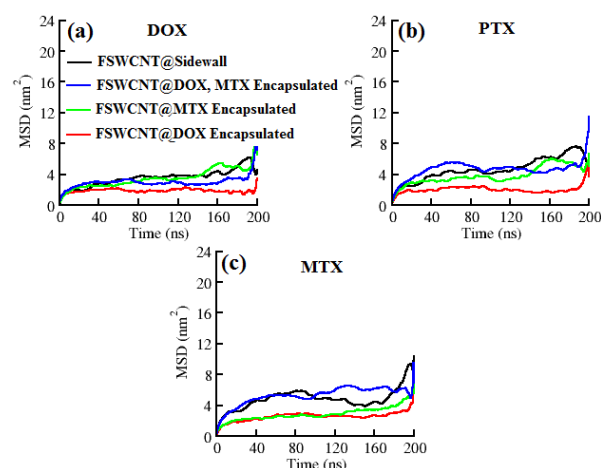
Fig. 1. Mean square displacement (MSD) versus the simulation time for (a) DOX, (b) PTX, and (c) MTX drug molecules in four studied systems.

Conclusions

MD simulations were carried out to investigate the co-loading of three anti-cancer drugs (DOX, PTX, and MTX) on/into CS functionalized SWCNT (FSWCNT). Strong affinity of all three drugs towards the FSWCNT substrate as well as their simultaneous adsorption are observed. According to the energy and dynamic analysis, the effective drug loading pattern is belong to the system including two DOX molecules encapsulated which can be desired system for delivery of these drugs.

References

[1] Shrestha, B; Wang, L; M. Brey, E; et al. (2021). Smart nanoparticle for chemo-based combinational therapy. *Pharmaceutics*, 13(6), 853-884.

[2] Aranaz, I; R. Alcantara; Civera, A; et al. (2021). Chitosan: An overview of its properties and applications. *Polymers*, 13(19), 3256-3282.

[3] Van Der Spoel, D., Lindahl, E., Hess, B., et al. (2005). Gromacs: fast, flexible, and free. *J. Comput. Chem*., 26 (4): 1701-1718.

Synthesis and Application of a Novel Ion-Imprinted Polymer as A Colorimetric Sensor for the Detection of Lead Ions

Nargess Yousefi-Limaee

Corresponding Author E-mail: yousefi-n@icrc.ac.ir

Department of Environmental Research, Institute for Color Science and Technology, Tehran, Iran.

Abstract: A new colorimetric chemosensor was synthesized for the detection of lead ions. In this regards, a novel ion-imprinted polymer nanoparticles was designed in which dithizone was used as a reagent for the detection of Pb^{2+} ions. The results indicated the successful application of sensor for trace detection of lead ions.

Keywords: Ion-imprinted polymer; Colorimetric sensor; Detection

Introduction

One of the noteworthy methods for the preparation of optical sensors is the use of imprinting technology [1]. Ion imprinted polymers are the lock-key system that are prepared by a complex reaction between a metal ion and a ligand followed by the polymerization reaction [2]. Ion-imprinted polymers are important due to their high selectivity and sensitivity for the preconcentration and detection of different metal ions [3].

Heavy metals produced in most industries cause the important environmental problems. Heavy metals damage the several organs including liver, nerves, and bones of human via blocking the functional groups of vital enzymes and also, are carcinogenic to human beings. Many industries discharge lots of toxic heavy metals such as Pb, Cd, Cu, Zn, and Ni to the environment. Therefore, the removal of heavy metals and detection of their levels are of interest for researchers [4].

Ion-imprinted technology is developed as a new separation technique which can be used as the preconcentration method as well as sensing properties by its design using proper ligand.

In this study, the novel colorimetric chemosensor based on ion-imprinted polymer was prepared for the detection of trace levels of Pb^{2+} ions. Moreover, the removal of lead ions was studied at optimized conditions and also, non-imprinted polymer was prepared in the absence of Pb^{2+}. The non- and ion-imprinted polymer were characterized using UV-Vis analysis, Scanning Electron Microscopy (SEM), and Fourier Transform Infrared Spectrometry (FT-IR). The results show the proper color change of chemosensor by lead ions in the presence of interfering ions.

Experimental Section

For the synthesis of IIPs, lead ions were stirred with dithizone as the complexing agent in ethanol for 30 min. Afterwards, hydroxyethylmethacrylate (HEMA) was added to the mixture as the functional monomer and stirred for 30 minutes. Then, the required amount of Ethylene glycol dimethacrylate (EGDMA) and tert-Butyl hydroperoxide (TBHP) was added as the crosslinker and initiator, respectively. The mixture was stirred for 30 min and the polymerization reaction was completed for 24 hours under a nitrogen atmosphere at 60 °C. The final product was washed with ethanol to remove unreacted reactants. The non-imprinted polymer was prepared using above protocol in the absence of lead ions.
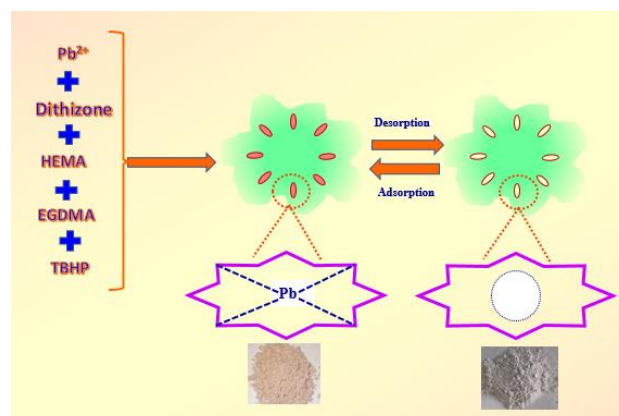
Fig.1: Schematic representation of colorimetric chemosensor-based ion-imprinted polymer synthesis.

Results and Discussion

After preparing the non- and ion-imprinted polymer, Fourier transform-infrared spectroscopy (FT-IR) and scanning electron microscopy (SEM) were used to identify the functional groups and morphology of the prepared sensor, respectively. FT-IR spectrum of NIP and IIP were represented in Figure 2. The peak appearing at 3440 cm^{-1} belongs to OH stretching vibration. The band at 2956 cm^{-1} is attributed to C-H stretching vibration. The band at 1732 cm^{-1} is cause by the stretching vibration of the carbonyl group. Also, the absorption band at 1461 cm^{-1} is related to C-C bending.

22nd Iranian Chemistry Congress (ICC22)
Iranian Research Organization for Science and
Technology (IROST)
03231-97589
13-15 May 2024

IROST

a)

b)
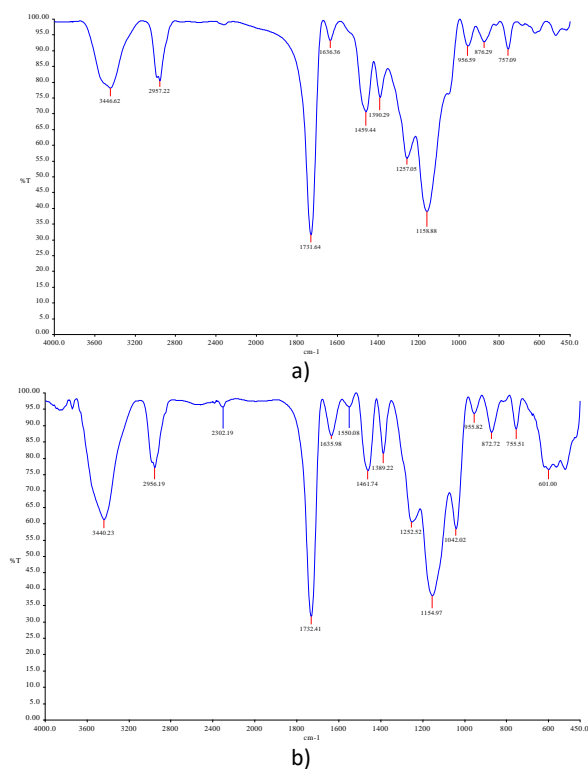
Fig.2: FT-IR spectrum of a) NIP and b) IIP.

The scanning electron microscopy image of prepared non- and ion-imprinted polymers are shown in Figure 3. The results show the spherical and uniform particles for both NIP and IIP.
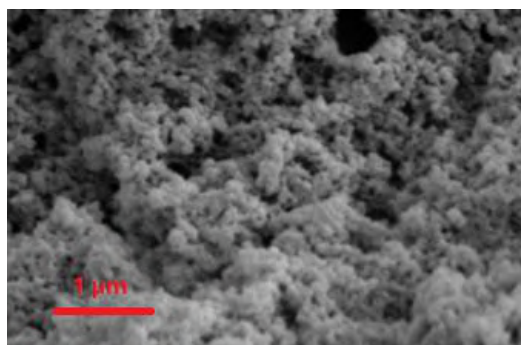
a)
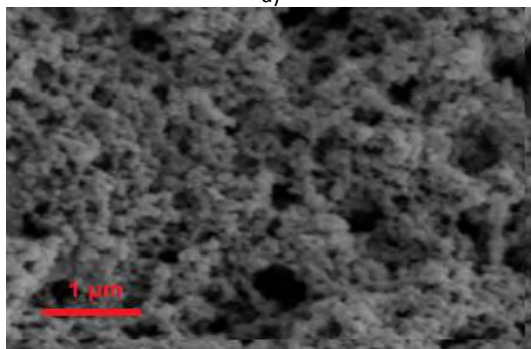
b)

Fig. 3: SEM images for a) NIP and b) IIP.

Conclusions

In this research, the selective removal and colorimetric properties of non- and ion-imprinted polymer were investigated usige dithizone as a ligand to create the colorimetric chemosensor for the detection of lead ions. The results indicated the successful application of the prepared sensor for the selective removal and trace detection of lead ions.

References

[1] Yousefi-Limaee, N., Rouhani, S., Olya, M.E., & Najafi, F. (2019). Selective 2, 4-dichlorophenoxyacetic acid optosensor employing a polyethersulfone nanofiber-coated fluorescent molecularly imprinted polymer. Polymer, 177, 73-83.

[2] Yousefi-Limaee, N., Rouhani, S., Olya, M.E., & Najafi, F. (2020). Selective recognition of herbicides in water using a fluorescent molecularly imprinted polymer sensor, Journal of Fluorescence, 30, 375-387.

[3] Behbahani, M., Salimi, S.H., Abandansari, S., Omidi, F., Salarian, M., & Esrafili, A. (2015). Application of a tailor-made polymer as a selective and sensitive colorimetric sensor for reliable detection of trace levels of uranyl ions in complex matrices, RSC Advances, 5(74), 59912-59920.

[4] Ao, X., & Guan, H., (2017). Preparation of Pb(II) ion-imprinted polymers and their application in selective removal from wastewater, Adsorption Science & Technology, 36(1-2), 774-787.

22nd Iranian Chemistry Congress (ICC22)
Iranian Research Organization for Science and Technology (IROST)
13-15 May 2024

03231-97589

IROST

Preparation of CQDs from natural resources for applications in optical sensors

Nargess Yousefi-Limaee*, Saba Tammari

Corresponding Author E-mail: yousefi-n@icrc.ac.ir

Department of Environmental Research, Institute for Color Science and Technology, Tehran, Iran.

Abstract: Carbon quantum dots (CQDs) are emerging as a promising category of luminescent nanomaterials. The preparation of CQDs from environmentally friendly sources has been increasingly considered. Therefore, in this investigation, CQDs with optical capability were hydrothermally prepared from Syzygium Cumini seeds for further utilization in optical sensor design.

Keywords: CQDS; Syzygium Cumini seeds; Hydrothermal

Introduction

Carbon dots, also known as carbon quantum dots (CQDs), have gained widespread attention globally for their diverse applications in sensors, photocatalysis, fluorescence bioimaging, drug delivery, and optical electronics. The presence of functional groups such as hydroxyl, carboxyl, carbonyl, epoxy, etc., on their surface ensures solubility in aqueous media [1]. The cost-effective and facile large-scale synthesis of CQDs contributes to their advantage as sensing probes [2]. Various carbon sources, including glucose, glycerol, sucrose, ascorbic acid, citric acid, and chitosan, have been utilized for CQD preparation. Multiple synthesis methods, such as hydrothermal, solvothermal, microwave-assisted, laser ablation, and electrochemical methods, have been developed for fluorescent CQDs [3]. Currently, there is a growing emphasis on utilizing natural and eco-friendly materials as carbon precursors for non-toxic CQD synthesis [4].

In this investigation, Syzygium Cumini seeds [5] are employed as a natural source of carbohydrates in the synthesis of Carbon Quantum Dots (CQDs). The fruits were procured from Bushehr, located in the south of Iran, and the seeds were manually extracted. The hydrothermal method was utilized to produce carbon dots, with water serving as the solvent. The solution was heated at high temperatures to facilitate the synthesis process.

Experimental Section

The Syzygium Cumini (S.C.) seeds were finely ground into powder using a grinder and stored in a cold place for future use. Subsequently, 1 g of the powder was dispersed in 60 mL of water using a magnetic stirrer, and the mixture was heated to 40 degrees Celsius to achieve an improved texture. For the synthesis of Carbon Quantum Dots (CQDs), the solution underwent a 12-hour heating process in an oven at 165 degrees Celsius, utilizing an autoclave to maximize pressure applied to the solution. After cooling the autoclave, the solution was transferred into Falcon tubes and centrifuged at a speed of 8000 rpm. This process was repeated until a yellow clear solution appeared. Finally, the solution was filtered using a 0.22-micron filter. Fig. 1 shows the preparation procedure of CQDs from Syzygium Cumini seeds.
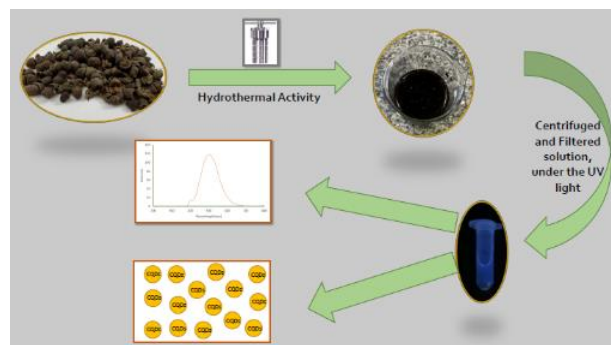
Fig.1: Schematic illustration of the synthesis of water-soluble fluorescent C-dots from S.C seeds.

Results and Discussion

Fourier Transform Infrared Analysis:

The peak at 3464 cm^{-1} corresponds to the elongation vibration of -OH. The peak at 2921 cm^{-1} indicates the stretching vibration of -CH3 and -CH2 bonds. The stretching vibration of C=O bonds in -COOC is represented by the peak at 1704 cm^{-1}. Peaks at 1605 and 1512 cm^{-1} signify the stretching vibration of C=C, characteristic of aromatic rings. The peaks at 1368, 1285, and 1203 cm^{-1} are attributed to C-O vibration in aromatic rings. The peak at 1045 cm^{-1} indicates aromatic ether presence. Lastly, peaks at 705 and 665 cm^{-1} signify the vibration of glycosides linkage.
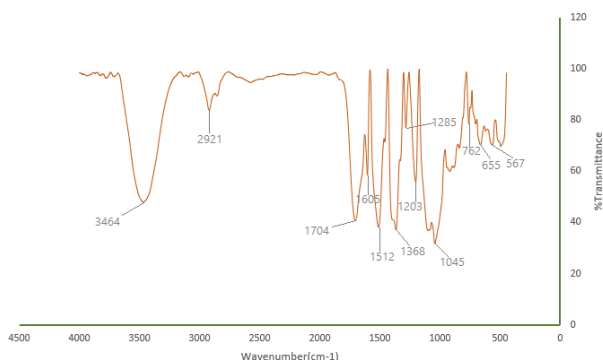
Fig.2: FT-IR analysis of CQDs prepared using Syzygium Cumini

UV-VIS Spectrometry:

The UV-Vis absorption spectra of Carbon Dots derived from Syzygium Cumini (S.C.) Seeds are illustrated in Figure 3. As shown in the figure, the maximum absorption of 2.8258 was obtained at 283 nm.
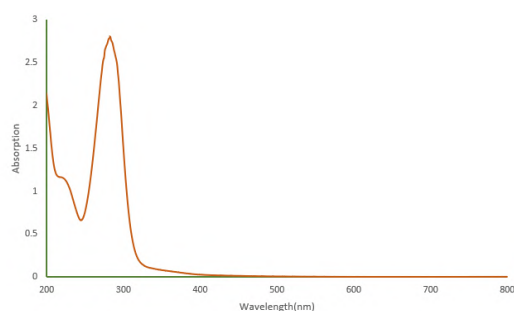
Fig.3: UV-VIS Spectrum of CQDs

PL Spectrometry:

The photoluminescence spectra of prepared CQDs is presented at Figure 4. As illustrated in the figure, the maximum emission intensity was attained at 512 nm.
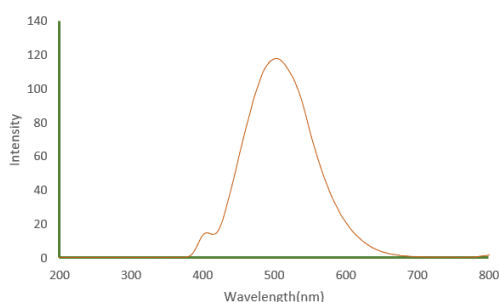
Fig.4: The photoluminescence spectra of CQDs

Conclusions

In conclusion, this method provides a green approach for synthesizing Carbon Quantum Dots (CQDs) using natural waste such as S.C. seeds. It not only offers an environmentally friendly solution but also proves to be a cost-effective and straightforward method for producing

a valuable product applicable in various domains. Another notable advantage of this experiment is the achievement of excellent fluorescence activity in the water-based solution of CQDs, making them high-performance optical imaging probes. Overall, this synthetic method demonstrates significant potential for large-scale synthesis of water-soluble C-dots.

References

[1] Das, R., Bandyopadhyay, R., & Pramanik, P. (2018). Carbon quantum dots from natural resource: A review, Materials today chemistry, 8, 96-109.

[2] Du, F., Zeng, F., Ming, Y,. & Wu, S. (2013). Carbon dots-based fluorescent probes for sensitive and selective detection of iodide, Microchimica Acta, 180, 453-460.

[3] Singh, H., Bamrah, A., Khatri, M., & Bhardwaj, N. (2020). One-pot hydrothermal synthesis and characterization of carbon quantum dots (CQDs), Materials Today: Proceedings, 28, 1891-1894.

[4] Kurian, M., & Paul, A. (2021). Recent trends in the use of green sources for carbon dot synthesis–A short review, Carbon Trends, 3, 100032.

[5] Dhanush, C., & Sethuraman, M. (2021). Independent hydrothermal synthesis of the undoped, nitrogen, boron and sulphur doped biogenic carbon nanodots and their potential application in the catalytic chemo-reduction of Alizarine yellow R azo dye, Spectrochimica Acta Part A: Molecular and Biomolecular Spectroscopy, 260, 119920.

Reduction in microbiological content of bee pollen by application of gamma irradiation followed by its phytochemical properties

Bahareh Dinimanesh [a], Atousa Aliahmadi [b], Hassan Rezadoost [a*]

Corresponding Author E-mail: h_rezadoost@sbu.ac.ir

[a] Department of Phytochemistry, Medicinal Plants and Drugs Research Institute, Shahid Beheshti University, Tehran, Iran

[b] Department of Biology, Medicinal Plants and Drugs Research Institute, Shahid Beheshti University, G.C., Tehran, Iran

Abstract: Bee pollen is a combination of plant pollen and honeybee secretions and nectar. Its components include protein, reducing and non-reducing sugars, lipids, vitamins and phenolic compounds. The purpose of this study was to investigate microbial contamination of pollen and its phytochemical characteristics before and after treatment with gamma irradiation.

Keywords: Bee pollen; Microbial Contamination; Gamma irradiation

Introduction

With seven million beehives, Iran ranks third in beekeeping in the world. Along with the honey production chain, other side products such as propolis, pollen grains, royal jelly and bee venom are also produced. Among beekeeping products, bee pollen has received commercial attention due to its high nutritional value, which contains important sources of energy and protein for humans and bees. Pollen grains are produced from the sticking together of pollen collected from flowers by bees in the form of irregular round masses along with plant nectar, secretions and bee saliva enzymes (such as amylase, catalase) or honey. Bees place pollen grains on their hind legs and carry them to the hive. The chemical composition of pollen depends on the plant source, geographical origin, soil type and bee kind. It contains all the amino acids needed by the human body. Its components include protein (5-60%), reducing and non-reducing sugars (13-55%), lipids (4-7%), raw fibers (0.3-20%) and vitamins and phenolic compounds. Due to its high amount of protein and amino acids, bee pollen is a good source of food for human, worker bees, males, larvae, and especially the queen bee. In nature, pollen is exposed to a wide range of pathogenic microorganisms. So when pollen is collected by worker bees, these microorganisms may be transferred to the bee colony. By using disinfection or sterilization methods to reduce or eliminate the microbial contamination in food, including bee pollen, the risks of infection and disease transmission in the hive can be greatly reduced. For this purpose, irradiation with gamma rays may be used. The effect of different doses of gamma radiation and on the nutritional content of pollen grains is very important because the main goal of this project is to reduce the microbial load of pollen grains while keeping its nutritional value constant.

Experimental Section

Pollen grains collected by bees were prepared for irradiation with doses of 2, 5 and 7 kGy. Pollen samples were irradiated with a research irradiator (Gamma cell 220) with a Cobalt-60 source with an activity of 4350 Curies. Gamma radiation was performed at an average rate of 1.05 Gy per second and with an accuracy of more than 90%. UV-Spectrophotometer method was used to measure total protein, carbohydrate and total phenol and flavnoid of samples before and after irradiation. Also, to determine the profile of phenolic acids and flavonoids in pollen grains by RP-HPLC-DAD method, a Knauer system (WellChrom, Germany) equipped with a K-1000 pump, a K-2800 diode array detector, an autosampler S3900 (Midas), a K-5004 analytical degasser, and a 2301 Rheodyneinjector with a 20 μL loop was used. Separation was achieved using a C18 column (4.6 mm × 250 mm, 5 μm), with a gradient elution program at a flow rate of 0.7 ml/min. Standard microbiological methods were applied to determine total aerobic bacteria, total fungi, *Escherichia coli*, Salmonella sp. counts in samples before and after irradiation

Results and Discussion

The result of irradiation with doses of 2, 5 and 7 kGy did not affect the total amount of protein, carbohydrates and phenolic acids in the pollen grain and their values were almost constant. By examining the amount of phenolic acids and flavonoids in control and irradiated pollen grains with HPLC , it was shown that their amount remains constant even in the higher doses. The total count of aerobic bacteria and fungi in the irradiated samples decreased with increasing dose. The number of colonies of *E. coli*, salmonella and bacteria in the control sample were zero.

22ⁿᵈ Iranian Chemistry Congress (ICC22)
Iranian Research Organization for Science and Technology (IROST)
13-15 May 2024

03231-97589

Table1: Phenolic compounds content identified by HPLC in pollen extract before and after irradiation(mg/g)

Active compounds	Control	2 kGy	5 kGy	7 kGy
Catchin	0.55±0.15	0.58±0.1	0.57±0.1	0.58±0.15
Chlorogenic acid	0.37±0.14	0.4±0.15	0.42±0.13	0.39±0.18
p-Coumaric acid	2.12±0.2	2.05±0.11	2.55±0.1	2.01±0.12
Ferulic acid	2.06±0.13	2.2±0.15	2.25±0.1	2.03±0.11
Rutin	3.95±0.15	3.9±0.15	3.97±0.16	3.92±0.15
Rosmarinic acid	0.84±0.18	0.86±0.1	0.88±0.12	0.89±0.11
Quercetin	3.55±0.25	3.57±0.1	3.62±0.1	3.66±0.15
kaempferol	3.45±0.14	3.4±0.1	3.48±0.16	3.44±0.16

Table2: Results obtained for the microbial contamination(cfu·g^{-1}) in the bee pollen

	Control	2 kGy	5 kGy	7 kGy
total aerobic bacteria	13.6×10^{3}	5.33×10^{3}	3×10^{3}	1×10^{3}
total fungi	50×10^{3}	12.75×10^{3}	6×10^{2}	1×10^{3}

Conclusions

Considering the reduction of the microbial load of pollen grains by gamma irradiation, it can be concluded that this method can be very efficient and effective in food and agriculture industries. Also, in addition to gamma radiation, other conventional methods such as ozone and cold plasma will be applied to reduce the microbial contamination of pollen grains in our ongoing study.

References

[1] de Arruda, V. A. S., Vieria dos Santos, A., Figueiredo Sampaio, D., da Silva Araújo, E., de Castro Peixoto, A. L., Estevinho, M. L. F., & Bicudo de Almeida-Muradian, L. (2017). Microbiological quality and physicochemical characterization of Brazilian bee pollen. *Journal of Apicultural Research*, *56*(3), 231-238.

[2] Bárbara, M. S., Machado, C. S., Sodré, G. D. S., Dias, L. G., Estevinho, L. M., & De Carvalho, C. A. L. (2015). Microbiological assessment, nutritional characterization and phenolic compounds of bee pollen from Mellipona mandacaia Smith, 1983. *Molecules*, *20*(7), 12525-12544.

[3] Hidalgo, E. Á., Hernandez-Flores, J. L., Moreno, V. D. A., López, M. R., Gómez, S. R., Cruz, M. A. V., ... & Campos-Guillén, J. (2020). Gamma irradiation effects on the microbial content in commercial bee pollen used for bumblebee mass rearing. *Radiation Physics and Chemistry*, *168*, 108511.

[4] Mauriello, G., De Prisco, A., Di Prisco, G., La Storia, A., & Caprio, E. (2017). Microbial characterization of bee pollen from the Vesuvius area collected by using three different traps. *Plos one*, *12*(9), e0183208.

[5] Campos, M. G., Anjos, O., Chica, M., Campoy, P., Nozkova, J., Almaraz-Abarca, N., ... & Carreck, N. L. (2021). Standard methods for pollen research. *Journal of Apicultural Research*, *60*(4), 1-109.

The ZnO-NiO Nano-Composite: Kinetic and Thermodynamic Study on The Sulfasalazine Photodegradation

Mahdieh Rezaei, Alireza Nezamzadeh-Ejhieh*

Corresponding Author E-mail: arnezamzadeh@iaush.ac.ir

Department of Chemistry, Shahreza Branch, Islamic Azad University, P.O. Box 311-86145, Shahreza, Isfahan, Iran.

Abstract: The coupled ZnO–NiO nano-composite (NC) was prepared and used in the photodegradation of sulfasalazine (SZ). The best photocatalytic activity was obtained at pH 6.5 (near the pHpzc: 7.6), 0.7 g/L of the catalyst, and 7 mg/L sulfasalazine (SZ). The frequency factor of 2.131×10^4 min^{-1} and the activation energy of 15.87 kJ/mol were obtained for the process by the Arrhenius equation. A negative activation ΔS (−0.22 kJ/mol) with the positive ΔH and ΔG values was obtained for the SZ photodegradation by the ZnO–NiO composite.

Keywords: Photocatalytic degradation, ZnO-NiO; Sulfasalazine, Kinetic and thermodynamic, Arrhenius equation, Activation energy

Introduction

Nowadays, the widespread presence of pharmaceutical materials in the environment created various potential adverse effects on ecological systems and as especial cases on human life. Besides the high toxicity of more of these compounds, their presence in the aquatic environment (drinking water, surface water, groundwater, and wastewater demands) can cause to their toxicity and their potential to induce drug resistance [1]. Sulfasalazine has been widely used for treating inflammatory bowel disease (e.g., ulcerative colitis and Crohn's disease) and rheumatoid arthritis. It is a conjugated drug that includes sulfapyridine (SPD) and 5-aminosalicylic acid (5-ASA). SZ with high environmental persistence can cause subtle chronic and unpredicted effects on aquatic organisms and ecosystems [2]. The semiconducting based photocatalysis has been widely used for removing various organic/inorganic pollutants from water/wastewater samples. Unfortunately, the recombination of e/h pairs diminishes the efficiency of this useful technique. So far doping, coupling, and supporting of semiconductors, a decrease in the size, and plasmonic materials have been used to diminish the e/h recombination that has been discussed sufficiently in the literature.

Experimental Section

Preparation of NiO/ZnO composites: For preparing a NiO/ZnO composite with a definite NiO:ZnO mole ratio, an adequate amount of each semiconductor NPs was added to an agate mortar. The mixture was thoroughly hand-mixed for 15 min [3]. The agate mortar was used to warrant that no impurities were added to the sample during the grinding process.

Results and Discussion

The coupled ZnO–NiO nano-composite (NC) was prepared and identified by powder X-ray diffraction (PXRD), scanning electron microscope (SEM), UV–Vis diffuse reflection spectroscopy (DRS) and Fourier transformation infrared spectroscopy (FTIR) characterization techniques. The crystallite sizes of about 6.7, 36.7 and 29.5 nm were obtained for the NiO, ZnO, and ZnO/NiO samples by the Williamson-Hall equation, and about of 33.5, 33.8 and 39.8 nm by the Scherrer equation, respectively. The energy dispersive X-Ray analysis (EDX) showed a NiO:ZnO mole ratio of 3.1 for the composite. The band gap energies of 3.49, 3.19, and 3.02 eV were estimated for the NiO, ZnO, and ZnO–NiO samples by using the absorption edge wavelengths of 355, 388, and 410, respectively. The pHpzc values of 9.3, 8.8, and 7.6 were also estimated for the NiO, ZnO, and ZnO–NiO samples respectively. At initial steps of the work about 42%, 60%, and 87% of a 10 mg/L SZ solution were degraded by the ZnO and NiO NPs and the ZnO–NiO NC, respectively. The best photocatalytic activity was obtained at pH 6.5 (near the pHpzc: 7.6), 0.7 g/L of the catalyst, and 7 mg/L sulfasalazine (SZ). The rate constants of 0.0904 min^{-1} ($t_{1/2}$ = 7.66 min) and 0.0915 min^{-1} ($t_{1/2}$ = 7.57 min) were obtained for the SZ photodegradation and mineralization processes, respectively. The frequency factor of 2.131×10^4 min^{-1} and the activation energy of 15.87 kJ/mol were obtained for the process by the Arrhenius equation. A negative activation ΔS (−0.22 kJ/mol) with the positive ΔH and ΔG values was obtained for the SZ photodegradation by the ZnO–NiO composite. Change in the UV-Vis spectra of SZ solution during the different removal process is shown in Fig. 1.

22nd Iranian Chemistry Congress (ICC22)
Iranian Research Organization for Science and
Technology (IROST)
13-15 May 2024

03231-97589

Method/catal.	C/C₀	Deg.%
a: Photolysis	1	0
b: Blank	-	
c: Surf. Ads.	0.93	7
d: ZnO	0.58	42
e: NiO	0.40	60
f: ZnO/NiO	0.13	87
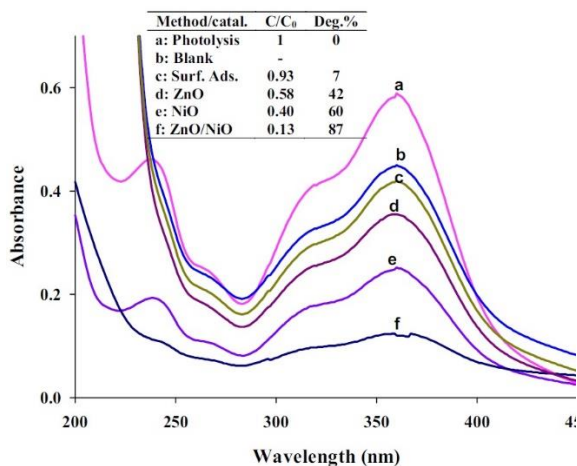
Fig. 1: Change in UV-Vis spectra of SZ solution during the mentioned removal processes.

Conclusions

The increased photoactivity of the coupled ZnO–NiO nano-composite was observed towards SZ which can be related to the better charge separation in the composite to the individual NiO and ZnO NPs. The best photocatalytic activity was obtained at pH 6.5 (near the pHpzc: 7.6) confirming that both charged SZ species and the charges accumulated on the catalyst surface have vital roles on the SZ photodegradation. The close rate constants of 0.0904 min^{-1} ($t_{1/2}$=7.66 min) and 0.0915 min^{-1} ($t_{1/2}$= 7.57 min) for the SZ photodegradation and the SZ mineralization processes, respectively, confirm that the SZ molecules and its photodegradation intermediates can be rapidly mineralized to water, carbon dioxide, and other sulfur and nitrogen contained inorganic species.

References

[1] Luo, Y., et al., *A review on the occurrence of micropollutants in the aquatic environment and their fate and removal during wastewater treatment.* Science of The Total Environment, 2014. **473-474**: p. 619-641.

[2] Wu, Q., *The fabrication of magnetic recyclable nitrogen modified titanium dioxide/strontium ferrite/diatomite heterojunction nanocomposite for enhanced visible-light-driven photodegradation of tetracycline.* International Journal of Hydrogen Energy, 2019. **44**(16): p. 8261-8272.

[3] Fazlali, F., A.r. Mahjoub, and R. Abazari, *A new route for synthesis of spherical NiO nanoparticles via emulsion nano-reactors with enhanced photocatalytic activity.* Solid State Sciences, 2015. **48**: p. 263-269.

Oxygen vacancy mediated TiO₂ -MoS₂ Heterostructure as an efficient photocatalyst for the Rhodamine B photodegradation

Mahdieyeh Rezaei[a], Ali A. Ensafi*[a,b], Esmaeil Heydari-Bafrooei's

Corresponding Author E-mail: Ensafi@iut.ac.ir

[a] Department of Chemistry, Isfahan University of Technology, Isfahan 84156-83111, Iran.

[b] Adjunct Professor, Department of Chemistry & Biochemistry, University of Arkansas, Fayetteville, AR 72701, USA.

Abstract: In this study, a heterojunction system comprising oxygen vacancies-mediated TiO_2 nanorods (TiO_{2-x}) modified with MoS_2 nanosheets (TiO_{2-x}-MoS_2) was prepared using the hydrothermal method and studied its photocatalytic activity toward Rhodamine B (RhB) degradation. The obtained results showed that the heterostructure significantly improved the photoinduced charge carrier separation efficiency, thereby reducing e^-/h^+ recombination.

Keywords: TiO_{2-x}-MoS_2, Oxygen vacancy, Kinetic and thermodynamic, Heterostructure photocatalyst, Scavenger agents, Arrhenius model.

Introduction

The rapid growth of the global population has coincided with increased industrialization, leading to a surge in environmental pollution [1]. In response, semiconductor photocatalysts have emerged as a promising solution, clean, green, economical, and efficient. Titanium dioxide (TiO_2) finds widespread use in environmental applications due to its long-term stability, potent oxidizing activity, resistance to photocorrosion, and relative nontoxicity [2]. However, its wide bandgap (3.2 eV) restricts its responsiveness primarily to the ultraviolet region, resulting in limited visible light absorption and insufficient photogenerated electrons. Various challenges associated with titanium dioxide have been extensively discussed in scientific literature [3]. Furthermore, photogenerated electrons and holes in TiO_2 tend to recombine rapidly, leading to decreased photocatalytic efficiency. To enhance TiO_2's performance, researchers have explored several strategies, including heterojunctions, doping, surface and morphology modifications, vacancy creation, and incorporation of noble metals [4]. Additionally, OVs facilitate the dissociation of H_2O molecules into hydroxyl groups, which then react with holes to generate hydroxyl radicals, further oxidizing pollutants [5]. This strategic utilization of OVs reduces the recombination of electron-hole pairs. recombination rate, enhancing the interfacial charge transfer reaction rate significantly [6].

MoS_2, as a dichalcogenide, arouses wide interest due to its suitable band gap for harvesting visible light. This makes it an attractive, earth-abundant photocatalyst for the photodegradation of organic pollutants. Despite having a small indirect bandgap (1.1-1.3 eV), bulk MoS_2 experiences fast charge recombination and cannot induce photocatalytic reactions [7].

RhB, commonly employed in textile, printing, paper, and food industries, can cause skin, eye, and respiratory tract irritation in both humans and animals. Given its hazardous properties, systematic endeavors to degrade RhB from aqueous solutions are deemed essential. For instance, Zheng et al. prepared g-C_3N_4/MoS_2 composites featuring abundant nitrogen (N) and sulfur (S) vacancies. These composites exhibit excellent performance in degrading both RhB and methyl orange [8].

In this study, we propose a gentle and efficient synthetic approach for creating defective functional materials that leverage the synergistic benefits of OVs and heterostructures within a TiO_{2-x}-MoS_2 composite. Our main objective is to enhance the photodegradation of RhB under UV-Vis irradiation.

Experimental Section

At first, the mixture of sodium molybdate dihydrate (240 mg) and TiO_{2-x} (160 mg) in deionized water (60 mL), was sonicated for 1 h. Then, thiourea (480 mg, 6.3mmol) was added into the slurry and stirred to form a homogeneous suspension. The mixture was then heated in an electric oven at 180 °C for 24 hours in a Teflon-lined stainless-steel autoclave. Preparation of TiO_{2-x}: An atmosphere thermal treatment was applied to TiO_2 nanorods to generate OV. To do so, the annealing step was carried out in a furnace min⁻¹ in a flow of ultrahigh purity Ar for 2h at 600 °C by the rate of 10 °C.

Results and Discussion

Oxygen vacancies-mediated TiO_2 nanorods (TiO_{2-x}) modified with MoS_2 nanosheets (TiO_{2-x}-MoS_2) was prepared using the hydrothermal method. The material was subsequently characterized using XRD, Raman

22nd Iranian Chemistry Congress (ICC22)
Iranian Research Organization for Science and Technology (IROST)
13-15 May 2024

03231-97589

spectroscopy, BET surface area analysis, FTIR, FESEM-EDX, TEM, DRS, and photoluminescence (PL) techniques. Compared to pure TiO_2, the TiO_{2-x}-MoS_2 heterostructure exhibited enhanced photocatalytic activity toward Rhodamine B (RhB). To optimize photodegradation performance, various experimental parameters, including mole ratio, pH, catalyst dosage, RhB concentration, and loading of the TiO_{2-x}-MoS_2 hybrid, were investigated. The heterostructure significantly improved the photoinduced charge carrier separation efficiency, thereby reducing e^-/h^+ recombination. The COD results align with the UV-Vis measurements conducted under the same conditions, which also indicate a degradation extent of 80%. The results of the scavengers effect indicate that the photocatalytic performance of RhB decreased with the addition of ascorbic acid, suggesting that %$^{\bullet}O_2^-$ played a key role in the oxidative degradation of RhB. In the proposed band gap diagram (Figure 1), electrons generated by photosynthesis are excited from the VB into the CB. These electrons transfer from the MoS_2 CB to the TiO_2 CB via the OV in TiO_{2-x}, where they accumulate for photocatalytic reactions. Furthermore, holes can transfer from the TiO_{2-x} VB to the MoS_2 VB, effectively separating the charge carriers and photogenerated electrons.
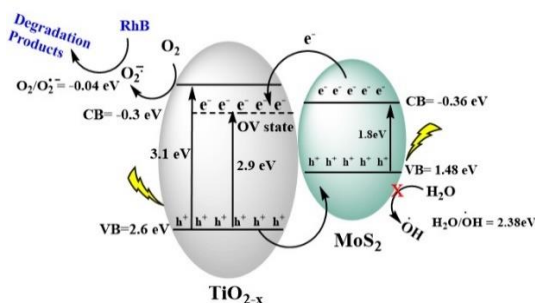
Fig.1: A schematic illustration showing the band structure of TiO_{2-x}-MoS_2 heterostructures and the mechanism of charge transfer proposed by this model.

Conclusions

In summary, we successfully synthesized MoS_2 nanosheets, an efficient dichalcogenide, decorating the surface of TiO_{2-x} nanoroads, a preferable metal oxide photocatalyst, using the hydrothermal method.

Thermal treatment led to an abundance of OVs on the TiO_2 surface, rendering TiO_{2-x} OV-rich with a broad optical absorption spectrum spanning visible to near-infrared (NIR) regions, as confirmed by EDX and UV-Vis absorption spectra. The heterogeneous interface between MoS_2 and TiO_2 promoted charge transfer and significantly enhanced photocatalytic performance compared to TiO_2 alone. The OVs improved charge separation efficiency and increased light absorption capacity. The obtained results showed

that a Type-II mechanism is more favorable for illustrating RhB photodegradation.

References

[1] Shi, J., et al., *Pollution control of wastewater from the coal chemical industry in China: Environmental management policy and technical standards.* Renewable and Sustainable Energy Reviews, 2021. **143**: p. 110883.

[2] Delekar, S.D., et al., *Structural and Optical Properties of Nanocrystalline TiO2 with Multiwalled Carbon Nanotubes and Its Photovoltaic Studies Using Ru(II) Sensitizers.* ACS Omega, 2018. **3**(3): p. 2743-2756.

[3] Dong, B., et al., *Species, engineering and characterizations of defects in TiO2-based photocatalyst.* Chinese Chemical Letters, 2018. **29**(5): p. 671-680.

[4] Fu, C., et al., *Photocatalytic enhancement of TiO2 by B and Zr co-doping and modulation of microstructure.* Applied Surface Science, 2016. **379**: p. 83-90.

[5] Nosaka, Y. and A. Nosaka, *Understanding Hydroxyl Radical (•OH) Generation Processes in Photocatalysis.* ACS Energy Letters, 2016. **1**(2): p. 356-359.

[6] Ortiz-Medina, J., et al., *Defect Engineering and Surface Functionalization of Nanocarbons for Metal-Free Catalysis.* Advanced Materials, 2019. **31**(13): p. 1805717.

[7] Chi, Z., et al., *The fabrication of atomically thin-MoS2 based photoanodes for photoelectrochemical energy conversion and environment remediation: A review.* Green Energy & Environment, 2022. **7**(3): p. 372-393.

[8] Zheng, J., B. Zhang, and Z. Wang, *Electron-assisted synthesis of g-C3N4/MoS2 composite with dual defects for enhanced visible-light-driven photocatalysis.* RSC Advances, 2021. **11**(1): p. 78-86.

Determining the Fatty Acid Profile of Tomato Seed Oil and Optimize the Extraction of Oil Using a High Shear Mixer Reactor

Deniz Khanmohammadi [a], Hassan Rezadoost [a], Masoud Rahimi [b]

Corresponding Author E-mail: iaupsstudeniz@gmail.com

[a] Department of Phytochemistry, Medicinal Plants and Drugs Research Institute, Shahid Beheshti University, Tehran, Iran.

[b] Shahid Beheshti University | SBU · Center for Medicinal Plant and Drug Research Institute PhD in Chemical, Petroleum and Gas Engineering.

Abstrac: Tomato seed oil is a vegetable oil extracted from tomato seeds.TSO contains various compounds including fatty acids. In this research, a new method using a high shear mixer for extraction was introduced and the highest extraction yield is 24.67 and linoleic acid is the most fatty acid of this oil.

Keywords: tomato seed oil (TSO); high shear mixer; extraction yield; linoleic acid

Introduction

Vegetable and edible oils are an indispensable part of the human daily food cycle and are widely used in the pharmaceutical and food industries and are rich sources of essential fatty acids such as omega 3, 6 and 9, which are beneficial for heart health and reduce the risk of heart diseases. Tomato seed is one of the food industry wastes from the tomato plant with the scientific name (Solanun lycopersicum) and,tomato is produced and consumed as one of the most consumed vegetables in the world and is rich in useful compounds such as carotenoids, phenolics and vitamins. Annually, a significant amount of tomato waste consists of skin and seeds and is produced in various industries, the yield of tomato waste is about 4.5 to 9 million tons, which provides a serious environmental and economic risk[1].

The nature of this seed includes various compounds such as saturated and unsaturated fatty acids and tocopherols. Tomato seed oil is an oil obtained from the seeds of the tomato plant .This oil was first studied in 1914 in the United States for extraction. Tomato seeds contain 20-36% oil with high unsaturated fatty acids and antioxidant properties, which are approved to prevent diseases such as arteriosclerosis, dilated blood vessels, thrombosis and high cholesterol.

Cold pressing method is one of the most economical methods of oil extraction from seeds. The obtained oil has a pleasant taste and aroma and retains all its nutritional value, often the amount of antioxidants and natural vitamins of cold-pressed oils is higher than that of oils extracted by other methods. The extraction of oil in this method is not complete and some of the oil remains inside the slag and causes the extraction efficiency to decrease, which can be mentioned as one of the disadvantages of this method.

The highest extraction yield of this oil belongs to the extraction with supercritical fluid method (SFE) with an efficiency of 25% ,in supercritical fluid extraction (SCFE), is used at the vapor-liquid critical point to extract tomato seed oil. The common solvent used is carbon dioxide; Because it is inert, abundant, non-flammable, non-toxic and can be easily recovered from the reaction streams, SFE offers advantages such as higher efficiency, better physicochemical properties of the extracted oils and compatibility with the environment[2].

In this study, high shear stress reactor was used as a new method to extract tomato seed oil, and the general mechanism of this method is that, in general, the working mechanism of a high shear mixer revolves around the creation of high shear forces through the rapid rotation of the blade. rotates, which enables efficient particle disintegration, dispersion, and mixing in various industrial processes, including extraction applications. which leads to a complete and uniform mixing or blending process.

The rotor or impeller rotates at high speed, creating a strong suction force and pulling the material in. Subsequently, the material is subjected to strong mechanical forces while passing through the narrow gap between the rotor and the stator. This process leads to the separation of particles and the formation of a homogeneous mixture or emulsion. The solvent used in this study is the organic solvent hexane, which is a suitable solvent for extracting fats, and this solvent is used even on an industrial scale.

In order to optimize the variables of extraction process by high shear stress reactor, Box Behnken model was used. Variables affecting extraction optimization include three factors, temperature, ratio of solvent to sample, time, which were investigated at three levels. In the optimization process, the percentage of extracting the dependent variable was selected as the answer. 17

22nd Iranian Chemistry Congress (ICC22)
Iranian Research Organization for Science and Technology (IROST)
13-15 May 2024

03231-97589

ISC

IROST

experiments were conducted to find the best reaction conditions and the central experiments showed a low coefficient of variation, which indicates the high repeatability and accuracy of these experiments.

Fig. 1. Tomato seeds

Experimental

To prepare the sample and to increase the contact surface of the solvent with the plant sample, the sample was powdered with an electric mill and the particle size was changed to 0.888 mm.according to the predetermined parameters. Solvent was added and complete mixing was done in a specified period of time, then the sample was passed through a filter paper and the solvent of the final material was evaporated by a rotary device and in order to determine the qualitative characteristics and quantitative analysis of the fatty acids of the oil by GC-FID device, the process of derivatization of fatty acids to convert them into methyl ester form and increase their volatility with potassium hydroxide, BF3 and methanol was done and then after adding hexane and water ,centrifuge at 4000 rpm, the upper layer containing fatty acids is injected into the device.

Results and Discussion

The results obtained in this research showed that the method of extracting oil from tomato seeds with the help of a high shear stress reactor had the highest yield percentage compared to other traditional methods. The optimal extraction efficiency was 24.65 ± 1% with the ratio (solvent to feed: 15 ml/g, time 35 minutes and temperature 25°C) and then its fatty acid profile was determined by the device and according to the results obtained, the highest percentage of fatty acids It belongs to (linoleic acid 52.5 % - oleic acid 20.92% - palmitic acid 16.68% - alpha linoleic 2.30% and stearic acid 4.41%) . There was no significant difference in the fatty acid composition of the oils with different extraction methods, which indicates the low impact of the extraction method on the fatty acid profile of tomato seed oil, and it can be said that the oil obtained by the high shear stress reactor method is a good alternative to the cold press method.

Table1: fatty acid profile of different extraction method

Extraction methode	Palmitic acid (C16:0)	Stearic acid (C18:0)	Oleic acid (C18:1)	Linoleic acid (C18:2)	Alpha linoleic acid (C18:3)A
Cold press	18	4.7	21	53	2.2
High shear	16.6	4.4	20.9	52.5	2.3

Fig. 2. High shear mixer

Conclusions

Tomato seed oil can be used as a suitable oil of vegetable origin and available from tomato waste with countless properties, and in this research, a new method for extracting oil with high efficiency compared to other methods has been investigated. And the oil obtained from this method was obtained with an extraction efficiency of 24.68%. The percentage composition of fatty acids of the obtained oil is similar to the cold pressing method, and the highest percentage of fatty acids belongs to linoleic acid with 52.5%, which is one of the essential fatty acids of the body. As a result, this method can be suggested as a method for oil extraction, and the advantages of this method compared to other methods are in terms of increasing the extraction yield of oil - less time , cost,and as well as preventing energy loss.

References

[1] Solaberrieta, I., et al., *Valorization of tomato seed by-products as a source of fatty acids and bioactive compounds by using advanced extraction techniques.* 2022. **11**(16): p. 2408.

[2] Sangeetha, K., et al., *Extraction, characterization, and application of tomato seed oil in the food industry: An updated review.* 2023. **11**: p. 100529.

22nd Iranian Chemistry Congress (ICC22)
Iranian Research Organization for Science and Technology (IROST)
13-15 May 2024

03231-97589

ISC

IROST

Ag-Catalyzed Cyclization Reaction of N'-(2-Alkynylbenzylidene)hydrazides and Acetylenedicarboxylate

Fatemeh Abdiyan Mobarakeh[a], Mohammad Rezaei-Gohar[a], Frank Rominger[b], Saeed Balalaie*[a]

Corresponding Author E-mail: balalaie@kntu.ac.ir

[a] Peptide Chemistry Research Institute, K. N. Toosi University of Technology, P. O. Box 15875-4416, Tehran, Iran.

[b] Organisch-Chemisches Institut der Universität Heidelberg, Im Neuenheimer Feld 271, 69120 Heidelberg, Germany.

Abstract: We describe sequential silver(I) salt catalyzed enantioselective and diastereoselective synthesis of a diversity of unprecedented fused heterocyclic compounds from the reaction of readily available N'-(2-alkynylbenzylidene)hydrazide with dialkyl acetylenedicarboxylates. This approach facilitates the selective preparation of tetracyclic ring-fused 1,6-Naphthyridines derivatives in moderated to good yields with high diversity.

Keywords: 1,6-Naphthyridines derivatives; N'-(2-alkynylbenzylidene)hydrazide; Dialkyl acetylenedicarboxylates.

Introduction

Tandem carbon-carbon bond formations are distinguished approach for the synthesis of structurally complex molecules from relatively simple starting materials in a convergent way.[1] On the other hand, the 1,6-naphthyridine and fused 1,6-naphthyridine scaffolds are represent prevalent structural motifs found in natural products and biologically active compounds. For example, 1,6-naphthyridine derivatives **A** and **B** dibenzo[b,h][1,6]naphthyridinecarboxamides **C** and imidazo[4,5-h [1,6]naphthyridin-2-ones **D** are inhibitors for VEGFR-2, MET, PDK1, and c-MET, respectively, which have potential applications in cancer therapeutics (Figure 1). In addition, 5,6,7,8-tetrahydro-1,6-naphthyridine derivatives E are potent HIV-1-integrase-allosteric-site inhibitors. Furthermore, pyrazolo[5,1-f][1,6]-naphthyridines **F** are CB2 receptor antagonists/inverseagonists. [2] Given the significance of the 1,6-naphthyridine motif in organic and medicinal chemistry, there is a strong emphasis on the development of efficient and stereoselective reactions for the synthesis of novel, multifunctionalized 1,6-naphthyridine and fused 1,6-naphthyridine derivatives.

The selection of a suitable bifuctional compound is an efficient approach for the synthesis of complex molecules. In continuation of our recent research to construct fused heteocyclic skeletons, 2-alkynyl 3-quinoline carbaldehyde was selected as starting material and its conversion to the desired hydrazide was used. These compounds have a huge potential to form 1,3-dipole. Meanwhile, due to the existence of tripe bond in the structure of molecules could add its potential for the cyclization reaction using Ag(I). [3]

We wish to report herein, the cyclization of N'-(2-alkynylbenzylidene)hydrazide **1** using Ag(I) and using it as a 1,3-dipole for the dipolar cycloaddition reaction with dialkyl acetylenedicarboxylates to construct the benzo[b]pyrazolo[5,1-f][1,6]naphthyridine-1,2-dicarboxylate **3** framework as a functionalized fused heterocyclic compound.
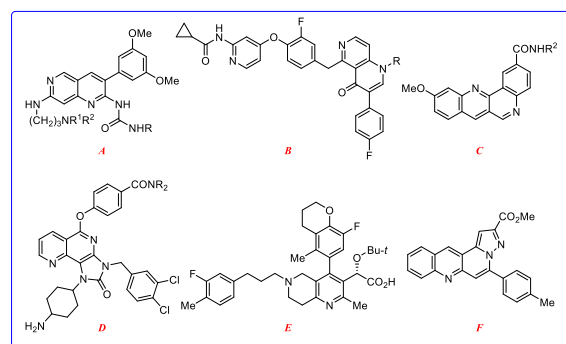
Fig.1: Selected examples of biologically active 1,6-naphthyridine derivatives and fused 1,6-naphthyridine compounds.
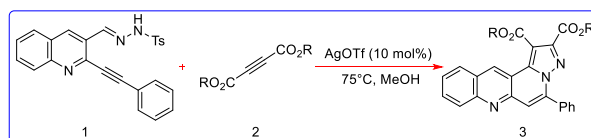
Scheme 1: Our Current Works.

To access this goal, a model reaction was selected and the reaction was studied in different Lewis acid such as AgOTf, AgNO$_3$, ZnCl$_2$, InCl$_3$, Sc(OTf)$_3$, CuCl$_2$ in different solvents were studied and the best results was obtained using 10 mol% AgOTf in metahnol at 75 °C.

22nd Iranian Chemistry Congress (ICC22)
Iranian Research Organization for Science and Technology (IROST)
13-15 May 2024

03231-97589

To validate our hypothesis, initial trials were carried out with the model reaction of N'-(2-alkynylbenzylidene)hydrazide derivatives of dialkyl acetylenedicarboxylates. The key results of the optimal conditions investigation are briefly summarized in Table 1.

Table 1. Optimization of the Reaction Conditions

Entry	Cat. (Mol %)	Solvent	Temp. (°C)	Yield (%)^B
1	-	MeOH	75	trace
2	InCl$_3$ (10)	MeOH	75	77
3	Sc(OTf)$_3$ (10)	MeOH	75	61
5	ZnCl$_2$ (10)	MeOH	75	63
6	CuCl$_2$ (10)	MeOH	75	68
7	AgNO$_3$ (10)	MeOH	75	83
8	AgOTf (10)	MeOH	75	92
9	AgOTf (5)	MeOH	75	85
10	AgOTf (15)	MeOH	75	43
11	AgOTf (20)	MeOH	75	31
12	AgOTf (10)	CH$_3$CN	75	81
13	AgOTf (10)	DCM	75	60
14	AgOTf (10)	Dioxane	75	43
15	AgOTf (10)	EtOH	75	84
16	AgOTf (10)	TFE	75	77
17	AgOTf (10)	MeOH	50	61

^{a}Reaction conditions: **1a** (0.2 mmol), **2a** (0.2 mmol), and catalyst (mol%) in 1.0 mL solvent. ^{b}Isolated yields

Experimental Section
To a Schlenk tube were added **1** (0.2 mmol), compound 2 (0.2 mmol) and MeOH (1 mL). The reaction was stirred at 75 °C in an oil bath for 12 h. The reaction process was monitored by thin-layer chromatography. The solvent of the reaction was removed under reduced pressure and then completion of the reaction was done on a preparative silica plate using *n*-hexane/EtOAc as an eluent to afford the products.

Results and Discussion

With the optimized reaction condition in hand, we screened the substrate scope to assess the generality and limitations of this novel tandem process.
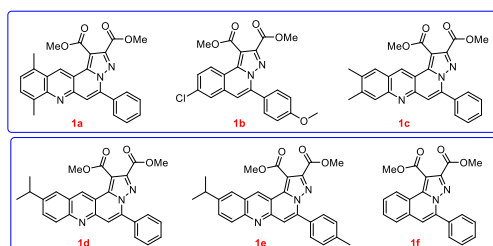
Scheme 2: Substrate scope.

Having these mentioned data in hand, we propose a plausible mechanism for the construction of benzo[b]pyrazolo[5,1-f][1,6]naphthyridine-1,2-dicarboxylate derivatives 3a-f. The Ag(I) has a dual role for the synthesis at first activation of the triple bond and also for the dipolar cycloaddition reaction it could act as a catalyst.
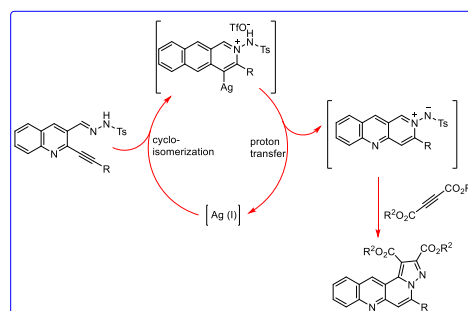
Scheme 3: Plausible reaction mechanism.

Conclusions
In summary, we have developed an efficient synthesis of benzo[b]pyrazolo[5,1-f][1,6]naphthyridine-1,2-dicarboxylate derivatives related to the natural products via domino cycloisomerization/dipolar-cycloaddition of readily available N'-(2-alkynylbenzylidene)hydrazides and acetylenedicarboxylate in the present of AgOTf as catalyst in methanol. Extend of the work in this area is in progress in our lab.

References

[1] Chen, Z., Ding, Q., Yu, X., & Wu, J. (2009). Silver Triflate-Catalyzed or Electrophile-Mediated Tandem Reaction of N'-(2-Alkynylbenzylidene) hydrazides with Dimethyl Acetylenedicarboxylate. *Advanced Synthesis & Catalysis*, *351*(10), 1692-1698.

[2] Thomas, M. G., De Rycker, M., Wall, R. J., Spinks, D., Epemolu, O., Manthri, S., & Gilbert, I. H. (2020). Identification and optimization of a series of 8-hydroxy naphthyridines with potent in vitro antileishmanial activity: initial SAR and assessment of in vivo activity. *Journal of Medicinal Chemistry*, *63*(17), 9523-9539.

[3] Wu, P., Zhang, Y., & Cheng, Y. (2022). Sequential Ag (I) salt and chiral N-Heterocyclic carbene catalysis enables enantioselective and diastereoselective construction of complex heterocyclic molecules and the switch of stereoselectivity. *The Journal of Organic Chemistry*, *87*(5), 2779-2796.

22nd Iranian Chemistry Congress (ICC22)
Iranian Research Organization for Science and Technology (IROST)
13-15 May 2024

03231-97589

IROST

Aryl sulfonyl hydrazide-Induced 1,6-Enyne Radical Cyclization under Copper Catalysis: Access to 3,4-Dihydronaphthalen-1(2H)-one Derivatives

Yeganeh Sadat Hosseini Nasab,[a] Saideh Rajai-Daryasarei,[a] Frank Rominger,[b] Saeed Balalaie*[a]

Corresponding Author E-mail: balalaie@kntu.ac.ir

[a] Peptide Chemistry Research Institute, K. N. Toosi University of Technology, P. O. Box 15875-4416, Tehran, Iran.

[b] Organisch-Chemisches Institut der Universität Heidelberg, Im Neuenheimer Feld 271, 69120 Heidelberg, Germany.

Abstract: We describe a fascinating approach to access 4-aroyl-3-aryl-3,4-dihydronaphthalen-1(2H)-one derivatives with moderate to good yields through the Cu-catalyzed radical cyclization/desulfonylation of 1,6-enynes with aryl sulfonyl hydrazide under air conditions. Significantly, this protocol involves an approach that works under mild reaction conditions and external oxidant free and represents an alternative and sustainable strategy for desulfonylation.

Keywords: 1,n-Enynes; Aryl sulfonyl hydrazide; Radical cyclization.

Introduction

1,n-Enynes are common and useful versatile building blocks for the construction of functionalized carbocyclic and heterocyclic frameworks in organic chemistry. In particular, cyclization reactions of 1,n-enynes through synergistic additions across C=C and C≡C bonds in a one-step operation have been recognized as one of the most powerful and straightforward strategies for the preparing complex molecular under mild conditions that found in numerous natural products, biologically active molecules, pharmaceuticals and material sciences.[1] Specifically, (E)-3-aryl-1-(2-(2-arylethynyl) aryl)prop-2-en-1-ones represent as one of the derivatives of 1,6-enynes and has been investigated in several radical cyclization reactions independently by organic chemists.[2] For instance, in 2011, Li and co-workers reported preparation of 1,4-naphthoquinones through the copper-catalyzed intramolecular oxidative 6-exo-trig cyclization of 1,6-enynes with H_2O in the presence of O_2 as the terminal oxidant as well as a reactant (Scheme 1a).[2b]

According to the intriguing reactive nature of 1,6-enynes and together with our interest in the development of the new radical reaction, we were encouraged to devise an efficient and simple methodology for the synthesis of novel carbocyclic compounds via radical reaction. Thus, we report herein a radical cyclization/desulfonylation of 1,6-enynes with aryl sulfonyl hydrazide to construct 4-aroyl-3-aryl-3,4-dihydronaphthalen-1(2H)-one derivatives under mild conditions (Scheme 1b).
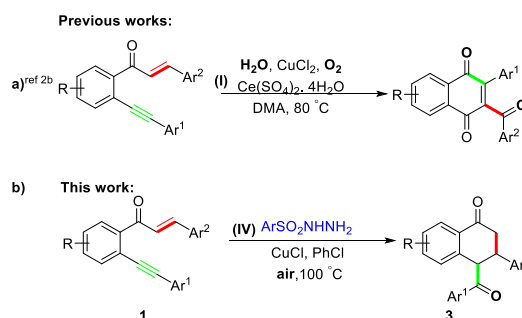
Scheme 1. Radical Cyclization of 1,6-Enynes to Construct Carbocyclic Compounds.

Experimental Section

Our initial efforts focused on the reaction between 1,6-enyne **1b** and arylsulfonylhyrazide **2** as model substrates to optimize the reaction conditions. As shown in Table 1.
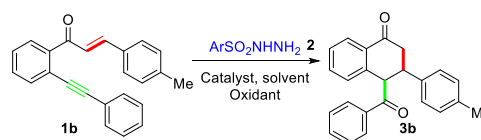
Table 1. Optimization of Reaction Conditions[a]

Entry	Oxidant (3.0 equiv.)	Catalysis (20 mol%)	Solvent	Yield (%)
1	$K_2S_2O_8$	CuCl	PhCl	65
2	TBHP	CuCl	PhCl	47
3	DTBP	CuCl	PhCl	55
4	-	**CuCl**	**PhCl**	**68**
5	-	CuCl	DMSO	15
6	-	CuCl	DMF	21
7	-	CuCl	CH_3CN	nr [b]
8	-	CuCl	PhCH₃	47

Entry	Oxidant (3.0 equiv.)	Catalysis (20 mol%)	Solvent	Yield (%)
9	-	CuCl	DCE	trace
10	-	CuCl	Dioxane	34
11	-	CuI	PhCl	nr
12	-	CuBr	PhCl	trace
13	-	Cu(OAc)$_2$	PhCl	46
14	-	CuO	PhCl	38
15	-	-	PhCl	nr
16[c]	-	CuCl	PhCl	70
17[d]	-	CuCl	PhCl	44
18[e]	-	CuCl	PhCl	42
19[f]	-	CuCl	PhCl	29
20[g]	-	CuCl	PhCl	nr
21[h]	-	CuCl	PhCl	32
22[i]	-	CuCl	PhCl	43

[a]Reaction conditions: **1b** (0.1 mmol), **2** (0.3 mmol), solvent (1.0 mL), at 100°C for 4 h. [b]No reaction.[c]CuCl (40 mol%), [d]CuCl (10 mol%). [e]At 80 °C, [f]At 50 °C, [g]under a N$_2$ atmosphere and dry solvent. [h]2 (1.5 equiv.), [i]O$_2$ (balloon).

Results and Discussion

With the optimized reaction conditions identified, was evaluated the scope and limitation of this radical cyclization using various 3-aryl-1-(2-(arylethynyl)aryl)prop-2-en-1-one derivatives **1a-1g** along with arylsulfonylhydrazid **2**. The results are summarized in Scheme 2.
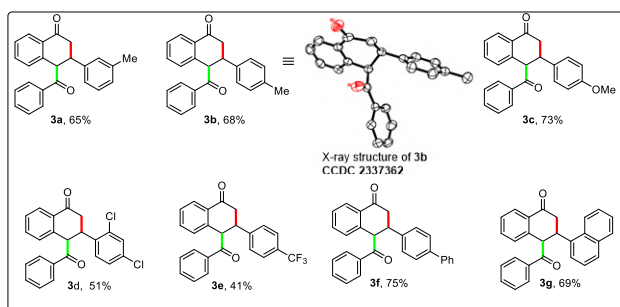
Scheme 2. Substrate Scope for the Construction of 4-Aroyl-3-aryl-3,4-dihydronaphthalen-1(2H)-ones.

Based on our presented experimental data and the previous reports[2 and 3] on the 1,6-enynes a plausible mechanism for this reaction is proposed in Scheme 3.

Conclusions

In summary, we have successfully presented an efficient and simple radical cyclization/desulfonylation of 1,6-enynes with aryl sulfonyl hydrazide in the presence of CuCl as catalyst under aerobic reaction conditions toward novel 4-aroyl-3-aryl-3,4-dihydronaphthalen-1(2H)-one derivatives. Additionally, a variety of 4-aroyl-3-aryl-3,4-dihydronaphthalen-1(2H)-one derivatives with high functional group tolerance were obtained in moderate to good yields. Mechanistic studies indicated that air atmosphere served as the oxygen source for C=O bond formation in this transformation. The attractive features of this protocol are the use readily available reagents, operational simplicity, aerobic reaction conditions and ability to gram-scale synthesis. Further investigations on the detailed mechanism and applications of this method are currently underway in our laboratory.
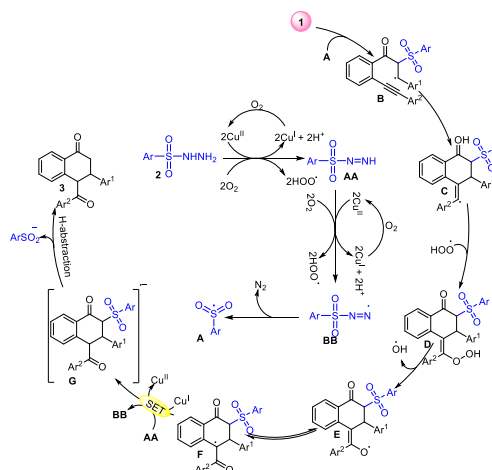
Scheme 3. Proposed Reaction Mechanism.

References

[1] (a) Li, Y., Pan, G. A., Luo, M. J., & Li, J. H. (2020). Radical-mediated oxidative annulations of 1, n-enynes involving C–H functionalization. *Chemical Communications*, *56*(51), 6907-6924; (b) Xuan, J., & Studer, A. (2017). Radical cascade cyclization of 1, n-enynes and diynes for the synthesis of carbocycles and heterocycles. *Chemical Society Reviews*, *46*(14), 4329-4346.

[2] (a) Qiu, S., Liang, R., Wang, Y., & Zhu, S. (2019). Domino reaction between Nitrosoarenes and Ynenones for catalyst-Free preparation of Indanone-Fused tetrahydroisoxazoles. *Organic Letters*, *21*(7), 2126-2129; (b) Wang, Z. Q., Zhang, W. W., Gong, L. B., Tang, R. Y., Yang, X. H., Liu, Y., & Li, J. H. (2011). Copper-Catalyzed Intramolecular Oxidative 6-exo-trig Cyclization of 1, 6-Enynes with H 2 O and O 2. *Angewandte Chemie International Edition*, *50*(38), 8968-8973.

[3] (a) Wei, W., Liu, C., Yang, D., Wen, J., You, J., Suo, Y., & Wang, H. (2013). Copper-catalyzed direct oxysulfonylation of alkenes with dioxygen and sulfonylhydrazides leading to β-ketosulfones. *Chemical Communications*, *49*(87), 10239-10241; (b) Chu, X. Q., Ge, D., Cui, Y. Y., Shen, Z. L., & Li, C. J. (2021). Desulfonylation via radical process: recent developments in organic synthesis. *Chemical Reviews*, *121*(20), 12548-12680.

Synthesis of derivatives of Sulfonyl acyl hydrazine under solvent free condition

Maryam Nedaei*, Gholamhassan Imanzadeh

Corresponding Author E-mail: Maryamnedaei67@yahoo.com

Department of Chemistry, Faculty of Sciences, University of Mohaghegh Ardabili, Ardabil, Iran.

Abstract Acyl hydrazides constitute very important moieties in organic chemistry and have been employed as starting materials for different transformations to many classes of organic compounds. In the present paper, we describe the synthesis of novel derivatives prepared by regioselective Michael addition to asymmetric hydrazide compounds. This chemoselectivity was experimentally studied employing different reaction conditions. Asymmetric hydrazide was synthesized via green chemistry approach.at the first acyl hydrazide was synthesized by using methyl benzoate and hydrazine hydrate. In the next step, mixture was reacted with the sulfonyl derivatives. finally finish, sulfonylacyl hydrazine was synthesized reacted with acrylates via regioselective Michael addition.

Keywords: Acylhydrazide, Michael addition, acrylates, acidic hydrogen, regioselective

Introduction

Hydrazides represent a class of organic compounds containing a nitrogen–nitrogen covalent bond with at least one acyl substituent [1]. They are used as starting materials for the synthesis of surfactants and of various heterocycles as of 1,2,4-triazoles [2], 1,3,4-thiadiazoles [3], or 1,3,4-oxadiazoles [3,4] with pharmacological activity [5]. Hydrazides are well known for their antitumor [6], anti-inflammatory, antibacterial [7], and analgesic [8], activities. on the other hand, Sulfonyl hydrazides constitute an important core structure for biologically active molecules. For examples, pharmaceutically interesting sulfonyl hydrazides have been synthesized for a potent suppressor of PGE2 production [9], potential anti-inflammatory agents [10], novel indoleamine 2,3-dioxygenase inhibitors [11], antibacterial agents [12]. This study, provides a succinct synthesis method of sulfonylacyl hydrazine derivatives which can be widely utilized in organic synthesis.

Experimental Section

All reactions were monitored by thin-layer chromatography on silica gel plates (60 Å, F254), visualizing with ultraviolet light. The structures of the synthesized compounds were confirmed by IR(KBr), ^{1}H NMR (400 MHz) and ^{13}C NMR (101 MHz) spectra.

General procedure for Synthesis of sulfonyl acyl hydrazine derivatives: Hydrazide was prepared by refluxing hydrazine hydrate with methyl benzoaet in ethanol at 80 C for 12 h. the mixture was left to cool down to room temperature.the resulting precipitate was filtered through a Buchner funnel with suction, and and recrystallized from ethanol. To synthesized Hydrazide, sulfonyl chloride and Pyridine added. reaction was into ice bath. After 2 h, the mixture was slowly poured into ice.

the resulting precipitate was filtered through a Buchner funnel with suctionand and was washed with distilled water. for synthesis hydrazine derivatives, sulfonylacy lhydrazine synthesized with acrylates was reaction in the presence K$_2$CO$_3$ as base and TBAB as catalyst in the room temperature for 12h.

R=Butyl, 2-Ethylhexyl
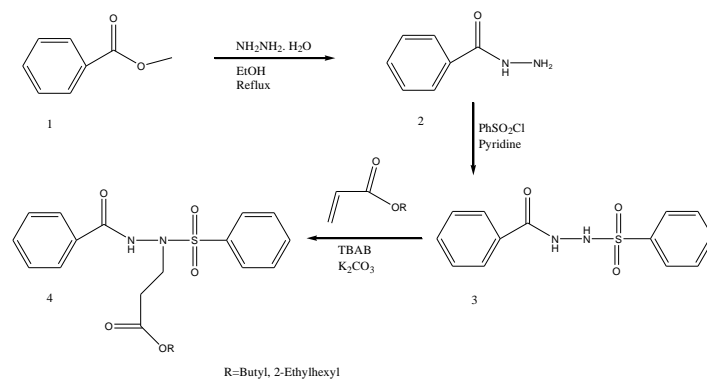
Results and Discussion

Sulfonylacyl hydrazine:Yield:90%, white color compound, m.p.:191-193 ^{0}C ,IR(KBr) 3311(N-H), 1671(CO), 1170(SO) , CH(3072).

22nd Iranian Chemistry Congress (ICC22)
Iranian Research Organization for Science and Technology (IROST)
13-15 May 2024

03231-97589

R	IR(KBr)	¹H NMR(CDCL₃)	C NMR(CDCL₃)
Butyl	3320 (N-H), 1736 (COO), SO(1163)	¹H NMR (400 MHz, CDCl3) δ 8.00 – 7.93 (m, 2H), 7.75 – 7.68 (m, 2H), 7.68 – 7.60 (m, 1H), 7.60 – 7.49 (m, 3H), 7.45 (td, J = 7.7, 1.4 Hz, 2H), 4.02 (dt, J = 21.2, 6.7 Hz, 4H), 2.78 (t, J = 6.6 Hz, 2H), 1.64 – 1.52 (m, 2H), 1.43 – 1.26 (m, 3H), 0.92 (t, J = 7.4 Hz, 3H), 0.11 (s, 1H)	13C NMR (101 MHz, CDCl3) δ 171.87, 165.87, 137.53, 133.68, 132.55, 131.76, 129.02, 128.82, 128.36, 127.31, 77.29, 64.96, 46.24, 33.63, 30.51, 29.74, 19.09, 13.72, 1.07.
2-Ethyl hexyl	3310 (N-H), 1735 (COO), SO(1167)	1H NMR (400 MHz, CDCl3) δ 8.31 (s, 0H), 8.00 – 7.93 (m, 1H), 7.75 – 7.68 (m, 1H), 7.68 – 7.49 (m, 2H), 7.45 (dd, J = 8.4, 7.0 Hz, 1H), 4.03 – 3.90 (m, 2H), 2.79 (t, J = 6.7 Hz, 1H), 1.54 (h, J = 6.0 Hz, 0H), 1.42 – 1.30 (m, 1H), 1.31 (s, 1H), 1.33 – 1.20 (m, 3H), 0.96 – 0.80 (m, 3H).	13C NMR (101 MHz, CDCl3) δ 171.99, 165.87, 137.50, 133.67, 132.54, 131.76, 129.02, 128.81, 128.36, 127.32, 67.53, 46.27, 38.59, 33.60, 30.28, 29.74, 28.88, 23.65, 22.98, 14.11, 10.94.

Conclusions

Sulfonylacyl hydrazines have two acidic hydrogen which produce a significant number of derivatives during an addition reactions. Was reaction of sulfonylacyl hydrazines with acrylates via regioselective Michael addition. We have successfully synthesized novel derivatives of Sulfonylacyl hydrazine under solvent free conditions aligns with green chemistry approach .

Reference

[1]. Mcnaught A.D., Wilkinson A. Compendium of Chemical Terminology: IUPAC Recommendations. 2nd ed. Blackwell Science; Oxford, UK: 1997.

[2]. Reichelt A., Falsey J.R., Rzasa R.M., Thiel O.R., Achmatowicz M.M., Larsen R.D., Zhang D. Palladium-catalyzed chemoselective monoarylation of hydrazides for the synthesis of [1,2,4] triazolo [4,3-a] pyridines. Org Lett. 2010;12:792–795. doi: 10.1021/ol902868q.

[3]. Abd Alla M.S., Hegab M.I., Abo Taleb N.A., Hasabelnaby S.M., Goudah A. Synthesis and anti-inflammatory evaluation of some condensed [4-(3,4-dimethylphenyl)-1(2H)-oxo-phthalazin-2-yl] acetic acid hydrazide. Eur. J. Med. Chem. 2010;45:1267–1277. doi: 10.1016/j.ejmech.2009.10.028.

[4]. Chandrakantha B., Shetty P., Nambiyar V., Isloor N., Isloor A.M. Synthesis, characterization and biological activity of some new 1,3,4-oxadiazole bearing 2-flouro-4-methoxy phenyl moiety. Eur. J. Med. Chem. 2010;45:1206–1210. doi: 10.1016/j.ejmech.2009.11.046.

[5]. Toliwal S., Jadav K., Patel K. Synthesis and Biological Evaluation of Fatty Hydrazides of By-products of Oil Processing Industry. Indian J. Pharm. Sci. 2009;71:144–148. doi: 10.4103/0250-474X.54282.

[6]. Mohareb R.M., Fleita D.H., Sakka O.K. Novel synthesis of hydrazide-hydrazone derivatives and their utilization in the synthesis of coumarin, pyridine, thiazole and thiophene derivatives with antitumor activity. Molecules. 2011;16:16–27. doi: 10.3390/molecules16010016.

[7]. Husain A. Amide derivatives of sulfonamides and isoniazid: Synthesis and biological evaluation. Acta Pol. Pharm. 2009;66:513–521.

[8]. Almasirad A., Hosseini R., Jalalizadeh H., Rahimi-Moghaddam Z., Abaeian N., Janafrooz M., Abbaspour M., Ziaee V., Dalvandi A., Shafiee A. Synthesis and analgesic activity of 2-phenoxybenzoic acid and N-phenylanthranilic acid hydrazides. Biol. Pharm. Bull. 2006;29:1180–1185. doi: 10.1248/bpb.29.1180.

[9].M.-F. Cheng, M.-S. Hung, J.-S. Song, S.-Y. Lin, F.-Y. Liao, M.-H. Wu, W. Hsiao, C.-L. Hsieh, J.-S. Wu, Y.-S. Chao, C. Shih, S.-Y. Wu, S.-H. Ueng.Discovery and structure–activity relationships of phenyl benzenesulfonylhydrazides as novel indoleamine 2,3-dioxygenase inhibitors

[10]. M. Kim, S. Lee, E.B. Park, K.J. Kim, H.H. Lee, J.-S. Shin, K. Fischer, A. Koeberle, O. Werz, K.-T. Lee, J.Y. Lee

Hit-to-lead optimization of phenylsulfonyl hydrazides for a potent suppressor of PGE2 production: synthesis, biological activity, and molecular docking study

[11]. E.B. Park, K.J. Kim, H.R. Jeong, J.K. Lee, H.J. Kim, H.H. Lee, J.W. Lim, J.-S. Shin, A. Koeberle, O. Werz, K.-T. Lee, J.Y. Lee

Synthesis, structure determination, and biological evaluation of phenylsulfonyl hydrazide derivatives as potential anti-inflammatory agents

[12].A.E. Dascalu, M. Rouleau Billam-Boz, A. Guinet, B. Rigo, E. Lipka Belloli, R.C. Hartkoorn, C. Ple, Preparation of hydrazide derivatives and their specific use as antibacterial agents by controlling Acinetobacter baumannii bacterium, PCT Int. Appl. (27 Aug 2020) 2020169682

Synthesis of 6/7/5-Fused Heterocyclic Skeletons through Transition-Metal-Free Intramolecular Double Hydrofunctionalization of Alkyne

Kimia Aghaie [a], Kamran Amiri [a], Mohammad Rezaei-Gohar [a], Frank Rominger [b], Saeed Balalaie*[a]

Corresponding Author E-mail: *Balalaie@kntu.ac.ir*

[a] Peptide Chemistry Research Institute, K. N. Toosi University of Technology, P. O. Box 15875-4416, Tehran, Iran.

[b] Organisch-Chemisches Institut der Universität Heidelberg, Im Neuenheimer Feld 271, D-69120 Heidelberg, Germany.

Abstract: We describe a novel intramolecular double hydrofunctionalization cyclization of alkyne with nitrogen and oxygen nucleophilic groups to construct valuable 6/7/5-fused heterocyclic products. This post-Groebke–Blackburn–Bienaymé reaction introduces a new class of functionalized isocyanides. Transition-metal-free cyclization, scale-up reaction, broad substrate scope, and high atom economy were some features of the present protocol.

Keywords: Double hydrofunctionalization; 6/7/5-fused heterocyclic; alkyne

Introduction

Synthesis of polyheterocyclic structures based on privileged scaffolds containing 6/7/5-fused heterocyclic components is of tremendous importance in modern organic chemistry [1]. Among them, oxazepine, oxazine, thiazine, and imidazole ring systems are privileged structural motifs in a wide variety of natural products and biologically active molecules [2]. Some drug structures are illustrated in Figure 1. Accordingly, the development of synthetic approaches for skeletons of this type has been a challenge in recent years.
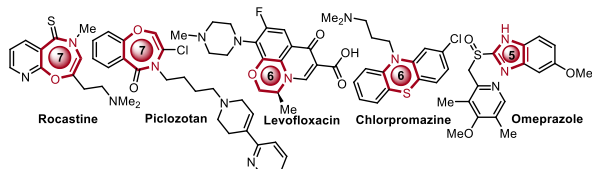
Fig. 1: Representative examples of drug-bearing oxazepine, oxazine, thiazine, and imidazole moieties.

The isocyanide scaffolds are one of the most significant classes of substrates to access the aforementioned heterocyclic skeletons [3]. In contrast to simple isocyanides, there are few studies of functionalized isocyanides that have not been developed [4]. Consequently, the design and synthesis of isocyanide containing different functional groups, such as alkynes, as an unsaturated system can be a valuable challenge.

Double hydrofunctionalization of nonpolar alkynes is a special and applicable method for the formation of complex heterocyclic compounds [5].

The previous observations and following our long-lasting interest in applying different types of isocyanides [6], led us to design and synthesize a new class of functionalized isocyanides with an alkyne moiety. With the suitable choice of other components in the Groebke–Blackburn–Bienaymé (GBB) reaction, we wish to access the

unprecedented 6/7/5-fused heterocyclic skeletons through intramolecular transition-metal-free double hydrofunctionalization (hydroamination and hydroalkoxylation) of nonactivated alkyne, which was completed upon preparative thin layer chromatography (PTLC) on silica gel plate. To the best of our knowledge, this synthetic approach has not been reported yet.

Under ascertained the optimized reaction conditions in hand, the generality, limitation, and substrate scope of the protocol were evaluated. Therefore, numerous R^1, R^2, and R^3 substituents on the different segments of isocyanide were investigated (Scheme 1).

Scheme 1. The substrate scope of fused-Oxazinopyridoimidazo oxazepine skeletons

22nd Iranian Chemistry Congress (ICC22)
Iranian Research Organization for Science and Technology (IROST)
13-15 May 2024

03231-97589

ISC

IROST

2i, 67 % **2j**, 74 % **2k**, 75 %

2l, 71 % **2m**, 74 % **2n**, 67 %

2o, 76 % **2p**, 84% **2q**, 82 %

2r, 69 % **2s**, 66 %
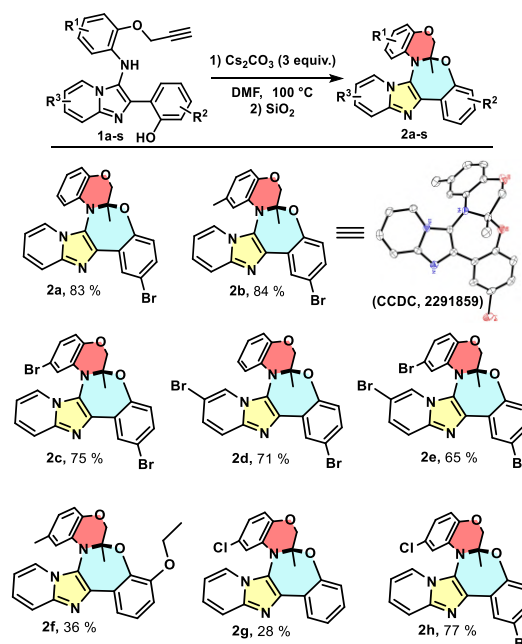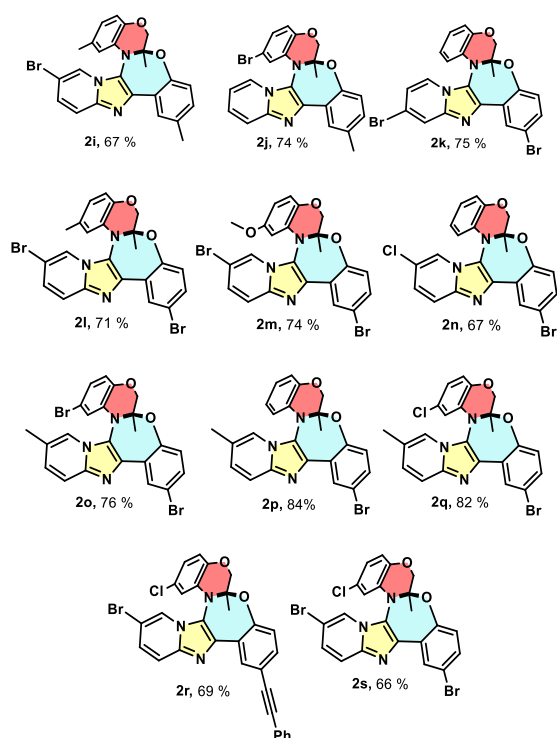
To further explore the adaptability and generality of the synthetic method, the 2-isocyanophenyl(prop-2-yn-1-yl)sulfane as a new type of isocyanide moiety was prepared and used for the syntheses of the desired product containing thiazine core (Scheme **2**).

Scheme 2. The substrate scope of fused-thiazinopyridoimidazo oxazepine skeletons

4a, 72 % **4b**, 73 % **4c**, 69 %

4d, 67 %
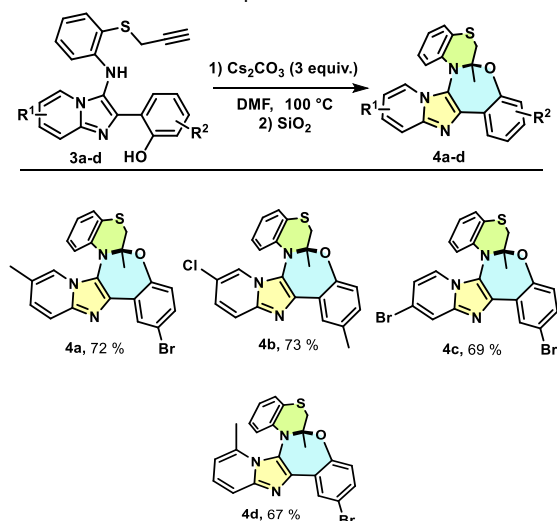
According to the literature precedents and the above results, a tentative mechanism was proposed and depicted in Scheme **3**.

Scheme 3. Plausible reaction mechanism
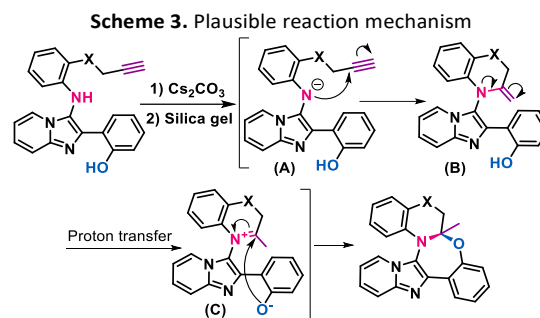
Conclusions

In conclusion, we have disclosed a novel functionalized isonitrile scaffold containing alkyne moiety and designed a new transition-metal-free double hydrofunctionalization reaction of alkyne that affords access to multi-fused heterocyclic frameworks. This protocol proceeds through the basic system. This synthetic route exhibited a high atom economy, simple operation, good functional group tolerance, broad substrate scope, scale-up synthesis, easy purification process, and good to high yields of the product. Further study and application of these isocyanides are currently underway in our laboratory

References

[1] Guo, S., Zhang, Z., Zhu, Y., Wei, Z., Zhang, X., & Fan, X. (2022). Rh (iii)-catalyzed substrate-dependent oxidative (spiro) annulation of isoquinolones with diazonaphthoquinones: selective access to new spirocyclic and oxepine-fused polycyclic compounds. *Organic Chemistry Frontiers*, 9(23), 6598-6605.

[2] a) Muthengi, A., Zhang, X., Dhawan, G., Zhang, W., Corsini, F., & Zhang, W. (2018). Sequential (3+ 2) cycloaddition and (5+ n) annulation for modular synthesis of dihydrobenzoxazines, tetrahydrobenzoxazepines and tetrahydrobenzoxazocines. *Green chemistry*, 20(13), 3134-3139. b) Yao, C., Bao, Y., Lu, T., & Zhou, Q. (2018). Stereoselective Synthesis of Functionalized Benzooxazepino [5, 4-a] isoindolone Derivatives via Cesium Carbonate Catalyzed Formal [5+ 2] Annulation of 2-(2-Hydroxyphenyl) isoindoline-1, 3-dione with Allenoates. *Organic letters*, 20(8), 2152-2155.

[3] Poulsen, M. Ø., Dastidar, S. G., Roy, D. S., Palchoudhuri, S., Kristiansen, J. E. H., & Fey, S. J. (2021). A Double-Edged Sword: Thioxanthenes Act on Both the Mind and the Microbiome. *Molecules*, 27(1), 196.

[4] (a) Chen, S., Oliva, M., Van Meervelt, L., Van der Eycken, E. V., & Sharma, U. K. (2021). Palladium-Catalyzed Domino Synthesis of 2, 3-Difunctionalized Indoles via Migratory Insertion of Isocyanides in Batch and Continuous Flow. Advanced Synthesis & Catalysis, 363(13), 3220-3226. (b) Su, S., Li, J., Sun, M., Zhao, H., Chen, Y., & Li, J. (2018). A domino reaction of 2-isocyanophenyloxyacrylate and aryne to synthesize arenes with vicinal olefin and benzoxazole. Chemical communications, 54(69), 9611-9614.

[5] Diéguez-Vázquez, A., Tzschucke, C. C., Lam, W. Y., & Ley, S. V. (2008). PtCl4-Catalyzed Domino Synthesis of Fused Bicyclic Acetals. Angewandte Chemie International Edition, 47(1), 209-212.

[6] Rezaei-Gohar, M., Amiri, K., Aghaie, K., Nayebzadeh, B., Ariafard, A., Shiri, F., ... & Balalaie, S. (2023). Domino Cyclization Reaction of o-Diisocyanoarenes for the Synthesis of Imidazo [1, 2-a] pyridinobenzimidazole Backbones. Organic Letters, 25(30), 5682-5686.

22nd Iranian Chemistry Congress (ICC22)
Iranian Research Organization for Science and Technology (IROST)
13-15 May 2024

03231-97589

IROST

Diastereoselective Construction of Spirocyclic Isobenzofurans *via* a Tandem Michael Addition/ 5-exo-dig Cyclization Reaction

Shaghayegh Mehdidoost,[a] Saideh Rajai-Daryasarei,[a] Sina Hosseini,[a] Frank Rominger,[b] Saeed Balalaie[a]*

Corresponding Author E-mail : *balalaie@kntu.ac.ir*

[a] Peptide Chemistry Research Institute, K. N. Toosi University of Technology, P. O. Box 15875-4416, Tehran, Iran.

[b]Organisch-Chemisches Institut der Universitat Heidelberg, Im Neuenheimer Feld 271, 69120 Heidelberg, Germany.

Abstract: A practical approach for efficient access to structurally complex multicyclic spirocyclic isobenzofurans is described via the cycloaddition reaction of 1,6-ynenone derivatives and 4-nitro-1,3-diarylbutan-1-ones with Cs_2CO_3 promotion in the presence of *L*-proline as catalyst. A range of multicyclic spirocyclic isobenzofuran products were obtained in good efficiency with good diastereoselectivities under mild conditions.

Keywords: Spirocyclic isobenzofurans; 1,6-ynenone; *L*-proline.

Introduction

Isobenzofuran and its derivatives are also one of the most important oxygen-containing heterocyclic compounds due to their presence in the structure of many essential compounds such as functional materials, bioactive compounds and natural products. Furthermore, these scaffolds have been extensively employed as useful building blocks and precursors of reaction intermediates in organic synthesis.[1] Owing to their significant value, the development of efficient and novel strategies for the preparation of isobenzofuran and its derivatives is an attractive research topic in medicinal chemistry and organic synthesis.

The cycloaddition reactions have been well-emerged as a versatile tool to construct various useful complex and functional molecules in the past decades.[2] In particular, cyclization reactions of 1,6-ynenones in a one-step operation have been drawn attention as one of the most powerful and straightforward strategies for the preparing complex molecular under mild conditions.[3] Hashmi and co-workers have developed an interesting approach to construct 6,6-spiroketal derivatives using reaction of 1,6-ynenones and dimedone in the presence of silver as catalyst via intermolecular Michael addition and a 6-endo-dig cyclization reaction (Scheme 1A).[3b] With our continuous interest in the heterocyclic molecules, a cycloaddition reaction was herein reported to access spiro-isobenzofuran through reaction of 1,6-ynenone derivatives and 4-nitro-1,3-diarylbutan-1-ones under a mild and transition metal-free conditions (Scheme 1B). This reaction leads to the formation of three new chemical bonds, two C–C bonds and one C–O bond through a sequence of Michael addition reaction on the C=C bond and tandem cyclization, and features broad scope with respect to 4-nitro-1,3-diarylbutan-1-ones containing various aryl groups as well as high diastereoselectivity.
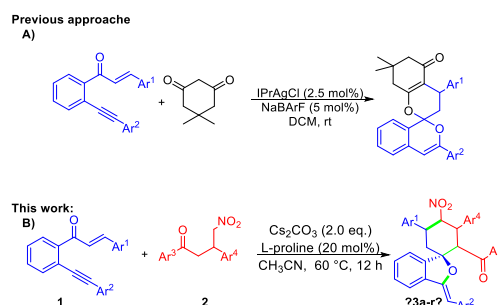
Scheme 1. New design for the synthesis of spiro-isobenzofurans.

Experimental Section

At the outset of our investigations, cyclization reaction of 1,6-ynenone **1a** and 4-nitro-1-phenyl-3-(p-tolyl)butan-1-one **2a** were selected as the model substrates to optimize the reaction conditions. As shown in Table 1.

Table 1. Optimization of the reaction conditions[a]

Entry	Base(2.0 eq.)	Solvent	Catalyst(20 mol%)	Yield (%)[b] **3a**
1	Na_2CO_3	CH_3CN	-	NR [c]
2	K_2CO_3	CH_3CN	-	20
3	Cs_2CO_3	CH_3CN	-	30
4	$NaHCO_3$	CH_3CN	-	NR

22nd Iranian Chemistry Congress (ICC22)
Iranian Research Organization for Science and Technology (IROST)
13-15 May 2024

03231-97589

Entry	Base(2.0 eq.)	Solvent	Catalyst(20 mol%)	Yield (%)[b] 3a
5	NEt₃	CH₃CN	-	20
6	DBU	CH₃CN	-	Trace
7	Cs₂CO₃	CH₃CN	*L*-Proline	70
8	Cs₂CO₃	EtOH	*L*-Proline	44
9	Cs₂CO₃	DCM	*L*-Proline	Trace
10	Cs₂CO₃	DMF	*L*-Proline	36
11	Cs₂CO₃	Toluen	*L*-Proline	NR
12	Cs₂CO₃	Dioxan	*L*-Proline	NR
13	Cs₂CO₃	CH₃CN	AgOTf	NR
14	Cs₂CO₃	CH₃CN	Sc(OTf)₃	Trace
15	Cs₂CO₃	CH₃CN	CuI	Trace
16	Cs₂CO₃	CH₃CN	InCl₃	Trace
17[d]	Cs₂CO₃	CH₃CN	*L*-Proline	70
18[e]	Cs₂CO₃	CH₃CN	*L*-Proline	55
19	-	CH₃CN	*L*-Proline	NR
20[f]	Cs₂CO₃	CH₃CN	*L*-Proline	69

[a]Reaction conditions: **1a** (0.25 mmol), **2a** (0.25 mmol), base and solvent (1.0 mL), at 60°C for 12 h. [b]Isolated yields. [c]No reaction.[d]Base 3.0 eq.[e]L-Proline 15 Mol%.[f]Reaction temperature 80°C.

Results and Discussion

With the optimized reaction conditions at hand, the synthesis of spiro-isobenzofuran derivatives **3** was pursued using various 1,6-ynenones **1** and 4-nitro-1,3-diarylbutan-1-one **2** derivatives (Scheme 2).
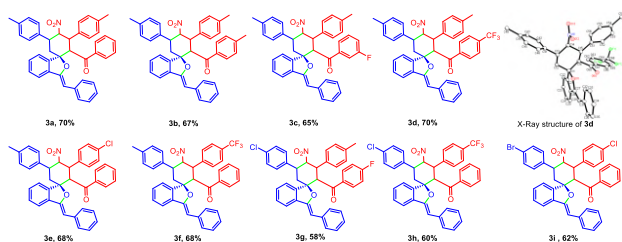
Scheme 2. Scope of the synthesis of spiro-isobenzofurans.

On the basis of the X-ray analysis of the single crystal of **3d** and the previous reports, a plausible reaction mechanism was proposed, as indicated in Scheme 3.

Conclusions

In conclusions, we have developed a transition metal-free atom economical strategy to access spiro-isobenzofuran derivatives through reaction of 1,6-ynenone derivatives and 4-nitro-1,3-diarylbutan-1-ones. This new tandem cyclization leads to form functionalized spirocyclic isobenzofurans with good diastereoselectivity. The present method features good functional group tolerance, high atom-economy, operational simplicity, mild and metal-free conditions and good yields of spirocyclic compounds.
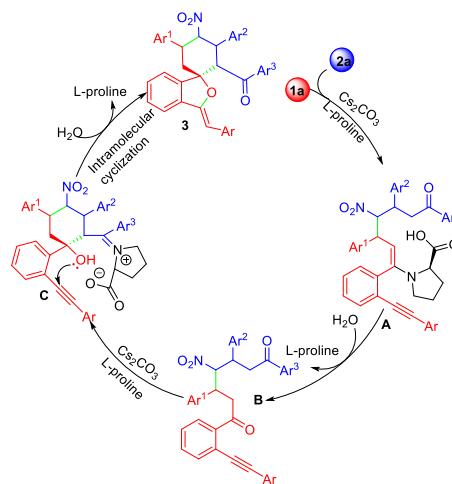
Scheme 3. Proposed mechanism.

References

[1]. (a) Wu, L., Hao, Y., Liu, Y., & Wang, Q. (2019). Visible-light-induced intramolecular sp 3 C–H oxidation of 2-alkyl-substituted benzamides for the synthesis of functionalized iminoisobenzofurans. *Chemical Communications*, *55*(92), 13908-13911.; (b) Zhang, T. S., Liu, S., Hao, W. J., & Jiang, B. (2023). Exploiting the reactivities of ortho-alkynyl aryl ketones: opportunities in designing catalytic annulation reactions. *Organic Chemistry Frontiers*, *10*(2), 570-589.

[2]. (a) Klier, L., Tur, F., Poulsen, P. H., & Jørgensen, K. A. (2017). Asymmetric cycloaddition reactions catalysed by diarylprolinol silyl ethers. *Chemical Society Reviews*, *46*(4), 1080-1102.; (b) García-Lacuna, J., Domínguez, G., & Pérez-Castells, J. (2020). Flow chemistry for cycloaddition reactions. *ChemSusChem*, *13*(19), 5138-5163.; (c) Thakur, A., & Louie, J. (2015). Advances in nickel-catalyzed cycloaddition reactions to construct carbocycles and heterocycles. *Accounts of Chemical Research*, *48*(8), 2354-2365.

[3]. (a) Ahrens, A., Heinrich, N. F., Kohl, S. R., Hokamp, M., Rudolph, M., Rominger, F., & Hashmi, A. S. K. (2019). A Silver-Catalyzed Modular Intermolecular Access to 6, 6-Spiroketals. *Advanced Synthesis & Catalysis*, *361*(24), 5605-5615.; (c) Qiu, S., Liang, R., Wang, Y., & Zhu, S. (2019). Domino reaction between Nitrosoarenes and Ynenones for catalyst-Free preparation of Indanone-Fused tetrahydroisoxazoles. *Organic Letters*, *21*(7), 2126-2129.

Synthesis of 2-sulfonamidoindolizine by 1,3-Dipolar Cycloaddition of Pyridinium Ylides with Benchtop Stabilized Ketenimines

Farhad Golmohammadi [a], Chiman Osmani [a], Frank Rominger [b], Saeed Balalaie [*a]

Corresponding Author E-mail: balalaie@kntu.ac.ir , golmohamadifarhad@gmail.com

[a] Peptide Chemistry Research Institute, K. N. Toosi University of Technology, 19697-64499 Tehran, Iran.

[b] Organisch-Chemisches Institut der Universitaet Heidelberg, 69120 Heidelberg, Germany.

Abstract: In this project, an efficient approach for the synthesis of multisubstituted 2-sulfonamidoindolizine derivatives was illustrated through the 1,3-dipolar cycloaddition reaction of pyridinium ylides with benchtop stabilized ketenimines. This method involves the [3+2] cycloaddition between pyridinium ylides and ketenimine species. The structure of the product was approved by ^{1}H-NMR, ^{13}C-NMR, HRMS and X-ray crystallography.

Keywords: 1,3-dipolar cycloaddition reactions; pyridinium ylide; ketenimine zwitterionic salts

Introduction

Nitrogen-containing heterocycles play a key role in both medicinal and materials chemistry. One of the most important *N*-fused heterocyclic skeletons is indolizine, which is composed of two condensed rings: a pyrrole-type five-membered ring and a pyridine-type six membered ring. Because of their diverse biological activities, photophysical properties, and using them as intermediates in the synthesis of other nitrogen heterocycles, indolizines have attracted the attention of organic and medicinal chemists. In the last few decades, 1,3-dipolar cycloaddition reactions of pyridinium ylide with various dipolarophiles such as alkynes, alkene, Electron-deficient ynamides, *O*-phosphorylated hydroxyketeneimines, allenes and *etc* has been used as a powerful synthetic tool for the preparation of indolizine derivatives[1].

Ketenimines are reactive species exhibiting a diverse array of synthetic applications parallel to their isoelectronic counterparts, ketenes and allenes. Because of the inherent instability and reactivity, ketenimines are normally generated in situ for their applications in organic synthesis. Very recently preparation of pyridine-stabilized ketenimine zwitterionic salts was reported by Sharma et all[2b] through click chemistry of alkynes and sulfonyl azides. This benchtop stabilized ketenimines have been utilized in various transformations such as 1.3-dipolar cycloaddition with isoquinoline N-oxides and [4+2] cycloadditios with 2-amino acetophenone for the synthesis of 2-aminoquinoline[2].

Herein, we disclose the development of a novel method to access highly functionalized 2-sulfonamidoindolizine derivatives through a metal free and base catalyzed 1,3-dipolar cycloaddition reactions of pyridinium ylide and pyridine-stabilized ketenimine salts (**Scheme 1**).
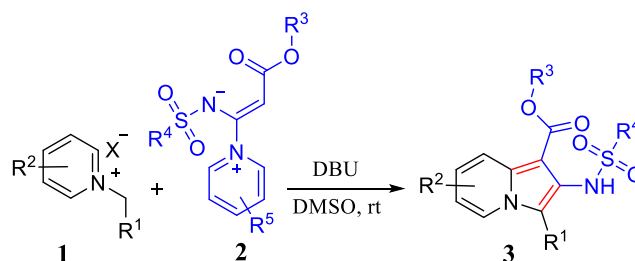
Scheme 1: 1,3-Dipolar Cycloaddition of Pyridinium Ylides and Ketenimine zwitterionic salts.

Experimental Section

The Pyridine salts **(1)** were synthesized according to the literature[1a].

The Ketenimine zwitterionic salts **(2)** were synthesized according to the literature[2a].

General procedure for the Synthesis of 2-sulfonamidoindolizine (3): Pyridinium Ylides **(1)** (0.24 mmol), Ketenimine **(2)** (0.2 mmol) and DBU (4.0 equiv) were added to a 25 mL Schlenk tube. Then DMSO (1.0 mL) were added to the reaction. The mixture was stirred for 15 h. The progress of the reaction was checked using TLC. After completion, EtOAc was added, and the mixture was washed with H_2O. The organic layers were combined, dried (Na_2SO_4), and concentrated in vacuo. The crude product was purified by column chromatography on silica gel to afford the corresponding product **(3)** in good to high yields.

Results and Discussion

For the synthesis of target product **3a** from starting materials **1a** and **2a**, the reaction conditions were initially optimized as shown in **Table 1**. In this regard, the model reaction of **1a** and **2a** was exposed to different inorganic and organic bases in various solvents. The best result was

22nd Iranian Chemistry Congress (ICC22)
Iranian Research Organization for Science and Technology (IROST)
13-15 May 2024

03231-97589

IROST

obtained using DBU as the base in DMSO at ambient temperature (**3a, 86 %**).
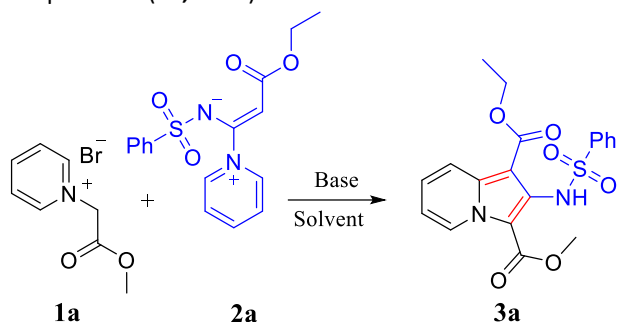
Table 1. Optimization of the Reaction Conditions for the Synthesis of 3a as a Model Reaction[a]

Entry	Base (4.0 equiv.)	Solvent	Yield (%)
1	K_2CO_3	MeOH	40
2	Cs_2CO_3	MeOH	45
3	DBU	MeOH	55
4	DBU	ACN	43
5	DBU	DMF	75
6	**DBU**	**DMSO**	**86**
7	DABCO	DMSO	65
8	KOtBu	DMSO	50
9	Et_3N	DMSO	30

[a]Reaction conditions: 1a (0.24 mmol), 2a (0.2 mmol), base (4.0 equiv) solvent (1.0 mL).

Table 2. Generality and scope of the 2-sulfonamidoindolizine **3a-l**[a]

3a, 86%   **3b**, 84%   **3c**, 84%   **3d**, 80%

3e, 30%   **3f**, 80%   **3g**, 83%   **3h**, 76%

3i, 79%   **3j**, 28%   **3k**, 93%   **3l**, 86%
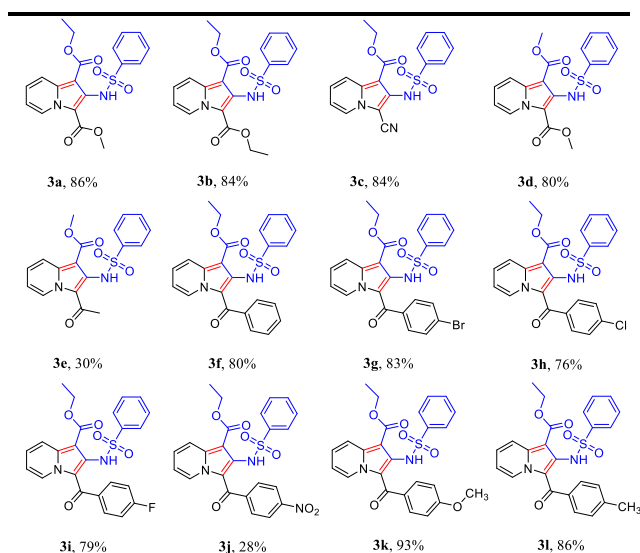
[a]All reactions were performed using Pyridinium Ylides 1a-L (0.24 mmol), Ketenimine zwitterionic salts 2a-b (0.2 mmol), DBU (4.0 equiv) in DMSO (1.0 mL).

To study the generality of these conditions to produce the 2-sulfonamidoindolizine derivatives, various pyridinium ylides **1a-l** were treated with ketenimine zwitterionic salts **2a-b** under optimized reaction conditions to obtain 2-sulfonamidoindolizine **3a-l.** The structure of products is shown in **Table 2**.

All multisubstituted indolizines were characterized by ^{1}H and ^{13}C-NMR, and high-resolution mass spectrometry (HRMS) spectral analyses. In addition, X-ray diffraction analysis of the product **3a** confirmed the formation of 2-sulfonamidoindolizine (**Fig 1**).
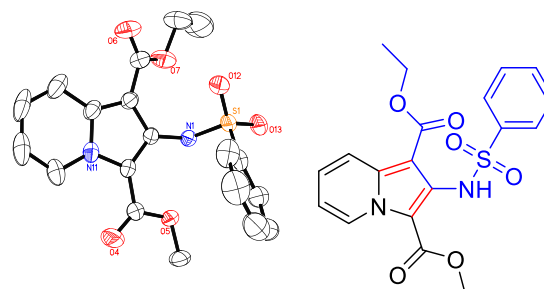
Fig.1: X-ray structure of product **3a**

Conclusions

In conclusion, we have demonstrated that the 1,3-dipolar cycloaddition of pyridinium ylides with pyridine-stabilized ketenimine zwitterionic salts provides a straightforward and convenient access to highly functionalized 2-sulfonamidoindolizine **3a-l**. The method is simple, safe, metal-free, and gives good to high yields of pure products. These products are valuable owing to the presence of sulfonamide as antibacterial agent. This reaction plays a remarkably important role in providing innovative ways for the preparation of new 2-sulfonamidoindolizine.

References

[1] (a) Sadowski, B., Klajn, J., Gryko, D. T. (2016). Recent advances in the synthesis of indolizines and their π-expanded analogues. *Organic & Biomolecular Chemistry*, *14*(33), 7804-7828. (b) Brioche, J., Meyer, C., & Cossy, J. (2015). Synthesis of 2-aminoindolizines by 1, 3-dipolar cycloaddition of pyridinium ylides with electron-deficient ynamides *Organic letters*, *17*(11), 2800-2803.

[2] (a) Hayatgheybi, S., Khosravi, H., Zahedian Tejeneki, H., Rominger, F., Bijanzadeh, H. R., & Balalaie, S. (2021). Synthesis of N-(Isoquinolin-1-yl) sulfonamides via Ag2O-catalyzed tandem reaction of ortho-alkynylbenzaldoximes with benchtop stabilized ketenimines. *Organic letters*, *23*(9), 3524-3529. (b) Massaro, N. P., Chatterji, A., & Sharma, I. (2019). Three-component approach to pyridine-stabilized ketenimines for the synthesis of diverse heterocycles. *The Journal of Organic Chemistry*, *84*(21), 13676-13685.

22nd Iranian Chemistry Congress (ICC22)
Iranian Research Organization for Science and Technology (IROST)
13-15 May 2024

03231-97589

IROST

Metal- and solvent-free domino reaction of 2-isocyanophenol esters to benzoxazines: long-range 1,5-acyl migration on 1,4-diazabutatriene

Alireza Akbari, Hormoz Khosravi, Saeed Balalaie *

Corresponding Author E-mail: Balalaie@kntu.ac.ir

Peptide Chemistry Research Institute, Department of Chemistry, K. N. Toosi University of Technology, P.O. Box 15875-4416, Tehran, Iran.

Abstract: The first example of intramolecular nucleophilic addition of 1,4-diazabutatriene to ester is disclosed. This approach provides a facile and versatile synthesis for functionalized 2H-1,4-benzoxazines through a metal-, reagent-, and solvent-free condition. Experimental and computational studies revealed the pivotal role of 1,5-acyl migration as the self-catalytic step in the reaction selectivity.

Keywords: 2-isocyanophenol esters; 1,5-acyl migration; 1,4-diazabutatriene

Introduction

Isocyanides, with their dual electronic nature, are known to be one of the most crucial building blocks in the construction of various nitrogen-containing heterocycles and carbocycles [1]. Although many reaction types of isocyanides are deep-rooted, such as multicomponent reactions, cycloadditions, or even insertion reactions, their dimerization has yet to be developed. This dimerization reaction leads to an unexploited heterocumulene, namely the 1,4-diazabutatriene, which has been used to synthesize N-heterocyclic compounds [2].

The sole application of 1,4-diazabutatriene, which has been well developed recently, was using them as a pericyclic reaction partner to produce azacycles, where the nitrogen atom was provided from the aforementioned heterocumulene. The reactivity of this cumulene as a 2π-component in [2+2]-cycloaddition reactions with itself, ketones, and alkynes just appeared after proposing its possible structure. Recently, Xu and Zhang disclosed a novel intramolecular [3+2]-cycloaddition of 1,4-diazabutatriene to yield the desired pyrrolo[3,4-b]indoles in catalyst-free condition, which reveals a different chemical potential of this intermediate in cycloaddition reactions [3].

Compared to various applications of 1,4-diazabutatrienes in pericyclic reactions, to the best of our knowledge,

nucleophilic addition is limited to only one example, which proposes participation of these intermediates in an intramolecular Michel addition to generate functionalized benzoxazinones [4].

Herein, we report an unprecedented migratory cycloisomerization of 1,4-diazabutatrienes involving a self-catalyzed long-range 1,5-acyl shift via nucleophilic addition to an acyl group giving access to a new library of 2H-1,4-benzoxazine structures through a green approach.

With the optimal conditions in hand, the reaction scope was evaluated using different aromatic isocyanides. The reaction tolerates a wide range of substrates bearing various functional groups such as electron-donating (-Me, -OMe), electron-withdrawing (-NO$_2$), heterocycle, and halogen groups (-Cl, -Br) at a variety of positions. In general, no solid evidence for a correlation between substrate structure and reactivity was observed. The probability of polymerization of the isocyanide group as well as the polarity of the isocyanide and the migrating acyl group (ester segment) may affect the yield obtained. Although the isocyanide-cyanide isomerization products 3 are detected as side products in two cases (3b and 3m), all the results show that the probability of this isomerization is low under optimized conditions (Table 1). In a gram scale experiment, reaction 2a was obtained with a good yield of 68%.

22nd Iranian Chemistry Congress (ICC22)
Iranian Research Organization for Science and Technology (IROST)
13-15 May 2024

03231-97589

IROST

Table 1 Substrate scope.

2a, 83% (68%)[b]
3a, N.D

2b, 67%

3b, 25%
CCDC 2337863

2c, 57%
3c, N.D

2d, 63%
3d, N.D

2e, 78%
3e, N.D

2f, 62%
3f, N.D

2g, 56%
3g, trace

2h, 55%
3h, N.D

2i, 37%
3i, N.D

2j, 43%
3j, N.D

2k, 46%
3k, N.D

2l, 58%
3l, trace

2m, 65%
3m, 33%

2n, 81%
3n, trace

2o, 66%
3o, N.D

2p, 47%
3p, N.D

Conclusions

Of particular significance is the discovery of the 1,5- acyl shifts observed in our study, a phenomenon that occurs in the absence of any catalyst, reagent, or solvent. The occurrence of this acyl shift starting from the 1,4-diazabutatriene intermediate represents a departure from conventional reaction pathways and underscores the importance of exploring alternative mechanisms in chemical transformations. This insight not only expands the understanding of the reactivity of 1,4-diazabutatrienes but also opens new avenues for developing greener and more sustainable synthetic methodologies in the synthesis of benzoxazine structures.

References

[1] Lygin, A. V., & de Meijere, A. (2010). Isocyanides in the synthesis of nitrogen heterocycles. *Angewandte Chemie International Edition*, *49*(48), 9094-9124.

[2] Marin-Luna, M., & Alajarin, M. (2020). The Elusive 1, 4-Diazabutatrienes: Lurking in the Shadows. *European Journal of Organic Chemistry*, *2020*(34), 5496-5500.

[3] Höfle, G., & Lange, B. (1977). N-Imidoyl Isocyanides. *Angewandte Chemie International Edition in English*, *16*(10), 727-728.

[4] Su, S., Hu, J., Cui, Y., Tang, C., Chen, Y., & Li, J. (2019). A formal (5+1) annulation reaction from heterodimerization of two different isocyanides: stereoselective synthesis of 2 H-benzo [b][1, 4] oxazin-2 one. *Chemical communications*, *55*(81), 12243-12246.

Mechanistic study

To elucidate the reaction mechanism, we carried out several control experiments and DFT calculations. First, a reaction starting from compound 1a was conducted in the presence of TEMPO under neat conditions, resulting in product 2a. This outcome suggests that the reaction is a non-radical reaction, as we were unable to scavenge any radical species, indicating the absence of radical intermediates.

Synthesis Of New Derivatives of pyrazol-5-yl benzenesulfonate Under Solvent-Free Conditions

Ali Mortazavi[*], Gholamhassan Imanzadeh, Seyedeh Simin dakhilpour

Corresponding Author E-mail: alimrtzv79@gmail.com

Department of Chemistry, Faculty of Sciences, University of Mohaghegh Ardabili, Ardabil, Iran.

Abstract: Pyrazolone, a five-membered heterocyclic structure involving two neighboring nitrogen atoms, serves as a core element with many properities. In this study a new derivative of pyrazol-5-yl benzenesulfonate were synthesized by Michael reaction under solvent free conditions. The regioselectivity of reactions is the most important feature of this organic method synthesis.

Keywords: Pyrazolone, green chemistry, solvent free, pyrazol-5-yl benzenesulfonate.
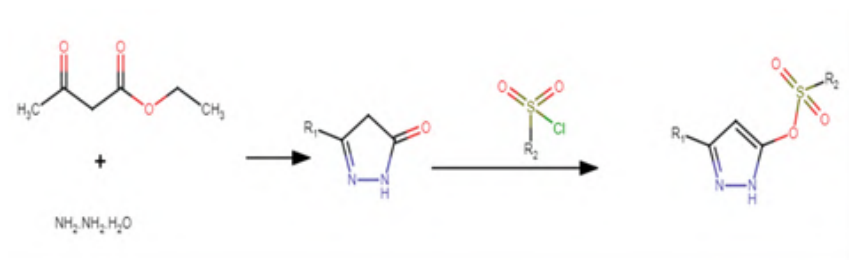
Introduction

In recent years, there has been intensive activity involving the synthesis and investigation of the biological activity of 2-pyrazolin-5-ones [1]. 5-Pyrazolones are very important class of heterocycles due to their biological and pharmacological activities [2], which exhibit anti- inflammatory [3], herbicidal [4], fungicidal [5], bactericidal [5], plant growth regulating properties [4], antipyretic properties [6] and act as protein kinase inhibitors [7]. Acyl-5-pyrazolones are a family of heterocyclic proligands and coordinated with some metal ions in anionic O 2-chelating mode [8]. In recent years, a number of FDA approved and commercially available drugs, both patented and non-patented, have been formulated using pyrazole derivatives [9]. This study, provides a succinct synthesis method of 5-Pyrazolones pharmacophore synthesis, making it a valuable reference guide for researchers exploring this field.

Experimental Section
Synthesis of 3-methyl-1H-pyrazol-5-yl 4-methylbenzenesulfonate

In this work, 3-methyl-1H-pyrazol-5(4H)-one (0.01 mol) was weighed and dissolved in 20 mL ethanol in a clean 250 mL single neck round bottom flask fitted with a reflux condenser. To this, pyridine (1 mL) and p-toluene sulfonyl chloride (0.01 mol) were added respectively, after which the mixture was refluxed for 18 h. The mixture was left to cool down to room temperature then slowly poured into ice. The resulting precipitate was filtered through a Buchner funnel with suction, and re-crystallized from ethanol.

Results and Discussion

Yield: 70%, Pale pink colored compound, m.p.: 116-117.4 °C
IR (KBr, cm-1): 3202(N-H), 3152(C-H), 1592,1458 (C=N), (C=C) ,1181-1197(SO3). ^{1}H NMR(CDCl3): 10.74 (s, 1H, NH)- 7.78 (d,2H, Ar)- 7.30 (d,2H, Ar)- 5.72 (s, 1H)- 2.43 (s, 3H, CH$_3$)- 2.24 (s, 3H, CH3). 13C NMR (63 MHz, CDCl3) δ 153.30, 144.75, 140.31, 131.57, 128.97, 127.71, 94.47, 20.94, 10.68.

22nd Iranian Chemistry Congress (ICC22)
Iranian Research Organization for Science and Technology (IROST)
13-15 May 2024

03231-97589

IROST

R	IR(KBr)	^{1}H NMR(CDCl$_3$)	C NMR(CDCl$_3$)
Ethyl	3152(CH),1736(COO),1592(C=C),1458(C=N),1181-1197(SO3).	1H NMR (400 MHz, CDCl3) δ 7.83 – 7.75 (m, 2H), 7.38 – 7.28 (m, 2H), 5.75 (d,1H), 4.19 – 4.05 (m, 4H), 2.74 (t,2H), 2.46 (s, 3H), 2.27 (d, 3H), 1.24 (t, 3H).	13C NMR (101 MHz, CDCl3) δ 170.83, 152.61, 145.37, 140.60, 132.46, 129.66, 128.61, 96.22, 60.84, 43.84, 34.15, 30.96, 28.78, 21.73, 14.13, 11.32.
Butyl	3152(CH),1736(COO),1592(C=C),1458(C=N),1181-1197(SO3).	1H NMR (400 MHz, CDCl3) δ 7.86 – 7.79 (m, 2H), 7.39 – 7.32 (m, 2H), 5.77 (t, 1H), 4.15 (t, 2H), 4.08 (t, 2H), 2.77 (t, 2H), 2.48 (s, 3H), 2.29 (d, 3H), 1.67 – 1.55 (m, 2H), 1.44 – 1.36 (m, 1H), 1.39 – 1.27 (m, 2H), 1.30 (s, 1H), 0.95 (t, 3H), 0.10 (s, 1H).	13C NMR (101 MHz, CDCl3) δ 170.98, 152.65, 145.30, 140.53, 132.59, 129.65, 128.65, 96.31, 77.27, 64.80, 43.88, 34.17, 30.55, 29.73, 21.76, 19.07, 13.70, 11.35, 1.06.
Hexyl	3152(CH),1736(COO),1592(C=C),1458(C=N),1181-1197(SO3).	1H NMR (400 MHz, CDCl3) δ 7.78 – 7.69 (m, 2H), 7.31 (d,1H), 5.68 (d, 1H), 4.09 (t, 2H), 4.01 (td, 2H), 2.71 (td, 2H), 2.42 (d,3H), 2.22 (d, 3H), 1.56 (t,2H), 1.34 – 1.22 (m, 6H), 0.91 – 0.81 (m, J = 2.8 Hz, 3H).	13C NMR (101 MHz, CDCl3) δ 170.82, 152.56, 145.38, 140.60, 132.40, 129.64, 128.53, 96.08, 64.91, 43.83, 34.05, 31.35, 28.44, 25.47, 22.48, 21.63, 13.98, 11.21.
2-Ethyl hexyl	3152(CH),1736(COO),1592(C=C),1458(C=N),1181-1197(SO3).	1H NMR (400 MHz, CDCl3) δ 7.78 – 7.70 (m, 2H), 7.33 – 7.26 (m, 2H), 5.68 (d, 1H), 4.09 (td, 2H), 3.95 (dd, 2H), 2.72 (td, 2H), 2.41 (d, 3H), 2.22 (d,3H), 2.13 (dd, 0H), 1.52 (dd, J = 12.1, 5.6 Hz, 1H), 1.36 – 1.21 (m, 8H), 0.85 (ddt, 6H).	13C NMR (101 MHz, CDCl3) δ 170.92, 152.55, 145.35, 140.54, 132.43, 129.63, 128.53, 96.09, 67.10, 43.85, 38.60, 34.04, 30.83, 30.23, 28.82, 23.58, 22.91, 21.63, 14.03, 11.21, 10.88.

Conclusions

We have successfully synthesized novel derivatives of 3-methyl-1H-pyrazol-5-yl 4-methylbenzenesulfonate using a phase-transfer catalysis (PTC) approach under solvent-free conditions, which aligns with the key principles of green chemistry. Notably, the Michael addition reaction of 3-methyl-1H-pyrazol-5-yl 4-methylbenzenesulfonate with acrylates proceeded efficiently at room temperature, further emphasizing the practicality and efficiency of our methodology.

References

[1] Sasson Y & Neumann R, Handbook of Phase Transfer Catalysis, (Chapman & Hall, New York) 1997.

[2] Scheibye S, El-Barbary A, Lawesson S O, Fritz H & Rihs G, Tetrahedron, 38, 1982, 3753.

[3] Hiremith S P, Rudresh K & Saundan A R I, Indian J Chem, 41B, 2002, 394.

[4] Joerg S, Reinhold G, Otto S, Joachim S H, Robert S & Klaus L, Ger Offen DE 3, 625, 686 (Cl C07D 231/22) Feb. (1988); Chem Abst, 108, 1988, 167465.

[5] Dhol P N, Achary T E & Nayak A, J Indian Chem Soc, 52, 1975, 1196.

[6] Souza F R, Souaza V T, Ratzlaff V, Borges L P, Olivera M R, Bonacorso H G, Zanatta N, Martina M A P & Mello C F, Eur J Pharma , 451 (2), 2002, 141.

[7] Singh J & Tripathy R, PCT Int Appl, 2001, 138.

[8] Cingolani A, Marchetti F, Pettinari C, Pettinari R, Skelton B W & White A H, Inorg Chem Comm, 7, 2004, 235.

[9] Nitulescu, G.M.; Stancov, G.; Seremet, O.C.; Nitulescu, G.; Mihai, D.P.; Duta-Bratu, C.G.; Barbuceanu, S.F.; Olaru, O.T. The Importance of the Pyrazole Scaffold in the Design of Protein Kinases Inhibitors as Targeted Anticancer Therapies. Molecules 2023, 28, 5359. [CrossRef].

Immobilization Of *Humicola Insolens* Lipase on Magnetic Nanoparticles ZrFe$_2$O$_4$@ UiO-66-NH$_2$

Saba Ghasemi*, Kowsar Azizi

Corresponding Author E-mail: Sb.ghasemi@iau.ac.ir

Department of Chemistry, Ilam Branch, Islamic Azad University, Ilam, Iran.

Abstract: *Humicola insolens* lipase was immobilized on magnetic nanoparticles ZrFe$_2$O$_4$@UiO-66-NH$_2$ via precipitation-crosslinking linkage method. This approach was very efficient in terms of enzyme loading, resulting in the immobilization of 333 mg·g^{-1} of HIL. Moreover, the immobilized derivative of enzyme showed broader pH and temperature tolerance relative to the soluble enzyme.

Keywords: *Humicola insolens* lipase; Immobilization; ZrFe$_2$O$_4$@UiO-66-NH$_2$.

Introduction

Lipases are considered as one of the most widely used biocatalysts in synthetic organic chemistry due to their versatility, mild reaction conditions, high selectivity, and broad substrate specificity [1, 2]. However, the applicability of soluble lipases in industry has been deterred duo to the poor stability under of processing conditions, difficulties in recovery from the reaction medium and reuse, and high cost of production [3, 4]. One of the available strategies to overcome these limitations is enzyme immobilization on an appropriate solid support, a method that has been proved to be simple and efficient [5]. Among reported supports for enzyme immobilization, metal-organic frameworks (MOFs) have drawn considerable attention owing to their well-defined structures. These solid supports exhibit distinct properties including high specific surface area, high thermal stability, desirable functionality, and adjustable porosity [6]. In this study, an attempt has been made to immobilize of *Humicola insolens* lipase (HIL) on magnetic nanoparticles ZrFe$_2$O$_4$@UiO-66-NH$_2$ by precipitation-crosslinking linkage attachment. Subsequently, the reusability and the effect of temperature and pH on the free and immobilized enzyme activity were investigated.

Experimental Section

1. Synthesis of ZrFe$_2$O$_4$ nanoparticles:

Briefly, 100 mL distilled water was added into a beaker and heated to 80 ºC, then 2.48 mmol (0.8 g) ZrOCl$_2$. 8H$_2$O and 4.9 mmol (0.98 g) FeCl$_2$.4H$_2$O were added under vigorous magnetic stirring. The mixture of reaction was kept at a temperature of 80 ºC and within a pH range of 10–12 by dropwise addition of NaOH (2 M) until the appearance of a black precipitate. The resulting precipitate was cooled to room temperature, collected through a magnet, and washed severally with deionized water.

2. Synthesis of ZrFe$_2$O$_4$@UiO-66-NH$_2$

Typically, 0.25 g of the prepared ZrFe$_2$O$_4$ nanoparticles was dispersed in 30 mL of DMF by sonication for 20 min. Then, 0.1 mmol (0.233 g) of zirconium (IV) chloride and 0.1 mmol (0.18 g) of 2-aminoterephthalic acid were added to the suspension of magnetic nanoparticles, followed by another 15 min of ultrasonication at room temperature. The mixture reaction was transferred into an autoclave and kept at 120°C for 24 h. After being cooled to room temperature, the obtained precipitate was collected with a magnet and and subjected to washing with N,N-dimethylformamide. The amount of enzyme bound to the carrier was estimated by Bradford assay at 595 nm , employing bovine serum albumin as a standard. The catalytic activity of both the immobilized and free form of HIL was assayed by monitoring the release of O-nitrophenol from p-nitrophenylbutyrate (p-NPB) as the substrate at 410 nm.

3. Immobilization of HILon ZrFe$_2$O$_4$@UiO-66-NH$_2$ nanoparticles

HIL was immobilized on the support following a previously described method with some modifications [7]. Lipase HIL was dissolved in phosphate buffer solution with a pH of 7 (40 mg mL^{-1}). Subsequently, 0.5 mL of this solution was added to as-prepared ZrFe$_2$O$_4$@UiO-66-NH$_2$ (20 mg). In the next step, 2.26 mL saturated ammonium sulfate solution was added into the mixture, which was then subjected to agitation at 4 °C for 30 min to precipitate the enzyme. After stirring for 30 min, 240 µL of glutaraldehyde solution (25%) was injected into the mixture. Continuing to stir for 2 h, the product was collected by a magnet and washed with PBS for three times.

Results and Discussion

Herein, ZrFe2O4@UiO-66-NH2 nanoparticles was chosen as a support for immobilization of *H. insolens* lipase by

22nd Iranian Chemistry Congress (ICC22)
Iranian Research Organization for Science and Technology (IROST)
13-15 May 2024

03231-97589

IROST

the method of precipitation-crosslinking. The obtained products were characterized using SEM, XRD, FT-IR spectra, and energy dispersive X-ray (EDX) spectroscopy (Fig. 1 and 2).
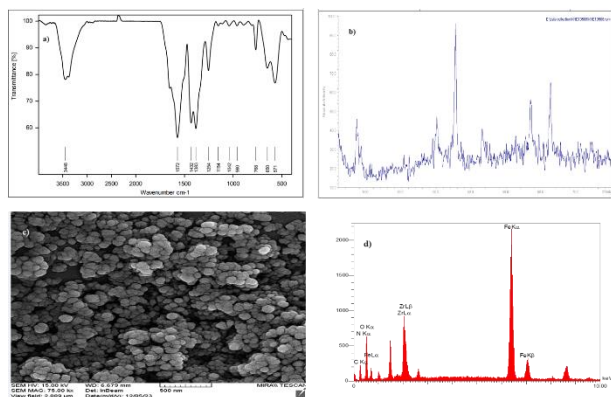
Fig.1: a) FTIR spectrum, b) XRD, c) SEM and d) EDX graph of the synthesised $ZrFe_2O_4$@UiO-66-NH_2 nanoparticles.
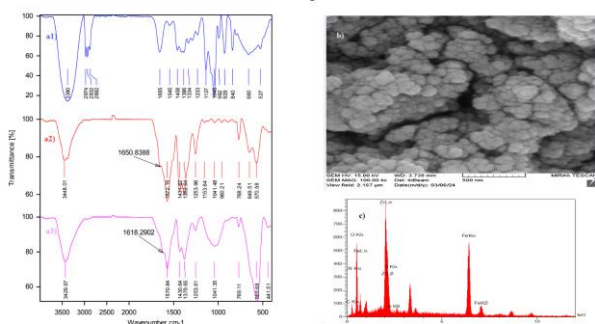
Fig.2: a) FTIR spectrum of a_1: HIL, a_2: $ZrFe_2O_4$@UiO-66-NH_2, and a_3: enzym immobilized on the support, b) SEM, and c) EDX graph of the immobilized enzym on the $ZrFe_2O_4$@UiO-66-NH_2 nanoparticles.

This method of immobilization was very efficient in terms of enzyme loading, reaching 333±5 mg/g support. Furthermore, the immobilized derivative of HIL showed the broader temperature and pH profiles in comparison to its soluble counterpart. The behavior of the soluble and immobilized enzyme was almost identical when exposed to alkaline pH values. However, a different behavior was observed under acidic pH conditions. The immobilized enzyme displayed a notable stability at pH 4 and it was able to maintain approximately 80% of its original activity after incubation for 1 hour. In contrast, the soluble enzyme retained only about 35% of its activity at this pH. Furthermore, the immobilized enzyme could retain more than 80% of its initial activity up to 3 cycles, after which it reduced to 20% over the subsequent two cycles.

Conclusions

In this study, a simple immobilization strategy, precipitation-crosslinking linkage method, was employed for the immobilization of HIL on the magnetic nanoparticles $ZrFe_2O_4$@UiO-66-NH_2. The thermal and pH stability of the immobilized derivative of enzyme was greatly improved, indicating potential for utilization in industrial applications

References

[1] Angajala, G., Pavan, P., Subashini, R. (2016). Lipases: An overview of its current challenges and prospectives in the revolution of biocatalysis. Biocatalysis and Agricultural Biotechnology, 7, 257-270. https://doi.org/10.1016/j.bcab.2016.07.001.

[2] Pereira, A. d. S., de Souza, A. H., Fraga, J. L., Villeneuve, P., Torres, A. G., Amaral, P. F. F. (2022) Lipases as Effective Green Biocatalysts for Phytosterol Esters' Production: A Review. Catalysts, 12(1), 88. https://doi.org/10.3390/catal12010088.

[3] Alikhani, N., Shahedi, M., Habibi, Z., Yousefi, M., Ghasemi, S., Mohammadi, M. (2022). A multi-component approach for co-immobilization of lipases on silica-coated magnetic nanoparticles: improving biodiesel production from waste cooking oil. Bioprocess and Biosystems Engineering, 45(12), 2043-2060. https://doi.org/10.1007/s00449-022-02808-7.

[4] Cheng, W., Nian, B. (2023). Computer-Aided Lipase Engineering for Improving Their Stability and Activity in the Food Industry: State of the Art. Molecules, 28(15), 5848.

[5] Xie, W., Xiong, J., Xiang, G. (2020). Enzyme immobilization on functionalized monolithic CNTs-Ni foam composite for highly active and stable biocatalysis in organic solvent. Molecular Catalysis, 483, 110714. https://doi.org/10.1016/j.mcat.2019.110714.

[6] Ghasemi, S., Yousefi, M., Nikseresht, A., Omidi, H. (2021). Covalent binding and in-situ immobilization of lipases on a flexible nanoporous material. Process Biochemistry, 102, 92-101. https://doi.org/10.1016/j.procbio.2020.12.013.

[7] Chen, J., Sun, B., Sun, C., Zhang, P., Xu, W., Liu, Y., Xiong, B., Tang, K. (2020) Immobilization of lipase AYS on UiO-66-NH_2 metal-organic framework nanoparticles as a recyclable biocatalyst for ester hydrolysis and kinetic resolution. Separation and Purification Technology, 251, 117398. https://doi.org/10.1016/j.seppur.2020.117398.

Synthesis of Flower-Like SnIn$_4$S$_8$/SmVO$_4$ Heterostructure Via a Hydrothermal Approach

Shahrzad Asoubar[a], Ali Mehrizad[b,*], Mohammad A. Behnajady[b], Mohammad Ebrahim Ramazani[a], Parvin Gharbani[c]

Corresponding Author E-mail: mehrizad@iaut.ac.ir

[a] Department of Environmental Engineering, Tabriz Branch, Islamic Azad University, Tabriz, Iran.

[b] Department of Chemistry, Tabriz Branch, Islamic Azad University, Tabriz, Iran.

[c] Department of Chemistry, Ahar Branch, Islamic Azad University, Ahar, Iran.

Abstract: This work reports the synthesis of stannum indium sulfide/samarium vanadate (SnIn$_4$S$_8$/SmVO$_4$) via a hydrothermal method. This heterostructure was characterized by different techniques. The results demonstrated that the distinct flower-like architecture of composite was obtained by hydrothermal approach which leads enlarged surface area and increasing the active sites of binary composite.

Keywords: SnIn$_4$S$_8$; SmVO$_4$; Hydrothermal

Introduction

Stannum indium sulfide (SnIn$_4$S$_8$) is a ternary chalcogenide semiconductor with potential uses in photocatalysis regarding its relatively narrow band gap, high stability, and strong visible-light absorption capacity. Generally, the short lifetime of photoinduced electron-hole (e$^-$-h$^+$) pairs dramatically restrict the performance of the simplex catalyst, where SnIn$_4$S$_8$ is no exception [1]. Fortunately, suitable strategies have been provided to overcome this main drawback including coupling of semiconductors with narrow and wide energy band gaps. In this respect, samarium vanadate (SmVO$_4$) can be considered a promising semiconductor candidate owning to its relatively narrow band gap, visible-light harvesting capability, and suitable band structure for photoredox reactions [2]. The capability of SmVO$_4$ to form heterojunctions with other semiconductors has been investigated in various studies [3-5]. This work aimed to synthesis of SnIn$_4$S$_8$/SmVO$_4$ using a hydrothermal method.

Experimental Section

The synthesis procedure of SnIn$_4$S$_8$/SmVO$_4$ was according to the following hierarchy: SnIn$_4$S$_8$ was prepared by solvothermal method proposed in the literature [6]. 1.25 mmol of SnCl$_4$.5H$_2$O and 5 mmol of InCl$_3$.4H$_2$O were dissolved in 150 mL of C$_2$H$_5$OH. Then, 12.5 mmol of CH$_3$CSNH$_2$ was added to the above solution. The obtained mixture was transferred into a Teflon-lined autoclave to be heated at 160 °C for 12 h. The final product was achieved by centrifuging, rinsing thrice with C$_2$H$_5$OH and deionized H$_2$O, and drying at 60 °C for 8 h. SmVO$_4$ was prepared via a precipitation method [3]. Equal molar ratios of Sm(NO$_3$)$_2$.6H$_2$O and NH$_4$VO$_3$ were separately dissolved in 50 mL of deionized H$_2$O. NH$_4$VO$_3$ solution was dropwise added into a round-bottom flask containing Sm(NO$_3$)$_2$.6H$_2$O solution under vigorously stirring, whiles the pH of mixture was kept at 7-8 using NH$_3$. Afterwards, the precipitates were collected centrifugally and rinsed with deionized H$_2$O to neutrality. The obtained product was oven-dried at 100 °C for 12 h, and calcined in furnace for 2 h at 500 °C. SnIn$_4$S$_8$/SmVO$_4$ composite was synthesized hydrothermally. Equal amounts of SnIn$_4$S$_8$ and SmVO$_4$ were separately dispersed in 100 mL of deionized H$_2$O under ultrasonication. Then, suspensions were transferred into a Teflon-lined autoclave and hold on 120 °C for 8 h. The final product was obtained by centrifuging, rinsing with deionized water, and drying at 80 °C for 8 h.

Results and Discussion

SnIn$_4$S$_8$/SmVO$_4$ heterostructure was characterized by different techniques including X-ray diffraction (XRD) and field emission scanning electron microscopy (FE-SEM).
For bare SnIn$_4$S$_8$, the XRD peaks appeared at 2θ angels of 9.65°, 19.10°, 28.20°, 32.80°, 47.82°, and 49.65° that correspond to the (200), (202), (600), (602), (174), and (001) planes of tetragonal phase SnIn$_4$S$_8$, respectively (JCPDS Card No. 42-1305) [7]. Similarly, for pure SmVO$_4$, seven distinct peaks appeared at 18.5°, 24.64°, 33.06°, 48.92°, 61.64°, 63.63°, and 69.4°, which are indexed with the (101), (200), (112), (312), (332), (204), and (224) planes of tetragonal phase SmVO$_4$, respectively (JCPDS Card No. 17-0876) [8]. In the case of SnIn$_4$S$_8$/SmVO$_4$, predominant diffraction peaks of SnIn$_4$S$_8$ and SmVO$_4$ were observed, confirming the successful formation of SnIn$_4$S$_8$/SmVO4 with strong interaction between them.
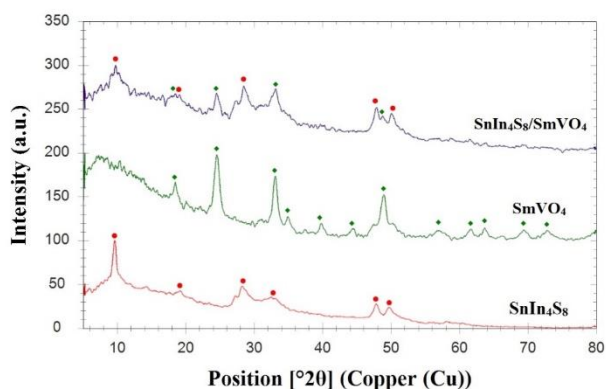
Fig.1: XRD patterns of synthesized samples.

The FE-SEM images of $SnIn_4S_8/SmVO_4$ with two magnifications are shown in Figs. 2a and 2b. Fig. 2a represents the formation of flower-like $SnIn_4S_8/SmVO_4$ microspheres. The high-magnification FE-SEM image (Fig. 2b) reveals that these microspheres were loosely assembled by numerous nanosheets.
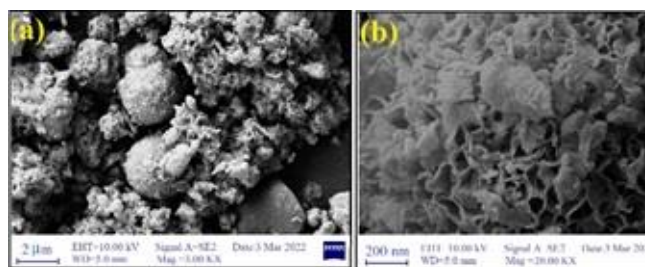
Fig.2: FE-SEM images of synthesized samples.

Conclusions

In this work, $SnIn_4S_8/SmVO_4$ heterostructure was prepared hydrothermally. The characterization results demonstrated that the distinct flower-like architecture of $SnIn_4S_8/SmVO_4$ composite was obtained by hydrothermal synthesis approach which leads enlarged surface area and increasing the active sites.

References

[1] Yan, T., Li, L., & Li, G. (2011). Solvothermal synthesis of hierarchical SnIn 4 S 8 microspheres and their application in photocatalysis. *Research on Chemical Intermediates*, *37*, 297-307.

[2] Ge, X., Zhang, Y., Wu, H., Zhou, M., & Lin, T. (2018). SmVO4 nanocrystals with dodecahedral shape: Controlled synthesis, growth mechanism and photoluminescent properties. *Materials Research Bulletin*, *97*, 81-88.

[3] Li, T., He, Y., Lin, H., Cai, J., Dong, L., Wang, X., & Weng, W. (2013). Synthesis, characterization and photocatalytic activity of visible-light plasmonic photocatalyst AgBr-SmVO4. *Applied Catalysis B: Environmental*, *138*, 95-103.

[4] Eghbali-Arani, M., Sobhani-Nasab, A., Rahimi-Nasrabadi, M., & Pourmasoud, S. (2018). Green synthesis and characterization of SmVO 4 nanoparticles in the presence of carbohydrates as capping agents with investigation of visible-light photocatalytic properties. *Journal of Electronic Materials*, *47*, 3757-3769.

[5] Chen, J., Xu, X., Feng, L., He, A., Liu, L., Li, X., & Chen, Y. (2020). One-step MOF assisted synthesis of SmVO4 nanorods for photocatalytic degradation of tetracycline under visible light. *Materials Letters*, *276*, 128213.

[6] Wang, L., Li, X., Teng, W., Zhao, Q., Shi, Y., Yue, R., & Chen, Y. (2013). Efficient photocatalytic reduction of aqueous Cr (VI) over flower-like SnIn4S8 microspheres under visible light illumination. *Journal of hazardous materials*, *244*, 681-688.

[7] Shen, C. H., Chen, Y., Xu, X. J., Li, X. Y., Wen, X. J., Liu, Z. T., ... & Fei, Z. H. (2021). Efficient photocatalytic H2 evolution and Cr (VI) reduction under visible light using a novel Z-scheme SnIn4S8/CeO2 heterojunction photocatalysts. *Journal of Hazardous Materials*, *416*, 126217.

[8] Quach, T. A., Becerra, J., Nguyen, D. T., Sakar, M., Vu, M. H., Dion, F., & Do, T. O. (2022). Direct Z-scheme mediated SmVO4/UiO-66-NH2 heterojunction nanocomposite for the degradation of antibiotic tetracycline hydrochloride molecules under sunlight. *Chemosphere*, *303*, 134861.

22nd Iranian Chemistry Congress (ICC22)
Iranian Research Organization for Science and Technology (IROST)
13-15 May 2024

03231-97589

Study of photocatalytic removal of hexavalent chromium ion from aqueous solutions by SnIn4S8

Shahrzad Asoubar[a], Ali Mehrizad[b,*], Mohammad A. Behnajady[b], Mohammad Ebrahim Ramazani[a], Parvin Gharbani[c]

Corresponding Author E-mail: mehrizad@iaut.ac.ir

[a] Department of Environmental Engineering, Tabriz Branch, Islamic Azad University, Tabriz, Iran.

[b] Department of Chemistry, Tabriz Branch, Islamic Azad University, Tabriz, Iran.

[c] Department of Chemistry, Ahar Branch, Islamic Azad University, Ahar, Iran.

Abstract: In this work, the photocatalytic performance of SnIn4S8 was studied in the removal of hexavalent chromium ion (Cr^{6+}). Response surface methodology (RSM) was employed to optimize the effective operating parameters. Obtained results demonstrated that the Cr^{6+} reduction reached 90.93% under RSM-based optimal conditions.

Keywords: SnIn4S8; Cr^{6+}; RSM

Introduction

Hexavalent chromium ion (Cr^{6+}) was introduced among the first category of hypertoxic water contaminants. When released directly into the water, such chemicals will cause irreparable damage to flora and fauna life by disrupting photosynthetic processes and cytotoxicity. Therefore, urgent action is necessary to prevent them from entering aquatic environments [1]. As one of the advanced oxidation processes, photocatalysis has demonstrated to be efficient at alleviating and eliminating a wide range of pollutants. The infrastructure of heterogeneous photocatalysis is based on the simultaneous use of the semiconductor catalyst and irradiation source, without the requirement for sophisticated equipment [2]. Stannum indium sulfide (SnIn4S8) is a ternary chalcogenide semiconductor with potential uses in photocatalysis regarding its relatively narrow band gap, high stability, and strong visible-light absorption capacity [3]. This work aimed to photocatalytic removal of hexavalent chromium ion from aqueous solutions by SnIn4S8.

Experimental Section

The experimental set-up consisted of a cylindrical Pyrex glass vessel, a 300 W halogen lamp (Osram, Germany), and a UV/IR cut-off optical filter. The cylindrical vessel was placed on a magnetic stirrer below the light source in a self-made enclosed wooden chamber equipped with a cooling fan. For each experimental run, a weighted amount of SnIn4S8 catalyst was introduced into 100 mL of the $K_2Cr_2O_7$ aqueous solution with specified concentration and pH values. After ultrasonically shaking for 2 min, the mixture was magnetically stirred in the light avoidance condition for 30 min to establish adsorption/desorption equilibrium. Next, the lamp and cooling fan were switched on, and the suspension was irradiated for a suitable duration at ambient temperature (~25 °C) and atmospheric pressure to trigger the photocatalytic reaction. Aliquots of 5 mL samples were taken for analysis at the designed time intervals, and centrifuged at 5,000 rpm for 10 min. The residual amounts of Cr^{6+} was measured spectrophotometrically using a single beam spectrophotometer (Shimadzu UV-Mini-1240) at corresponding maximum wavelength. Equation (1) was used to calculate the removal efficiency of the Cr^{6+}.

$$\text{Removal(\%)} = \frac{(C_0 - C_t)}{C_0} \times 100 \tag{1}$$

where C_0 and C_t are the liquid concentration (mg L^{-1}) of Cr^{6+} at initial time and time t, respectively.

Results and Discussion

As mentioned in the experimental section, the effect of four influential factors was studied during 30 RSM-designed experiments to find the optimal condition for photocatalytic Cr^{6+} reduction.

Based on the results the binary interaction of solution pH with the initial Cr^{6+} concentration, catalyst dosage, and irradiation time have pivotal roles in the photocatalytic reduction of Cr^{6+} which are graphically illustrated by 3D response surfaces in Figs. 1a-c.

22nd Iranian Chemistry Congress (ICC22)
Iranian Research Organization for Science and Technology (IROST)
13-15 May 2024

03231-97589
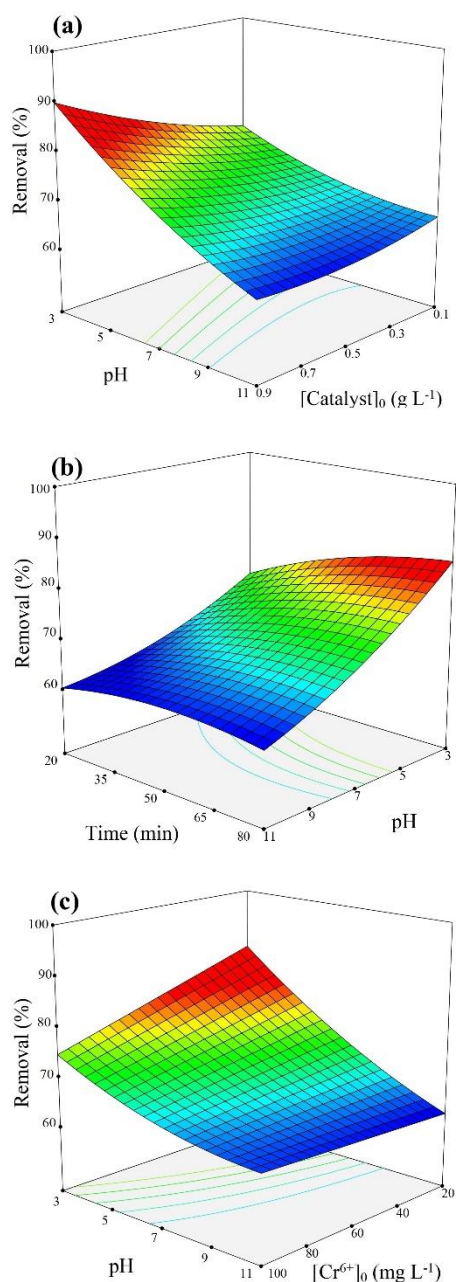
Fig.1: Response surface plots of the Cr^{6+} removal efficiency as a function of operational factors.

As shown in Figs. 1a–c, acidic pHs were favorable to the photocatalytic reduction of Cr^{6+}. In Figs. 1a and 1b, the pH interactions with catalyst dosage and irradiation time show that increasing the catalyst amount and irradiation duration in relatively strong acidic environments increases the efficiency. This enhancement might be due to the increased available active sites and the possibility of creating more active species. Besides, according to Fig. 1c, the removal efficiency was decreased at higher Cr^{6+} concentrations because of huge amounts of Cr^{6+} ions and the non-responsiveness of involved active species [4].

Conclusions

In this research, the photocatalytic activity of $SnIn_4S_8$ was evaluated in the removal of Cr^{6+} ion under visible light irradiation. RSM was employed to optimize the effective operating variables (initial Cr^{6+} concentration, photocatalyst's amount, pH, and irradiation time). Based on the results the binary interaction of solution pH with the initial Cr^{6+} concentration, catalyst dosage, and irradiation time have pivotal roles in the photocatalytic reduction of Cr^{6+}. It was observed that the Cr^{6+} reduction reched 90.93% under RSM-based optimal conditions.

References

[1] Ou, B., Wang, J., Wu, Y., Zhao, S., & Wang, Z. (2020). Efficient removal of Cr (VI) by magnetic and recyclable calcined CoFe-LDH/g-C3N4 via the synergy of adsorption and photocatalysis under visible light. Chemical engineering journal, 380, 122600.

[2] Mehrizad, A., & Gharbani, P. (2016). Removal of methylene blue from aqueous solution using nano-TiO2/UV process: optimization by response surface methodology. *Progress in Color, Colorants and Coatings*, *9*(2), 135-143.

[3] Yan, T., Li, L., & Li, G. (2011). Solvothermal synthesis of hierarchical SnIn 4 S 8 microspheres and their application in photocatalysis. *Research on Chemical Intermediates*, *37*, 297-307.

[4] Shen, C. H., Chen, Y., Xu, X. J., Li, X. Y., Wen, X. J., Liu, Z. T., & Fei, Z. H. (2021). Efficient photocatalytic H2 evolution and Cr (VI) reduction under visible light using a novel Z-scheme SnIn4S8/CeO2 heterojunction photocatalysts. *Journal of Hazardous Materials*, *416*, 126217.

Using A Plant Exosome to Improve the Biocompatibility of Zeolitic Imidazolate Framework Nanocarriers

Adeleh Saffar [a], Ahmad Reza Bahrami [a,b], Amir Sh. Saljooghi [c,d*], Maryam M. Matin[a,d*]

Corresponding Author E-mail: Saljooghi@um.ac.ir; Matin@um.ac.ir

[a] Department of Biology, Faculty of Science, Ferdowsi University of Mashhad, Mashhad, Iran.

[b] Industrial Biotechnology Research Group, Institute of Biotechnology, Ferdowsi University of Mashhad, Mashhad, Iran.

[c] Department of Chemistry, Faculty of Science, Ferdowsi University of Mashhad, Mashhad, Iran.

[d] Novel Diagnostics and Therapeutics Research Group, Institute of Biotechnology, Ferdowsi University of Mashhad, Mashhad, Iran.

Abstract: A novel core-shell nanocarrier consisting of doxorubicin-loaded ZIF-8 (core) enveloped by a plant exosome (shell) was established. The proper synthesis of the nanocarrier was confirmed by physical characterization. Nanoparticle coating led to a reduced hemolysis rate and enhanced immune evasion, indicating improved biocompatibility.

Keywords: ZIF-8; core; plant exosome

Introduction

The advent of nanotechnology-based drug delivery systems (DDS) has created new hope for addressing the challenges associated with chemotherapy medication usage. Metal-organic frameworks (MOFs), composed of metal ions and organic linkers, have attracted much attention due to their properties, including a large surface area, adjustable pore shape and size, and the ability to control surface behavior. The zeolite imidazolate framework (ZIF-8) (as a subgroup of MOFs) composed of zinc ions and imidazole units has been extensively investigated in biomedical applications. Notably, ZIF-8 has been found to decompose under the acidic pH of the tumor microenvironment. This pH-responsive nanocarrier is an ideal candidate for cancer research. Therefore, these nanocarriers overcome limitations such as the insolubility and low half-life of chemotherapeutic drugs and uncontrolled drug release compared to conventional ones [1] [2]. On the other hand, a frequently employed strategy to improve the pharmacokinetics and accumulation at tumor sites involves surface modification of DDS with organic materials with good biocompatibility. This approach minimizes DDS clearance by the immune system, increases blood circulation time, and enhances DDS effectiveness [3].

In this research, a novel biocompatible DDS was prepared, including ZIF-8 as the core of DDS for doxorubicin (DOX) delivery to cancer cells and a plant exosome as an outer shell.

Experimental Section

ZIF-8/DOX was synthesized by the one-pot method [4]. In the next step, ZIF-8/DOX coating with a plant exosome was performed. After the physical characterization of the nanocarrier, drug loading capacity (LC %) was calculated. Two tests for biocompatibility evaluation were conducted: 1: A hemolysis test to check the feasibility of the intravenous injection of nanocarrier. To this aim, 4% (v/v) erythrocyte suspensions were prepared and mixed with various concentrations of coated ZIF-8/DOX and uncoated ones (25-800 µg/ml) and incubated at 37 °C for 4h. After that, the supernatant absorbance of the samples was measured at 545nm by a UV-vis spectrophotometer [5].

2: Evaluation of immune scape: An in vitro experiment was conducted to assess the uptake of nanocarriers by the RAW 264.7 murine macrophage cell line (immune cell) via flow cytometry analysis [6].

Results and Discussion

The successful synthesis of ZIF-8/DOX was confirmed by observing characteristic peaks (including Zn-N stretching at 422 cm^{-1}, C-N stretching bands at 1145 and 995 cm^{-1}) in Fourier transform infrared (FT-IR) spectra (Fig.1). The loading capacity (LC %) of DOX was 23%.

22nd Iranian Chemistry Congress (ICC22)
Iranian Research Organization for Science and
Technology (IROST)
13-15 May 2024

03231-97589
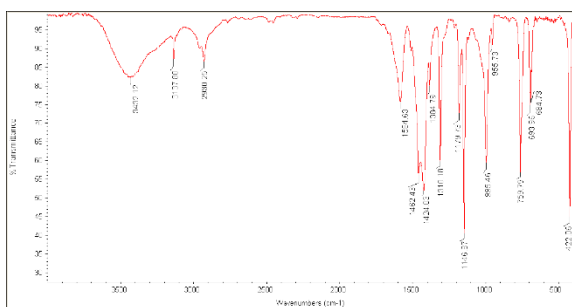
Fig.1: Fourier transform infrared (FTIR) analysis

The released hemoglobin as an indicator of red blood cell (RBC) membrane rupture was measured. The low rate of hemolysis in RBCs treated with coated nanocarriers compared to uncoated ones indicates the biocompatibility of the existing coating (Fig.2).
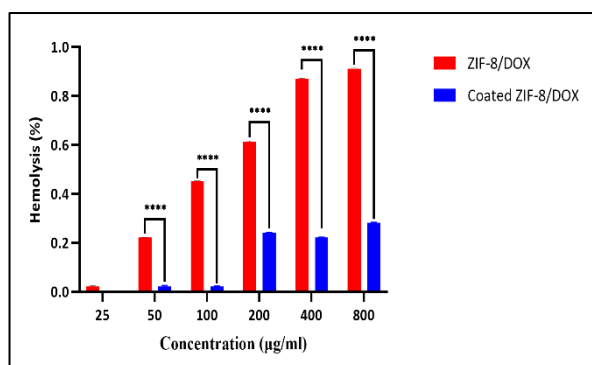
Fig.2: Hemolysis percentage of samples

In the next experiment, the uptake of coated and uncoated ZIF-8/DOX by immune cells was investigated. The foreign nanoparticles are rapidly cleared by immune cells. Flow cytometry results indicated a significantly lower uptake of coated nanocarriers compared to uncoated ones by immune cells. The improved immune escape of coated ZIF-8/DOX can be attributed to the coating layer (Fig.3).

Conclusions

The core-shell nanocarrier fabrication using this plant exosome introduced a novel strategy for DDS improvement to achieve superior antitumor outcomes.

References

[1] Wei, Q. Y., He, K. M., Chen, J. L., Xu, Y. M., & Lau, A. T. Y. (2019). Phytofabrication of nanoparticles as novel drugs for anticancer applications. Molecules, 24(23), 4246. https://doi.org/10.3390/molecules24234246.

[2] Shu, F., Lv, D., Song, X. L., Huang, B., Wang, C., Yu, Y., & Zhao, S. C. (2018). Fabrication of a hyaluronic acid conjugated metal organic framework for targeted drug delivery and magnetic resonance imaging. RSC Advances, 8(12), 6581–6589. https://doi.org/10.1039/c7ra12969f.

[3] Lin, Y., Zhong, Y., Chen, Y., Li, L., Chen, G., Zhang, J., Li, P., Zhou, C., Sun, Y., Ma, Y., Xie, Z., & Liao, Q. (2020). Ligand-Modified Erythrocyte Membrane-Cloaked Metal-Organic Framework Nanoparticles for Targeted Antitumor Therapy. Molecular pharmaceutics, 17(9), 3328–3341. https://doi.org/10.1021/acs.molpharmaceut.0c00421.

[4] Zheng, H., Zhang, Y., Liu, L., Wan, W., Guo, P., Nyström, A. M., & Zou, X. (2016). One-pot Synthesis of Metal-Organic Frameworks with Encapsulated Target Molecules and Their Applications for Controlled Drug Delivery. Journal of the American Chemical Society, 138(3), 962–968. https://doi.org/10.1021/jacs.5b11720.

[5] Zhao, Z., Liu, Z., Hua, Y., Pan, Y., Yi, G., Wu, S., He, C., Zhang, Y., & Yang, Y. (2022). Biomimetic ZIF8 Nanosystem with Tumor Hypoxia Relief Ability to Enhance Chemo-Photothermal Synergistic Therapy. Frontiers in pharmacology, 13, 850534. https://doi.org/10.3389/fphar.2022.850534.

[6] Lv, W., Han, Z., Li, Y., Huang, Y., Sun, J., Lu, X., & Liu, C. (2021). Exosome-coated zeolitic imidazolate framework nanoparticles for intracellular detection of ATP. Chinese Journal of Chemistry, 39(8), 2107-2112.

Fig.3: Uptake of the synthesized nanocarriers by macrophage cells

Wound Healing of Nanofiber Comprising Chitosan Thiourea/Poly(Vinyl Alcohol) Embedded Mpeg-CUR for Second-Degree Burn Injuries

Alireza Shaabani [a], Nastaran Sayyari *[b]

Corresponding Author E-mail : nastaransayyari72@gmail.com

[a] Department of Polymer & Materials Chemistry, Faculty of Chemistry and Petroleum Sciences, Shahid Beheshti University, G.C, 1983969411, Tehran, Iran.

[b] School of Medicine, Qom University of Medical Sciences, Qom, Iran.

Abstract: In this study, pegylated curcumin (mPEG-CUR) was integrated into chitosan thiourea (CST) nanofibers as a novel multifunctional wound healing nanofiber for treating second-degree burn wounds. CST-based uniform nanofiber with 5 wt% mPEG-CUR has good breathability, excellent dimensional stability, and outstanding antimicrobial activity with any cytotoxicity to normal fibroblast cells.

Keywords: Chitosan; Nanofiber; Chitosan thiourea; Wound healing

Introduction

Chitosan, originating from chitin, is renowned for its immune response activation, wound-healing capabilities, and degradability. Enhancing its antimicrobial effects through derivatives like thiourea is beneficial, as this functional group displays antibacterial and insecticidal properties. Novel nanofibers utilizing chitosan derivatives, such as chitosan thiourea, and incorporating antimicrobial and antioxidant elements like pegylated curcumin can present an effective approach for managing second-degree burn wounds.

Curcumin (CUR), derived from turmeric, showcases exceptional antibacterial, antioxidant, anti-inflammatory, and skin tissue regeneration properties, making it a promising natural agent for wound healing. However, its low aqueous solubility challenges its bioavailability and stability, necessitating higher doses for efficacy. PEGylating curcumin (mPEG-CUR) enhances its hydrophilicity, effectively boosting its antioxidant, antimicrobial, and wound-healing benefits [1].

Experimental Section

Synthesis of the CST: For the synthesis of CST, 15.2 gr of NH_4SCN was dissolved in 100 mL of absolute ethanol. Then, 16.1 gr of CS (medium molecular weight) was added to the solution. We allowed the mixture to form a suspension and refluxed it for 16 h. After the reaction was complete, the reaction flask was cooled to room temperature. The mixture was filtered, purified with acetone, and dried at 60 °C (Degree of thiourea substitution = 36.2%, from CHNS/O elemental analysis).

Synthesis of the mPEG-CUR: First, the 2 mmol of the mPEG (2000 Da) was dissolved in 100 mL fresh dried tetrahydrofuran (THF). After adding 2.1 mmol toluene diisocyanate, the mixture was stirred for 6 h at 40 °C. Then, the 2 mmol CUR in 100 mL dried THF was added and stirred overnight. The solution was concentrated, precipitated in cold diethyl ether, filtered, and washed with cold diethyl ether. The obtained product was dried in a vacuum oven at room temperature overnight.

Preparation of electrospinning solution: The electrospinning solution was prepared by dissolving 0.2 of CST and CS in 10 g aqueous poly(vinyl alcohol) (PVA, 72000 Da) solution (8 wt%) for 5 h at 60 °C using magnetic stirring in the present or absence of mPEG-CUR (50 mg) as shown in Table. 1. 1 cc of acetic acid was used to completely dissolve CS and CST.

Table 1: Different ratios of materials in bioink composition

Sample	PVA (g)	CS (g)	CST (g)	mPEG-CUR (mg)
PC0	10	0.2	0.0	50
PCT0	10	0.0	0.2	50
PC5	10	0.2	0.0	50
PCT5	10	0.0	0.2	50

Results and Discussion

The CST showed peaks at 2880 & 2922 cm^{-1}, 2065 cm^{-1}, 1429 cm^{-1}, and 1257 cm^{-1} which related to the stretching vibrations of the $-CH_x-$, NC=S, N-C-S, and C=S, respectively [2]. Moreover, the mPEG-CUR showed peaks at 1600 cm^{-1}, 1506 cm^{-1} & 1630 cm^{-1}, 1280 cm^{-1}, 1153 cm^{-1}, 2887 cm^{-1}, and 1100 cm^{-1} which attributed to the stretching vibrations of the benzene ring, mixed C=O and C=C groups, aromatic C−O, C−O−C, C−H (of mPEG unit), and C−O−C (mPEG unit), respectively [1].

22nd Iranian Chemistry Congress (ICC22)
Iranian Research Organization for Science and
Technology (IROST)
13-15 May 2024

03231-97589
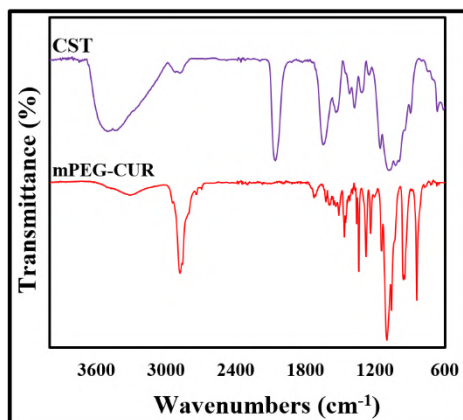
Fig.1: FT-IR spectrum of CST and mPEG-CUR

As observed in Fig. 2, all nanofibers have uniform and bead-less morphology. Moreover, nanofibers with average diameters of 105±24 nm (PC0), 124±28 nm (PCT0), 134±34 nm (PC5), and 149±31 nm (PCT5) were formed. The nanofiber diameter rises as the mPEG-CUR content increases, attributed to the heightened viscosity of the electrospinning solution upon the addition of mPEG-CUR.
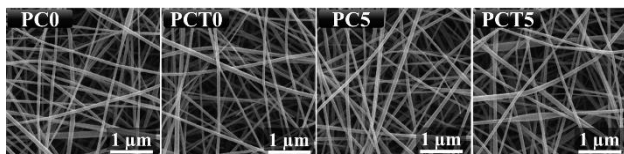
Fig. 2. SEM images of the different nanofibers
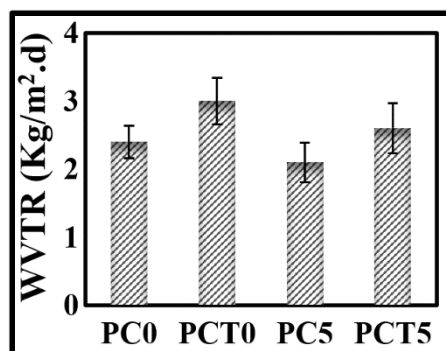
Fig. 3. The WVTR rate of the different nanofibers

Fig. 2 shows the water vapor transmission rate (WVTR) of the electrospun nanofibers. The results indicate that the WVTR rates range from 2.1±0.37 to 3.0±0.29 kg/m².day. The findings fall within the recommended range of 2.0 to 2.5 kg/m².day for an effective wound dressing, suggesting that these nanofibers are suitable for use in wound dressing applications [3].

The 2,2-diphenyl-1-picrylhydrazyl (DPPH) test was conducted to assess the antioxidant properties of nanofibers. Extracting mPEG-CUR from methanol showed that the antioxidant activity of nanofibers improves with time, suggesting that the biological activity of the nanofibers remains intact even after undergoing electrospinning and heat treatment. As anticipated, the antioxidant activity of the nanofibers rises with a higher concentration of mPEG-CUR. The antioxidant effects of mPEG-CUR are primarily linked to the loss of phenoxyl and hydroxy groups upon the creation of phenoxyl radicals.
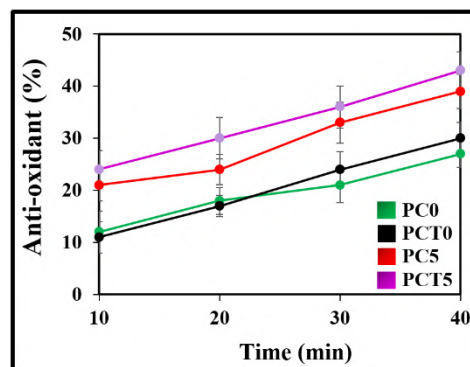
Fig. 3. Anti-oxidant activity of the different nanofibers

Conclusions

In summary, an electrospinning process was used to successfully create multifunctional nanofibers for burn wound healing, featuring antibacterial and skin regeneration properties. SEM analysis confirmed that the nanofibers containing mPEG-CUR in PC5 and PCT5 formulations displayed uniform, bead-free structures and excellent WVTR rate. These findings suggest that this innovative approach to nanofiber fabrication holds great potential for the advancement of novel wound dressings.

References

[1]. Shaabani, A., Bizari, D., & Khoshmohabat, H. (2023). PEGylated curcumin-loaded poly (vinyl alcohol)/Zwitterionic poly (sulfobetaine vinylimidazole)-grafted chitosan nanofiber as a second-degree burn wound dressing. *Carbohydrate Polymers*, *321*, 121307.

[2]. Al-Saidi, H. M. (2016). Biosorption using chitosan thiourea polymer as an extraction and preconcentration technique for copper prior to its determination in environmental and food samples by flame atomic absorption spectrometry: Synthesis, characterization and analytical applications. *International journal of biological macromolecules*, *93*, 390-401.

[3]. Guo, Y., Zhou, W., Wang, L., Dong, Y., Yu, J., Li, X., & Ding, B. (2019). Stretchable PDMS embedded fibrous membranes based on an ethanol solvent system for waterproof and breathable applications. ACS Applied Bio Materials, 2(12), 5949-5956.

22nd Iranian Chemistry Congress (ICC22)
Iranian Research Organization for Science and Technology (IROST)
13-15 May 2024

03231-97589

IROST

Synthesis of Amorphous Porous Organic Polymer Functionalized With Nitrogen Rich Graphitic Carbon Nitride

Seyed Mahdi Mejmarian Esfahani, Nahid Khandan*, Yasamin Bide*

Corresponding Author E-mail: **khandan@irost.org, y.bide@irost.ir**

Department of Chemical Technologies, Iranian Research Organization for Science and Technology (IROST), Tehran, Iran.

Abstract: The porosity and adaptability of porous organic polymers (POPs) in gas separation, catalysis, and energy applications are vital. This study covered the synthesis of a porous organic polymer using melamine and terephthaloyl chloride through a simple pathway. The in-situ growth of nitrogen rich graphitic carbon nitride on the synthesized POP was reported in this work. Various analyzes including scanning electron microscope (SEM) and Fourier transform infrared spectrometry (FTIR) were employed to characterize and follow up the synthetic procedure.

Keywords: Porous organic polymer (POP); graphitic carbon nitride; melamine.

Introduction

Porous organic polymers (POPs) represent a new field of study in porous material science. POPs are a class of multidimensional porous network materials composed of strong covalent bonds between different organic building blocks with different topologies and geometries [1]. POPs can be broadly classified into two groups: crystalline (such as covalent organic frameworks) and amorphous (such as hyper-cross-linked polymers, conjugated microporous polymers, intrinsic microporous polymers, and porous aromatic frameworks) [2].POPs have garnered a lot of interest and research attention because of their many advantages, which include high intrinsic porosity, light weight, excellent stability, and pre-designed and adjustable structures and functions. These materials are highly useful for heterogeneous catalysts, chemical and biological sensing, gas storage and separation, photoelectric conversion, energy storage and conversion, and other applications. By altering their component parts, the porous structure, the pores' sizes, and the surfaces of this structure can all be created and modified for a particular use [3].POPs are commonly synthesized using the following techniques: microwave synthesis, solvothermal synthesis, ionothermal synthesis and room-temperature synthesis [4].A class of porous aromatic frameworks known as PAF was created in 2011 by Teng Ben and associates. These materials are stable in the majority of solvents, including alcohols, acetone, and DMF[5].Amin Abid and associates created POPs in a class of polymers with high cross-linking in 2021, dubbed HCP-PN. When this structure was heated to 273 K, it adsorbed roughly 72 mg of carbon dioxide for every gram of adsorbent [6].

Experimental Section
Materials:

The following materials were purchased from Merck in Germany: melamine, DMSO, triethylamine, terephthaloyl chloride, and methanol.

Synthesis of GN-POP:

A sample of graphitic carbon nitride (GN) was prepared via calcination. In order to obtain graphitic carbon nitride with extra amine groups, 350 °C was used as the temperature for calcination. In detail, 5 g of melamine in an alumina crucible was heated to 350 °C from room temperature in a tube furnace at a rate of 2.5 °C min^{-1} under an N_2 atmosphere at ambient pressure and kept for 4 h at 350 °C. GN-POP were synthesized by thermal polymerization. In detail, 252 mg of melamine, 63 mg of GN-melamine, 15 mL of DMSO, 0.5 mL of triethanolamine, and 609 mg of Terephthaloyl chloride were added to a 100 mL single-necked flask and stirred for 20 min at 25 °C. Then, The mixture was heated for 6 hours at 190 °C under inert conditions using a Dean–Stark apparatus. Following that, the material underwent three methanol washes before being separated via centrifugation.

Results and Discussion

Melamine, terephthaloyl chloride, and graphitic carbon nitride derived from melamine were condensed to create an amorphous organic polymer functionalized with nitrogen-rich graphitic carbon nitride (GN-POP).There are several ways to synthesize this structure, including mechanical and microwave methods.

Fourier transform infrared spectroscopic analysis(FTIR):
FTIR analysis was used for identifying molecular species and functional groups of the synthesized materials.

22nd Iranian Chemistry Congress (ICC22)
Iranian Research Organization for Science and Technology (IROST)
13-15 May 2024

03231-97589

IROST

The FTIR spectra of the as-syntheszied HN have been displayed in Figure 1 showing the peak at 3400 cm^{-1} due the OH and NH groups.
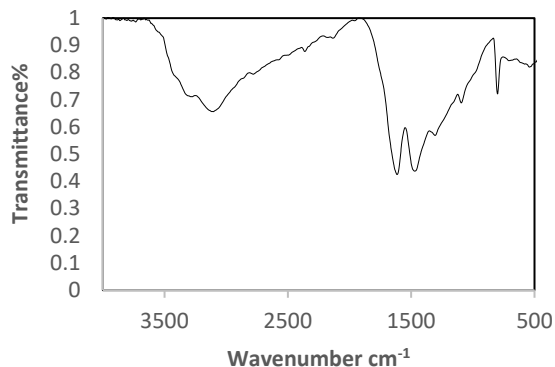
Fig.1: FTIR spectrum of GN.

Figure 2 shows the FTIR spectrum of the as-prepared GN-POP. The peaks in the 1600 cm^{-1} region are related to CN rings [7].
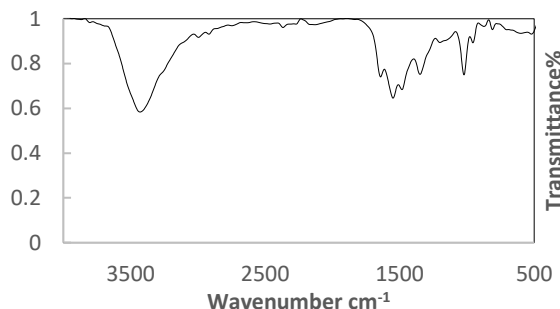
Fig.2: Diagram showing the Fourier transform infrared spectroscopy analysis (GN_POP).

Scanning electron microscope analysis (SEM):

Using a scanning electron microscope, the morphology of the as-synthesized GN-POP was investigated. The dimensions and shape of synthesized particles are easily observed via the SEM images. Through SEM analysis, the surface morphology of the synthesized GN-POP was examined (Figure 3).
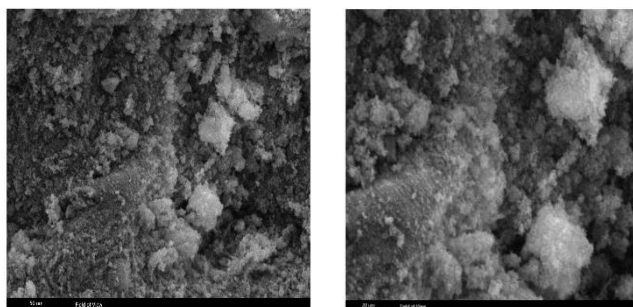
Fig.3: SEM images obtained from GN-POP.

Conclusions

In conclusion, we have described the synthesis of a chemically stable, porous organic polymer. In this work, we used in situ procedure to synthesize GN-POP. In two stages of synthesis, we first transformed melamine into graphitic carbon nitride in a furnace with a nitrogen atmosphere. Additionally, POP functionalized with nitrogen rich graphitic carbon nitride was prepared using melamine and terephthaloyl chloride. The bands related to the CN rings are visible in the FTIR analysis. The mesoporous structure and the spherical nanoparticles are visible in the SEM image.

References

[1] Raganati, F., F. Miccio, and P. Ammendola, *Adsorption of carbon dioxide for post-combustion capture: A review.* energy & fuels, 2021. 35(16): p. 12845-12868.

[2] Ben-Mansour, R., et al., *Carbon capture by physical adsorption: materials, experimental investigations and numerical modeling and simulations–a review.* Applied Energy, 2016. 161: p. 225-255.

[3] Abuzeid, H.R., A.F. EL-Mahdy, and S.-W. Kuo, *Covalent organic frameworks: Design principles, synthetic strategies, and diverse applications.* Giant, 2021. **6**: p. 100054.

[4] Diaz de Grenu, B., et al., *Microwave-assisted synthesis of covalent organic frameworks: A review.* ChemSusChem, 2021. 14(1): p. 208-233.

[5] Ben, T., et al., *Gas storage in porous aromatic frameworks (PAFs).* Energy & Environmental Science, 2011. 4(10): p. 3991-3999.

[6] Abid, A., et al., *Eco-Friendly Phosphorus and Nitrogen-Rich Inorganic–Organic Hybrid Hypercross-linked Porous Polymers via a Low-Cost Strategy.* Macromolecules, 2021. **54**(12): p. 5848-5855.

[7] Ou, H., et al., *One-pot synthesis of gC 3 N 4-doped amine-rich porous organic polymer for chlorophenol removal.* Environmental Science: Nano, 2018. **5**(1): p. 169-182.

Cationic Dye Removal from Industrial Wastewater by Chemical Surface Modified Cellulose as an Adsorbent

Elaheh Gharehkhani, Sahar Rahmati*

Corresponding Author E-mail: sahar.rahmati121358@gmail.com

Department of Chemistry, Islamic Azad University, Saveh Branch, Saveh, Iran.

Abstract: Chemical surface modification was done on cellulose fibers and its absorption capacity was increased as alkaline dye absorbent. Optimizing the dye removal conditions using DOE by CCD method was done on the amount of adsorbent, contact time, pH and initial dye concentration in the simulated wastewater and the results were analyzed.

Keywords: Dye removal; Experiment design; Surface modification; Cellulose; Adsorbent

Introduction

Cellulose is the most abundant raw organic material in nature with unique physical and chemical properties, easy access, renewable and degradability, and has many capabilities in micro to nanometer scales. Cellulosic fibers are usually obtained by cellulose extracted from trees or woody plants, although protein fibers are also used. Hydroxyl groups on the surface of cellulose and sulfonate and phosphonate groups, which are linked to its surface as a result of chemical modification, can selectively absorb pollutants in wastewater [1].

The chemical modification of the surface of cellulose fibers based on functional groups that have a high affinity for certain compounds shows that it can be expected to increase the absorption capacity for water-soluble pollutants. This strategy was successfully carried out to increase the absorption of heavy metal ions by the bonds of selected structures [2]. Carboxylated cellulose has been extensively studied for the adsorption of cationic dyes. In this article, the removal of color by cellulose and paper is discussed, which has not been observed in other articles. Cellulosic materials naturally have unique structural, mechanical and optical properties. The special potentials of cellulosic materials such as high surface to volume, low environmental impact, functionality and stability can be used in water and wastewater treatment technology [3].

In order to remove color pollutants from chemical industry wastewater and prevent to enter the environment, especially alkaline dyes that have high intensity and can be seen in low concentrations, chemically modified cellulose was used. The amount of adsorbent, contact time, pH and initial concentration of dye, optimized by design of experiment (DOE) through RSM, CCD [4] with certain number of experiments.

Experimental Section

Carboxylated cellulose was prepared by adding sulfuric acid and then maleic anhydride to pure cellulose.
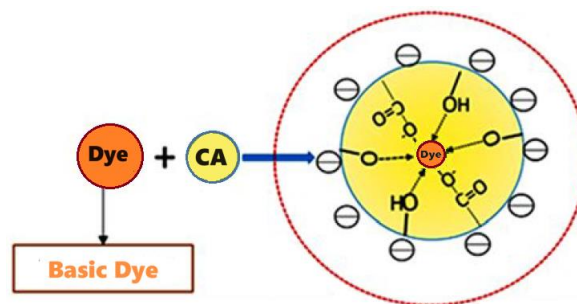
Fig.1: Preparation of carboxylated cellulose adsorbent and how to surround the phenazole red dye molecule

Some cationic dyes such as CHROMAFIX BlACK GDRE (MIX) was dissolved in water with different concentrations and according to the table of tests determined by Design Expert software, the amount of dye removal from the simulated wastewater was tested. The influences of several parameters (contact time, pH, absorbent dose, initial concentration) were evaluated to determine the best adsorption conditions.

Table1: Test program specified by Design expert software (amount and range of effective factors in dye removal)

Run	Block	Factor1 A:Initial dye conC mg/l	Factor 2 B:Absorbend dose g/l	Factor 3 C:Mixing Time min	Factor 4 D:pH -
1	Block 1	30	3.5	90	7
2	Block 1	40	5	120	5
3	Block 1	40	5	120	9
4	Block 1	40	2	120	9
5	Block 1	20	5	120	9
6	Block 1	20	5	120	5
7	Block 1	30	3.5	90	7
8	Block 1	40	2	120	5
9	Block 1	30	0.5	90	7
10	Block 1	30	3.5	90	7
11	Block 1	10	3.5	90	7
12	Block 1	50	3.5	90	7
13	Block 1	30	3.5	90	11
14	Block 1	20	5	60	5
15	Block 1	30	3.5	90	7
16	Block 1	20	2	60	5
17	Block 1	20	2	120	5
18	Block 1	20	2	60	9
19	Block 1	20	5	60	9
20	Block 1	40	2	60	9
21	Block 1	20	2	120	9
22	Block 1	40	5	60	5
23	Block 1	40	5	60	9
24	Block 1	40	2	60	5
25	Block 1	30	3.5	30	7
26	Block 1	30	3.5	90	3
27	Block 1	30	3.5	50	7
28	Block 1	30	3.5	90	7
29	Block 1	30	6.5	90	7
30	Block 1	30	3.5	90	7

Results and Discussion

In this work, a novel absorbent CNM with abundant carboxyl was synthesized and characterized with SEM, AFM, FT-IR, XRD and TGA.
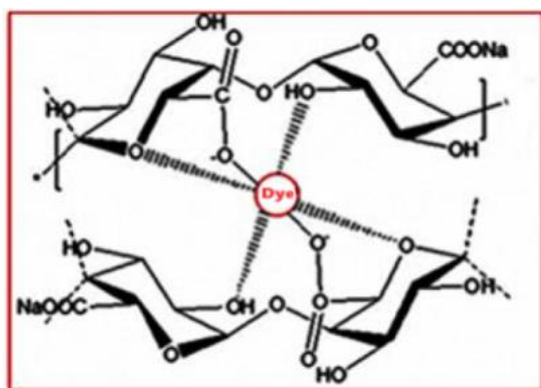
Fig.2: How to bond absorbent functional groups with amine groups of dyes

Adsorption results show that CNM can be efficiently used for removal cationic dyes from aqueous solutions. The removal capacity for them was investigated systematically. The adsorption rate was encouraging, and 80% of removal percentage was reached within 120

min, initial concentation 50 ppm and absorbent doase 3 g/L.

Conclusions

Although dye removal with paper made from virgin pulp is done with a higher percentage from paper made from recycled pulp, the absorption by recycled one is a more cost-effective method. Also, cellulose fibers are very suitable for absorbing and separating pollutants due to having a surface with the possibility of chemical modification. In this view , biological methods can also be effective for dye removing.

References

[1] Ramalingam S., SenthilKumar P., (2015). Novel adsorbent from agricultural waste (cashew NUT shell) form ethylene blue dye removal: Optimization by response surface methodology, Water Resources and Industry, 11, 64-70. http: // dx. doi. org/ 10.1016/ j.wri. 2015.07.002.

[2] Weiying Z., Mengying Y., Zhenlin Y., Dan C., Xiao L. (2019). A Novel Cu(II) Ion-Imprinted Alginate -Chitosan Complex Adsorbent for Selective Separation of Cu(II) from Aqueous Solution, Polymer Bulletin, 76, 1861-1876. https://doi.org/10.1007/s00289-018-2433-8.

[3] Yanmei Z., Min Z., Xiaoyi H., Xinhai W., Jingyang N., and Tongsen M. (2013). Adsorption of Cationic Dyes on a Cellulose-Based Multicarboxyl Adsorbent, J. Chem. Eng. Data,58,2, 413- 421. https: //doi. org/10.1021/je301140c.

[4] Han Q., Yanmei Z., Fang Y., Enze W., Yinghao M., Qi H., Lanfang P., Tongsen M., (2015). Effective removal of cationic dyes using carboxylate-functionalized cellulose nanocrystals, Chemosphere, 141, 297-303. https: //doi. org/ 10.1016/j.chemosphere.2015.07.078

[◦] Dehghani M. H., Pour shabanian M., Heidari nejad Z. (2018), Experimental data on the adsorption of Reactive Red 198 from aqueous solution using Fe3O4 nanoparticles: Optimization by response surface methodology with central composite design, Data in Brief 19 (2018) 2126- 2132. http: //dx. doi. Org /10.1016 /j. dib. 2018. 07. 008.

Magnetic hydrogels in cartilage repair

Behafarin Batmanghelich [a], Zahra Mohammadi [*b]

Corresponding Author E-mail: mohamadiz@ut.ac.ir

[a] MSc Student, Bioceramic and Implant Laboratory, Department of Life Science Engineering, Collage of Interdisciplinary Science and Technology, University of Tehran, Tehran, Iran.
[b] Faculty member, Bioceramic and Implant Laboratory, Department of Life Science Engineering, Collage of Interdisciplinary Science and Technology, University of Tehran, Tehran, Iran.

Abstract: Cartilage injuries are common in the elderly, causing tissue destruction. Treatment methods include tissue engineering scaffolds such as hydrogels, but magnetic hydrogels provide strength and mimic cartilage tissue. In this paper, polyacrylamide polymer and iron oxide nanoparticles are used to prepare this hydrogel. This hydrogel was synthesized using the grafting method and obtained good mechanical properties and stimulated the growth and repair of cartilage tissue.
Keywords: Magnetic Hydrogels, Scaffold, Cartilage repair

Introduction

Cartilage injuries, one of the most common causes of arthroscopic knee injury, affect more than 60% of patients and 50% of the elderly population over 65 years of age [1]. These disorders occur due to mechanical load and long-term wear, limiting cell proliferation and preventing regeneration. Cartilage tissue includes water, chondrocytes, collagen, and proteoglycans, of which water is the most important component [2] The schematic of cartilage structure is shown in Fig. 1. Current treatments like cartilage grafts may not mimic native tissue structure, cause inflammation, or require a second surgery. Tissue engineering offers new solutions using scaffolds, cells, and growth factors, while regeneration depends on cytokines and growth factors. Magnetic hydrogels have been introduced in biomedical applications to improve the biological activity of cells, tissues, or organs. These hydrogels improve cell function and growth and can promote the differentiation of bone mesenchymal stem cell and contribute to the construction of cartilage scaffolds [3]. [In this paper, the structure and properties of magnetic hydrogels are presented and the in vivo and *in vitro* results of the samples are discussed.
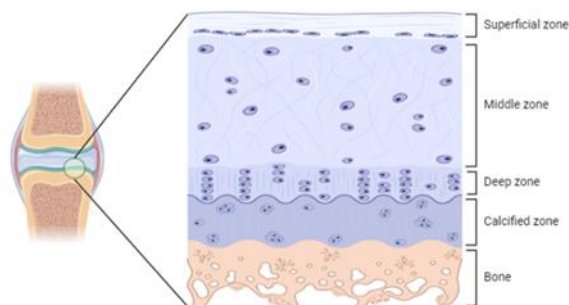
Fig.1: Schematic of Cartilage structure

Experimental Section

Various polymers such as polyacrylamide, magnetic nanoparticles such as iron oxide particles, and grafting methods have been used to prepare this hydrogel.
In this method, a covalent bond is created between the magnetic particles and the hydrogel network, and several functional groups are partially grafted on the surface of the magnetic nanoparticles, which are known as nano cross-linkers, and cause the formation of bonds between magnetic particles and hydrogel monomers.

Results and Discussion

The iron oxide nanoparticles were well dispersed in the hydrogel and as a result, isotropic magnetic properties appeared in the hydrogel. Using the FT-IR technique, the strength of covalent bonding of nanoparticles with hydrogel was measured. FT-IR spectra of Iron oxide before and after modification is shown in Fig.2 The hydrogel was also evaluated using SEM. It was found that the iron oxide particles established a strong covalent bond with the hydrogel and such a porous structure emerged in it. The SEM image of the hydrogel with 1000× magnification is shown in Fig. 3. Also, the mechanical strength of the hydrogel using this technique increased significantly compared to the hydrogel without iron oxide nanoparticles. It was also found in laboratory experiments that electromagnetic fields can direct the hydrogel to the defect site so that growth factors or mesenchymal stem cells can be placed there. Also after placing the hydrogel, growth factors and mesenchymal stem cells are released from it and then they adhere to the surface, and proliferate. Finally, a unified tissue is formed like native cartilage tissue. Both *in vivo* and *in vitro* cartilage growth is enhanced by the presence of an external electromagnetic field, which also increases the differentiation of mesenchymal stem cells.

22nd Iranian Chemistry Congress (ICC22)
Iranian Research Organization for Science and Technology (IROST)
03231-97589
13-15 May 2024

IROST
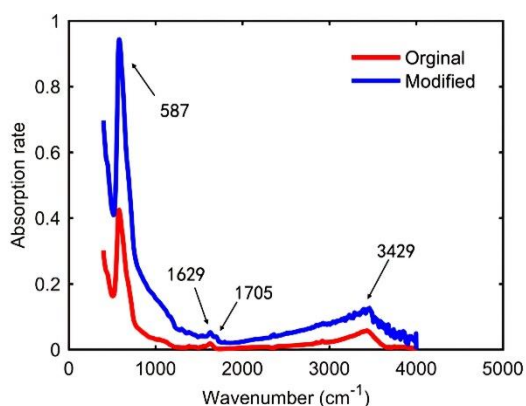
Fig.2: FT-IR spectrum of Iron oxide before and after modification

Fig.3: SEM image of hydrogel with 1000× magnification

Conclusions

Magnetic hydrogels have shown promise for the treatment of cartilage lesions by influencing stem cell fate and chondrocyte activity. Magnetic hydrogels can effectively deliver and release growth factors and provide additional benefits. Magnetic strength affects tissue development, regeneration and homeostasis. This research shows that the use of electromagnetic fields can help advance the field of regenerative medicine to regenerate cartilage tissue. Magnetic nanoparticles can control the microstructure by applying noncontact magnetic forces or mechanical stresses at the microscopic level, potentially leading to cell growth and differentiation. Although these results were promising, further research in this area is under consideration.

References

[1] Bączkowicz D, Majorczyk E, Kręcisz K. Age-Related impairment of quality of joint motion in vibroarthrographic signal analysis. BioMed Research International. 2015;2015:1-7. doi:10.1155/2015/591707

[2] Asadi N, Alizadeh E, Salehi R, Khalandi B, Davaran S, Akbarzadeh A. Nanocomposite hydrogels for cartilage tissue engineering: a review. Artificial Cells, Nanomedicine, and Biotechnology. 2017;46(3):465-471. doi:10.1080/21691401.2017.1345924

[3] Ross C, Ang DC, Almeida-Porada G. Targeting mesenchymal stromal Cells/Pericytes (MSCs) with pulsed electromagnetic field (PEMF) has the potential to treat rheumatoid arthritis. Frontiers in Immunology. 2019;10. doi:10.3389/fimmu.2019.00266

22nd Iranian Chemistry Congress (ICC22)
Iranian Research Organization for Science and Technology (IROST)
13-15 May 2024

03231-97589

IROST

Impact of Mechanical Stress on the Swelling Capacity of Polyacrylamide/AMPS Hydrogel during Folding Cycles

Zahra Mohammadi [a], Fatemeh Hosseini Beydokhti [b], Zahra Mohammadi [*c]

Corresponding Author E-mail: mohamadiz@ut.ac.ir

[a] MSc Student, Bioceramic and Implant Laboratory, Department of Life Science Engineering, Collage of Interdisciplinary Science and Technology, University of Tehran, Tehran, Iran.
[b] Department of Material Science and Engineering, Sharif University of Technology, P. O. Box 11365-11155, Tehran, Iran.
[c] Faculty member, Bioceramic and Implant Laboratory, Department of Life Science Engineering, Collage of Interdisciplinary Science and Technology, University of Tehran, Tehran, Iran.

Abstract: Bio-inspired perspiration cooling fabric could be a promising combination to address the need for water retention and cooling. One of the key components of this cooling system is a layer of superabsorbent hydrogel that automatically releases the stored moisture under the temperature difference with the environment.

Keywords: Acrylamide, Cotton fabric, swelling

Introduction

With their hydrophilic nature and cross-linked structure, hydrogels absorb water while maintaining their original consistency, while suffering irreversible mechanical damage due to the absence of an efficient mechanism. Several studies have focused on the development of physically and chemically cross-linked hydrogels with enhanced mechanical properties. Chemically crosslinked hydrogels possess favorable mechanical properties and water stability due to their strong covalent bonds, stronger than non-covalent bonds. However, most of the chemical hydrogels prevent water penetration and swelling in the structure, creating challenges for designing an optimal hydrogel.

2-Acrylamido-2-methyl-1-propane sulfonic acid (AMPS) is a strong electrolyte monomer widely used in the preparation of superabsorbent polymers. These polymers have a high swelling capacity that is not affected by pH changes. Meanwhile, Poly-(AMPS) (PAMPS) hydrogels as attractive materials find applications in biomedical engineering, food industry, agriculture, and water treatment. Figure 1 shows the schematic of AMPS and AMM polymerization. However, PAMPS hydrogels are typically formed through non-covalent cross-links, resulting in weak mechanical properties. Recent research investigates physically cross-linked PAMPS hydrogels formed via self-initiated thermal free-radical polymerization. Although these gels are highly stretchable, their mechanical properties are limited and they easily dissolve in aqueous media due to weak hydrogen bonding interactions between PAMPS chains. In this article, the behavior of swelling capacity of hydrogel after bearing mechanical stress during folding cycles is investigated.
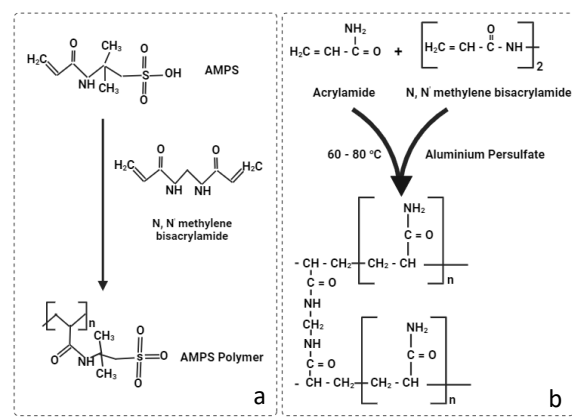
Fig.1: a) Schematic of AMPS Polymerization and b) AMM Polymerization

Experimental Section

Materials: 2-Acrylamido-2-methylpropane sulfonic acid (AMPS, 282731, Sigma Aldrich), Acrylamide (Sigma Aldrich), Ammonium persulfate (APS, A3678, Sigma Aldrich), and N,N'-Methylenebisacrylamide (MBA, 146072, SigmaAldrich) and plain linen as the fabric part for wearing were used.

Hydrogel synthesis: The synthesis of this hydrogel consists of two steps. First, a monomer solution is created by mixing 0.8 g of AMPS and 2 g of Acrylamide with 20 g of deionized water. Second, a binding (crosslinker) and priming(initiator) solution was prepared by mixing 600 μL of 0.4 wt% solution of MBA and 100 μL of 5 wt% solution of APS in deionized water. The monomer and crosslinker solutions are then combined. The resulting mixture is gassed and heated to 70 degrees Celsius until it gels. Fabrics are immersed in the solution, and the sample is dried in an oven at 50 degrees for 15 minutes.

22nd Iranian Chemistry Congress (ICC22)
Iranian Research Organization for Science and Technology (IROST)
13-15 May 2024

03231-97589

IROST

Results and Discussion

The covalently cross-linked network structure of PAMPS hydrogels leads to brittle behavior even under low strains. The incorporation of AM segments into the physical network of PAMPS increases the molecular weight of the primary chains, which leads to an increase in the mechanical strength of the hydrogels. Cross-linked PAMs, especially when partially hydrolyzed to produce acrylic acid segments, are superabsorbent gels.
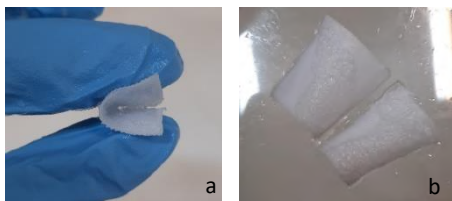
Fig.2: a)Fabric with swollen hydrogel under mechanical folding stresses b) unfold fabric with hydrogel

PAMPS/DMAA hydrogels exhibit high modulus (up to 0.41 MPa), ultimate tensile strength (up to 0.57 MPa), and elongation (~1000%) along with excellent swelling capacity (up to 1700 g/g) [1]. Considering the structure of the gel and the higher amount of acrylamide, it can be predicted that the mechanical test of the gel without fabric will bring better mechanical results. Also, the hydrogel in a completely dry state has suitable flexibility and does not crumble, fall, or separate from the fabric. Mechanical testing, considering the use of textiles, was carried out in two cases after bearing tensile stresses during folding and before (Figure 2), without the fabric substrate, the sample loses its application even if the gel is still stable. The fabric structure returned to its previous state after enduring each stretch step. Finally, after enduring 400 cycles, in the folded state, 50% of the hydrogel volume in the fabric was deformed. Due to the structure of the thread and fabric sheath, the hydrogel had coarse pores in micro dimensions, which may cause faster drying than the capacities reported in other articles due to the increase in the contact surface with the environment.

After complete drying, the samples were weighted for swelling test and then placed in tap water at room temperature to be weighed at desired time intervals. The swelling percentage was calculated in each time period until the swelling rate reached a constant value. By increasing the heat received during polymerization, the polymer chains form longer and more cross-links and gain more elasticity. The results reported a swelling rate of up to 200%. The reason for this difference with similar researches was the use of this gel on fabric and the effect of thread and sheath on the heterogeneity of the gel structure.
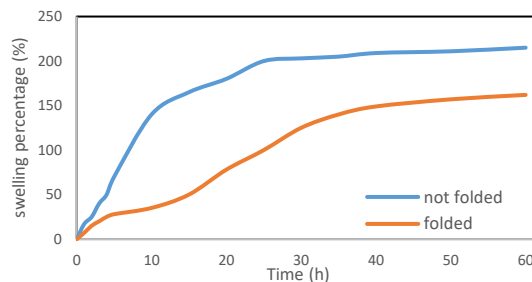
Fig.3: Graph of percentage swelling of AAm/AMPS hydrogel before and after tensial stresses

Despite the deformation after folding, the fabric sample still showed a suitable amount of swelling and water retention (Figure 3). Due to degradation and physical damage to the chains and uniformity of the structure, the water holding capacity decreased by approximately 23%. It was also observed that the hydrogel reaches a constant swelling rate over a longer period of time.

A previous study [2] performed simultaneous measurements of global and local elastic properties in PAM hydrogels. Four compositions of PAM hydrogels were evaluated, the stiffer gels showed negligible changes in elastic modulus over time during swelling tests, while the softer gels exhibited a decrease in elastic modulus during one-day swelling. This indicates that swelling significantly affects the elastic properties of PAM, especially for gels with low monomer concentration and cross-linking. In our study despite a much lower amount of crosslinking than even the softest hydrogel in aforementioned study, not only did our hydrogel maintain its structure and integrity but it also showed great swelling after applying cyclic tensile stress.

Conclusions

Hydrogels with high water content and reversible water affinity can provide a promising platform for bio-mimetic temperature reduction. As a model, a covalently networked acrylamide/AMPS hydrogel was chosen as a basis for creating a low-cost and easy-to-make hydrogel. These samples have a high water storage capacity despite cyclic mechanical stresses.

References

[1] Su, E., Yurtsever, M., & Okay, O. (2019). A Self-Healing and Highly Stretchable Polyelectrolyte Hydrogel via Cooperative Hydrogen Bonding as a Superabsorbent Polymer. Macromolecules, 52(9), 3257-3267. Doi: 10.1021/acs.macromol.9b00032

[2] Subramani, R., Izquierdo-Alvarez, A., Bhattacharya, P., Meerts, M., Moldenaers, P., Ramon, H., & Van Oosterwyck, H. (2020). The Influence of Swelling on Elastic Properties of Polyacrylamide Hydrogels. Frontiers in Materials, 7:212. Doi: 10.3389/fmats.2020.00212

22nd Iranian Chemistry Congress (ICC22)
Iranian Research Organization for Science and Technology (IROST)
13-15 May 2024

03231-97589

IROST

Synthesis and Characterization of Keratin Electrospun Nanofibers Containing Organic Metal Framework for Skin Restoration

Shaghayegh Kohzadi [a], Zahra Mohammadi [*b]

Corresponding Author E-mail: mohamadiz@ut.ac.ir

[a] PhD Candidate, Bioceramic and Implant Laboratory, Department of Life Science Engineering, Collage of Interdisciplinary Science and Technology, University of Tehran, Tehran, Iran.
[b] Faculty member, Bioceramic and Implant Laboratory, Department of Life Science Engineering, Collage of Interdisciplinary Science and Technology, University of Tehran, Tehran, Iran.

Abstract: This study explores the potential of electrospun keratin nanofibers containing metal-organic frameworks (MOFs), which have shown promising properties for skin restoration. Keratin offers a biocompatible scaffold, while MOFs enhance cell interaction. In this article, the synthesis and properties of keratin nanofibers incorporating Cu-BTC MOF have been investigated.

Keywords: Keratin, Metal-Organic Framework, Nanofiber

Introduction

The skin is the largest organ in the human body and its proper functioning is essential for overall health. Skin injuries, such as burns, ulcers, and chronic wounds, can significantly impact quality of life and require extensive medical treatment. As a result, there is a growing need for innovative therapies that can promote skin restoration and tissue regeneration. One promising approach is the use of nanofibers, which have shown great potential in skin tissue engineering applications. Nanofibers are extremely small in diameter, ranging from 100 to 1000 nm, and can be tailored to mimic the structure and function of native skin tissue [1]. Additionally, the addition of bioactive molecules, such as growth factors and enzymes, can enhance the biocompatibility of nanofibers and promote cell adhesion and proliferation. Electrospinning is a versatile technique that has been widely used to produce nanofibers from various biomaterials, including keratin. However, the incorporation of metals and metal-organic frameworks (MOFs) into electrospun nanofibers has shown great potential to increase their bioactivity and biocompatibility. Cu-BTC MOF is a novel MOF that has been shown to exhibit excellent biocompatibility and bioactivity, making it an ideal candidate for skin tissue engineering applications [2]. In this study, we investigate the use of electrospinning, a versatile and widely used technique for producing nanofibers, to fabricate keratin nanofibers containing Cu-BTC MOF (copper-based metal-organic framework) for skin restoration.

Experimental Section

Material: Keratin ($C_4H_9N_3O_2 \cdot H_2O$, Merck), Hydrochloric Acid (HCL, Sigma Aldrich), Copper Nitrate (Cu $(NO_3)_2$, Sigma Aldrich), 1,3,5-Benzenetricarboxylic Acid (BTC, $C_9H_6O_6$, Merck), Ethylene Dichloride ($C_2H_4Cl_2$, Sigma Aldrich).

Preparation of Keratin Solution: Keratin was dissolved in 0.1 M HCl solution with a concentration of 10 mg/mL. The solution was then filtered through a 0.2 μm filter to remove any impurities.

Preparation of Cu-BTC MOF: Cu-BTC MOF was synthesized according to a previously reported method. Briefly, copper nitrate and 1,3,5-benzenetricarboxylic acid (BTC) were dissolved in ethylene dichloride to form a metal complex solution. The solution was then added to a mixture of trifluoroacetic acid and water, and the resulting solution was stirred slowly for 24 hours at room temperature. The resulting precipitate was collected by centrifugation and washed with ethanol to obtain the Cu-BTC MOF.

Electrospinning: Keratin solution and Cu-BTC MOF were mixed at a ratio of 10:1 (w/w) and then applied to a rotating collector via a syringe. The collector was placed in a glove box under vacuum, and a voltage of 15 kV was applied for 30 minutes to produce nanofibers. Then the obtained nanofibers were washed with ethanol and water to remove any impurities.

Characterization: The structure and composition of the nanofibers were characterized using SEM (Scanning Electron Microscopy), TEM (Transmission Electron Microscopy), XRD (X-ray Diffraction), and FTIR (Fourier Transform Infrared Spectroscopy).

Results and Discussion

SEM analysis revealed that the nanofibers had a uniform morphology with diameters of 50-100 nm, indicating that the electrospinning process was successful in producing uniform nanofibers (fig 1(a)). The presence of CU-BTC MOF in the nanofibers was confirmed through TEM

22nd Iranian Chemistry Congress (ICC22)
Iranian Research Organization for Science and Technology (IROST)
13-15 May 2024

03231-97589

analysis (fig 1(b)), which showed that the CU-BTC MOF was evenly distributed throughout the nanofibers.
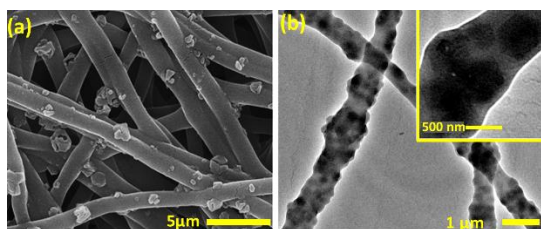
Fig 1: SEM and TEM images of keratin nanofibers containing MOF (a,b)

XRD analysis showed that the nanofibers had a high degree of crystallinity, indicating that the keratin was well-ordered and had a high degree of crystallinity. Two strong peaks at 2θ=10° and at 27° were assigned to α-helix and β-sheet, respectively (fig 3). This crystallinity was found to increase with the addition of Cu-BTC MOF, which promoted the formation of more regular and stable nanofibers.
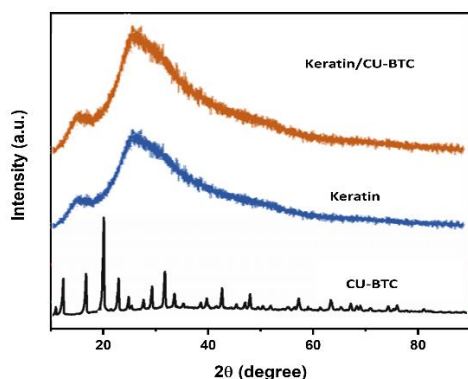
Fig 2: XRD patterns of CU-BTC MOF, Keratin nanofibers, and keratin/CU-BTC nanofibers

The FTIR spectrum of the keratin nanofibers showed characteristic peaks at 1650 cm^{-1} (amide I), 1700 cm^{-1} (amide II), 2950 cm^{-1} (C=O stretching), and 3400 cm^{-1} (C-O-C stretching) [3]. The absence of other significant peaks indicates that the keratin is well-ordered and has no significant impurities. The FTIR spectrum of keratin nanofibers containing CU-BTC MOF showed similar peaks as pure keratin nanofibers, indicating that CU-BTC MOF was evenly distributed throughout the nanofibers. In addition, some new peaks appeared at 1300 cm^{-1} (C=O stretching of CU-BTC MOF), 1100 cm^{-1} (C-O-C stretching of CU-BTC MOF), and 800 cm^{-1} (aromatic ring stretching of CU-BTC MOF) [4]. These peaks indicated the successful incorporation of CU-BTC MOF into keratin nanofibers (fig 3). FTIR analysis showed that the content of CU-BTC MOF in the nanofibers was about 10%. This was consistent with the weight ratio of keratin to CU-BTC MOF used in the electrospinning process.
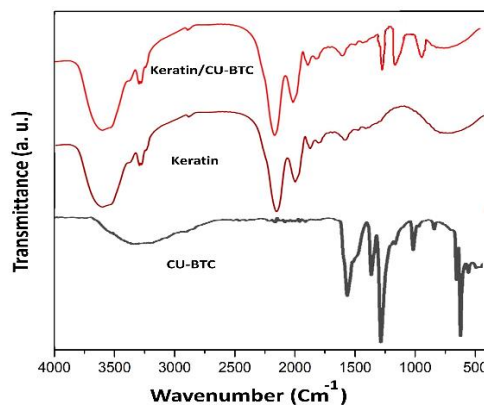
Fig 3: FTIR spectra of CU-BTC MOF, Keratin nanofibers and keratin/CU-BTC nanofibers

Conclusions

In conclusion, the present study demonstrated the successful incorporation of CU-BTC MOF into keratin nanofibers via electrospinning. The obtained nanofibers showed improved conductivity compared to pure keratin nanofibers, indicating that the CU-BTC MOF particles were evenly dispersed throughout the nanofiber matrix. FTIR analysis revealed that the CU-BTC MOF was successfully incorporated into the nanofibers without significant changes in keratin structure. The successful incorporation of CU-BTC MOF into keratin nanofibers via electrospinning is a promising approach to create suitable biomaterials for skin restoration applications.

References

[1] Eslahi, N., Soleimani, F., Lotfi, R., Mohandes, F., Simchi, A., & Razavi, M. (2024). How biomimetic nanofibers advance the realm of cutaneous wound management: The state-of-the-art and future prospects. *Progress in Materials Science*, 101293.

[2] Bigham, A., Islami, N., Khosravi, A., Zarepour, A., Iravani, S., & Zarrabi, A. (2024). MOFs and MOF-Based Composites as Next-Generation Materials for Wound Healing and Dressings. *Small*, 2311903.

[3] Yang, J., Lei, T., Yang, X., Fan, J., Wu, H., He, S., ... & Liu, Y. (2023). Investigation of Keratin/Poly (ethylene oxide) Nanofiber Membrane Prepared with Different Post-crosslinking Method. *Fibers and Polymers*, 24(2), 715-727.

[4] Liu, L., Zhang, H., Peng, L., Wang, D., Zhang, Y., Yan, B., Liu, X. (2023). A copper-metal organic framework enhances the photothermal and chemodynamic properties of polydopamine for melanoma therapy. *Acta Biomaterialia*, 158, 660-672.

22nd Iranian Chemistry Congress (ICC22)
Iranian Research Organization for Science and Technology (IROST)
13-15 May 2024

03231-97589

IROST

Onion Extract: A Green and Eco-friendly Catalyst for MW-Assisted Solvent-less Synthesis of Pyrroles via Paal–Knorr Reaction

Omid Marvi

Corresponding Author E-mail: omid_marvi@pnu.ac.ir

Department of Chemistry, Payame Noor University, PO Box 19395-3697, Tehran, Iran.

Abstract: In this study, we have developed an environmental friendly and highly efficient method for onion extract catalyzed microwave- induced solvent- free synthesis of pyrroles via Paal–Knorr reaction. This method is applicable to a wide range of aromatic/aliphatic/heterocyclic primary amines with 2,5- hexanedione, and affords the various pyrrole derivatives in good to excellent yields (up to 98%) in an eco-friendly solvent-less procedure under microwave irradiation at reaction temperature 80° C. The use of onion extract makes the process environmentally benign.

Keywords: Pyrroles; Onion extract; Eco-friendly; Paal–Knorr; Microwave

Introduction

Pyrrole moieties are one of the most important classes of heterocyclic compounds, being present in a large number of naturally occurring, biological, and drug molecules [1-4]. The growing importance of these heterocycles as intermediates in pharmaceutical and chemical processes has led to considerable effort to develop a variety of methodologies for their synthesis. Among the various methods developed for straightforward synthesis of pyrrole ring, Paal–Knorr cyclization and the Clauson-Kaas reaction have received considerable attention dueto their use of readily available starting materials [6, 7].

Among catalysts reported for the Paal–Knorr reaction, Lewis acid catalysts are the most widely adopted, e.g., $Bi(NO_3)_3$-$5H_2O$, $Sc(OTf)_3$, $SnCl_2$_$2H_2O$, $RuCl_3$, $CoCl_2$, $InCl_3$, $InBr_3$ or $In(OTf)_3$, $ZrCl_4$, $Ga(OTf)_3$, $AlCl_3$/PS, $ZrOCl_2$-$8H_2O$, $UO_2(NO_3)_2$-$6H_2O$, CuI/C, $SbCl_3$/SiO_2, $BiCl_3$/SiO_2, $GaCl_3$/PS, $Al(DS)_3$, MgI_2-$(OEt_2)_n$, $FePO_4$, and MgI_2 [8]. However, the classical Paal–Knorr reaction, in which a 1,4 diketone is condensed with an amine, continues to be the most attractive method for the synthesis of pyrroles [9-11]. Despite its popularity, the Paal–Knorr reaction suffers from limitations such as drastic reaction conditions, high cost, poor yields, tedious workup and longer reaction time. Therefore, the development of milder and nonhazardous methods for pyrrole synthesis continues to be a very important area of investigation. Moreover, in the case of some of the metal based Lewis acid catalyzed reactions, toxic to the environment. Hence, these methods environmentally unsound, especially with regard to a potential large-scale synthesis. Though the different methods are available for the synthesis of pyrroles, we report herein a simple, efficient green protocol for the synthesis of pyrrole derivatives under mild conditions.

Experimental Section

In a typical reaction, hexane-2,5-dione (1.0 mmol) and onion extract (0.5 mL) were mixed thoroughly for 1 min. Then aniline (1.1 mmol) was added and the mixture was irradiated in a reaction vessel of a Synthwave 402 Prolabo focused microwave reactor (manufactured by M/S Prolabo, 54 rue Roger Salengro, Cedex, France) for 1 min after setting reaction temperature at 80°C and power at 40% (maximum output 300 W). During the reaction the temperature was not allowed to rise above 80°C (by setting the programmer). After completing the reaction (monitored by TLC, n-hexane/ ethyl acetate, 1/3), water (10 mL) was added to the reaction mixture in order to remove the catalyst. The obtained solution was extracted by ethyl acetate (1×15 mL), and the organic layer was separated and dried over Na_2SO_4.The separated organic phase was evaporated under reduced pressure to give the corresponding solid pyrrole 4a, that was washed thoroughly with water, dried, and then recrystallized from methanol. The oily products were purified by column chromatography using hexane and ethyl acetate as the eluent.

Results and Discussion

The reaction was proceeded smoothly in the presence of onion extract (0.5 mL) to afford pyrroles in good to excellent (**Fig 1**, **Table 1**). Results summarized in the Table 1 indicate the scope and generality of the reaction with respect to the various pimary amines. In most cases, the reaction proceeded expeditiously, although the yield was highly dependent on the substrate used. The nature of the substituents on the aromatic ring of pimary amines has different influences.

22nd Iranian Chemistry Congress (ICC22)
Iranian Research Organization for Science and Technology (IROST)
13-15 May 2024

03231-97589

IROST
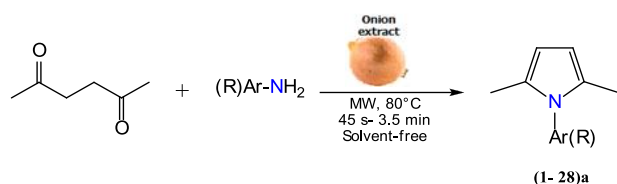
Fig.1: Onion extract catalyzed solvent- free Paal–Knorr synthesis of pyrroles under MWI

Table1: The yields and reaction times for onion extract-mediated MW-assisted synthesis of pyrroles

1a, 1 min, 96 % **2a**, 1 min, 95% **3a**, 2 min, 93% **4a**, 1.5 min, 93 % **5a**, 1.5 min, 92%

6a, 2 min, 90% **7a**, 2.5 min, 90 % **8a**, 45 s, 98% **9a**, 3 min, 89% **10a**, 2 min, 90 %

11a, 1.5 min, 89% **12a**, 1.5 min, 94% **13a**, 3.5 min, 90% **14a**, 3.5 min, 91% **15a**, 3.5 min, 90%

16a, 2.5 min, 92% **17a**, 2.5 min, 94% **18a**, 3 min, 92% **19a**, 3 min, 93% **20a**, 2 min, 95%

21a, 2 min, 92 % **22a**, 1.5 min, 91 % **23a**, 1.5 min, 92% **24a**, 1.5 min, 94% **25a**, 1 min, 97%

26a, 1 min, 96% **27a**, 1 min, 95% **28a**, 1 min. 98%

References

[1] Este´vez, V.; Villacampa, M.; Mene´ndez, J.C. *Chem. Soc. Rev.* **2010**, *39*, 4402. https://doi.org/10.1039/b917644f

[2] Zheng, Y.; Wang, Y.; Zhou, Z. *Chem. Commun.* **2015**, *51*, 16652. https://doi.org/10.1039/C5CC05624A

[3] Dasari, R.; La Clair, J.J.; Kornienko, A. *Chem Bio Chem* **2017**, *18*, 1792. https://doi.org/10.1002/cbic.201700210

[4] Zhang, L.; Zhang, J.; Ma, J.; Cheng, D.-J. Tan, B. *J. Am. Chem. Soc.* **2017**, *139*, 1714. https://doi.org/10.1021/jacs.6b09634

[5] Fleige, M.; Glorius, F. *Chem. Eur. J.* **2017**, *23*, 10773. https://doi.org/10.1002/chem.201703008

[6] Joshi, S.D.; More, U.A.; Kulkarni, V.H.; Aminabhavi, T.M. *Curr. Org. Chem.* **2013**, *17*, 2279. https://doi.org/10.2147/RRMC.S80395

[7] Wang, P.; Ma, F.-P.; Zhang, Z.-H. *J. Mol. Liq.* **2014,** *198*, 259. https://doi.org/10.6023/cjoc202206002

[8] Aghapoor, K.; Mohsenzadeh, F.; Darabi, H. R.; Rastgar S. *Res. Chem. Intermed.* **2018**, *44*, 4063. https://link.springer.com/article/10.1007/s11164-018-3355-7

[9] Wang, B.; Gu, Y.; Luo, C.; Yang, T.; Yang, L.; Suo, J. *Tetrahedron Lett.* **2004**, *45*, 3417. https://doi.org/10.1016/j.tetlet.2004.03.012

[10] Banik, B.K.; Banik, I.; Renteriaa, M.; Dasgupta, S.K. *Tetrahedron Lett.* **2005**, *46*, 2643. https://doi.org/10.1016/j.tetlet.2005.02.103

[11] Chen, J.; Wu, H.; Zheng, Z.; Jin, C.; Zhang, X.; Su, W. *Tetrahedron Lett.* **2006**, *47*, 5383. https://doi.org/10.1016/j.tetlet.2006.05.085

Conclusions

In conclusion, onion extract was found to be a highly efficient and convenient catalyst for the preparation of pyrroles in good to excellent yields. This method provides several advantages including mild reaction conditions, clean reaction profiles, small quantity of the catalyst, operational and experimental simplicity. This green protocol makes this process environmental friendly and applicable for the large scale synthesis of pyrrole derivatives.

22nd Iranian Chemistry Congress (ICC22)
Iranian Research Organization for Science and Technology (IROST)
13-15 May 2024

03231-97589

Onion Extract (*Allium Cepa L.*): A Green and Eco-friendly Catalyst for the MW-Assisted Solvent-Free Synthesis of 5-Substituted 1*H*-Tetrazoles

Omid Marvi

Corresponding Author E-mail: omid_marvi@pnu.ac.ir

Department of Chemistry, Payame Noor University, PO Box 19395-3697, Tehran, Iran.

Abstract: 5-Substituted-1*H*-tetrazoles can be synthesized from the corresponding nitriles by reaction with NaN_3 using the efficient and green onion extract catalyst under microwave irradiation and solvent- free conditions in good to excellent yields (up to 98%) and very short reaction times. This method is applicable to a wide range of aryl and alkyl nitriles with sodium azide in solvent-free media, and affords the various tetrazole derivatives in an eco-friendly solvent-less procedure under microwave irradiation at reaction temperature 120 °C. The use of onion extract makes the process environmentally benign.

Keywords: Microwave; Onion extract; Tetrazole; Eco-friendly

Introduction

Tetrazoles which represent an important class of heterocycles are an increasingly popular functionality with wide ranging applications. For tetrazole ring construction the synthetic equivalents of sodium azide or organic azides and cyanides, isocyanides, isocyanates or isothiocyanates are used most frequently. They can be brought into the reaction as individual compounds or generated directly in a reaction medium [1].

Other methods of the tetrazole ring synthesis are based on the reaction of amines with triethyl orthoformate and sodium azide [2], the [3+2] cycloaddition of isocyanides with TMSN3 under the influence of various catalysts and the reaction of primary amines with orthocarboxylic acid ester/ sodium azide reported in several more recent reports are more practical [3]. The use of $In(OTf)_3$ and $Yb(OTf)_3$ as catalysts for this three component transformation has been reported utilizing alcoholic solvents or neat at high temperatures (100 °C) [4]. Catalysis by 1-n-butylimidazolium tetrafluoroborate with $NaN_3/CH(OEt)_3$ has also been shown, but it requires high temperatures [5]. Some of these methods have one or more of the following drawbacks: expensive and toxic metal catalysts, harsh reaction conditions, refluxing for a prolonged period of time and tedious work-ups. Therefore, the development of milder and nonhazardous methods for tetrazole ring synthesis continues to be a very important area of investigation.

Allium cepa L. is one of the most widely cultivated and used plants, and its bulb (onion) is used as both food and medicine. Onions (*A. cepa* L.) possess strong, characteristic aromas and flavors, which have made them important ingredients of various food items. Onions and onion flavors (essential oil) are important seasonings widely used in food processing. It has been shown that onion possesses various biological properties, including antibiotic, antidiabetic, antioxidant, antiatherogenic, and anticancer effects [6].

Experimental Section

In a typical experiment (synthesis of 2a), 4-nitrobenzonitrile (0.39 g, 2 mmol) and onion extract (0.5 mL) were mixed thoroughly for 1 min. Then sodium azide (0.2 g, 3 mmol) was added and the mixture was irradiated in a reaction vessel of a Synthwave 402 Prolabo focused microwave reactor (manufactured by M/S Prolabo, 54 rue Roger Salengro, Cedex, France) for 1 min after setting reaction temperature at 120°C and power at 50% (maximum output 300 W). During the reaction the temperature was not allowed to rise above 120°C (by setting the programmer). After completion of the reaction (as indicated by TLC), ethyl acetate (40 mL) and 6 N HCl (20 mL) was added to the reaction mixture and stirred vigorously. The resultant organic layer was separated and the aqueous layer was extracted with ethyl acetate (30 mL). The combined organic layer was washed with water (10 mL) and concentrated to give a crude product. Column chromatography using silica gel gave pure product 5-(4-nitrophenyl)-1*H*-tetrazole (**2a**).

Results and Discussion

Results summarized in the TABLE 1 indicate the scope and generality of the reaction with respect to the various nitriles. In most cases, the reaction proceeded expeditiously, although the yield was dependent on the substrate used. The nature of the substituents on the aromatic ring of benzonitriles has different influences. The presence of the electron-withdrawing substituents (such as nitro, bromo, chloro and cyano) give high yields of products compared to benzonitrile (compounds **1-4a**). It was also found that benzonitrile derivatives bearing electron-donoring groups such as methyl and ethyl, for

weak electron-withdrawing nature and steric hindrance led to poor yield (compounds (**6, 7, 10, 14**, **15)a**).
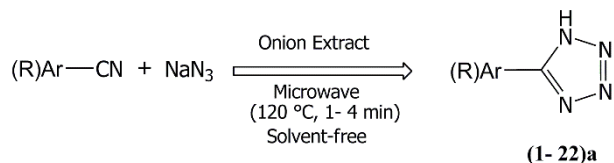
Fig.1: Onion extract catalyzed solvent- free synthesis of tetrazoles under MWI

Table1: The yields and reaction times for onion extract-mediated MW-assisted synthesis of tetrazoles

1a, 95%, 1min **2a**, 94%, 1 min **3a**, 91 %, 1.5 min **4a**, 92%, 1 min

5a, 88%, 2min **6a**, 84%, 2.5 min **7a**, 82 %, 3 min **8a**, 93%, 2 min

9a, 85%, 3min **10a**, 81%, 4 min **11a**, 84 %, 3 min **12a**, 85%, 2.5 min

13a, 93%, 1min **14a**, 83%, 4 min **15a**, 85 %, 4 min **16a**, 88%, 2 min

17a, 97%, 1min **18a**, 92%, 2.5 min **19a**, 91 %, 2.5 min **20a**, 92%, 1 min

21a, 84 %, 3 min **22a**, 89%, 2.5 min

Conclusions

In conclusion, onion extract was found to be a highly efficient and convenient catalyst for the preparation of pyrroles in good to excellent yields. This method provides several advantages including mild reaction conditions, clean reaction profiles, small quantity of the catalyst, operational and experimental simplicity. This green protocol makes this process environmental friendly and applicable for the large scale synthesis of pyrrole derivatives.

References

[1] Sharghi, H., Ebrahimpourmoghaddam, S., Doroodmand, and M. M. *J. Organomet. Chem.* 2013, vol. 738(6), p. 41. https://doi.org/10.1016/j.jorganchem.2013.04.013

[2] Boland, Y., Hertsens, P., Marchand-Brynaert, J., and Garcia, Y. *Synthesis* 2006, vol. 9, p. 1504. https://doi.org/10.1055/s-2006-926439

[3] Jin, T., Kamijo, S., and Yamamoto, Y., *Tetrahedron Lett.* 2004, vol. 45, p. 9435. https://doi.org/10.1016/j.tetlet.2004.10.103

[4] Su, W.-K., Hong, Z., Shan, W.-G., and Zhang, X.-X., *Eur. J. Org. Chem.* 2006, p. 2723. https://doi.org/10.1002/ejoc.200600007

[5] Potewar, T.M., Siddiqui, S.A., Lahoti, R.J., and Srinivasan, K.V., *Tetrahedron Lett.* 2007, vol. 48, p. 1721. http://dx.doi.org/10.4236/ijoc.2015.52009

[6] Khalilzadeh, M. A., and Borzoo, M., *J. Food Drug Anal.* 2016, vol. 24, p. 796. https://doi.org/10.1016/j.jfda.2016.05.004

22ⁿᵈ Iranian Chemistry Congress (ICC22)
Iranian Research Organization for Science and Technology (IROST)
13-15 May 2024

03231-97589

IROST

22nd Iranian Chemistry Congress (ICC22)
Iranian Research Organization for Science and Technology (IROST)
13-15 May 2024

03231-97589

IROST

Rapid and Sensitive Detection of Malachite Green Residues in Fish Tissues Using Hand-Held Ion Mobility Spectrometry

Amir Hossein Alinoori, Saeed Hajialigol, Seyed Alireza Ghorashi, Farkhondeh Saliminezhad, Hamed Sheikhbahaee

Corresponding Author E-mail: ahalinoori@yahoo.co.uk

Institute of Materials and Energy, Isfahan, Iran.

Abstract: Malachite green (MG) is widely used in aquaculture and industries, but its toxicity raises concerns. This study investigates the potential of Hand-held ion mobility spectrometry for rapid and sensitive detection of MG in fish tissues, with a limit of detection of 1 ng and as a rapid and easy to use methods.

Keywords: Hand-held ion mobility spectrometry; Malachite green; identification and quantification

Introduction

Malachite green (MG) is a widely used ectoparasiticide, fungicide, and antiseptic in fish farming, despite its potential carcinogenic, mutagenic, and teratogenic effects [1,2]. When absorbed by fish, MG is rapidly reduced to its non-chromophorous metabolite, leuco-malachite green (LMG), which is the prevalent residue found in treated aquatic animals [3].

The use of MG in edible fish species, such as trout and eel, has been recognized as a public health threat since 1933 [2]. Due to its adverse effects, the use of MG is banned in the European Union, and its administration is only permitted in specific national fish hatcheries in the USA [2].

Several analytical methods have been developed for the determination of MG and LMG residues in aquatic animal tissues, including HPLC with post-column oxidation and absorbance or mass spectrometry detection, as well as GC-MS and LC-APCI-MS [4]. These methods have been applied to various fish species, such as trout, catfish, and hake [5]. The ability of IMS to rapidly and selectively detect a wide range of compounds has made it an indispensable tool in modern analytical chemistry [6-7].

The need for a robust and reliable analytical method for the control of MG residues in (cultured) aquatic animals has become increasingly important due to the ban on its use and its potential adverse effects in humans [2].

Experimental Section

The Hand-held-IMS was designed and constructed at the Institute of Materials and Energy, Isfahan, Iran. The device includes a novel sample inlet, an ionization chamber, a shutter-grid, a separation chamber, an ion collector, and voltage generators. The ionization cell volume was reduced, and the device is equipped with a radioactive 63Ni ionization source.

The sample inlet allows a continuous stream of the gas carrying the analytes to pass through the ionization chamber, where the ions formed are effectively focused before entering the separation chamber. Fish fillets were cut, frozen, and homogenized with dry ice. Fortified samples were prepared by spiking thawed tissue with known concentrations of MG.

The extraction process involved adding ammonium acetate buffer, HAH solution, and p-TSA solution to the tissue, followed by the addition of acetonitrile and alumina. The mixture was then centrifuged, and the supernatant was analyzed using the Hand-held-IMS device.

Results and Discussion

After optimization of the hand-held IMS parameters, the instrument's response was utilized to evaluate its sensitivity and capability for the identification and quantification of MG in fish tissue samples, as shown in Fig. 1. Upon the addition of successive aliquots of malachite green, ranging for 2 ngr, 5 ngr and 10 ngr, the area of ion mobility peak of MG exhibited a linear increase corresponding to the increasing concentration of MG in the fish tissue samples. This demonstrates the excellent sensitivity and linearity of the IMS technique for the reliable detection and quantification of MG residues in aquatic animal matrices, which is crucial for the effective control and monitoring of this banned substance in the aquaculture industry.

As shown in Fig. 2, the calibration of the IMS response area to MG concentration illustrated that the ion mobility signal was proportional to the concentration of malachite green.

22nd Iranian Chemistry Congress (ICC22)
Iranian Research Organization for Science and Technology (IROST)
13-15 May 2024

03231-97589

IROST
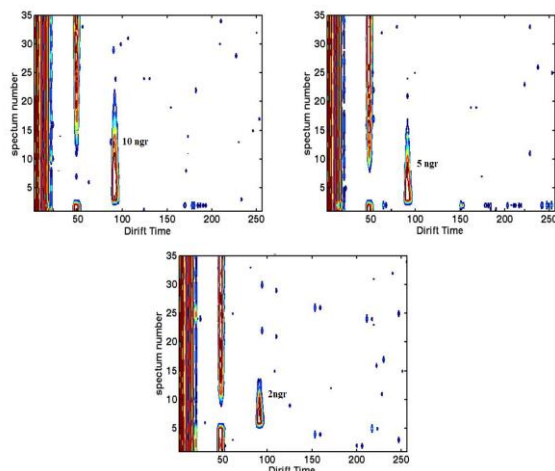
Fig.1: Linear calibration plot of peak current value vs. the concentration of malachite green

The ion mobility signal versus the concentration of malachite green was linear in the range from 1 to 10 ngr (R = 0.979). The detection limit could be calculated to be 0.25 ngr according to the formula 3.3 Sa/b at a signal-to-noise ratio of 3, where Sa was the standard deviation of the background signal and b was the slope of the calibration curve. The limit of quantification (0.75 ngr) was also obtained based on 10 sa/b. The detection limit is lower than those obtained using other analytical techniques, demonstrating the excellent sensitivity and selectivity of the IMS method for the detection of malachite green in complex matrices.
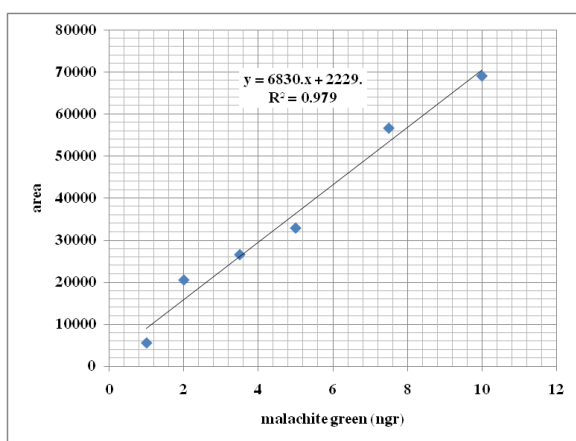
Fig.2: Linear calibration plot of peak area value vs. the concentration of malachite green

Conclusions

The present study demonstrates the potential of hand-held ion mobility spectrometry (IMS) for the rapid and sensitive detection of malachite green (MG) residues in fish tissues. The developed IMS method exhibits excellent sensitivity, with a limit of detection of 0.25 ng and a limit of quantification of 0.75 ng for MG in the fish tissue

samples. The linear calibration plot of the IMS response area versus the concentration of malachite green in the range of 1-10 ng (R = 0.979) further confirms the reliability and quantitative capabilities of the technique. Compared to other analytical methods reported in the literature, the IMS approach offers superior sensitivity and selectivity for the identification and quantification of MG in complex aquatic animal matrices. This makes the hand-held IMS a promising tool for the rapid and on-site monitoring of this banned substance in the aquaculture industry, ensuring food safety and compliance with regulatory standards.

References

[1] Hajialigol, S., & Masoum, S. (2019). Optimization of biosorption potential of nano biomass derived from walnut shell for the removal of Malachite Green from liquids solution: Experimental design approaches. Journal of Molecular Liquids, 286, 110904. https://doi.org/10.1016/j.molliq.2019.110904

[2] Srivastava, S., Sinha, R., & Roy, D. (2004). Toxicological effects of malachite green. Aquatic Toxicology, 66(3), 319–329. https://doi.org/10.1016/j.aquatox.2003.09.008

[3] Tan, Z., Xing, L., Guo, M., Wang, H., Jiang, Y., Li, Z., & Zhai, Y. (2011). Persistence of malachite green and leucomalachite green in perch (Lateolabrax japonicus). Chinese Journal of Oceanology and Limnology, 29(3), 647–655. https://doi.org/10.1007/s00343-011-0141-4

[4] van de Riet, J. M., Murphy, C. J., Pearce, J. N., Potter, R. A., & Burns, B. G. (2005). Determination of Malachite Green and Leucomalachite Green in a Variety of Aquacultured Products by Liquid Chromatography with Tandem Mass Spectrometry Detection. Journal of AOAC INTERNATIONAL, 88(3), 744–749. https://doi.org/10.1093/jaoac/88.3.744

[5] Fallah, A. A., & Barani, A. (2014). Determination of malachite green residues in farmed rainbow trout in Iran. Food Control, 40, 100–105. https://doi.org/10.1016/j.foodcont.2013.11.045

[6] Hajialigol, S., Ghorashi, S. A., Alinoori, A. H., Torabpour, A., & Azimi, M. (2012). Thermal Solid Sample Introduction–Fast Gas Chromatography–Low Flow Ion Mobility Spectrometry as a field screening detection system. Journal of Chromatography A, 1268, 123–129. https://doi.org/10.1016/j.chroma.2012.10.010

[7] Parastar, H., & Weller, P. (2024). Towards greener volatilomics: Is GC-IMS the new Swiss army knife of gas phase analysis? TrAC. Trends in Analytical Chemistry, 170, 117438–117438. https://doi.org/10.1016/j.trac.2023.117438

22nd Iranian Chemistry Congress (ICC22)
Iranian Research Organization for Science and Technology (IROST)
13-15 May 2024

03231-97589

IROST

Computational Study of CO, NO, and NO₂ adsorption on $A_{1-x}A'_xB_{1-y}B'_yO_6$ (A: Ce, La & B: Fe, Cu, Zn) bouble perovskites

Hanieh Zarintorang[a], Razieh Habibpour[*a], Eslam Kashi[*a], Mehdi Zamani[b]

Corresponding Author E-mail: Habibpour@irost.ir, Kashi@irost.ir

[a] Department of Chemical Technology, Iranian Research Organization for Science and Technology (IROST), Tehran, Iran.

[b] School of Chemistry, Damghan University, Damghan, Iran.

Abstract: The adsorption of CO, NO, and NO₂ molecules on the $A_{1-x}A'_xB_{1-y}B'_yO_3$ (A: Ce, La & B: Fe, Cu, Zn) double perovskites was investigated using density functional theory calculations. The adsorption energies of CO, NO, and NO₂ were estimated to ranging from -11 to -31 kcal/mol, -7 to -19 kcal/mol, and -27 to -39 kcal/mol, respectively. The most stable adsorption configurations are those in which the C or N atoms the adsorbates are close to the Fe and Zn atoms of the perovskite surface, respectively.

Keywords: DFT (PBE/DNP); Double perovskite; Ce/La rare earths; Fe/Cu transition metals

Introduction

Density functional theory calculations at the (PBE/DNP) level are employed to study the ground state of $A_{1-x}A'_xB_{1-y}B'_yO_6$ (A: Ce, La & B: Fe, Cu, Zn) bouble perovskites. Various configurations are considered to find out its most stable phase. Double perovskite materials, with their unique properties and potential applications, have garnered much attention in recent years [1, 2]. Considering the chemical flexibility of possible $A_{1-x}A'_xB_{1-y}B'_yO_6$, the composition of different cations in the periodic table offers an enormous number of double perovskite oxides in which the charge balance is maintained by considering those elements that satisfy $2Q_A + Q_{B'} + Q_{B''} = 12$ [3, 4].

Experimental Section

The adsorption of CO, NO, and NO₂ molecules on the 18 $A_{1-x}A'_xB_{1-y}B'_yO_3$ (A: Ce, La & B: Fe, Cu, Zn) double perovskites was investigated using density functional theory at the (PBE/DNP) level. Optimized geometries for bulk structure and (100) surfaces of $La_2Ce_2FeCuZn_2O_{12}$ double perovskite is shown in Figure 1. In this study, we will explore the preferential adsorption sites and propose specific active centers for CO, NO, and NO₂ adsorption on $A_{1-x}A'_xB_{1-y}B'_yO_6$ (A: Ce, La & B: Fe, Cu, Zn) bouble perovskites.

Results and Discussion

DFT (PBE/DNP) calculated initial and optimized geometries, total, relative and adsorption energies, and electronic parameters for adsorption of CO, NO, and NO₂ molecule over (100) surface of $La_2Ce_2FeCuZn_2O_{12}$ double perovskite are presented in Table 1, Table 2, and Table 3, respectively. The adsorption energies of CO, NO, and NO₂ were estimated to ranging from -11 to -31 kcal/mol, -7 to -19 kcal/mol, and -27 to -39 kcal/mol, respectively. It was found that the chemical nature of the B cation influences

greatly the CO, NO, and NO₂ conversion and its variation with adsorption temperature.
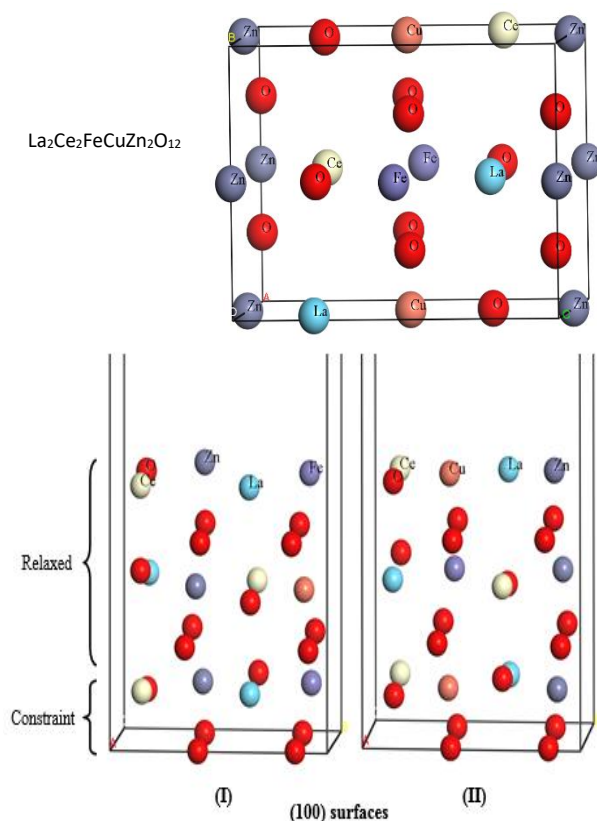
$La_2Ce_2FeCuZn_2O_{12}$

Fig.1: Optimized geometries for bulk structure and (100) surfaces of $La_2Ce_2FeCuZn_2O_{12}$ double perovskite.

22nd Iranian Chemistry Congress (ICC22)
Iranian Research Organization for Science and Technology (IROST)
13-15 May 2024

03231-97589

IROST

Table1: initial and optimized geometries, total, relative and adsorption energies, and electronic parameters for adsorption of CO molecule over (100) surface of $La_2Ce_2FeCuZn_2O_{12}$ double perovskite

E_{tot} (Ha)	E_{rel} (kcal/mol)	E_{ads} (kcal/mol)	E_{HOMO} (eV)	E_{LUMO} (eV)	E_{gap} (eV)	E_F (eV)
-4041	0 (Min)	-44.27	-5.48	-4.78	0.69	-5.1

Table2: initial and optimized geometries, total, relative and adsorption energies, and electronic parameters for adsorption of NO molecule over (100) surface of $La_2Ce_2FeCuZn_2O_{12}$ double perovskite

E_{tot} (Ha)	E_{rel} (kcal/mol)	E_{ads} (kcal/mol)	E_{HOMO} (eV)	E_{LUMO} (eV)	E_{gap} (eV)	E_F (eV)
-4131	0 (Min)	-19.69	-5.66	-4.98	0.70	-5.1

Table3: initial and optimized geometries, total, relative and adsorption energies, and electronic parameters for adsorption of NO_2 molecule over (100) surface of $La_2Ce_2FeCuZn_2O_{12}$ double perovskite

E_{tot} (Ha)	E_{rel} (kcal/mol)	E_{ads} (kcal/mol)	E_{HOMO} (eV)	E_{LUMO} (eV)	E_{gap} (eV)	E_F (eV)
-4133	0 (Min)	-39.95	-5.31	-4.80	0.51	-5.2

CO absorption does not eliminate the adsorbent band gap, but NO and NO_2 absorption makes the adsorbent a conductor by eliminating the band gap. It was shown in Figure 2.
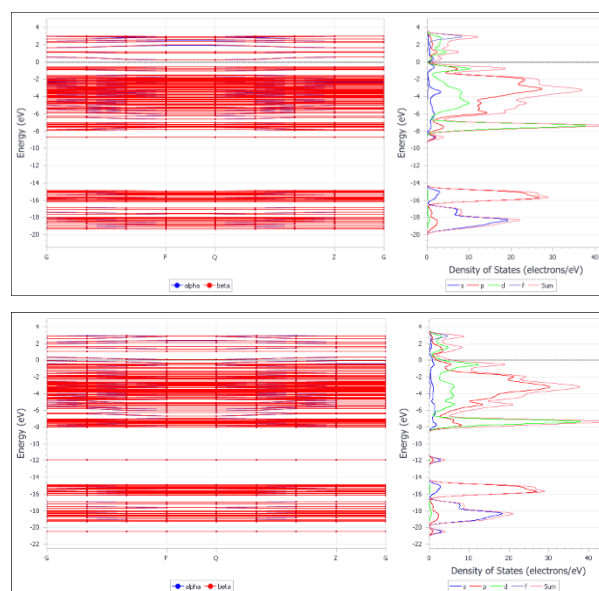
Fig.2: DFT (PBE/DNP) calculated band structure and PDOS diagram for adsorption of CO and NO molecule over (100) surface of $La_2Ce_2FeCuZn_2O_{12}$ double perovskite.

Conclusions

All synthesized perovskites were prepared using sol-gel method. Based on the computational results, CO absorption does not eliminate the adsorbent band gap, but NO and NO_2 absorption makes the adsorbent a conductor by eliminating the band gap.

References

[1] Hammami, R., et al., Surface science, 603(20), pp.3057-3067, 2009.

[2] Haye, E., et al., Journal of Alloys and Compounds, 657, pp.631-638, 2016.

[3] Ateia, E.E., et al., Journal of Inorganic and Organometallic Polymers and Materials, 31, pp.1713-1725, 2021.

[4] Chen, C. and Ciucci, F., Chemistry of Materials, 28(19), pp.7058-7065, 2016.

Morphology of $A_{1-x}A'_xB_{1-y}B'_yO_6$ (A: Ce, La & B: Fe, Cu, Zn) bouble perovskites with Zn doping in B-site

Hanieh Zarintorang, Razieh Habibpour*, Eslam Kashi*

Corresponding Author E-mail: Habibpour@irost.ir, Kashi@irost.ir

Department of Chemical Technology, Iranian Research Organization for Science and Technology (IROST), Tehran, Iran.

Abstract: The computational and experimental investigations of the structure and crystal-chemistry of the $A_{1-x}A'_xB_{1-y}B'_yO_6$ (A: Ce, La & B: Fe, Cu, Zn) double are reported. Polycrystalline $A_{1-x}A'_xB_{1-y}B'_yO_6$ perovskites were synthesized by the sol–gel method and their structure and morphology were investigated using DFT calculations at PBE/DNP level of theory and FE-SEM/EDS analysis. The characterization results indicate that the main effects of the partial substitution of B-metal with Zn elements are the maintenance of the hexagonal structure of the perovskite and the increase in reducibility and oxygen mobility. All structures were optimized and computational electro-chemical properties was reported. Based on these results, changing the chemical composition of perovskites has a significant effect on their electronic properties and it is expected to be effective in their efficiency to convert CO, NO and NO_2 polluting gases. Also, all the synthesized perovskites have a flaky plate structure and it remains constant with the change in their chemical composition.

Keywords: Double perovskite; Ce/La rare earths; Fe/Cu transition metals; Zn doping; Sol-gel

Introduction

In this research work, 18 perovskite-type mixed oxides were prepared based on transition metals Fe, Cu and Zn and rare earth metals Ce and La by sol-gel method. Unburnt hydrocarbons (UHC), carbon monoxide (CO), and nitrogen oxides (NOx) are the major noxious gases present in the exhaust of internal combustion engines. [1]. The catalytic activity of perovskite-type oxides is largely controlled by the nature of the B-site cation. The role of the A-site cation was found to be less decisive in the studied systems. However, partial substitution at the A-site by a cation of different valence can form oxygen vacancies and/or change the oxidation state of the B-site cation, which enhances substancially the catalytic properties of the material [2].

Experimental Section

All synthesized perovskites were prepared using sol-gel method. In this method, we first set the temperature of the water bath to 60 °C. We dissolve each of the weighed metal salts with a small amount of water. To dissolve the La salt and EDTA, we place the solution at 100°C. Then a 5-liter beaker was placed in a water bath, and then all copper, iron, lanthanum, zinc, and cerium salts were poured into it. Chemical composition of all 18 synthesized double perovskites is given in table 1. As can be seen, the effect of the presence and absence of transition metals Fe, Cu and Zn has been investigated in these structures. The change in the amount of iron, the change in the amount of copper, and in the third column, the change in the amount of zinc have been reported. The first composition of each column does not contain the corresponding investigated metal.

Table1: Chemical composition of 18 synthesized double perovskites

(1) $La_{0.5}Ce_{0.5}Cu_{0.5}Zn_{0.5}O_6$
(2) $La_{0.5}Ce_{0.5}Fe_{0.1}Cu_{0.45}Zn_{0.45}O_6$
(3) $La_{0.5}Ce_{0.5}Fe_{0.2}Cu_{0.4}Zn_{0.4}O_6$
(4) $La_{0.5}Ce_{0.5}Fe_{0.3}Cu_{0.35}Zn_{0.35}O_6$
(5) $La_{0.5}Ce_{0.5}Fe_{0.4}Cu_{0.3}Zn_{0.3}O_6$
(6) $La_{0.5}Ce_{0.5}Fe_{0.5}Cu_{0.25}Zn_{0.25}O_{36}$
(7) $La_{0.5}Ce_{0.5}Fe_{0.5}Zn_{0.5}O_6$
(8) $La_{0.5}Ce_{0.5}Fe_{0.45}Cu_{0.1}Zn_{0.45}O_6$
(9) $La_{0.5}Ce_{0.5}Fe_{0.4}Cu_{0.2}Zn_{0.4}O_6$
(10) $La_{0.5}Ce_{0.5}Fe_{0.35}Cu_{0.3}Zn_{0.35}O_6$
(11) $La_{0.5}Ce_{0.5}Fe_{0.3}Cu_{0.4}Zn_{0.3}O_6$
(12) $La_{0.5}Ce_{0.5}Fe_{0.25}Cu_{0.5}Zn_{0.25}O_6$
(13) $La_{0.5}Ce_{0.5}Fe_{0.5}Cu_{0.5}O_6$
(14) $La_{0.5}Ce_{0.5}Fe_{0.45}Cu_{0.45}Zn_{0.1}O_6$
(15) $La_{0.5}Ce_{0.5}Fe_{0.4}Cu_{0.4}Zn_{0.2}O_6$
(16) $La_{0.5}Ce_{0.5}Fe_{0.35}Cu_{0.35}Zn_{0.3}O_6$
(17) $La_{0.5}Ce_{0.5}Fe_{0.3}Cu_{0.3}Zn_{0.4}O_6$
(18) $La_{0.5}Ce_{0.5}Fe_{0.25}Cu_{0.25}Zn_{0.5}O_6$

Results and Discussion

In order to investigate the morphology of the synthesized perovskites and their elemental analysis, FE-SEM images and corresponding EDS diagrams are shown in Figures 1 and 2, respectively. As can be seen, all the synthesized perovskites have a flaky plate structure and it remains constant with the change in their chemical composition.

22nd Iranian Chemistry Congress (ICC22)
Iranian Research Organization for Science and Technology (IROST)
13-15 May 2024

03231-97589

IROST
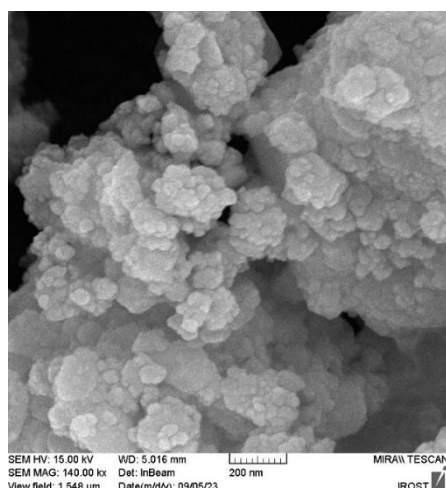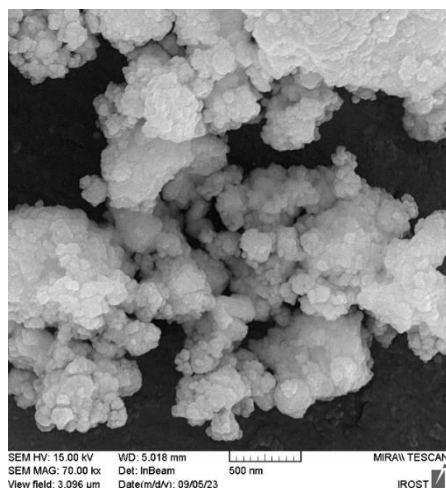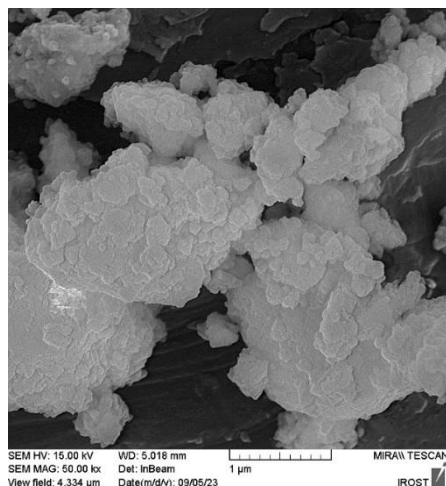
Fig.1: FE-SEM images of $La_2Ce_2FeCuZn_2O_{12}$ double perovskite with magnifications of 1 μm, 500 nm, and 200 nm.
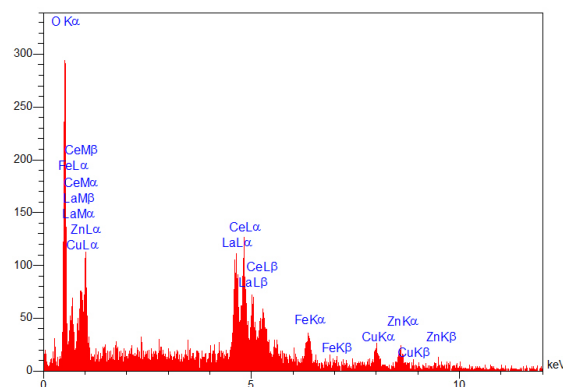
Fig.2: Energy dispersive X-ray spectroscopy (EDS) spectra of $La_{0.5}Ce_{0.5}Fe_{0.4}Cu_{0.4}Zn_{0.2}O_6$ perovskite.

Figure 3 shows the performance of the perovskite catalysts in the conversion of UHC, CO, and NO_X gases.
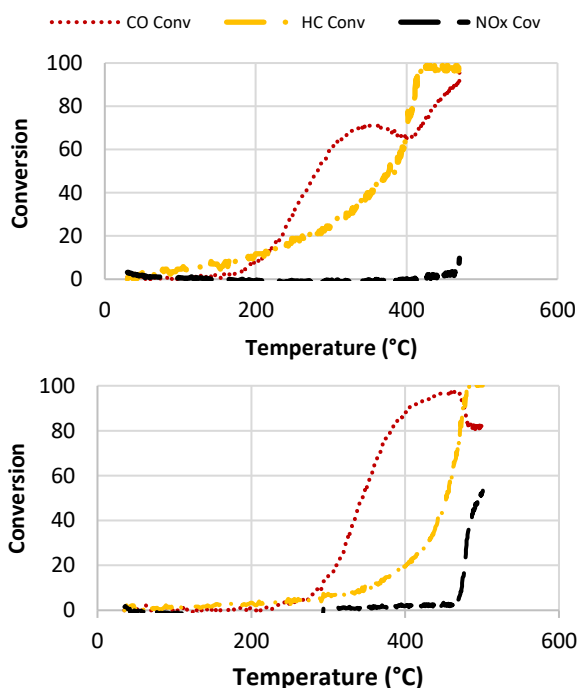
Fig.3: The performance of the $La_{0.5}Ce_{0.5}Fe_{0.4}Cu_{0.4}Zn_{0.2}O_6$ and $La_{0.5}Ce_{0.5}Fe_{0.3}Cu_{0.3}Zn_{0.4}O_6$ perovskite catalysts in the conversion of UHC, CO, and NO_X gases.

Conclusions

All synthesized perovskites were prepared using sol-gel method. Based on the performance experiment results, Increasing the amount of Zn in the composition of perovskite greatly increases the NO_X conversion.

References

[1] Raimondi, G., et al., Chemistry of Materials, 32(19), pp.8502-8511, 2020.

[2] Zhang, L., et al., Inorganic chemistry, 56(9), pp.5210-5218, 2017.

Structural and Electro-chemical Properties of Double Perovskites Based on Rare Earth Elements (Ce/La) and Transition Metals (Fe, Cu, and Zn)

Hanieh Zarintorang[a], Razieh Habibpour[*a], Eslam Kashi[*a], Mehdi Zamani[b]

Corresponding Author E-mail: Habibpour@irost.ir, Kashi@irost.ir

[a] Department of Chemical Technology, Iranian Research Organization for Science and Technology (IROST), Tehran, Iran.

[b] School of Chemistry, Damghan University, Damghan, Iran.

Abstract: $A_{1-x}A'_xB_{1-y}B'_yO_6$ (A: Ce, La & B: Fe, Cu, Zn) perovskite-type mixed oxides were synthesized by the sol–gel method. The characterization results indicate that the main effects of the partial substitution of B-metal with Zn elements are the maintenance of the hexagonal structure of the perovskite and the increase in reducibility and oxygen mobility. All structures was optimized and computational electro-chemical properties was reported. Based on these results, changing the chemical composition of perovskites has a significant effect on their electronic properties and it is expected to be effective in their efficiency to convert CO, NO and NO_2 polluting gases. $La_{0.5}Ce_{0.5}Fe_{0.4}Cu_{0.4}Zn_{0.2}O_3$ is the most active catalyst for improving CO and UHC oxidation, as it is the most reducible, and because is able to evolve oxygen at intermediate temperatures. $La_{0.5}Ce_{0.5}Fe_{0.3}Cu_{0.3}Zn_{0.4}O_3$ is the most active catalyst for NO_x reduction.

Keywords: Perovskite mixed oxides; Ce/La rare earths; Fe/Cu/Zn transition metals; Sol-gel

Introduction

In this research work, 18 perovskite-type mixed oxides were prepared based on transition metals Fe, Cu and Zn and rare earth metals Ce and La by sol-gel method. Unburnt hydrocarbons (UHC), carbon monoxide (CO), and nitrogen oxides (NO_x) are the major noxious gases present in the exhaust of internal combustion engines. [1]. The catalytic activity of perovskite-type oxides is largely controlled by the nature of the B-site cation. The role of the A-site cation was found to be less decisive in the studied systems. However, partial substitution at the A-site by a cation of different valence can form oxygen vacancies and/or change the oxidation state of the B-site cation, which enhances substancially the catalytic properties of the material [2].

Experimental Section

All synthesized perovskites were prepared using sol-gel method. In this method, we first set the temperature of the water bath to 60 °C. We dissolve each of the weighed metal salts with a small amount of water. To dissolve the La salt and EDTA, we place the solution at 100°C. Then a 5-liter beaker was placed in a water bath, and then all copper, iron, lanthanum, zinc, and cerium salts were poured into it. The color of samples without copper (including iron and zinc) is yellow, the color of the samples without iron (including copper and zinc) is blue and for the samples including copper and iron (with any amount of zinc) it is green (Figure 1).
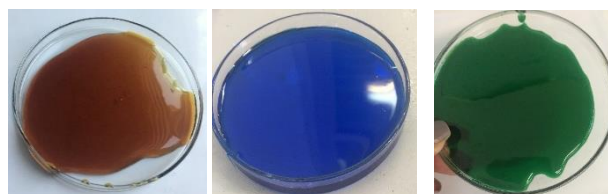
Fig.1: $A_{1-x}A'_xB_{1-y}B'_yO_6$ (A: Ce, La & B: Fe, Cu, Zn) perovskite-type mixed oxides without copper (yellow), without iron (blue), and including copper and iron (green).

Results and Discussion

In order to check the thermal stability and also to determine the calcination temperature of the synthesized perovskite catalysts, the thermal decomposition diagram of the catalyst precursors is shown in Figure 2.
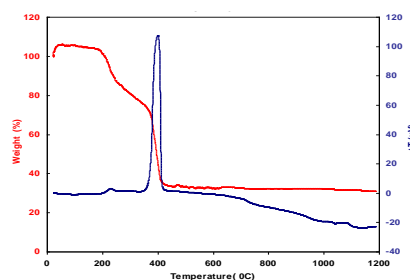
Fig.2: TGA and DSC curves in red and blue color, respectively from 25 to 1200 °C.

22nd Iranian Chemistry Congress (ICC22)
Iranian Research Organization for Science and Technology (IROST)
13-15 May 2024

03231-97589

IROST

As can be seen above the temperature of 700°C, weight change does not occur and this temperature is suitable for performing the calcination process and converting the catalyst precursor to perovskite oxide compound. In Figure 3, a schematic of the changes in valence band edge (HOMO), conduction band edge (LUMO) and conduction and valence band energy gap (E_{gap}) values for structures with different chemical composition at the lowest energy value at the PBE/DNP level of theory is provided.
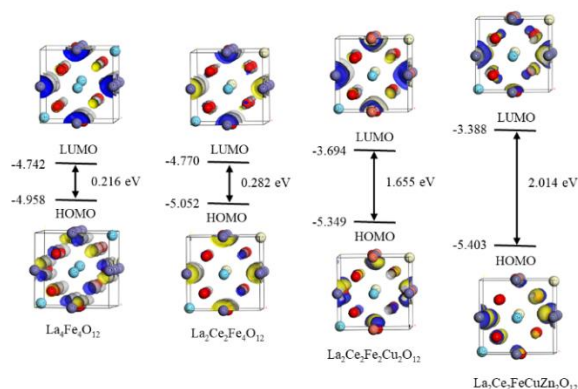
Fig.3: Schematic of the changes in HOMO, LUMO and energy E_{gap} values for structures with different chemical composition at the lowest energy value at the PBE/DNP level of theory.

Figures 4-6 show the band structures and PDOS diagrams of $La_2Ce_2Fe_4O_{12}$, $La_2Ce_2Fe_2Cu_2O_{12}$, and $La_2Ce_2FeCuZn_2O_{12}$ perovskite structures, respectively.
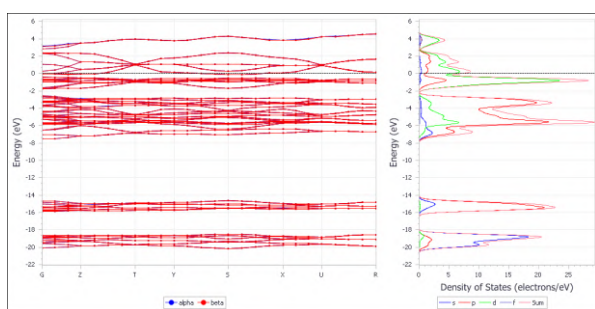
Fig.4: band structures and PDOS diagrams of $La_2Ce_2Fe_4O_{12}$ perovskite structure.
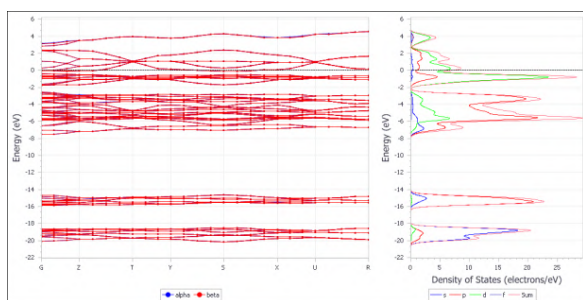
Fig.5: band structures and PDOS diagrams of $La_2Ce_2Fe_2Cu_2O_{12}$ perovskite structure.
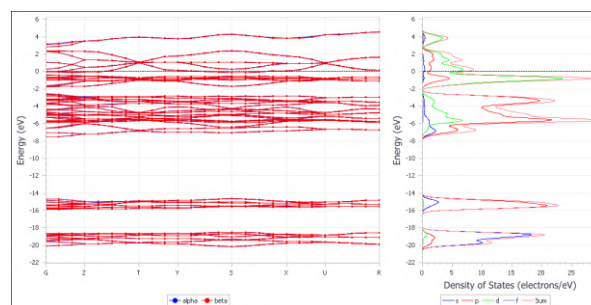
Fig.6: band structures and PDOS diagrams of $La_2Ce_2FeCuZn_2O_{12}$ perovskite structure.

In order to confirm the formation of the perovskite structure, the XRD spectrum of a synthesized perovskite sample ($La_2Ce_2FeCuZn_2O_{12}$) is shown in Figure 7a. The sharp peak at 32° along with the smaller peak at 28° and the peaks at 48° and 57° are indicators of the perovskite structure, which can also be seen in the XRD spectrum of the perovskite sample reported in other scientific sources in Figure 7b.
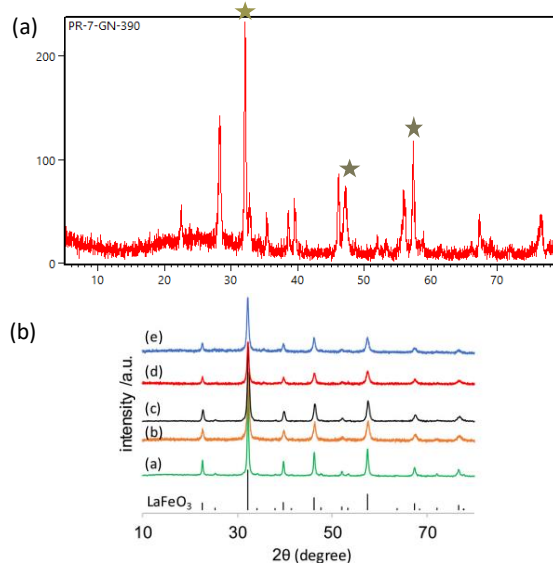
Fig.7: The XRD pattern of synthesized $La_2Ce_2FeCuZn_2O_{12}$ perovskite (a) and reported in other scientific sources (b).

Conclusions

All synthesized perovskites were prepared using sol-gel method. Based on the computational and experimental results, changing the chemical composition of perovskites has a significant effect on their electronic properties and it is expected to be effective in their efficiency to convert CO, NO and NO_2 polluting gases.

References

[1] Ghezali, N., et al., Crystals, 14(2), p.191, 2024.
[2] Bibi, I., et al., Results in Physics, 26, p.104392, 2021.

Determining the optimal amount of D2EHPA and TBP extractants in the solvent extraction of nickel and cadmium from the filter cake of cold purification of zinc production factory.

Maryam Ranjbar, Razieh Habibpour, Eslam Kashi, Hasan Zamanian, Amir Pazouki, Zahra Bagherpour

Corresponding Author E-mail: marandjbar@irost.ir

Department of Chemical Technology, Iranian Research Organization for Science and Technology IROST, Tehran,

3313193685, Iran.

Abstract: Solvent extraction is widely used and on a commercial scale as a method with selective extraction in this study, we try to achieve the highest amount of cadmium and nickel extraction from the cadmium cold purification cake filter by using the optimal amount of the combination of D2EHPA and TBP extractors. Different quantities of extractors were examined and tested. The highest amount of extraction in of D2EHPA = 22.5 ml, TBP = 7.5 ml and 402 = 20 ml. It is done with 50 ml of distilled water and the ambient temperature was achieved under rotation and at PH=8-9 in time = 30 min.

Write your abstract here, not more than 50 words. Please do not change the format of different parts of the text. (Font: Calibri 10)

Keywords: cold purification cake of cadmium; Solvent extraction; D2EHPA; TBP

Introduction

Hydrometallurgical extraction is based on acidic or alkaline leaching, and the metal in question is considered to be soluble and pulp-shaped for recovery and subsidence by various methods, including ION Exchange, electrolysis, etc [1]. Various techniques have been used to recover and separate metals from solutions of different concentrations of complexes, such as surface absorption of materials, ion exchange, solvent extraction, and caromatography. Solvent extraction is widely used and on a commercial scale as a method with selective extraction [2]. Various techniques have been used to recover and separate metals from solutions of different concentrations of complexes, such as surface absorption of materials, ion exchange, solvent extraction, and caromatography. Solvent extraction is widely used and on a commercial scale as a method with selective extraction.[2] Metals with more electrical properties than zinc are deposited and separated into cakes.[3] Zinc plant waste contains significant amounts of zinc, manganese, cadmium, nickel and cobalt [2]. Soluble extraction of nickel from an acidic sulfate solution of carboxyl acids (versatile acids) and alkaline derivatives of phosphoric acids and such as D2EHPA are used. Extractors have less selectivity on other metals such as manganese iron and cobalt [4]. Acidarganophosphorus extractors are widely used in soluble extraction of various metal ions [3]. Various techniques have been used to recover and separate metals from complex solutions with different concentrations, such as surface adsorption, ion exchange, solvent extraction and chromatography. Solvent extraction is widely used on a commercial scale as a selective extraction method [3]. Metals that have more electrical properties than zinc are deposited in the form of cakes and separated [1]. The tailings of zinc factories contain significant amounts of zinc, manganese, cadmium, nickel and cobalt [3]. Solvent extraction of nickel from acid sulfate solution is used from carboxylic acids (Versatic acids) and alkaline derivatives from phosphoric acids such as D2EHPA. Extractors have less selectivity on other metals such as manganese, iron and cobalt [3]. Organophosphorus acid extractors are widely used in the solvent extraction of various metal ions [3].

Experimental Section

The extraction operation is performed with the help of D2EHPA extractant in kerosene solvent which is used as kerosene and combined with (tributyl phosphate) TBP. At this stage, after drying at 150ºC oven, the cold cadmium purification cake is leached with sulfuric acid 0.65 mol/liter for 2 hours at room temperature. The filter was brought to a volume of 100 ml and 25 ml was used for solvent extraction. For the solvent extraction of filter cake cold purification of cadmium, the organic phase is a combination of D2EHPA, TBP and Solvent 402 as kerosene, 25 ml of which is added to 25 ml of the pulp obtained from five times of leaching. The sample prepared at different temperatures between 25 and 70 degrees Celsius with D2EHPA concentration between 5% and 40% of the aqueous phase and TBP concentration between zero and 15% of the organic phase and contact time between the two phases from 5 minutes to 60 minutes was subjected to solvent extraction. By performing different tests in different conditions and

22nd Iranian Chemistry Congress (ICC22)
Iranian Research Organization for Science and Technology (IROST)
13-15 May 2024

03231-97589

IROST

different percentages of the extractant, the optimal amount of the extractant in constant laboratory conditions was determined as the following combination. D2EHPA =22.5 ml , TBP = 7.5 ml , 402 = 20 ml

The determined composition is dissolved in 50 ml of distilled water and used as an extractant with a ratio of 1:1 with the leaching solution.

Results and Discussion

Solvent extraction was performed with the combination of D2EHPA, TBP and 402 with a ratio of 1:1 with leaching solution. In order to obtain the optimal amount of extractant, several samples with different compositions were examined under constant laboratory conditions. Different percentages of extractants were used. After extraction, the aqueous phase and the charged organic phase are separated from each other by a centrifuge, and the aqueous phase is subjected to an atomic absorption test to determine the percentage of remaining and unextracted elements.

Table1: Amounts of extractants under constant conditions of temperature and reaction time

	A	B	C	D
D2EHPA	22.5	13.75	31.25	13.75
TBP	7.5	3.75	11.25	11.25
Temperature	38	38	38	38
Time	33	33	33	33
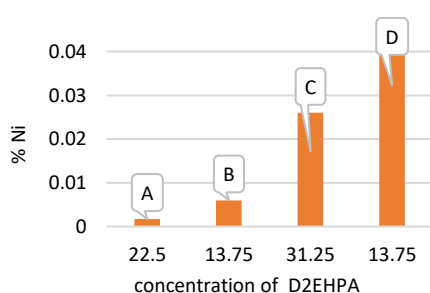
Fig.1: Effect of D2EHPA& TBP concentration on nickel extraction

Table2: Amounts of extractants under constant conditions of temperature and reaction time

	A	B	C	D	E
D2EHPA	22.5	31.25	31.25	13.75	22.5
TBP	7.5	3.75	3.75	11.25	7.5
Temperature	38	38	38	38	70
Time	33	33	33	33	33
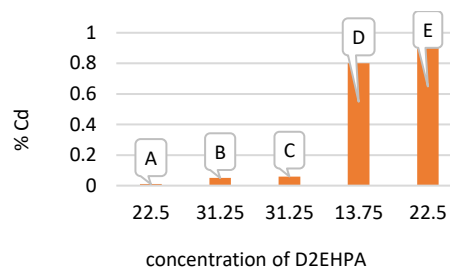
Fig.2: Effect of D2EHPA& TBP concentration on codmium extraction

It can be seen that the most optimal result is related to the column A where the amount of cadmium and nickel remaining in the aqueous phase is minimal. And almost all the mentioned elements have been transferred to the organic phase. For further investigation, the temperature of the extractor was increased to 70 degrees with fixed values in column E , and it can be seen that the minimum amount of extraction has taken place.

Conclusions

In order to achieve the highest efficiency in the solvent extraction process of nickel and cadmium from the cold filter cake, the composition of the organic phase must be optimal, for this purpose, various experiments and tests were conducted under the specified laboratory conditions, and the composition of the organic phase used was thus determined. The extraction was done at room temperature and under magnetic rotation for 33 minutes.

D2EHPA= 22.5 ml, TBP= 7.5 ml, 402= 20 ml

References

[1]Safarzadeh,M.hawan,D.Birinci,M,N and Moradkhani,D. "Reductive leaching of cobalt from zinc plant purification residues" , Hydrometallurgy 106 , Volume 106, Issues 1–2, 51–57, 2011

[2 Seyed Mehdi Kani, O. Azizitorghabeh, A and Rashchi, F. "Recovery of Zn(II), Mn(II) and Co(II) from the zinc plant residue using the solvent extraction with CYANEX 302 and D2EHPA/TBP" , Minerals EngineeringVolume 169, 106944, August 2021.

[3] Michael, J . Murdoch, J.Mackenzie. "Process for the recovery of nickel" , Cognis IP Management GmbH, US5976218a USA, 1996.

Application of GO-g-PCA Composite as a Coating for Paperboards

Reza Beiranvand[*,a,b], Aliasghar Engashte-vahed[a]

Corresponding Author E-mail: Rezabeiranvand.lu@gmail.com

[a] Quality Control Department, Pishro Kaghaz Negar Pars Factory, Shekohieh Industrial Town, Qom, Iran.

[b] Department of Analytical Chemistry, Faculty of Chemistry, Lorestan University, Khorramabad, Iran.

Abstract: In this study, the impact of coating a trace amount of GO-g-PCA composite on a paperboard sample was examined. The findings indicate that the water absorption and tensile, tear, and stiffness properties of the modified paperboard have increased by 4 to 19 percent.
Keywords: Graphene Oxide; Coating; Paperboard

Introduction

Polymeric coatings are becoming popular for protecting surfaces and they can help keep the surface working properly [1]. Organic coatings are one type of polymeric coating that can protect surfaces from damage. They work by creating a barrier between the surface and the environment. This helps keep the surface from getting damaged by things like rust and abrasion. Organic coatings can be used on many different surfaces, like metals, plastic, and paperboard [2]. They can improve how long the surface will last and also make it look better.

Graphene, an allotrope form of carbon, has revolutionized the field of composite materials due to its unique properties such as a high specific surface area, mechanical, electrical, and thermal characteristics [3]. Graphene oxide (GO), an oxidized form of graphene, has emerged as a strong alternative to graphene because of its structural similarity to graphite. GO has remarkable mechanical strength, chemical stability, and thermal stability. When used in a composite, GO often forms a three-dimensional layered sheet that sustains the coating's integrity by preventing the exchange of volatile compounds with the external environment [4].

In the presented research, graphene oxide, on which citric acid was polymerized, has been proposed as a promising option for surface coating. This is due to the significant increase in OH groups on the surface of GO that results from citric acid polymerization (GO-g-PCA). This composite was used for the first time to cover paperboard in this study, and the results demonstrate the potential of GO-g-PCA composite for surface coating applications.

Experimental Section

The process for making GO-g-PCA was done using the method described by Sarlak et al. [5]. First, 0.5 g of GO and 25 g of citric acid were put into a polymerization ampoule. Then, the container was stirred in three steps: 1) at 120 °C for 45 minutes, 2) at 140 °C for 90 minutes, and 3) at 160 °C for 2 hours. Water was removed from the container using a vacuum pump. After that, the composite was taken out of the container using Tetrahydrofuran as a solvent and then filtered. This made a sticky dark brown solution.

The conventional immersion method was utilized to coat the GO-g-PCA composite onto the paperboard. A 2 wt% GO-g-PCA solution was prepared in 100 ml ethanol, and the desired paperboard was subsequently immersed in it. After 30 min, the solution was discarded, and the coated paperboard was dried at 50°C for 4 hours. Finally, grammage, thickness, Cobb 60, tensile, stiffness, tearing, and water absorption tests were conducted on the coated paperboard. All the tests are conducted according to the International Organization for Standardization (ISO).

Results and Discussion

Figure 1 shows the schematic of the immersing coating system, where both sides of the paperboard are immersed uniformly. In this method, enough time should be considered to absorb the GO-g-PCA composite on and inside the paperboard so that the coating can be done successfully. the GO-g-PCA composite, there are many carboxyl functional groups in the structure of the GO-g-PCA, which increases its reactivity to the paperboard [6].
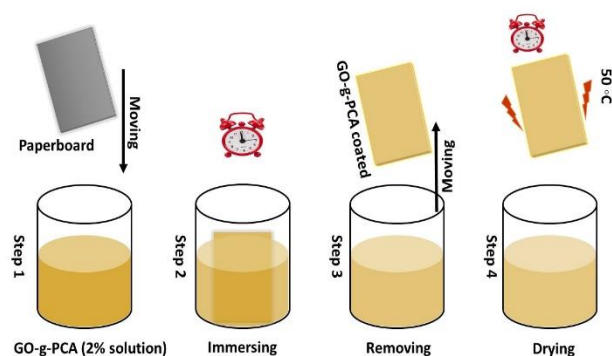
Fig.1: Scheme of Immersion Coating Method

22nd Iranian Chemistry Congress (ICC22)
Iranian Research Organization for Science and Technology (IROST)
13-15 May 2024

03231-97589

IROST

When GO-g-PCA composite is added to the paperboard, it changes the physical properties of the paperboard. By weaving the GO-g-PCA into the paperboard's structure, we can see clear changes in the examined characteristics. Table 1 shows the results of the tensile, stiffness, tearing, and Cobb 60 tests. These results reveal that the modified paperboard's surface has become hydrophilic, which is different from its original hydrophobic nature. The modified paperboard has shown an increase in performance between 4 and 19 percent in the desired parameters.

Conclusions

We utilized a GO-g-PCA composite to study the physical changes in paperboard, which had not been previously studied. Even a trace amount of composite applied to a 20 x 30 cm^2 paperboard surface significantly improved the paperboard's physical properties including tensile strength, tear resistance, water absorption, and stiffness. This suggests that GO-g-PCA composite could be a promising alternative to traditional paperboard-strengthening agents. Further research in this area could lead to the development of more durable and sustainable paperboard products, with less environmental impact.

Table 1: Result of Physical Analysis.

Title of Test	Pristine Paperboard	GO-g-PCA@Paperboard
Grammage (g/m^2)	155	158
Thickness (micron)	240	244
Cobb 60 (g/m^2)	36	56
Tension Stress (N)	137.1	145.2
Tensile Strength (kN/m)	9.14	9.68
Elongation (%)	1.39	1.59
Energy Absorption (J/m^2)	77.6	92.8
Tear (mN)	774.9	830.1
Stiffness (mN)	100	110

References

[1] Randis, R., Darmadi, D. B., Gapsari, F., Sonief, A. A. A., Akpan, E. D., & Ebenso, E. E. (2023). The potential of nanocomposite-based coatings for corrosion protection of metals: A Review. Journal of Molecular Liquids, 123067.

[2] Basak, S., Dangate, M. S., & Samy, S. (2024). Oil-and water-resistant paper coatings: A review. Progress in Organic Coatings, 186, 107938.

[3] Nasir, S., Hussein, M. Z., Zainal, Z., & Yusof, N. A. (2018). Carbon-based nanomaterials/allotropes: A glimpse of their synthesis, properties and some applications. Materials, 11(2), 295.

[4] Chen, D., Feng, H., & Li, J. (2012). Graphene oxide: preparation, functionalization, and electrochemical applications. Chemical reviews, 112(11), 6027-6053.

[5] Sarlak, N., & Meyer, T. J. (2017). Fabrication of completely water soluble graphene oxides graft poly citric acid using different oxidation methods and comparison of them. Journal of Molecular Liquids, 243, 654-663.

Study of Soy Protein as an Unique Biopolymer in Modern Bio-Composite Systems

Fateme Sabouri*, Vahid Khakyzadeh

Corresponding Author E-mail: Sabouri137@yahoo.com

Department of Chemistry, Faculty of basic science, Khajeh Nasir Toosi University of Technology, Tehran, Iran.

Abstract: Using polymers based on biological materials, rather than those based on petroleum, to create eco-friendly biologically degradable materials has gained popularity in recent years. Today, scientists advise choosing polymers that are naturally eco-friendly. So, soybean contains 90% protein, which is a cheap, easily accessible, and biodegradable ingredient biopolymer. Soy protein is often combined with biopolymers or nanomaterials to improve its properties and for its successful applications. An appealing aspect of it is its use in numerous industrial fields. Soy protein-based blends/composites/nanocomposites are gaining great attention in packaging, medical, and other sectors and have applications in food packaging, medical sector, horticultural applications, wood adhesive agents, and in the green development of batteries. Due to this, the extraction of this protein is significant; in this article, we will deal with the extraction of soy protein as a biopolymer.

Keywords: Soy protein; Biopolymer; Biodegradable polymers; Protein

Introduction

Biopolymers are a leading class of functional material suitable for high-value applications and are of great interest to researchers and professionals across various disciplines. Today, biodegradable polymers based on renewable resources are more popular, and attention has been focused on biopolymers as starting materials [1]. Plant protein is the major biopolymers in crops because of It is a renewable and biodegradable biopolymer. Among these plant proteins, soy protein has the advantage of being economically competitive[2].

As shown in Table1, Soy generally consists of protein, lipids, carbohydrates, fibre, and phytic acid, and they are the most important representative of legume proteins due to their high protein level and well-balanced amino-acid composition [3].

Table1: Nutritional composition of soybean

compounds	%	Description
Protein	40	2S, 7S, 11S, 15S
lipids	20	Triglycerides, Phospholipid, Unsaponifiable matter
Carbohydrates	25	Complex carbohydrates
fiber	5	Crude fiber
phytic acid	1.5	$C_6H_{18}O_{24}P_6$

Soy protein has high thermal stability and is a complex mixture containing various proteins [4], legume protein such as soy protein isolate (SPI), which has relatively lower water solubility, higher surface hydrophobicity, and a higher tendency of aggregation [5].

It is well known that more than 90% of soy protein includes a group called globulin, which consists of four components: 2S, 7S, 11S, and 15S. The 2S consists of low molecular weight polypeptides (8000 to 20000 Daltons) and comprises the soybean trypsin inhibitors. The 15S protein is a dimer of glycinin. Most of the stored proteins are 7S and 11S groups; their names are glycine(11S) and β-conglycinin (7S) [6, 7].

To obtain the desired biopolymer, we need to extract protein from the soybean plant source optimally; in the following, we will examine the extraction method of this protein.

Experimental Section

The conventional approach for obtaining vegetable protein is alkaline extraction and acid precipitation [8]. This method yields a protein with high purity and a large quantity, making it a crucial technique in protein research and actual production. Additionally, this method is uncomplicated and cost-effective, making it ideal for large-scale industrial protein production.

First, 0.025 M NaCl was dissolved in 100 ml water, and then 3 g of sifted soybean meal was added to the solution and stirred. According to the reports, extraction of soy protein is done in acidic and alkaline pH. Considering that in acidic pH, the possibility of protein denaturation and damage to its structure is higher, acidic (pH=2) and primary (pH=10) were selected and compared. To adjust the PH, NaOH and HCl were used and separated from the fibre through centrifugation. Eventually, the supernatant and sediment separated, and the residue was put at room temperature to dry completely. The dried deposit is our protein.

22nd Iranian Chemistry Congress (ICC22)
Iranian Research Organization for Science and Technology (IROST)
13-15 May 2024

03231-97589

IROST
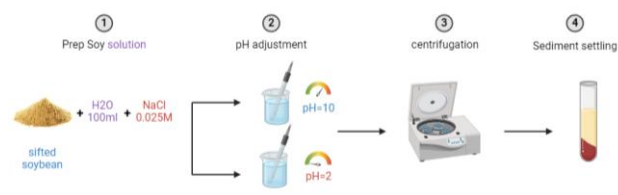
Fig.1: Soy protein extraction

Results and Discussion

The yield of this extraction method was calculated to be 62.26%.

The structure of soy proteins is dynamic and subject to change at different conditions (e.g., pH, ionic strength, reducing agents, temperature). So, the Characteristics of soy proteins are, in turn, strongly dependent on the interplay between the chemical structure of the protein and environmental factors. The pH, temperature, and ionic strength effects depend on the soy protein's properties. The stability and reactivity of soy proteins in producing soy protein-based materials, such as nanocomposites, are influenced by their surface charge, hydrophobicity, and charge density. These properties are primarily dictated by the structural characteristics of the soy proteins and external factors such as pH and ionic strength.

One of the main limiting factors of using soy protein is its inherent low solubility. As a mixture of 7S and 11S proteins, the isolated soybean protein exhibits a similar solubility profile. The solubility of SPI is influenced by multiple factors, such as dissolution temperature, pH, and ionic strength, with the lowest solubility (≈10%) at pH 4.6 (isoelectric point). Adjustment of pH is an effective method to modify the properties of soy protein products, either alone or in conjunction with heating. The solubility of soybean proteins is substantially increased by adjustment of the pH at 11-12. Furthermore, the type of ions in the protein solution also influences protein solubility.

In general, the pH level in the protein extraction process should be such that its structure is not denatured.

As thermal treatments induce a conformational change in the soy proteins, they can further alter the supramolecular structure, producing protein aggregates of different sizes depending on the heating condition. At temperatures higher than 90 °C, the 11S protein forms insoluble aggregates that consist exclusively of the basic peptide. The primary force driving aggregation in this context is hydrophobic interaction. Interestingly, 11S does not form aggregates when incubated with the 7S fraction. Due to their higher specific surface area, smaller soybean particles lead to higher recovery of soybean protein regardless of the extraction method.

Conclusions

Soy protein (SP) based materials are gaining increasing interest for biochemical applications because of their tailorable biodegradability, abundance, and relative inexpensiveness. Analysis of the available literature indicates that soy protein can be fabricated into different shapes, being relatively easy to process by solvent- or melt-based techniques. Furthermore, soy protein can be blended with other synthetic and natural polymers and with inorganic materials to improve the mechanical properties and the bioactive behaviour for several demands. It can also be used as a biological substrate in the preparation of other compounds Recently, soy protein based bionanocomposites show potential applications and has proven to be a promising option in improving mechanical and moisture barrier properties.

References

[1] Baranwal, J., et al., Biopolymer: A sustainable material for food and medical applications. Polymers, 2022. 14(5): p. 983.

[2] Ly, Y.-P., L. Johnson, and J. Jane, Soy protein as biopolymer, in Biopolymers from renewable resources. 1998, Springer. p. 144-176.

[3] Yuan, Y., et al., Associative interactions between chitosan and soy protein fractions: Effects of pH, mixing ratio, heat treatment and ionic strength. Food Research International, 2014. 55: p. 207-214.

[4] Preece, K., N. Hooshyar, and N. Zuidam, Whole soybean protein extraction processes: A review. Innovative Food Science & Emerging Technologies, 2017. 43: p. 163-172.

[5] Feng, S., et al., The impacts of complexation and glycated conjugation on the performance of soy protein isolate-gum Arabic composites at the O/W interface for emulsion-based delivery systems. Food Hydrocolloids, 2023. 135: p. 108168.

[6] Lee, E.-J. and G.-P. Hong, Effect of the double heating cycle on the thermal gelling properties of vicilin fractions from soy, mung bean, red bean and their mixture with soy glycinin. Food Hydrocolloids, 2022: p. 108370.

[7] Klupšaitė, D. and G. Juodeikienė, Legume: Composition, protein extraction and functional properties. A review. Chemical Technology, 2015. 66(1): p. 5-12.

[8] Furong Hou, W.D., Wenjuan Qu, Ayobami Olayemi Oladejo , Feng Xiong , Weiwei Zhang, Ronghai He , Haile Ma Alkali solution extraction of rice residue protein isolates: Influence of alkali concentration on protein functional, structural properties and lysinoalanine formation. Food Chemistry, 2017. 218.

Investigation of stability criteria for asphaltene in crude oil

Saman Mirmarghabi*, Masoud Bahrami Babaheidari, Pouya Hosseini far, Mohsen Mahmoudi, Seyed Mohammad-Amin Hosseini Moghaddam

Corresponding Author E-mail: S.Mirmarghabi@gmail.com

Ahwaz Faculty of Petroleum, Petroleum University of Technology (P.U.T), Kut-e-Abdollah, Ahwaz, 6198144471, Iran.

Abstract: In the production, transportation, and refining of crude oil, a significant challenge arises from the instability and deposition of asphaltene. Currently, several indexes have been developed to forecast asphaltene stability in crude oil. Some of these proposed indexes are SCP, MJM, JM, and others. In the current study, the laboratory data, the data under investigation, and the indexes for the SARA analysis of 85 oil samples were compared and analyzed. The accuracy of the indexes in distinguishing between stable and unstable oils was individually assessed. Based on the findings of this investigation, CSI demonstrated the most reliable performance, whereas QQA exhibited the least effective performance.

Keywords: Asphaltene; Stability of crude oil; SCP, MJM, JM, ANJIS, QQA, CII, CSI, SI, SP; SARA Analysis.

Introduction

Asphaltenes are complex molecules that, along with saturates, resins, and aromatics, comprise crude oil. They are the heaviest and most polar components of crude oil. Based on their solubility, asphaltenes are soluble in aromatic solvents such as toluene or benzene, but insoluble in low molecular weight alkanes like n-heptane. Similar to waxes and gas hydrates, asphaltenes create flow assurance issues in wells, production pipelines, and other high-flow-rate production facilities such as separators and heat exchangers. Asphaltenes can separate from crude oil due to pressure changes (depressurization below the onset pressure of asphaltenes), temperature conditions, or changes in the oil composition. Therefore, the possibility of asphaltene deposition in wells and flowlines is a major concern for the oil and gas industry [1].

Given the presented content, the prediction of crude oil stability holds significant importance from the perspective of asphaltene deposition. There are various methods available for determining the stability and instability of a crude oil sample, and one of these methods is the use of SARA analysis-based indexes. The primary focus of this research paper lies on examining this specific aspect.

Experimental Section

The stability and instability of asphaltene in crude oil can be analyzed through operational conditions data. In this study, a total of 85 samples of crude oil were examined. Among these samples, laboratory test data was accessible for 11 samples, while the remaining 74 samples were obtained from various articles. The data collected specifically focused on the analysis of SARA (Saturates, Aromatics, Resins, and Asphaltenes) in the corresponding crude oil. Out of the total data, it was found that 43 crude oils were reported to be stable, while 42 crude oils were reported to be unstable in terms of asphaltene precipitation.

Results and Discussion

In this section, the collected data is used to examine and evaluate the CII, SI, CSI, SCP, ANJIS, JP, MJP, and QQA indexes. For each index, the number of accurate predictions for stable and unstable oils, which are available, is shown in Table 1.

In Figures 1 and 2, the indexes were compared and analysed separately based on the percentage of predictions for stable and unstable oils.

Based on the results obtained in Figure 1, it can be concluded that the SCP, SI, and JM indexes have performed better predictions for stable oils compared to the others. Additionally, the CII and QQA indexes have shown the weakest predictions.

In the following, the results obtained from Figure 2, which pertains to unstable oils, are examined. It can be observed that the QQA, CSI, CII, and ANJIS indices have shown better predictions compared to the other indices. Additionally, it was observed that the SI and JM indices, despite performing well in predicting stable oils, have exhibited the weakest predictions for unstable oils.

22nd Iranian Chemistry Congress (ICC22)
Iranian Research Organization for Science and Technology (IROST)
13-15 May 2024

03231-97589

IROST

Table1: The Primary Statistical Population of each Index

Index	Total Data Stable	Total Data Unstable
CII	15	36
SI	34	23
CSI	30	38
ANJIS	29	36
SP	24	33
Ave-SCP	35	25
JM	33	22
MJM	27	27
QQA	4	42

The results obtained have revealed that some indexes perform well in predicting stable oils, while others are more suitable for unstable oils. Furthermore, to investigate the stability and instability of a particular oil, the indexes are generally examined. The percentage of each index is calculated based on equation 1.

$$\%\text{Index}_i = \left(\frac{\text{Total Data Stable}_i + \text{Total Data Unstable}_i}{\text{Total Data}} *100 \right) \quad (1)$$
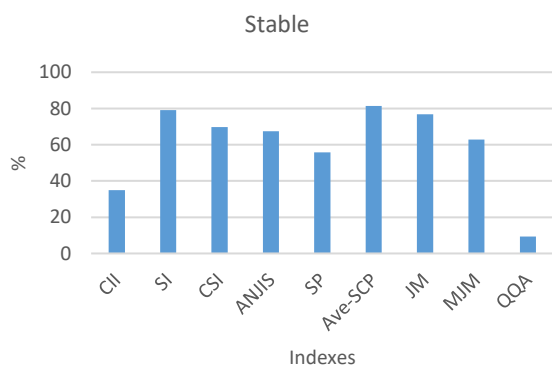
Fig.1. Comparison the accuracy of indexes in stable oils
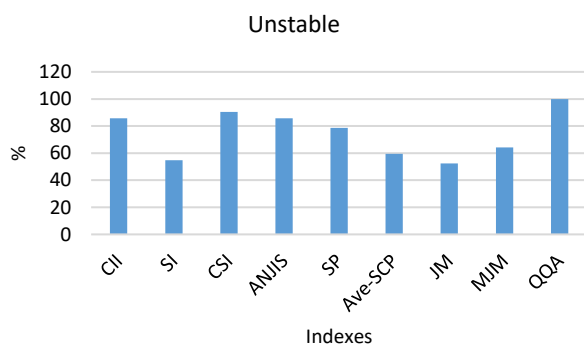
Fig.2. Comparison the accuracy of indexes of instable oils

According to the results obtained from equation 1, the indexes are examined in Figure 3.
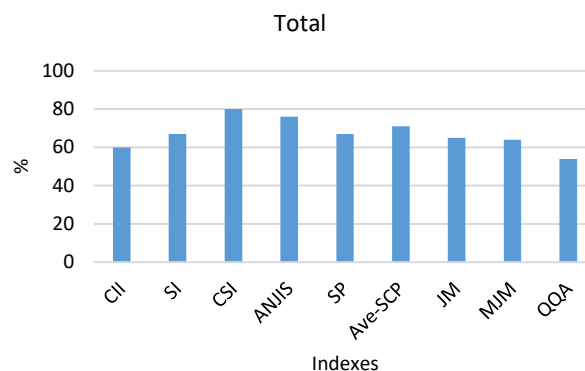
Fig.3. Comparison of accuracy of indexes in total samples

Based on the results obtained in Figure 4.3, the CSI and ANJIS indexes have shown better predictions compared to the other indices. Additionally, the CII and QQA indexes had the weakest predictions.

Conclusions

According to the findings of this study, stable oils demonstrated higher accuracy when evaluated using the SCP and SI indexes, whereas unstable oils showed better accuracy when assessed using the QQI and CSI indexes, compared to the other indexes. Nevertheless, overall, the CSI and ANJIS indexes exhibited superior accuracy compared to the other indexes.

References

[1] J. L. Creek, "Freedom of action in the state of asphaltenes: Escape from conventional wisdom," *Energy & fuels,* vol. 19, no. 4, pp. 1212-1224, 2005.

22nd Iranian Chemistry Congress (ICC22)
Iranian Research Organization for Science and Technology (IROST)
13-15 May 2024

03231-97589

IROST

Proposing the most environmentally friendly bio-methanol production process from synthesis oil through waste heat recovery and environmental optimization

Abolghasem Kazemi *[a], Zahra Kazemi [b]

Corresponding Author E-mail: abolghasemkazemi@gmail.com

[a] Chemical, Oil and Gas Engineering Department, Shiraz University of Technology, Shiraz, Iran.

[b] Chemistry Department, Farhangian University, Isfahan, Iran.

Abstract: This study presents rigorous environmental, technical, and economic optimization of bio-methanol production process using a novel methodology. Through adopting the optimal scenario, the carbon footprint can be reduced by 70.6%/kg_Methanol. A reduction of 2.176 million tons of CO_2-eq/year emissions per percentage of the methanol market it captured is feasible.

Keywords: bio-methanol; bioprocess; environment; CO_2 emissions; Evolutionary Optimization;

Introduction

The pyrolysis-derived bio-oil typically consists of a variety of compounds including acetic acid, acetol, guaiacol, water, propanoic acid, furfural, phenol, and numerous others [1,2]. Due to its corrosive nature and thermal instability, bio-oil is generally unsuitable for direct utilization in burners [1]. Nevertheless, the abundance of organic compounds in bio-oil presents an intriguing opportunity for its application in the production of biofuels and other hydrocarbons [1, 3].

No prior publication has documented the environmental evaluation and methodical optimization of the bio-oil to methanol conversion process.

Hence, this study aims to tackle the aforementioned deficiencies in the bio-oil to methanol process by employing a unique multi-objective optimization approach utilizing genetic algorithm (GA).

Fig.1: schematic representation of the process's interactions with the environment [5]

Methods

According to [4], the initial point and input stream for the procedure were presumed. The feed bio-oil was assumed to consist of particular compounds such as acetic acid, guaiacol, acetol, and water. Three crucial objective functions were chosen in this study to encompass the technical, economic, and environmental aspects of the process. Economics aspects were modeled according to [4]. The optimization process focused on the following selected objective functions:

- Minimizing process' global warming potential (GWP).
- Minimizing process' total annualized costs (TAC)
- Maximizing the methanol production rate.

A schematic diagram illustrating the primary environmental factors considered is presented in Fig.1.

The environmental consequences were computed using the environmental footprints (EF) approach. It was presumed that the electricity generated from the procedure would substitute the consumption of electricity from a natural gas (NG)-powered grid.

Results and Discussion

Fig.2 illustrates that relocating the operation of the process from the base operating system to the optimal Pareto front can lead to significant enhancements in the performance of the process. According to Fig.2, it is feasible to achieve the same methanol production rate as in the base case while reducing the environmental burdens of the process from 6.0E+09 to 4.0E+09 kgCO$_2$-eq/kgMethanol (33.3% reduction). Alternatively, it is possible to maintain the same global warming impact as the base operating system while increasing the methanol
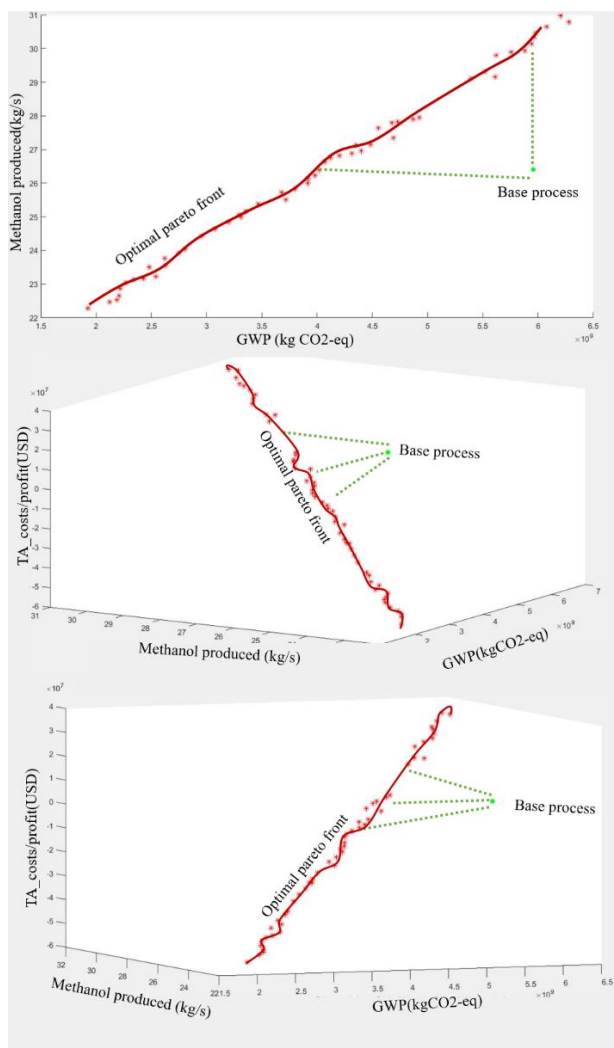
Fig.2: Optimal pareto front compared to the base case performance [5]

Fig.3: Specific carbon footpring and acidification potential of the process under operation [5]

production rate from 26.2 to 30.1 kg/s, thereby achieving a 15.0% increase in production rate.

Fig.3 illustrates the global warming and acidification potential of the process per kilogram of methanol. However, by incorporating ORC and optimizing the process, the global warming potential per kilogram of product decreases to 121 grams of CO_2-equivalent, and the acidification potential decreases to -209 millimoles of H^+-eq. It is crucial to highlight that the negative acidification potential is a result of the connection to the reduction of a natural gas-based power plant, which subsequently reduces the usage of natural gas and its associated emissions in the alternative power plant. These results suggest that if this combined methanol/power production technology reaches the commercialization stage and captures 5% of the global methanol market, it could lead to a reduction of 10.88 million tons of CO_2-equivalent emissions per year.

Conclusions

The findings demonstrated the significant impact of environmental optimization and ORC on the performance of the process. By implementing the most efficient process, it was discovered that the annual rate of return could be increased by 15.1% and the GWP could be reduced by 70.5%. Additionally, it was revealed that once this technology is brought into the commercial market, for every percentage of the methanol market it captures, it will contribute to a reduction of 2.176 million tons CO_2-eq/year in emissions. The results also indicated that incorporating ORC would result in a 2.8% higher annual rate of return and a 22.6% decrease in GWP (per kg methanol produced) compared to sub-optimal operation without ORC.

References

[1] Pinheiro Pires, A. P., Arauzo, J., Fonts, I., Domine, M. E., Fernandez Arroyo, A., Garcia-Perez, M. E., ... & Garcia-Perez, M. (2019). Challenges and opportunities for bio-oil refining: A review. Energy & fuels, 33(6), 4683-4720.

[2] Li, X., Jiang, Y., Li, C., Fan, M., Zhang, L., Zhang, S., ... & Hu, X. (2022). Pyrolysis of sawdust coupled with steam reforming for simultaneously production of heavy organics and hydrogen. Fuel, 330, 125515.

[3] Wang, H., Gross, A., & Liu, J. (2022). Influence of methanol addition on bio-oil thermal stability and corrosivity. Chemical Engineering Journal, 433, 133692.

[4] Ng, K. S., & Sadhukhan, J. (2011). Process integration and economic analysis of bio-oil platform for the production of methanol and combined heat and power. Biomass and Bioenergy, 35(3), 1153-1169.

[5] Kazemi, A., Kazemi, Z., & Pourmohamadi, M. (2024). Combined bio-methanol and power production from bio-oil: proposing a clean bio-process through waste heat recovery and environmental optimization. *Chemical Engineering and Processing-Process Intensification*, 109807.

An efficient one-step process for the synthesis of hexahydro-6H-thiazolo[3,2-a]quinolin-6-one derivatives based on heterocyclic ketene aminals .

Zeinab Amiri, Mohammad Bayat[*]

Corresponding Author E-mail: *bayat_mo@yahoo.com; m.bayat@sci.ikiu.ac.ir*

Department of Chemistry, Faculty of Science, Imam Khomeini International University, Qazvin, Iran.

Abstract: A straightforward method has been created to produce thiazoloquinoline derivatives through a single-step reaction involving l,l-dimethylthio-2-nitroethene, cysteamine hydrochloride, aromatic aldehydes, and cyclohexane-1,3-dione in the presence of Triethylamine in a H_2O and C_2H_5OH mixture. The series of consecutive reactions includes Knoevenagel condensation, Michael addition, intramolecular cyclization, and imine-enamine tautomerization. The key benefits of this approach include rapid reaction times, accessibility of initial compounds, high atom efficiency, straightforward purification of products, and the use of water/ethanol as environmentally friendly solvents.
Keywords: Heterocyclic aromatic systems.; single-step synthesis; aromatic aldehydes

Introduction

Multicomponent reactions (MCRs) have become a highly efficient and potent tool in contemporary synthetic organic chemistry due to their esteemed characteristics [1]. They provide benefits like simplicity and efficiency in comparison to traditional chemical reactions, along with selectivity, convergence, and atom economy [2]. HKAs, or Heterocyclic Ketene Aminals (figure 1), are a class of compounds that have shown potential biological activity. Some examples of biological active compounds containing HKAs include antiviral, antibacterial, antifungal, and anticancer agents. These compounds have been studied for their potential in drug development and medicinal chemistry [3].

Experimental Section

A combination of cysteamine hydrochloride (0.113 g, 1mmol), 1,1-bis(methylthio)-2-nitro ethylene (0.165 g, 1mmol), 10mL H_2O/EtOH (1:1), and triethylamine (140 µL, 1mmol) was heated under reflux in a 50-mL flask for 6 hours. Upon completion of the reaction (monitored by TLC, ethyl acetate/n-hexane, 1:1), aromatic aldehyde (1mmol) and cyclohexane-1,3-dione (0.112 g, 1mmol) were introduced to the reaction mixture, which was then stirred under reflux for the duration specified in Table **1**. Subsequently, the reaction mixture was cooled to room temperature, filtered to obtain the crude product, and the solid was washed with water/ethanol (1:1) to yield product 5 in a satisfactory yield.

Results and Discussion

Initially, a series of thiazoloquinoline derivatives **5a-5l** was obtained in excellent yields through the four-component reaction of cysteamine hydrochloride **1**, l,l-bis(methylthio)-2-nitroethene **2**, aromatic aldehydes **3**, and 1,3-cyclohexanone **4** in the presence of Et3N in a green solvent, EtOH, under reflux conditions for 20-60 minutes (Scheme **1**).
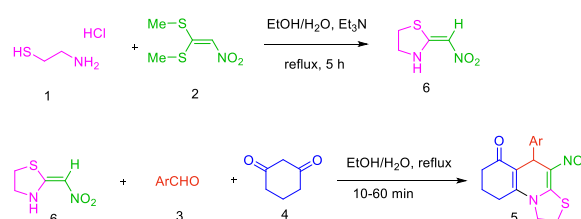
Scheme 2: Synthetic scheme for the products 5.

The identification of compound 5a was based on analysis of their IR, ^{1}H NMR, ^{13}C NMR, and mass spectra. The mass spectrum of **5a** showed a molecular ion peak at m/z 328, consistent with the suggested structure. The IR spectrum of this conformation exhibited absorption bands related to C=O stretching (1654 cm^{-1}) also 1539, 1438, and 1215 cm^{-1} owing to the NO_2 and C-N groups. The ^{1}H NMR spectrum of **5a** revealed multiple signals for the CH_2 and CH_2S groups, two multiplets for the CH_2N group, a singlet for the CH group, and two multiplets for the aromatic region (δ 7.13-7.17, 7.23-7.27 ppm) (Figure 2). The ^{1}H-decoupled ^{13}C NMR spectrum of **5a** displayed **17** distinguished resonances.

22nd Iranian Chemistry Congress (ICC22)
Iranian Research Organization for Science and
Technology (IROST)
13-15 May 2024

03231-97589
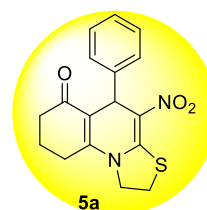
4-nitro-5-phenyl-1,2,5,7,8,9-hexahydro-6H-thiazolo[3,2-a]quinolin-6-one **(5a):** Yellow powder; Yield: 0.315 g (96%); m.p. 296-298°C. IR (KBr) (v_{max}/cm^{-1}): 1654 (C=O), 1539 and 1438 (NO$_2$), 1254 (C-N). ^{1}H NMR (300MHz, DMSO): 1.75-1.84 (m, 1H, CH$_2$), 1.96-2.02 (m, 1H, CH$_2$), 2.24-2.28 (m, 2H, CH$_2$), 2.66-2.89 (m, 2H, CH$_2$), 3.39-3.43 (m, 2H, CH$_2$S), 4.20-4.27 (m, 1H, CH$_2$N), 4.44-4.50 (m, 1H, CH$_2$N), 5.28 (s, 1H, CH), 7.13-7.18 (m, 2H, Ar), 7.23-7.27 (m, 3H, Ar). ^{13}C NMR (75.4MHz, DMSO): 20.3, 25.9, 28.1, 35.8, 37.2, 51.4, 116.2, 123.3, 126.6, 127.7 (2C), 128.0 (2C), 143.7, 150.5, 156.7, 194.4. m/z (%) = 328 (M$^+$, 18), 282 (13), 251 (100), 205 (20), 177 (5), 149 (10). Anal. Calcd. for C$_{17}$H$_{16}$N$_2$O$_3$S (328.39): C, 62.18; H, 4.91; N, 8.53; O, 14.62; S, 9.76

component reactions and evaluation of their cytotoxic activity. Bioorg Med Chem Lett 2011: 7119-7123. Doi:10.1016/j.bmcl.2011.09.082

[2] Ganem, B. (2009). Strategies for Innovation in Multicomponent Reaction Design. Acc Chem Res 2009: 463-472. Doi:10.1021/ar800214s

[3] Han, L., Feng, Y., Luo, M., Yuan, Z., Shao, X., Xu, X., & Li, Zh. (2016). 2,2,2-Trifluoroethanol activated one-pot Mannich-like reaction of β-nitroenamines, secondary amines, and aromatic aldehydes. Tetrahedron Lett 2016: 2727-2731. DOi:doi.org/10.1016/j.tetlet.2016.05.023
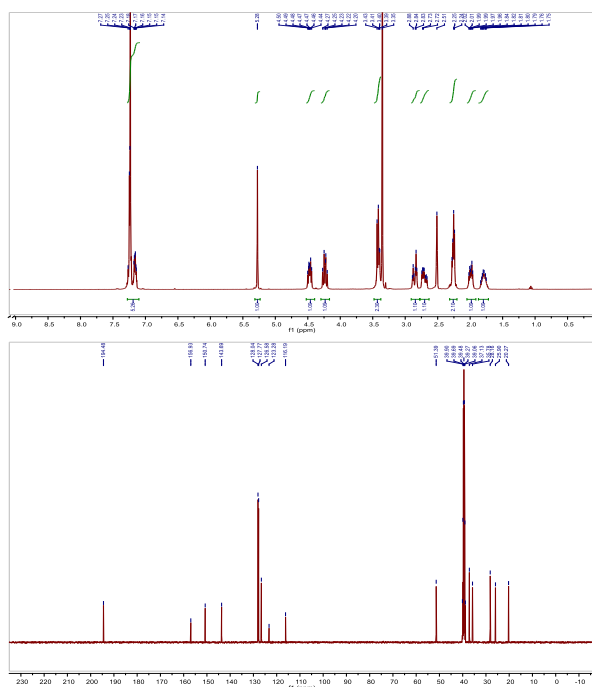
Conclusions

In conclusion, we have outlined a highly effective one-step method for producing thiazoloquinolines with good yields by reacting aromatic aldehydes with 2-(nitromethylene)thiazolidine and 1,3-cyclohexane-dione under mild conditions. This synthesis exemplifies green chemistry principles as it utilizes water and ethanol as the solvent. Additionally, the method offers advantages such as straightforward reaction process, exceptional selectivity, readily available reactants, high yields, and eliminates the need for isolating products using column chromatography.

References

[1] Shi, F., Xiao-Ning, Z., Zhang, G., Ma, N., Jiang, B., & Tu, Sh. (2011). Facile synthesis of new 4-aza-podophyllotoxin analogs via microwave-assisted multi-

22nd Iranian Chemistry Congress (ICC22)
Iranian Research Organization for Science and Technology (IROST)
13-15 May 2024

03231-97589

A one-pot four-component approach to synthesis of novel spiro[acenaphthylene-1,4'-chromene]-3'-carbonitrile and spiro[acenaphthylene-1,1'-pyrano[2,3-c]chromene]-2'-carboxylate derivatives

Zeinab Amiri, Mohammad Bayat

Corresponding Author E-mail: bayat_mo@yahoo.com; m.bayat@sci.ikiu.ac.ir

Department of Chemistry, Faculty of Science, Imam Khomeini International University, Qazvin, Iran.

Abstract: An efficient one-pot four-component condensation reaction of acenaphthoquinone, malononitrile derivatives or 2-cyanoacetamide and triazolamino-chromen-2-one and triazolamino-dimethylcyclohex-2-en-1-one in ethanol for the combinatorial synthesis of novel spiro[acenaphthylene-1,4'-chromene]-3'-carbonitrile and spiro[acenaphthylene-1,1'-pyrano[2,3-c]chromene]-2'-carboxylate derivatives has been achieved. The significant features of this reaction include, short reaction time, no column chromatographic purification, excellent yield, avoidance of environmentally hazardous solvents and catalyst-free condition, operational simplicity and readily available starting materials.
Keywords: Acenaphthenequinone; Spiroacenaphthoquinone; 3-Amino-1,2,4-triazole; Dimedone

Introduction

Multi-component reactions (MCRs) are an important tool of chemical variation for the efficient synthesis of natural products and Pharmaceutical compounds for the discovery of biological drugs.[1] A notable property of MCRs is their ability to produce multifunctionalized compounds from simple starting materials.[2] Therefore, a possible method for generating biologically active nitrogen containing heterocycles through MCRs has attracted much attention in recent decades.[3] N-heterocyclic compounds are widely found in biologically active pharmaceuticals and natural products such as vitamins, hormones, and alkaloids, as well as in good, specialized chemicals.[4]

Experimental Section

A mixture of acenaphthoquinone 1 (0.182g, 1mmol), malononitrile (0.661g, 1mmol) and triazolamino-dimethylcyclohex-2-en-1-one (0.206g, 1mmol) 3 in EtOH (5 ml) with catalyst nano-SiO₂ was stirred at room temperature condition for 20 minute. The progress of the reaction was monitored by TLC using EtOAc / n-hexane (1:1) as eluent, the reaction mixture after completion of the reaction, the solid was washed with ethanol (95%, 5 mL) to obtain the pure product 4a (94% yield). Spiroacenaphthylene derivatives were analytically pure without recrystallization.

Results and Discussion

Initially, the four-component reaction of acenaphthoquinone **1**, malononitrile derivatives or 2-cyanoacetamide **2** and triazolamino-chromen-2-one or triazolamino-dimethylcyclohex-2-en-1-one **3** in ethanol as solvent with nano-SiO₂ catalyst under reflux for 20-30 minute, afforded a series of spiro[acenaphthylene-1,4'-chromene]-3'-carbonitrile and spiro[acenaphthylene-1,1'-pyrano[2,3-c]chromene]-2'-carboxylate 4 in 88-94 % yields in (Table 2) and (Scheme 1). The effects of solvents and catalyst were evaluated for this model reaction, and the results are summarized in (Table 1).
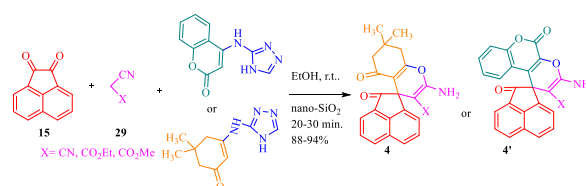
Scheme 1: Synthetic scheme for the products 4.

The ^{1}H NMR spectrum of **4a** exhibited recognized as arising from CH₃ group (δ = 0.92 ppm) and CH₃ group (δ = 0.94 ppm), CH₂ group (δ = 1.97 ppm) and CH₂ group (δ = 2.53 ppm) and one sharp singlets due to a NH₂ group (δ = 7.24 ppm), and NH group (δ = 8.16 ppm), which were determined by D₂O exchange. The phenyl moiety gave rise to characteristic signals in the aromatic region of the spectrum. ^{1}H decoupled ^{13}C NMR spectrum showed 25 distinct signals in agreement with the proposed structure. Resonances due to Cspiro, 2 CH₃, CN, and 2 C=O appeared at δ = 58.4, 27.6, 27.9, 108.0 and 195.8, 204.1 respectively.

22nd Iranian Chemistry Congress (ICC22)
Iranian Research Organization for Science and Technology (IROST)
13-15 May 2024

03231-97589
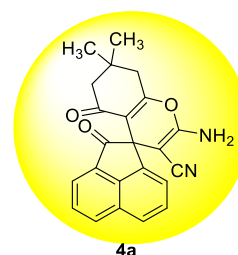
3'-Amino-7',7'-dimethyl-2,5'-dioxo-1'-(4H-1,2,4-triazol-3-yl)-5',6',7',8'-tetrahydro-1'H,2H-spiro[acenaphthylene-1,4'-quinoline]-2'-carbonitrile

(4a): White powder, Yield (94%). Mp: 301-303 °C, IR (KBr), v_{max}: 3364, 3297 (NH$_2$), 3183 (NH), 2950, 2871, 2190, 1715 (C=O), 1666, 1599, 1344, 1216, 1162, 1050, 760, 551 cm^{-1}. ^{1}H NMR (300 MHz, DMSO-d_6) δ: 0.92 (s, 3 H, CH$_3$), 0.94 (s, 3 H, CH$_3$),1.97 (s, 2 H, CH$_2$), 2.53 (s, 2 H, CH$_2$), 7.24 (s, 2 H, NH$_2$), 7.29 (d, $^3J_{HH}$ = 6 Hz, 1 H, ArH), 7.55 (t, $^3J_{HH}$ = 6 Hz, 2 H, ArH), 7.72 (t, $^3J_{HH}$ = 6 Hz, 2 H, ArH), 7.82 (s, 1 H, CH), 7.84 (d, $^3J_{HH}$ = 3 Hz, 1 H, ArH), 8.16 (d, $^3J_{HH}$ = 9 Hz, 1 H, NH). ^{13}C NMR (75 MHz, CDCl$_3$-d_1) δ: 27.6, 27.9, 32.5, 50.1, 51.4, 58.4 (C$_{spiro}$), 72.4, 74.7, 87.8, 91.3, 108.0, 108.1, 112.5, 117.9, 120.3, 121.9, 125.0, 128.9, 129.4, 130.3, 131.9, 132.6, 140.5, 140.9, 143.7, 146.1, 147.2, 149.2, 155.1, 159.2, 162.2, 165.0, 168.4, 195.8 (C=O), 204.1 (C=O). MS (EI) m/z (%):370 (17), 326 (17), 286 (100), 259 (26), 230 (12), 188 (11), 163 (4), 140 (1), 115 (2), 83 (8), 55 (5). Anal. Calcd for C$_{25}$H$_{20}$N$_6$O$_2$ (436.48): C, 68.80; H, 4.62; N, 19.25; O, 7.33.

This procedure has advantages of excellent yields, neutral and mild reaction condition, no toxic byproducts, available starting material, simple experimental and work-up procedure. Moreover the substances can be mixed without any further activation or modification.

References

[1] Bienayme H, Hulme C, Oddon G, Schmitt P (2000) Maximizing synthetic efficiency: multi-component transformations lead the way. Chem Eur J 2000:3321-3329. Doi: 10.1002/1521-3765(20000915)6:18%3C3321::aid-chem3321%3E3.0.co;2-a

[2] Sarkar R, Mukhopadhyay C (2014) L-Proline catalyzed expeditious multicomponent protocol for the synthesis of fused N-substituted-2-pyridone derivatives in aqueous medium. Tetrahedron Lett 2014:2618-2624. DOi: 10.1016/j.tetlet.2014.02.123

[3] Kozyr AV, Chenko LP, Kolesnikow AV, Zelenova N A (2002) Anti-DNA autoantibodies reveal toxicity to tumor cell lines. Immunol Lett 2002:41-47. Doi: 10.1016/s0165-2478(01)00308-x

Conclusions

This work represents a successful synthesis of a new class of spiro[acenaphthylene-1,4'-quinoline and spiro[acenaphthylene-1,1'-chromeno[3,4-b]pyridine derivatives via four components reaction between acenaphthoquinone, malononitrile derivatives or 2-cyanoacetamide and triazolamino-chromen-2-one and triazolamino-dimethylcyclohex-2-en-1-one. This reaction proceeded with catalyst nano-SiO$_2$ in excellent yields.

22ⁿᵈ Iranian Chemistry Congress (ICC22)
Iranian Research Organization for Science and Technology (IROST)
13-15 May 2024

03231-97589

IROST

An efficient synthesis of new diphenyl-hexahydroquinoline-3-carboxamide derivatives via a fourcomponent cascade reaction

Zeinab Amiri, Mohammad Bayat*

Corresponding Author E-mail : bayat_mo@yahoo.com; m.bayat@sci.ikiu.ac.ir

Department of Chemistry, Faculty of Science, Imam Khomeini International University, Qazvin, Iran.

Abstract: A straightforward method for producing oxoquinoline carboxamide derivatives is outlined, involving a one-pot, multi-component reaction. This process utilizes enaminones generated from the addition of cyclohexane-1,3-dione to various anilines, along with aromatic aldehydes and cyanoacetamide. The optimal reaction conditions were determined to be the use of EtOH/H2O (1:1) as the solvent at 80 °C, with piperidine as the catalyst. The reactions were found to be completed within 5–25 minutes, yielding good to high amounts of product (74–85%). This approach encompasses Michael reaction, imine-enamine tautomerization, and cyclization sequences. The identification of the products' structures was based on their IR, mass, 1H NMR, and 13C NMR spectra. This method incorporates several important features such as simple operation under mild conditions, easy accessibility of reactants, straightforward workup procedure, high atom economy, and the use of ethanol/water as an environmentally friendly solvent.
Keywords: Cyclohexane-1,3-dione; Anilines; Aromatic aldehydes; Cyanoacetamide

Introduction

Multi-component reactions (MCRs) are highly regarded in the fields of organic and medicinal chemistry [1] due to their convergence, simplicity of execution, high yields, efficiency, waste reduction, and atom economy [2]. The availability of easily accessible starting materials and the simplicity of one-pot procedures make MCRs a powerful tool for achieving synthetic efficiency. In particular, the multi-component synthesis of polyfunctionalized heterocyclic compounds has become increasingly challenging in organic and medicinal chemistry [3].

Experimental Section

A combination of cyclohexane-1,3-dione 1 (1 mmol, 0.112 g) and aniline 2 (1 mmol) was subjected to melting at 80 °C for 60 minutes. Following this, ethanol/water (1:1, 5 mL) was introduced, and the resulting solution was stirred for 10 minutes at 80 °C. Subsequently, aromatic aldehyde 3 (1 mmol), cyanoacetamide 4 (1 mmol, 0.084 g), and one drop of piperidine were added, and the solution was stirred at reflux for the duration indicated in Table 2. After reaching completion as confirmed by TLC, the reaction mixture was allowed to cool to room temperature, and the resulting precipitate was filtered and washed with ethanol/water (1:1) to obtain product 5 in satisfactory yields.

Results and Discussion

The synthesis of oxoquinoline carboxamide derivatives 5a-o was achieved through a one-pot, multi-component reaction involving enaminones resulting from the combination of acyclohexane-1,3-dione 1 and various anilines 2 under solvent-free conditions at 80 °C. Aromatic aldehydes 3 and cyanoacetamide 4 were added in the presence of a catalytic amount of piperidine, using EtOH/H2O (1:1) as a green solvent at 80 °C. This process yielded the desired products in good yields, as depicted in Scheme **1**.
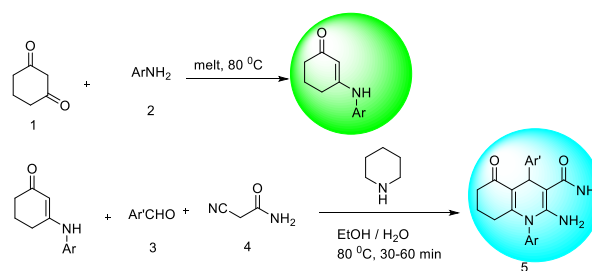
Scheme 1: Synthetic scheme for the products 5.

The structures of compounds 5a-o were determined from their IR, mass, ¹H NMR, and ¹³C NMR spectra. For example, the ¹H NMR spectrum of 5a displayed characteristic peaks corresponding to various functional groups. The mass spectrum of 5a showed the molecular ion peak at m/z 456, consistent with the proposed structure. The 1H-decoupled ¹³C NMR spectrum of 5a confirmed the proposed structure with 20 distinct resonances. The IR spectrum of 5a exhibited characteristic absorption bands at 3471, 3355, 1626, 1483, and 1267 cm−1 due to specific functional groups.

22nd Iranian Chemistry Congress (ICC22)
Iranian Research Organization for Science and Technology (IROST)
03231-97589
13-15 May 2024

IROST

5b
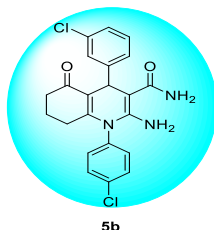
2-Amino-1,4-bis(4-chlorophenyl)-5-oxo-1,4,5,6,7,8-hexahydroquinoline-3-carboxamide (5a): White powder, mp: 258-260 ^{0}C, 0.312 g, Yield: 73%. IR (KBr) (υ_{max} /cm^{-1}): 3421 (NH$_2$), 3340 (NH$_2$), 1632 (C=O), 1465 (Ar), 1374, 1265 (C-N). ^{1}H NMR (300 MHz, DMSO): δ 1.49-1.52 (2H, m, CH$_2$), 1.78-1.82 (2H, m, CH$_2$), 2.19-2.30 (2H, m, CH$_2$), 4.92 (1H, s, CH), 6.44 (2H, s, NH$_2$), 7.18 (2H, d, $^3J_{HH}$ = 6 Hz, NH$_2$), 7.28-7.35 (2H, m, Ar), 7.42 (2H, d, $^3J_{HH}$ = 6 Hz, Ar), 7.49 (1H, s, Ar), 7.66 (2H, d, $^3J_{HH}$ = 6 Hz, Ar). ^{13}C NMR (75.4 MHz, DMSO): δ 20.4 (CH$_2$), 27.8 (CH$_2$), 33.7 (CH$_2$), 36.1 (CH), 72.9, 114.1, 125.4, 125.9, 127.5, 129.9, 132.0, 132.2, 134.0, 135.3, 150.3, 150.6, 151.8, 171.6 (C=O), 194.6 (C=O). MS (EI, 70 eV): m/z (%) = 428 (M$^+$, 2), 383 (100), 316 (47), 299 (47), 273 (12), 232 (11), 164 (9), 127 (15), 111 (19), 89 (47), 75 (31), 55 (17).

straightforward experimental procedures, short reaction times, easy purification without the need for chromatography, and compatibility with a range of functional groups make this method appealing for synthesizing various derivatives.

References

[1] del Corte, X., de Marigorta, E.M., Palacios, F., & Vicario, J. (2019). A Brønsted Acid-Catalyzed Multicomponent Reaction for the Synthesis of Highly Functionalized γ-Lactam Derivatives. Molecules 2019: 2951-2958.Doi :10.3390/molecules24162951

[2] Wiemann, J., Fischer, L., Kessler, J., Strohl, D. & Csuk, R. (2018). Ugi multicomponent-reaction: Syntheses of cytotoxic dehydroabietylamine derivatives. Bioorg.Chem. 2018: 567-576. DOi:10.1016/j.bioorg.2018.09.014

[3] Yu, S., Hua, R., Fu, X., Liu, G., Zhang, D., Jia, S., Qiu, H., Hu, W. (2019). Asymmetric Multicomponent Reactions for Efficient Construction of Homopropargyl Amine Carboxylic Esters. Org. Lett. 2019: 5737-5741. DOi: 10.1021/acs.orglett.9b02139

Conclusions

In summary, this study presents an effective approach for quickly producing a novel group of oxoquinoline carboxamide derivatives through a one-step, multi-component reaction involving dimedone, different anilines, aromatic aldehydes, and cyanoacetamide. The use of mild reaction conditions, high yields,

22nd Iranian Chemistry Congress (ICC22)
Iranian Research Organization for Science and Technology (IROST)
13-15 May 2024

03231-97589

ISC
Islamic World Science Citation Center

IROST

An efficient, novel, simple and recyclable α-Fe₂O₃@MoS₂@Ni nanocomposite with excellent catalytic function for the degradation of Acid Blue-113 as an organic pollutant

Iman Rezaei*[a], Iliya nazeriyeh [b], Raoofeh Sattari Nobarzad [c], Forouzan Shahri [a], Narges Dehghani [a]

Corresponding Author E-mail: rezae.imaan@gmail.com

[a]Department of Chemistry, Faculty of Sciences, University of Guilan, P.O. Box 41335-1914, Rasht, Iran.
[b]Department of Medical Sciences, Faculty of Medicinal Chemistry, Islamic Azad University of Medical Sciences, P.O. Box 19395/1495, Tehran, Iran.
[c]Department of Chemistry, Faculty of Science, University of Maragheh, P.O. Box 55181-83111, Maragheh, Iran.

Abstract: In this research, an effectual, novel and recyclable nanocomposite (α-Fe₂O₃@MoS₂@Ni) was synthesized and checked with spectroscopic and microscopic techniques (FT-IR, XRD, SEM, EDX and VSM). The effectiveness of α-Fe₂O₃@MoS₂@Ni nanocomposite for Fenton-like and visible light photocatalysis was investigated using the degradation of Acid Blue-113 and analysis of the process was evaluated by response surface methodology (RSM). The Acid Blue-113 was removed at the optimal conditions of pH 6.5, 5.50 mg nanocomposite, 0.5 ml H_2O_2 and 15 min (> 99%). high catalytic Function, facile synthesis and reusability of the synthesized nanocomposite makes it an excellent catalyst in order to the degradation of organic pollutants.

Keywords: Photocatalysis, Photo-Fenton, Fe₂O₃, MoS₂, Nickel, Nanocomposite

Introduction

Water pollution is a significant environmental concern worldwide, particularly due to the discharge of industrial wastewater containing various dyes. Acid Blue-113 is one such dye commonly used in textile industries, which poses a serious threat to aquatic ecosystems and human health. Therefore, effective methods for the removal of Acid Blue-113 from wastewater are urgently needed. In recent years, nanotechnology has emerged as a promising approach for water treatment due to its high efficiency and low cost. Among various nanomaterials, iron oxide-based molybdenum disulfide nanocomposites have gained considerable attention for their exceptional adsorption properties [1-3]. MoS₂-based nanocomposites have shown great potential in removing various pollutants from water, including heavy metals and organic dyes. The adsorption capacity of the Fe₂O₃-MoS₂ nanocomposite will be evaluated by conducting batch experiments under different operating conditions such as initial dye concentration, pH, contact time, and temperature. The kinetics and thermodynamics of the adsorption process will also be studied to understand the mechanism behind the removal of Acid Blue 113 by the iron oxide-based molybdenum disulfide nanocomposite. Furthermore, the effects of coexisting ions and other common pollutants present in industrial wastewater on the adsorption efficiency will be investigated. This information will help assess the feasibility of using Fe₂O₃-MoS₂ nanocomposite for large-scale wastewater treatment applications [4, 5]. Overall, this study aims to contribute to the development of efficient and sustainable methods for removing Acid Blue 113 dye from industrial wastewater. The results obtained from this research could potentially pave the way for the implementation of MoS₂ nanocomposite-based technologies in water treatment plants, leading to a cleaner and healthier environment.
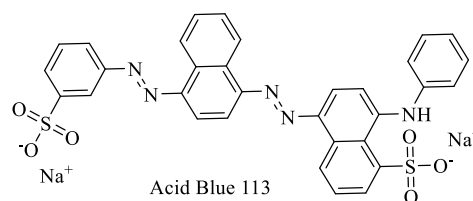
Fig.1. the structure of Acid Blue-113

Experimental Section

Synthesis of α-Fe₂O₃@MoS₂@Ni nanocomposite

α-Fe₂O₃@MoS₂@Ni nanocatalyst was synthesized according to the reported articles [1-3]. 10 mg of α-Fe₂O₃@MoS₂@Ni was stirred in 10 ml of EtOH by ultrasonic to give suspension I, Then, 40 mmol NiCl₂.6H₂O was dissolved in 15 ml pure water and then 4% diluted ammonia was dropped into the Nickel Chloride solution until the turbid solution be clear (solution II). Finally, solution II was mixed with suspension I, and the ultimate suspension was refluxed for 2 hours. The resulting product was removed using a foreign magnet 1.4 tesla, washed with hot water frequently, and dried at 100 ℃ for 6 hours at oven to give α-Fe₂O₃@MoS₂@Ni as a dark brown solid.

22nd Iranian Chemistry Congress (ICC22)
Iranian Research Organization for Science and
Technology (IROST)
13-15 May 2024

03231-97589

Results and Discussion

Preparation and characterization of the catalyst

The α-Fe_2O_3@MoS_2 was synthesized according to the resent reports [1-3]. Then, the α-Fe_2O_3@MoS_2 in EtOH (suspension I) reacted with Nickel Chloride in 4% water/NH_3 solution (suspension II) at 80 °C for 2 hours. The resulted α-Fe_2O_3@MoS_2@Ni nanomagnetic particles was prepares and purified by washing several times with pure water. The structure of the α-Fe_2O_3@MoS_2@Ni nanocomposite was spectroscopic and microscopic methods (FT-IR, XRD, EDX, SEM and VSM).

XRD analysis:

the XRD analysis of α-Fe_2O_3@MoS_2@Ni nanocomposite. The XRD analysis of α-Fe_2O_3@MoS_2@Ni shows diffraction peaks at around 2θ= 14.7°, 33.4°, 36.8° and 59.7° which are related to the MoS_2 (JCPDS card No. 37-1492). Diffraction peaks at around 2θ = 32.5°, 35.8°, 40.3°, and 49.6° are also related to the α-Fe_2O_3 (JCPDS File No. 79-0007). The peaks at 2θ = 32.7°, 35.3° and 39.4° are related to the FeS phase (JCPDS card No. 37-0477). The average size of the nanocomposite was calculated to be about 60 nm by the Scherrer equation.

SEM image

The morphology and particle size of the α-Fe_2O_3@MoS_2@Ni nanocomposite were obtained using Scanning Electron Microscope technique. According to the SEM images of α-Fe_2O_3@MoS_2@Ni nanocomposite the spherical morphology is confirmed for the nanocomposite. The obtained average size of the synthesized nanocomposite is about 65 nm.

EDX analysis

The results of EDX analysis of α-Fe_2O_3@MoS_2@Ni nanocatalyst verified the existence of Iron, Oxygen, Sulfur, Molybdenum and Nickel atoms in the nanocomposite structure.

FT-IR spectrum

In the FT-IR analysis of α-Fe_2O_3@MoS_2@Ni nanocompisite the band at 566 cm^{-1} belongs to the stretching vibration of Fe-O. The stretching vibration of Mo-O band is appeared at 1043 cm^{-1}. The broad band at 3437 cm^{-1} is related to the stretching vibrations of the O-H groups and adsorbed water.

VSM image

The VSM curve of the α-Fe_2O_3@MoS_2@Ni nanocomposite was investigated using vibrating sample magnetometer at 25℃. The results cleared that the α-Fe_2O_3@MoS_2@Ni nanocomposite could be have superparamagnetic behavior at room temperature. The magnetic properties of nanocomposite led to the easy removal and then recyclability of the catalyst trough applying an external magnet.

Conclusions

The α-Fe_2O_3@MoS_2@Ni nanocomposite was successfully synthesized in this study using a simple hydrothermal method. A new combined heterogeneous Fenton-like/visible light photocatalytic system was created by simultaneously introducing α-Fe_2O_3@MoS_2@Ni, H_2O_2, and visible light. The magnetic nanocomposite exhibited excellent catalytic performance in removing the stubborn azo dye, Acid Blue-113, and could be reused. RSM based on CCRD was effectively utilized to analyze the performance of the photo-Fenton-like process. Almost complete removal of the dye was achieved at pH 6.5, 0.5 ml H_2O_2, 5.50 mg catalyst, and 15 minutes. Under optimal conditions, the VL/α-Fe_2O_3@MoS_2@Ni/H_2O_2 system showed higher dye degradation compared to the catalyst/VL and catalyst/H_2O_2 systems, indicating a synergistic effect between Fenton-like and VL photocatalysis in generating reactive oxygen species (ROS). This research may contribute to the design of new multifunctional photocatalytic systems with outstanding catalytic activity for eliminating persistent organic pollutants.

References

[1] Yang, X., Sun, H., Zhang, L., Zhao, L., Lian, J. and Jiang, Q., (2016) High efficient photo-Fenton catalyst of α-Fe_2O_3/MoS_2 hierarchical nanoheterostructures: reutilization for supercapacitors. Scientific Reports, 6 (1) 31591, doi.org/10.1038/srep31591.

[2] Yin, M., Wang, Y., Yu, L., Wang, H., Zhu, Y., Li, C. (2020). Ag nanoparticles-modified Fe_2O_3@MoS_2 core-shell micro/nanocomposites for high-performance NO_2 gas detection at low temperature. Journal of Alloys and Compounds, 829, 154471, doi.org/10.1016/j.jallcom.2020.154471.

[3] Uma, K., Muniranthinam, E., Chong, S., Yang, T. C., Lin, J. H. (2020) Fabrication of hybrid catalyst ZnO Nanorod/α-Fe_2O_3 composites for hydrogen evolution reaction. Crystals, 10 (5), 356, doi.org/10.3390/cryst10050356.

[4] Rezaei, I., Mamaghani, M. (2021) An efficient green synthesis of polyfunctional pyrazole-triazole hybrids and bis-triazoles via chromium incorporated fluorapatite encapsulated iron oxide nanocatalyst. Current Chemistry Letters, 10 (4), 445-458,

[5] Rezaei, I., Mamaghani, M. (2021) Green synthesis of bis pyrazole-triazole and azo-linked triazole hybrids using an efficient and novel cobalt nanocatalyst. Reaction Kinetics, Mechanisms and Catalysis, 134, 385-400, doi.org/10.1007/s11144-021-02076-8.

Extraction and purification of safranal and crocin from saffron in pilot-scale

Majid Javanmard

Corresponding Author Email: javanmard@irost.ir

Department of Chemical Engineering, Iranian Research Organization for Sciece & Technology (IROST), Tehran-Iran.

Abstract: Saffron is a flowering plant with the scientific name Crocus Sativus L. According to ancient Iranian medicine, saffron is hot and dry, and in recent years, several researches have been conducted on saffron and safranal. This plant has antidepressant effects and is used to the extent of antidepressants such as fluoxetine and imipramine. Its effective ingredients, including crocin and safranal, have inhibitory properties in the treatment of cancer. In this project, safranal and crocin were extracted and chromatography and infrared spectrometry tests were performed. Safranal is the main aromatic substance of saffron, and the method used in this study was the extraction of safranal by vacuum distillation. The best solvent was 50% methanol with a ratio of 1:20 with a safranal content of 56 ppm. Also, in this study, total crocin was extracted from saffron stigmas by crystallization method. 80% ethanol was chosen as the best extraction solvent. The crystallization process was done in one and two steps.

The crocin crystals obtained from the first crystallization were of low purity, and as a result, they were subjected to the second crystallization. The purity of crocin crystals was checked using HPLC. The purity of the total crystallized crocin in this work was more than 97%. The results of the present study showed that the crystallization of crocin from saffron and the extraction of safranal from saffron cream by vacuum distillation improved the extraction from the saffron plant, and this solution can be suggested to increase the economic productivity of saffron.

Keywords: Crocin, safranal, saffron, purity percentage, crystalization

References

[1] Abdulrauf, L. B.; Sirhan, A. H.; Tan, G. H. Recent developments and applications of liquid phase microextraction in fruits and vegetables analysis. J. Sep. Sci. 2012, 35, 3540–3553.

[2] Agha-Hosseini, M., Kashani, L., Aleyaseen, A., Ghoreishi, A., Rahmanpour, H., Zarrinara, A., Akhondzadeh, S., 2008. Crocus sativus L.(saffron) in the treatment of premenstrual syndrome: a double-blind, randomised and placebo-controlled trial. BJOG: An International Journal of Obstetrics and Gynaecology 115, 515-519.

[3] Akhondzadeh, S., Fallah-Pour, H., Afkham, K., Jamshidi, A.-H., Khalighi-Cigaroudi, F., 2004. Comparison of Crocus sativus L. and imipramine in the treatment of mild to moderate depression: a pilot double-blind randomized trial [ISRCTN45683816]. BMC Complementary and Alternative Medicine 4, 1.

Low saturated fatty acid frying oil formulation by rice bran oil as a substitute for palm oil

Mohammad Mahdi Garshasbi [a], Amir Gholitabar Omrani [b] Majid Javanmard Dakheli [c*] Hila Javanmard Dakheli [c]

Corresponding author: Email: javanmard@irost.ir

[a] Laboratory Supervisor, Quality Control department, Margarine Co., Tehran, Iran.

[b] R&D laboratory Supervisor, R&D Department, Margarine Co., Tehran, Iran.

[a,c] Food Technologies Group, Department of Chemical Engineering, Iranian Research Organization for Science and Technology (IROST), Tehran, Iran.

Abstract: Because of the limitations of regulatory organizations for the saturated fatty acids content, rice bran oil, due to its desirable physical, chemical, and nutritional properties, can be a suitable alternative to palm oil. The rice bran oil as one of the components of frying oil for household consumption was studied. Modeling is by experiment design methodology (mixture design). Oxidative and chemical parameters such as smoke point, peroxide value growth, anisidine value growth, stability, and total polar materials were statistically evaluated and assessed as indicators for frying oil behavior. The optimized frying oil formulation includes 2.13% sunflower, 22.75% canola, and 75.12% rice bran oil. Insignificant differences between predicted values of the indicators and the actual ones (p <0.05) indicate the appropriate validation of the model. Therefore, rice bran oil can be good for health due to its good fatty acid profile, its special phytosterol (gamma-oryzanol), and reduced oxidative growth of the oil during frying.

Keywords: Rice bran oil, frying, experimental design, mixture design

MATERIALS AND METHODS

The oils are refined SFO, CNO, and RBO, and their specifications represent in table 1. All measured parameters are in the range of the relevant national standards.

Table 1: initial specifications of oils

oil type	acidity	moisture	Peroxide value	Anisidine value	explanation
SFO	0.042	0.01	0.1	4.1	In accordance with ISIRI 1300
CNO	0.036	0.013	0	4.6	In accordance with ISIRI 4093
SBO	0.049	0.012	0.1	3.9	In accordance with ISIRI 6658

Results and Discussion

According to the equation obtained for stability, the lowest coefficient belongs to sunflower oil. The interaction of rice bran oil with canola oil has a considerably lower effect on peroxide growth because linoleic acid is at least 50% less than sunflower oil. In other words, rice bran oil has an appreciably better performance than sunflower oil in growing peroxide.

Regarding the behavior of each oil, despite increasing the coefficients of rice bran and canola oils, they still have better performance than sunflower oil.

Conclusions

The present study showed that rice bran oil is suitable for household frying oil of its unique nutritional and chemical properties. Its stability and smoke point are higher than other conventional frying oils. Because of its good fatty acid profile, one of its most essential features represents its resistance to increasing TPM. TPM is a significant indicator of frying oil and a measure of its acceptance or disposal. The obtained optimal formulation depicts that rice bran oil is suitable for improving the oxidation parameters and can be replaced as an alternative to frying oil components.

References

[1] Amarbir K et al (2020) Changes in chemical properties and oxidative stability of refined vegetable oils during short-term deep-frying cycles, J Food Process Preserv.; 00:e14445.

[2] Li, X., Li, J., Yong, W., Cao, P., & Liu, Y. (2017). Effects of frying oils' fatty acids profile on the formation of polar lipids components and their retention in french fries over deep-frying process. Food Chemistry, 237, 98-105.

Magnetic dispersive solid phase extraction of diazinon in onion using a spherical nanostructure magnetic nanobiosorbent

Mahboube Shirani *[a], Mahboobeh Amiranipour [b], Saied Shafiei[c]

Corresponding Author E-mail: m.shirani@ujiroft.ac.ir

[a] Department of Chemistry, Faculty of Science, University of Jiroft, Jiroft, P. O. Box 7867161167, Iran.

[b] Central Library, University of Jiroft, Jiroft, 7867161167, Iran.

[c] Soil Science Department, Faculty of Agriculture University of Jiroft, Iran.

Abstract: In this research study, magnetic sporopollenin as biological polymer was prepared and used for magnetic dispersive solid phase extraction of diazinon. The effect of influential parameters was studied. At optimum conditions, the linear range of 0.1-300 $\mu g\ kg^{-1}$, LOD of 0.32 $\mu g\ kg^{-1}$ and LOQ of 0.15 $\mu g\ kg^{-1}$ were achieved. The potential of the method was evaluated in onion. The repeatability (intra–day precision (n=)) of ≤ 2.5% and reproducibility (inter–day precision, days=5, n=3) of ≤3.3 % and were appraise at two concentration levels (10 and 50 µg kg-1 of diazinon). High relative recoveries of 93.8-101.1 % confirmed high potential of the presented method.

Keywords: Diazinon; Magnetic dispersive solid phase extraction; Onion

Introduction

This There has been an incredible increase in the use of agricultural chemicals including fertilizers and pesticides to meet the food needs of billions people while substantially decreasing the proportion of the population who go hungry [1]. Despite their significant contribution to agricultural production, there is a general consensus that high applications of pesticides can increase toxins in water, soil, air, and agricultural and livestock products such as fruits, vegetables, milk and meat etc., causing immense risks to health [2]. Therefore, there have been in the past numerous attempts to qualitatively and quantitatively assay the pesticide residue in agricultural and livestock products. Solid phase extraction (SPE) as one of the most conventional extraction methods has been widely used in separation of various pollutants. There are many developments in SPE [3]. Magnetic dispersive solid phase extarction (MDSPE) is a developed form of SPE which has been used in many sceintific studies to preconcentrate and separate pollutant [4]. At this method, small amounts of the mangnetic sorbent is added to the analyte solution and after shaking, sonication, or vigoration, the sorbent will b easily separated from the medium using an external magnet. Then, the sorbent will be eluted with a suitable sorbent to desorb the analyte. Easy separation of the magnetic sorbent, short extarction time and low consumption of the sorbent are the advantages of this method [5]. In this study, magnetic sporopollenin (MSP) as biological polymer was prepared and used as the sorbent to adsorb diazinon from eggplant and determined by GC-MS. The effect of influential parameters was studied.

Experimental Section

To 20 mL sample solution in a falcon tube with the pH value of 6, 12 mg of MSP was added and vortexed intensely for 5 min. The sorbent was sedimented using an external magnet. After that, the analyte was desorbed using 100 µL acetonitril. The mixture was sonicated and after separation of the sorbent with the magnet, 2 µL of the upper phase was analyzed with GC-MS. The calibration curve was obtained through matrix match method.

Results and Discussion

text has been formatted and styled. (Font: Calibri 10) The prepared sorbent was characerized with FT-IR and SEM-EDX, and VSM. The SEM images of the sorbent is shown in Fig. 1 in which the nanostructure morphology of the magnetic sporopollenin is obvious. The effect of influential parameters including pH, amount of sorbent, extarction time, type and volume of elution solvent were investigated and the results ae shown in Fig. 2.

Fig. 1: The SEM image of MSP

22nd Iranian Chemistry Congress (ICC22)
Iranian Research Organization for Science and Technology (IROST)
13-15 May 2024

03231-97589

IROST
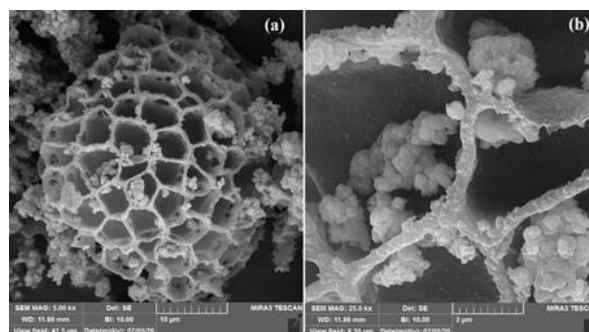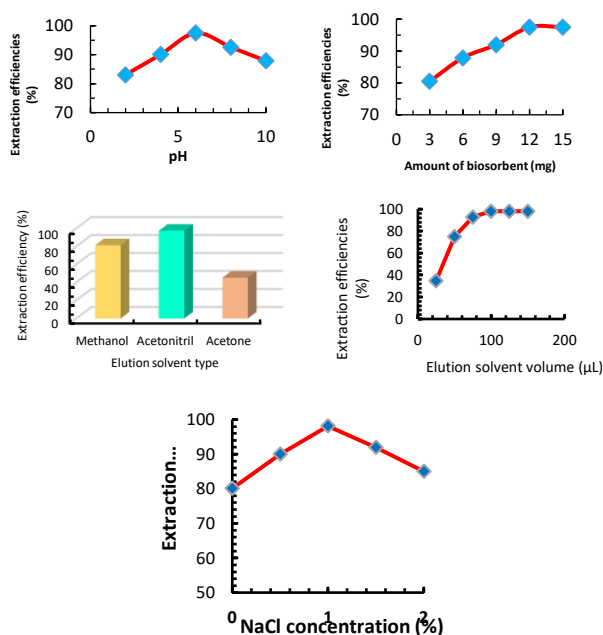
Fig. 2: The effect of influential parameters on the extraction of diazinon

The optimum conditions of pH of 6, amount of sorbent of 12 mg, acetonitrile as the elution solvent with the volume of 100 µL, and the NaCl concentration of 1 (w/v %) were obtained.

The analytical performance of the method was also investigated and the linear range of 0.1-300 µg kg^{-1}, LOD of 0.32 µg kg^{-1} and LOQ of 0.15 µg kg^{-1} were achieved. The potential of the method was evaluated in onion. The repeatability (intra–day precision (n=)) of ≤ 2.5% and reproducibility (inter–day precision, days=5, n=3) of ≤3.3 % and were appraise at two concentration levels (10 and 50 µg kg-1 of diazinon). High relative recoveries of 93.8-101.1 % confirmed high potential of the presented method.

Conclusions

In this research work, magnetic sporopollenin as an efficient nanobiosorbent were synthetized and used for magnetic dispersive SPE. At this present method, diazinon as a comon organophosphorus pesticide was separated and preconcentrated from onion and detected by GC-MS. To investigate the performance of the method and also to increase the sensitivity of the detection, all analytical parameters were achieved by matrix match methodology. Rapidity, simplicity, good linearity, low LODs and LOQs, high repeatability and reproducibility are the prevailing features of the method.

References

[1] Bagheri, V., Naseri, A., Sajedi-Amin, S., Soylak, M., & Zhang, Z. (2024). Using Fe3O4-graphene oxide-modified chitosan with melamine magnetic nanocomposite in the removal and magnetic dispersive solid-phase microextraction of Cr (VI) ion in aquatic samples. *Chemical Papers*, *78*(1), 381-396. https://doi.org/10.1007/s11696-023-03096-5

[2] Chen, R., Qiao, X., Liu, F., & Chen, X. (2023). Amino acid ionic liquid–based magnetic dispersive solid-phase extraction for benzimidazole residue analysis in fruit juice and human serum based on theoretical screening. *Food Chemistry*, *404*, 134695. https://doi.org/https://doi.org/10.1016/j.foodchem.2022.134695

[3] Płotka-Wasylka, J., Jatkowska, N., Paszkiewicz, M., Caban, M., Fares, M. Y., Dogan, A., . . . de la Guardia, M. (2023). Miniaturized Solid Phase Extraction techniques for different kind of pollutants analysis: State of the art and future perspectives – PART 1. *TrAC Trends in Analytical Chemistry*, *162*, 117034. https://doi.org/https://doi.org/10.1016/j.trac.2023.117034

[4] Shirani, M., Aslani, A., Ansari, F., Parandi, E., Nodeh, H. R., & Jahanmard, E. (2023). Zirconium oxide/titanium oxide nanorod decorated nickel foam as an efficient sorbent in syringe filter based solid-phase extraction of pesticides in some vegetables. *Microchemical Journal*, *189*, 108507. https://doi.org/https://doi.org/10.1016/j.microc.2023.108507

[5] Suseela, M. N. L., Viswanadh, M. K., Mehata, A. K., Priya, V., Vikas, Setia, A., . . . Muthu, M. S. (2023). Advances in solid-phase extraction techniques: Role of nanosorbents for the enrichment of antibiotics for analytical quantification. *Journal of Chromatography A*, *1695*, 463937. https://doi.org/https://doi.org/10.1016/j.chroma.2023.463937

Magnetic dispersive solid phase extraction of nickel and cobalt from water samples using magnetic nanofluid

Mahboube Shirani *[a], Mahboobeh Amiranipour [b]

Corresponding Author E-mail: m.shirani@ujiroft.ac.ir

[a] Department of Chemistry, Faculty of Science, University of Jiroft, Jiroft, P. O. Box 7867161167, Iran.

[b] Central Library, University of Jiroft, Jiroft, 7867161167, Iran

Abstract: In this research study, the combination of $Fe_3O_4@SiO_2$ nanocomposite as the nanostructure and a deep eutectic solvent (oceanic acid: cumarine) and dispersive solid phase extraction was used as a green method for simultaneous separation and preconcentartion of nickel and cobalt which determined by MP-AES. The effect of important parameters was studied. At optimum conditions, the linear range of 10-500 µg kg^{-1}, LOD of 3.2 and 3.1 µg kg^{-1} and LOQ of 10.5, 10.3 µg kg^{-1} were achieved for nickel and cobalt respectively. The repeatability (intra–day precision (n=5)) of ≤ 2.6 and 2.5 % for nickel and cobalt respectively and reproducibility (inter–day precision, days=5, n=3) of ≤3.3 % and were appraise at two concentration levels (50 and 100 µg kg^{-1}). High relative recoveries of 91.2-99.3 % confirmed high potential of the presented method.

Keywords: Magnetic dispersive solid phase extraction; Nickel; Cobalt

Introduction

The considerable usage of heavy metals in various industrial areas causes a great concern on environmental pollution. Heavy metals can accumulate in the environment in the stages of production, utilization and disposal [1]. As a result, this pollution may lead to serious health concerns in humans. Heavy metals such as cobalt and nickel are usually present at trace levels in environmental samples and many of them are toxic even at very low concentrations. Their main sources in the environment include domestic, industrial, agricultural and pharmaceutical effluents. However, in cases when it is not possible to use a sensitive analytical technique, the preconcentration stage is necessary. The daily intakes of 50-200 µg/day, 5-50 µg/day are recommended for nickel, cobalt respectively. Prevalent SPE suffers from large consumption of toxic organic conditioning and elution solvents, presentation of contaminated SPE sorbent to the environment, and exhausting process. Magnetic dispersive solid phase extarction (MDSPE) is a developed form of SPE which has been used in many sceintific studies to preconcentrate and separate pollutant [2]. At this method, small amounts of the mangnetic sorbent is added to the analyte solution and after shaking, sonication, or vigoration, the sorbent will b easily separated from the medium using an external magnet. Then, the sorbent will be eluted with a suitable sorbent to desorb the analyte. Easy separation of the magnetic sorbent, short extarction time and low consumption of the sorbent are the advantages of this method. In this study, magnetic nanofluid based octatonic acid: cumarin as eutectic solvent and $Fe_3O_4@SiO_2$ (MNF) which was prepared in our previous work [3], was used as the sorbent to adsorb Ni and Co from eggplant and determined by GC-MS. The effect of influential parameters was studied.

Experimental Section

To 40 mL sample solution in a falcon tube with the pH value of 8, 20 mg of MSP was added and vortexed intensely for 5 min. The sorbent was sedimented using an external magnet. After that, the analyte was desorbed using 200 µL nitric acid (0.1 mol L^{-1}). The mixture was sonicated and after separation of the sorbent with the magnet, the upper phase was analyzed with MP-AES.

Results and Discussion

To achive the highest extraction efficiencies, the influence of important factors including pH, the volume of MNF, extraction time, type and volume of desorption solvent, desorption time, ionic strength, and sample volume were considered. FT-IR, VSM, and SEM used to charazterized the synthetized MNF and the results ae shown in Fig. 2.
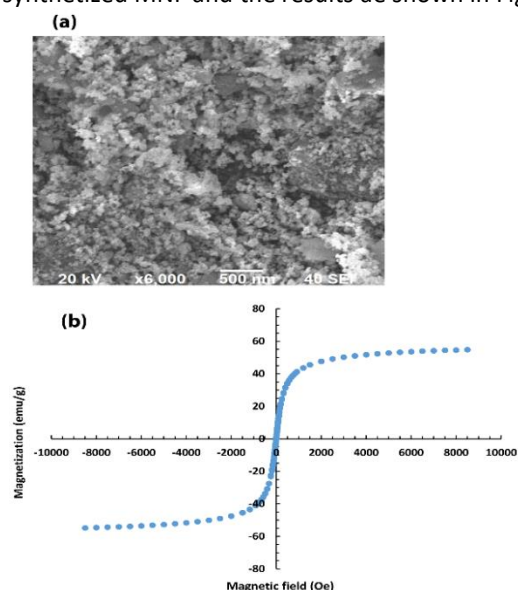
Fig. 1: The SEM image and VSM images of MNF

22nd Iranian Chemistry Congress (ICC22)
Iranian Research Organization for Science and Technology (IROST)
13-15 May 2024

03231-97589
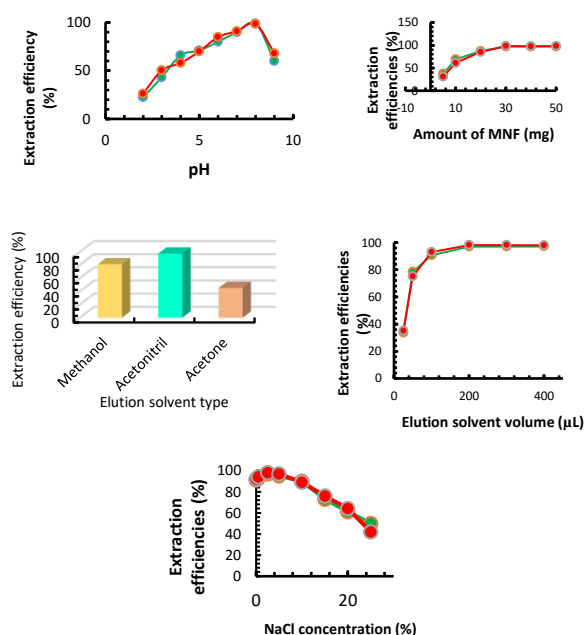
Fig. 2: The effect of influential parameters on the extraction of nickel and cobalt

The optimum conditions of pH of 8, amount of sorbent of 20 mg, nitric acid as the elution solvent with the volume of 200 µL, and the NaCl concentration of 5 (w/v %) were obtained.

The analytical performance of the method was also investigated and the linear range of 0.1-300 µg kg^{-1}, LOD of 0.32 µg kg^{-1} and LOQ of 0.15 µg kg^{-1} were achieved. The potential of the method was evaluated in onion. The repeatability (intra–day precision (n=)) of ≤ 2.5% and reproducibility (inter–day precision, days=5, n=3) of ≤3.3 % and were appraise at two concentration levels (10 and 50 µg kg^{-1}). High relative recoveries of 93.8-101.1 % confirmed high potential of the presented method.

Conclusions
In this research study, magnetic nanofluid was synthetized and used for soild phase extraction of nickel and cobalt from water samples. Environmentally-friendly analytical method owing to usage of the magnetic nanofluid, short extraction time, easy operational extraction process, low detection limit, good linearity are the significances of the proposed method.

References
[1] Hussein, A. R., Gburi, M. S., Muslim, N. M., & Azooz, E. A. (2023). A greenness evaluation and environmental aspects of solidified floating organic drop microextraction for metals: A review. *Trends in Environmental Analytical Chemistry*, *37*, e00194. https://doi.org/https://doi.org/10.1016/j.teac.2022.e00194 1016/j.microc.2023.109149

[2] Shirani, M., Faraji, M., Rashidi Nodeh, H., Akbari-adergani, B., & Sepahi, S. (2023). An efficient deep eutectic magnetic nano gel for rapid ultrasound-assisted dispersive µ-solid phase extraction of residue of tetracyclines in food samples. *Journal of Food Science and Technology*. https://doi.org/10.1007/s13197-023-05798-w

[3] Shirani, M., Salari, F., Habibollahi, S., & Akbari, A. (2020). Needle hub in-syringe solid phase extraction based a novel functionalized biopolyamide for simultaneous green separation/preconcentration and determination of cobalt, nickel, and chromium (III) in food and environmental samples with micro sampling flame atomic absorption spectrometry. *Microchemical Journal*, *152*, 104340. https://doi.org/https://doi.org/10.1016/j.microc.2019.104340

Recovery of Zinc and Copper from Brass Slag by Hydro-metallurgical Method with Selective or Cumulative Approach

Saeid Karimi [a], Bahram Behnajady [b], Javad Moghaddam [c]

Corresponding Author E-mail: s.karimi@hut.ac.ir

[a] Department of Metallurgy and Materials Engineering, Hamedan University of Technology, Hamedan, 65169-13733, Iran.

[b] Research Centre of Advanced Materials, Faculty of Materials Engineering, Sahand University of Technology, Sahand New Town, Tabriz, Iran.

[c] Department of Materials Science, Faculty of Engineering, University of Zanjan, Zanjan, 45371-38791, Iran.

Abstract: In this study, the recovery of Zn and Cu from brass furnace slag using the hydro-metallurgical method has been investigated. Sulfuric acid as a leaching agent and oxidizing agents including H_2O_2, HNO_3, and air have been employed. According to the results, selective leaching followed by cumulative leaching can be utilized as an effective method for the recovery of Zn and Cu metals.

Keywords: Zn recovery, Leach residue, Sulfate baking, Water washing.

Introduction

The brass smelting slag is a solid byproduct resulting from the recycling process of scrap brass, containing heavy metals like Zn, Cu, and Pb [1]. Numerous studies have been dedicated to enhancing the leaching of metals by hydrometallurgical recovery process for Cu and Zn from brass slag. For instance, several researchers have investigated the recovery of Cu and Zn from brass alloy slag using sulfuric acid [2–6]. The major issue with using sulfuric acid is the lack of selective dissolution of Zn and Cu. Additionally, under harsh conditions with high temperature and acidity, complete efficiency in Zn extraction is not achieved. Therefore, in this study, the dissolution of Zn and Cu in sulfuric acid was investigated in both cumulative and selective manners, using different oxidizing agents.

Experimental Section

In this study, brass slag containing 50.1% Zn and 16.3% Cu was used as the raw material. Other materials including HNO_3, H_2O_2, and sulfuric acid of laboratory purity were utilized. An L/S of 6.25 mL/g and a temperature of 70 °C were considered for brass slag leaching. The solution was agitated for 2 h in all experiments. In the first strategy, selective leaching of Zn and Cu was conducted by adjusting the pH in the range from 2.5 to 4. In the second stage of the first strategy, cumulative leaching in sulfuric acid with the addition of HNO_3 and H_2O_2 as the oxidizing agent was performed. In the second strategy, cumulative leaching was carried out using sulfuric acid and oxidizing agents including H_2O_2, HNO_3, and air.

Results and Discussion

Fig. 1 illustrates the results of the first stage of selective leaching of brass slag in sulfuric acid. According to the results shown in Fig. 1, it can be observed that the Zn efficiency decreases with increasing pH, from 85.1% at pH

2.0 to 67.8% at pH 4. A similar trend is observed for Cu. It appears that pH 3.0 is the optimal value for selective leaching, where Zn efficiency is around 80% and Cu efficiency is below 10%.
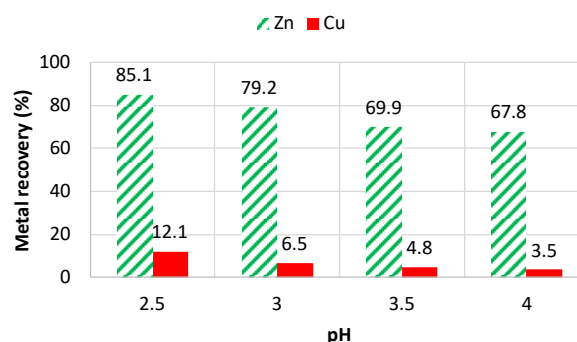
Fig. 1. Zn and Cu recovery of the first stage of selective leaching of brass slag in sulfuric acid (first strategy).

In the second stage of the first strategy, leaching of the residue from the first stage was carried out in sulfuric acid to achieve 100% efficiency for each metal by adding two oxidizing agents, HNO_3 and H_2O_2 (Fig. 2). According to Fig. 2, it can be observed that the simultaneous addition of two oxidizing agents at the amounts of 25 mL HNO_3 and 125 mL H_2O_2 brings the dissolution efficiency of Zn and Cu to 100%. This is while adding 20 mL HNO_3 and 55 mL H_2O_2 results in Zn and Cu dissolution efficiencies of 99.8% and 75%, respectively.

In the second strategy, cumulative leaching of Zn and Cu was investigated by adding various oxidizing agents. Fig. 3 illustrates the results of cumulative leaching of Zn and Cu from brass slag in sulfuric acid. It is evident from the results that without adding HNO_3 and with pH adjustment to approximately 1.5, 88.2% of Zn and 13.3% of Cu are dissolved. However, by adding HNO_3 as an oxidizing agent at a quantity of 20 mL, the Cu efficiency improved by approximately 7% and reached 20.1%. Due to the low

22nd Iranian Chemistry Congress (ICC22)
Iranian Research Organization for Science and
Technology (IROST)
13-15 May 2024

03231-97589

efficiency of Cu, oxygen purging was employed in the next stage, resulting in the recovery of 32.7% Cu and 89.4% Zn. Despite oxygen purging, satisfactory efficiency was not achieved. However, by adding 30 mL HNO$_3$ and 50 mL H$_2$O$_2$, it can be observed that Zn efficiency reached 92.6% and Cu efficiency reached approximately 51.4%. Despite the extensive use of oxidizing agents and the creation of strong leaching conditions, all Zn and Cu can not be dissolved. Therefore, the cumulative leaching method was not effective, and selective leaching was chosen as the primary option for the recovery of Zn and Cu from brass slag.
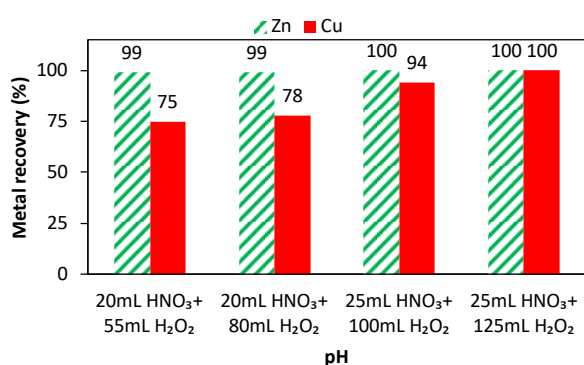
Fig. 2. Results of Zn and Cu recovery in cumulative leaching of the residue based on the first strategy.
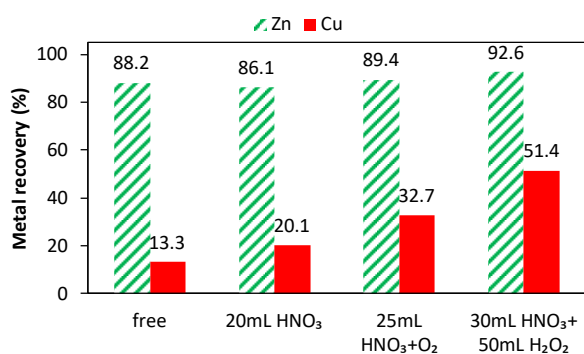
Fig. 3. Results of Zn and Cu recovery in cumulative leaching of brass slag (second strategy).

Conclusions

In this study, the dissolution of Zn and Cu was investigated in both cumulative and selective approaches with sulfuric acid as the leaching agent and different oxidizing agents. The key findings are as follows:

1. Selective leaching in the pH range of 2.5 to 4 shows a decrease in Zn and Cu efficiency with increasing pH. The optimal pH for selective dissolution was chosen as pH 3.0, and under these conditions, approximately 80% of Zn and 6.5% of Cu were dissolved.

2. Cumulative leaching of the residue from the first stage (selective leaching approach) in sulfuric acid as the leaching agent and HNO$_3$ and H$_2$O$_2$ as the oxidizing agents shows that with the addition of 25 mL of HNO$_3$ and 125 mL of H$_2$O$_2$, all Zn and Cu become soluble.

3. The results of cumulative leaching of brass slag in sulfuric acid solvent and oxidizing agents including H$_2$O$_2$, HNO$_3$, and air indicate dissolution of approximately 92.6% of Zn and 51.4% of Cu under the best conditions, which is not economically and industrially feasible.

Aknowledgement

References
[1] Xia Z, Zhang X, Huang X, Yang S, Chen Y, Ye L. Hydrometallurgical stepwise recovery of copper and zinc from smelting slag of waste brass in ammonium chloride solution. Hydrometallurgy 2020;197:105475. https://doi.org/10.1016/j.hydromet.2020.105475.

[2] Abdel Basir SM, Rabah MA. Hydrometallurgical recovery of metal values from brass melting slag. Hydrometallurgy 1999;53:31–44. https://doi.org/10.1016/S0304-386X(99)00030-4.

[3] Kilicarslan A, Saridede MN. Treatment of Industrial Brass Wastes for the Recovery of Copper and Zinc. Sep Sci Technol 2015;50:286–91. https://doi.org/10.1080/01496395.2014.952304.

[4] Martins JM, Guimarães AS, Dutra AJB, Mansur MB. Hydrometallurgical separation of zinc and copper from waste brass ashes using solvent extraction with D2EHPA. Journal of Materials Research and Technology 2020;9:2319–30. https://doi.org/10.1016/j.jmrt.2019.12.063.

[5] Shi G, Liao Y, Su B, Zhang Y, Wang W, Xi J. Kinetics of copper extraction from copper smelting slag by pressure oxidative leaching with sulfuric acid. Sep Purif Technol 2020;241:116699. https://doi.org/10.1016/j.seppur.2020.116699.

[6] Maleki F, Ghasemi S, Heidarpour A. Recycling of brass melting slag through the high-temperature oxidation-leaching process. Sustainable Environment Research 2022;32:24. https://doi.org/10.1186/s42834-022-00135-w.

Feasibility study of sulfate baking of leaching residue in the process of Zn extraction with Fe$_2$(SO$_4$)$_3$

Saeid Karimi [a], Bahram Behnajady [b], Javad Moghaddam [c]

Corresponding Author E-mail: s.karimi@hut.ac.ir

[a] Department of Metallurgy and Materials Engineering, Hamedan University of Technology, Hamedan, 65169-13733, Iran.

[b] Research Centre of Advanced Materials, Faculty of Materials Engineering, Sahand University of Technology, Sahand New Town, Tabriz, Iran.

[c] Department of Materials Science, Faculty of Engineering, University of Zanjan, Zanjan, 45371-38791, Iran.

Abstract: The study explores Zn extraction from leaching residue (LR) via sulfate baking. Results show sulfate baking enhances Zn extraction efficiency from LR, maintaining low impurity levels. Increasing Fe$_2$(SO$_4$)$_3$/LR boosts efficiency by about 15% (from 52.8% to 68.1%). Lowering S/L in washing improves Zn recovery.

Keywords: Zn recovery, Leach residue, Sulfate baking, Water washing.

Introduction

The production of Zn in Iran primarily relies on the hydrometallurgical method of dissolving oxide sources of this metal in sulfuric acid [1]. Through the optimization of dissolution parameters like temperature, time, pH, and stirring speed, approximately 95% dissolution efficiency can be achieved [2]. However, due to the incomplete separation of sulfide and oxide compounds and the presence of refractory compounds (such as Zn ferrite) in the raw material, attaining over 95% efficiency is improbable in most mineral materials [3]. Therefore, various methods have been employed to extract this portion of the mineral substance to ensure the dissolution of all Zn-containing materials. One of these methods is increasing the grinding of leaching residue (LR), aiming to enhance dissolution efficiency by reducing particle size and creating localized strain. However, this method is typically avoided due to its inability to achieve satisfactory efficiencies and high energy consumption. Another method involves sulfate baking of LR, utilizing compounds containing sulfate such as sulfuric acid [4], ammonium sulfate [5], and Fe$_2$(SO$_4$)$_3$ [6]. Therefore, in this study, the sulfate baking of LR generated from the leaching process of Zn production using Fe$_2$(SO$_4$)$_3$ has been evaluated.

Experimental Section

The LR from the Zn production process was used as the primary material for conducting the tests, the chemical analysis of which is presented in Table 1. Additionally, laboratory-grade Fe$_2$(SO$_4$)$_3$ and H$_2$SO$_4$ were used for conducting the tests.

Table 1. Chemical analysis of LR from Zn production process

Analysis	Main elements (%)			Trace elements (ppm)				
	Zn	Fe	Pb	Ni	Cd	Co	Cu	Mn
content	3.21	8.49	2.14	55	255	19	355	209

In this study, for the Zn recovery from the LR, initially, the conventional method involving washing in water with a pH of approximately 3.5 at room temperature was carried out. This experiment was conducted in comparison with the sulfate baking method under conditions of 150 g of LR in 500 mL of acidic water with a pH of 3.5. For sulfate baking, three experiments were conducted under different conditions to reduce the Zn content in the LR to below 1 wt. %. In the first test, 150 g of dried LR residue was mixed with 22 g of Fe$_2$(SO$_4$)$_3$ and then heated at 650 °C for 2 h. After cooling in the air, the resulting residue was subjected to washing in 500 mL of water without any additives for 1.5 h. The second experiment repeated the first test, with the difference in the cooling method inside the furnace. The washing step of the resulting residue was also carried out in 500 mL of water for 1.5 h. In the third experiment, instead of using LR, neutralization stage residue (NSR) was used. A quantity of 100 g of dried NSR was mixed with 15 g of Fe$_2$(SO$_4$)$_3$ and then heated at 650 °C for 2 h. After cooling, the dissolution operation in water was performed at room temperature with S/L ratios of 0.5 and 0.25 without adding any additives for 1.5 h.

Results and Discussion

In the conventional washing experiment, which involves adding 150 g of LR to 500 mL of water, the Zn content decreased from 3.2 % to 2.2 %, indicating zinc recovery of 17.9 %. Therefore, the obtained efficiency is below 20 %, which is considered relatively low. In the first baking experiment, where the LR was mixed with Fe$_2$(SO$_4$)$_3$ and subjected to sulfate baking at a temperature of 650 °C, followed by washing in water, the results were obtained as shown in Table 2. According to the obtained Zn concentration and the volume of leach liquor (LL), the Zn recovery was determined to be 52.8 %. A comparison with the conventional method reveals that the efficiency has roughly tripled, while impurities remain at normal levels.

22nd Iranian Chemistry Congress (ICC22)
Iranian Research Organization for Science and Technology (IROST)
13-15 May 2024

03231-97589

IROST

Specifically, the iron dissolution efficiency was found to be 1.4 %, indicating a negligible dissolution. Additionally, the analysis of the water-washing LR (WLR) is also provided in Table 2.

Table 2. Results of sulfate baking of LR with $Fe_2(SO_4)_3$ and water washing

Metals	Zn	Fe	Pb	Ni	Cd	Co	Cu	Mn
LL (ppm)	8200	562	3.5	20	27	2	69	67
WLR (ppm)	1.5×10^4	1.1×10^4	2.9×10^4	45	146	12	172	129

One of the important analyses in the Zn extraction process is the analysis of Zn residue in aqua regia, sulfuric acid, and water. The Zn content in the aqua regia indicates the total Zn present in the LR, while the sulfuric acid analysis shows the soluble Zn content with sulfuric acid solvent. The Zn content in water also indicates the sulfate Zn content in the residue. The lower the Zn content in aqua regia, sulfuric acid and water, the better the washing process is performed. The difference in Zn between aqua regia and sulfuric acid demonstrates a portion that is insoluble and mostly in the form of Zn sulfide. However, the difference between sulfuric acid and water indicates a lack of sulfate supply through the process. Table 3 shows the analysis of the initial LR and WLR. As observed, the Zn content in the initial LR was approximately 3.2 %, which decreased to 1.5 % with the sulfate baking process $Fe_2(SO_4)_3$, by providing sulfate and breaking the structure, also reduced its content from 2.2 to 1.3 % in the LR. However, the Zn content in water is almost similar for both.

Table 3. Chemical analysis of initial LR and LR resulting from sulfate baking and water washing

Zn (ppm)	Aqua regia	H_2SO_4	Water
Initial	32100	22300	5981
Sulfate roasting	14900	13300	6507

The repetition of the sulfate baking process in the second experiment yielded an efficiency of 62 %, which approximately confirms the results of the previous stage. In this phase, the LR resulting from the washing process was 1.3 %. However, in the third experiment, with sulfate baking followed by water washing at two S/L of 0.5 and 0.25, the Zn content in the aqua regia present in the WLR was found to be 1.5 and 0.8 %, respectively. As evident, with the reduction in the S/L, the conditions for Zn recovery have improved, resulting in a lower Zn content remaining in the final residue. The efficiencies of these two stages were 68.1 and 86.4 %, respectively.

Conclusions

In this study, the feasibility of sulfate baking of the LR from Zn production using $Fe_2(SO_4)_3$ was evaluated. The key findings are as follows:

1 -The conventional water washing process yielded an efficiency of approximately 17.9 %, which is very low.

2 -Sulfate baking of the LR, followed by water washing, results in a reduction in the Zn content in the final residue. The efficiency increased almost threefold, reaching 52.8 %.

3- Increasing the ratio of $Fe_2(SO_4)_3$ and reducing S/L during the water washing stage led to an increase in the Zn metal recovery to 86.4 %.

Aknowledgement

References

[1] Ahmadpour H-A, Eng C, Kalbasi M, Hedayati A, Ahmadpour A. Optimization of Energy and Production Process Modeling of Zn. World Appl Sci J 2010;11.

[2] Saidi M, Kadkhodayan H. Experimental and theoretical evaluation of Zn recovery from Zn oxide ore: process optimization and simulation using Aspen Plus software. International Journal of Chemical Reactor Engineering 2020;0. https://doi.org/10.1515/ijcre-2019-0187.

[3] Li Y, Liu H, Peng B, Min X, Hu M, Peng N, et al. Study on separating of Zn and iron from Zn leaching residues by roasting with ammonium sulphate. Hydrometallurgy 2015;158:42–8. https://doi.org/10.1016/j.hydromet.2015.10.004.

[4] Guler E, Seyrankaya A, Cocen I. Effect of sulfation roasting on metal extraction from Cinkur Zn leach residue. J Ore Dress 2008;10:1–10.

[5] Fekete F, Lázár K, Keszler AM, Jánosity A, Zhibin L, Szilágyi IM, et al. Recycling the industrial waste ZnFe2O4 from hot-dip galvanization sludge. J Therm Anal Calorim 2018;134:1863–72. https://doi.org/10.1007/s10973-018-7849-8.

[6] Grudinsky P, Pankratov D, Kovalev D, Grigoreva D, Dyubanov V. Comprehensive Study on the Mechanism of Sulfating Roasting of Zn Plant Residue with Iron Sulfates. Materials 2021;14:5020. https://doi.org/10.3390/ma14175020.

NO₂ Adsorption in Carbon Nanocone with Various Apex Angles by Monte Carlo Simulation

Vahid Sokhanvaran*, Mohammadbagher Ghoryani, Behzad Haghighi

Corresponding Author E-mail: sokhanvaran@neyshabur.ac.ir

Department of Physics and Chemistry, Faculty of Basic Sciences and Engineering, University of Neyshabur, Neyshabur, Iran.

Abstract: This study aimed to investigate the adsorption of nitrogen dioxide at ambient temperature and pressure range of 0.0 to 1000 kPa using Monte Carlo simulation method. At first, the NO_2 absorption in the carbon nanocone with various apex angles was investigated. The simulation results showed that the nanocone with angle of 240º has the highest amount of absorption. Therefore, this nanocone was used to continue the simulation. Also, the results indicated that the absorption isotherm of gas in nanocone is type-I, and the amount of NO_2 gas absorption in the nanocone with angle of 240º is 2.03 mmol/g under ambient conditions.

Keywords: Adsorption; Carbon Nanocone; Apex Angle; Monte Carlo

Introduction

Carbon nanocones (CNCs) have been observed since 1968 or even earlier on the surface of naturally occurring graphite. Carbon allotropes such as CNCs were proposed as possible gas storage devices [1]. According to the World Health Organization (WHO), 1 in 8 of all worldwide deaths are caused by air pollution [2]. The nitrogen oxides (NO_x), including NO_2, NO, and N_2O_4, belong to the most prominent air pollutants that originate environmental pollution and represent a health hazard for humans and animals [3]. As a result of the increasing industrialization of several developing countries, nitrogen dioxide is constantly present in the atmosphere. This gas has a high solubility in water and is colorless, non-flammable, and corrosive [2]. The presence of NO_2 in the atmosphere has a significant impact on air pollution, including acid rain, photochemical smog, greenhouse effect, and ozone layer depletion [4]. To the best of our knowledge, no known research has tested the effectiveness of NO_2 molecules adsorbing in carbon nanocone using a computational technique. Therefore, in this work, we decide to study the nitrogen dioxide adsorption in the carbon nonocone by Monte Carlo simulation.

Computational Section

The Grand Canonical Monte Carlo (GCMC) technique was used to calculate the equilibrium adsorption isotherm of NO_2 gas molecules. We keep the temperature fixed at 298.15 K. Three Monte Carlo moves, insertion, deletion, and translations, are employed with the respective probabilities being 1.0, 1.0, and 1.0. For generating the adsorption isotherms, the Monte Carlo simulations are conducted at different chemical potentials (μ) so as to span the region between 0-1000 kPa. In this thermodynamic ensemble, the temperature (T), volume (V) and chemical potential (μ) of the system are kept fixed, while the total number of molecules (N) is allowed to fluctuate. Periodic boundary conditions were applied in all three dimensions. The potential parameters for nitrogen dioxide (σ_N=3.24 Å, σ_O=2.93 Å), (ε_N=50.202 K, ε_O= 62.289 K) was taken from Ref. [5]. The number of the unit cells of CNCs adopted in the simulations is 4 × 2 × 2, so that enough molecules are accommodated to guarantee the simulation accuracy. For each state point, GCMC simulation consisted of 1×10^6 steps to guarantee equilibration followed by 1×10^6 steps to sample the desired thermodynamic properties. The multi-propose simulation code (MuSiC) of molecular simulation package was used for all simulations [6].

Results and Discussion

The adsorption was characterized by the absolute adsorption, which counts the total number of gas molecules in the CNC system expressed as adsorbed gas/carbon. At first, to investigate the effect of the angles of CNC on the amount of gas absorption, Monte Carlo simulations of the NO_2 absorption in CNC with 60º, 120º, 180º, 240º, 300º angles at temperature of 298.15 K and pressure of 1 atmosphere was done. The absorption values are given in Table (1).

Table 1: NO₂ adsorption in CNC with different angle.

Angle	60º	120º	180º	240º	300º
NO₂ Adsorbed (mmol/g)	1.04	1.26	1.72	2.03	0.043

The results of Table 1**,** show that the highest amount of nitrogen dioxide gas absorption is in the CNC with an angle of 240º. So based on this result, a CNC with 240º was used to continue the simulation of NO_2 absorption. In order to investigate the gas adsorption capacity at about room temperature, the simulated adsorption isotherms of NO_2 in the CNC in the range of 0–1000 kPa at 298.15 K are presented in Figure 1.

22nd Iranian Chemistry Congress (ICC22)
Iranian Research Organization for Science and Technology (IROST)
13-15 May 2024

03231-97589
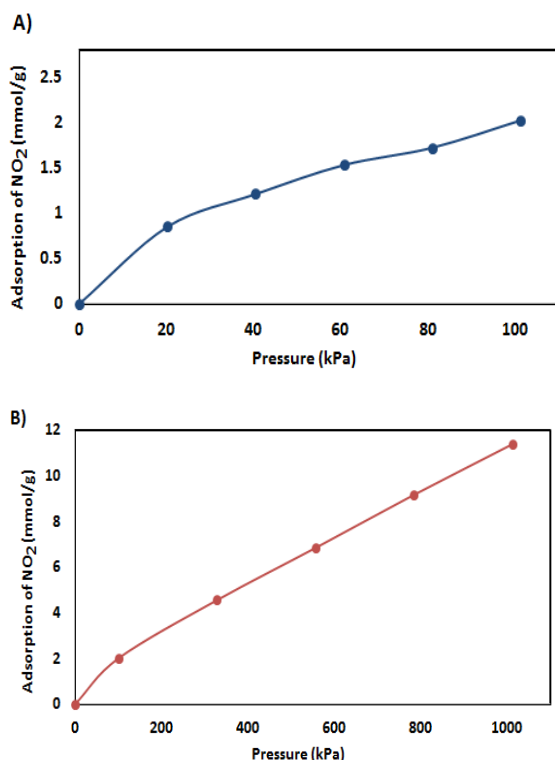
Fig. 1: The simulated adsorption isotherms of nitrogen dioxide in CNC at A) 0-100 kPa and B) 100-1000 kPa.

As can be seen from Figure 1, the highest adsorption capacity at low pressure is 2.03 mmol/g and at high pressures is 11.37 mmol/g. Also, the adsorption behavior revealed a type-I isotherm indicating a microporous material.

Conclusions

In this research, we calculated the adsorption isotherms of nitrogen dioxide in the CNC using Monte Carlo simulation. Our results showed that, 1) The comparison of absorption in CNCs with different angles showed that the CNC with a vertex angle of $240°$ is the most suitable for NO_2 adsorption. 2) The maximum amount of NO_2 absorption in the CNC with a vertex angle of $240°$ is 11.37 mmol/g at 1000 kPa and 298.15 K.

References

[1] Nazeer, W., Farooq, A., Younas, M., Munir, M., & Kang, S. M. (2018). On molecular descriptors of carbon nanocones. Biomolecules, 8(3), 92. https://doi.org/10.3390/biom8030092

[2] Seehamart, K., Busayaporn, W., & Chanajaree, R. (2023). Molecular adsorption and self-diffusion of NO_2, SO_2, and their binary mixture in MIL-47 (V) material. RSC advances, 13(28), 19207-19219. https://doi.org/10.1039/D3RA02724D

[3] Chokbunpiam, T., Chanajaree, R., Caro, J., Janke, W., Remsungnen, T., Hannongbua, S., & Fritzsche, S. (2019). Separation of nitrogen dioxide from the gas mixture with nitrogen by use of ZIF materials; computer simulation studies. Computational Materials Science, 168, 246-252. https://doi.org/10.1016/j.commatsci.2019.05.025

[4] Muhammad, A. A., & Umar, U. (2022). Adsorption of SO_2 and NO_2 on ZrO_2 (1 1 0) surface: Density functional theory and molecular dynamic simulation studies. Journal of Chemistry Letters, 3(3), 135-143. https://doi.org/10.22034/JCHEMLETT.2023.363900.1088

[5] Thompho, S., Fritzsche, S., Chokbunpiam, T., Remsungnen, T., Janke, W., & Hannongbua, S. (2021). Adsorption and the chemical reaction $N_2O_4 \leftrightarrow 2NO_2$ in the presence of N_2 in a gas phase connected with a carbon nanotube. ACS omega, 6(27), 17342-17352. https://doi.org/10.1021/acsomega.1c01459

[6] Gupta, A., Chempath, S., Sanborn, M. J., Clark, L. A., & Snurr, R. Q. (2003). Object-oriented programming paradigms for molecular modeling. Molecular Simulation, 29(1), 29-46. https://doi.org/10.1080/0892702031000065719

22nd Iranian Chemistry Congress (ICC22)
Iranian Research Organization for Science and Technology (IROST)
13-15 May 2024

03231-97589

Temperature Effect on the SO₂ Adsorption in Carbon Nanocone by GCMC Simulation

Vahid Sokhanvaran*, Mohammadbagher Ghoryani, Behzad Haghighi

Corresponding Author E-mail: sokhanvaran@neyshabur.ac.ir

Department of Physics and Chemistry, Faculty of Basic Sciences and Engineering, University of Neyshabur, Neyshabur, Iran.

Abstract: Sulfur oxides (SO_2) is principal pollutant in the atmosphere due to its harmful impact on human health and environment. We used Grand Canonical Monte Carlo (GCMC) molecular simulations to study SO_2 gas adsorption in carbon nanocone. To investigate the effect of temperature on the amount of gas absorption in the nanocone, the simulations were performed at 348.15, 298.15 and 248.15 K temperatures. The results indicated that as the temperature was increased, the amount of gas absorption decreased.

Keywords: Temperature; Simulation; Adsorption

Introduction

Gases that contain sulfur are the most harmful and highly toxic. Most pollution in the form of carbon and sulfur emissions comes from burning fossil fuels such as coal, petroleum, natural gas processing, and natural sources. Sulfur dioxide is a major atmospheric pollutant that contributes to acid rain and has substantial impacts on human health, terrestrial, aquatic ecosystems and industrial gas post-processing. Researchers have recently made considerable experimental and computational attempts to explore the effective removal of SO_2 from gaseous emissions and mixtures. Their efforts showed that adsorption within porous materials has been shown to be one effective approach for capturing gases [1]. The excessive emissions of pollution gas to the atmosphere will lead to the formation of acid rain that does not only have a serious impact on the environment, but also raises a great threat to human health. Therefore, the removal of SO_2 from flue gas becomes a key issue for protecting air environment [2]. Solid adsorbents present a promising alternative to wet desulfurization units, as they can be regenerated without release into the environment. In the literature, there are several experimental studies investigating adsorbents such as activated carbons zeolites, and MOFs, for the removal of sulfur gases from flue gas [3]. However, to the best of our knowledge, molecular simulations studies were mostly focused on carbon capture, and much less attention has been given to the removals of SO_2. The above mentioned, has motivated us to investigate the adsorption of SO_2 toxic gas in carbon nanocone (CNC) using Monte Carlo simulation.

Computational Section

The calculated adsorption equilibrium of sulfur dioxide in the carbon nanocone was carried out in the grand canonical Monte Carlo ensemble by means of a typical Metropolis algorithm for the importance sampling of the configuration space. The sorption isotherm was obtained by computing averages of the number of sorbate molecules, N, over a large number of equilibrated configurations, as a function of the fugacity. GCMC simulations were performed using the multipurpose simulation code (MuSIC) [4]. The CNC structure was treated as rigid with frozen atoms during simulation. The relative frequencies of displacement, insertion, and deletion moves were 1:1:1, respectively. Simulation cells consisted of 16 supercells were created for carbon nanocone structure. Lorentz-Berthelot combining rules were used to calculate the Lennard-Jones cross-parameters for all gas-nanocone interactions with a short-range cutoff radius of 16.4 Å. Electrostatic interactions were taken into consideration. A total of 2 million moves were performed in each simulation; the first half of these moves were used for equilibration and were not included when calculating gas loadings. The Lennard-Jones (LJ) parameters with partial charges which follow equation (1),

$$U(r_{ij}) = 4\varepsilon_{ij}\left[\left(\frac{\sigma_{ij}}{r_{ij}}\right)^{12} - \left(\frac{\sigma_{ij}}{r_{ij}}\right)^{6}\right] + \frac{1}{4\pi\varepsilon_0}\frac{q_iq_j}{r_{ij}} \qquad (1)$$

Where ε_{ij} is the well depth, σ_{ij} is the LJ distance, and r_{ij} is the distance between two interacting atoms i and j. The potential parameters between two different species were obtained from the Lorenz-Berthelot mixing rule written as equations (2) and (3)

$$\sigma_{ij} = \frac{(\sigma_{ii}+\sigma_{jj})}{2} \qquad (2)$$

$$\varepsilon_{ij} = \sqrt{\varepsilon_{ii}\varepsilon_{jj}} \qquad (3)$$

The (LJ) parameters with partial charges are summerized in Table 1.

Table 1. The LJ Parameters of SO₂ [5] and CNC [6].

Molecules	Atom	σ (Å)	ε (K)	Charge
SO₂	S	3.585	154.4	0.47
	O	2.993	62.3	-0.235
CNC	C	3.4	28.2	0.0

Results and Discussion

The GCMC simulation adsorption isotherm of SO₂ results in CNC in the range of 0–100 kPa at 248.15, 298.15 and 348.15 K temperatures, are depicted in Figure 1.
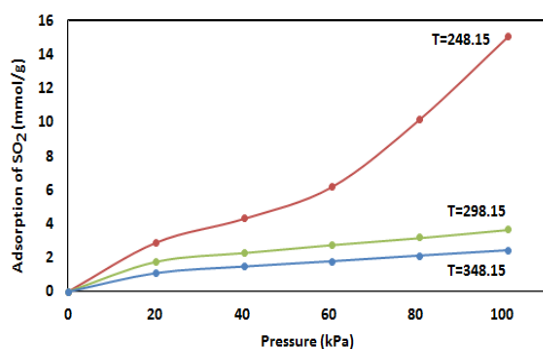
Fig.1: The simulated adsorption isotherms of SO₂ on carbon nanocone at 248.15, 298.15 and 348.15 K.

It is obvious that the sulfur dioxide adsorption amounts in the CNC decreased with increasing temperature. So, at the temperature of 348.15 K, the lowest amount of absorption has taken place. The maximum amount of simulated absorption for SO₂ is 15.06 mmol/g at 248.15 K temperature. The amount of SO₂ adsorbed on CNC at 100 kPa and 248.15 K is 4.1 times that of 298.15 K and 6.2 times that of 348.15 K.

Conclusions

We have presented a detailed simulation study of SO₂ adsorption at 248.15, 298.15, and 348.15 K in CNCs. It is found that the adsorption isotherm curves for SO₂ adsorption at 348.15 and 298.15 temperatures in CNC are of type-I and 248.15 K is of type-V according to the IUPAC classification.

References

[1] Zhang, D., Jing, X., Sholl, D. S., & Sinnott, S. B. (2018). Molecular simulation of capture of sulfur-containing gases by porous aromatic frameworks. The Journal of Physical Chemistry C, 122(32), 18456-18467. https://doi.org/10.1021/acs.jpcc.8b03767

[2] Li, Z., Liao, F., Jiang, F., Liu, B., Ban, S., Chen, G., ... & Sun, Y. (2016). Capture of H₂S and SO₂ from trace sulfur containing gas mixture by functionalized UiO-66 (Zr) materials: A molecular simulation study. Fluid Phase Equilibria, 427, 259-267. https://doi.org/10.1016/j.fluid.2016.07.020

[3] Jacobs, J. H., Chou, N., Lesage, K. L., Xiao, Y., Hill, J. M., & Marriott, R. A. (2023). Investigating activated carbons for SO₂ adsorption in wet flue gas. Fuel, 353, 129239. https://doi.org/10.1016/j.fuel.2023.129239

[4] Gupta, A., Chempath, S., Sanborn, M. J., Clark, L. A., & Snurr, R. Q. (2003). Object-oriented programming paradigms for molecular modeling. Molecular Simulation, 29(1), 29-46. https://doi.org/10.1080/0892702031000065719

[5] Peng, X., Jain, S. K., & Singh, J. K. (2017). Adsorption and separation of N₂/CH₄/CO₂/SO₂ gases in disordered carbons obtained using hybrid reverse Monte Carlo simulations. The Journal of Physical Chemistry C, 121(25), 13457-13473. https://doi.org/10.1021/acs.jpcc.7b01925

[6] Gotzias, A., Heiberg-Andersen, H., Kainourgiakis, M., & Steriotis, T. (2010). Grand canonical Monte Carlo simulations of hydrogen adsorption in carbon cones. Applied Surface Science, 256(17), 5226-5231. https://doi.org/10.1016/j.apsusc.2009.12.108

Effect of light stress on *Spirulina platensis* productivity and phycocyanin and chlorophyll content

Raziyeh Rostami, Hossein Delavari Amrei*, Hamed Azami

Corresponding Author E-mail: h.delavari@ub.ac.ir

Department of Chemical Engineering, Faculty of Engineering, University of Bojnord, Bojnord, Iran.

Abstract: *Spirulina* is one of the microalgae that has been widely used in the food, cosmetic and pharmaceutical industries. Like all organisms, the application of various stresses can affect the growth rate and intracellular content of *spirulina*. In this research, *Spirulina platensis* microalgae was exposed to light shock after a 6-day growth period, and the light intensity was increased from 2000 lux to 6000 lux. The results showed that due to the applied stress, Biomass productivity decreased by about 10%. Of course, the beginning of this decrease happened almost on the 8th day. Also, the content of phycocyanin decreased by 40% due to stress. However, the results related to chlorophyll content showed an increase of about 10%.

Keywords: *Spirulina* ; light stress; biomass; phycocyanin

Introduction

Adaptation is the process by which all living forms attain the ability to sustain in the changing environment. Bacteria, algae, fungi, protistans, and micro-invertebrates live in almost all of the habitats available on Earth, from the so-called 'normal ambient' environments to the harshest places [1]. Microalgae have an incredible ability to adapt to these abnormal ambients. Such environments are also known as 'stress' that pushes the entity to undergo physiological and chemical changes to thrive in the changing environment [2].

Light with appropriate wavelength and intensity can also be one of the key factors that affect or control biomass production. Manipulation of light intensity changes the types and levels of secondary metabolites such as phenols and flavonoids, which in turn affect antioxidant activities [3].

Various researches have been conducted on the effect of light intensity and light stress on the growth of microalgae [4-6].

In this research, microalgae *Spirulina platensis* was placed under 24/0 light cycle, and the light intensity was increased three times during the growth period, so that the microalgae was under stress caused by light intensity, and its growth rate, chlorophyll and phycocyanin content were investigated.

Experimental Section

Prepare the culture medium:
NaHco3, NaCl, NaNo3, K2Hpo4, CaCl2, MgSo4, FeSo4, EDTA, H3Bo3, MnCl2, ZnSo4, Na2moo4, Cuso4 along with spirulina platensis at a temperature of 25 degrees Celsius and an approximate pH of 9.5 in a 2000 liter container and placed in 1 Erlenmeyer flasks. We poured one liter under the same conditions with the same amount of ventilation as the white LED lamps under the light intensity of 2000 Lux and light/dark cycle 24/0. After 6 days, one of the samples was placed under light stress and the intensity of on it increased to 6000 lux. In Table 1, culture condition for different sample is presented.

Table 1. Different samples condition.

sample	Light intensity (lux)	
	Until the 6th day	After the 6th day
1	2000	2000
2	2000	6000

Measurement of phycocyanin:
The extraction of phycocyanin protein was done by sodium hydrogen phosphate as buffer solution. Phycocyanin concentration was estimated using equation 1:

$$C_{pc} = \frac{A_{620} - 0.474 A_{652}}{5.34} \qquad (1)$$

A_{620}: Absorption at 620 nm for supernatant liquid

A_{652}: Absorption rate at 652 nm for supernatant liquid that the concentration of phycocyanin is obtained in terms of mg/ml.

Measuring the content of chlorophyll-a:
The extraction of phycocyanin protein was done by methanol as chlorophyll solvent. Finally, to determine the amount of chlorophyll-a, the absorbance of the obtained sample was obtained at wavelengths of 666 and 653 nm using a UV/Vis spectrophotometer and obtained from equation 2:

$$\text{Cholorophyll} - a = 11.75 \times OD_{666} - 2.350 \times OD_{653} \qquad (2)$$

22nd Iranian Chemistry Congress (ICC22)
Iranian Research Organization for Science and Technology (IROST)
13-15 May 2024

03231-97589

Results and discussion:
Time course for *Spirulina* growth for different sample is presented in Fig. 1. Until the sixth day, both samples have shown almost the same growth. Due to the application of the shock on the sixth day, the growth for the samples has changed from the following days. Although the light intensity for sample 2 has increased from 2000 lux to 6000 lux, but its growth rate is lower than that of sample 1, that is, the sample whose light intensity remains at 2000 lux. In fact, application of shock has decreased the growth of *Spirulina plaensis* with a 3-fold increase in light.
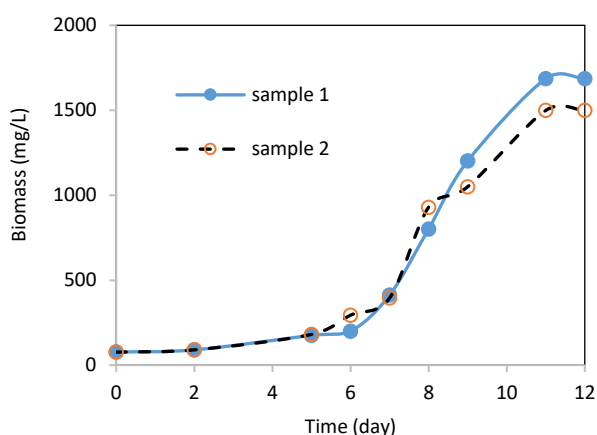
Fig. 1. Time course of growth for sample 1 and 2.

Results in Table 2 shows that applying the shock has caused biomass productivity to decrease by 10%. Also, phycocyanin content has decreased by about 40%, but in any case, chlorophyll content has increased by about 15%. It seems that the application of shock caused the destruction or lack of production of phycocyanin molecules in the cells. Regarding chlorophyll, it can be said that due to the increase in light intensity, cells have shown a greater tendency to produce chlorophyll-a.

Table 2: Productivity and chlorophyll-a and phycocyanin cotent for different sample.

Sample	Productivity (mg L^{-1} day^{-1})	Cholorophyll-a (g-Chla/g-algae %)	Phycocyanin (g-phyco/g-algae%)
1	134	0.6	10.0
2	119	0.7	6.1

Conclusions
Every organism experiences stress, although the way in which it is expressed differs according its level of organisation. From the botanist's point of view, stress can be described as a state in which increasing demands made upon a plant lead to an initial destabilization of functions, followed by normalization and improved resistance [7]. If the limits of tolerance are exceeded and the adaptive

capacity is overtaxed, permanent damage or even death may result. The results of this research showed that the application of light stress reduced the growth of *Spirulina* platensis. Of course, more research is needed to investigate other light intensities. Also, the content of phycocyanin has decreased under the influence of stress. However, the chlorophyll content has increased.

References
[1] Woese, C.R., O. Kandler, and M.L. Wheelis, *Towards a natural system of organisms: proposal for the domains Archaea, Bacteria, and Eucarya.* Proceedings of the National Academy of Sciences, 1990. **87**(12): p. 4576-4579.

[2] Borowitzka, M.A., *The 'stress' concept in microalgal biology—homeostasis, acclimation and adaptation.* Journal of applied phycology, 2018. **30**: p. 2815-2825.

[3] Chojnacka, K. and A. Noworyta, *Evaluation of Spirulina sp. growth in photoautotrophic, heterotrophic and mixotrophic cultures.* Enzyme and microbial technology, 2004. **34**(5): p. 461-465.

[4] Chen, Y.-C., *The effect of shifts in medium types on the growth and morphology of Spirulina platensis (Arthrospira platensis).* Journal of Marine Science and Technology, 2011. **19**(5): p. 13.

[5] Bachchhav, M.B., M.V. Kulkarni, and A.G. Ingale, *Enhanced phycocyanin production from Spirulina platensis using light emitting diode.* Journal of The Institution of Engineers (India): Series E, 2017. **98**: p. 41-45.

[6] Zhang, X.-W., Y.-M. Zhang, and F. Chen, *Application of mathematical models to the determination optimal glucose concentration and light intensity for mixotrophic culture of Spirulina platensis.* Process Biochemistry, 1999. **34**(5): p. 477-481.

[7] Borowitzka, M.A., The 'stress' concept in microalgal biology—homeostasis, acclimation and adap. Journal of Applied Phycology, 2018. 30, 2815–2825.

22nd Iranian Chemistry Congress (ICC22)
Iranian Research Organization for Science and Technology (IROST)
13-15 May 2024

03231-97589

IROST

The effect of magnetic field produced by neodymium magnets on the productivity and chlorophyll content of *Spirulina platensis*

Mahdi Yazdani [a], Hossein Delavari Amrei [*a], Ebrahim Mohammadi Razi [b]

Corresponding Author E-mail: h.delavari@ub.ac.ir

[a] Department of Chemical Engineering, Faculty of Engineering, University of Bojnord, Bojnord, Iran.

[b] Department of Physics, Faculty of Basic Sciences, University of Bojnord, Bojnord, Iran.

Abstract: Magnetic fields affect the metabolism of microorganisms such as microalgae. These fields have their effect on the speed of photosynthesis and the percentage composition of macromolecules inside the cell and can be inhibitory, stimulating and ineffective on the growth of microorganisms. For this purpose, in the present study, the biomass productivity and chlorophyll content of *Spirulina platensis* under a static magnetic field of 2.5 mT in cylindrical photobioreactors was investigated. The obtained results showed that the static magnetic field with an intensity of 2.5 mT increased the biomass productivity by 38%. However, no change was observed in the chlorophyll-*a* content.

Keywords: Magnetic field; Microalgae; Productivity; Chlorophyll content

Introduction

Spirulina are among the most important species that are an excellent source of proteins, carbohydrates and vitamins, which have found a special place in the human diet due to their high nutritional value [1]. Recently, magnetic field has been used in the growth process of different types of microorganisms. Numerous studies have shown differences in cell behavior when cells are exposed to magnetic fields [2-5]. that their effect may be positive or negative in growth processes and changes in metabolism, based on the findings, these changes depend on the frequency, intensity and time of performance. The potential link between the magnetic field and its effect on living organisms is that it causes oxidative stress, that is, MF can change the energy levels and direction of electron spin, thus increasing the activity, concentration, and lifetime of free radicals [2] The use of magnetic field has advantages such as being cheap, simple to use, non-toxic and non-toxic. The present study aims to evaluate the effect of medium intensity magnetic field, which is created using neodymium magnets, on the growth and biomass production of *Spirulina platensis*. The chlorophyll content has also been investigated.

Experimental Section

Microorganism: In this research, the microalgae Spirulina platensis was used, which was obtained from the Scientific and Industrial Research Organization of Iran (IROST) and cultivated in Zaruk's culture medium.

Construction of photobioreactor and cultivation of microalgae: To investigate the effect of magnetic field, two cylindrical photobioreactors with a volume of 250 cc were used, one as a test sample and the other as a control, on one of them there were 16 neodymium magnets with a certain and equal distance and the effect of the field. A static magnet with an intensity of 2.5 millitesa (mT) was installed and 16 pieces of foil with the same size were placed on top of each other to equalize the conditions. The diameter of the cylinders was 3.75 cm and the active height of cultivation was 25 cm. Each cylinder was filled with 210 ml of culture medium and 40 ml as inoculum. Both photobioreactors were used with the same aeration and the same light intensity of 6000 lux.

Growth measurement: To measure the amount of growth and biomass, samples were taken every day and OD at 680 nm entered in the following formula that gives us the amount of dry weight:

$$X\left(\frac{mg}{L}\right) = 666.5\, OD_{680} + 56.7$$

Measurement of chlorophyll: To measure the amount of chlorophyll on the first day of cultivation, 5 cc was removed from the original cultured sample, and after centrifugation and complete sedimentation of the microalgae, the clear liquid above it was removed, then the same amount of the removed yeast was added to the distilled water. After complete mixing, it was placed in a centrifuge, after the clear liquid settled on top, it was removed and the same amount of methanol was added to it to reach a volume of 5 cc, and it was placed on a shaker for 5 minutes until Mix completely, the sample was placed in the refrigerator for 24 hours, then after 24 hours, the sample was centrifuged to separate the remaining solids from the color of the seed. Finally, to determine the amount of chlorophyll, the sample was placed in the spectrophotometer. The absorbance was at

22nd Iranian Chemistry Congress (ICC22)
Iranian Research Organization for Science and Technology (IROST)
13-15 May 2024

ISC
03231-97589

IROST

666 wavelengths. nm and 653 nm were recorded and placed in the following formula:

$$Cholorophyll - a = 11.75 \times OD_{666} - 2.350 \times OD_{653}$$

Results and Discussion

The effect of a static magnetic field with an intensity of 2.5 millitesla on the growth and amount of chlorophyll production of spirulina microalgae was investigated and the results showed that applying this field on the microalgae significantly increased the amount of biomass production. Time course for cell growth is shown in Fig. 1. Also, bimass productivity and chlorophyll content are presented in Table 1. The results showed biomass productivity under the magnetic field increased by 38%. As a result, this method can be used as an effective method to increase the amount biomass. In fact, the magnetic field activates the ions and the polarization of bipolars has a great effect in the cell. The materials inside the culture medium are dissolved in the form of ions and the magnetic field increases the activity of these ions, as a result, it causes the microalgae to use more of the materials in the culture medium, and this increases the growth and production of biomass [2]. Also, the concentration of chlorophyll has increased in the culture medium under the magnetic field. This phenomenon was due to the increase in the growth rate in the sample under the magnetic field. But checking the chlorophyll content, as shown in Table 1, shows that the intracellular chlorophyll content has not changed.
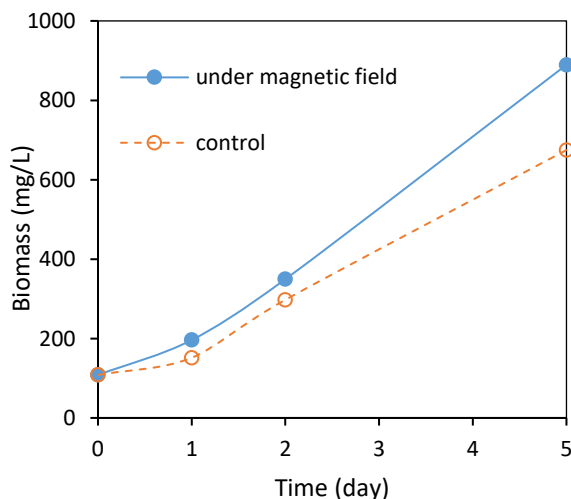
Fig. 1: Time course for cell growth

Table1: biomass productivity and chlorophyll content.

sample	Productivity (mg L^{-1} day^{-1})	Chlorophyll-a content (g-chl/g-algae %)
control	113.3	0.35
Under MF	156.2	0.36

Conclusions

Studies have shown that the use of a magnetic field in the cultivation of microalgae has a significant effect on the growth as well as the production of biological compounds. However, the effects of this application may stimulate or inhibit the growth and production of biological compounds. In order to obtain acceptable results, for each type of microalgae, the intensity and type of field, the time of exposure to the field, the length of the cultivation period and the devices used to apply this field must be evaluated. In the current project, the static magnetic field used has increased the growth of *Spirulina platensis*. However, no change was observed in the chlorophyll-*a* content. Considering that the application of the field does not introduce any chemical substances into the environment, then this technology is a zero-emission technology in this field.

References:

[1] Khan, Z., Bhadouria, P., and Bisen, P. S., Nutritional and Therapeutic Potential of Spirulina. Current Pharmaceutical Biotechnology, 2005. 6(5): 373-379.

[2] Nemani, N., Delavari Amrei, H., Yazdani, M., The effects of static magnetic field on the growth of microalgae Nannochloropsis and Spirulina in a bubble column photobioreactor and investigation on the growth models. Journal of Aquaculture Science, 2022. 10(2): 47-57

[3] Font, Y.S. et al., The effect of magnetic field treatment on the cultivation of microalgae: An overview of involved mechanisms. Journal of applied phycology, 2023. 35: 1525–1536.

[4] Moon, J.-D. and H.-S. Chung, *Acceleration of germination of tomato seed by applying AC electric and magnetic fields.* Journal of electrostatics, 2000. **48**(2): 103-114.

[5] Pilla, A., D. Muehsam, and M. Markov, *A dynamical systems/Larmor precession model for weak magnetic field bioeffects: Ion binding and orientation of bound water molecules.* Bioelectrochemistry and Bioenergetics, 1997. **43**(2): 239-249.

Chemical Reactivity of Amrinone's Tautomers: A Theoretical DFT Study Using Fukui Functions Analysis

Azimeh Davarpanah, Amir Abdolmaleki*

Corresponding Author E-mail: abdolmaleki@shirazu.ac.ir

Department of Chemistry, College of Sciences, University of Shiraz, Shiraz, Iran.

Abstract: In this article, the cardiovascular disorders' drug amrinone was studied by DFT/B3LYP/6-311++G(d,p) to investigate its tautomers' local and global chemical reactivity through Fukui functions and dual descriptors analysis. The results indicated that tautomer C has more chemical reactivity than others. The findings suggest amrinone's potential applications in new fields.

Keywords: Amrinone; Chemical reactivity; Fukui functions

Introduction

Amrinone, also known as inamrinone, is a bipyridine lactam that may improve the prognosis of individuals suffering from congestive cardiovascular disorders. [1,2] This I-class cardiotonic inotropic drug increases cellular levels of cyclic adenosine monophosphate (cAMP) by blocking the phosphodiesterase (PDE3) enzyme. [1,2] Heart failure and stroke have become the most frequent diseases nowadays, and amrinone plays an important role in the prevention or control of them. [1,2]

The X-ray crystallographic studies in other literature illustrated that the amrinone molecule was found to be almost planar in the crystalline state. [2] However, significant structural differences have been suggested for the solution state compared to the crystalline phase, leading to a twisted structure. [2] Also, theoretical abinitio studies of this compound's tautomers have indicated the existence of a significant and non-negligible difference in their structural energy and electronic properties. [1,2]

Despite what has been mentioned, there have not been any complete, accurate, and reliable studies that have investigated and compared the local and global chemical reactivity of amrinone's tautomers. This is very important for targeting this compound to be used in various chemical, industrial, and pharmacological novel applications.

In this article, we have investigated amrinone's three stable tautomers by Fukui functions and dual-descriptors analysis of frontier orbitals to study the local and global chemical reactivity parameters. The theoretical quantum study was executed in this work based on DFT theory using the Gaussian 09 suite of programs [3], B3LYP method, and 6-311++G(d,p) basis set.

Results and Discussion
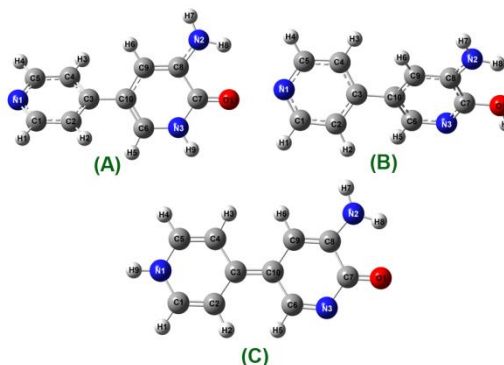
Fig.1: The structural energy and geometric optimization of amrinone's three stable tautomers

The results of quantum theoretical calculations for geometric-energic optimization of amrinone tautomers based on DFT/B3LYP/6-311++G(d,p) (**Fig.1**) illustrated that the tautomer C is almost flat, unlike other tautomers of this compound.

The theoretically calculated global chemical reactivity parameters for all three amrinone's tautomers (**Table 1**) indicated that tautomer B is the most stable and tautomer C is the most unstable form of the compound. Also, tautomer C has a much lower HOMO-LUMO gap of energy ($\Delta E_{LUMO-HOMO}$) in comparison with the other tautomers, and this tautomer is placed in the range of semiconductors with low electrical resistance, unlike others. This low gap of energy is related to the more stable LUMO and much more unstable HOMO orbitals compared to the other tautomers. Also, tautomer C has a higher electrophilicity and nucleophilicity index than the other tautomers simultaneously.

22nd Iranian Chemistry Congress (ICC22)
Iranian Research Organization for Science and Technology (IROST)
13-15 May 2024

03231-97589

ISC

IROST

Table 1: Global chemical reactivity parameters from theoretical DFT/B3LYP/6-311++G(d,p) calculations for all three amrinone's tautomers.

Chemical reactivity parameters	Unite	Amrinone's tautomers		
		A	**B**	**C**
Total electronic energy (E):	(eV)	-17033.2859	-17033.0459	-17032.1347
Energy of HOMO (E_{HOMO}):	(eV)	-5.2055	-5.4599	-4.3911
Energy of LUMO (E_{LUMO}):	(eV)	-1.0561	-1.0142	-1.8835
HOMO-LUMO gap of Energies ($\Delta E_{LUMO-HOMO}$):	(eV)	4.1494	4.4457	2.5076
Vertical ionization potential (IP):	(eV)	7.0802	7.3339	6.0991
Adiabatic ionization energy (IEA):	(eV)	-0.6622	-0.7089	0.2218
Electronegativity (χ):	(eV)	3.2090	3.3125	3.1604
Chemical potential (μ):	(eV)	-3.2090	-3.3125	-3.1604
Global hardness(η):	(eV)	7.7424	8.0427	5.8773
Global softness (S):	(eV^{-1})	0.1292	0.1243	0.1701
Electrophilicity index (ω):	(eV)	0.6650	0.6822	0.8497
Nucleophilicity index (N):	(eV)	3.9157	3.6613	4.7301

The presented results of the theoretical calculations in **Fig.2** and **3** indicated that the highest condensed local electrophilicity and nucleophilicity indexes are related to "N1" and "O1" atoms for tautomer A, were detected at "N1" and "N2" atoms of tautomer B, and were observed at "O1" and "N2" atoms in tautomer C, respectively.
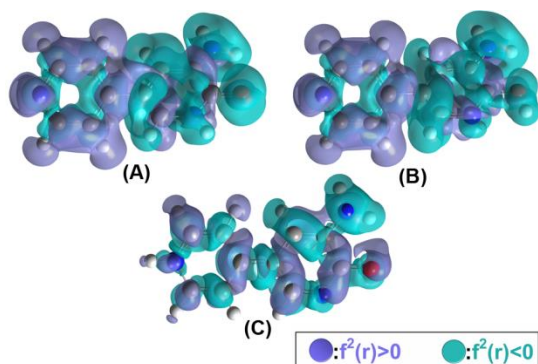
Fig.2: Isosurface maps of orbital weighted double descriptors of amrinone's three stable tautomers.
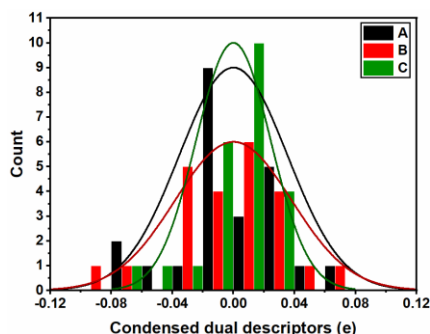
Fig.3: Local condensed dual-descriptors' distribution chart for all atoms of the three tautomers of amrinone (A, B, and C).

In **Fig.2**, the regions with electrophilic and nucleophilic behaviours are marked with purple and green colours, respectively. Also, the comparison of the charts in **Fig.3** has clearly revealed the shift of local

condensed dual descriptors' distribution to more positive values in the smaller domain for tautomer C compared to the tautomers A and B.

Conclusions

Our local and global chemical reactivity parameters' theoretical DFT study of amrinone's three stable tautomers through the Fukui functions and dual-descriptors analysis' results illustrated that this heart failure drug's tautomer C has the most chemical reactivity due to its so much lower $\Delta E_{LUMO-HOMO}$, more unstable HOMO and more stable LUMO orbitals, higher electrophilicity and nucleophilicity global index, less structural stability, and flatness compared with tautomers A and B. Also, the local and global regions with electrophilic and nucleophilic behaviours are marked for all amrinone's tautomers.

These results provide future studies' background, including the feasibility of using this compound in new chemical, industrial, and pharmacological applications.

References

[1] Türker, L. (2022). Some Tautomers of Amrinone and Their Interaction with Calcium Cation - DFT Treatment. Earthline Journal of Chemical Sciences, 9(2), 209–226. https://doi.org/10.34198/ejcs.9223.209226.

[2] Celik, S., Akyuz, S., Ozel, A.E. and Akalin, E. (2022). Vibrational Spectroscopic and Molecular Docking Studies of Amrinone, a Cardiotonic Inotropic Drug. Оптика И Спектроскопия, Springer, 130(2), 236. https://doi.org/10.21883/os.2022.02.51988.1011-21.

[3] Frisch, M., Trucks, G.W., Schlegel, H.B., Scuseria, G.E., Robb, M.A., Cheeseman, J.R., Scalmani, G., Barone, V., Mennucci, B., Petersson, G.A., Nakatsuji, H., Caricato, M., Li, X., Hratchian, H.P., Izmaylov (2009) Gaussian 09, Revision D. 01, Gaussian Inc., Wallingford CT,. Gaussian, Inc., Wallingford CT.

Synthesis of *N*-Tosyl Aldimine Derivatives in the Presence of Magnetically Nanocatalyst Fe₃O₄@Cuo and Ionic Liquids

Akram Ashouri, Faride Ghasemhasani, Somayeh Pouryan

Corresponding Author E-mail: ak.ashouri@gmail.com

Laboratory of Asymmetric Synthesis, Department of Chemistry, Faculty of Science, University of Kurdistan, Sanandaj, Iran.

Abstract: The synthesis of aromatic *N*-sulfonyl imine derivatives, was carried out in the presence of a magnetic CuO@Fe₃O₄ nanocatalyst and imidazolium-based ionic liquids as a co-catalyst to increase the reaction yield. FT-IR, AAS, EDAX, SEM, and VSM techniques were used to identify and confirm the structure of the CuO@Fe₃O₄ nanocatalyst. The structure of the ionic liquids and imines was identified, analyzed, and characterized using melting point and FT-IR, ^{1}H-NMR, and ^{13}C-NMR spectroscopy methods.

Keywords: nanocatalyst; imine; ionic liquid

Introduction

Imines are chemical compounds containing a carbon-nitrogen double bond (C=N). They play a key role as intermediates in the synthesis of nitrogen-containing compounds. Imines are inherently electron-rich due to their electron deficiency. These activating groups can also act as auxiliaries for chirality [1]. Magnetic nanocatalysts have been recognized as a prime choice to accelerate chemical reactions for many years. In addition to being inexpensive and having catalytic power to promote reactions, they can often be easily prepared from the base metal iron and, most importantly, they can be recycled multiple times without significant loss of selectivity and catalytic activity [2]. Ionic liquids have found wide applications and have had a special impact in various fields over the past few decades. Their applications included as catalysts and co-catalysts in the synthesis of chemical compounds and electrochemistry[3].

Experimental Section

Magnetic nanocatalysts Fe₃O₄ and CuO@Fe₃O₄ were first synthesized. Imidazolium-based ionic liquids, required as co-catalysts, were synthesized *via* a one-step or two-step reaction based on imidazolium. In the next step, anion exchange was performed with acidic anions. The reaction of aromatic aldehyde with *p*-toluene sulfonamide was carried out in the presence of the magnetic nanocatalyst CuO@Fe₃O₄ and ionic liquids as the auxiliary catalyst. The reaction was optimized under various conditions of solvents, temperatures, etc. The desired imines were synthesized under the optimized conditions (Scheme 1).
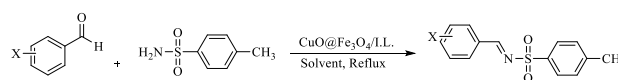
Scheme1: *N*-sulfonyl imine derivatives

Results and Discussion
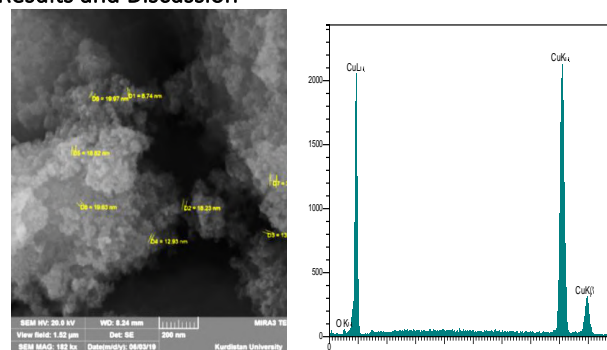
Fig.1: SEM and EDX of nanocatalyst CuO/Fe₃O₄
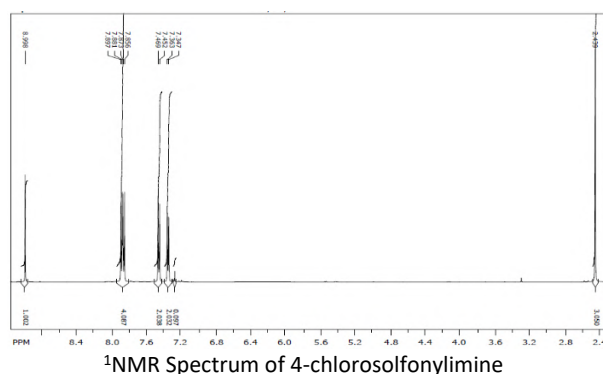
^{1}NMR Spectrum of 4-chlorosolfonylimine

22nd Iranian Chemistry Congress (ICC22)
Iranian Research Organization for Science and
Technology (IROST)
13-15 May 2024

03231-97589

Conclusions

In this research, aromatic *N*-sulfonyl imine compounds were synthesized with higher yields *via* the reaction of sulfonamide with aromatic aldehydes in the presence of magnetic CuO@Fe3O4 nanocatalysts and imidazolium-based ionic liquids as co-catalysts.

References

[1] Xie, Z., Song, Y., Xu, L., Guo, Y. (2018). Rapid Synthesis of N-Tosylhydrazones under Solvent-Free Conditions and Their Potential Application Against Human Triple Negative Breast Cancer. *ChemistryOpen*, *7*(12), 977-983.

[2] Atarod, M., & Safari, J. (2020). Comparative study of CuO, Fe_3O_4 and $CuFe_2O_4$/CuO over montm-orillonite clay: green synthesis, characterization and catalytic activity. *Chemistry-Select*, *5*(28), 8394-8404.

[3] McNeice, P., Marr, P. C., & Marr, A. C. (2021). Basic ionic liquids for catalysis: the road to greater stability. *Catalysis Science & Technology*, *11*(3), 726-741.

22nd Iranian Chemistry Congress (ICC22)
Iranian Research Organization for Science and Technology (IROST)
13-15 May 2024

03231-97589

IROST

Enantioselective Reduction of *N*-Soulphonyl Ketimine by Heterogeneous Chiral Ligand

Behzad Nasiri, Akram Ashouri

Corresponding Author E-mail: ak.ashouri@gmail.com

Laboratory of Asymmetric Synthesis, Department of Chemistry, Faculty of Science, University of Kurdistan, Sanandaj, Iran.

Abstract: Catalytic asymmetric hydrogenation of *N*-sulfonyl ketimine represents one of the most direct and efficient methods for the construction of chiral *N*-sulfonyl amines derivatives and was carried out in the presence of a magnetic nanoligand, and $PdCl_2$ to prepare organometallic catalysts and tartaric acid as acid to increase the reaction yield. FT-IR, AAS, EDAX, SEM, VSM, and TEM techniques were used to identify and confirm the structure of the nanoligand.

Keywords: Reduction; Chiral Ligand; amines; nanoligands

Introduction

Asymmetric hydrogenation is one of the most prominent and easy methods to produce optically pure compounds in both academic and industrial scales [1]. Due to high price of chiral catalysts applying in asymmetric reactions developed in recent years [2].

Organometallic palladium complexes have been used in a wide range of synthetic organic reactions, particularly in enantioselective reactions .

Chiral amines are essential building blocks in pharmaceuticals and agrochemicals. They can be achieved by enantioselective arylation or reduction reactions [3,4].

In this project, we utilized magnetic nano ligand for the enantioselective reduction of protected imines. The nano ligand can be recovered after the reaction and reused multiple times for this reaction.

Experimental Section

Synthesis of nano ligand

First, Fe_3O_4 was synthesized according to a known procedure [5]. It was then dissolved in aqueous NH_4OH (pH= 11), and chiral phosphine bidenate was added to this solution. After 10 hours, the nanoligand was separated, washed with ethanol and pure water, and dried for 20 hours at 110 °C (Fig. 1).

Asymmetric reaction procedure

Substrate A (0.2 mmol), L-tartaric acid (20 mol %), $PdCl_2$ (5 mol %), and nanoligand (3 mg) were dissolved in dichloromethane (1 mL) and stirred under H_2 at room temperature for 24 hours to yield the product (Scheme.1).

Results and Discussion

The reaction was optimized under different conditions of solvent, temperature, and different loading of nanoligand and metal, and the best result is shown in the Fig.1.
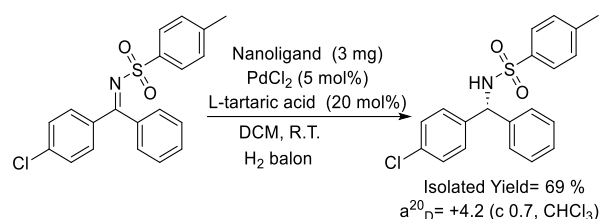
Scheme.1: Synthesis of chiral *N*-Sulfonyl amines derivatives

Nanoligand (3 mg)
$PdCl_2$ (5 mol%)
L-tartaric acid (20 mol%)
DCM, R.T.
H_2 balon

Isolated Yield= 69 %
a^{20}_D= +4.2 (c 0.7, $CHCl_3$)
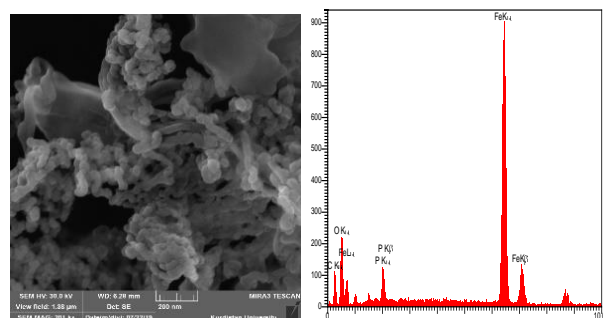
Fig.1: SEM and EDX of nanoligand
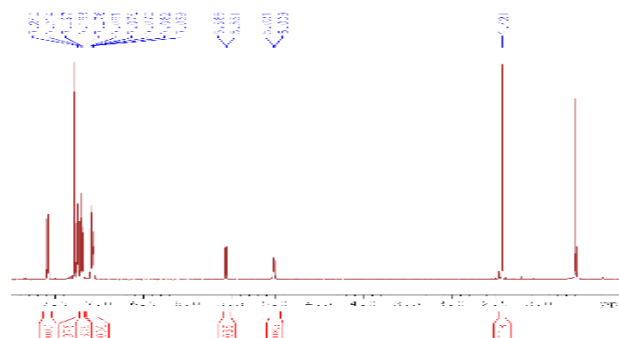
Fig.2: [1]NMR Spectrum of 4-Chlorosolfonylamine

Conclusions

In summary, we prepared a new chiral magnetic nano ligand which was used as a heterogeneous catalyst for the enantioselective reduction of ketimine. The reaction resulted in moderate yield and ee, and the catalyst was efficiently reused three times.

22nd Iranian Chemistry Congress (ICC22)
Iranian Research Organization for Science and Technology (IROST)
13-15 May 2024

03231-97589

References

[1] Lu, B., Yu, J., Zhang, X., & Chen, G. Q. (2024). Recent advances on catalytic asymmetric hydrogenation of oximes and oxime ethers. Tetrahedron Letters, 154914.

[2] Tetour, D., Novotná, M., Tatýrek, J., Máková, V., Stuchlík, M., Hobbs, C., ... & Hodačová, J. (2024). Preparations of spherical nanoparticles of chiral Cinchona alkaloid-based bridged silsesquioxanes and their use in heterogeneous catalysis of enantioselective reactions. Nanoscale.

[3] Gavrilov, K. N., Chuchelkin, I. V., Gavrilov, V. K., Zheglov, S. V., Firsin, I. D., Trunina, V. M., ... & Goulioukina, N. S. (2023). Hemilabile diamidophosphite-thioether ligands with a β-hydroxy sulfide backbone: palladium (II) complexesand asymmetric allylic substitution. Organometallics, 42(15), 1985-1996.

[4] Xu, M. M., Xie, P. P., He, J. X., Zhang, Y. Z., Zheng, C., & Cai, Q. (2024). Enantioselective Cross-[4+ 2]-Cycloaddition/Decarboxylation of 2-Pyrones by Cooperative Catalysis of the Pd (0)/NHC Complex and Chiral Phosphoric Acid. Journal of the American Chemical Society.

[5] Rezayati, S., Ahmadi, Y., & Ramazani, A. (2023). Synthesis of the Picolylamine copper complex immobilized on the Core-Shell Fe_3O_4 nanomagnetic particles and its application in the organic transformation. Inorganica Chimica Acta, 544, 121203.

22nd Iranian Chemistry Congress (ICC22)
Iranian Research Organization for Science and Technology (IROST)
13-15 May 2024

03231-97589

IROST

The effect of ultrasonic waves on the synthesis of yttrium oxide nanostructure and its application in the degradation of methylene blue pollutant

Mohsen Asdpour[a], Darush Afzali[b], Zahra Afzali[a]

Corresponding Author E-mail: mohsenasdpour79@gmail.com

[a] Department of Nanotechnology, Graduate University of Advanced Technology, Kerman, Iran.

[b] Department of Environment, Institute of Science and High Technology and Environmental Sciences, Graduate University of Advanced Technology, Kerman, Iran.

Abstract: One of the effective methods that has been noticed in recent years for the synthesis of nanostructured materials is the use of ultrasound waves to perform chemical reactions. The nanostructure of yttrium oxide was synthesized by the method of ultrasonic waves, and the necessary parameters for the destruction of methylene blue pollutant optimization and investigated.
Keywords: Yttrium oxide; Sonocatalyst.; Destruction Methylene blue

Introduction

Nowadays, there has been significant progress in the synthesis of nanostructures in catalytic industries. One of these methods is the synthesis of nanostructures using ultrasonic waves [1]. Ultrasonic waves are a process that occurs due to the application of ultrasonic waves to a solution, including the formation, growth and bursting of bubbles. It is in the liquid and is known as cavitation. Bubble growth is caused by the penetration of solvent vapor into the bubble and continues until the bubble bursts [2]. The bursting of the bubble causes the release of energy locally and allows the chemical reaction to take place [3]. Due to the sonocatalytic properties of yttrium oxide, it is possible to make yttrium oxide nanoparticles and investigate its use as a sonocatalyst in future degradation .

Experimental Section

1.1 Materials

Yttrium(III) nitrate hexahydrate/ Sodium Hydroxide / Methylene Blue / Hydrochloric Acid

1.2 Synthesis

Synthesis by hydrothermal method, 0.1 M yttrium nitrate aqueous solution in a 100 ml flask was brought up to volume with distilled water. Then, 1 M sodium hydroxide aqueous solution was brought up to volume in a 100 ml flask with distilled water. 0.1 M aqueous yttrium nitrate solution was applied using an ultrasonic probe device with an intensity of 250. Then, one molar sodium hydroxide solution was added to the yttrium nitrate solution to form a precipitate. We put the obtained solution in the autoclave and put it in the oven at 200 degrees Celsius for two hours, then the pollutant in the solution was washed and separated with distilled water. We dried the obtained final deposit and then placed it in the furnace for calcination at 850 degrees Celsius for one and a half hours and the deposit of nanostructure of yttrium oxide was synthesized and checked for the removal of methylene blue.

Identification
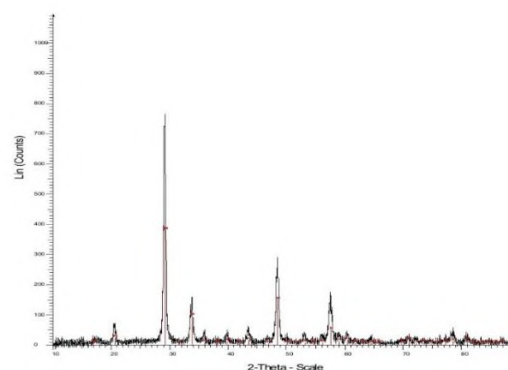
Fig.1: XRD pattern of yttrium oxide nanoparticles
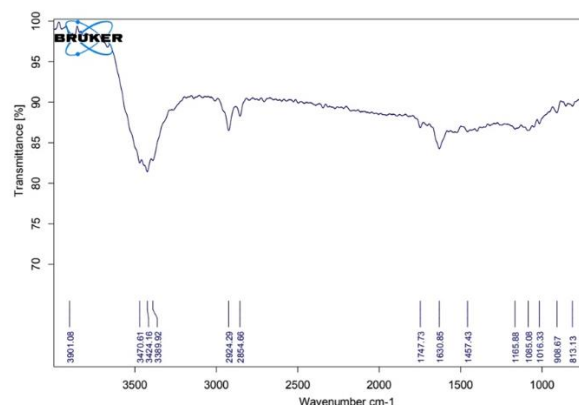
Fig2: FTIR spectrum of yttrium oxide nanoparticles

Picture 1,During the analysis, it was checked by the XRD pattern, which is used to determine the size of

22nd Iranian Chemistry Congress (ICC22)
Iranian Research Organization for Science and Technology (IROST)
13-15 May 2024

03231-97589

nanoparticles and crystal characterization of the material, and it showed that the yttrium oxide sample was synthesized in a crystalline form [7].

Picture2, FT_IR analysis is usually used to investigate chemical bonds and functional groups. By using this test (FT_IR), it is possible to determine the presence or absence or the change of a bond in the substance. FTIR spectrum has two main absorption areas. In the region of the first spectrum, the peak is between 550 and 700 cm. They are assigned to yttria, which shows the stretching frequency of the Y-O molecule. In the second region, the peaks between 3400 and 3450 cm^{-1} are the precursors of the water molecule group. This was found to be due to the absorption of moisture from O-H [8].

Table1: Origin of FTIR absorption bands in yttrium oxide nanoparticles

Origin	Wave number (cm^{-1})	Modes of vibration
Y_2O_3	550_700	Y_O stretching
H_2O absorption of Y_2O_3 from atmosphere	3400 _3450	O_H stretching

Conclusions

In the hydrothermal method, which was carried out in the direction of the synthesis of yttrium oxide nanostructure using ultrasonic waves. There was a good effect on the rate of sediment formation using ultrasonic waves. And the synthesized nanostructure had a good effect on the destruction of industrial waste.

References

[1] Li, Z., Dong, J., Zhang, H., Zhang, Y., Wang, H., Cui, X., & Wang, Z. (2021). Sonochemical catalysis as a unique strategy for the fabrication of nano-/micro-structured inorganics. *Nanoscale Advances*, *3*(1), 41-72. https://doi.org/10.1039/D0NA00753F

[2] Shchukin, D. G., Skorb, E., Belova, V., & Möhwald, H. (2011). Ultrasonic cavitation at solid surfaces. *Advanced Materials*, *23*(17), 1922-1934. https://doi.org/10.1002/adma.201004494

[3]. Suslick, K. S. (1989). The chemical effects of ultrasound. *Scientific American*, *260*(2), 80-87.

[4] Srinivasan, R., Yogamalar, R., & Bose, A. C. (2010). Structural and optical studies of yttrium oxide nanoparticles synthesized by co-precipitation method. *Materials Research Bulletin*, *45*(9), 1165-1170. https://doi.org/10.1016/j.materresbull.2010.05.020

[5] Kottaisamy, M., Jeyakumar, D., Jagannathan, R., & Rao, M. M. (1996). Yttrium oxide: Eu3+ red phosphor by self-propagating high temperature synthesis. *Materials Research Bulletin*, *31*(8), 1013-1020. https://doi.org/10.1016/S0025-5408(96)00077-3

Simultaneous extraction of nitrogen and sulfur contents from fuel Using Deep Eutectic Solvents: A Parametric Study

Leila Zarin[a], Javad Saien[b], Dara dastan[c], Farnaz Jafari[b]

[a] Department of Chemistry, combined cycle power plant, Sanandaj, Iran.

[b] Department of Applied Chemistry, Faculty of Chemistry and Petroleum Sciences University of Buali Sina, Hamedan, Iran.

[c] Faculty of Pharmacy, Department of Pharmacology, Hamadan University of Medical Sciences, Iran.

Abstract: Ultra-deep desulfurization/denitrogenation technologies are critical for cleaner oils with low impurity and consequent better air quality. In this regard and considering the drawbacks of conventional methods of Hydrodesulfurization and hydrodenitrogenation, the novel and simultaneous extractive desulfurization/denitrogenation utilizing green and designable solvents Concerning has been proposed. The used DES is composed of methyltriphenylphosphonium bromide (MTPPBr) and para-toluene sulfonic acid (PTSA) in a particular molar ratio of (0.3 (MTPPBr):0.7 (PTSA)). A simulated fuel based on n-heptane including Thiophene (TH) and pyridine (PY) as harmful pollutants found in fuel has been examined. The influence of fuel matrices and initial concentration of impurities on the extraction efficiency has been assessed. In comparison to conventional DESs, the novel DES demonstrated improved extraction capability to 87% and 98% for desulfurization and denitrogenation process, respectively.

Keywords: Simultaneous desulfurization/denitrogenation, Deep eutectic solvents, Model fuel, Thiophene, Pyridine.

Introduction

Long-term energy outlooks predict the dominant role of fossil fuels as energy sources for at least more two decades due to the rising demand of along with the development of the industries. Although, the environment degradation and public health are the inevitable drawbacks of the current fossil fuel consumption which has led to numerous global challenges. In this regard, the more stringent regulations are adopting for reducing fuel impurities and producing ultra-low sulfur and nitrogen fuels. Hydrodesulfurization (HDS) and hydrodenitrogenation (HDN) are the industrually used approches to separate sulfur and nitrogene compounds from refined products. However, the large-scale utilization of these methods has been restricted due to the requirement of expensive catalysts, large amounts of hydrogen under high temperatures and pressures. furthermore, HDS and HDN are less effective in the removal of heterocyclic sulfur and nitrogen compounds. With regard to the above problems and challenges faced with HDS and HDN, the potential of various alternative techniques such as oxidation, adsorption, extraction, or and bio-based processes, have been widely evaluated. Among these methods, the extractive desulfurization/denitrogenation which is based on the consumption of extractant solvents to particularly eliminate the sulfur and nitrogen compounds from liquid fuel with the advantages of the simplicity of process under mild conditions, low energy consumption, as well as lower temperature and pressure and using the green solvents have gained researcher attentions.

Moreover, the emerging generation of green and designable solvents including ionic liquid (IL) and deep eutectic solvent (DES) has the potential benefits for effective extraction of fuel impurities. Deep eutectic solvents (DESs) which composed of the hydrogen-bond acceptor (HBA) and hydrogen-bond donor (HBD), have the potential of selectively removing sulfur and nitrogen compounds from fuel to achieve deep desulfurization with low melting points and vapour pressure [1, 2].

In this work, the simultaneous removing of thiophene and pyridine as sulfur and nitrogen compounds in model fuel via extraction approach with utilizing novel DES solvent has been investigated.

Experimental Section

Materials

DES preparation: The proposed DESs was formulated with combining methyltriphenylphosphonium bromide as HBA and para-toluene sulfonic acid as HBD at various molar ratios ranging from 1:1 to 1:9. The specific organic HBA: HBD molar ratio employed in this study was determined based on achieving a homogeneous liquid DES at room temperature. After those two compositions become liquid with heating, the system was stirred [2]. All reagents were procured from the chemical suppliers Merck. Considering heptane as the bases of the model, several hydrocarbons were also introduced to modulate gasoline (simulated gasoline) as indicated in Table 1[3].

22nd Iranian Chemistry Congress (ICC22)
Iranian Research Organization for Science and Technology (IROST)
13-15 May 2024

03231-97589

IROST

Table 1: Specifications of the different multicomponent simulated fuel

Basic model fuel	Simulated gasoline
n-Heptane, 99.37 wt%	n-Heptane, 29.81 wt%
Thiophene, 0.15 wt%	n-Hexane, 29.81 wt%
Pyridine, 0.15 wt%	Isooctane, 29.81 wt%
	Thiophene, 0.15 wt%
	Pyridine, 0.15 wt%

Extraction procedure: The individual and simultaneous extractive desulfurization/denitrogenation processes were performed at constant temperature of 25 °C. In each experiment, the DES and simulated fuel were mixed with volume ratio of 1:1. Then the mixture was stirred for 60 min in a water bath and settled for one hour. After that, the upper layer (fuel phase) was collected and analysed by GC-FID in order to quantify the amount of sulfur and/or nitrogen compounds [3]. The extraction efficiency of sulfur/nitrogen compounds removal was calculated from following formula:

$$\text{extractio efficincy (\%)} = \frac{C_i - C_f}{C_i} \times 100$$

Where C_i and C_f are initial and final concentration of sulfur/nitrogen compounds in model fuel, respectively.

Results and Discussion
Effect of the fuel matrix
Concerning the comprehensive investigation of extractive desulfurization/denitrogenation process, the influence of the simultaneous presence of both compounds of thiophene and pyridine in several hydrocarbons has been assessed. The results presented in Figure 1 (a) and (b) revealed that the extraction efficiency of both sulfur and nitrogen impurities boosts in presence of hydrocarbons. The reason is attributed to the increasing tendency of polar solvents to impurity.
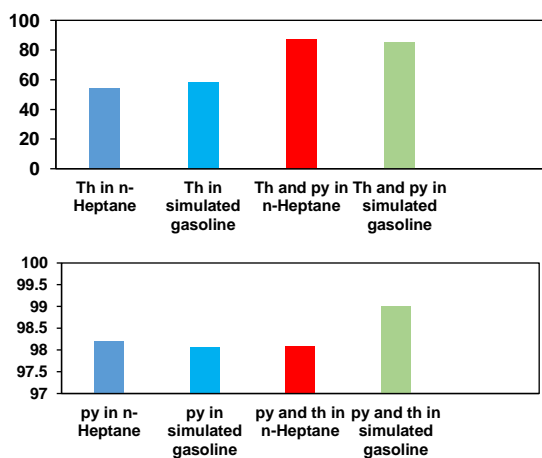
Fig.1: extraction efficiency of thiophene(a) and pyridine (b) in various fuel matrix.

Effect of Initial Concentration of fuel impurities
The influence of initial concentration thiophene and pyridine on their extraction efficiency are depicted in Figure 2. As revealed, the extraction efficiency of pyridine is relatively independent of initial concentration. Nevertheless, the extraction efficiency of thiophene is significantly decreased with increasing its initial concentration in model fuel. The observed trend is apparently attributed to this fact that the solvent reaches to its maximum capacity as high concentrations of thiophene accumulate in the DES phase preventing further extraction. Interestingly, for extraction of pyridine, the dominant acid and base interactions could overcome to the saturation factor of solvent and improve the extraction capacity.
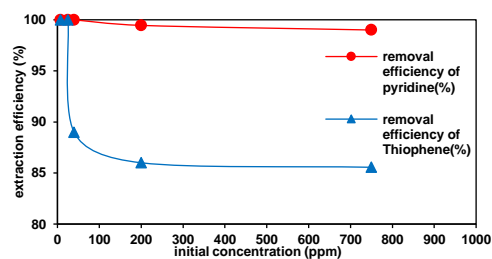
Fig.2: The extraction efficiency of the sulfur and nitrogen compounds with different initial concentration.

Conclusions:
The ability of novel DES for extracting two main sulfur and nitrogen impurity in model fuel, thiophene and pyridine was proved with high efficiency of 87% and 98%, respectively. A success combination of desulfurization and denitrogenation processes capable of almost completely extraction of the most fule contaminates model fuel under mild conditions was achieved. Taking sustainability into account further research was undertaken to evaluate extractability of the proposed DES.

References
[1] Hizaddin, H. F., Hadj-Kali, M. K., Ramalingam, A., & Ali Hashim, M. (2016). Extractive Denitrogenation of Diesel Fuel Using Deep Eutectic Solvents. J. Chem. Thermodyn, 95, 164–173. https://doi.org/10.1016/j.jct.2015.12.009.
[2] Hansen, B. B., Spittle, S., Poe, D., Zhang, Y., Klein, J. M., & Horton, L. (2020). A Deep Eutectic Solvents: A Review of Fundamentals and Applications. ACS. Chem. Rev. 121, 1232-1285. https://doi.org/10.1021/acs.chemrev.0c00385.
[3] Lima, F, Dave, M, Silvestre, AJD, Branco, LC, & Marrucho IM. (2019). Concurrent desulfurization and denitrogenation of fuels using deep eutectic solvents. ACS Sustain. Chem. Eng,7(13),11341–11349. https://doi.org/10.1021/acssuschemeng.9b00877[20]

Elimination of methylene blue from aqueous solutions by using a magnetic nanocomposite containing zinc ferrite spinel

Sania Sanjabi, Alireza Salehirad*

Corresponding Author E-mail: salehirad@irost.ir

Department of chemical Technologies, Iranian Research Organization for Science and Technology (IROST), Tehran, Iran.

Abstract: In this paper, $MgAl_2O_4$/$ZnFe_2O_4$/zeolite A nano composite was utilized as a new adsorbent to removal methylene blue (MB) from aqueous solutions. The nano composite was synthesized by co-precipitation method. To determine the characterization of nanoparticles several analyses such as BET, SEM, EDX, FT-IR, XRD and VSM were executed.
Keywords: $MgAl_2O_4$/$ZnFe_2O_4$/zeolite A nano composite; Methylene blue; aqueous solutions.

Introduction
The fabric industry is one of the most important basic industries any country, that is the biggest water polluters in the world. This wastewater contains a variety of organic compounds and toxic substances that are harmful to humans, animals and aquatic organisms [1]. Methylene blue (MB) is one of the most widely used dyes in the fabric industry. This is the most common color combination used for dyeing Cotton, wool and silk, temporary hair color and paper color [2]. There are different methods to remove color from industrial wastewater, including: chemical oxidation [3], biological method [4], adsorption [5], and electrodialysis [6]. Recent developments in in the field of eliminating dyes have led to renewed interested in adsorption, because of its easy functioning process, high separation performance and low-cost [7].

Experimental Section
1-Preparation of $MgAl_2O_4$/$ZnFe_2O_4$/zeolite 4A nano composites: Magnetic nanoparticles were synthesized by the co-precipitation method. An aquas solution of Zn $(NO_3)_2$.$6H_2O$ and Fe $(NO_3)_3$.$9H_2O$ with a molar ratio of 1:2 (Zn: Fe) was stirred at 800C for 90 min. After that, the obtained mixture was placed in ultrasonic batch at 80 0C for 30 min. The precipitate was magnetically separated, washed and dried at 120 0C. Finally, the black precipitates were heated at 600 0C for 4 hr. In this paper $MgAl_2O4$/$ZnFe_2O_4$/zeolite A nano composites with mass ratios of $MgAl_2O_4$, $ZnFe_2O_4$ were prepared and surveyed MB adsorption on samples.

To prepare nanocomposites, to an aquas solution containing certain amounts of Mg $(NO_3)_2$.$6H_2O$ and Al $(NO_3)_3$.$9H_2O$ (Mg: Al molar ratio was 1:2) stirring at 80 ^{0}C, an ammonia solution was slowly added until pH 10 obtained. The resulting mixture was aged at 80 0C for 90 min. The certain amounts the prepared $ZnFe_2O4$ nanoparticle was added to the mixture. The obtained suspension was stirred for 90 min and followed by ultra sonication treatment for 15 min. Then the sample was dried at 110 0C. Ultimately, the achieved precipitate calcinated at 800 0C for 4 hr.

Results and Discussion
Characterization of $MgAl_2O_4$/$ZnFe_2O_4$/zeolite A nanocomposite Experiments). The magnetic behavior of $MgAl_2O_4$/$ZnFe_2O_4$/zeolite A nano composite was studied with by the VSM analysis at 300 0K and is shown in Fig. 1, that displays a typical shape like a letter ''S''. The curve of synthesized nanocomposite, indicates superparamagnetic behaviour with a zero coercivity and they have little hysteresis, remanence.
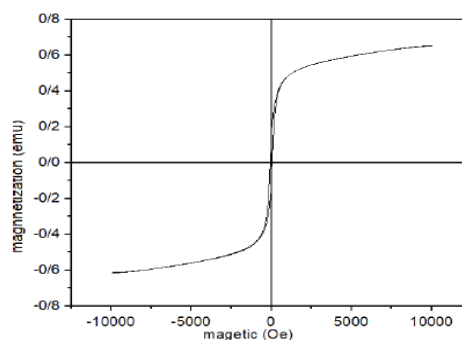
Fig.1: The magnetization curves measured at 300 K for $MgAl_2O_4$/ $ZnFe_2O_4$/zeolite A

Thermodynamic studies
Thermodynamic parameters; Free energy (G), enthalpy (H) and entropy (S) for the adsorption of dye on nanocomposites have been calculated using the following equations.

22nd Iranian Chemistry Congress (ICC22)
Iranian Research Organization for Science and Technology (IROST)
13-15 May 2024

03231-97589

IROST

$$Ln\left(\frac{Q_{em}}{C_e}\right) = \frac{\Delta S}{R} - \frac{\Delta H}{RT}$$

$$\Delta G = \Delta H - T\Delta S$$

Values of ΔG were calculated by Eq. The values of thermodynamic parameters are shown in Table 1. The negative values of free energy is confirmed the feasibility of the adsorption process and its automatical nature. Further, the positive values of ΔH shows that the adsorption process is endothermic and the adsorption is favorable at higher temperatures, the positive values of ΔS describes that the adsorption process is random at the adsorbent-solution interface .
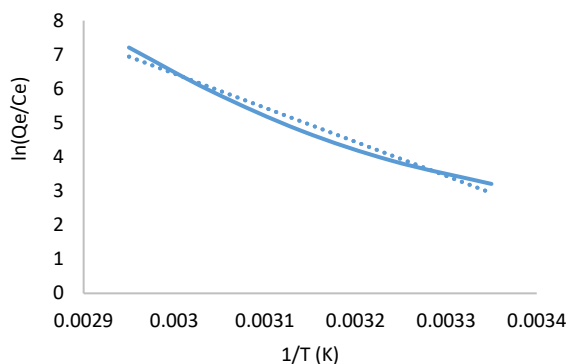
Fig. 2: Plot of ln (Qe/Ce) versus 1/T to give thermodynamic parameters.

Table1: Thermodynamic parameters for adsorption of MB

Dye concentration mg/l	ΔH (kJ/mol)	ΔG (kJ/mol)	ΔS (kJ/mol/K)
40	94.2	-8.4	4.36

Conclusions

The present study investigated the adsorption of MB from aqueous solutions by $MgAl_2O_4/ZnFe_2O_4/Zeolite$ A magnetic nanocomposite. The best conditions for the adsorption of MB dye were taken at temperature of 45 °C, adsorbent dosage of 0.2 g/L, and initial dye concentration of 40 mg/l, contact time of 35 min and pH of 11. The maximum adsorption capacity of MB was 119.3 mg/g and removal efficiency was 98.3%. The positive enthalpy Change for the adsorption process confirms the endothermic nature of the adsorption.

References

[1] E.N. El-Qada, S.J. Allen, G.M. Walker. (2006). Adsorption of methylene blue onto activated carbon produced from steam activated bituminous coal: a study of equilibrium adsorption isotherm, Chem. Eng. J. 124 103–110. https://doi.org/10.1016/j.cej.2006.08.015.

[2] S.M. Sidik, A.A. Jalil, S. Triwahyono, S.H. Adam, M.A.H. Satar, B.H. Hameed.(2012). Modified oil palm leaves adsorbent with enhanced hydrophobicity for crude oilremoval, Chem.Eng.J.203,9–18. https://doi.org/10.1016/j.cej.2012.06.132

[3] A.R. Ribeiro, O.C. Nunes, M.F.R. Pereira, A.M.T. Silva. (2015). an overview on the advanced oxidation processes applied for the treatment of water pollutants defined In the recently launched directive. Environ. Int. 75, 33–51 https://doi.org/10.1016/j.envint.2014.10.027

[4] I. M. Banat, and S. Datel. (1996). Microbial decolorization of textile dye containing effluents: A Review, BioresourceTechnol.58,217–227. https://doi.org/10.1016/S0960-8524(96)00113-7

[5] H. Hamad, Z. Ezzeddine, F. Lakis, H. Rammal, M. Srour, A. Hijazi. (2016). An insight into the removal of Cu (II) and Pb (II) by aminopropyl-modified mesoporous carbon CMK-3: adsorption capacity and mechanism, Mater. Chem.Phys.178,57–64. https://doi.org/10.1016/j.matchemphys.2016.04.062

[6] B. Karabacakoglu, F. Tezakil, A. Guvenc. (2015). Removal of hardness by electrodialysis using homogeneous and heterogeneous ion exchange membranes, Desalin. Water Treat 54, 8–14. https://doi.org/10.1080/19443994.2014.880159

22nd Iranian Chemistry Congress (ICC22)
Iranian Research Organization for Science and Technology (IROST)
13-15 May 2024

03231-97589

IROST

Hydrogels With Self-Healing and Multi Responsive Properties as Wound Dressing for Skin Wound Healing

Sheyda moradi [a], Mohammad Reza Zamanloo [*a], Zaynab Ahmadian [b]

Corresponding Author E-mail : *mrzamanloo@uma.ac.ir*

[a] Department of Chemistry, Faculty of Science, University of Mohaghegh Ardabili, Ardabil, Iran.

[b] Department of Pharmaceutics, Faculty of Pharmacy, Lorestan University of Medical Science, Khorramabad, Iran.

Abstract: Designing wound dressing materials with self-healing properties has great practical significance in healthcare. Here, we designed a kind of self-healing micelle/hydrogel composites with multi-functions as wound dressing. By combining the dynamic Schiff base and cross-linking, the hydrogel was prepared by mixing chitosan (CS) and aldehyde-terminated micelle (CHO-PCL-PEG-PCL-CHO) under physiological conditions.
Keywords: *hydrogel*; *Schiff base*; *micelle*.

Introduction

Skin damage is one of the most common physical injuries throughout human history [1]. Among these novel dressing materials fabricated in recent years, hydrogel with high water content and biocompatibility is a promising candidate for practical application [2, 3]. hydrogels, by providing a porous structure and suitable swelling ratio, hydrogel matrix can allow for oxygen presence, absorb the exudates, and maintain a moist healing environment [4] to promote wound healing. Then, unlike traditional wound dressing (gauze and cotton wool), bioactive molecules loaded hydrogel dressings exhibited desirable biological activity by releasing encapsulated drug from the hydrogel matrix. In this work, we combined the dynamic Schiff base bond as dynamic crosslinking in one hydrogel to get excellent mechanical properties and self-healing ability. hydrogel was prepared by mixing chitosan (CS) and aldehyde-terminated micelle (micelle-CHO) under physiological conditions.

Experimental Section

The hydrogels were prepared by mixing CS solution (5%) and micelle-CHO solution in a ratio of 2:3 (v/v) at 25°c. Therefore the hydrogel formed by Schiff base reaction between the amine group of CS and the aldehyde group of a micelle. The method of recording the gelation time is the tube inversion method.

Results and Discussion

The hydrogel CS-Micelle (CS-M) with controlled composition was obtained by Schiff base reaction of chitosan solution with aldehyde-terminated micelle (CHO-PCL-PEG-PCL-CHO), Fig 1. IR was utilized to approve the structures, Fig. 2a.
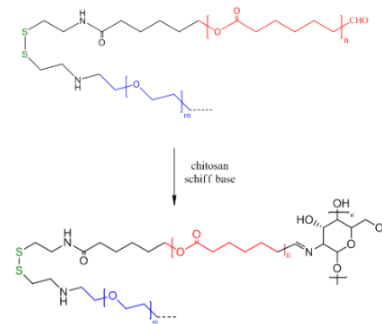
Fig. 1: The reaction pathway of hydrogel.

The peak at 1720 cm^{-1} in micelle-CHO was the stretching vibration of -C=O bond of the aldehyde group, suggesting that -CHO was successfully introduced to micelle [32]. A peak at 1640 cm^{-1} in CS-M hydrogel appeared due to the characteristic absorption of the newly formed Schiff base from the amine group of CS and aldehyde group of micelle-CHO.

The morphologies of hydrogels were observed by SEM. The hydrogel showed porous structures (Fig. 2b). The average diameter pore of CS-M was 80 μm, and this is show the increased crosslinking densities in the hydrogel. Hence, with the porous structure, the CS-M hydrogel has potential as a wound dressing material.
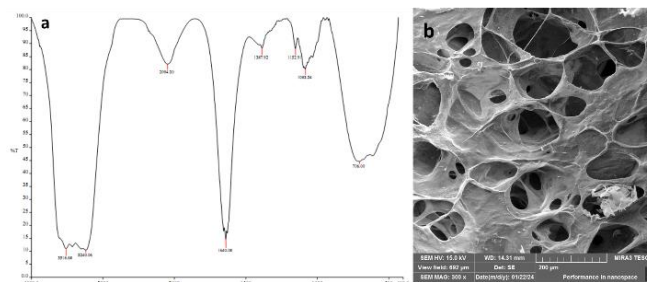
Fig.2: Characterization of CS-M hydrogel. a) FT IR spectra of the hydrogel CS-M .b) SEM image of hydrogel.

22nd Iranian Chemistry Congress (ICC22)
Iranian Research Organization for Science and
Technology (IROST)
03231-97589
13-15 May 2024

IROST

The swelling percentage and water absorption of CS-M hydrogel with different micelle concentrations are shown (Fig. 3). Swellability for hydrogel made with different concentrations of micelles in PBS with 5.5 and pH 7.4 was investigated. The results indicated a very fast and high swelling of the hydrogel in PBS (pH 5.5). The slope of the inflation percentage is much higher in the early hours. The percentage of swelling in the concentration of 0.4 g/mL is higher than other concentrations, although this difference is much more noticeable in the early hours than in the final hours. The results also indicate that the percentage of swelling in all concentrations and all times at pH 5.5 is higher than pH 7.4.
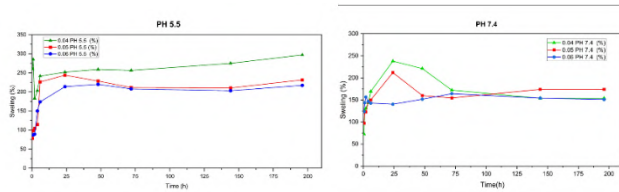
Fig.3: Swelling and water absorption of CS-M hydrogel with different micelle concentrations and in PBS (pH 4.7, 5.5), (n=3; mean ± SD).

Conclusion

The CS/M hydrogels were successfully synthesized based on CS and CHO-PCL-PEG-PCL-CHO copolymer under physiological conditions. These hydrogels exhibited similar to human soft tissue, tunable gelation time, good pH-dependent ability, and Appropriate swelling which could effectively used in the wound healing process.

References

[1] X. Zhao., H. Wu., B. Guo., R. Dong., Y. Qiu., P.X. Ma. (2017). Antibacterial anti-oxidant electroactive injectable hydrogel as self-healing wound dressing with hemostasis and adhesiveness for cutaneous wound healing. Biomaterials, 122, 34-47. https://doi.org/10.1016/j.biomaterials.2017.01.011.

[2] B. Guo., P.X. Ma. (2018). Conducting polymers for tissue engineering. Biomacromolecules, 19(6), 1764-1782. https://doi.org/10.1021/acs.biomac.8b00276.

[3] [6] B. Guo., L. Glavas., A. C. Albertsson. (2013). Albertsson, Biodegradable and electrically conducting polymers for biomedical applications. Pro. Polym. Sci. 38(9),1263-1286. https://doi.org/10.1016/j.progpolymsci.2013.06.003.

[4] Z. Fan., B. Liu., J. Wang., S. Zhang., Q. Lin., P. Gong., L. Ma., S. Yang. (2014). A novel wound dressing based on Ag/graphene polymer hydrogel: effectively kill bacteria and accelerate wound healing. Adv. Funct. Mater. 24(25), 3933-3943. https://doi.org/10.1002/adfm.201304202.

Synthesis of Coumarin derivatives using biobased Ti (IV) under different conditions

Ramtin Moradi Chafjiri, Abdolhamid Bamoniri*

Corresponding Author E-mail: bamoniri@kashanu.ac.ir

Department of Organic Chemistry, Faculty of Chemistry, University of Kashan, Kashan, Iran.

Abstract: In this research use bio-based Ti (IV) as a catalyst in the synthesis of coumarin, which improves stability and catalytic activity. This process catalyses phenolic-aldehyde reactions and offers potential applications in materials, aroma, and agricultural research. Among the advantages, we can mention the cost-effectiveness, efficiency and ease of separation and purification. Products were identified using spectroscopic ways.

Keywords: Coumarin; Phenol derivatives; Green chemistry

Introduction

Strong heterogeneous catalysts have received plenty of attention in this area from both financial and natural contemplations because they offer more focal points than homogeneous catalysts, such as shorter reaction times, the capacity to be utilized again at different times, a decrease in the rate of gear erosion, and a reduction in waste items. Thus, extensive efforts are underway to replace standard fluid corrosive catalysts with heterogeneous fluid acidic catalysts. Improved soundness, reusability, and advanced catalytic action are among the benefits of using nanocellulose as support for titanium tetrachloride catalysts. A sufficient catalyst must be present when an aldehyde condenses with phenol or derivatives to produce a mixture of coumarins [1-3]. An effective catalyst in this reaction is titanium tetrachloride stabilized on nanocellulose, which promotes the organization of the carbon-carbon bond between the phenolic molecule and the aldehyde. The catalyst has a robust foundation to anticipate filtering and accelerate the overall productivity of the reaction when nanocellulose is present as support [4]. Coumarin derivatives have been the focus of extensive investigation due to their wide variety of biological activity and potential use in various contexts. Different approaches, including multi-component responses and traditional courses like Pechmann condensation, Knoevenagel condensation, Perkin response, and Wittig condensation responses, have been used to unite these subsidiaries. Additionally, multistep responses have been used to create contemporary coumarin subordinates with enhanced characteristics. NMR spectroscopy and FT-IR are two characterization techniques that have been used to analyse the generated molecules. The invention of effective and eco-friendly developed processes, especially the topsy-turvy organocatalyzed mix, has made it feasible to obtain the 2H-chromen-2-one core of coumarin derivatives [5-7]. Because of their various applications and possible bioactivities, coumarin subordinates have generally been a subject of great interest. In the field of natural chemistry, the union of coumarin subsidiaries has attracted quite a bit of attention due to their wide range of biological activities and uses. Subordinates of coumarin have a wide range of natural activities, including antioxidant, anti-inflammatory, antibacterial, and anticancer effects [8]. Because of these characteristics, coumarin derivatives are attractive prospects for improving underutilized medications for many therapeutic uses. Furthermore, coumarin derivatives have been found beneficial in materials research, scent, and agriculture [9]. Conventionally designed methods often rely on condensation reactions between salicylates or salicylaldehyde and other carbonyl molecules, like aldehydes or ketones. These strategies have given rise to a strong base for the blending of a wide variety of coumarin subordinates. However, with the advancement of natural union, more modern and potent tactics have been developed. These consist of one-pot multi-component reactions, enzymatic modifications, microwave-assisted processes, and move metal-catalysed activities. These contemporary methods have increased the variety of potential structures, but they haven't really improved the competence and submission of coumarin subsidiaries [10-12]. Natural chemists have not been the only ones interested in the union of coumarin subsidiaries; therapeutic chemists and pharmaceutical specialists have also become attracted by it [13,14].

Experimental Section

1mmol of phenol derivatives was added to 1mmol β-keto esters and a catalytic amount of Bio-based Ti (IV) was stirred at 130°C when the reaction was complete, the mixture was solved in hot isopropyl alcohol for separated insoluble catalyst by filtration. monitoring the reaction with TLC in n-hexane and ethyl acetoacetate (7:3). The catalyst can use for four times again.

22nd Iranian Chemistry Congress (ICC22)
Iranian Research Organization for Science and
Technology (IROST)
13-15 May 2024

03231-97589

Results and Discussion

The use of Nanocellulose as a support for TiCl$_4$ catalyst displayed several advantages in the synthesis of Coumarin. The high surface area and porosity of Nanocellulose provide a suitable environment for the efficient immobilization of the catalyst. This immobilization improves the catalyst's stability and minimizes its leaching during reaction, resulting in enhanced efficiency and reusability.The optimized reaction conditions played a crucial role in achieving higher yields and selectivities of the desired Coumarin products. The reusability of the TiCl$_4$ supported on Nanocellulose catalyst is a notable advantage from both economic and environmental points of view. The catalyst's stability and ease of separation allow for multiple cycles of the reaction without significant loss in catalytic activity (Fig.1).
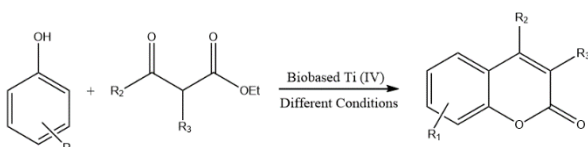
Fig.1: Preparations of Coumarin derivatives

Table 1: Result

Entry	Phenol derivetives	Product	Time (min)	Yield (%)
1	2-hydroxy-4-methyl phenol	7-hydroxy-4,5-di methyl Coumarin	120	97
2	2-methyl phenol	7,4- dimethyl Coumarin	180	96
3	Resorcinol	7-hydroxy -4-methyl Coumarin	120	94

Conclusions

In conclusion, the synthesis of coumarins using Bio-based Ti (IV) is a promising approach in organic chemistry, offering enhanced catalytic activity and stability. Further research in this area may lead to the development of novel coumarin derivatives with diverse biological activities. For future work researcher in all over the world can repeat this research used electrosynthesis.

References

[1] Van Velthoven, N., Henrion, M., Dallenes, J., Krajnc, A., Bugaev, A. L., Liu, P., ... & De Vos, D. E. (2020). S, O-functionalized metal–organic frameworks as heterogeneous single-site catalysts for the oxidative alkenylation of arenes via C–H activation. *Acs Catalysis*, *10*(9), 5077-5085.

[2] Sekewael, S. J., Pratika, R. A., Hauli, L., Amin, A. K., Utami, M., & Wijaya, K. (2022). Recent progress on sulfated nanozirconia as a solid acid catalyst in the hydrocracking reaction. *Catalysts*, *12*(2), 191.

[3] Dhali, K., Ghasemlou, M., Daver, F., Cass, P., & Adhikari, B. (2021). A review of nanocellulose as a new

material towards environmental sustainability. *Science of the Total Environment*, *775*, 145871.

[4] Xu, T., Song, Q., Liu, K., Liu, H., Pan, J., Liu, W., ... & Zhang, K. (2023). Nanocellulose-assisted construction of multifunctional MXene-based aerogels with engineering biomimetic texture for pressure sensor and compressible electrode. *Nano-Micro Letters*, *15*(1),98.

[5] Chen, L., Abdalkarim, S. Y. H., Yu, H., Chen, X., Tang, D., Li, Y., & Tam, K. C. (2022). Nanocellulose-based functional materials for advanced energy and sensor applications. *Nano Research*, *15*(8), 7432-7452.

[6] Muravyev, N. V., Pivkina, A. N., & Koga, N. (2019). Critical appraisal of kinetic calculation methods applied to overlapping multistep reactions. *Molecules*, *24*(12), 2298.

[7] Jia, Q., Yan, Z. C., Li, Y., Liu, J., Ding, Y., Liu, Y., Chen, Y. (2021). Synthesis of well-defined di-and triblock acrylic copolymers consisting of hard poly (dicyclopentanyl acrylate) and soft poly (alkyl acrylate) segments by organocatalyzed group transfer polymerization and their glass transition behavior. *Polymer Chemistry*, *12*(23), 3427-3440.

[8] Rawat, A., & Reddy, A. V. B. (2022). Recent advances on anticancer activity of coumarin derivatives. *European Journal of Medicinal Chemistry Reports*, *5*, 100038.

[9] Fayed, E. A., Nosseir, E. S., Atef, A., & El-Kalyoubi, S. A. (2022). In vitro antimicrobial evaluation and in silico studies of coumarin derivatives tagged with pyrano-pyridine and pyrano-pyrimidine moieties as DNA gyrase inhibitors. *Molecular Diversity*, 1-23.

[10] Pattar, S. V., Adhoni, S. A., Kamanavalli, C. M., & Kumbar, S. S. (2020). In silico molecular docking studies and MM/GBSA analysis of coumarin-carbonodithioate hybrid derivatives divulge the anticancer potential against breast cancer. *Beni-Suef University journal of basic and applied sciences*, *9*(1), 1-10.

[11] Tolba, M., El-Dean, A., Geies, A., Radwan, S., Zaki, R., Sayed, M., ... & Abdel-Raheem, S. (2022). An overview on synthesis and reactions of coumarin based compounds. *Current Chemistry Letters*, *11*(1), 29-42.

[12] Boutin, R., Koh, S., & Tam, W. (2019). Recent advances in transition metal-catalyzed reactions ofoxabenzonorbornadiene. *Current Organic Synthesis*, *16*(4), 460-484.

[13] Patil, S. M., Martiz, R. M., Satish, A. M., Shbeer, A. M., Ageel, M., Al-Ghorbani, M., Ramu, R. (2022). Discovery of novel coumarin derivatives as potential dual inhibitors against α-glucosidase and α-amylase for the management of post-prandial hyperglycemia via molecular modelling approaches. *Molecules*, *27*(12), 3888.

[14] Aksakal, R., Mertens, C., Soete, M., Badi, N., & Du Prez, F. (2021). Applications of discrete synthetic macromolecules in life and materials science: recent and future trends. *Advanced Science*, *8*(6), 2004038.

Investigating Intramolecular Hydrogen Bonding of Triketone Compounds with N and S Heteroatoms

Mohaddese Hosnan, Mostafa Fazli[*]

Corresponding Author E-mail: mfazli@semnan.ac.ir

Faculty of Chemistry, University of Semnan, Iran.

Abstract: In the current study, the intramolecular hydrogen bonds of triketone compounds in the vicinity of heteroatoms in ++G**311-6 system have been investigated. Bader's quantum theory of atoms in molecules (QTAIM) was also applied here to get more details about the nature of hydrogen bonds using the AIM program. Correlations between hydrogen bond strength and different parameters were also analyzed. Also, a comparison for electron delocalization in systems containing O, N, and S heteroatoms is presented.

Keywords: Destabilization of π electron**;** heteroatom; AIM; triketone; theoretical methods

Investigating different parameters of hydrogen bonding of bicyclic compounds

Mohaddese Hosnan, Mostafa Fazli*

Corresponding Author E-mail: mfazli@semnan.ac.ir

Faculty of Chemistry, University of Semnan, Iran.

Abstract: In this study, emphasizing the importance of computational chemistry and its applications, hydrogen bonds in adjacent bicyclic systems in the presence of heteroatoms have been investigated. The investigated systems have been optimized at the MP2 level of theory and using the ++G**311-6 standard base series. Also, to find topological properties, the quantum theory of Mr. Bieder about "atoms in molecules" has been used.

Keywords: Computational Chemistry; Gaussian; Resonance Assisted Hydrogen Bonding

Introduction

In recent years, researches in the field of computational chemistry have increased. Conducting such studies with the advancement of computer software that pay more attention to easy applications. In these studies, there is no need for the basis and theory part of the software, and the user does not need to know the tools used in the calculations. In computational and theoretical chemistry, I cannot use the word and concept of "exact". Very few aspects of chemistry can I calculate accurately. But basically, all aspects of chemistry are expressed with "quantitative and approximate" calculations [1]. The biggest mistake a computational chemist makes is to think that all calculated numbers are exact. However, even though everything is not fully resolved, some qualitative or approximate accounts such as ab-initio and semi-empirical methods can be useful in chemistry to make the researcher. Have a prediction of the subject under review. Among the types of computational chemistry methods, molecular dynamics and molecular mechanics simulations can be mentioned. Computational chemistry has many applications, one of the most important of which is building a model of a molecular system before making that molecule in the laboratory [2]. Comparison of computer models may not be perfect, but they are effective for checking about 90% of compounds. This method is very useful. Because making a compound may require months of laboratory work and of course spending a lot of raw materials. Another application of computational chemistry is a more detailed and complete investigation of a problem. For example, determining the properties of a molecule computationally is much easier than laboratory methods. In addition, by using computational methods, one can find an insight into features such as molecular bonds, which is not possible using laboratory methods [3].

The mechanism of electron destabilization in monocyclic RAHB systems (malonaldehyde, acetyl, acetone, etc.) was investigated by Gilly and his colleagues. This mechanism is very different in two-ring systems compared to single-ring systems. In these systems, there is a single ring resonance in each of the rings of these compounds. Based on this single ring resonance, there is a π bond participation effect, or in other words, π electron delocalization (RAHB) in each of the rings of this molecule independently. In the upper part of the molecule (in the bridge of hydrogen bonds) there is also an anti-participation effect for σ bonds. Therefore, the hydrogen bonds formed in this molecule are strengthened through the destabilization of the π electron (RAHB) in the lower part of the electron and weakened through the two-way polarization caused by the anti-participation effect in the upper part of the molecule. Hence the hydrogen bonds formed in this molecule are called resonance assisted hydrogen bonds (RAHB) [4]. Since there is a single ring resonance in each of the rings of these compounds, it is possible to evaluate the destabilization of the π electron by determining the value of Q in each of the rings of this molecule. Since there is a single ring resonance in each of the rings of these compounds, it is possible to evaluate the destabilization of the π electron by determining the value of Q in each of the rings of this molecule. According to Gilli's expression, for RAHB systems, the value of Q decreases, which indicates an increase in the destabilization of the π electron and greater equality of the corresponding single and double conjugated bonds, and as a result, an increase in the strength of the hydrogen bond. The Q values for both ring compounds have been investigated. Compounds with OH proton donors have the lowest Q value compared to SH and HNH proton donors [4]. For compounds that have N and S heteroatoms, the comparison of Q values is as follows:

$$HN–H\cdots O\cdots H–HN > HN–H\cdots O\cdots H–O$$
$$S–H\cdots O\cdots H–S > S–H\cdots O\cdots H–O$$

22nd Iranian Chemistry Congress (ICC22)
Iranian Research Organization for Science and Technology (IROST)
13-15 May 2024

03231-97589
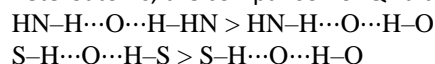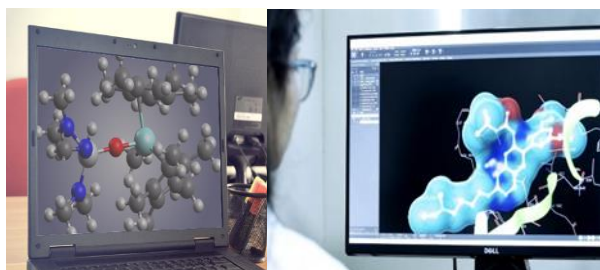
Fig.1 Schematic of Computational chemistry.

Experimental Section

In the research work, calculations were done using AIM 09 Gaussian software. The studied systems are optimized at MP2 level of theory and using ++G**311-6 standard base series. Also, the quantum theory of "atoms in molecules" by Mr. Bider was used to find topological properties.

Results and Discussion

All the systems investigated in this study have been completely optimized at the level of the base MP2/6-++G**311-6 series. The amount of hydrogen bond energy for both rings (EHB1, EHB2) of all systems along with the sum of these values (EHB1 + EHB2 = EHB) are presented in Table (1) The amount of hydrogen bond energy using the values of electron potential energy density (V(r)) is calculated in HBCP and Spinoza's relation. A detailed examination of the calculated results in the table shows that the strongest hydrogen bond is created when the system has an O-H proton-donating bond. Comparing the systems with S–H and HNH proton donor bonds, the hydrogen bond energy is higher for the S–H group. Therefore, the strongest hydrogen bond for systems with N heteroatoms is the -HN compound (EHBT = -24.78) H···O···H–O and for systems with S, the combination –S–H···O···H (EHBT = -23.84) O is formed.

Table1: Comparison of Q and λ parameters with the amount of hydrogen bond energy.

The table of geometrical parameters, including the length

Ring 1		Ring2				
Donor	Acceptor	Donor	H-bridge	Q	λ	E_{HBT}
HNH	O	OH	HN-H….O….H-O	0.312	0.067	-24.78
HNH	O	HNH	HN-H….O….H-NH	0.372	0.0596	-14.8
SH	O	OH	S-H…..O…..H-O	0.715	0.162	-23.84
SH	O	SH	S-H…..O….H-S	1.156	-0.066	-16.20

of links and the angles of various types of connections, has been obtained for both rings of the investigated systems. Therefore, it can be concluded that the shorter the length of the H...O bonds and the larger the X-H...O angle (X=HN,S,O), the stronger the hydrogen bond (Table2).

Table2: Table of geometrical parameters in terms of A^0.

Ring 1		Ring2											
Donor	Acceptor	Donor	Hbridge	$r_{c=c}$	$r_{H...o}$	r_{c-c}	$r_{c=o}$	$r_{c=c}$	r_{c-o}	r_{c-c}	$r_{c=o}$	$r_{H...o}$
HNH	O	OH	HN-H...O...H-O	1.371	1.952	1.446	1.269	1.364	1.330	1.457	1.269	1.640
HNH	O	HNH	HN-H...O....H-NH	1.368	1.94	1.456	1.261	1.368	-	1.457	1.261	1.943
SH	O	OH	S-H…..O…..H-O	1.361	1.934	1.463	1.262	1.367	1.325	1.452	1.262	1.654
SH	O	SH	S-H…..O…..H-S	1.361	1.904	1.464	1.251	1.361	-	1.465	1.251	1.904

Conclusions

In recent years, researches in the field of computational chemistry have increased. Conducting such studies simultaneously with the progress of computer software that is easy to use has been more attention. In these studies, it is not necessary to know the basis and theory part of the software, and the user does not need to know all the concepts used in calculations. Therefore, in this study, computational chemistry and its applications are reviewed and examples are given.
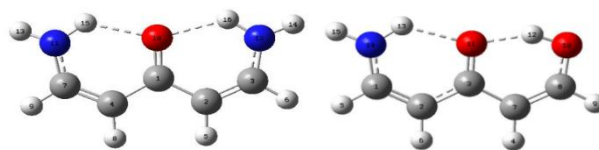
Fig.2: Molecular graph and contour plot of two-ring system.

References

[1] Young, D. (2004). Computational chemistry: a practical guide for applying techniques to real world problems. John Wiley & Sons.

[2] Atkins, P. W., & Friedman, R. S. (2011). *Molecular quantum mechanics*. Oxford university press.

[3] Gilli, G., Bertolami, V., Ferretti, V., & Gilli, P. (1993). Resonance-assisted hydrogen bonding. III. Formation of intermolecular hydrogen-bonded chains in crystals of β-diketone enols and its relevance to molecular association. Acta Crystallographic Section B: Structural Science, 49(3), 564-576.

[4] Bertolami, V., Gilli, P., Ferretti, V., & Gilli, G. (1991). Evidence for resonance-assisted hydrogen bonding. 2. Intercorrelation between crystal structure and spectroscopic parameters in eight intramolecularly hydrogen bonded 1, 3-diaryl-1, 3-propanedione enols. *Journal of the American Chemical Society*, 113(13), 4917-4925.

22ⁿᵈ Iranian Chemistry Congress (ICC22)
Iranian Research Organization for Science and Technology (IROST)
13-15 May 2024

03231-97589

IROST

Lanthanide Complex Based on Urea Ligand as Homogeneous Catalyst

haniyeh lazar Soleimani, Taraneh hajiashrafi*

Corresponding Author E-mail : t.hajiashrafi@alzahra.ac.ir

Abstract A new lanthanide-coordination complex containing 1,3-di(pyrimidin-2-yl)urea (LH) linker, namely $[La(LH)_2Cl_2(MeOH)_2] \cdot H_2O$, was synthesized and characterized using X-ray crystallography and spectroscopic methods. In this compound, two LH ligands are coordinated from pyrimidine nitrogens and urea oxygens to the lanthanum metal, with two LH ligands for each lanthanum metal. In the structure of this complex, the LH ligand acts as a bidentate, and a metal-ligand complex is formed with a ratio of 1:2. Crystallographic studies of the structure of this compound show that it crystallizes in $P\bar{1}$ space group of the triclinic system. This compound can be a promising homogeneous catalyst for organic transformations.

Keywords: Lanthanide complexes; X-ray crystal structure; coordination compound

Introduction

Rare earth elements (RE) are under investigation due to their significant advantages, such as low environmental impact and compatibility with organic interfaces.[1] The coordination chemistry of lanthanides has garnered increasing attention, given its crucial applications in fields like medicine, catalysis, and materials science. Lanthanide complexes find widespread use in various applications, serving as chromophores for catalysts in organometallic chemistry and as fluorescent probes. These applications necessitate a profound understanding of the coordination properties of lanthanide ions.[2] In recent years, urea ligands have become a focus of researchers due to their NH-C=O-NH active sites. The NH components form hydrogen bonds with metal salts, leading to the coordination of these ligands with lanthanide metal salts and the subsequent formation of lanthanide complexes. Consequently, we are working on synthesizing a new lanthanide metal complex based on urea ligands. This group of compounds has demonstrated remarkable growth in material and supramolecular chemistry owing to its diverse structural roles, high coordination numbers, and magnetic properties.[3]

Experimental Section
Synthesis of La-coordination compound

$[La(LH)_2Cl_2(MeOH)_2] \cdot H_2O$:

0.1 mmol (0.371 mg) of lanthanum(III) chloride heptahydrate and 0.2 (0.432 mg)mmol of 1,3-di(pyrimidin-2-yl)urea (LH) were added to 12 ml of MeOH as a solvent and stirred on the heater for 3 hours at 50°C. After several attempts, some colorless crystals were obtained.
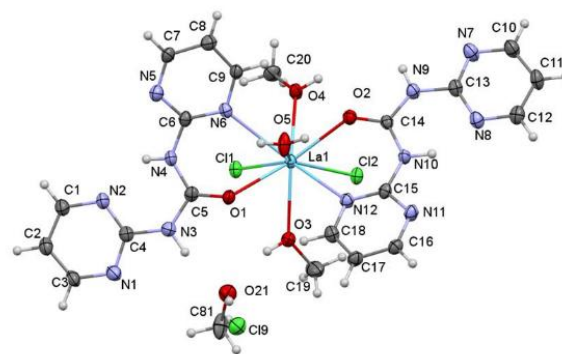
Fig.1: ORTEP scheme of the coordination complex; thermal ellipsoids are displayed at the 50% probability level and naming is done on non-hydrogen atoms.

Results and Discussion

Compound $[La(LH)_2Cl_2(MeOH)_2] \cdot H_2O$ was synthesized through the reaction between 1,3-di(pyrimidin-2-yl)urea (LH) and the corresponding $LaCl_3 \cdot 7H_2O$ salts, using the slow evaporation technique to produce crystals suitable for X-ray analysis (Fig. 1). The La-O bond is in the range of 2.578-2.501 Å, and for La-N, it is in the range of 2.791-2.769 Å. Crystal data: a = 6.9540(14) Å, b = 21.108(4) Å, c = 42.696(9) Å, β = 85.38(3)°, Z = 8.
In the LH FT-IR spectrum, a peak appears at 3220 cm⁻¹, corresponding to the OH stretching vibration of the urea group, while the CO stretching vibration in urea is observed at 1652 cm⁻¹.

Table1: selected bond distance (Å) and angles (◦) for complex

Bond distance		Bond angle	
La1-O1	2.501	Cl2-La1-Cl1	87.19(2)
La2-O2	2.517	Cl2-La1-O2	73.67(5)
La3-O3	2.575	Cl2-La1-O1	139.55(5)
La4-O4	2.560	Cl2-La1-O5	136.46(5)

22nd Iranian Chemistry Congress (ICC22)
Iranian Research Organization for Science and
Technology (IROST)

03231-97589

13-15 May 2024

IROST

Bond distance		Bond angle	
La5-O5	2.508	Cl2-La1-O4	78.67(5)
La1-N6	2.784	Cl2-La1-N12	79.29(6)
La1-N12	2.778	Cl2-La1-O3	76.30(5)
La1-Cl1	2.879	Cl2-La1-N6	146.40(6)
La1-Cl12	2.881	Cl1-La1-O2	139.74(5)

Conclusions

In summary, we have presented a novel lanthanum coordination complex incorporating 1,3-di(pyrimidin-2-yl)urea (LH).The solid-state structure of these compounds was investigated. Geometrical analysis revealed a distorted triclinic nine-coordination geometry for the metal center. This compound can be a promising homogeneous catalyst for organic transformations. These findings contribute valuable insights into the structural and spectroscopic properties of the synthesized compound, laying the foundation for further exploration and applications in the field.

References

[1]   G. KONG, L. LIU, J. LU, C. CHE, and Z. ZHONG, "Study on lanthanum salt conversion coating modified with citric acid on hot dip galvanized steel," *J. Rare Earths*, vol. 28, no. 3, pp. 461–465, 2010, doi: 10.1016/S1002-0721(09)60134-4.

[2]   T. Hajiashrafi, A. N. Kharat, J. A. Love, and B. O. Patrick, "Synthesis, characterization and crystal structure of three new lanthanide (III) complexes with the [(6-methyl-2-pyridyl)methyl]bis (2-pyridylmethyl)amine (MeTPA) ligand; New precursors for lanthanide (III) oxide nano-particles," *Polyhedron*, vol. 60, pp. 30–38, 2013, doi: 10.1016/j.poly.2013.04.061.

[3]   S. Khanjani and A. Morsali, "New nano-particle La(III) supramolecular compound as a precursor for preparation of lanthanum oxybromide-, hydroxide-, and oxide-nanostructures," *J. Coord. Chem.*, vol. 62, no. 20, pp. 3343–3350, 2009, doi: 10.1080/00958970903082184.

Reaction of arylidene malononitriles and N-1-adamantyl acetoacetamide: Synthesis of novel adamantane-4H-Pyran Hybrids

Hafez Janizadeh, Adeleh Moshtaghi Zonouz*

Corresponding Author E-mail: adelehmz@yahoo.com

Departement of Chemistry, Faculty of Science, Azarbijan Shahid Madani University, Tabriz, Iran.

Abstract: Novel 4H-pyrans incorporating an adamantane moiety were synthesized by the sequential Michael addition/cyclization reaction of arylidene malononitriles and N-1-adamantyl acetoacetamide. The 2-pyrone derivatives are formed upon hydrolysis of the iminopyran intermediates resulting from the intramolecular cyclization by nucleophilic attack of the hydroxyl group on the cyano group.

Keywords: Adamantane motif; Diamondoid; 4H-pyran; Amantadine; Nanodiamond

Introduction

The syntheses of 4H-pyrans derivatives have attracted great interest due to the biological and pharmacological activities [1]. Diamondoids are cage-saturated hydrocarbon molecules and superimposable on the diamond lattice, which can be described as hydrogen-terminated nanodiamonds [2]. Adamantane with the $C_{10}H_{16}$ formula is the smallest diamondoid. Until now eight drugs with adamantyl scaffold have been approved and exist in the world pharmaceutical market. Moreover, the unique properties of adamantane, including the size, lipophilicity, rigidity, and biocompatibility make it special for modification of known drugs through an add-on strategy. In many cases, the incorporation of the bulky lipophilic adamantyl moiety into the known drugs has improved their pharmacological properties without increasing toxicity, and resulted in many promising drug candidates with an adamantane moiety [2, 3]. Since the combination of adamantane moiety with other pharmacophores on the same scaffold, in most cases, leads to more potent biologically active compounds or drugs, we decided to synthesize novel 4H-pyran derivatives incorporating an adamantane moiety.

Experimental Section

Synthesis of N-(adamantan-1-yl) acetoacetamide: To a stirred mixture of ethyl acetoacetate (0.27 mL, 2.11mmol) in dry toluene (10 mL) at 105 °C, a solution of 1-adamantylamine (220 mg, 1.46 mmol) in dry toluene (5 mL) was added dropwise (over 50 min). Then the catalytic amount of triethylamine was added. The mixture was stirred at this temperature under an argon atmosphere for 19 h. On completion of the reaction, the solvent was removed under reduced pressure. The concentrate was left open overnight. The yellow solid was obtained with an excellent yield (95%) and was used without any further purification.
Yield: 325 mg (95%); yellow solid; mp 70-73 °C; IR (KBr): ū= 3315 (NH), 2908, 2851 (C-H), 1725 (C=O); 1642 (NH-C=O) cm⁻¹; ¹H NMR (DMSO-d₆, 500 MHz): δ = 1.60 (s, 6H, Ad), 1.92 (s, 6H, Ad), 1.95 (s, 3H, Ad), 2.11 (s, 3H, CH₃), 3.21 (s, 2H, CH₂), 7.56 (s, 1H, NH) ppm; ¹³C NMR (DMSO-d₆, 125 MHz): δ = 28.7, 36.0, 40.9, 52.3 (C-Ad), 29.7 (CH₃), 50.9 (CH₂), 165.3 (C=O), 203.4 (C=O) ppm.

Typical procedure for the Synthesis of arylidene malononitrile derivatives: A mixture of Malononitrile (1 mmol) and aromatic aldehydes (1 mmol) was in ethanol (3 mL) at room temperature for 30 min. The arylidene malononitrile as crystallian solid was obtained in excellent yield, and was used without any further purification.

Typical Procedure for the synthesis of 4H-pyrans derivatives: A mixture of Arylidine malononitrile (**2**) (1 mmol), N-(adamantan-1-yl)acetoacetamide (**1**) (220 mg, 1 mmol), and ammonium acetate (1.5 mmol, 0.12 g) was thoroughly mixed in a mortar by grinding till the completion of reaction as indicated by TLC. After work up,recrystallization and the coloumn chromatography 2-pyrone derivative (**3**) and 2-amino pyran derivative (**4**) were obtained in high yield.

Results and Discussion

In order to preparation of 4H-pyrans, firstly, N-(adamantan-1-yl)acetoacetamide (**1**) (a β-keto amide), as an adamantane-containing active methylene compound, was prepared by nucleophilic amidation of ethyl acetoacetate with 1-adamantylamine (amantadine) in the presence of a catalytic amount of triethylamine (5 mol %) in refluxing toluene under an argon atmosphere [4]. Then, arylidene malononitriles (**2**) were prepared by the Knovenagel condensation reaction of malononitrile and aromatic aldehydes under reflux condition in ethanol at room temperature for 30 min. [5]. Next, tandem Micheal addition/cyclization reaction of N-(adamant-1-yl)acetoacetamide (**1**) (1 mmol) and arylidene malononitrile (**2**) (1 mmol), in the presence of ammonium acetate (1.5 mmol) under solvent-free conditions at room temperature on grinding gave a

22nd Iranian Chemistry Congress (ICC22)
Iranian Research Organization for Science and
Technology (IROST)
13-15 May 2024

03231-97589

IROST

crude solid. To the crude residue was added dichloromethane and water. The organic layer was separated and dried over anhydrous Na_2SO_4 and concentrated in vacuo. Crystallized of crude product from ethanol gave the white solid, whish spectral data approve the 2-pyrone structure (**3**). The evaporation of mother liquore and purification of it by flash chromatography to give 2-amino-pyran derivatives (**4**) (Scheme1).
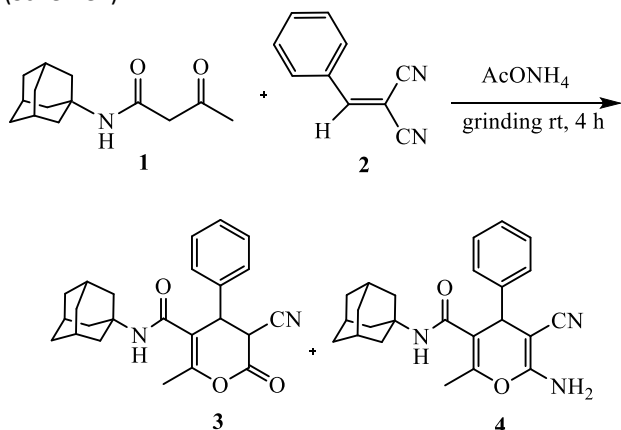
Scheme 1: Synthesis of 2-pyrone and 2-amino-pyran

The proposed mechanism for the synthesis of 4H-pyran derivatives was shown in (Scheme2). Tandem Micheal addition/cyclization reaction of N-(adamant-1-yl) acetoacetamide (**1**) and arylidene malononitrile (2) gave the imino pyran intermediate (**5**). The intermediate (**5**) upon hydrolysis to give 2-pyrone derivatie (**3**), and by imine-enamine tautomerization to afford 2-amino-pyran derivative (**4**).

Conclusions

In summary, we have developed for the first time a convenient and highly efficient add-on strategy to generate 4H-pyrans incorporating adamantane moiety. In order to introduce adamantane moiety on the 4H-pyrans skeletone, adamantylated active methylene compound (**1**) was prepared and used in reaction with arylidene malononitrile derivatives. We hope the size, rigidity, and approximately spherical shape of adamantane as a lipophilic bullet can influence and modify the physico–chemical features of these 4H-pyran-based scaffolds.
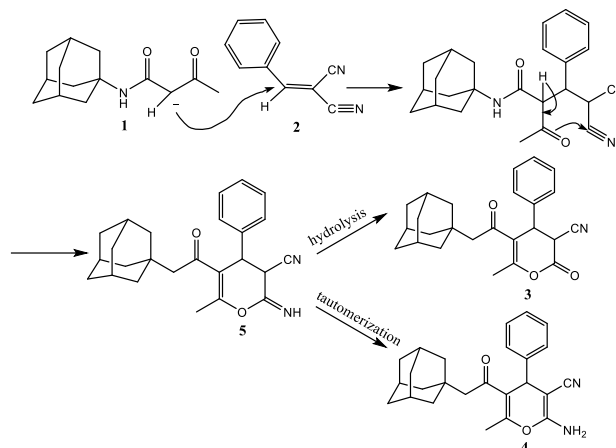
Scheme 2: The proposed mechanism for the synthesis of 4H-pyran derivatives **3** and 4

References

[1] Patil, U. P., Patil, R. C., & Patil, S. S. (2020). Waste mussel shell as a highly efficient heterogeneous catalyst for the synthesis of polyfunctionalized 4H-pyrans in aqueous media. *Reaction, Kinetics, Mechanisms and Catalysis* 129(2), 679-691. ttps://doi.org/10.1007/s11144-020-01743-6.

[2] Wanka, L., Iqbal, K., & Schreiner, P. R. (2013). The lipophilic bullet hits the targets: medicinal chemistry of adamantane derivatives. Chemical reviews, 113(5), 3516-3604. https://doi.org/10.1021/cr100264t.

[3] Sibiryakova, A. E., Shiryaev, V. A., Reznikov, A. N., Kabanova, A. A., & Klimochkin, Y. N. (2019). Asymmetric Synthesis of Adamantyl GABA Analogues. Synthesis, 51(02), 463-469. https://doi.org/10.1055/s-0037-1610824.

[4] Abkar Aras, M., & Moshtaghi Zonouz, A. (2023). Synthesis of novel adamantane-containing dihydropyrimidines utilizing Biginelli condensation reaction. Journal of Sulfur Chemistry, 44(3), 361-376. https://doi.org/10.1080/17415993.2023.2166348.

[5] Johari, S., Johan, M. R., & Khaligh, N. G. (2024). Mechanism study and preparing (hetero) arylidene malononitriles through a greener and scalable catalytic strategy. Journal of Molecular Structure, 1302, 137422. https://doi.org/10.1016/j.molstruc.2023.137422.

[6] Moshtaghi, Z. A., Ghaffari, P., & Pourreza, A. (2022). Synthesis of Pyrimidine Hybrids Based on 4H-Pyran and 4H-Chromene Privileged Structures. Letters in Organic Chemistry, 19(11), 993-998. https://doi.org/10.2174/1570178619666220209154646.

Spectroscopic (FT-IR, UV-Vis), first-order hyperpolarizability, HOMO and LUMO analysis of N-phenylpyrazine-2-carboxamide ligand Derivatives by density functional methods

Samira Fadaei [a], Robabeh Alizadeh [*a], Vahid Amani [b], Pouya Doaei [c]

Corresponding Author E-mail: r.alizadeh@du.ac.ir

[a] School of Chemistry, Damghan University, Damghan, Iran.

[b] Department of Chemistry Education, Farhangian University, P.O. Box 14665-889, Tehran, Iran.

[c] School of Chemistry, Gachsaran University, Gachsaran, Iran.

Abstract: In the present work, a theoretical study was carried out to study the molecular structure and FMO for N-(2-ethoxyphenyl)pyrazine-2-carboxamide (HL) in density functional theory (DFT) using B3LYP (Becke-3–Lee–Yang–Parr) functional and 6-311+G(d,p) basis set. Time-dependent DFT (TD-DFT) to study the UV–vis has been performed absorption behavior. Hirshfeld calculations were used to quantitatively analyze the different intermolecular interactions in the crystal structure of the ligand.

Keywords: Carboxamide DFT; Mulliken; B3LYP

Introduction

The carboxamide linkage, [–C(O)NH–], is considered one of the most vital and widespread functional groups in nature, and an important ligand-construction unit for coordination chemists which has attracted much attention [1].

Experimental Section

The computational studies were carried out utilizing the GAUSSIAN 16, and Gauss View 6.0. The geometry optimization of the ligand HL was performed using the DFT/B3LYP technique of the Gaussian program with 6-311G+(d, p) basis set. Electronic transition calculations were performed using the TDDFT/B3LYP function basis set [3].

-0.0619 0.0619
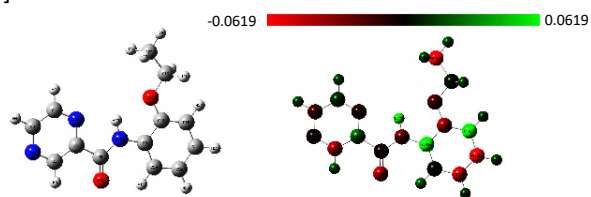
Fig.1: Optimized geometries and Mulliken's atomic charges distributions

Results and Discussion

The calculated IR spectrum is recorded in the region of 4000-400 cm^{-1} and the gas phase. The N-H stretching vibration is expected in the region 3500-3300 cm^{-1} [3] and for the title compound, this mode is assigned at 3540 cm^{-1}. The Carbonyl stretching frequency is in the range of 1700-1600 cm^{-1}, and the theoretical carbonyl stretching frequency of the HL compound is 1634 cm^{-1} which confirms the presence of the carbonyl group. The HOMO

and LUMO orbitals for ligand and complex were calculated at the B3LYP/6-311+G (d,p). Molecular atomic charges were computed by MPA using the aforementioned basis set to calculate the MEP of the title molecule. Analyzing the results, the N28 atom has a negative atomic charge (-0.25), whereas the H29 atom linking to N28 has a larger positive atomic charge than other hydrogen atoms in the gas phase (0.39). This is due to N-H…N hydrogen bond. HOMO of HL was localized on the phenyl core, oxygen methoxy group, and the linker, whereas LUMO was on the pyrazine core and the linker. The resulting MEP map with a range of −5.072 e^{-2} to 5.072 e^{-2} depicts its potential distribution. In the NMR spectrum, the theoretical and experimental chemical shift values show a good agreement with each other.

-5.072 e^{-2} 5.072 e^{-21}

LUMO - 0.08546

0.13471 eV

HOMO - 0.22035

HL1
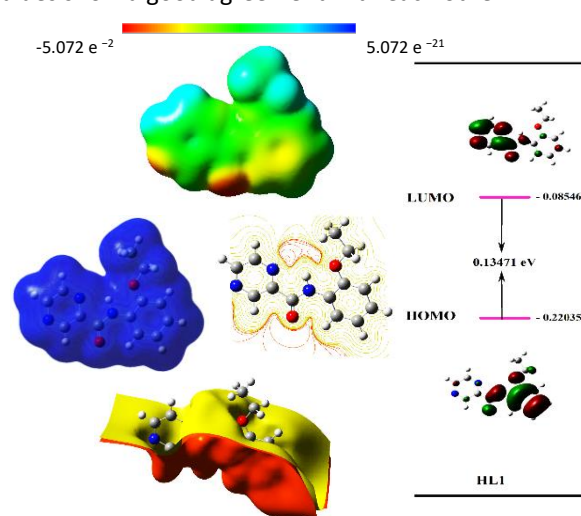
Fig.2: The electrostatic potential contour surface (ESP), Iso-surface plot of ESP contour map, total electron density (TED) plot, HOMO-LUMO and energy gaps of the HL
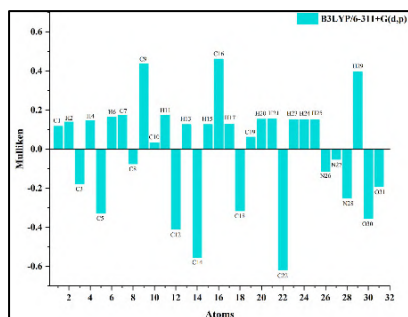
Fig.3: Histogram of atomic charge distribution graph (MPA)

Table1: Calculated energy values (eV) of ligand

Parameters	HL (eV)	Parameters	HL (eV)
HOMO	-0.22035	η	0.067445
LUMO	-0.08546	σ	7.41345
HOMO-1	-0.24887	μ	-0.15290
LUMO+1	-0.06260	ω	0.173326
E_g	-0.13471	χ	0.15290
IA	0.22035	ΔN_{max}	-2.2670
EA	0.08546		

Conclusions

We compared the X-ray diffraction crystal structure of compounds with the DFT-optimized structure. Frequency calculation has been done on this optimized geometry. The results indicate that the complex is a local minimum, without any imaginary frequency. Optimized structural parameters were then used for the calculation of vibrational wavenumbers. The positive value of all the calculated wavenumbers confirms the stability of optimized geometry. The results of our calculations show that the calculated bond lengths and angles are similar to those determined by the crystal structure. Theoretical calculations confirmed good agreement between experimental and calculated results.
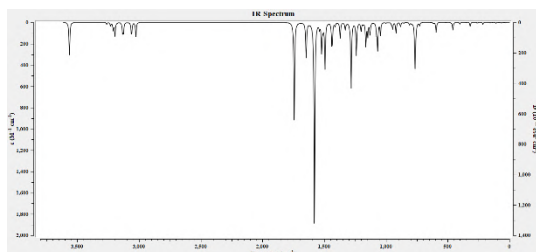
Fig.4: Theoretical FTIR spectra of HL ligand

References

[1] Khayer, K., & Haque, T. (2023). Density Functional Theory Calculation on the Structural, Electronic, and Optical Properties of Fluorene-Based Azo Compounds. ACS Omega, 5(9), 4507-4531. https://doi.org/10.1021/acsomega.9b03839.

[2] Adeyemi, J.O.; Olasunkanmi, L.O.; Fadaka, A.O.; Sibuyi, N.R.S.; Oyedeji, A.O.; & Onwudiwe, D.C. (2022). Synthesis, Theoretical Calculation, and Biological Studies of Mono- and Diphenyltin(IV) Complexes of N-Methyl-N-hydroxyethyldithiocarbamate. Molecules, 27(9), 2947-2969. https://doi.org/10.3390/molecules27092947.

[3] Boraei, A.T.A.; Haukka, M.; Sarhan, A.A.M.; Soliman, S.M.; & Barakat, A. (2021). Intramolecular Hydrogen Bond, Hirshfeld Analysis, AIM; DFT Studies of Pyran-2,4-dione Derivatives. Crystals, 11(8), 896-918. https://doi.org/10.3390/cryst11080896.

Table2: Theoretical NMR isotropic chemical shifts

Atom	Calculated B3LYP/ 6-311+G(d,p)	Atom	Calculated B3LYP/ 6-311+G(d,p)
29-H	10.612	8-C	165.250
6-H	9.754	18-C	154.290
11-H	9.126	3-C	153.745
4-H	9.010	7-C	150.913
2-H	8.834	5-C	150.562
15-H	7.274	1-C	148.290
13-H	7.191	9-C	133.381
17-H	7.084	14-C	128.629
20-H	4.122	12-C	124.205
21-H	4.121	10-C	122.628
23-H	1.716	16-C	113.813
24-H	1.715	19-C	66.324
25-H	1.490	22-C	15.407

Table3: Dipole moments, static electronic polarizabilities

Ligand			
Atom	Charge	Dipole Moment	Dipole Moment
1 C	0.116100	μ_x= -1.5774	γ_{xxxx}= -5444.9176
2 H	0.137244	μ_y= 5.0783	γ_{xxxz}= -0.0849
3 C	-0.176366	μ_z= -0.0008	γ_{zzzy}= -0.0050
4 H	0.145008	μ_{tot}= 5.3177 D	γ_{xxyz}= -0.0082
5 C	-0.326319	α_{xx}= -96.5660	γ_{yyyy}= -2072.2338
6 H	0.162971	α_{xy}= 5.3608	γ_{yyyx}= 1.4923
7 C	0.173634	α_{yy}= -100.2283	γ_{xxyy}= -1115.6616
8 C	-0.073702	α_{xz}= -0.0029	γ_{yyxz}= -0.0110
9 C	0.436207	α_{zz}= -108.7048	γ_{zzzz}= -132.5222
10 C	0.032228	α_{yz}= 0.0021	γ_{yyyz}= 0.0230
11 H	0.173209	β_{xxx}= -59.7502	γ_{xxzz}= -984.8129
12 C	-0.408780	β_{xxy}= 60.3636	γ_{zzxy}= -30.0397
13 H	0.124786	β_{yyz}= -0.0077	γ_{xxxy}= 201.6031
14 C	-0.551772	β_{yyy}= 42.6796	γ_{zzzx}= 0.0001
15 H	0.125227	β_{xxz}= -0.0027	γ_{yyzz}= -395.8138
16 C	0.460657	β_{xyz}= -0.0030	$\Delta\alpha$= 7.90055
17 H	0.126481	β_{zzz}= 0.0026	η_α= 1.6094
18 C	-0.314419	β_{xzz}= 8.3111	α^{iso}= -15.09165×10⁻²⁴
19 C	0.060052	β_{xyy}= -16.9966	β_{tot}= 505.8457×10⁻³³
20 H	0.152880	β_{yzz}= 6.6456	γ_{tot}= -12735.044×10⁻⁴⁰
21 H	0.152914		
22 C	-0.618677		
23 H	0.151112		
24 H	0.151113		
25 H	0.148462		
26 N	-0.111740		
27 N	-0.051287		
28 N	-0.249340		
29 H	0.395039		
30 O	-0.353329		
31 O	-0.189593		

Synthesis, characterization, spectroscopic investigation, and crystal structure determination of a new copper(II) complex with the N-(2-methoxyphenyl)pyrazine-2-carboxamide ligand

Samira Fadaei [a], Robabeh Alizadeh[*a], Vahid Amani [b], Raziyeh Arab Ahmadi [c]

Corresponding Author E-mail: r.alizadeh@du.ac.ir

[a] School of Chemistry, Damghan University, Damghan, Iran.

[b] Department of Chemistry Education, Farhangian University, P.O. Box 14665-889, Tehran, Iran.

[c] Chemistry Department, Payame Noor University (PNU), Tehran, Iran

Abstract: In the present work, the new Cu(II) complex has been designed and synthesized from the reaction of $CuCl_2.3H_2O$ with N-(2-mthoxyphenyl)pyrazine-2-Carboxamide Ligand (HL). The crystal and molecular structure of the coordination polymer complex $[Cu(L)Cl]_n$, has been determined by X-ray crystallography, IR, and UV-Vis. The ligand L acts as a tridentate unsymmetrical ligand.

Keywords: Cu (II) Complex; Crystal Structure; Carboxamide, Pyrazine

Introduction

Transition metal complexes have attracted enormous attention over the past few decades in the area of materials science, especially for their applications as functional materials. Despite all transition metals, copper has gained much attention due to its enormous biological potential. Also, transition metal complexes have a great diversity in their mode of action [1]. Subtle factors, for example, the coordination environment of the central metal ion, the type of metal, and the nature of solvents used for crystallization, often affect the coordination modes and the nuclearity of the resulting metal complexes. The synthesis of transition metal complexes with ligands containing carboxamide functionality has attracted attention due to their potential applications in medicine, catalysis, and the construction of functional materials and ion-selective electrodes [2-3]. Pyrazine-2-carboxamide derivatives have found wide applications in the fields of chemistry, biology, and biotechnology. In an effort toward the development of new applications for carboxamide ligands, the synthesis, characterization, and properties of the new complex [Cu(L)], is reported. The ligand can coordinate with the metal center in several different modes, depending on whether the base was present in the synthesis.

Experimental Section

5 mL methanolic solution of HL (0.2 mmol, 0.046 g) and triethylamine (0.2 mmol, 0.7ml, catalyst) in methanol was slowly added to a 5 mL methanolic solution of copper chloride dihydrate (0.2 mmol, 0.034 g) under stirring to give a light green solution. Then the mixture was stirred for 40 min at 40 °C. X-ray-quality single crystals were obtained after slow evaporation of the solvent over five weeks. The resulting crystals were isolated to conduct the single-crystal X-ray analysis. The compound was characterized as $[Cu(L)Cl]_n$. Yield (81%). m.p >250°C.

Results and Discussion

The FTIR spectra were recorded in the range of 4000–400 cm^{-1} as a KBr pellet at room temperature providing information about the coordination mode when the free ligand is coordinated to metal ions. The lack of the N–H stretching band in the IR spectrum of the complex confirms that the ligand is coordinated in its deprotonated form [4].

The UV–Vis data of the new complex $[Cu(L)Cl]_n$ in acetonitrile show two bands in the region of 260 and 301 nm, assigned to the intra-ligand $\pi{\rightarrow}\pi^*$ (of aromatic rings) and $n{\rightarrow}\pi^*$ (of electron pairs of carboxamide-O atom) transitions. As expected these bands were slightly shifted relative to the corresponding bands in the free ligand. A low-intensity band ($\varepsilon = 22.46$ M^{-1} L cm^{-1}) observed at 454 nm in the electronic spectrum of the complex is attributed to the ligand field transition of the copper(II) complex.

As shown in Table 1, the single crystal was developed in the monoclinic crystal system with the space group $P2_1/c$. There is a significant interaction between the Cu(II) ion of one molecule and the pyrazine nitrogen atom of the adjacent molecule to form a polymeric compound with a Cu–N(neighbor) distance of (2.334(6)Å). The Cu1-N3 (pyrazine) (1.919(5)Å) distance is shorter than the Cu1-N1(pyrazine) (2.017(6)Å), and Cu1–O2(methoxy) (2.088(5)Å). This is consistent with the fact that the deprotonated amide nitrogen is a very strong s donor.

22nd Iranian Chemistry Congress (ICC22)
Iranian Research Organization for Science and Technology (IROST)
13-15 May 2024

03231-97589

Table 1: Crystallographic parameters, data collection, and refinement details for Complex

Crystal Data	
Chemical formula	$C_{12}H_{12}ClCN_3O_3$
Formula weight	345.25
Temperature (K)	298
Crystal system	Monoclinic
Space group	$P2_1/c$
a (Å)	10.5070(17)
b (Å)	12.782(2)
c (Å)	10.5612(15)
α (°)	90
β (°)	109.510(11)
γ (°)	90
V (Å3)	1336.9(4)
Z	4
Calculated density (g/cm^{-3})	1.715
Crystal size (mm)	0.02 × 0.30 × 0.35
μ (mm^{-1})	1.843
F (000)	700
ϑ Ranges (°)	2.59, 27.00
Index ranges	$-13 \leq h \leq 13$; $-16 \leq k \leq 16$; $-13 \leq l \leq 11$
Absorption correction	Multi-scan
T_{min}, T_{max}	0.0852, 0.3210
Reflections collected	11996
Independent reflections	2926 (0.098)
(R_{int})	2029
Data/restraints/parameters	2926 /8/190
Goodness-of-fit on F^2	1.110
Final R indices [$I>2\sigma (I)$]	R1 = 0.0846, wR2 = 0.1719
R indices (all data)	R1 = 0.0965, wR2 = 0.1897
Max./min. $\Delta\rho$ (e Å^{-3})	-0.66 and 0.87
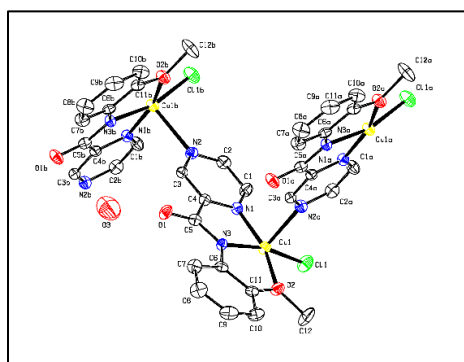
Fig.1: ORTEP diagram of the asymmetric unit with the atom numbering scheme used for copper complex with 30% thermal probability ellipsoids.
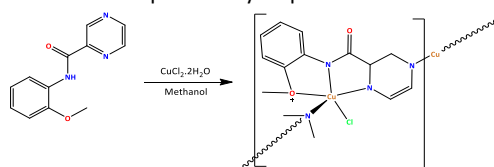
Fig.2: Synthesis of complex and copper ion chelation in methanol

Conclusions

In summary, in the present study, a carboxamide-Cu(II) complex in a simple and one-step process was successfully designed and synthesized and characterized by various spectroscopic techniques Copper(II) ion adopts a distorted square pyramidal (4 + 1) coordination in this complex, and in the solid state, the Cu(II) complex is stabilized by interactions between Cu(II) ions and pyrazine nitrogen atoms of the neighbor molecule to form a polymeric compound. Further research on the applications and biological properties of complexes, such as antibacterial and antifungal properties and comparing them with the corresponding ligands, in order to investigate the possibility of using the target compounds in biological systems, is also one of the other goals of this study that will be evaluated.

References

[1] Ambrożkiewicz, W.; Kučerová-Chlupáčová, M.; Janďourek, O.; Konečná, K.; Paterová, P.; Bárta, P.; Vinšová, J.; Doležal, M.; & Zitko, J. (2020). 5-Alkylamino-N-phenylpyrazine-2-carboxamides: Design, Preparation, and Antimycobacterial Evaluation. *Molecules*, *25*(7), 1561-1582. https://doi.org/10.3390/molecules25071561

[2] Liu, X., Shi, T., Xu, C., Zhu, M., & Wang, Y. (2023). A highly selective and sensitive ICT-based Cu2+ fluorescent probe and its application in bioimaging. Ecotoxicology and Environmental Safety, 262(7), 115127-115149. https://doi.org/10.1016/j.ecoenv.2023.115127.

[3] Jandourek, O.; Tauchman, M.; Paterova, P.; Konecna, K.; Navratilova, L.; Kubicek, V.; Holas, O.; Zitko, J.; & Dolezal, M. (2017). Synthesis of Novel Pyrazinamide Derivatives Based on 3-Chloropyrazine-2-carboxamide and Their Antimicrobial Evaluation. *Molecules*, *22*, 223-243. https://doi.org/10.3390/molecules22020223.

[4] Meghdadi, S., Amirnasr, M., Moein Sadat, S.B.H., Mereiter, K., & Amiri, A. (2014). Benign synthesis of the unsymmetrical ligand N-(8-quinolyl)quinoline-2-carboxamide (Hqcq) and the varied crystal chemistry of its Cu(II), Zn(II), and Cd(II) complexes bearing acetato and aqua co-ligands. Monatsh Chem 145(10), 1583–1594. https://doi.org/10.1007/s00706-014-1232-7.

Using a flower-like MoS2 as a sunlight-assisted photocatalyst for degradation of Eosin Y

Samira Saeednia*[a], Parvaneh Iranmanesh [b], Sobhan Abbasi [a]

s.saaednia@vru.ac.ir , Sobhanabbasi239@gmail.com

[a] Department of Chemistry, Faculty of Sciences, Vali-e-Asr University of Rafsanjan, Rafsanjan, Iran

[b] Department of Physics, Faculty of Sciences, Vali-e-Asr University of Rafsanjan, Rafsanjan, Iran.

Abstract: A bottom-up approach was used to synthesize molybdenum disulfide nanostructures. The flower-like MoS2 nanosheets were synthesized by hydrothermal method using a thio Schiff base ligand as a sulfur source and simultaneously as a capping agent. In the study of photocatalytic activity, the effective amount of the catalyst was optimized and the recovery ability of the catalyst was also investigated.

Keywords: Molybdenum disulfide; Hydrothermal; Photocatalyst

Introduction

Among all metal sulfides, transition metal dichalcogenides have unique properties which have attracted the attention of researchers[1,2,3] . Molybdenum disulfide (MoS2) is an inorganic compound of the transition metal dichalcogenide (TMD) serie. MoS2 has a hexagonal crystalline structure which in its most common 2H form shows a unit symmetry. In such structure, Mo ions are surrounded by six sulfur anions in a trigonal prismatic arrangement interstices. MoS2 possesses a tunable band gap that depends on the number of MoS2 layers[4]. MoS2 has layered structure composing of S–Mo–S three layers bound by the weak Van der Waals forces, resulting in materials with fascinating properties[5].

Experimental Section

All of the chemical reagents used in this experiment were analytical grade. In a typical synthesis, 0.17 g of ammonium hepta molybdate (NH4)$_6$Mo$_7$O$_{24}$.4H$_2$O) and 0.328 g of 1- benzylidene thiourea (C$_8$H$_8$N$_2$S) were dissolved in 15 mL deionized water separately, then these two solutions were blended together and stirred for about 1 h at room temperature until it was mixed homogenously. At the next step, the precipitated solution was transferred to a Teflon-line stainless steel autoclave and sealed tightly and heated for 24 h at 200 °C. The solution was not disturbed during the heating period. After the end of the reaction and coolness the autoclave to room temperature, the resulting black precipitate was gathered. To remove the un-reacted materials, the obtained precipitate was washed various time with absolute ethanol and distilled water respectively. The degradation of dyes (eosin Y) was carried out under natural sunlight. The experiment was carried out on a sunny day (11:00 am-3:00 pm) in the month of June, location-Rafsanjan City, Kerman (Iran). In a typical experiment, 0.01 g of the MoS2 powders suspended in 100 mL of 10 ppm dye solution. This solution stirred in the dark for 1 h to achieve adsorption-desorption equilibrium between the photocatalyst and dye solution. The aqueous solution was then exposed to natural sunlight under constant stirring. After every 30 min, 2 ml of degraded solution was collected and followed by centrifuge at 2100 rpm. The obtained filtrates were then examined by measuring absorption peak at 510 nm for eosin Y to identify variation in concentration of dye at different irradiance time.

Results and Discussion

So far, the degradation of toxic dyes by many metal nanostructures has been investigated and studied [6,7]. In this work, we have synthesized flower-like MoS2 nanosheets [8] sample as a photocatalyst for the degradation of eosin Y dye under natural sunlight irradiation. The photocatalytic activity of the synthesized MoS2 were examined using of absorbance plots over 200 to 800 nm of wavelength. Initially, the dye solution sample was first collected in the presence of photocatalyst in the dark. Here, we found no noticeable change in the color of the dye and only a slight decrease in absorbance. This partial decrease is due to the surface adsorption of dye on the surface of MoS2 nanosheets. Even so, when the photocatalyst sample was added to the solution of eosin Y and placed under sunlight for 1.5 h, the dye absorption peak decreased due to effective photocatalysis reactions (Figure 1).

The estimated photocatalyst degradation efficiency of photocatalyst sample were found to be 98%, under 1.5 of natural sunlight irradiation.

22nd Iranian Chemistry Congress (ICC22)
Iranian Research Organization for Science and Technology (IROST)
13-15 May 2024

03231-97589
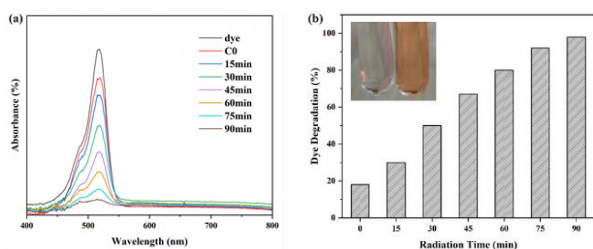
Fig.1: Time-dependent optical absorbance spectra for the eosin solution containing the synthesized MoS_2 nanosheets after its exposure to sun light for different durations (b) the dye degradation percentage.

To obtain the minimum amount of photocatalyst, other experiments were conducted in which smaller amounts of the photocatalyst were used. As seen in Table 1, the minimum effective amount of MoS_2 is 0.0025 g. In smaller quantities of photocatalyst, the process of dye degradation is not done as well and the photocatalytic activity decreases noticeably.

Table1: Effect of photocatalyst amount on percentage of dye degradation

Amount of Photocatalyst (g)	Degradation of Eosin Y (%)
0.01	98
0.005	97
0.0025	93
0.0013	56

In order to investigate the possibility of reusing the catalyst, after each experiment, the photocatalyst was separated from the reaction solution by centrifugation, washed several times with distilled water, and used again in the dye degradation reaction.
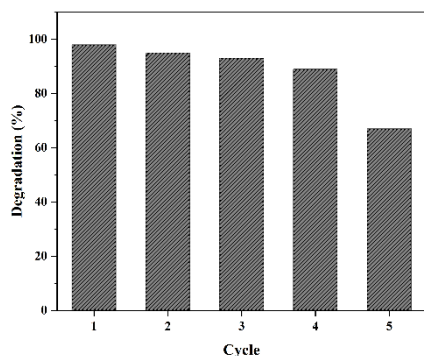
Fig.2: Degradation percentage in different cycles of photocatalyst reusing

Conclusions

Considering that the hydrothermal method, which is a simple, environmentally benign and economical technique, this method was used for the successful synthesis of flower-like MoS_2 nanosheets. In this hydrothermal method, the thio Schiff-based (1-benzylidene thiourea) was used as both a sulfur source and a capping and complexing agent which resulted in less use of chemicals and less time and cost. The activity of synthesized molybdenum disulfide was investigated for photodegradation of eosin Y dye under natural sunlight illumination. 95% photodegradation percentages under sunlight illumination were estimated for eosin Y within 1.5h. The minimum effective amount of photocatalyst was determined to be 0.0025 g. The applied photocatalyst up to 4 times for eosin Y has the ability to recover with very good efficiency.

References

[1] Chen, E., Xu, W., Chen, J., & Warner, J. H. (2020). 2D layered noble metal dichalcogenides (Pt, Pd, Se, S) for electronics and energy applications. *Materials Today Advances*, *7*, 100076.

[2] Kanade, C. K., Seok, H., Kanade, V. K., Aydin, K., Kim, H. U., Mitta, S. B., ... & Kim, T. (2021). Low-temperature and large-scale production of a transition metal sulfide vertical heterostructure and its application for photodetectors. *ACS Applied Materials & Interfaces*, *13*(7), 8710-8717.

[3] Liang, Q., Zhang, Q., Zhao, X., Liu, M., & Wee, A. T. (2021). Defect engineering of two-dimensional transition-metal dichalcogenides: applications, challenges, and opportunities. ACS nano, 15(2), 2165-2181.

[4] Akram, H., Mateos-Pedrero, C., Gallegos-Suárez, E., Guerrero-Ruíz, A., Chafik, T., & Rodríguez-Ramos, I. (2014). Effect of electrolytes nature and concentration on the morphology and structure of MoS2 nanomaterials prepared using one-pot solvothermal method. Applied Surface Science, 307, 319-326

[5] Akram, H., Mateos-Pedrero, C., Gallegos-Suárez, E., Allali, N., Chafik, T., Rodriguez-Ramos, I., & Ruiz, A. G. (2012). Low solvothermal synthesis and characterization of hollow nanospheres molybdenum sulfide. Journal of nanoscience and nanotechnology,12(8), 6679-6685

[6]Pourjafari, D., Saeednia, S., Iranmanesh, P., & Hatefi Ardakani, M. (2019). Preparation and Photocatalyst Properties of Zinc Sulfide Using a Distinct Sulfur Source: 1-Benzylidenethiourea. Journal of Cluster Science, 30, 571-580.

[7] Khorasanipour, N., Iranmanesh, P., Saeednia, S., & Yazdi, S. T. (2023). Photocatalytic degradation of Naphthol Green in aqueous solution through the reusable ZnS/MoS2/Fe3O4 magnetic nanocomposite. Surfaces and Interfaces, 36, 102613.

[8] Saeednia, S., Iranmanesh, P. & Abbasi, S., (1402). Solvothermal synthesis and characterization of nano molybdenum disulfide, 22nd Iranian Inorganic Chemistry Conference, Sanandaj, Kordestan

Investigating the Effect of Mn Addition on Fischer-Tropsch Synthesis during CO Hydrogenation on Graphene Oxide using DFT

Hanieh Bakhtiari, Saeedeh Sarabadani Tafreshi, Majid Abdouss

Corresponding Author E-mail: s.s.tafreshi@aut.ac.ir

Department of Chemistry, Amirkabir University of Technology, No. 350, Hafez Avenue, Valiasr Square, Tehran, Iran.

Abstract: Our study explored the potential of Mn-doped Graphene Oxide (GO) as a catalyst in reducing air pollution by converting carbon monoxide (CO) into valuable hydrocarbons, CH_4 and CH_3OH. We identified low and high-energy barrier reactions and concluded that Mn-doped GO holds promising capabilities as a catalyst. We employed DFT calculations to explore both thermodynamic and kinetic properties.

Keywords: Carbon monoxide hydrogenation; CH_4; catalyst; Mn-doped graphene oxide; DFT

Introduction

A study published in the journal of Applied Surface Science investigated the ability of transition metals (TMs) to bind to graphene nanoflakes (GNFs) and found that Mn-GNFs had a relatively high CO adsorption energy. Literature has shown that metal-doped graphene and graphene oxide surfaces also have high catalytic activity for CO hydrogenation. The deviations from classical Fischer-Tropsch reactions can be attributed to the unique properties of the graphene oxide substrate and the tailored manganese catalysis. Also, the role of OH functional groups and how the introduction of hydroxyl groups on the graphene oxide surface leads to the formation of intermediates that are subsequently transformed into hydrocarbon products with the help of manganese. [1] We can highlight that the graphene oxide surface provides an ideal environment for selective reactions, while the manganese catalyst plays a crucial role in directing the selectivity towards smaller hydrocarbons. [2,3]

Computational Detail

We conducted periodic plane-wave density functional theory (DFT) [4] calculations to examine the adsorption of CO and its reactivity on the surfaces of GO doped with manganese. This methodology ensured a rigorous approach to our investigations, enabling us to gain valuable insights into the CO adsorption and reactivity of Mn-doped GO surfaces. [5–7] VASP is employed to approximate solutions to the many-body Schrödinger equation through DFT by solving the Kohn-Sham equations. To calculate the total energy, we utilized the Perdew–Burke–Ernzerhof (PBE) variant of the generalized gradient approximation (GGA). [8] The inclusion of the long-range van der Waals (vdW) forces improves the energy description of each system, therefore, employed DFT-D3, the method of Grimme as implemented in VASP. [9]

Results and Discussion

Among the molecules studied, CH_2 has the lowest adsorption energy (-5.58 eV), indicating its greater stability on the catalyst surface and probable participation in hydrocarbon production. CH_2OH, while having lower adsorption energy (-3.61 eV) compared to CH_2 and CH_2OH in CH_3OH formation, still stands as a relatively stable molecule, suggesting its potential involvement in hydrocarbon generation. CO, having the lowest adsorption energy (-1.35 eV) among all molecules, is the least stable and might have a less significant role in the reaction on this catalyst surface. [10] (Table1)

Table1: Adsorption energies of intermediates on the Mn-doped GO surface.

	E_{ads} (eV)		E_{ads} (eV)
CO	-1.35	CH_2OH	-3.61
HCO	-3.27	CH_2	-5.58
CH_2O	-2.04	CH_3	-3.48

During a chemical reaction, the participating molecules absorb thermal energy from their surroundings. When a reactant molecule absorbs sufficient energy to reach what's known as the transition state, the reaction can proceed.

22ⁿᵈ Iranian Chemistry Congress (ICC22)
Iranian Research Organization for Science and
Technology (IROST)
13-15 May 2024

03231-97589
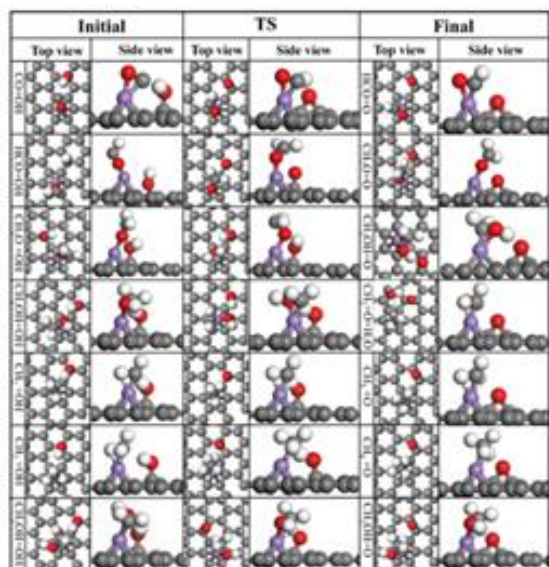
Figure 1 shows the initia, transition, and final states of all studied reactions. Table 2 indicates the activation energies of the reactions catalyzed by manganese (Mn), a metal that efficiently converts carbon monoxide (CO) to methane (CH_4) and methanol (CH_3OH) in FT synthesis. The reaction $CH_2O+OH \rightarrow CH_2OH+O$ demands an activation energy of 3.86 eV, making it more favorable at higher temperatures.[11] On the other hand, the reaction $CH_2OH +OH \rightarrow CH_2+O+H_2O$ benefits from a low activation energy of 0.80 eV, signifying higher efficiency at lower temperatures.(Table 2)[12]

Table 2: Calculated activation energies (E_{act}) for all reactions on the Mn-doped GO surface.

Reactions	E_{act} (eV)	Reactions	E_{act} (eV)
$CO+OH \rightarrow HCO+O$	2.48	$CH_2OH+OH \rightarrow CH_2+O+H_2O$	0.80
$HCO+OH \rightarrow CH_2O+O$	0.48	$CH_2+OH \rightarrow CH_3+O$	0.36
$CH_2O+OH \rightarrow CH_2OH+O$	3.86	$CH_3+OH \rightarrow CH_4+O$	1.35
$CH_2OH+OH \rightarrow CH_3OH+O$	1.66		

Conclusions

The hydrogenation method utilizes the GO surface as a source of hydrogen atoms, requiring the conversion of hydroxyl groups to epoxy groups within the mechanism. The catalyst's suitability is confirmed by these results, which ultimately explain the spontaneous progression of the reaction even with high activation energy. By comparing the calculated results with data from relevant sources, it is revealed that the use of GO as a surface material characterized by a larger surface area and lighter weight significantly increases the effectiveness of the required reactions. Overall, the presence of manganese as a catalyst, along with the utilization of GO as a suitable surface possessing a substantial surface area and hosting hydroxyl and epoxy groups, proved efficient in expediting the reaction.

References

[1] M. Luo, Z. Liang, C. Liu, X. Qi, M. Chen, R.U.R. Sagar, H. Yang, T. Liang, Single–atom manganese and nitrogen co-doped graphene as low-cost catalysts for the efficient CO oxidation at room temperature, Appl Surf Sci 536 (2021) 147809.

[2] W. Gao, The chemistry of graphene oxide, Graphene Oxide: Reduction Recipes, Spectroscopy, and Applications (2015) 61–95.

[3] W. Gao, Graphene oxide: reduction recipes, spectroscopy, and applications, Springer, 2015.

[4] H. Ahmad, M. Fan, D. Hui, Graphene oxide incorporated functional materials: A review, Compos B Eng 145 (2018) 270–280.

[5] W. Gao, The chemistry of graphene oxide, Graphene Oxide: Reduction Recipes, Spectroscopy, and Applications (2015) 61–95.

[6] W. Gao, Graphene oxide: reduction recipes, spectroscopy, and applications, Springer, 2015.

[7] Y. Chen, Y. Gui, X. Chen, Adsorption and gas-sensing properties of C2H4, CH4, H2, H2O on metal oxides (CuO, NiO) modified SnS2 monolayer: A DFT study, Results Phys 28 (2021) 104680. https://doi.org/https://doi.org/10.1016/j.rinp.2021.104 680.

[8] S. Sarabadani Tafreshi, N. Taghizade, M. Sharifian, S. Panahi, M. Torkashvand, N.H. de Leeuw, A density functional theory study of CO2 hydrogenation on carbon-terminated TaC (111) surface, Reaction Kinetics, Mechanisms and Catalysis 136 (2023) 1945–1963.

[9] S. Grimme, S. Ehrlich, L. Goerigk, Effect of the damping function in dispersion corrected density functional theory, J Comput Chem 32 (2011) 1456–1465.

[10] X. Sun, S. Luan, H. Shen, S. Lei, Effect of metal doping on carbon monoxide adsorption on phosphorene: A first-principles study, Superlattices Microstruct 124 (2018) 168–175.

[11] C.B. Reuter, R. Zhang, O.R. Yehia, Y. Rezgui, Y. Ju, Counterflow flame experiments and chemical kinetic modeling of dimethyl ether/methane mixtures, Combust Flame 196 (2018) 1–10.

[12] C.-R. Chang, B. Long, X.-F. Yang, J. Li, Theoretical studies on the synergetic effects of Au–Pd bimetallic catalysts in the selective oxidation of methanol, The Journal of Physical Chemistry C 119 (2015) 16072–16081.

22nd Iranian Chemistry Congress (ICC22)
Iranian Research Organization for Science and Technology (IROST)
13-15 May 2024

03231-97589

IROST

Phytochemical study of the lichen Species *Evernia prunastri* in Iran and investigation of its antioxidant biological activity

Atieh Saleh Nejad *[a], Mahdi Moridi Farimani [a], Mohammad Sohrabi [b]

Corresponding Author E-mail: *atieh.saleh.70@gmail.com*

[a] Department of Phytochemistry, Medicinal Plants and Drugs Research Institute, Shahid Beheshti University, Tehran, Iran.

[b] Iranian Research Organization for science and technology (IROST), Tehran, Iran.

Abstract: This study was conducted to investigate the secondary metabolites of lichen *Evernia prunastri*, and evaluate the amount of total phenol and antioxidant activity of its acetone and ethanol extracts. To identify secondary metabolites, TLC and Spot test methods were used.

Keywords: *Evernia*; Secondary metabolites, Total phenol, Antioxidant activity

Introduction

Lichens are symbiotic organisms formed by a fungus and one or more photosynthetic partners. some of them are called medicinal lichens due to the presence of various effective substances. Lichen synthesizes a great variety of secondary metabolites, and many of them are unique which offer a vast potential for discovering novel classes of antioxidant substances. Their diverse and scarcely studied metabolites facilitate adaptability to extreme living conditions. Since synthetic drugs have few effects, the need for research and the emergence of natural bioactive compounds has expanded. We investigated *E.prunastri*, one of the most important commercial lichens in the world, especially in France, for its antioxidant potential [1][2].

Experimental Section

E. prunastri lichen was collected from the forests of *Arasbaran*. The TLC method was used to identify the secondary metabolites. *P. acetabulum* species was used as an internal control in determining the R_f of the substances. Three solvent systems were used as mobile phase in this study: System A: toluene, 1, 4-Dioxane, acetic acid (180:60:8 v/v/v); System B: n-hexane, diethyl ether, formic acid (130:1000:20 v/v/v) and system C: toluene, acetic acid (200:30 v/v). 10% sulfuric acid was used as a reagent. In addition, the spot test method was used as an auxiliary method to identify metabolites. KOH, NaOCl, and PPD reagents were used. A spotting test was performed under a stereomicroscope to detect the color change better. Acetone and ethanol extracts of *Evernia prunastri* were obtained using the maceration method to check the antioxidant activity, and the extraction efficiency was calculated for all two extracts. Based on the colorimetric method of Folin–Ciocalteu and according to gallic acid, the amount of phenol was measured. The antioxidant property of the extracts was evaluated based on the inhibition of DPPH free radicals and their IC_{50} was compared.

Results and Discussion

The results showed that the acetone extract had a higher extraction efficiency. The substances identified using TLC and spot tests included atranorin and evernic acid. The amounts of phenolic compounds extracted by acetone were more than ethanol extract, although the extraction efficiency by ethanol was higher than acetone. The results of DPPH free radical inhibitory activity showed that in all investigated concentrations, the inhibitory activity of acetone extract is more than that of ethanol extracts.
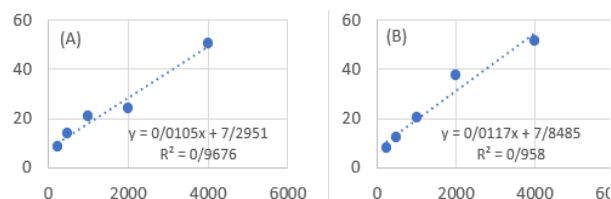
Fig.1: % inhibition vs concentration for a) Ethanol and b) Acetone extracts

Table1: Comparison of extracts

Extracts	Efficiency	Total phenol	IC50
Acetone	21.96	192.28 ± 9.18	3602.692
Ethanol	26.40	90.06 ± 13.35	4067.133

Conclusions

The results showed a direct relationship between the number of phenolic compounds and DPPH free radical inhibitory activity.

References

[1] S. Dudani and G. Ecology, "Sahyadri Shilapushpa : Lichen Chemistry," no. January. 2011.

[2] A. Shcherbakova, A. A. S. U. Göransson, O. G. A. Turanov, and D. Kochkin, "Antimicrobial and antioxidant activity of Evernia prunastri extracts and their isolates," World J. Microbiol. Biotechnol., vol. 37, no. 8, pp. 1–14, 2021.

Analytical analysis of the elemental composition of *Usnea articulata* to evaluate the potential of lichen as a pollution indicator

Atieh Saleh Nejad [*a], Mahdi Moridi Farimani [a], Mohammad Sohrabi [b]

Corresponding Author E-mail: *atieh.saleh.70@gmail.com*

[a] Department of Phytochemistry, Medicinal Plants and Drugs Research Institute, Shahid Beheshti University, Tehran, Iran.

[b] Iranian Research Organization for science and technology (IROST), Tehran, Iran.

Abstract: A study was carried out to determine the concentration of trace elements Cd, Cr, Cu, Fe, Mn, Ni, Pb, and Zn in *usnea articulata* to evaluate the potential of lichen as a pollution indicator. The sample was analyzed by using ICP-OES. Before analyses, species was cleaned, dried, pulverized, and digested in a dilute nitric acid solution.

Keywords: Lichen; *U. articulata*; Elementals; ICP-OES, Pollution indicator

Introduction

Plants have been used as bioindicators for many years to detect environmental changes. Lichens are one of the most valuable biomonitors of atmospheric pollution with other growth such as moss and fungi. Most species of lichen have a wide geographical distribution, which allows for a study of pollution covering wide areas and its high capacity to accumulate metals [1]. Lichen are very sensitive to changes in their surrounding environment. Lichens also can absorb pollutants such as trace metals from airborne particles, and then accumulate and saturate the metals. This is due to their structure and anatomy. The ability of different types of lichens to accumulate metals from the surroundings is different depending upon their species. Lichen can be used as sensitive indicators to estimate the biological effect of pollutants by measuring changes at the community or population level, and as accumulative monitors of persistent pollutants, by assaying their trace element contents [2]. The inductively coupled plasma-optical emission spectrometer (ICP-OES) is an analytical instrument with a sensitivity that is suitable for trace metal analyses. It is widely used in industries such as environment, geology, chemistry, material science, nuclear and clinical research [3].

Experimental

lichen was collected from the area in the forests of Noor Heights. the sample was ground into powder and homogenized. About 1 g was weighed accurately and digested using 12 ml HNO_3 and 2 ml H_2O_2. The digested sample was diluted to 100 ml using deionized distilled water as preparation for analysis using (ICP-OES). Trace elements were determined by using inductively coupled plasma-optical emission spectrometry for (Cd, Cr, Cu, Fe, Mn, Ni, Pb, and Zn).

Results and Discussion

The concentrations of elements are shown in Table 1. The obtained results showed that this species is free of contamination with elements such as Pb, Cd, etc. The data obtained could be valuable for future studies when researchers can sample the same lichen species found in contaminated areas. We believe the values obtained in this study are representative of clean areas in Iran.

Table 1: The concentration of trace metals in *U. articulata*

Cd	Cr	Cu	Fe	Mn	Ni	Pb	ZN	Metals
0.007	0.028	0.094	2.593	0.214	0.017	0.339	0.326	C (µg/g)

Conclusions

For future studies, it is recommended that sampling should be done in different locations. A sample of lichen of the same species should be collected in an area that is polluted and other areas where the level of pollution is variable. This is to evaluate the potential of lichens as a pollution indicator.

References

[1] Burton, M. A. (1986). Biological monitoring of environmental contaminants (plants) (pp. viii+-247).

[2] Pearson, L. C. (1973). Air pollution and lichen physiology: progress and problems. Air pollution and lichens, 224-237.

[3] Grohse, P. M. (1999). Trace element analysis of airborne particles by atomic absorption spectroscopy, inductively coupled plasma-atomic emission spectroscopy, and inductively coupled plasma-mass spectrometry. Elemental Analysis of Airborne Particles. Advances in Environmental, Industrial and Process Control Technologies, 1, 1-65.

Exploring Antibacterial Properties of Acetone and Ethanol Extracts from *Usnea articulata* Lichen Using the Antibiotic Sensitivity Test

Atieh Saleh Nejad [*a], Mahdi Moridi Farimani [a], Mohammad Sohrabi [b]

Corresponding Author E-mail: *atieh.saleh.70@gmail.com*

[a] Department of Phytochemistry, Medicinal Plants and Drugs Research Institute, Shahid Beheshti University, Tehran, Iran.
[b] Iranian Research Organization for science and technology (IROST), Tehran, Iran.

Abstract: *Usnea* species exhibit intriguing medicinal properties. In this study, we investigated the antibacterial properties of acetone and ethanol extracts obtained from *Usnea articulata* lichen. Specifically, we assessed their effects on both gram-positive (*S. aureus*) and gram-negative (*E. coli*) bacteria using the antibiogram test.

Keywords: Lichen; Usnea; *Usnea articulata*; Antibacterial; Antibiogram test

Introduction

Lichens, fascinating symbiotic organisms, have long been utilized in traditional herbal medicine by communities worldwide [1]. In our study, we specifically investigated the impact of acetone and ethanol extracts from U.articulata lichen on inhibiting the growth of E. coli and S. aureus.

Experimental Section

In this study, we prepared various concentrations of ethanol and acetone extracts (5 to 350 mg/ml) to assess their antibacterial activity. We utilized standard microbial strains of S. aureus (ATCC25923) and E. coli (ATCC8739). The antimicrobial potential of the extracts was evaluated using the agar diffusion method. DMSO served as the negative control. The antibiotic sensitivity of bacterial isolates was determined using the Kirby-Bauer method. A suspension of bacteria with a 0.5 Mc-Farland turbidity was prepared. The bacterial suspension was cultivated on Mueller-Hinton agar medium. After a brief incubation period, antibiotic discs were aseptically placed on the agar plate at appropriate distances. The plates were then incubated at 37°C for 24 h. The diameter of the zone of inhibition around each antibiotic disc was measured [2]. By referring to the 2010 CLSI standard tables, the antibiotic sensitivity of the isolates was determined. The antibiotic discs used in this study were prepared by the Padtan Teb company (Table 1).

Table 1: Used antibiotic discs

Name	Disc content (µg/ml)	Name	Disc content (µg/ml)
Kanamycin	30	Gentamicin	10
Tetracycline	30	Vancomycin	30
Ceftriaxone	30	Streptomycin	10
Ciprofloxacin	5	Trimethoprim-Sulfamethoxazole	1.25-23.75
Imipenem	10		

Results and Discussion

Based on the obtained results, only the ethanol extract of lichen at a concentration of 350 mg/ml exhibited antimicrobial properties against both bacteria. The inhibition zone diameter (IZ) for the ethanolic extract was 15 ± 2.8 mm against *Staphylococcus aureus* bacteria and 16.5 ± 2.12 mm against *Escherichia coli* bacteria. The antibiogram test results indicated that all antibiotics were effective against the bacteria, except for vancomycin and trimethoprim-sulfamethoxazole, which were resistant to Staphylococcus aureus bacteria (fig 1). These findings suggest that the ethanolic extract of Usnea articulata lichen could be used as a potent antibacterial compound, especially at high concentrations.
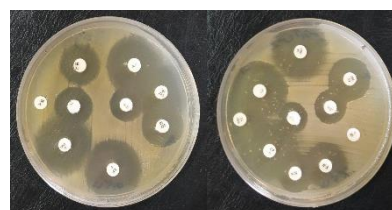
Fig 1: Formation of inhibition zone around antibiotic disks

Conclusions

The ethanolic extract from this *usnea* species presents a promising alternative to chemical antibiotics for treating diseases caused by bacterial strains that have developed resistance.

References

[1] Adjeng, A. N. T., Darmawan, A., Susilowati, P. E., Vika, B., Musdalifah, A., Usman, U., ... & Maulidiyah, M. (2023, May). Antibacterials activity of Escherichia coli and Salmonella typhi by acetone extract of the lichen Usnea sp. In AIP Conference Proceedings (Vol. 2719, No. 1). AIP Publishing.

[2] Hudzicki, J. (2009). Kirby-Bauer disk diffusion susceptibility test protocol. American society for microbiology, 15(1), 1-23.

Novel in silico designed inhibitor for BTK enzyme and B-cell lymphoma treatment by natural fragments

Aliasghar Behzadi *, Alireza Fattahi

Corresponding Author E-mail: aliasghar.behzadi@ch.sharif.edu

Organic chemistry department, Faculty of Chemistry, Sharif university of technology, Tehran, Iran.

Abstract: Bruton's tyrosine kinase (BTK) has been discovered by its critical role in B cell receptor signaling pathway, and for inhibition of malignant B cell growth as well. In this work, we have successfully designed a new inhibitor for BTK enzyme, using natural fragments by in silico studies.

Keywords: anti-cancer drug; computational drug design; BTK

Introduction

Bruton's tyrosine kinase (BTK) has been discovered by its critical role in B cell receptor signaling pathway. In this regard, BTK was recognized to be a promising target for inhibition in B-cell lymphoma treatment so as to hinder wild growth of malignant B-cells[1]. There are two categoary of mechanism which related medicines concruent, covalent and non-covalent binding. Based on non-covalent drugs are a newly defined type which pre dominant the other group by less mutation causing and ease of excreation[2]. Futuremore, by taking prevously experimenrtally designed and approaved non-covalent drug for medical use, Pirtobrutinib[3], we have successfully designed new potential inhibitor consisted of natural fragments, using computational methods.

Experimental Section

Physical features of Pirtobrutinib such as electrostatic potential map (EPM), polar surface area (PSA) and hydrogen bonding ability of the structure was evaluated, along with EPM of BTK enzyme. A set of ligands were prepared, by mimicking the same features; structurally optimized, evaluated and compared with Pirtobrutinib. Sorted structures with reliable results were chosen for Molecular Dynamic (MD) studies for precise simulation of protein-ligand contact.

Results and Discussion

On the basis of MD studies related analyzes were obtained; RMSD, RMSF, Radius of gyration and minimun distance of ligand with protein binding site redues. One ligand has shown similar and in number of cases better and acceptable results.
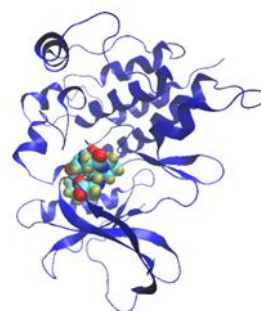
Fig.1: the complex of designed structure and BTK enzyme produced from MD simulation result

Conclusion

By taking FDA approved Pirtobrutinib's strucutre as the template, we have successfully designrd new structure as inhibitor for BTK enzymes which overcomes two matter of importance. First, the pharmacokinetic aspect by utilizing natural fragments and second, by mimicing physical features of Pirtobrutinib. In this regard the designed structure offers more adoptable action with human body, lowering side effects.

References

[1] Ponader, S., & Burger, J. A. (2014). Bruton's tyrosine kinase: from X-linked agammaglobulinemia toward targeted therapy for B-cell malignancies. Journal of clinical oncology: official journal of the American Society of Clinical Oncology, 32(17), 1830–1839.

[2] Rozkiewicz, D., Hermanowicz, J. M., Kwiatkowska, I., Krupa, A., & Pawlak, D. (2023). Bruton's Tyrosine Kinase Inhibitors (BTKIs): Review of Preclinical Studies and Evaluation of Clinical Trials. Molecules (Basel, Switzerland), 28(5),2400.

[3] Aslan, B., Kismali, G., Iles, L. R., Manyam, G. C., Ayres, M. L., Chen, L. S., ... & Gandhi, V. (2022). Pirtobrutinib inhibits wild-type and mutant Bruton's tyrosine kinase-mediated signaling in chronic lymphocytic leukemia. Blood cancer journal, 12(5), 80.

22nd Iranian Chemistry Congress (ICC22)
Iranian Research Organization for Science and Technology (IROST)
13-15 May 2024

03231-97589

IROST

Synthesis of pyridopyrimidines using borane trifluoride supported on nanocellulose as a catalyst

Zahra Imani, Abdolhamid Bamoniri *

Corresponding Author E-mail: bamoniri@kashanu.ac.ir

Department of Organic Chemistry, Faculty of Chemistry, University of Kashan, Kashan, IR Iran.

Abstract: In this study, borane trifluoride supported on nanocellulose was successfully utilized as a catalyst for the synthesis of pyridopyrimidines under various conditions. The efficient and eco-friendly nature of this catalyst opens up new possibilities for the development of novel organic compounds.

Keywords: Pyridopyrimidine; Nanocellulose; Multi component reaction; Solvent free

Introduction

Multicomponent reactions (MCR's) have become very important in modern organic chemistry [1]. Unlike the step by step reactions, MCR's provide a convenient synthetic method to generate products of one step structural complexity and minimize waste as the number of reagents, solvents, and adsorbents are significantly reduced. Therefore, MCRs rely on an eco-friendly green synthetic methodology [2-4]. Heterocycles integrated pyridopyrimidine verified substantial biological features and are found in the basic skeleton of many drugs [5-7]. pyrido[2,3-d] pyrimidines are found in various bioactive compounds with bactericidal, antipyretic, antitumor, pharmaceutical, and antihistaminic characteristics [8]. This nano-cellulose could be used as supporters for boron trifluoride (BF3) and make a new, biodegradable, inexpensive and eco-friendly bio-catalyst. The synthesis of heterocyclic compounds holds immense significance in the field of organic chemistry due to their wide-ranging applications in medicinal chemistry and material science. Among these heterocycles, pyridopyrimidines have gained significant attention owing to their diverse pharmacological properties and their potential as building blocks for drug discovery. In recent years, the development of efficient and environmentally-friendly catalysts for heterocycle synthesis has become a prime focus for researchers. One promising catalyst that has emerged is borane trifluoride (BF3) supported on nanocellulose, an innovative nanomaterial derived from cellulose . Nanocellulose, a nanoscale form of cellulose, offers unique structural, mechanical, and surface properties, making it an ideal platform for catalyst support . When combined with BF3, the resulting catalyst system demonstrates extraordinary efficiency and selectivity in the synthesis of pyridopyrimidines. The advantages of utilizing borane trifluoride supported on nanocellulose as a catalyst are multifoil. Firstly, BF3 provides a Lewis acidic character that promotes the activation of reactants, thereby enhancing reaction rates. Additionally, nanocellulose acts as a solid support, facilitating the immobilization of the catalyst and providing enhanced stability and reusability. The synthesis of pyridopyrimidines using this catalyst system has been found to be highly efficient, providing excellent yields with good functional group tolerance. The protocol involves a simple and straightforward procedure, making it applicable for large-scale synthesis [9-11].

Experimental Section

Preparation of nano-BF3/cellulose:

In a well-ventilated system, BF3 (4 mL) was added drop wise to the mixture of nano-cellulose (1.6 g) in chloroform (10 mL). The mixture was stirred for one hour at room temperature. The resulted suspension was filtered, washed with chloroform and dried at room temperature.

Preparation of pyridopyrimidines:

A mixture of aromatic aldehydes(1mmol), barbituric acid (1mmol), dimedone (1mmol) and ammonium acetate(1mmol) with 0.1 g catalyst was stirred under solvent free conditions at 70 ^{0}C for the required time. The progress of reaction was monitored by TLC. the catalyst was separated using simple filtration and the solid precipitate was several times washed with water and then dried to obtain the crude product. Finally, the pure products were obtained through recrystallization

Results and Discussion

The use of Nanocellulose as a support for BF3 catalyst displayed several advantages in the synthesis of pyridopyrimidines. The high surface area and porosity of Nanocellulose provide a suitable environment for the efficient immobilization of the catalyst. This immobilization improves the catalyst's stability and minimizes its leaching during reaction, resulting in enhanced efficiency and reusability.The optimized reaction conditions played a crucial role in achieving higher yields and selectivities of the desired pyridopyrimidine products. The reusability of the BF3 supported on Nanocellulose catalyst is a notable advantage from both economic and environmental points of view. The catalyst's stability and ease of separation allow for multiple cycles of the reaction without significant loss in catalytic activity.(scheme1)

22nd Iranian Chemistry Congress (ICC22)
Iranian Research Organization for Science and Technology (IROST)
13-15 May 2024

03231-97589
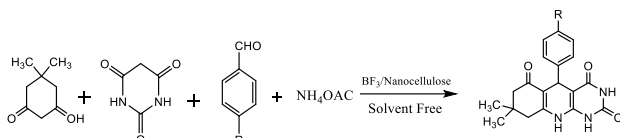
Scheme 1

Table1: Results

Entry	Benzaldehyde derivates	Time (min)	Yield (%)
1	4-cl	35	98
2	4-NO$_2$	35	96
3	4-OMe	45	92

Conclusions

In conclusion, the synthesis of pyridopyrimidines using BF3 supported on Nanocellulose as a catalyst proved to be an effective and sustainable approach. The optimized reaction conditions, including temperature, solvent, and reaction time, significantly influenced the yield and selectivity of pyridopyrimidines. The BF3 supported on Nanocellulose catalyst exhibited excellent catalytic activity, stability, and reusability, making it a promising candidate for future applications in pyridopyrimidine synthesis. These findings contribute to the advancement of sustainable catalysis in the field of organic chemistry.

References

[1] Zhu, J., & Bienaymé, H. (Eds.). (2006). *Multicomponent reactions*. John Wiley & Sons.

[2] Pellissier, H. (2013). Stereocontrolled domino reactions. *Chemical Reviews*, *113*(1), 442-524.

[3] Volla, C. M., Atodiresei, I., & Rueping, M. (2014). Catalytic C–C bond-forming multi-component cascade or domino reactions: Pushing the boundaries of complexity in asymmetric organocatalysis. *Chemical eviews*, *114*(4), 2390-2431.

[4] Chauhan, P., Mahajan, S., & Enders, D. (2017). Achieving molecular complexity via stereoselective multiple domino reactions promoted by a secondary amine organocatalyst. *Accounts of Chemical Research*, *50*(11), 2809-2821.

[5] Gao, X., Cen, L., Li, F., Wen, R., Yan, H., Yao, H., & Zhu, S. (2018). Oral administration of indole substituted dipyrido [2, 3-d] pyrimidine derivative exhibits anti-tumor activity via inhibiting AKT and ERK1/2 on hepatocellular carcinoma. *Biochemical and biophysical research communications*, *505*(3), 761-767.

[6] Jahan Shahi, P., Mamaghani, M., Haghbin, F., Nia, R. H., Rassa, M. (2018). One-pot chemoselective synthesis of novel pyrrole-substituted pyrido [2, 3-d] pyrimidines using [γ-Fe2O3@ HAp-SO3H] as an efficient nanocatalyst. *Journal of Molecular Structure*, *1155*, 520-529.

[7] Kumar, R. N., Dev, G. J., Ravikumar, N., Swaroop, D. K., Debanjan, B., Bharath, G., Rao, A. G. (2016). Synthesis of novel triazole/isoxazole functionalized 7-trifluoromethyl) pyrido [2, 3-d] pyrimidine derivatives as promising anticancer and antibacterial agents. *Bioorganic & Medicinal Chemistry Letters*, *26*(12), 2927-2930.

[8] Darias, V., Abdallah, S. S., Tello, M. L., Delgado, L. D., & Vega, S. (1994). NSAI activity study of 4-phenyl-2-thioxo-benzo [4, 5] thieno [2, 3-d] pyrimidine derivatives. *Archiv der Pharmazie*, *327*(12), 779-783.

[9] Safajoo, N., Mirjalili, B. B. F., & Bamoniri, A. (2021). A facile and clean synthesis of indenopyrido [2, 3-d] pyrimidines in the presence of Fe3O4@ NCs/Cu (II) as bio-Based magnetic nano-catalyst. *Polycyclic Aromatic Compounds*, *41*(6), 1241-1248.

[10] Osanlou, F., Nemati, F., & Sabaqian, S. (2017). An eco-friendly and magnetized biopolymer cellulose-based heterogeneous acid catalyst for facile synthesis of functionalized pyrimido [4, 5-b] quinolines and indeno fused pyrido [2, 3-d] pyrimidines in water. *Research on Chemical Intermediates*, *43*, 2159-2174.

[11] Ji, S. J., Ni, S. N., Yang, F., Shi, J. W., Dou, G. L., Li, X. Y., Shi, D. Q. (2008). An efficient synthesis of pyrimido [4, 5-b] quinoline and indeno [2', 1': 5, 6] pyrido [2, 3-d] pyrimidine derivatives via multicomponent reactions in ionic liquid. *Journal of Heterocyclic Chemistry*, *45*(3), 693-702.

Eco-Friendly Synthesis of Highly Efficient Nanocomposite for the Treatment of Tannery Wastewater

Farnam Manavi [a], Mohammad Reza Allahgoli Ghasri [*a], Shervin Ahmadi [b], Sima Habibi [a]

Corresponding Author E-mail: dr.mr.ghasri@gmail.com

[a] Department of Chemistry, College of Science, Yadegar-e-Imam Khomeini (RAH) Shahr-e-Rey Branch, Islamic Azad University, Tehran, Iran.

[b] Iran Polymer and Petrochemical Institute (IPPI), PO BOX 14965-115, Tehran, Iran.

Abstract: The study presents a novel approach for synthesizing a CuO-PP-MAH nanocomposite to reduce biological oxygen demand (BOD) and chemical oxygen demand (COD) levels in tannery wastewater. It integrates Copper Oxide nanoparticles into polymeric nanocomposites via an eco-friendly technique. The resulting nanocomposite demonstrates high catalytic efficiency, offering scalability for industrial use.

Keywords: CuO nanocomposite; Tannery wastewater; BOD; COD

Introduction

The leather industry is economically significant in many countries, yet its wastewater poses environmental challenges due to high levels of toxic contaminants. Stringent emission standards aim to address these concerns, but challenges persist due to the complex composition of effluents. Researchers have explored physicochemical methods to decontaminate wastewater, with metal/metal oxide nanoparticle-based nanocomposites showing promise [1]. Notably, copper/copper oxide (CuO) polymer composites exhibit remarkable properties, including photocatalytic and antimicrobial capabilities [2]. Various preparation methods have been employed, such as ex-situ and in-situ techniques, to synthesize these composites. Polypropylene (PP) is widely used as a thermoplastic polymer, and incorporating CuO nanoparticles into PP matrices has shown antibacterial and adsorbent properties [3]. Preventing nanoparticle agglomeration within the polymer matrix is crucial, with immobilization on diverse polymeric supports being a promising strategy. Maleic acid functionalization of the polymeric matrix has been explored to mitigate agglomeration issues. A novel method involving melt mixing and extrusion was developed to synthesize CuO-PP-MAH nanocomposites wherein CuO nanoparticles are immobilized onto maleic anhydride grafted polypropylene (PP-MAH) without toxic solvents, yielding a high-surface-area catalyst for wastewater treatment. Characterization techniques including Field Emission Scanning Electron Microscopy (FESEM), Transmission Electron Microscopy (TEM), and Fourier-Transform Infrared Spectroscopy (FTIR), were utilized to analyze the nanocomposites, demonstrating their potential for COD and BOD reduction in tannery wastewater, with reductions exceeding 70%. These findings highlight the promise of CuO-MAH-PP nanocomposites as stable and reusable catalysts for wastewater treatment.

Experimental Section

This section focuses on synthesizing a copper metal nanopolymer through in-situ melt mixing and extrusion techniques for reducing BOD and COD levels in tannery wastewater. Commercially procured chemicals, primarily from reputable suppliers such as Merck and Sigma-Aldrich were used. Instrumental analysis involved acquiring FTIR spectra, morphological studies using SEM coupled with Energy-Dispersive X-ray spectroscopy (EDX) tests, and determining copper content through Inductively Coupled Plasma Atomic Emission Spectroscopy (ICP-AES) and EDX analysis. The synthesis of PP-MAH involved bulk polymerization of polypropylene granules with maleic anhydride monomer, followed by grafting CuO onto PP-MAH using a co-rotating twin screw extruder with potassium hydroxide as the catalyst. Tannery wastewater treatment experiments were conducted in batch reactors using various quantities of CuO-PP-MAH nanocomposite. Reduction percentages of COD and BOD considering initial and final concentrationswere calculated. Desorption and regeneration studies involved sequential washing with 1 M HCl and 1 M NaOH to regenerate exhausted material, followed by drying and multiple cycles of "sorption-desorption-regeneration" to evaluate adsorbent capacity.

Results and Discussion

The preparation and characterization of CuO-PP-MAH nanocomposite were examined utilizing FTIR spectroscopy. The FTIR spectra illustrated distinct signatures confirming the functionalization of polypropylene with MAH and the presence of CuO nanoparticles on the polymer substrate.

22nd Iranian Chemistry Congress (ICC22)
Iranian Research Organization for Science and Technology (IROST)
13-15 May 2024

03231-97589

IROST
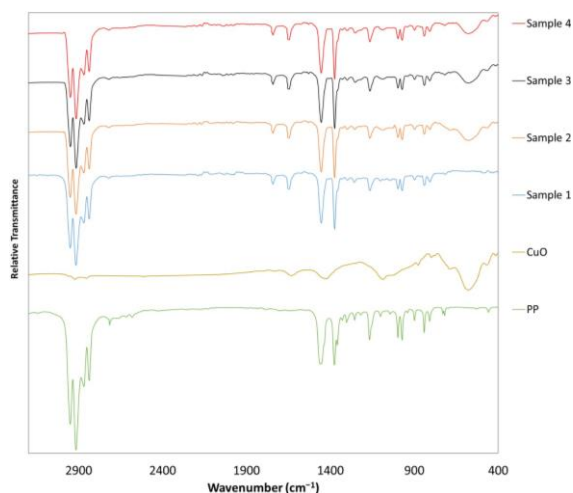
Fig.1: FTIR spectra for PP, CuO and (PP-MAH), (CuO-PP-MAH)

The SEM analysis revealed the morphological characteristics of CuO-PP-MAH nanocomposites.
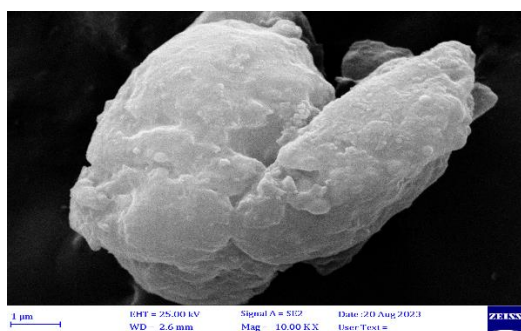
Fig.2: SEM micrograph

The EDX analysis confirmed the elemental composition of the polymer surface, aligning with expected nominal weight percentages. The TEM microscopy images further confirmed the presence of CuO nanoparticles within the matrix at nanoscale dimensions. The influence of CuO content on the efficiency of the nanocomposite in COD and BOD reduction was examined. Results showed enhanced activity with increased CuO content, with 1 wt% CuO-PP-MAH exhibiting superior performance despite observed nanoparticle clustering. Treatment duration significantly influenced the reduction in BOD and COD levels, with over 75% reduction achieved within the initial 60 minutes. The equilibrium was reached after 80 minutes, attributed to adsorption on the nanocomposite's external surface, followed by diffusion into its pores. The dosage of CuO-PP-MAH significantly affected BOD and COD reduction, with enhanced reduction observed up to 20 g dosage. The plateau reduction observed thereafter was attributed to intra-particle diffusion concurrent with adsorption dominance. The developed nanocomposite exhibited exceptional regenerative capacity, with over 70% reduction in BOD and COD maintained after six sorption-desorption cycles, highlighting its potential for practical application in wastewater treatment.

Conclusions

The paper presents a novel methodology for creating CuO-PP-MAH nanocomposites to reduce BOD and COD levels in tannery wastewater using an environmentally friendly approach that avoids toxic solvents. The nanocomposites, characterized using various techniques including FTIR, SEM, EDX, and TEM, exhibit well-dispersed and firmly attached CuO nanoparticles on the MAH-grafted PP matrix. These nanocomposites effectively treat tannery wastewater, achieving significant reductions of over 70% in BOD and COD, with sustained performance over multiple regeneration cycles. The findings highlight the potential of CuO-PP-MAH as a stable and efficient catalyst for mitigating pollutants in industrial wastewater treatment.

References

[1] Singh, P. P. (2018). Environmental remediation by nanoadsorbents-based polymer nanocomposite. In New polymer nanocomposites for environmental remediation (pp. 223-241). Elsevier. https://doi.org/10.1016/B978-0-12-811033-1.00010-X

[2] Tamayo, L., Azócar, M., Kogan, M., Riveros, A., & Páez, M. (2016). Copper-polymer nanocomposites: An excellent and cost-effective biocide for use on antibacterial surfaces. Materials Science and Engineering: C, 69, 1391-1409. https://doi.org/10.1016/j.msec.2016.08.041

[3] Palza, H., Gutiérrez, S., Delgado, K., Salazar, O., Fuenzalida, V., Avila, J. I., ... & Quijada, R. (2010). Toward tailor-made biocide materials based on poly (propylene)/copper nanoparticles. Macromolecular rapid communications, 31(6), 563-567. https://doi.org/10.1002/marc.200900791

Synthesis of 2,4,5-tri substituted imidazole derivatives in the presence of nano kaolin supported by Sn(IV) tetrachloride under ultrasonic conditions

Seyed Mehdi Kanani, Abdolhamid Bamoniri[*]

Corresponding Author E-mail: bamoniri@kashanu.ac.ir

Department of Organic Chemistry, Faculty of Chemistry, University of Kashan, Kashan, Iran.

Abstract: Imidazole derivatives, vital in pharmacology and industry, are efficiently synthesized using a novel nanokaolin Lewis acid catalyst supported by Sn(IV) tetrachloride. This green approach confirms high yields, rapid reactions, and versatility through ultrasonic methods and addresses concerns about solvent toxicity.

Keywords: One-pot synthesis, ultrasonic, Trisubstituted imidazoles, Green chemistry, nano kaolin

Introduction

Imidazole derivatives with a unique five-membered ring structure and significant biological effects are essential in pharmaceuticals and various industries [1]. However, concerns about the toxicity of organic solvents have led to the adoption of green chemistry approaches [2]. In this context, a novel Lewis acid catalyst with nano kaolin with Sn(IV) tetrachloride enables the efficient synthesis of 2,4,5-trisubstituted imidazoles in a one-pot reaction. This catalyst offers high yields, fast reaction rates, and simplified protocols that have been validated through various characterization techniques [3]. In addition, the versatility and efficiency of the catalyst using ultrasonic techniques have been demonstrated under different conditions [4]. Imidazole derivatives are a significant class of compounds with wide applications in pharmacology, agriculture, and materials science [5,6]. The distinctive structure of imidazole, which has a five-membered ring with two nitrogen atoms, is essential for its diverse biological activities and medicinal properties [7]. These compounds are used in making painkillers, anti-tumor agents, anti-inflammatory drugs, pesticides, fungicides, and even in photography processes [8]. Despite being useful, conventional synthesis methods for imidazole derivatives often rely on organic solvents such as chloroform and carbon tetrachloride, which are of concern due to their toxicity and environmental effects [9]. With increasing environmental awareness and regulatory pressures, there is a concerted effort to develop greener and more sustainable synthetic routes to imidazole derivatives[10]. A promising approach in this field involves the use of Lewis acid catalysts supported by environmentally friendly materials [11]. A combination of nano kaolin, a clay mineral with excellent adsorption properties and high surface area, as a support matrix, and Sn(IV) tetrachloride as an active Lewis acid catalyst has emerged as a powerful system for the efficient synthesis of 2,4,5-trisubstituted imidazoles [12-14]. Nano kaolin provides a stable and recyclable platform for the catalyst and increases its performance and stability. The synthesis of 2,4,5-trisubstituted imidazoles was carried out using a Lewis acid catalyst with nano kaolin through a one-pot multicomponent reaction [15,16].

Experimental Section

This reaction included the condensation of benzyl derivatives, 1,2-diketone, aromatic aldehydes, and ammonium acetate salt in the presence of a catalyst [17]. Reaction conditions, including catalyst loading, temperature, and reaction time, were optimized to maximize yield and product purity. The synthesized imidazole derivatives were characterized using various analytical techniques, including ^{1}H NMR, ^{13}C NMR, and FT-IR spectroscopy, confirming the successful formation of the desired products with the expected structural features. In addition, the catalyst itself was fully characterized using techniques such as FT-IR, XRD, SEM, TEM, EDS, and TGA to elucidate its composition, structure, and thermal stability [18]. Lewis acid catalyst with nano kaolin showed excellent catalytic activity in the synthesis of 2,4,5-trisubstituted imidazoles [19].

Synthesis of 2,4,5-tri substituted imidazole derivatives

A mixture containing benzaldehyde derivatives (1 mmol), 1,2-diketone (1 mmol), and NH$_4$OAc (1.2 mmol) as a source of ammonia underwent ultrasonic irradiation for 10-15 minutes at 40 °C and 60 W power. The reaction progress was tracked using thin-layer chromatography (TLC). Upon completion, the reaction's purity and yield were determined through double redistillation [20].

Results and Discussion

The nano kaolin-supported Lewis acid catalyst exhibited excellent catalytic activity in the synthesis of 2,4,5-trisubstituted imidazoles. The reaction proceeded smoothly under mild conditions, yielding high product yields within a short reaction time. The simplicity of the reaction setup and the straightforward workup procedure further underscored the practicality of this approach for large-scale synthesis.
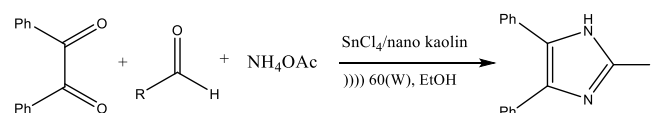
Scheme.1: Synthesis of 2,4,5-tri substituted imidazoles

Table1: 2,4,5-tri substituted imidazoles

Entry	1,2-Diketone	ArCHO	Yield (%)
1	Benzyl	3,4,5-(OMe)$_3$	93
2	4,4'-(OMe)$_2$ Benzyl	m-OMe	87
3	Benzyl	p-CN	94

The catalyst's performance was evaluated under different reaction conditions, including ultrasonic methods. In each case, the catalyst demonstrated remarkable versatility and efficiency, highlighting its robustness across diverse synthetic environments. Notably, ultrasonic-assisted reactions showed enhanced reaction rates and

22nd Iranian Chemistry Congress (ICC22)
Iranian Research Organization for Science and Technology (IROST)
13-15 May 2024

03231-97589

improved product yields, emphasizing the potential of this method for accelerating the synthesis of imidazole derivative

4,5-diphenyl-2-(3,4,5-trimethoxyphenyl)-1H-imidazole:

Mp:162-165 ˚C, FT-IR [ū (cm^{-1}), KBr]: 3444, 2932, 2838, 2616, 1635, 1241-1126, 766-696, ^{1}H NMR (400 MHz, DMSO-d_6) δ(ppm):3.72(s, 3H, CH$_3$), 3.88(s, 6H, CH$_3$), 7.22(d, 1H, *J*=4Hz, ArH), 7.31(t, 3H, *J*=8Hz, ArH), 7.41(t, 3H, *J*=8Hz, ArH), 7.46(s, 1H, ArH), 7.49(t, 2H, *J*=8Hz, ArH), 7.56(d, 2H, *J*=8Hz, ArH), 12.63(s, 1H, NH)

2-(2-methoxyphenyl)-4,5-bis(4-methoxyphenyl)-1H-imidazole:
Mp:284-286 ˚C, FT-IR [ū (cm^{-1}), KBr]: 3436, 2927, 2844, 2532, 1705-1651, 1249-1175, 744-686, ^{1}H NMR (400 MHz, DMSO-d_6) δ(ppm): 3.75(s, 3H, CH$_3$), 3.80(s, 3H, CH$_3$), 3.92(s, 3H, CH$_3$), 6.85(d, 2H, *J*=8Hz, ArH), 6.99(d, 2H, *J*=8Hz, ArH), 7.05(t, 1H, *J*=8Hz, ArH), 7.15(d, 1H, *J*=8Hz, ArH), 7.38(t, 3H, *J*=8Hz, ArH), 7.43(d, 2H, *J*=8Hz, ArH), 8.03(d, 1H, *J*=8Hz, ArH), 11.69(s, 1H, NH)

4-(4,5-diphenyl-1H-imidazol-2-yl)benzonitrile:
Mp: 276-278 ˚C, FT-IR [ū (cm-1), KBr]: 3424, 2251, 2125, 1653, 1394, 824, 761, 623, ^{1}H NMR (400 MHz, DMSO-d_6) δ(ppm):7.29-7.55(m, 10H, ArH), 7.95(d, 2H, *J*=8Hz, ArH), 8.25(d, 2H, *J*=8Hz, ArH), 13.04(s, 1H, NH)

Conclusions

In conclusion, the development of a nanokaolin-supported Lewis acid catalyst has revolutionized the synthesis of 2,4,5-trisubstituted imidazoles, offering a greener and more efficient alternative to conventional methods. The catalyst's high activity, coupled with its recyclability and stability on the nano kaolin support, makes it a promising candidate for sustainable synthesis processes in pharmaceutical and chemical industries. Further research may focus on exploring additional applications of this catalyst system and optimizing reaction conditions for broader synthetic utility.

References

[1] Al Munsur, A. Z.; Roy, H. N.; Imon, M. K., Highly efficient and metal-free synthesis of tri- and tetrasubstituted imidazole catalyzed by 3-picolinic acid. *Arabian Journal of Chemistry* **2020,** *13* (12), 8807-8814.

[2] Mohammadi Ziarani, G.; Badiei, A.; Lashgari, N.; Farahani, Z., Efficient one-pot synthesis of 2,4,5-trisubstituted and 1,2,4,5-tetrasubstituted imidazoles using SBA-Pr-SO3H as a green nano catalyst. *Journal of Saudi Chemical Society* **2016,** *20* (4), 419-427.

[3] Bansal, R.; Soni, P. K.; Halve, A. K., Green Synthesis of 1,2,4,5-Tetrasubstituted and 2,4,5-Trisubstituted Imidazole Derivatives Involving One-pot Multicomponent Reaction. *Journal of Heterocyclic Chemistry* **2018,** *55*, (6), 1308-1312.

[4] Nawaz, A.; Kumar, P., Thermocatalytic pyrolysis of Sesbania bispinosa biomass over Y-zeolite catalyst towards clean fuel and valuable chemicals. *Energy* **2023,** *263*, 125684.

[5] Kumar, B. V.; Ramesh, B.; Kameswaran, S.; Supraja, N.; Pitchika, G. K., Zinc Oxide Nanoparticles Synthesis Using Herbal Plant Extracts and Its Applications. In *Agricultural and Environmental Nanotechnology: Novel Technologies and their Ecological Impact*, Springer: 2023; 221-249.

[6] Mohammadi Ziarani, G.; Badiei, A.; Lashgari, N.; Farahani, Z., Efficient one-pot synthesis of 2,4,5-trisubstituted and 1,2,4,5-tetrasubstituted imidazoles using SBA-Pr-SO3H as a green nano catalyst. *Journal of Saudi Chemical Society* **2016,** *20* (4), 419-427.

[7] Abdelmonsef, A. H.; El-Saghier, A. M.; Kadry, A. M., Ultrasound-assisted green synthesis of triazole-based azomethine/thiazolidin-4-one hybrid inhibitors for cancer therapy through targeting dysregulation signatures of some Rab proteins. *Green Chemistry Letters and Reviews* **2023,** *16* (1), 2150394.

[8] Vasu, A.; Naresh, M.; Sai, G. K.; Rohini, Y. D.; Murali, B.; Ramulamma, M ;.Ramunaidu, A.; Narender, N., A heterogeneous catalytic strategy for facile production of benzimidazoles and quinoxalines from primary amines using the Al-MCM-41 catalyst. *Green Chemistry* **2021,** *23* (23), 9439-9446.

[9] Matiichuk, Y.; Grozav, A.; Kostyshyn, L.; Yakovychuk, N.; Chaban, T.; Martyak, R.; Matiychuk, V., Synthesis ,Antimicrobial and Anticancer Activities of 1-Aryl-4-[(5-Aryl-2-Furyl) Carbonothioyl] Piperazines. *Biointerface Biointerface Research in Applied Chemistry,* **2022,** *12*, 706-717.

[10]Londhe, B. S.; Khillare, S. L.; Nalawade, A. M.; Mane, R. A., Ultrasound assisted synthesis of 2, 4, 5-triarylimidazoles catalyzed by baker's yeast. *International Journal of Research in Engineering and Science* **2021,** *9* (1), 79-84.

[11]Gupta, S.; Lakshman, M., Magnetic Nano Cobalt Ferrite: An efficient recoverable catalyst for synthesis of 2,4,5-trisubstituted imidazoles. *Journal of Medicinal and Chemical Sciences* **2019,** *2* (2), 51-54.

[12]Kulkarni, M. S.; Mamgain, R.; Saravate, K.; Nagarkar, R. R., One pot solvent-free synthesis of 2, 4, 5-trisubstituted imidazoles using wet cyanuric chloride. *Journal of Pharmaceutical Innovation,* **2018,** *7* (1), 153-155.

[13]Manteghi, F.; Zakeri, F.; Guy, O. J.; Tehrani, Z., MIL-101 (Cr), an efficient heterogeneous catalyst for one pot synthesis of 2, 4, 5-tri substituted imidazoles under solvent free conditions. *Nanomaterials* **2021,** *11* (4), 845.

[14]Naidoo, S.; Jeena, V., One-Pot, Two-Step Metal and Acid-Free Synthesis of Trisubstituted Imidazole Derivatives via Oxidation of Internal Alkynes Using an Iodine/DMSO System. *European Journal of Organic Chemistry* **2019,** *2019* (5), 1107-1113.

[15]Parthiban, D.; Karunakaran, R. J., Benzethonium chloride catalyzed one pot synthesis of 2, 4, 5-trisubstituted imidazoles and 1, 2, 4, 5-tetrasubstituted imidazoles in aqueous ethanol as a green solvent. *Oriental Journal of Chemistry* **2018** ,34(6) ,3004-3034.

[16]Imran, M.; Bawadekji, A.; Alotaibi, N., Synthesis and evaluation of antimicrobial properties of some azole derivatives. *Tropical Journal of Pharmaceutical Research* **2020,** *19* (2), 377-382.

[17]Sari, S.; Kart, D.; Öztürk, N.; Kaynak, F. B.; Gencel, M.; Taşkor, G.; Karakurt, A.; Sarac, S.; Eşsiz, Ş.; Dalkara, S., Discovery of new azoles with potent activity against Candida spp. and Candida albicans biofilms through virtual screening. *European Journal of Medicinal Chemistry* **2019,** *179*, 634-648.

[18]Sadeghian, S.; Gholami, A.; Khabnadideh, S.; Razmi, R.; Sadeghian, I.; Ghasemi, Y.; Rezaei, Z., Evaluation of Antibacterial and Anticandidal Activities of Some Imidazole, Benzimidazole and Benztriazole Derivatives. *Trends in Pharmaceutical Sciences* **2022,** *8* (2), 75-84.

[19]Zhang, Q.; Li, S. Z.; Queneau, Y.; Soulère, L., Synthesis of new 1, 4-and 1, 5-disubstituted N-ethyl acetate and N-α-butyro-γ-lactone alkylimidazole derivatives as N-acylhomoserine lactone analogs. *Journal of Heterocyclic Chemistry* **2021,** *58* (12), 2298-2303.

[20]Mueller, L. G.; Chao, A.; AlWedi, E.; Fleming, F. F., One-step synthesis of imidazoles from Asmic (anisylsulfanylmethyl isocyanide). *Beilstein Journal of Organic Chemistry* **2021,** *17* (1), 1499-1502.

22nd Iranian Chemistry Congress (ICC22)
Iranian Research Organization for Science and Technology (IROST)
13-15 May 2024

03231-97589

IROST

Simultaneous kinetic spectrophotometric determination of nitroglycerin and nitrocellulose in double base solid propellants

Ali Reza Zarei *, Kobra Mardi

Corresponding Author E-mail: zarei1349@gmail.com

Faculty of Chemistry and Chemical Engineering, Malek Ashtar University of Technology, Tehran, 15875-1774, Iran

Abstract: The proposed method is based on alkaline hydrolysis of NG and NC, and followed by colored reaction of released nitrite with a diazotizable aromatic amine in acidic media and produce azo product and finally simultaneous determination of NG and NC was done by mean centering of ratio kinetic profiles that allows rapid and accurate determination of NG and NC. Under optimum conditions, the results allow simultaneous determination of NG and NC in the range of 0.2-5.0 µg mL^{-1} and 0.5-10 µg mL^{-1}, respectively. The limit of detections was 0.1 µg mL^{-1} and 0.25 µg mL^{-1} for NG and NC respectively. The relative standard deviations (RSD) were <4%. In comparison with military standard 286 the relative errors were obtained between -3.1- 2.3 %

Keywords: Nitroglycerine, Nitrocellulose, Simultaneous spectrophotometric determination, Mean centering of ratio kinetic profiles, DB solid propellants.

Introduction

Double base propellants (DB) contain energetic polymer, generally nitrocellulose, plasticized into a gel by an energetic plasticizer, generally nitroglycerine that these compounds used in rocket and gun applications as energetic base materials since the late 1800s [1]. Due to role and high application of NG and NC in DB propellants, determination of them is necessary. mean centering of ratio spectra method (MC) has been developed as a simple for analysis of binary or ternary mixtures [3]. Also, mean centering of ratio kinetic profiles can be used for separation and simultaneous determination of binary mixtures by kinetic methods [4]. The objective of this study is to evaluate the applicability of UV-Vis spectrophotometric technique based on mean centering of ratio kinetic profiles for simultaneous determination of NG and NC in DB propellants.

Procedure

An appropriate aliquot of the solution containing 0.2-5.0 µg mL^{-1} NG and 0.5-10 µg mL^{-1} NC was transferred to 10 mL volumetric flasks, then 2 mL of 2 mol L^{-1} sodium hydroxide were added to 10 mL volumetric flasks and placed in water bath at 40°C and stopwatch was started just after addition of the sodium hydroxide solution and hydrolysis was investigated in 3 min intervals in the range of 0-20 min. After these time intervals for hydrolysis process, 2 mL of 5 mol L^{-1} sulphuric acid solution, 1 mL of 0.1 % w/v of paranitroaniline (PNA) and 1 mL of diphenylamine were added and diluted to the mark with DI water and a portion of solution was transferred to the quartz cell to measure absorbance change with hydrolysis time so, the kinetic profiles for the solutions containing NG and NC with different concentrations were recorded at 534 nm in the time range 0-20 min with 3 min intervals.

Sample preparation of DB propellant for NG and NC determination

In order extraction of NG and NC from DB propellant, for each analysis, about 0.2 ± 0.1 g of sample was weighed and transferred to 100 mL baker and dissolved in 20 mL of acetone solvent and the resulting solution was transferred into 100 mL flask and made up to mark with mixture of water/ acetone (50:50) solution.

Results and discussion

Hydrolysis of NG and NC can be done in alkaline media and produced nitrite ion (NO$_2^-$) that reaction of NO$_2^-$ with PNA in the presence of diphenylamine (as a coupling agent) in acidic media can produce an azo dye. Thus, concentration of NG and NC can be determined spectrophotometrically by measuring of the absorption of colored solutions reaction of NO$_2^-$ with PNA at 534 nm. The result revealed that the hydrolysis of NG in alkaline media can be completed after addition of sodium hydroxide solution in 40 °C; while, hydrolysis of NC was relatively slow and its hydrolysis rates can be accelerated by increasing temperature and time (Fig. 1).
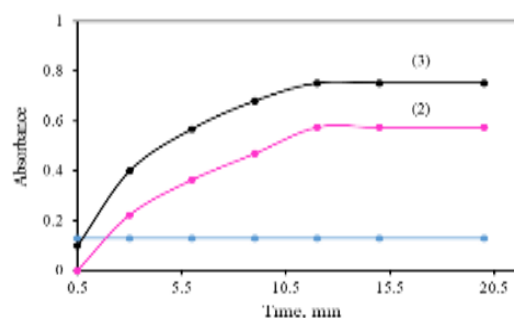
Fig.1: Absorption kinetic profiles for 0.30 µg mL^{-1} NG (1), 3.0 µg mL^{-1} NC (2) and their mixture (3)

22nd **Iranian Chemistry Congress (ICC22)**
Iranian Research Organization for Science and Technology (IROST)
13-15 May 2024

03231-97589

ISC

IROST

Application of MC of ratio kinetic profiles for simultaneous determination of NG and NC in DB propellants

For creating of individual calibration curves, absorption kinetic profiles of the standard solutions of NG with different concentrations were recorded and stored in the time range 0.5–20 min with 3min intervals (Fig. 2a) and ratio profiles for NG were obtained by dividing the kinetic profiles of NG by the normalized kinetic profile of the NC (Fig. 2b). Mean centering (MC) of the ratio profiles for NG were obtained in the time range of 3–20 min (Fig. 2c). The concentration of NG was determined by measuring the amplitude at 3 min corresponding to a maximum time shown of mean centering profiles. The same procedure was done for NC.
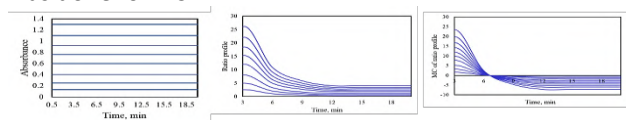
Fig. 2. The absorption kinetic profiles for the standard solutions of the NG with different concentrations (0.2-5.0 µg mL^{-1}) at 534 nm (a), the ratio profiles (b) and the MC of ratio profiles (c).
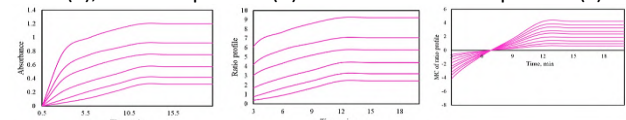
Fig. 3. The absorption kinetic profiles for the standard solutions of the NC with different concentrations (0.5-10.0 µg mL^{-1}) at 534 nm (a), the ratio profiles (b) and the MC of ratio profiles (c).

Optimization of parameters affecting simultaneous determination of NG and NC

Hydrolysis process of NG and NC occurs in an alkaline media, so, the concentration of sodium hydroxide was investigated in the range of 0.1- 0.6 mol L^{-1}. the hydrolysis process of NG and NC was completed in 0.4 mol L^{-1} of sodium hydroxide.

The effect of temperature was investigated in the range of 25-60 ℃**.** increasing of temperature did not cause considerable change in absorbance of NG, while for the NC, by increasing of temperature the absorbance of system was increased up to 40 ℃ with time and remained constant above it. So, optimum conditions for determination of nitrite ion from hydrolysis process of NG and NC were chosen as follows: The H$_2$SO$_4$ concentration: 1.0 mol L^{-1}, concentration of PNA as diazotizable aromatic amin: 0.02 % (w/v), and concentration of diphenylamine as a coupling agent: 0.02 % (w/v).

Analytical performance and method validation

The limits of detection were 0.1 µg mL^{-1} and 0.25 µg mL^{-1} respectively for NG and NC and on the basis of (S/N=10), the LOQ values   were 0.33 µg mL^{-1} and 0.83 µg mL^{-1} respectively for NG and NC.

Application of proposed method

In order to verification of the suggested was done by *military standard 286* method in DB propellant. The obtained results (Table 1), revealed that there are no egregious differences between two methods.

Conclusion

Proposed method revealed that UV-Vis spectrophotometric technique based on mean centering of ratio kinetic profiles method is a simple, fast, accurate, sensitive and user-friendly approach for resolving of binary mixtures of NG and NC in DB propellants.

DB propellant	Analyte	Proposed method		Standard method (MIL-STD-286)
		Found% in DB propellant	Relative error,%	Found% in DB propellant
Propellant 1	NG	28.9 ±0.3	+ 2.3	28.25 ± 0.45
	NC	53.0± 0.6	-2.21	54.2 ± 0.58
Propellant 2	NG	30.3 ± 0.42	-3.1	31.3 ± 0.55
	NC	57.3 ± 0.7	+1.95	56.2 ± 0.68

References

[1] Zou, X., Zhang, W., Gu, Y., Fu, X., Zhang, Z., Ge, Z., Luo, Y. (2020). A study on the effect of four thermoplastic elastomers on the properties of double-base propellants. The Royal Society of Chemistry Advanes, 10, 428883-428889. DOI: http://doi.org/10.1039/D0RA08370D

[2] Chajistamatiou , A. S., Bakeas, E. B. (2016). A rapid method for the identification of nitrocellulose in high explosives and smokeless powders using GC–EI–MS. Talanta.1, 192-201. DOI: https://doi: 10.1016/j.talanta.2016.01.038

[3] Afkhami, A. Bahram, M. (2005). Talanta. Mean centering of ratio spectra as a new spectrophotometric method for the analysis of binary and ternary mixtures.66, 712-720. https://doi.org/10.1016/j.talanta.2004.12.004

[4] Afkhami, A., Bahram, M. (2005). A novel spectrophotometric method for the simultaneous kinetic analysis of ternary mixtures by mean centering of ratio kinetic profiles. Talanta. 68, 1148-1155 DOI: https://doi.org/10.1016/j.talanta.2005.07.017

Synthesis of polysubstituted pyridines via nitrogen-doped graphene catalyzed one-pot multicomponent reaction under solvent-free conditions

Zahra Movahed, Hassan Valizadeh*, Farzaneh Mirzaei

Corresponding Author E-mail: hvalizadeh2@yahoo.com

Department of chemistry, Faculty of science, Azarbaijan Shahid Madani University, Tabriz, Iran.

Abstract: Nitrogen-doped graphene as a dual acid–base catalyst efficiently catalyzes the multicomponent reaction between arylaldehydes, diethylacetylenedicarboxylates, malononitrile and ammoniumacetate under solvent-free conditions at 80°C. Polysubstituted pyridine derivatives were produced in high to excellent yields and in short reaction times. The structures of the synthesized pyridines were established by Ft-IR, ^{1}H and ^{13}C NMR spectroscopic analysis. The advantages of this method include the in-situ oxidation of prepared 1,4-dihydropyridines, one-pot procedure, solventless system, operational simplicity and no column chromatography.

Keywords: Nitrogen-Doped Graphene; Multicomponent Reaction; Pyridine

Introduction

Nitrogen containing heterocyclic compounds is a very attractive research field for chemists, because of existence of those molecules as fundamental frameworks in various natural products and pharmaceuticals [1]. In particular, pyridines are important six-membered heterocycles that play important roles in many medicinal and biological activities like being anti-microbal, anti-bacterial, anti-viral, anti-tumor, anti-oxidant, anti-diabetic, anti-cancer, anti-inflammatory [2-4]. At first Arthur Hantzsch prepared symmetrically substituted 1,4-dihydropyridines (1,4-DHP) via four-component one-pot procedure in 1882 [5]. To the best of our knowledge, it was not many reports about the direct preparation of pyridines from the MCR of arylaldehydes with dialkylacetylenedicarboxylate, malononitrile and ammonium acetate. Although some successful procedures have been reported for this aromatization purpose, most of these procedures suffer from several

disadvantages and drawbacks such as long reaction times, low yields of oxidation and low selectivity.

Graphene quantum dots have attracted considerable attention of chemists because of their unique properties such as: stability, non-toxicity, good water solubility, biocompatibility [6-7]. Doping heteroatoms in GQDs can modify its electronic and chemical properties which expands their application [8-9]. Here, we wish to report efficient synthesis of polysubstituted pyridine derivatives in high to excellent yields. Nitrogen- doped graphene quantum dots were used as a highly effective catalyst in the four-component reaction between arylaldehydes, diethylacetylenedicarboxylates (DEAD), malononitrile and ammoniumacetate under solvent-free conditions at 80°C (Scheme 1). In-situ oxidation of 1,4-dihydropyridines afforded to pyridines in this procedure. Polysubstituted pyridine derivatives were prepared in high to excellent yields and in short reaction times.
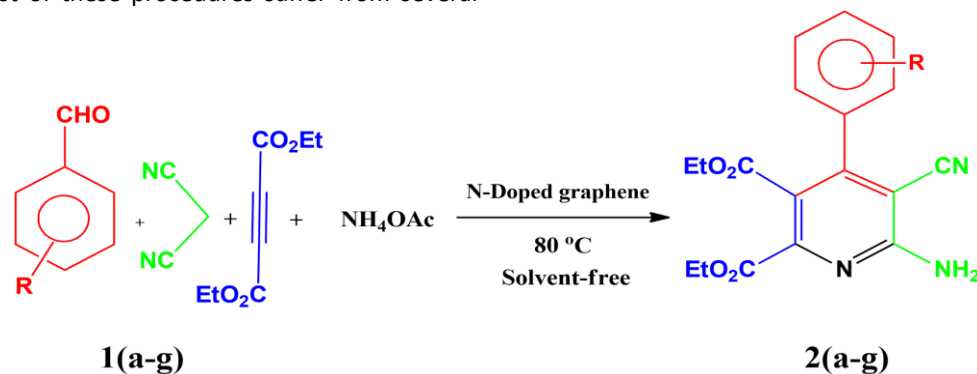
Fig.1: Synthesis of polysubstituted pyridines via multicomponent reaction

22nd Iranian Chemistry Congress (ICC22)
Iranian Research Organization for Science and Technology (IROST)
13-15 May 2024

03231-97589

ISC

IROST

Experimental Section

Synthesize of NGQDs

The NGQDs were synthesized microwave-assisted. 2 g of citric acid and 1.2 g of urea (1:2 molar ratio) were dissolved in 3 mL of deionized water. Then were placed in the microwave cell and heated under microwave irradiation to 180 ℃ with full power (1000 W) for 120 min. After heating they were allowed to cool to room temprature. The dark brown solution was centrifuged with ethanol to remove unreacted urea. Then the solution was dried in an oven at 70 ℃, and the dark brown powder was stored at room temprature.

General procedure for the synthesis of polysubstituted pyridins (2a-g)

Benzaldehyde derivatives (1 mmol), DEAD (1 mmol), malononitrile (1 mmol) and ammoniumacetate (1 mmol) were mixed thoroughly. N-doped graphene (0.007 mg) was added and the mixture was stirred at 80 ºC. After completion of the reaction, as indicated by TLC (ethyl acetate/n-hexane, 1/2), the mixture was extracted using ethyl acetate. Ethyl acetate was evaporated using a rotary evaporator at 45ºC and the crude product was further purified by recrystallization from a suitable solvent (ethyl acetate/n-hexane) to give pure products **2a-g**.

Results and Discussion

Using of N-doped graphene as a catalyst was examined and it was found that aforementioned 1,4-DHP was oxidized to the related pyridine derivative **2a**. The reaction was completed in a shorter reaction time and significantly higher yield in the presence of catalyst. It was found that the best yield of the product was obtained using 1/1/1/1 molar ratios of benzaldehyde/ DEAD/ malononitrile/ ammoniumacetate in the presence of catalyst (0.007 mg/1mmol of **1a**). Diethyl 2-amino-3-cyano-4-phenyl-5,6-dicarboxylate was isolated in 98% yield under these conditions. To the best of our knowledge this is the first report about the in-situ synthesis of pyridines via the above described four-component reaction. The efficiency of catalyst in this reaction is likely supported by the presence of carboxylic and amino groups on the surface of catalyst. Different benzaldehyde derivatives were examined for exploring of the scope of this promising reaction.

No significance difference in products yields were seen from the reaction of benzaldehydes containing electron donating groups in comparison with those containing electron-withdrawing groups. Catalyst was readily recovered by extraction of the reaction mixture with ethyl acetate (5ml×5), and its recyclability was investigated. Preparation of products **2a** and **2b** in the presence of four times recycled catalyst and the results are in comparable yields to the fresh catalyst.

Conclusions

In conclusion, we have introduced a one-pot synthesis of polysubstituted pyridine derivatives from simple and readily available precursors. It was found that N-doped graphene is a highly efficient, mild and convenient catalyst for the synthesis of pyridines via a four component reaction. This approach includes some important aspects such as in-situ oxidation of 1,4-dihydropyridines, the ease of the work-up procedure which the products can be isolated without chromatography and excellent yields, make this protocol a useful and attractive method for the synthesis of pyridine derivatives.

References

[1] Kerru, N., Maddila, S., & Jonnalagadda, S. B. (2019). Design of carbon-carbon and carbon-heteroatom bond formation reactions under green conditions. *Current Organic Chemistry*, *23*(28), 3154-3190.

[2] Altaf, A. A., Shahzad, A., Gul, Z., Rasool, N., Badshah, A., Lal, B., & Khan, E. (2015). A review on the medicinal importance of pyridine derivatives. *J. Drug Des. Med. Chem*, *1*(1), 1-11.

[3] Abdel-Raheem, S., El-Dean, A., Abd-Ella, A., Al-Taifi, E., Hassanien, R., El-Sayed, M., ... & Bakhit, E. (2021). A concise review on some synthetic routes and applications of pyridine scaffold compounds. *Current Chemistry Letters*, *10*(4), 337-362.

[4] Maddila, S., Maddila, S. N., Jonnalagadda, S. B., & Lavanya, P. (2016). Reusable Ce-V Loaded Alumina Catalyst for Multicomponent Synthesis of Substituted Pyridines in Green Media. *Journal of Heterocyclic Chemistry*, *53*(2), 658-664.

[5] Hantzsch, A. (1882). Justus Liebigs Ann. *Chem*, *215*, 1-5.

[6] Tian, P., Tang, L., Teng, K. S., & Lau, S. P. (2018). Graphene quantum dots from chemistry to applications. *Materials today chemistry*, *10*, 221-258.

[7] Du, Z., Shen, S. L., Tang, Z. H., & Yang, J. H. (2021). Graphene quantum dots-based heterogeneous catalysts. *New Carbon Materials*, *36*(3), 449-467.

[8] Gu, S., Hsieh, C. T., Lin, T. W., Yuan, C. Y., Gandomi, Y. A., Chang, J. K., & Li, J. (2018). Atomic layer oxidation on graphene sheets for tuning their oxidation levels, electrical conductivities, and band gaps. *Nanoscale*, *10*(33), 15521-15528.

[9] Rivera, L. M., Fajardo, S., Arévalo, M. D. C., García, G., & Pastor, E. (2017). S-and N-doped graphene nanomaterials for the oxygen reduction reaction. *Catalysts*, *7*(9), 278.

Development of Conductivity Methods -Cation Conductivity or Acid Conductivity and Suppressed Conductivity - for the Measurement of Trace Anions

Behzad Tayari Kalajahi[*], Seyedeh Hanieh Sajadi Kalajahi, Sara Tayari Kalajahi

Corresponding Author E-mail: tayari.kalajahi@ gmail.com

Mobin Energy Persian Gulf Co.

Abstract: Suppressed conductivity and cation conductivity were used for measuring and monitoring of low concentration of inorganic anions in ultrapure water of MOBIN energy's powerplant. A rapid and accurate test and low detection limits(ppb) provides a suitable means for preventing possible damage to equipment in powerplant

Keywords: cation conductivity; acid conductivity; CO_2 suppressor

Introduction

Cation conductivity is a very useful measurment of potentially harmful acidic impurities (anions).It is the conductivity of water after it passes through a cation exchange column in which cations are replaced by the hydrogen cation which is a strong contributor to conductivity and makes the measurement very sensitive.caton conductivity is used to seprate the conductivity caused by the dissolved sollidsfrom the conductivity caused by the water treatment chemicals

In the suppressed conductivity is used for removing CO_2 from the eluent flow before detection .This method improves the detection limits and eliminates the systm peak

Experimental Section

Cation conductivity

When power plant water passes thrugh the cation resin bed ,the resin exchange any positive ions in the solution for hydrogen ions. If a salt such as KNO_3 passes through the resin k^+ ions is held in the bed and an H^+ ions is released. In so doing 1 ppm of KNO_3 (which has a conductivity of approximately 10.50 µs/cm is converted to 1 ppm HNO_3 acid(which has a conductivity of approximately 24.8 µs/cm in like manner other salt are converted to their corresponding acids which have 2 to 6 times the coductivity of the corresponding salt.This shown in figure 1

Suppression method

The sample (KNO_3) were injected using direct injection technique .The analyte ions were separated on aselective ion exchange column using high-purity mobile phase (carbonate/hydrogen carbonate eluent for NO_3^- ,PO_4^- AND SO_4^{2-} and sodium hydroide for the detemination of F^-

and CL^- ions and detected using the suppressed conductivity detection method. This shown in figure 2
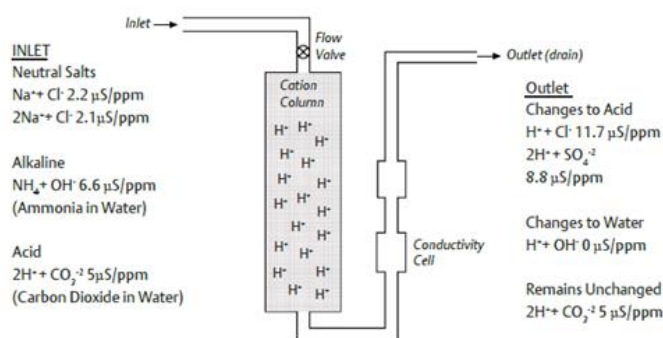
Fig.1

Test Conditions

Eluent: 5.0 mmol/L Na2CO3 - 0.3 mmol/L NaOH
Flow: 0.800 mL/min
Temperature: 45.0 °C
Pressure: 10.81 MPa
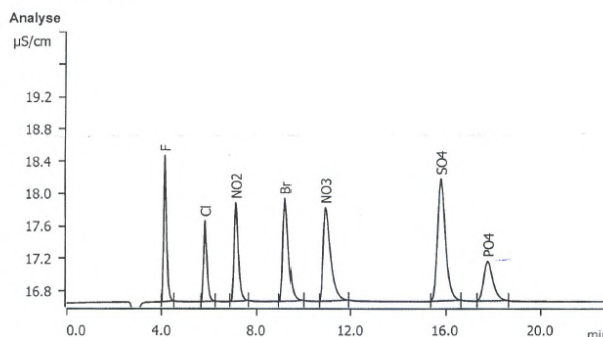
Fig.2: Sepration of standard anions on columns

22nd Iranian Chemistry Congress (ICC22)
Iranian Research Organization for Science and Technology (IROST)
13-15 May 2024

03231-97589

ISC

IROST

Results and Discussion

A regression line was obtained by plotting the coductivity verses cocenteration using least square methodThe relationship between the two parameter is linear with correlation coefficient $r^2 > .998$ for all methodes. This shown in figure 3

y = 14.593x + 9.522
$R^2 = 0.9989$

Specefic Conduct

y = 9.4254x + 1.1424
$R^2 = 0.9999$

Acid Conduct

y = 0.4797x - 0.0292
$R^2 = 1$

CO2 Suppressor
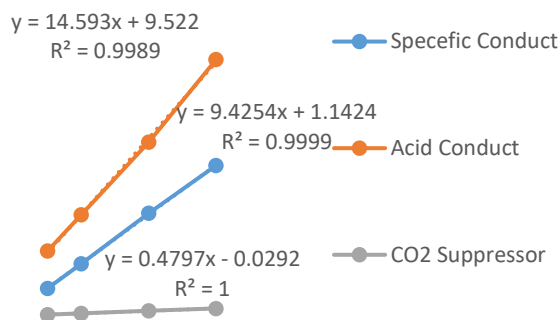
Fig.3: regression line for conductivity methodsConductivity vs concentration

Table1: Conductivity measurement before and after hydrogen exchange treatment

CONC N-NO$_3$(ppm)	SpecificConduct(μs)	CationConduct (μs)
1	10.50	24.8
2	19.90	38.6
4	39.2	66.4
6	57.5	98

Table2: Suppressed Conductivity -Retention Time 10.9 min

CONC N-NO$_3$(ppm)	SuppressedConductivity(μs)
1	0.535
2	1.083
4	2.226
6	3.341

Conclusions

Coductivity with no treatment is abulk -property detection methode because it measures coductivity in cluding analytes , anions,cations.

Cation coductivity is a useful tool for monitoring return condensate for low level of contamination by anions such as NO$_3^-$,Cl$^-$. Thus the cation coductivity cab be thought of as a" condutivity amplifier " for mineral and organic acid contaminants, increasing the sensitivity of the conductivity analyzer to lowlevels of contamination

In suppressed coductivity the background conductance of the eluent is lower than th overall conductance of the analyte, resulting in lower detection limits. The suppressed technique is for separating and detection of inorganic anions.

The determination of the major inorganic anions in ultra pure water samples was the main analytical task in thiswork amied at developing coductivity method for monitoring the chemical impurities in water- steam samples of MOBIN ENERGY PERSIAN GULF CO 's power plant

References

[1] Am. Soc. Mech.Engrrs.,29W. 39th St., New York, Power Test Code, "Determination of Quality of Steam, Part 2, 1940

[2] INDUSTRIAL AND ENGINEERING CHEMISTRY, VOL 47. 1955

[3] J.Serb.chem.Soc.70(7)995-1003(2005)

22nd Iranian Chemistry Congress (ICC22)
Iranian Research Organization for Science and Technology (IROST)
13-15 May 2024

03231-97589

IROST

Green CO₂ capture using carbonic anhydrase model enzyme: DFT approach

Mina Ghiasi* and Hanane Sadat Eghtedari

Corresponding Author E-mail: ghiasi@alzahra.ac.ir

Department of Physical Chemistry and NanoChemistry, Faculty of Chemistry, Alzahra University, P.O. Box: 1993893973, Tehran, Iran.

Abstract: The catalytic cycle of carbonic anhydrase (CA) enzyme using the immobilization of CA active site model on mesoporous silica amin-functionalized by 3-aminopropyltriethoxysilane (APTES) and using glutaraldehyde linker as a green biocatalyst was investigated employing DFT calculations in the gas and solvent to CO_2 capture.

Keywords: Carbonic anhydrase; CO_2 capture; Mechanism; DFT calculations

Introduction

presently one of the most challenging issues that confronts human society is global warming as environmental degradation. The steady increase in CO_2 emission into the atmosphere attributed to Industrial activities, deforestation, and urbanization poses a significant threat. The excessive amount of anthropogenic CO_2 as one of the main components of greenhouse gases (GHGs) leads to the depletion of the ozone layer, the temperature rise of the Earth, and subsequent climate change (Sekoai & Yoro, 2016). Burning fossil fuels, due to power, heat generation, and transportation is the primary source of CO_2. CO_2 capture (CC) technology has gained global acceptance as a viable solution which is a rescuer approach that makes possible the utilization of fossil fuels while reducing the emission of CO_2 (Koerner & Klopatek, 2002). Utilizing carbonic anhydrase (CA) as a catalyst in an alternative solvent in CO_2 capture has become prominent due to its significant advantages, including non-toxicity, high selectivity, biodegradability, lower capture cost, and green in comparison with other methods (like amine-based process). CA is a capable metalloenzyme typically with zinc in the active site, which exists in nature. CA catalyzes biological processes in humans and other living organisms, the vital reaction of interconversion of carbon dioxide and water to bicarbonate and protons speedily as its turnover rate ranges from 10^4 to 10^6 molecules of CO_2 per molecule of CA per second based on the wild form. (Effendi & Ng, 2019). In the present study, our attention focuses on several mechanism aspects: (1) the details of the nucleophilic attack of the zinc-bond hydroxide ion on CO2, (2) the study of different transition states through the reaction path, (3) the study of solvent effect on reaction mechanism and calculation of thermodynamic functions.

Methodology

The geometric structures of carbonic anhydrase model enzyme, ES complex, product complexes, intermediates (Int), and transition states (TS) were fully geometry optimized employing a hybrid Hartree-Fock- density functional scheme, the adiabatic connection method– Becke three-parameter with Lee-Yang-Parr (B3LYP) functional of density functional theory (DFT) with the standard 6-31G* basis set. The QST2 procedure has been used to search for transition states. Intrinsic reaction coordinate (IRC) calculations were employed to ensure the identity of the reactants and products corresponding to each transition structure. To evaluate the effects of solvent, we employed a polarized continuum model, PCM, (Maeda et al., 2015) for water solvent. All calculations were performed using Gaussian 09 software.
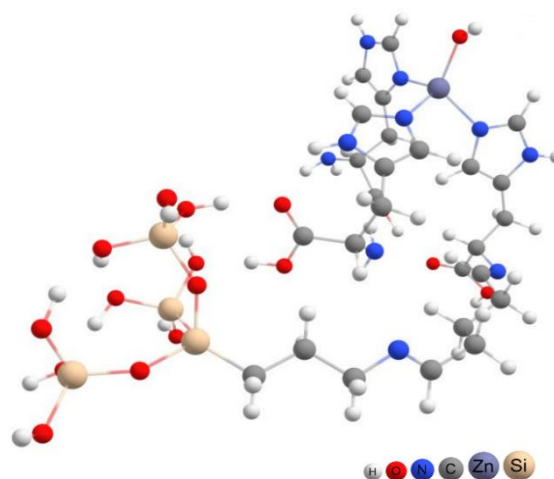
Fig.1: Optimized geometry of model Enzyme in the water solvent.

22nd Iranian Chemistry Congress (ICC22)
Iranian Research Organization for Science and
Technology (IROST)
13-15 May 2024

03231-97589

IROST
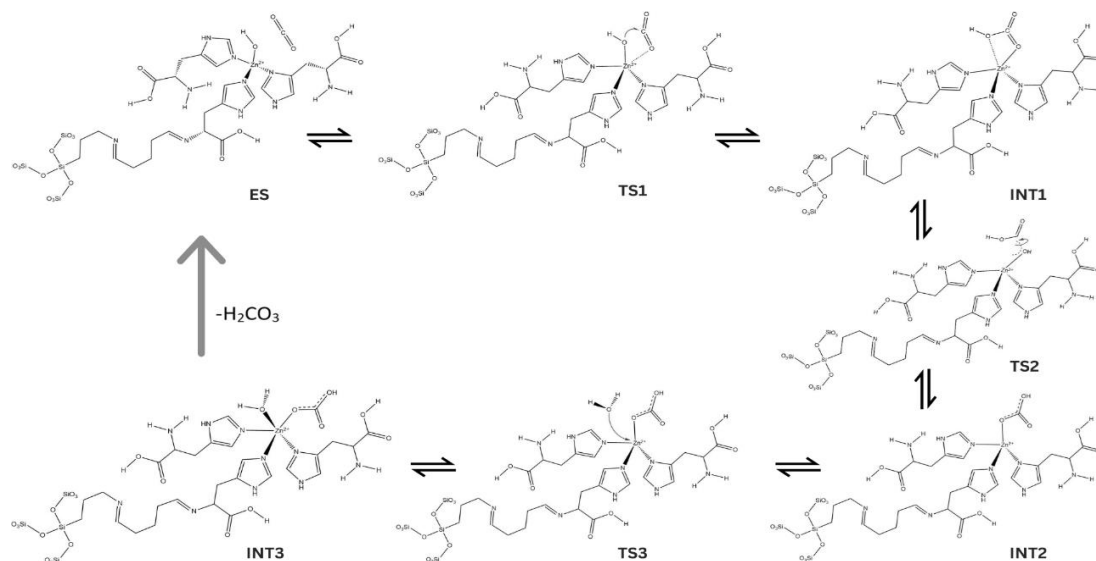
Fig. 2: Schematic representation of the catalytic mechanism of CA enzyme, catalyzed CO_2 hydration

Results and Discussion

The structure of the model enzyme of carbonic anhydrase II (CAII) was fully optimized at B3LYP/6-31G* level of calculations with no initial symmetry restrictions. In the following, the fully optimized geometries in the gas phase were re-optimized by considering the solvent effect using the PCM method in the water solvent, Figure 1 shows the optimized geometry of the immobilized CA model enzyme on mesoporous silica. As Figure 2 indicates the mechanism starts with a nucleophilic attack of zinc bond hydroxide lone pairs on the CO_2 molecule leading to form the first intermediate structure (ES), Figure 3. In the second step, the first transition state with about 42.74 kcal/mol barrier energy is formed. The third step is the binding of water molecule and the release of HCO_3^-. The geometry of the transition state has been found using scan, QST2, and QST3 procedures. Imaginary frequency confirms the transition state.
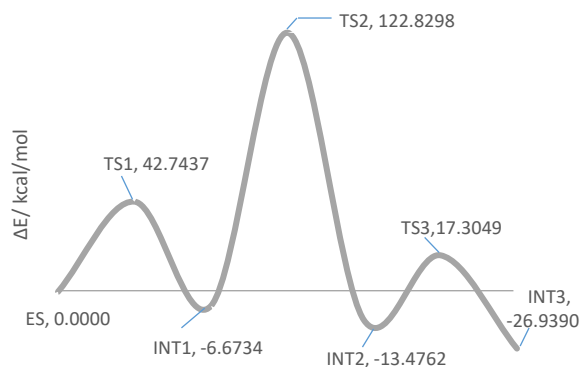
Fig. 3: Calculated variation energy through the reaction path

Conclusions

In the present study, we have extended our investigations of the carbonic anhydrase catalytic cycle with the CA immobilized on mesoporous silica complex as a model system for the hydration of CO_2 molecule employing DFT calculations. The results present a simplified model for the CO_2 hydration mechanism by the model system of CA involves different steps: in the first step, the zinc-bound OH has a nucleophilic attack on the CO_2 molecule to generate the first intermediate. In the second step the first intermediate converts to the second intermediate. The third step is the binding of a water molecule and the release of HCO_3^-.

References

[1] Effendi, S. S. W., & Ng, I.-S. (2019). The prospective and potential of carbonic anhydrase for carbon dioxide sequestration: A critical review. *Process Biochemistry*, *87*, 55-65.

[2] Koerner, B., & Klopatek, J. (2002). Anthropogenic and natural CO_2 emission sources in an arid urban environment. *Environmental Pollution*, *116*, S45-S51.

[3] Maeda, S., Harabuchi, Y., Ono, Y., Taketsugu, T., & Morokuma, K. (2015). Intrinsic reaction coordinate: Calculation, bifurcation, and automated search. *International Journal of Quantum Chemistry*, *115*(5), 258-269.

[4] Sekoai, P. T., & Yoro, K. O. (2016). Biofuel development initiatives in Sub-Saharan Africa: opportunities and challenges. *Climate*, *4*(2), 33.

Synthesis, characterization and catalytic application of Fe$_3$O$_4$/ ethyleneammonium tungestophosphate Nano-composite in the synthesis of Spiro[4H-chromene-4,3'-indolin-2-one]S

Sina Sheidaei*, K. Rad-Moghadam *, M.A. Zanjanchi ^{c}, Roghayeh Pasyar

Corresponding Author E-mail: Sinasheidaei@gmail.com

Faculty of Science, Chemistry Department, University of Guilan, Rasht, Iran.

Abstract: The magnetic nanoparticles of Fe3O4@C2H4NH3 [Li2PW12O40] were synthesized. The resulting product contains the ammonium group on the magnetic scaffold. The catalytic activities of Fe3O4@C2H4NH3 [Li2PW12O40] and Fe3O4@C2H4NH2 were studied through their application in one-pot synthesis of some spiro[4H-chromene-4,3'-indolin-2-one] s. The synthesis was based on a three-component reaction.
Keywords: Magnetic Nanoparticles, Heteropolyacid, Catalyst, Green Chemistry

Introduction

In recent years, there has been a great interest in the creation of biocompatible nanostructures due to the vast number of uses that may be found for them as well as their unique features. Researchers have focused particularly on magnetic nanoparticles among these nanostructures because of their unusual magnetic properties. This is partly because of how simple it is to separate them, how much overall surface area they have, and how easily they can be changed to act as nanocatalysts. In the current investigation, a novel category of magnetic nanoparticles was conceived of and put to use as a catalyst for the synthesis of spiro [4H-chromene-4,3-indolin-2-ones] via a three-component reaction. This was accomplished by using the nanoparticles as a starting material. [1-3]

The catalyst that is being discussed here is an example of a heterogeneous catalyst, and the fact that it possesses the superparamagnetic feature allows it to be extracted from reaction mixtures with relative ease. The majority of magnetic catalysts have the drawback of having their catalytically active component stuck to the surface of the magnetic support by physisorption forces. This is one of the most significant disadvantages of magnetic catalysts. In most cases, these forces are quite mild, which makes it possible for the active component to be easily leached away during use. On the other hand, a low density of active sites is produced on the surface of the nano-catalysts as a result of grafting catalytically active molecules onto the surface of the magnetic supports. In order to overcome these limitations, the purpose of this research was to graft Kegin-type heteropolyacid onto the surface of magnetite nanoparticles and then link these nanoparticles to the support using an ionic bond.

When compared to homogeneous catalysts, heterogeneous catalysts have improved thermal stability in the solid phase. This is one of the advantages of heterogeneous catalysts. This quality makes it possible to achieve higher reaction temperatures, which, when compared to other factors affecting the rate of the reaction, can result in an increased yield and an improvement in the reaction's overall efficiency. [4-5]

The literature places spiro-oxindole alkaloids within the category of oxindoles, and a significant number of the oxindole family's members are found in naturally occurring compounds [11]. The preferential structure of the spiro-oxindole scaffold, which is made from two essential substructures, is one of the defining characteristics of this scaffold. The oxindole moiety is one of these units. It is multifunctionalized, meaning that it is capable of serving as both an H-bond donor and an acceptor. Because of this one-of-a-kind characteristic, the scaffold is able to interact successfully with a wide variety of biological targets. In the context of this inquiry, the second moiety is a 4H-pyran ring that has been connected to the C-3 of oxindole at its 4-position through a fusion. Controlling liposolubility and a variety of other physicochemical properties can be accomplished through the application of spiro-oxindole [13]. Researchers have been very interested in spirooxindole for a considerable amount of time because of its unique spatial structure and notable biological features. This curiosity has persisted over a long length of time.

Experimental Section

1.1.1 Nano-Particle Synthesis:

The technique for the manufacture of Fe3O4 magnetic particles was carried out in a manner that was comparable to that which was described in other works [9-10], albeit with certain adjustments. An appropriate amount of Fe3O4 nanoparticles was equally dispersed in

22nd Iranian Chemistry Congress (ICC22)
Iranian Research Organization for Science and Technology (IROST)
13-15 May 2024

03231-97589

IROST

a solvent containing diamine and sodium acetate in an amount equal to 100 millilitres. The size-controlling agent was sodium acetate. After that, the ethylenediamine@Fe3O4 nanoparticles were washed many times using a solution that contained both ethanol and deionized water. The resultant substrate was evenly disseminated in ethanol, after which the hetero-acid was added and the mixture was agitated for a period of twenty-four hours. The precipitate that was produced was dried in an oven at a temperature of 60 degrees Celsius while also being subjected to reduced pressure. [10]

1.1.2 Synthesis method:

In order to successfully synthesize spiro-oxindoles, it is customarily necessary to adhere to a well-established protocol, as outlined by Fereydooni et al. [13]. In order to carry out this technique of synthesis, precisely measured amounts of each of the three components, together with the nanocatalyst, are mixed together. After that, the resulting reaction mixture is heated to 70 degrees Celsius and stirred while thin-layer chromatography (TLC) is used to monitor how much farther away the reaction is getting.

Results and Discussion

The goal of this research is to create a novel magnetic nano-catalyst by starting with magnetite nanoparticles densely functionalized with surface amino groups and then grafting a Kegin-type heteropolyacid to the surface of the magnetite nanoparticles using ionic bonding. The nano-composite that was generated in this manner proved to be an effective catalyst in the process of enabling the synthesis of some spiro-oxindoles from three separate components. By synthesizing ten different spiro-oxindole derivatives, we were able to demonstrate the effectiveness, dependability, and substrate scope of the approach. It was determined that the structure of the products could be deduced from their NMR data, and this was validated by comparing their physical data with that which was given in the scientific literature. In comparison to other methods, all of the items were manufactured with relatively high yields, in relatively short amounts of time, and in settings that were not harmful to the surrounding environment [13].
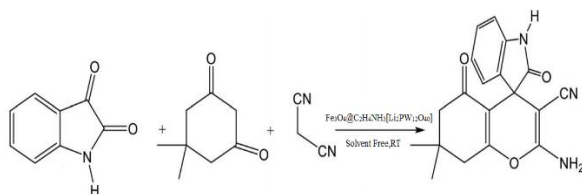
Fig.1: 3×4 Supercells used for three-component synthesis of the spiro-oxindoles (Font: Calibri 9)

Conclusions

While synthesis was based on a three-component reaction, and the optimized conditions were achieved by examining the effects of solvent, temperature, type, and amount of catalyst on the reaction time and yield of the model product.

References

[1] Ghanbaripour, R., Mohammadpoor-Baltork, I., Moghadam, M., Khosropour, A. R., Tangestaninejad, S., Mirkhani, V. (2012). "Microwave-promoted efficient conversion of acetophenones to 1, 3, 5-triarylbenzenes catalyzed by $H_3PW_{12}O_{40}$ and nano-silica supported $H_3PW_{12}O_{40}$ as reusable catalysts". *Polyhedron*, *31*(1), 721-728.

[2] Chu, W., Yang, X., Shan, Y., Ye, X., Wu, Y. (1996). "Immobilization of the heteropoly acid (HPA) $H_4SiW_{12}O_{40}$ (SiW_{12}) on mesoporous molecular sieves (HMS and MCM-41) and their catalytic behavior". *Catalysis Letters*, *42*(3), 201-208.

[3] Shojaei, A. F., Shams-Nateri, A., Ghomashpasand, M. (2015). "Comparative study of photocatalytic activities of magnetically separable $WO_3/TiO_2/Fe_3O_4$ nanocomposites and TiO_2, WO_3/TiO_2 and TiO_2/Fe_3O_4 under visible light irradiation". *Superlattices and Microstructures*, *88*, 211-224.

[4] Shojaei, A. F., Tabatabaeian, K., Zanjanchi, M. A., Moafi, H. F., Modirpanah, N. (2015). "Synthesis, characterization and study of catalytic activity of Silver doped ZnO nanocomposite as an efficient catalyst for selective oxidation of benzyl alcohol". *Chemical Sciences*, *127*(3), 481-491

[5] http: //en. Wikipedia. org/ Wiki/ Homogeneous-Catalysis.

[6] http: //en. Wikipedia. org/ Wiki/Heterogeneous-Catalysis

[7] Shirini, F., Khaligh, N. G. (2012). "Poly (4-vinylpyridine) catalyzed chemoselective O-TMS protection of alcohols and phenols and N-Boc protection of amines". *Iranian Chemical Society*, *9*(4), 495-502.

[8] Kong, L., Chen, W., Ma, D., Yang, Y., Liu, S., Huang, S. (2012). "Size control of $Au@Cu_2O$ octahedra for excellent photocatalytic performance". *Materials Chemistry*, *22*(2), 719-724.

[9] C. Qus, H.B. Yang, D.W. Ren, Magnetite nanoparticles prepared by precipitation from partially reduced ferric chloride aqueous solutions, J. Colloid Interface Sci. 215 (1999) 190–192

[10] P. Berger, N.B. Adelman, K.J. Bechman, Preparation and properties of an aqueous ferro fluid, J. Chem. Edu. 76 (1999) 448–943.

[11] Kaur M, Singh M, Chadha N, et al. Oxindole: a chemical prism carrying plethora of therapeutic benefits. Eur J Med Chem. 2016;123:858–894

[12] Tantawy MA, Nafie MS, Elmegeed GA, et al. Auspicious role of the steroidal heterocyclic derivatives as a platform for anti-cancer drugs. Bioorg Chem. 2017;73:128–146

[13] Jannat Freidooni, Kurosh Rad-Moghadam & Maedeh Saeedi-Mirakmahaleh (2022) ZrO_2 and Rice-Husk-Xanthate Adduct: An Efficient Bioderived Catalyst for Synthesis of Spiro[4H-pyran-4,3'-indoline]s, PolycyclicAromaticCompounds, 42:10, 7217-7231, DOI: 10.1080/10406638.2021.1998145

One-pot synthesis of pyridopyrimidines *via* reaction of enaminones or uracils with *in situ* generated Chalcones

Amin Arman, Najmeh Nowrouzi *

Corresponding Author E-mail: nowrouzi@pgu.ac.ir

Department of Chemistry, Faculty of Nano and Bio Science and Technology, Persian Gulf University, Bushehr.

Abstract: A one-pot reaction is presented for the synthesis of pyridopyrimidine and quinoline derivatives, which are nitrogen-containing heterocyclic compounds with various medicinal properties. Chalcone derivatives are generated *in situ* from the reaction of aldehyde and ketone derivatives, then trapped by enaminone or uracil to produce the corresponding pyrido[2,3-d] pyrimidine and quinoline derivatives.

Keywords: Pyridopyrimidine; Quinoline; Chalcone; Enaminone; Uracil

Introduction

The study of the chemistry of heterocyclic compounds is very important for the discovery of new drugs. Many heterocyclic compounds such as pyrrole, pyrrolidine, pyrimidine, furan, thiophene, pyrrolopyridine, pyridine, and thiazole show significant biological activities. Among these compounds, pyrimidines are of special importance [1]. Pyridopyrimidines are formed by fusing pyridine and pyrimidine rings. The presence of pyridopyrimidines in the structure of some vital drugs has caused more interest in the synthesis of these compounds [2]. Pyrido[2,3-d] pyrimidines are compounds with various medicinal effects such as antihypertensive [3], analgesic, anti-inflammatory [4], vascular relaxant [5], antiviral [6], antibacterial [7] and antihistaminic [8].

Due to the importance of pyridopyrimidine in various drugs, many synthetic methods have been used in the synthesis of these compounds. In 2012, Verma and co-workers reported a two-component reaction for preparation of pyrido[2,3-d] pyrimidine form uracil and diethyl 2-ethoxy malonate using water as a solvent under reflux conditions with excellent yield [9]. A method for preparation of 4,3,2,1-tetrahydropyrido[2,3-d] pyrimidines has been reported by Ramati and his colleagues via a three-component reaction between benzyl cyanide, aminouracil, and aromatic aldehyde [10]. In another study, a three-component reaction, between 6-amino-2-mercaptopyrimidine-4-yl, malononitrile, and aromatic aldehydes has been reported for the synthesis of 2-thiooxo-4,3,2,1-tetrahydropyrido[2,3-d] pyrimidines in good yield using sodium lauryl sulfate as the catalyst [11]. Pyrido[2,3-d] pyrimidine derivatives can also be synthesized through the Diels-Alder reaction. In 2008, Valderama and *et al.* prepared 8,5,4,3,2,1-hexahydropyrido [2,3-d] pyrimidine derivatives in high yield from the reaction of 6-amino-3,1-dimethyluracil, aromatic aldehydes and diethyl ethylene dicarboxylate in the presence of *L*-proline as the catalyst [12]. In another attempt, Hayakawa and co-workers synthesized 4,3-

dihydropyrido [2,3-d] pyrimidine derivatives in high yield using 6-aminouracil and electron-rich enamines in water as a solvent [13].

One of the principles of green chemistry for the synthesis of compounds is the use of safe solvents in chemical reactions. Water is known as a green solvent because it is non-flammable, non-corrosive, non-toxic, cheap and readily available. In this study, we reported a one-pot synthesis of pyrido[2,3-d] pyrimidine derivatives using ketones and aldehydes with enaminone or uracil derivatives in ethanol and water (Scheme 1).
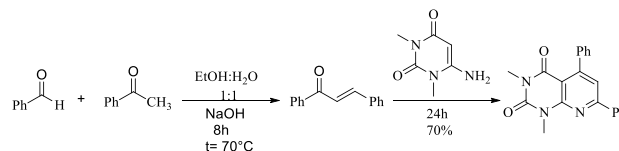
Scheme 1: preparation of 1,3-dimethyl-5,7-diphenylpyrido[2,3-d] pyrimidine-2,4(1H,3H)-dione

Results and Discussion

The obtained results are satisfactory and the good yield of the products is a confirmation of the good progress of the coupling reaction of chalcone with enaminone and uracil derivatives. By examining the electronic effects, we concluded that the desired reaction is associated with good results both in the case of benzaldehydes with electron-withdrawing and electron-donating groups. For instance, changing the substitution from hydrogen to methyl, *N,N*-dimethyl, methoxy, chlorine, and nitro on benzaldehyde did not cause a noticeable change in the reaction yield. Acetophenone, *p*-methylacetophenone and *p*-chloroacetophenone have also produced the desired products with similar efficiencies in the reaction with different aldehydes. In the second step of the reaction, uracil derivatives (6-aminouracil and 1,3-dimethyl-6-aminouracil), dimedone-derived enaminones and 4-aminocoumarin were used. In all cases, the product was obtained in good to excellent yield, although in the case of uracil derivatives, where the products are

22nd Iranian Chemistry Congress (ICC22)
Iranian Research Organization for Science and Technology (IROST)
13-15 May 2024

03231-97589

IROST

separated from the reaction mixture as a precipitate, the yields were a little higher.

Experimental Section

Acetophenone (1 mmol), benzaldehyde (1.2 mmol) and sodium hydroxide (0.1 mmol) were added to a test tube containing water and ethanol in the ratio of 1:1 (2 mL). The reaction mixture was allowed to stir in an oil bath at 70°C. The progress of the reaction was monitored by thin layer chromatography (TLC). After complete consumption of acetophenone (8 hours) and formation of chalcone intermediate, uracil or enaminone (0.8 mmol) was added to the reaction mixture. After the reaction is complete, it was poured into cold water and extracted with ethyl acetate (3×15 mL). The combined organic extracts were concentrated and the crude product was purified by column chromatography on silica gel using ethyl acetate/*n*-hexane as an eluent.

Conclusions

In summary, in this study, a new and effective method for the synthesis of pyrido[2,3-d] pyrimidines *via* a one-pot process were presented. In this research, various benzaldehydes and acetophenones were reacted with uracil and enaminone derivatives to produce the corresponding pyrido[2,3-d] pyrimidines in good to excellent yields. Simple procedure, one-pot reaction, no need for catalyst, easy access to raw materials, normal atmospheric conditions and high yield of products were advantages of the present method.

References

[1] Dinakaran, V. S., Bomma, B., & Srinivasan, K. K. (2012). Fused pyrimidines: The heterocycle of diverse biological and pharmacological significance. *Der Pharma Chemica*, *4*(1), 255-265. [Google Scholar]

[2] Dongre, R. S., Bhat, A. R., & Meshram, J. S. (2014). Anticancer activity of assorted annulated pyrimidine: a comprehensive review. *Am J Pharm Tech Res*, *4*(1), 138-155. [Google Scholar]

[3] Shamroukh, A. H., Rashad, A. E., & Abdelmegeid, F. M. (2016). The chemistry of pyrido [2, 3-d] pyrimidines and their applications. *J. Chem. Pharm. Res*, *8*(3), 734-772.

[Google Scholar]

[4] El-Gazzar, A. R. B., & Hafez, H. N. (2009). Synthesis of 4-substituted pyrido [2, 3-d] pyrimidin-4 (1H)-one as analgesic and anti-inflammatory agents. *Bioorganic & medicinal chemistry letters*, *19*(13), 3392-3397.

https://doi.org/10.1016/j.bmcl.2009.05.044

[5] Pastor, A., Alajarin, R., Vaquero, J. J., Alvarez-Builla, J., de Casa-Juana, M. F., Sunkel, C., ... & Sanz-Aparicio, J. (1994). Synthesis and structure of new pyrido [2, 3-d] pyrimidine derivatives with calcium channel antagonist activity. *Tetrahedron*, *50*(27), 8085-8098.

https://doi.org/10.1016/S0040-4020(01)85291-1

[6] Nasr, M. N., & Gineinah, M. M. (2002). Pyrido [2, 3-d] pyrimidines and Pyrimido [5', 4': 5, 6] pyrido [2, 3-d] pyrimidines as New Antiviral Agents: Synthesis and Biological Activity. *Archiv*

der Pharmazie: An International Journal Pharmaceutical and Medicinal Chemistry, *335*(6), 289-295. https://doi.org/10.1002/1521-4184(200208) 335:6<289::AID-ARDP289>3.0.CO;2-Z

[7] Matsumoto, J., & Minami, S. (1975). Pyrido [2, 3-d] pyrimidine antibacterial agents. 3. 8-alkyl-and 8-vinyl-5, 8-dihydro-5-oxo-2-(1-piperazinyl) pyrido [2, 3-d] pyrimidine-6-carboxylic acids and their derivatives. *Journal of Medicinal Chemistry*, *18*(1), 74-79.

https://doi.org/10.1021/jm00235a017

[8] Quintela, J., Peinador, C., Botana, L., Estévez, M., & Riguera, R. (1997). Synthesis and antihistaminic activity of 2-guanadino-3-cyanopyridines and pyrido [2, 3-d]-pyrimidines. *Bioorganic & medicinal chemistry*, *5*(8), 1543. https://doi.org/10.1016/S0968-0896(97)00108-9

[9] Verma, G. K., Raghuvanshi, K., Kumar, R., & Singh, M. S. (2012). An efficient one-pot three-component synthesis of functionalized pyrimido [4, 5-b] quinolines and indeno fused pyrido [2, 3-d] pyrimidines in water. *Tetrahedron Letters*, *53*(4), 399-402.

https://doi.org/10.1016/j.tetlet.2011.11.047

[10] Rahmati, A., & Khalesi, Z. (2012). Catalyst free synthesis of fused pyrido [2, 3-d] pyrimidines and pyrazolo [3, 4-b] pyridines in water. *Chinese Chemical Letters*, *23*(10), 1149-1152.

https://doi.org/10.1016/j.cclet.2012.08.009

[11] Li, S. H., Shen, Y. H., Gao, N., & Li, J. T. (2010). One-Pot Synthesis of Some New Pyrido [2, 3-d] pyrimidine Derivatives Catalyzed by Sodium Lauryl Sulfate in Aqueous Media. *Journal of Chemistry*, *7*, 779-784.

https://doi.org/10.1155/2010/230707

[12] Valderrama, J. A., & Vásquez, D. (2008). Design and synthesis of angucyclinone AB-pyrido [2, 3-d] pyrimidine analogues. *Tetrahedron Letters*, *49*(4), 703-706.

https://doi.org/10.1016/j.tetlet.2007.11.133

[13] Hayakawa, M., Kaizawa, H., Moritomo, H., Koizumi, T., Ohishi, T., Yamano, M., ... & Parker, P. (2007). Synthesis and biological evaluation of pyrido [3', 2': 4, 5] furo [3, 2-d] pyrimidine derivatives as novel PI3 kinase p110α inhibitors. *Bioorganic & medicinal chemistry letters*, *17*(9), 2438-2442.

https://doi.org/10.1016/j.bmcl.2007.02.032

The use of chromium hexacarbonyl as carbon monoxide source in the synthesis of pyrido[2,3-d] pyrimidines

Hamed Ahmadi, Najmeh Nowrouzi*

Corresponding Author E-mail: nowrouzi@pgu.ac.ir

Department of Chemistry, Faculty of Nano and Bio Science and Technology, Persian Gulf University, Bushehr 75169 Iran.

Abstract: In this study, the multicomponent reaction between aryl iodides, phenylacetylene, chromium hexacarbonyl and uracil or enaminone derivatives in the presence of palladium acetate as a catalyst for the one-pot synthesis of pyrido[2,3-d] pyrimidines is described.

Keywords: Carbonylation; Chromium hexacarbonyl; Pyridopyrimidine; Palladium acetate; Phenyl acetylene; Aryl halide; Uracil; enaminone

Introduction

Due to the importance of carbonylation reactions, many studies have been carried out in the field of these reactions. The first transition-metal catalyzed carbonylation reaction by carbon monoxide gas was reported in 1963 by Hack [1]. Despite the high use of carbon monoxide gas in industrial processes, in organic synthesis, it is not desirable to carry out the reactions in the presence of this gas. Carbon monoxide is a very poisonous gas that has no specific color and smell. Its affinity with blood hemoglobin is about 200 times higher than that of oxygen gas. In addition to carbon monoxide toxicity, these reactions require high gas pressure and high temperatures, as well as special tools for using, storing and transporting gas. In this way, it is important to develop methods to carry out carbonylation reactions without direct use of gas and to find suitable alternatives for it. So far, several sources of carbonylation have been introduced as a substitute for carbon monoxide gas, including formic acid and its derivatives, aldehydes, carbamoylsilane, carbamoylstannane, and metal carbonyls. Metal carbonyls are solid and stable carbonyl sources that can be easily used [2-5]. These compounds are much more desirable than other carbonyl sources because cleavage of a carbon-carbon bond in organic carbonyls requires much more energy than removing the carbonyl ligand from the complexes. Therefore, the aim of this study is to use chromium hexacarbonyl as a carbonylating source in the one-pot synthesis of pyrido[2,3-*d*] pyrimidines which are compounds with diverse pharmacological effects [6-12].

Experimental Section

In a test tube containing *N,N*-dimethylformamide (2 ml), Iodobenzene (1.0 mmol), chromium hexacarbonyl (1.0 mmol), phenyl acetylene (1.4 mmol), uracil (1.5 mmol), sodium acetate (3.0 mmol) and palladium acetate (0.01 mmol) were added. the reaction mixture was allowed to stir in an oil bath at 100 °C. The progress of the reaction was monitored by thin layer chromatography (TLC). After 24 hours and cooling the reaction mixture to room temperature, the product was extracted using ethyl acetate (3×1 mL). Finally, the pure product was obtained by column chromatography using *n*-hexane/ethyl acetate as eluent.

Results and Discussion

Different phenyl iodides were reacted with phenylacetylene and uracils under optimal conditions. These reactions were easily carried out under optimal conditions and high yields of the respective products were obtained. Examining the electron effects showed that the desired reaction in the case of iodobenzenes with electron-donating groups and electron-withdrawing groups is associated with good results. Enaminones, like uracils, participated in this reaction and formed the product with favorable yields. The reaction of bromobenzene with phenylacetylene and 6-amino-1,3-dimethyluracil under optimal conditions did not result in a product. Chlorobenzene was also inactive under the current catalytic conditions.
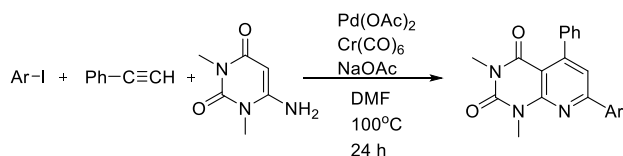
Scheme 1: Preparation of 1,3-dimethyl-5,7-diphenylpyrido[2,3-d]pyrimidin-2,4-(1H,3H)-dione

22nd Iranian Chemistry Congress (ICC22)
Iranian Research Organization for Science and Technology (IROST)
13-15 May 2024

03231-97589

Conclusions

In the present method, pyrido[3,2-d]pyrimidines were synthesized using phenylacetylene and phenyliodides during a palladium-catalyzed carbonylation reaction using chromium hexacarbonyl as a carbonyl source. One-pot and one-step reaction is one of the advantages of this method. Also, chromium hexacarbonyl, in addition to being a stable carbonyl source and a suitable substitute for gaseous carbon monoxide, also plays a role as a reducer, and there is no need to use an additional reducer in the reaction medium. These reactions did not need a ligand either.

References

[1] Heck, R. F. *J. Am. Chem. Soc*. 1967, *5546*. https://doi.org/10.1002/9781118905074.ch05

[2] Odell, L. R.;Russo, F.; Larhed, M. *Synlett* 2012, *23*, 685. DOI: 10.1055/s-0031-1290350

[3] Larhed, M.; Kaiser, N. F.; Hallberg, K. *J. Comb. Chem*. 2002, *4*, 109. DOI: 10.1021/cc010085f

[4] Nowrouzi, N.; Mozaffari, M. *Eur. J. Org. Chem*. 2019, 7541. https://doi.org/10.1002/ejoc.201901273

[5] Nowrouzi, N.; Abbasi, M.; Mozaffari, M. *Appl. Organomet. Chem*. 2019, 5049. https://doi.org/10.1002/aoc.5049

[6] Abdelhameed, Osama M. Darwesh, O. M. El-Shahatc, M. *Heliyon,* 2020, e04956. https://doi: 10.1016/j.heliyon. 2020.e04956.

[7] Shamroukh, A.; Rashad, A.; Abdelmegeid, F. J. *Chem. Pharm. Res*. 2016, *8*, 734. ISSN: 0975-7384

[8] El-Gazzar, A. B. A.; Hafez, H. N. *Bioorg. Med. Chem. Lett*. 2009, *19*, 3392. https://doi.org/10.1016/j.bmcl.2009.05.044

[9] Pastor, A.; Alajarin, R.; Vaquero, J. J.; Alvarez-Builla, J.; Casa-Juana, M. F.; Sunkel, C.; Priego, J. G.; Fonseca, I. J. *Tetrahedron*. 1994, *50*, 8085. https://doi.org/10.1016/S0040-4020(01)85291-1

[10] Moreno, E.; Plano, D.; Lamberto, I.; Font, M.; Encío, I.; Palop, J. A.; Sanmartín, C. Eur. J. *Med. Chem*. 2012, *47*, 283. https://doi.org/10.1016/j.ejmech.2011.10.056

[11] Nasr, M. N.; Gineinah, M. M. *Arch. Pharm. Pharm. Med. Chem*. 2002, *6*, 289. https://doi.org/10.1002/1521-4184(200208)335:6<289::AID-ARDP289>3.0.CO;2-Z

[12] Matsumoto, J.; Minami, S. J. *Med. Chem*.1975, *18*, 74. https://doi.org/10.1021/jm00235a017

Theoretical Study of the Structural, Electronic, and stability properties of LiBeN half-Heusler Compound from DFT Methods.

Ebrahim Nemati-Kande[a]*, Farzaneh Hosseini[a], Sima Mahmoudi[a,b]

Corresponding Author E-mail: e.nemati@urmia.ac.ir.

[a] Department of Physical Chemistry, Faculty of Chemistry, Urmia University, Urmia, Iran.

[b] Department of Physics, Faculty of Sciences, Urmia University, Urmia, Iran.

Abstract: In this project, the structural, electronic, optical, and stability behaviours of the LiBeN half-Heusler compound was studied using GGA and HSE exchange correlation functionals. The results show that this compound is stable from a dynamic point of view. The calculated electronic band gap also indicates the semiconducting nature of the compound.

Keywords: Half-Heusler; electronic structure; Density functional theory

Introduction

The crystal lattice of half-Heusler (hH) ternary compounds is described by the space group F-43m[1]. These compounds have a general formula of XYZ, where X is a more electropositive transition metal, Y is a less electropositive transition metal, and Z is heavy main group element. For the half-Heusler compounds XYZ one FCC sublattice remains unoccupied (C1b structure)[2].
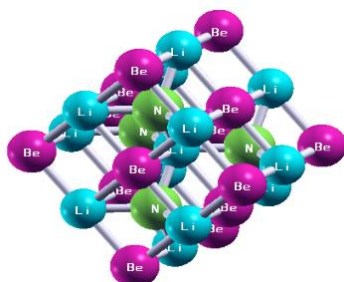
Fig.1: The relaxed unit cell of the LiBeN half-Heusler Compound.

Computational details

In the present work, the full-potential DFT approach as implemented in the Quantum espresso package was used. We used the generalized gradient approximation (GGA) of Perdew-Burke-Ernzerhof (PBE) and hybrid functional of the Heyd Scuseria-Ernzerh (HSE). The kinetic energy cutoff considered for the wave function is equal to 100 Ry and the cutoff Kinetic energy for charge density expansion was set at 500 Ry. Also, to optimize the network structure, energy uncertainty of 10^{-12} has been considered. Also, to calculate the lattice stability and the phonon dispersion curve and the phonon density of state, the PHONOPY package has been used. A well converged k-point mesh set of 20×20×20 w as used in relaxtaion and electronic calculations. However, in phonon calculation a less dense k-mesh of 16×16×16 with a 3×3×3 supercell was used.

Results and Discussion

The chemical formula for a hH material is XYZ and crystallize in the C1b structure. The X, Y, and Z atoms' Wyckoff locations result in three interpenetrating FCC lattices. The LiBeN structure can be found space group F-43m. 4a (0,0,0), 4b (1/2, 1/2, 1/2), and 4c (1/4, 1/4, 1/4) are the atomic locations, which is shown in Fig. 1.

The calculation of the band structure helps us to understand the shape of the fermi surface. The band gap is one of the most useful aspects of the band structure, as it influences strongly the electrical and optical properties of the material. The electronic band structure calculations were performed using the GGA and HSE functionals, which is shown in Fig. 2. For calculating the band structure high symmetry point (X→L→Γ→X→W→K→Γ) is considered, while the fermi energy level is considered to be at 0.0 eV. As can be seen in Fig. 3, the minimum value of the band gap occurs at the gamma and X points. These results show that this compound has a semiconductor nature.
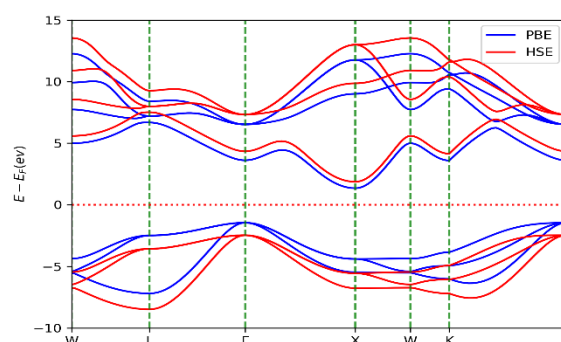
Fig. 2: Electronic band structure of the LiBeN hH compound using the PBE (blue) and HSE (red) functionals.

22nd Iranian Chemistry Congress (ICC22)
Iranian Research Organization for Science and
Technology (IROST)
13-15 May 2024

03231-97589

IROST
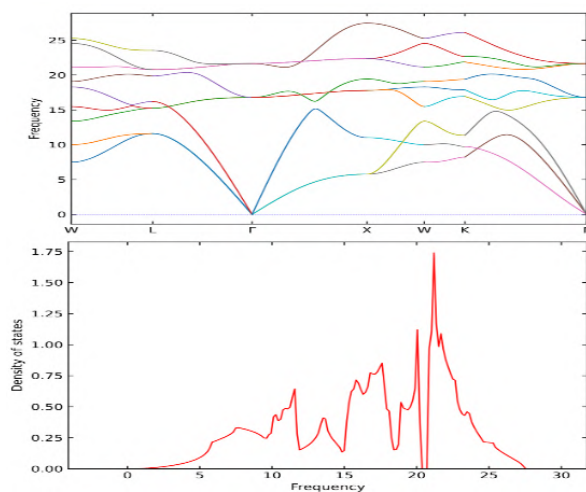
Fig. 3: The phonon scattering band structure (top), and
phonon density of states (bottom) of LiBeN hH compound.

In order to check the dynamic stability of LiBeN hH
compound, we also calculated phonon scattering curves
and phonon density of states. The Fig. 3 shows the
phonon scattering curve and the phonon density of
states. It can be seen that, the phonon spectrum obtained
for the LiBeN compound in all directions shows a positive
phonon frequency in the Brillion region. Therfore this
compound is dynamically stable in the hH structure.

Conclusions

According to the obtained results, the studied compound
is dynamically stable and the band gap obtained with the
GGA and HSE approximations shows that this compound
is a semiconductor.

References

[1] 1. Ojha, A., R.K. Sabat, and S. Bathula,
*Advancement in half-Heusler thermoelectric
materials and strategies to enhance the
thermoelectric performance.* Materials Science in
Semiconductor Processing, 2024. **171**: p. 107996.
https://doi.org/10.1016/j.mssp.2023.107996

[2] 2. Islam, M. and M.A.R. Sheikh, *A comprehensive
DFT study on the physical properties of XCrAl (X= Fe,
Co, Ni, Cu) half-Heusler alloys for applications in
high-temperature technology.* Physica B: Condensed
Matter, 2023. **668**: p. 415244.
https://doi.org/10.1016/j.physb.2023.415244

22nd Iranian Chemistry Congress (ICC22)
Iranian Research Organization for Science and Technology (IROST)
13-15 May 2024

03231-97589

ISC

IROST

BiOIBr/Polydopamine coated on TiO₂ nanotubes arrays-based signal-off photoelectrochemical sensor for high sensitivity detection of Betamethasone sodium phosphate

Mohana Abassi, Majid Arvand*, Maryam Farahmand Habibi

Corresponding author E-mail: arvand@guilan.ac.ir

Electroanalytical Chemistry Laboratory, Faculty of Chemistry, University of Guilan, Rasht, Iran.

Abstract: Betamethasone sodium phosphate (BSP) is an anti-inflammatory and immunosuppressive drug used for various skin and systemic conditions, and its measurement can aid in treatment optimization and safety monitoring. In this study, a photoelectrochemical sensor using BiOIBr/polydopamine (BiOIBr/PDA) on titanium dioxide nanotubes (TiO₂ NTs) for sensitive determination of BSP was presented.

Keywords: Photoelectrochemical sensor; Betamethasone sodium phosphate; Polydopamine; BiOIBr

Introduction

Photoelectrochemistry is a phenomenon in which photoactive materials, when excited, exchange electrons with certain substances, leading to changes in light currents. Photoelectrochemical measurement is a rapidly developed and emerging analytical method using photoactive substances. In this method, photoactive substances are stimulated by external light, generating a flow of photons that can correspond to the concentration of the analyte present in the solution. TiO₂, a type of semiconductor, is prepared from titanium anodizing, enhancing resistance against corrosion, increasing surface area, and also sufficiently absorbing the analyte. Polydopamine, synthesized through oxidative polymerization of dopamine, requires no specific or special process and can polymerize on the surface of any material with good adhesive properties. Due to abundant catechol groups, polydopamine can adhere via covalent interaction to various molecules, including metals and metal oxide surfaces (such as Fe₂O₃, ZrO₂, and TiO₂). Moreover, polydopamine possesses high light harvesting capability, high electrical conductivity, good biocompatibility, and rapid electron transfer rate. Another advantage of polydopamine is its electron donor capability in the PEC system, which significantly diminishes recombination of electrons and holes created by light.

Experimental Section

The well-ordered TiO₂ NTs were made through a modified one-step anodization TiO₂ NTs were made by anodizing Ti foils in NH₄F solution at 25 V for 2 h and annealing them at 450°C for 2.5 h. In continue, BiOIBr nanostructures were fabricated on the TiO₂ NTs substrate by hydrothermal synthesis in a Teflon-lined autoclave with KI, Bi(NO₃)₃, and KBr at 160°C for 10 h. The sample was washed and dried before characterization. Finally, the progamebale chronoamperometry technique was employed in an electrolyte solution containing CaCl₂, NaH₂PO₄, and dopamine for constructing the PDA.

Results and Discussion

To evaluate the photoelectrochemical behavior of different electrodes, the photocurrents of TiO₂ NTs, TiO₂ NTs/BiOIBr, TiO₂ NTs/PDA, and TiO₂ NTs/BiOIBr/PDA electrodes were measured in a phosphate buffer solution (0.1 M, pH = 7.3) under UV light irradiation. As shown, the bare TiO₂ NTs electrode showed very low photocurrent response, while the TiO₂ NTs/BiOIBr, and TiO₂ NTs/PDA electrode exhibited a greatly enhanced anodic photocurrent response. After modifying the surface of the TiO₂ NTs with BiOIBr/PDA, the photocurrent response significantly increased. This enhancement was attributed to the synergistic effect between the BiOIBr and PDA, which efficiently facilitated the photocarriers separation and inhibited the photoinduced electron-hole pairs recombination. Consequently, the PEC efficiency was greatly improved. The photoelectrochemical behavior of BSP on the surface of the TiO₂ NTs/BiOIBr/PDA electrode was studied in a 0.1 M phosphate buffer (pH = 7.3) under UV light irradiation at a potential of 0.1 V using the chronoamperometry technique. As shown, in the blank electrolyte (in the absence of BSP), the TiO₂ NTs/BiOIBr/PDA electrode represented a high photocurrent signal. However, when 100 μM BSP was added to the electrolyte, the photocurrent of the TiO₂ NTs/BiOIBr/PDA electrode decreased considerably. The drastic decrease in photocurrent can be attributed to the interaction between BSP and the TiO₂ NTs/BiOIBr/PDA, which increases steric hindrance and hinders electron

22nd Iranian Chemistry Congress (ICC22)
Iranian Research Organization for Science and Technology (IROST)
03231-97589
13-15 May 2024

IROST

transfer on the electrode surface, thus declining the photocurrent signal.
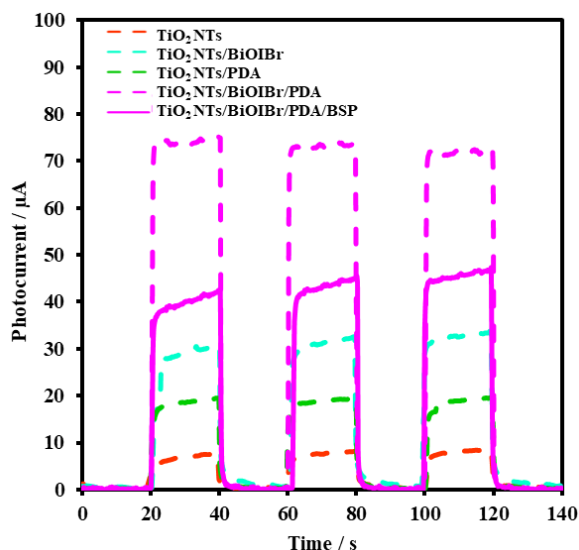
Fig. 1: Photocurrent response of TiO$_2$ NTs, TiO$_2$ NTs/BiOIBr, TiO$_2$ NTs/PDA, TiO$_2$ NTs/BiOIBr/PDA, and TiO$_2$ NTs/BiOIBr/PDA/BSP in 100 µM phosphate buffer (pH = 7.3).

Conclusions

In this study, a photoelectrochemical sensor for fast and high sensitive determination of BSP using an TiO$_2$ NTs/BiOIBr/PDA was developed. In the optimum conditions, the calibration curve was linear for BSP in the concentration range from 10^{-10} to 10^{-6} M, with a detection limit of 5×10^{-11} M.

References

[1] Tuchiu, B. M., Stefan-van Staden, R. I., & van Staden, J. K. F. (2023). Fast on-site simultaneous electroanalysis of fusidic acid and betamethasone in pharmaceuticals and water samples using novel stochastic platform. *Electrochemistry Communications*, 157, 107625. https://doi.org/10.1016/j.elecom.2023.107625.

[2] Goyal, R. N., & Bishnoi, S. (2010). Effect of single walled carbon nanotube–cetyltrimethyl ammonium bromide nanocomposite film modified pyrolytic graphite on the determination of betamethasone in human urine. *Colloids and Surfaces B: Biointerfaces*, 77, 200–205. https://doi.org/10.1016/j.colsurfb.2010.01.024.

[3] Hasani, S., Arvand, M., & Habibi, M. F. (2023). Efficient "on–off" photoelectrochemical sensing platform with layer-by-layer assembly of titanium dioxide nanotube arrays and silver@zinc sulfide nanoparticles for unbiased and accurate monitoring of clonazepam. *Microchemical Journal*, 185, 108253. https://doi.org/10.1016/j.microc.2022.108253

22nd Iranian Chemistry Congress (ICC22)
Iranian Research Organization for Science and Technology (IROST)
13-15 May 2024

03231-97589

IROST

Three-component reaction of Isoquinoline and acetylenic esters in the presence of phenylthiourea derivatives

Rahimeh Hajinasiri

Corresponding Author E-mail: rhmhajinasiri@yahoo.com

Department of Chemistry, Qaemshahr Branch, Islamic Azad University, Qaemshahr, Iran.

Abstract: An efficient and one-pot method is described for the yliden acetate derivatives *via* simple reaction of dialkylacetylenedicarboxylate and phenylthiourea derivatives in the presence of isoquinoline, promoted component, under solvent-free conditions. The good yields of the products are synthetic advantage of this environmentally friendly method.

Keywords: Isoquinoline; Phenylthiourea; Thiazolan; Green Chemistry; Benzyl Phenylthiourea; Yliden Acetates.

Introduction

Derivatives of thiazolidinone ring systems are known to act as anti-HIV infections [1], analgesic, anti-bacterial, anti-convulsant, anti parasitic, potential anti-inflammatory, and herbicidal agents [2–7]. Due to the biological activities of thiazolidinones ring, several methods for their synthesis have been illustrated in the literature [8].

Experimental Section

Dialkyl acetylenedicarboxylate 2 (2 mmol) was slowly added to a magnetically stirred mixture of an phenylthiourea 3 (2 mmol) and isoquinoline 1 (2 mmol), and the reaction mixture was stirred for 4 h at room temperature. After completion of the reaction as indicated by TLC, the residue was purified by column chromatography over silica gel (Merck 230-400 mesh) using an n-hexane-EtOAc mixture (6:1) as eluant to afford the pure compounds 4.

Results and Discussion

In this method, isoquinoline **1** promoted reaction of dialkylacetylenedicarboxylates **2** and phenylthiourea **3**, as promoted component for the synthesis of yliden acetates drivatives (Fig 1). This precedure is performed under solvent free conditions and as green and enviromentally route. Also, the performance of this reaction at room temprature is another advantage. The structures of compounds were apparent from the ^{1}H NMR, ^{13}C NMR and IR spectra.

The ^{1}H NMR spectrum of methyl 2-(1-benzyl-5-oxo-3-phenyl-2-thioxotetrahydro-4H-imidazol-4-yliden) acetate displayed three peeks at δ 3.73, 5.07 and 5.34 ppm for the methoxy group, benzylic and olefinic protons, respectively, along with characteristic multiplet signals for the aromatics moiety. The proton-decoupled ^{13}C NMR spectrum of methyl 2-(1-benzyl-5-oxo-3-phenyl-2-thioxotetrahydro-4H-imidazol-4-yliden) acetate showed 15 signals in agreement with the proposed structure.

A possible mechanism for the synthesis of compounds **4** is proposed in Fig 2. The zwitterionic intermediate **5** produced from the reaction of isoquinoline and dialkyl acetylenedicarboxylate is subsequently protonated by a phenylthiourea **3** and formed intermediate **6**. The conjugate base of phenylthiourea attacked to intermediate **6** and removed isoquinoline ring as leaving group and compound **7** was produced. Then, nucleophilic attack of NH on carbonyl synthesized compound **4**.
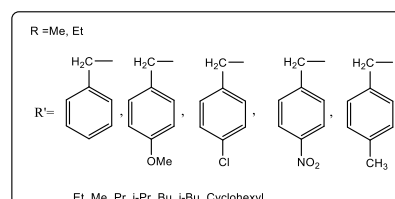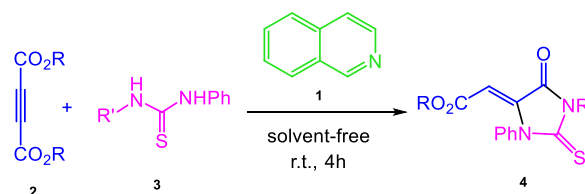
Fig.1: Synthesis of yliden acetates

1+2
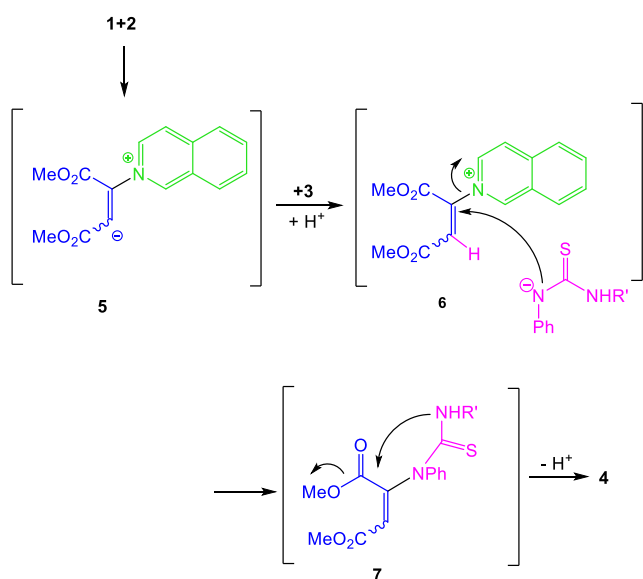
Fig. 2.: Possible mechanism for the formation of compounds 4.

Conclusions

In conclusion we have reported a convenient one-pot route for the synthesis of yliden acetates by reaction between isoquinoline, dialkyl acetylenedicarboxylate and phenylthiourea, under solvent-free conditions at room temperature.

References

[1] Barreca, M.L., Balzarini, J., Chimirri, A., De Clercq, E., De Luca, L., Holtje, H.D., Holtje, M., Monforte, A.M., Monforte, P., Pannecouque, C., Rao, A., Zappala, M. (2002). Design, synthesis, structure– activity relationships, and molecular modeling studies of 2, 3-diaryl-1, 3-thiazolidin-4-ones as potent anti-HIV agents. J. Med. Chem., 45, 5410.

[2] Li, Y.X., Wang, S.H., Li, Z.M., Su, N., Zhao, W.G. (2006). Synthesis of novel 2-phenylsulfonylhydrazono-3-(2', 3', 4', 6'-tetra-O-acetyl-β-d-glucopyranosyl) thiazolidine-4-ones from thiosemicarbazide precursors. Carbohydrate Res. 341, 2867.

[3] Kucukguzel, G., Kocatepe, A., De Clercq, E., Sahin, F., Gulluce, M. (2006). Synthesis and biological activity of 4-thiazolidinones, thiosemicarbazides derived from diflunisal hydrazide. Eur. J. Med. Chem. 41, 353.

[4] Kato, T., Ozaki, T., Tamura, K., Suzuki, Y., Akima, M., Ohi, N. (1998). Novel Calcium Antagonists with Both Calcium Overload Inhibition and Antioxidant Activity. 1. 2-(3,5-Di-tert-butyl-4-hydroxyphenyl)-3-(aminopropyl)thiazolidinones. J. Med. Chem., 41, 4309.

[5] Tenorio, R.P., Carvalho, C.S., Pessanha, C.S., de Lima, J.G., de Faria, A.R., Alves, A.J., de Melo, E.J.T., Goes, A.J.S. (2005). Synthesis of thiosemicarbazone and 4-thiazolidinone derivatives and their in vitro anti-Toxoplasma gondii activity. Bioorg. Med. Chem. Lett., 15, 2575.

[6] Kucukguzel, S.G., Oruc, E.E., Rollas, S., Sahin, F., Ozbek, A. (2002). Synthesis, characterisation and biological activity of novel 4-thiazolidinones, 1, 3, 4-oxadiazoles and some related compounds. Eur. J. Med. Chem., **2002**, *37*, 197.

[7] Shih, M.H., Ke, F.Y. (2004). Syntheses and evaluation of antioxidant activity of sydnonyl substituted thiazolidinone and thiazoline derivatives. *Bioorg. Med. Chem.*, *12*, 4633.

[8] Short, F.W., Littleton, B.C., Johnson, J.L. (1971). Chem. Ind. (London), 705.

22nd Iranian Chemistry Congress (ICC22)
Iranian Research Organization for Science and Technology (IROST)
13-15 May 2024

03231-97589

IROST

Synthesis of 1,3-thiazole derivatives catalyzed by ZNO-nanorods

Rahimeh Hajinasiri

Corresponding Author E-mail: rhmhajinasiri@yahoo.com

Department of Chemistry, Qaemshahr Branch, Islamic Azad University, Qaemshahr, Iran.

Abstract: 1,3-Thiazole derivatives are produced by environmentally multicomponent reactions of primary amines, isothiosyanates and alkyl bromides under solvent-free conditions using ZnO-nanorod structures as catalyst. These reactions were not performed without catalyst. The catalyst showed significant reusable activity.

Keywords: Alkyl bromides; isothiosyanates; multicomponent reactions; ZnO-Nanorod; primary amines.

Introduction

Thiazoles have an important effect in nature. For instance, the thiazolium ring that exists in vitamin B1 works as an electron cavity and its coenzyme form is significant for the decarboxylation of α-keto-acids. Some pesticides have a thiazole nucleus are famous in agriculture. Large numbers of thiazole derivatives have appeared as active pharmaceutical ingredients in some drugs for their potential anti-inflammatory anti-tumour, anti-hyperlipidemic, anti-hypertensive, anti-HIV infections [1-3].

Herein we describe a general, rapid, high yielding and green synthetic protocol for wide variety thiazole derivatives from amines, alkyl bromids and alkyl or aryl isothiocyanates by nanorod ZnO (Fig. 1).
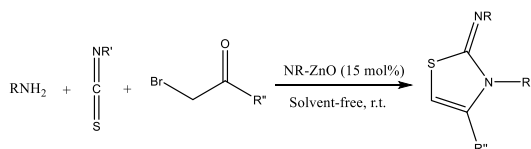
Fig.1: Reaction of amines, isothiocyanates and alkylbromid.

Experimental Section

General Procedure for the Preparation of Nanorod ZnO (NR-ZnO)

Sodium hydroxide (0.44 g) was dissolved in 75 mL of distilled water under vigorous stirring at room temprature. Afterwards, with the addition of SDS (1.57 g) and $Zn(AcO)_2.2H_2O$ (0.6 g) to the mixture, the solution was refluxed for 1.5 h at 80 $^\circ$C (pH=14). The product was collected by filtration and washed with distilled water and ethanol (96%) several times [34].

General Procedure for Preparation of Compounds 4

To a stirred mixture of amines (2 mmol), alkyl bromides (2 mmol) was added nanorod ZnO (15% mol). After 10 min isothiocyanates (2 mmol) was added at room temperature. The mixture was stirred for about 3h (TLC monitoring). The viscous residue was purified by column chromatography on silica gel (Merck 230-400 mesh) using n-hexane-EtOAc (7:1) as eluent.

Results and Discussion

ZnO nanoparticles were achieved from the reaction between $Zn(AcO)_2.2H_2O$ and NaOH by reflux technique devoid of including pattern. Nanorod morphology was produced by SDS. SDS was utilized as a directing driving force to control ZnO nanostructure morphologies. The morphology of the product was checked by SEM (Fig. 2). The length and diameter of nanorods were 300-600 nm and 50-70 nm, respectively. The XRD image of ZnO with usual morphologies that synthesized by this technique is demonstrated in Fig. 3. All the peaks in the pattern matched to the wurtzite structure of ZnO, which can be listed on the basis of JCPDS file No. 36-1451.
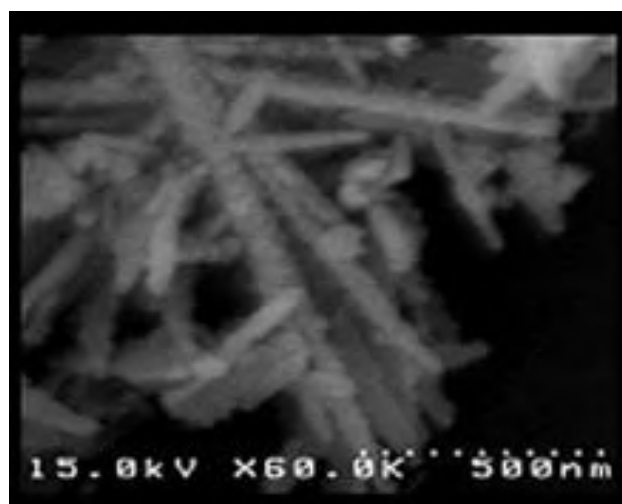
Fig.2: SEM images of nanorod (NR-ZnO).

22nd Iranian Chemistry Congress (ICC22)
Iranian Research Organization for Science and Technology (IROST)
13-15 May 2024

03231-97589

IROST
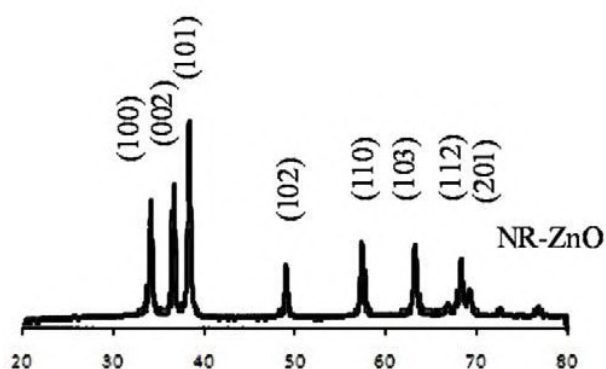
Fig.3: XRD spectra of nanorod ZnO (NR-ZnO).

In the next step, the one-pot three-component reactions of primary amines **1**, alkyl bromides **3** and isothiocyanates **2** under solvent free conditions using nanorod ZnO (15 mol%) are performrd. The catalyst can be resolved three times without considerable defeat of activity.

Mechanistically, it is possible that the reaction includes the first formation **6** between the amine and the isothiocyanates, which reacts with the alkyl bromides to generate **7**. Cyclization of this intermediate followed by dehydration affords thiazoles. NR-ZnO has Lewis acid sites (Zn^{2+}) and Lewis basic sites (O^{2-}). In this reaction, the Zn^{2+} sites are interact with sulfur group in isothiocyanate compounds, alkyl bromides and O^{2-} site of ZnO nanostructures taking up a proton of **8** to produce **4** (Scheme 2). The detailed formation mechanism of product needs to be further investigated.
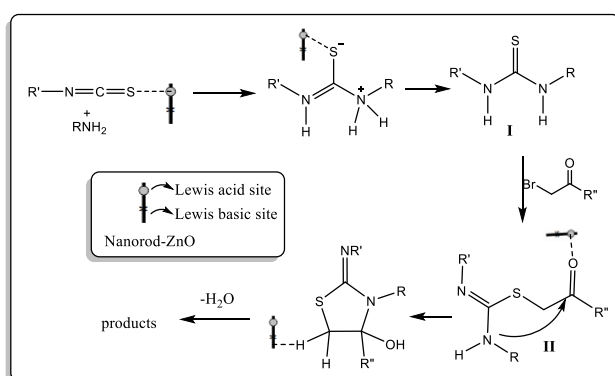
Fig.4: Proposed mechanism for the preparation of 4.

Conclusions

In conclusion, we disclose a general, rapid, high yielding and green synthetic protocol for synthesis of thiazole derivatives *via* the one-pot three-component reactions of primary amines, alkyl bromides and isothiocyanates under solvent free conditions using nanorod ZnO.

Expansion of such catalysts has outcome in more economical and environmentally friendly chemistry replacing unsteady or toxic catalysts.

References

[1] Abdel-Aziz, H. M., Gomha, S.i M., Salaheldin, T. A., Hassaneen, H. Synthesis, Characterization and Molecular Docking of Novel Bioactive Thiazolyl-Thiazole Derivatives as Promising Cytotoxic Antitumor Drug. Molecules, 2016, 21,3.

[2] Eman, M. H. A., Sobhi; M. G., Thoraya, A. F., Mohamed, M. A., Synthesis of New Thiazole Derivatives as Antitumor Agents . Curr. Org. Synth., 13, 2016, 456-465.

[3] Mahesh; T. C., Shivani; P., Palmi; M., Pathik, S. B., Thiazole: A Review on Chemistry, Synthesis and Therapeutic Importance of its Derivatives. Curr. Top. Med. Chem., 16, 2016, 2841-2862.

Investigating the Physical Properties of Paperboards and Their Applications in the Filtration of Cadmium Ions

Reza Beiranvand [a,c], Elahe Gharekhani [b], Hossein Gharebeiglou [b], Aliasghar Engashte-vahed [c]

Corresponding Author E-mail: Rezabeiranvand.lu@gmail.com

[a] Department of Analytical Chemistry, Faculty of Chemistry, Lorestan University, Khorramabad, Iran.

[b] Department of Chemistry, Faculty of Science, Islamic Azad University, Saveh, Iran.

[c] Quality Control Department, Pishro Kaghaz Negar Pars Factory, Shekohieh Industrial Town, Qom, Iran.

Abstract: We compared bagasse and recycled paperboard to see which one was better at filtering cadmium ions and had better physical properties. Recycled paperboard had better physical properties than bagasse paperboard. Both paperboards were effective in filtering cadmium, but Bagasse paperboard had higher performance than recycled paperboard.

Keywords: Bagasse; Recycled paperboard; Filtration; Physical properties

Introduction

In today's world, there is a constant and increasing demand for paper and paperboard products, which is unfortunately not being met by the available resources. The paper industry heavily relies on indigenous hardwood resources, which are becoming increasingly scarce. As a result, the industry is exploring other options for raw material fibers, including wheat residues, rice, barley, sugarcane bagasse, and recycling. Non-wood fibers now account for 9% of paper fibers worldwide, with bagasse pulp being particularly popular in the pulp and paper industry in recent years. This type of pulp is used to create paperboard for glasses, among other things. Additionally, the paper recycling industry is a vital part of the present era, providing a significant portion of the raw material needs of various paper and paperboard industries. By utilizing these alternative raw materials and recycling paper products, the industry can help alleviate the strain on limited forest resources while still meeting the growing demands for paper products [1-3].

This particular study is centered around investigating the physical properties and successful elimination of Cadmium metal from aqueous solutions through the use of two separate paperboard types. One of these paperboard types is composed of unprocessed bagasse pulp, while the other is made from recycled materials. The study's primary objective is to examine and evaluate a variety of parameters, such as the filtration of Cadmium ions, water absorption, grammage, thickness, tensile, and stiffness characteristics. This analysis aims to offer a comprehensive understanding of the effectiveness of these paperboards when attempting to remove Cadmium ions from an aqueous solution. By conducting this study, a greater understanding of the interplay between these parameters will be gained, and more effective methods for removing Cadmium ions from water-based solutions can potentially be developed.

Experimental Section

The paperboard sample based on bagasse pulp (bagasse paperboard) was purchased from Pars Paper Industry Company, and the recycled material-based paperboard sample (recycled paperboard) was purchased from Rasha Caspian Iranian Company. Machines for grammage, thickness, tension, and stiffness tests were procured from Hangzhou Company, China. Additionally, Cadmium nitrate tetrahydrate $Cd(NO_3)_2 \cdot 4H_2O$ was from Merck Company, Germany. All the tests have been carried out according to the instructions of the International Organization for Standardization (ISO). The paperboard is fragmented into small pieces and packed into a syringe to begin the filtration process. The solution consisting of cadmium metal is then slowly flowed through the syringe twice. The percentage of filtration efficiency is calculated by analyzing the adsorption difference between the feed and filtered solution (Flame atomic absorption spectroscopy).

Results and Discussion

The use of bagasse as a raw material in the paper industry has multiple advantages. It helps reduce costs and environmental impacts associated with forest management and harvesting. Bagasse fibers have properties that are similar to wood fibers, making them suitable for producing various types of paper, such as industrial and packaging papers, newsprint, and paperboard. Paperboard is an essential product that mainly gets made from O.C.C processes, which stands for old corrugated containers. This product contributes to economic and environmental sustainability by reducing the wastage of resources. It is an excellent example of a circular economy, where existing materials and resources are used. The use of paperboard in the packaging industry has many cost benefits, such as saving resources, reducing

greenhouse gases, managing consumption, reducing costs, and protecting ecosystems.

Due to the clarity of the components of each paperboard sample, it is expected that the properties investigated in this research for the recycled paperboard are at a higher level and stronger than the bagasse paperboard. In total, the results of water absorption, grammage, thickness, tensile, and stiffness tests are listed in Table 1.

Table 1: Result of Physical Analysis of Paperboards

Title of Test	Bagasse paper	Recycled paper
Water absorption (% in 3 h)	31.2 ± 1.20	48.1 ± 0.71
Grammage (g/m²)	178.69 ± 2.91	180.15 ± 3.40
Thickness (micron)	243.93 ± 8.54	248.10 ± 5.61
MD Tensile force (N)	143.31 ± 1.61	172.56 ± 8.76
MD Tensile Strength (kN/m)	9.53 ± 0.26	11.58 ± 0.63
MD Elongation (%)	1.40 ± 0.05	1.12 ± 0.55
MD Stiffness (mN)	57.40 ± 1.69	78.17 ± 4.70

Based on the findings presented in Table 1, it can be inferred that the physical properties of recycled paperboard are superior to those of bagasse paperboard. Specifically, the recycled paperboard exhibits higher levels of thickness, tensile strength, stiffness force, and water absorption compared to the bagasse paperboard.

The comparison of the filtration of cadmium metal ions in an aqueous solution by two different paperboard samples with varying concentrations (20-80 ppm) was conducted. The results are depicted in Figure 1. The findings of the experiment show that the bagasse paperboard sample has demonstrated higher filtration ability and performance in comparison to the recycled paperboard sample.

Conclusions

The research findings suggest that recycled paperboard exhibits better durability and resistance in physical properties, which could potentially make it a superior choice for a range of industrial applications, particularly packaging. Further, the study has established that the bagasse-based paperboard is an effective material for filtering cadmium metal ions from aqueous solutions. This finding highlights the potential of paperboards for use in relevant industries that require efficient filtration capabilities. Overall, the study provides valuable insights into the properties and potential applications of these paperboards in various industrial domains.
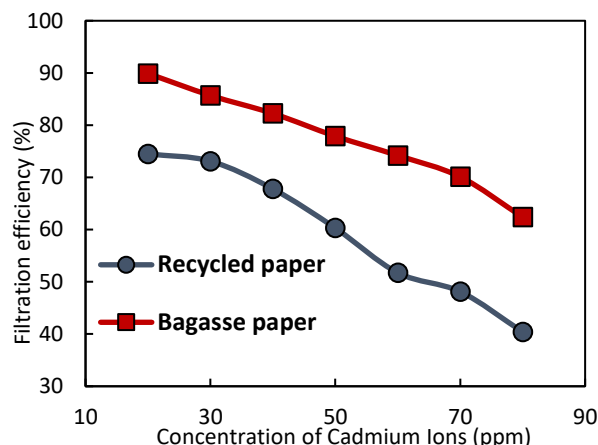
Fig.1: Filtration of Cd^{2+} By Bagasse and Recycled Paperboards

References

[1] Worku, L. A., Bachheti, A., Bachheti, R. K., Rodrigues Reis, C. E., & Chandel, A. K. (2023). Agricultural residues as raw materials for pulp and paper production: Overview and applications on membrane fabrication. *Membranes*, *13*(2), 228. DOI: https://doi.org/10.3390/membranes13020228.

[2] Mahmud, M. A., Belal, S. A., & Gafur, M. A. (2023). Development of a biocomposite material using sugarcane bagasse and modified starch for packaging purposes. Journal of Materials Research and Technology, 24, 1856-1874. DOI: https://doi.org/10.1016/j.jmrt.2023.03.083

[3] Tikhomirova, E., Aleksandrov, D., Tofanica, B. M., & Mikhailidi, A. (2024). Evaluation of Recycled Paperboard Properties and Characteristics. Applied Sciences, 14(4), 1661. DOI: https://doi.org/10.3390/app14041661.

22nd Iranian Chemistry Congress (ICC22)
Iranian Research Organization for Science and Technology (IROST)
13-15 May 2024

03231-97589

IROST

Introduction of MoS₂-FeS₂ with S-Vacancy Defect as an Efficient Bifunctional Electrocatalyst for Hydrogen Evolution Reaction and Ferrocyanide and Iodide Oxidation Reactions

Hossein Ashrafi, Morteza Akhond*, Behzad Haghighi*

Corresponding Author E-mail: bhaghighi@shirazu.ac.ir

Professor Massoumi Laboratory, Department of Chemistry, Shiraz University, Shiraz 71454, Iran.

Abstract: The electrocatalytic behavior of the prepared MoS₂-FeS₂ nanocube composite was investigated for hydrogen evolution (HER), iodide oxidation (IOR), and ferrocyanide oxidation (FOR) reactions. The overpotentials required to perform HER-OER, HER-IOR, and HER-FOR using MoS₂-FeS₂ as an electrocatalyst were significantly less than those of traditional Pt/C and RuO₂ electrocatalysts.

Keywords: Hydrogen Evolution Reaction; Iodide Oxidation Reaction; Overpotential

Introduction

The water-splitting process involves a hydrogen evolution reaction (HER) at the cathode and an oxygen evolution reaction (OER) at the anode. The theoretical voltage for water splitting is 1.23 V, but commercial electrolyzers typically operate at voltages higher than 1.8 V [1]. The anodic OER is a sluggish reaction and a large overpotential or an efficient electrocatalyst is required to achieve water dissociation. So, the slow anodic OER is the main reason for the increased energy consumption, and the produced O_2 at the anode is less needed for further uses [2]. Recently, a cost-effective and energy-saving method for hydrogen production has been proposed based on the substituting of the traditional anodic OER (water oxidation) with oxidation of a chemical substrate, such as hydrazine, urea, iodide, amines, and alcohols at the anode using an inexpensive metal electrocatalyst. Among the mentioned substituted oxidation reactions, iodide oxidation reaction (IOR) and ferrocyanide oxidation reaction (FOR) are the most appropriate anodic reactions to produce hydrogen and value-added products [3].

Experimental Section

Five mg of MoS₂-FeS₂ was dispersed in 1.0 mL of ethanol containing 0.1 % of Nafion with ultrasonic agitation for an hour to achieve a well dispersed suspension. Then, 3 μL of the prepared suspension was placed on the surface of a glassy carbon electrode (3 mm diameter). The prepared modified electrode, GCE/MoS₂-FeS₂, was dried in air and ready for use. Then the electrocatalytic performances of the prepared MoS₂-FeS₂ towards HER, IOR, and FOR were evaluated using linear sweep voltammetry (LSV).

Results and Discussion

After optimization of MoS₂-FeS₂ analogs and Mo/Fe mole ratio, the structural and morphological characterizations of MoS₂-FeS₂ were performed (Fig.1).
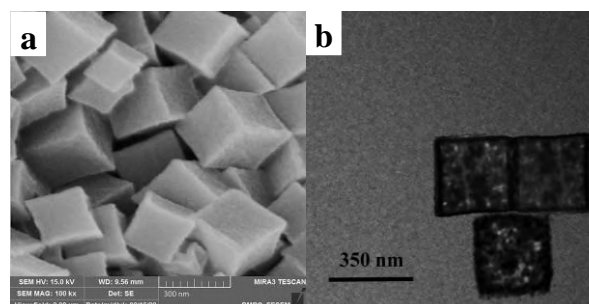
Fig.1: (**a**) FESEM and (**b**) TEM of MoS₂-FeS₂ nanocubes.

The electrocatalytic performance of MoS₂-FeS₂ towards HER, IOR, and FOR in different pHs was investigated (Fig.2). The result proved that alkaline media had better performance for MoS₂-FeS₂ towards HER and acidic media had better performance IOR and FOR. Also, the Stability of MoS₂-FeS₂ towards HER, IOR, and FOR was evaluated using chronoamperometry and cyclic voltammetry and the result showed that exhibited excellent resistance to surface poisoning compared to the Pt/C and RuO₂ electrode. The polarization curves for HER-OER, HER-IOR, and HER-FOR using the modified MoS₂-FeS₂ electrode showed that at a current density of 10 mA cm⁻² the required (over)potentials were about 2.08, 0.82, and 0.65 V, respectively (Fig.3).
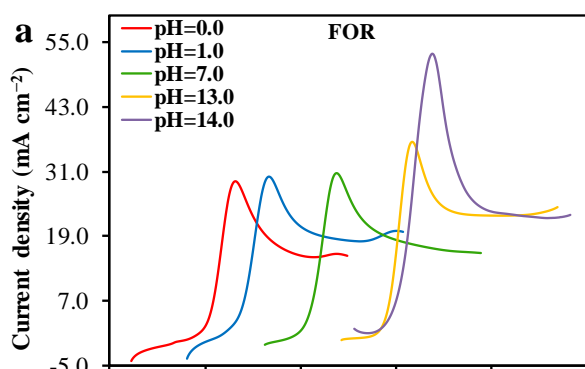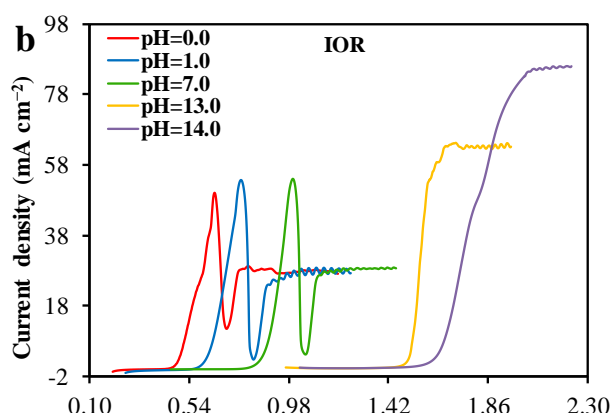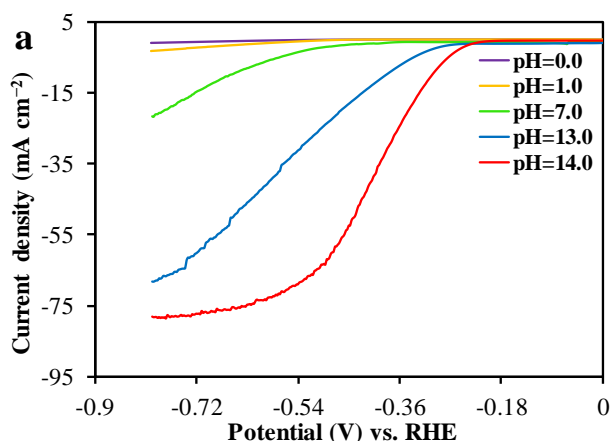
22nd Iranian Chemistry Congress (ICC22)
Iranian Research Organization for Science and Technology (IROST)
13-15 May 2024

03231-97589

IROST
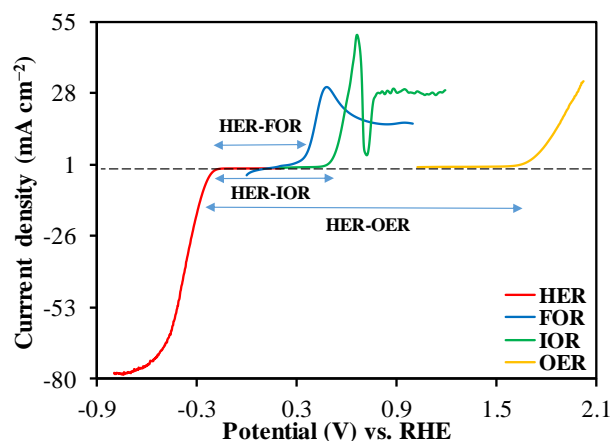
Fig.3: The plot of overpotential required to perform HER-OER, HER-IOR, and HER-FOR at a current density of 10 mA cm^{-2} using GCE modified with MoS$_2$-FeS$_2$.

Conclusions

In this study, MoS$_2$-FeS$_2$ with a well-defined nanocubes morphology and an average size of 280 nm were synthesized and successfully applied for HER-OER, HER-IOR, and HER-FOR compared to the traditional Pt/C and RuO$_2$ electrocatalyst. The exceptional electrocatalytic performance of MoS$_2$-FeS$_2$ in terms of reduced overpotential, enhanced charge transfer rate, and improved Tafel slope, long-term stability, and durability was attributed to its well-defined morphology, the presence of numerous edge sites, defects, and sulfur vacancies, the synergistic effects between MoS$_2$ and FeS$_2$ and minimal structural degradation. The findings of this study highlight the promising potential of the MoS$_2$-FeS$_2$ as an efficient and durable electrocatalyst for HER, IOR, and FOR in energy conversion and storage systems.

References

[1] You, B. and Sun, Y. (2018). Innovative strategies for electrocatalytic water splitting. Accounts of chemical research, 51(7), 1571-1580.

https://doi.org/10.1021/acs.accounts.8b00002.

[2] Dessie, T.A., Huang, W.-H., Adam, D.B., Awoke, Y.A., Wang, C.-H., Chen, J.-L., Pao, C.-W., Habtu, N.G., Tsai, M.-C., and Su, W.-N. (2022). Efficient H$_2$ Evolution Coupled with Anodic Oxidation of Iodide over Defective Carbon-Supported Single-Atom Mo-N$_4$ Electrocatalyst. Nano Letters, 22(18), 7311-7317.

https://doi.org/10.1021/acs.nanolett.2c01229.

[3] Wang, T., Cao, X., and Jiao, L. (2022). Progress in hydrogen production coupled with electrochemical oxidation of small molecules. *Angewandte Chemie International Edition*, *61*(51), e202213328.

Fig.2: (a, b, and c) The effect of pH on the overpotentials and kinetics required for HER, IOR, and FOR reactions using MoS2-FeS2 electrode.

Phosphatidylcholine: A green catalyst for one-pot synthesis of pyrido[2,3-d:5,6-d']-dipyrimidines

Roodabeh Azari, Masoumeh Abedini*

Corresponding Author E-mail: mabedini@guilan.ac.ir

Department of Chemistry, College of Science, University of Guilan, 41335-19141, Rasht, Iran.

Abstract: In the present study, a green one-pot synthesis of pyrido[2,3-d:5,6-d']dipyrimidines is reported, using biocompatible phosphatidylcholine. This method boasts broad compatibility, rapid reaction times (20-45 min), excellent yields (up to 97%), simplified product isolation, green solvent utilization, and catalyst reusability (4 times) with minimal activity loss.

Keywords: Phosphatidylcholine; Multi-component reactions; Pyrido[2,3-d:5,6-d']dipyrimidines; Barbituric acid

Introduction

Multicomponent reactions [1] (MCRs) play an important role in synthetic organic chemistry due to the ability to produce complex molecules from three or more starting materials in one step without isolating the intermediates in the process. As compared to multistep reactions, they have numerous advantages, including high atom-economy, high yield, low cost, short reaction times, and eco-friendliness [2]. These reactions can be used to prepare derivatives of pyrido[2,3-d:5,6-d']dipyrimidines [3,4]. They represent a significant class of heterocyclic compounds [5] exhibiting diverse biological activities [6], including antitumor [7], anti-HIV [8], anti allergic, anti-leishmanal [9], vasodilator [10], antiviral, antibacterial [11], potassium sparing [12] anti inflammatory [13], antifolate [14], antihypertensive, antimicrobial [15], calcium channel antagonists [16], tuber-culostatic [17] properties. Several synthetic approaches have been developed for these heterocycles, often involving multi-step procedures with harsh reaction conditions CoFe$_2$O$_4$@SiO$_2$-PA-CC-Guanidine-SA [18] ،CuFe$_2$O$_4$ NPs [19] ،[H-NMP]$^+$[HSO$_4$]$^-$ [20] ،CuFe$_2$O$_4$ [21] ،[DMSPDE][Cl] [22] Despite the fact that many of these methods are suitable, most of them have significant disadvantages, such as low yields, long reaction times, and harsh conditions [18]. Consequently, the search for simpler and more efficient methods remains ongoing.

One of the most important protein sources used in oil production is soy [23]. It is also considered the only current dominant source of lecithin. Lecithin is made by removing phospholipids from edible oil. The valuable food components of soy lecithin are phospholipids or phosphoglycerides. These lipids are known as the main building blocks of cell membranes and as a result, cells need them essential for growth, maturation, and optimal function. Phospholipids are composed of glycerol, fatty acids, phosphate, and poly-hydroxy groups [24]. Among the main phospholipids in oilseeds, phosphatidylethanolamine (PE), phosphatidylinositol (PI),

phosphatidylcholine (PC), and phosphatidic acid (PA) can be named [25]. These compounds are used in the food, pharmaceutical, and healthcare industries and are effective in cardiovascular health, liver, reproduction, growth, memory enhancement, liver protection, and cholesterol reduction [26]. The most abundant phospholipid in soy lecithin is phosphatidylcholine (PC), which accounts for about 50% of the total phospholipid content. PC is a phospholipid composed of two molecules of glycerol, two fatty acids, and one molecule of choline. It is one of the most abundant phospholipids found in cell membranes and plays an important role in the structure and function of the membrane [27]. Further, it is a key component of cell membranes and contributes to various biological processes, including Neurotransmission, Fat metabolism, Membrane transport, Emulsification, Immune function & Brain health [28].

In this context, developing efficient and eco-friendly methods is highly desirable. Herein, we report a novel and efficient one-pot reaction for the synthesis of pyrido[2,3-d:5,6-d']dipyrimidines from readily available starting materials and under mild conditions. The key features of this protocol include:

Phosphatidylcholine (PC) catalysis: Replacing traditional metal catalysts with biocompatible PC offers a greener and more sustainable approach.

High efficiency: Excellent yields (up to 97%) and short reaction times (20-45 minutes) demonstrate the effectiveness of this methodology.

Substituent control: Tuning the substituents on the aromatic aldehydes allows for tailoring the reaction efficiency and product diversity.

Experimental section

Chemicals and solvents used were purchased mainly from Merck in Germany, Fluka in Switzerland, Aldrich in the United States, and Radkimiagaran Co. in Iran. Progress of

22nd Iranian Chemistry Congress (ICC22)
Iranian Research Organization for Science and Technology (IROST)
13-15 May 2024

03231-97589

IROST

reactions was monitored by thin layer chromatography (TLC) using Merck 254F60 silica gel-coated aluminum sheets. Whatman 42 filter paper with low permeability was used. Melting points were determined by electrothermal apparatus in degrees Celsius. FT-IR spectra were obtained using a Bruker PS-15 FT-IR spectrometer by preparing KBr discs. The vibrational frequencies mentioned are reported in wavenumbers (cm^{-1}).

In distilled water, 20 mg of PC, barbituric acid or thiobarbituric acid (2 mmol), ammonium acetate (1 mmol), and aldehyde (1 mmol) were stirred at 80 °C for the appropriate duration. Monitor the reaction progress by TLC using a mixture of n-hexane: ethyl acetate: methanol (6:3:2). Upon completion, cool the mixture and filter the solid product. Wash with 5 mL of distilled water and recrystallization with hot ethanol to obtain the pure product with high yield (Table1).

Catalytic activity:

The initial optimization was performed using 4-chlorobenzaldehyde as a model substrate.

Table1: Influence of different conditions on the preparation of pyrido[2,3-d:5,6-d']dipyrimidine derivative from 4-chlorobenzaldehyde in the presence of phosphatidylcholine catalyst[a]

Row	Solvent	Condition	Amount of Catalyst (mg)	Time (min)	Conversion (%)
1	Water	R.T	20	60	100
2	Water	80°C	15	40	100
3[b]	Water	80°C	20	20	100
4	Solvent free	50°C	20	50	100

[a]Reaction condition: 1 mmol of aldehyde, 2 mmol of barbituric acid or thiobarbituric acid, 1 mmol of ammonium acetate and 20 mg of the catalyst in water.
[b]Optimum conditions

Following the general procedure with thiobarbituric acid, the reaction afforded the desired product in 97% yield with 20 mg of catalyst in water at 80°C for 20 minutes. Further experiments confirmed the effectiveness of phosphatidylcholine as a catalyst for this reaction with both barbituric and thiobarbituric acid (Fig.1).
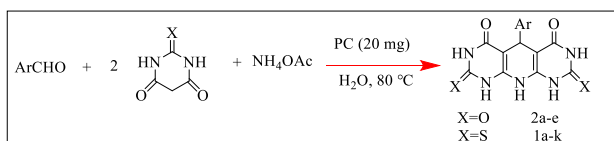
Fig.1: Optimum conditions for the synthesis of pyrido[2,3-d:5,6-d'] dipyrimidines in the presence of phosphatidylcholine as catalyst

The optimized reaction conditions were then applied to various aromatic aldehydes with diverse electron-donating and electron-withdrawing substituents (Table2).

Table2: Preparation of pyrido[2,3-d:5,6-d']dipyrimidine derivatives in the presence of phosphatidylcholine under optimal conditions

Row	Aldehyde	X	Time (min)	Yield (%)	Melting Point (°C)	Ref
1	Benzaldehyde(1a)	S	25	90	220-215 (observed), 211 (reported) Dec.	[21]
2	3-MeO-benzaldehyde (1b)	S	40	91	235-238 (observed), 242 (reported) Dec.	[19]
3	4-MeO-benzaldehyde (1c)	S	20	94	270-273 (observed), 280 (reported) Dec.	[20]
4	2-NO₂-benzaldehyde (1d)	S	25	95	226-230 (observed), 230 (reported) Dec.	[20]
5	4-NO₂-benzaldehyde (1e)	S	30	93	260-263 (observed), 269 (reported) Dec.	[21]
6	3-Br-benzaldehyde (1f)	S	40	97	232-240 (observed), 246-248 (reported) Dec.	[22]
7	4-Cl-benzaldehyde (1g)	S	20	97	250-253 (observed), 257 (reported) Dec.	[20]
8	N,N-diMe-benzaldehyde (1h)	S	32	94	282-289 (observed), 300< (reported) Dec.	[18]
9	Terephthalaldehyde (1i)	S	25	95	286-290 (observed), 300 (reported) Dec.	[21]

22nd Iranian Chemistry Congress (ICC22)
Iranian Research Organization for Science and Technology (IROST)
13-15 May 2024

03231-97589

ISC

IROST

Row	Aldehyde	X	Time (min)	Yield (%)	Melting Point (°C)	Ref
10	4-Br-benzaldehyde (1j)	S	20	94	>300 (observed), 380 (reported) Dec.	[29]
11	2-OH-benzaldehyde (1k)	S	60	95	285-288 (observed), 308 (reported) Dec.	[9]
12	4-Cl-benzaldehyde (2a)	O	30	97	280-294 (observed), 302-300 (reported) Dec.	[30]
13	Benzaldehyde (2b)	O	45	95	288-278 (observed), 280-279 (reported) Dec.	[31]
14	2-OH-benzaldehyde (2c)	O	38	96	235-230 (observed), 212-210 (reported) Dec.	[32]
15	4-OH-benzaldehyde (2d)	O	30	95	>300 (observed), >300 (reported) Dec.	[33]
16	4-MeO-benzaldehyde (2e)	O	40	95	280-273 (observed), 278-277 (reported) Dec.	[34]

Reaction condition: 1 mmol of aldehyde, 2 mmol of barbituric acid or thiobarbituric acid, 1 mmol of ammonium acetate and 20 mg of the catalyst in water at 80°C.

The results revealed that the substituent effect manifested similarly for both barbituric and thiobarbituric acid: substrates with electron-withdrawing groups generally reacted faster and yielded higher products compared to those with electron-donating groups. The overall method proved versatile and effective with various substituent positions and types for both barbituric and thiobarbituric acid starting materials. This approach uses "barbituric acid or thiobarbituric acid" consistently, emphasizes the similar behavior of these starting materials while acknowledging both options, and maintains clarity in the discussion of results.

The obtained products were characterized by melting points and infrared (IR) spectroscopy. The observed IR spectra exhibited characteristic peaks for the pyrido[2,3-d:5,6-d']dipyrimidine core, confirming the successful synthesis of the target compounds.

Based on the experimental observations and literature precedents, a five-step mechanism involving PC-assisted activation and condensation steps is proposed. The key steps include:

PC facilitates the activation of thiobarbituric acid through electrostatic interactions. The activated thiobarbituric acid attacks the aldehyde in a nucleophilic addition reaction, forming an intermediate (a) with water elimination (step 1). A second thiobarbituric acid molecule reacts with ammonium acetate, generating another intermediate (b) (step 2). The two intermediates undergo condensation, driven by PC, to form a larger intermediate (c) (step 3). An intramolecular cyclization forms the last intermediate (d) (step 4). Finally, water loss leads to the desired pyrido[2,3-d:5,6-d']dipyrimidine product (step 5) (Fig.2) [23].
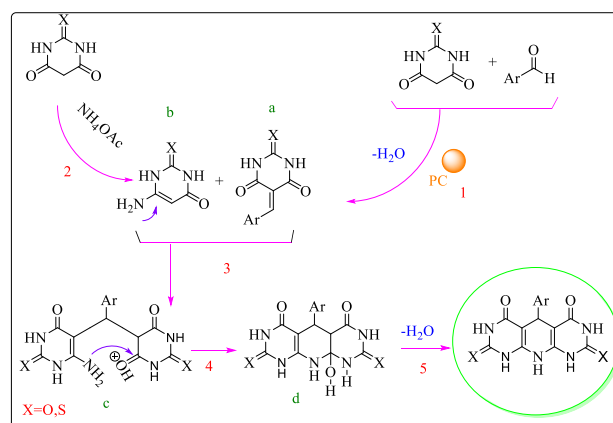
Fig.2: Synthesis mechanism of pyrido[2,3-d:5,6-d']dipyrimidine derivatives in the presence of phosphatidylcholine as catalyst

Results and discussion

To compare the performance of phosphatidylcholine (PC) with some of the catalysts that have been reported to date, a table is provided. As can be seen, PC has performed better in terms of reaction time and yield. The high yield of products, the use of mild conditions, and the use of less catalyst are among the advantages of the present method (Table3).

22nd Iranian Chemistry Congress (ICC22)
Iranian Research Organization for Science and Technology (IROST)
13-15 May 2024

03231-97589

ISC

IROST

Table3: Comparison of the performance of phosphatidylcholine with respect to different catalysts in the synthesis of pyrido[2,3-d:5,6-d']dipyrimidine derivative from 4-chlorobenzaldehyde

Catalyst	Condition	Yield (%)	Time (min)	Catalyst (mg)	Ref
CoFe$_2$O$_4$@ SiO$_2$-PA^a-CC^b-Guanidine-SA^c	H$_2$O, R.T	90	20	60	[17]
CuFe$_2$O$_4$ NPs	H$_2$O, R.T	99	25	10	[18]
[H-NMP^d]$^+$ [HSO4]$^-$	H$_2$O, US	98	5	15	[19]
CuFe$_2$O$_4$	H$_2$O, US	98	4	10	[20]
[DMSPDE^e] [Cl]	Solvent free/ 110℃	90	5	20	[21]
PC	H$_2$O, 80℃	97	20	20	-

^{a}PA: 3-aminopropyltrimethoxysilane, ^{b}CC: Cyanuric chloride, ^{c}SA: Sulfonic acid, ^{d}NMP: N-methyl-2-pyrrolidone, ^{e}DMSPDE: Nano-2-(dimethylamino)-N-(silica-n-propyl)-N,N-dimethylethanaminium chloride

Based on the results presented in the table, phosphatidylcholine (PC) is a highly effective catalyst for the synthesis of nitrogen-containing heterocyclic compounds. It achieves a high reaction yield (97%) in a short reaction time (20 minutes) with a low catalyst loading (20 mg). These results are comparable to, or even better than, those obtained with other catalysts, including metal-based catalysts and organic catalysts. In addition to its high efficiency, PC is also a natural compound that is non-toxic and environmentally friendly. This makes it a promising alternative to conventional catalysts for the synthesis of nitrogen-containing heterocyclic compounds.

To investigate the reusability of phosphatidylcholine, the reaction of preparing 4-chlorobenzaldehyde derivative was selected and investigated. After completion of the reaction, by adding water to the reaction mixture, the soluble catalyst was separated from the product by filter paper and after evaporation of the solvent and drying at 70 degrees Celsius, it was reused. The recovered catalyst can be used up to 4 stages without losing a significant amount of catalytic activity (Fig.3).
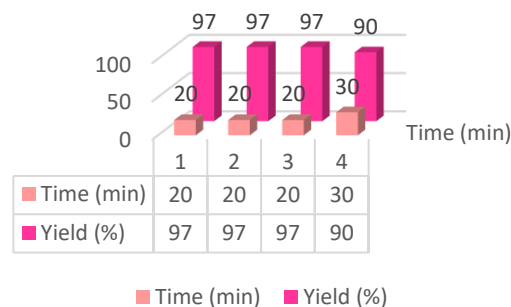
Fig.3: Investigating the activity of recovered phosphatidylcholine in the synthesis of pyrido[2,3-d:5,6-d']dipyrimidine derivative from 4-chlorobenzaldehyde

The study also found that the recovered catalyst can be easily separated from the product by filtration. This makes it easy to reuse the catalyst without the need for any additional purification steps. Overall, the results of this study suggest that PC is a promising candidate for the synthesis of 4-chlorobenzaldehyde derivative. It is a highly efficient catalyst that can be used repeatedly without losing its catalytic activity.

Conclusions

This work presents a novel and efficient one-pot synthesis of pyrido[2,3-d:5,6-d']dipyrimidines from readily available starting materials under mild conditions using biocompatible phosphatidylcholine as a catalyst. This green and sustainable method provides excellent yields in short reaction times with tunable product diversity based on substituent effects.

References

[1] Fatehi, A., Ghorbani-Vaghei, R., Alavinia, S., & Mahmoodi, J. (2020). Synthesis of quinazoline derivatives catalyzed by a new efficient reusable nanomagnetic catalyst supported with functionalized piperidinium benzene-1, 3-disulfonate ionic liquid. Chemistry Select, 5, 944-951.

[2] Alizadeh, A., Rezvanian, A., & Mokhtari, J. (2011). Solvent-free and efficient synthesis of highly functionalized cyclohexa-1, 3-diene derivatives via a novel one-pot three-component reaction. Synthesis, 2011, 3491-3495.

[3] Jalili, F., Zarei, M., Zolfigol, M. A., Rostamnia, S., & Moosavi-Zare, A. R. (2020). SBA-15/PrN (CH$_2$PO$_3$H$_2$)$_2$ as a novel and efficient mesoporous solid acid catalyst with phosphorous acid tags and its application on the synthesis of new pyrimido [4,5-b] quinolones and pyrido [2,3-d] pyrimidines via anomeric based oxidation. Microporous and Mesoporous Materials, 294, 237-244.

[4] Ghorbani-Vaghei, R., & Sarmast, N. (2018). Hexamethylenetetramine grafted layered double hydroxides as a novel and green heterogeneous ionic liquid catalyst for the synthesis of pyrido [2,3-d] pyrimidine derivatives. Research on Chemical Intermediates, 44, 4483-4501.

[5] Ghorbani-Vaghei, R., Alavinia, S., & Sarmast, N. (2018). Fe$_3$O$_4$@SiO$_2$@propyl-ANDSA: A new catalyst for the synthesis of tetrazoloquinazolines. Applied Organometallic Chemistry, 32, 237-244.

22nd Iranian Chemistry Congress (ICC22)
Iranian Research Organization for Science and Technology (IROST)
13-15 May 2024

03231-97589

[6] Azarifar, D., & Sheikh, D. (2013). ZrOCl₂·8H₂O: An efficient, ecofriendly, and recyclable catalyst for ultrasound-accelerated, one-pot, solvent-free synthesis of 8-aryl-7, 8-dihydro-[1, 3] dioxolo [4, 5-g] quinolin-6-(5 H)-one and 4-aryl-3, 4-dihydroquinolin-2 (1 H)-one derivatives. Synthetic Communications, 43, 2517-2526.

[V] Kovacs, J. A., Allegra, C. J., Swan, J. C., Drake, J. C., Parrillo, J. E., Chabner, B. A., & Masur, H. (1988). Potent antipneumocystis and antitoxoplasma activities of piritrexim, a lipid-soluble antifolate. Antimicrobial Agents and Chemotherapy, 32, 430-433.

[8] Rawal, R. K., Tripathi, R., Katti, S. B., Pannecouque, C., & De Clercq, E. (2007). Synthesis and evaluation of 2-(2, 6-dihalophenyl)-3-pyrimidinyl-1, 3-thiazolidin-4-one analogues as anti-HIV-1 agents. Bioorganic & Medicinal Chemistry, 15, 3134-3142.

[9] Naeimi, H., Didar, A., & Rashid, Z. (2017). Microwave-assisted synthesis of pyrido-dipyrimidines using magnetically CuFe₂O₄ nanoparticles as an efficient, reusable, and powerful catalyst in water. Journal of the Iranian Chemical Society, 14, 377-385.

[10] Kidwai, M., Mohan, R., & Saxena, S. (2003). Solid-supported Hantzsch—Biginelli reaction for syntheses of pyrimidine derivatives. Russian Chemical Bulletin, 52, 2457-2460.

[11] Broom, A. D., Shim, J. L., & Anderson, G. L. (1976). Pyrido [2, 3-d] pyrimidines. IV. Synthetic studies leading to various oxopyrido [2, 3-d] pyrimidines. The Journal of Organic Chemistry, 41, 1095-1099.

[12] Monge, A., Martinez-Merino, V., Sanmartin, C., Fernandez, F. J., Ochoa, M. C., Bellver, C., & Fernandez-Alvarez, E. (1989). 2-Arylamino-4-oxo-3, 4-dihydropyrido [2, 3-d] pyrimidines: Synthesis and diuretic activity. European Journal of Medicinal Chemistry, 24, 209-216.

[13] Kolla, V. E., Deyanov, A. B., Nazmetdinov, F. Y., Kashina, Z. N., & Drovosekova, L. P. (1993). Investigation of the anti-inflammatory and analgesic activity of 2-substituted 1-aryl-6-carboxy (carbethoxy)-7-methyl-4-oxo-1, 4-dihydropyrido [2, 3-d] pyrimidines. Pharmaceutical Chemistry Journal, 27, 635-636.

[14] Rosowsky, A., Mota, C. E., & Queener, S. F. (1995). Synthesis and antifolate activity of 2, 4-diamino-5, 6, 7, 8-tetrahydropyrido [4, 3-d] pyrimidine analogues of trimetrexate and piritrexim. Journal of Heterocyclic Chemistry, 32, 335-340.

[15] Donkor, I. O., Klein, C. L., Liang, L., Zhu, N., Bradley, E., & Clark, A. M. (1995). Synthesis and antimicrobial activity of 6, 7-annulated pyrido [2, 3-d] pyrimidines. Journal of Pharmaceutical Sciences, 84, 661-664.

[16] Pastor, A., Alajarin, R., Vaquero, J. J., Alvarez-Builla, J., de Casa-Juana, M. F., Sunkel, C., & Sanz-Aparicio, J. (1994). Synthesis and structure of new pyrido [2, 3-d] pyrimidine derivatives with calcium channel antagonist activity. Tetrahedron, 50, 8085-8098.

[17] Bystryakova, I. D., Burova, O. A., Chelysheva, G. M., Zhilinkova, S. V., Smirnova, N. M., & Safonova, T. S. (1991). Synthesis and biological activity of pyridol [2, 3-d] pyrimidines. Pharmaceutical Chemistry Journal, 25, 874-876.

[18] Rostami, H., & Shiri, L. (2021). One-pot synthesis of pyrido [2, 3-d: 5, 6-d'] dipyrimidines using CoFe₂O₄@ SiO₂-PA-CC-guanidine-SA magnetic nanoparticles in water. Applied Organometallic Chemistry, 35, 6293-6303.

[19] Naeimi, H., & Didar, A. (2017). Facile one-pot four component synthesis of pyrido[2,3-d:6,5-d'] dipyrimidines catalyzed by CuFe₂O₄ magnetic nanoparticles in water. Journal of Molecular Structure, 1137, 626-633.

[20] Naeimi, H., Didar, A., Rashid, Z., & Zahraie, Z. (2017). Sonochemical synthesis of pyrido[2,3-d:6,5-d']-dipyrimidines catalyzed by [HNMP]⁺[HSO4]⁻ and their antimicrobial activity studies. The Journal of Antibiotics, 70, 845-852.

[21] Naeimi, H., & Didar, A. (2017). Efficient sonochemical green reaction of aldehyde, thiobarbituric acid and ammonium acetate using magnetically recyclable nanocatalyst in water. Ultrasonics Sonochemistry, 34, 889-895.

[22] Zare, A., Kohzadian, A., Abshirini, Z., Sajadikhah, S. S., Phipps, J., Benamara, M., & Beyzavi, M. H. (2019). Nano-2-(dimethylamino)-N-(silica-n-propyl)-N,N-dimethylethanaminium chloride as a novel basic catalyst for the efficient synthesis of pyrido [2,3-d:6,5-d'] dipyrimidines. New Journal of Chemistry, 43, 2247-2257.

[23] Backhed, F., Ley, R. E., Sonnenburg, J. L., Peterson, D. A., & Gordon, J. I. (2005). Host-bacterial mutualism in the human intestine. Science, 307, 1915-1920.

[24] Duerkop, B. A., Vaishnava, S., & Hooper, L. V. (2009). Immune responses to the microbiota at the intestinal mucosal surface. Immunity, 31, 368-376.

[26] Hausmann, M., & Rogler, G. (2008). Immune-non immune networks in intestinal inflammation. Current Drug Targets, 9, 388-394.

[26] Swidsinski, A., Ladhoff, A., Pernthaler, A., Swidsinski, S., Loening–Baucke, V., Ortner, M., & Lochs, H. (2002). Mucosal flora in inflammatory bowel disease. Gastroenterology, 122, 44-54.

[27] Chen, Y., Hills, B. A., & Hills, Y. C. (2005). Unsaturated phosphatidylcholine and its application in surgical adhesion. ANZ Journal of Surgery, 75, 1111-1114.

[28] Sousa, A. A., Lopes, D. L., Emerenciano, M. G., Nora, L., Souza, C. F., Baldissera, M. D., & Da Silva, A. S. (2020). Phosphatidylcholine in diets of juvenile Nile tilapia in a biofloc technology system: Effects on performance, energy metabolism and the antioxidant system. Aquaculture, 515, 734574-734601.

[29] Mohamed, M. S., Awad, S. M., & Sayed, A. I. (2010). Synthesis of certain pyrimidine derivatives as antimicrobial agents and anti-inflammatory agents. Molecules, 15, 1882-1890.

[30] Saeidiroshan, H., & Moradi, L. (2019). Immobilization of Cu (II) on MWCNTs@ L-His as a new high efficient reusable catalyst for the synthesis of pyrido [2, 3-d: 5, 6-d'] dipyrimidine derivatives. Journal of Organometallic Chemistry, 893, 1-10.

[30] Bhosle, M. R., Khillare, L. D., Mali, J. R., Sarkate, A. P., Lokwani, D. K., & Tiwari, S. V. (2018). DIPEAc promoted one-pot synthesis of dihydropyrido [2, 3-d: 6, 5-d'] dipyrimidinetetraone and pyrimido [4, 5-d] pyrimidine derivatives as potent tyrosinase inhibitors and anticancer agents: in vitro screening, molecular docking and ADMET predictions. New Journal of Chemistry, 42, 18621-18632.

[32] Kidwai, M., & Singhal, K. (2007). Aqua-mediated one-pot synthesis and aromatization of pyrimido-fused 1, 4-dihydropyridine derivatives using ammonium salts. Canadian Journal of Chemistry, 85, 400-405.

[33] Rostamizadeh, S., Tahershamsi, L., & Zekri, N. (2015). An efficient, one-pot synthesis of pyrido [2, 3-d: 6, 5-d'] dipyrimidines using SBA-15-supported sulfonic acid nanocatalyst under solvent-free conditions. Journal of the Iranian Chemical Society, 12, 1381-1389.

[34] Ziarani, G. M., Gholamzadeh, P., Badiei, A., Asadi, S., & Soorki, A. A. (2015). Application of SBA-15 functionalized sulfonic acid (SBA-Pr-SO₃H) as an efficient nanoreactor in the one-pot synthesis of pyrido [2,3-d] pyrimidine. Journal of the Chilean Chemical Society, 60, 2975-2978.

Preparation of modified carbon paste electrode to potentiometric determination of mercury

Masoumeh Jafari, Leila Hajiaghababaei, Jamshid Najafpour, Ashraf Sadat Shahvelayati

Corresponding Author E-mail: masomeh.jafari2020@gmail.com

Department of Chemistry, Yadegar-e-Imam Khomeini (RAH) Shahre Rey Branch, Islamic Azad University, Tehran, Iran.

Abstract: 1-(4,6-dimethyl pyrimidin-2-yl)-3-phenylthiourea was synthesized and used as new modifier in the carbon paste electrode. The best electrode response was obtained by 12% ionophore, 70% graphite powder and 18% paraffin oil. The Hg^{2+} selective CPE showed a Nernstian slop of 29.1 mV/decade within the concentration range of 3×10^{-2} to 7×10^{-8} mol L^{-1}. The electrode has short response time of less than 5 s and was used successfully to potentiometric determination of Hg^{2+}.

Keywords: 1-(4,6-dimethyl pyrimidin-2-yl)-3-phenylthiourea; Carbon Paste Electrode; potentiometry; Hg^{2+}

Introduction

When toxic metals enter the environment because of global industrialization and have caused serious effects on human health. For example, mercury(Hg) compounds have many applications in mining for example extraction of gold and some industrial processes. In lamp producing factories, Hg is used in the production of fluorecent light bulbs, they have been used as fungicides to protect plants against infections. Hg often poses a high ecotoxicological risk for aquatic organisms due to its hight toxicity, bioaccgentic effects and mtagenicity[1]. Therefore, it is a critical issue to measure this ion.

Using the analytical methods such as atomic absorption spectroscopy(AAS) and inductively coupled plasma-atomic emission spectroscopy(ICP-AES) are performed to determine the level of metals like mercury but, these procedures have some disadvantages based on the cost and time of routine analysis and the tedious sample preparation process. Therefore, many researches are being done to find new simple and rapid methods. Electrochemical sensors provide a low-cost and convenient method for the detection of variable analytes which has higher sensitivity in their responses. carbon paste electrodes(CPE) as a simple and low-cost instrument have higher easy renewability of the surface, stability of response, lower ohmic resistance, and not requiring the internal solution . Extensively, carbon paste electrodes can be simply modified with different kinds of organic or inorganic modifiers. Electrode modification allows the researcher to design electrodes for different purposes and application[2].

In this research, we synthesized 1-(4,6-dimethyl pyrimidin-2-yl)-3-phenylthiourea for the first time and used it as new modifier ligand to fabricate modified carbon paste electrodes to measurement of Hg^{2+} ion potentiometrically.

Experimental Section

For fabricating modified CPE, the past was prepared by mixing different amounts of the synthesized ligand powder as modifier and different amounts of graphite and parafin oil. When mixture was homogenized, the prepared paste was carefully packed into the tube tip to prevent possible air gaps. Electrical contact was established by inserting a copper wire into the CPE opposite end. Before usage, a piece of paper was used to smooth the carbon paste's external surface. The electrode was conditioned for 24 h by soaking in a 1.0×10^{-3} mol L^{-1} of Hg^{2+} solution and as a working electrode is placed next to the reference electrode for potential measurement.

Results and Discussion

Electrode composition. The best composition of the carbon paste electrodes was found. For this purpose, several electrodes were fabricated with different compositions (Table1). Best modified CPE was made by combining 70% of graphite powder with 18% of paraffin and 12% ionophore (no.4). According to the Table, an increase in ligand level in the CPE (no. 1 - 4) from 5 to 12 mg led to an increased slope of the calibration curve from 6.1 mV/decade to 29.0 mV/decade. Improving the response of electrode by increasing the ionophores amounts shows the affinity of 1-(4,6-dimethyl pyrimidin-2-yl)-3-phenylthiourea to Hg^{2+}.

Table1: Optimizing the prepared carbon paste composition

No	Graphite	paraffin	ionophore	Slop(mV/decade)
1	73	22	5	6.1
2	72	21	7	16.2
3	65	25	10	21.5
4	70	18	12	29.0

22nd Iranian Chemistry Congress (ICC22)
Iranian Research Organization for Science and Technology (IROST)
13-15 May 2024

03231-97589

Effects of pH on the modified CPE response. The effect of the solution's pH on the response of the proposed modified electrodes was investigated in 1.0× 10^{-3} mol/ L mercury (II) solution with various pH values (2 to 11) (Fig.1). During all experiments, potential response of electrode was maintained constant in the pH range of 3 to 8.5 for Hg^{2+}. This result suggests the good performance of the sensor in this pH range.
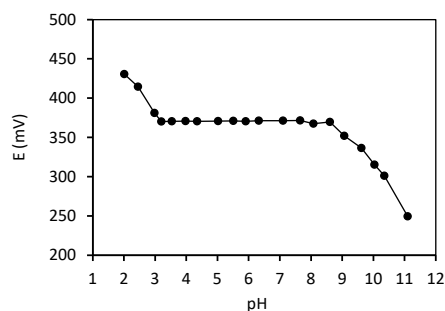
Fig.1: The effects of pH on the potential response of the Hg^{2+} selective CPE.

The calibration curve of modified CPE. in this step, working range of the modified CPE was evaluated. The electrode showed a linear concentration range of 3 × 10^{-2} to 7 × 10^{-8} mol/L for Hg^{2+} (Fig. 2). Also, detection limit of the proposed electrode was 5 × 10^{-8} mol/L.
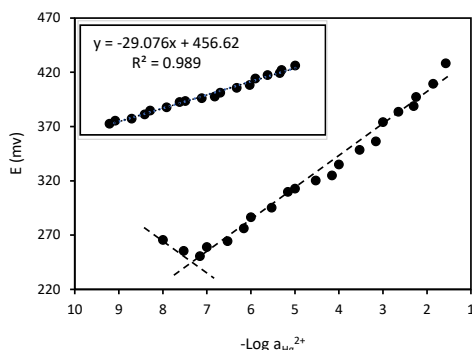
Fig.2: calibration curve of the Hg^{2+} selective CPE.

The response time of modified CPE.
Response time is the time required for the potential response to obtain values within ±1 mV of the ultimate equilibrium potential [3]. The average response time was about 3-5 s in low to high concentrations in the case of the Hg^{2+} selective CPE. This short response time indicates the desired result of the electrode.

Interference study. The selectivity coefficients of the electrode were assessed by the well-known Matched Potential Method (MPM) [4]. In MPM, first, the changes in the potentials by altering the primary ion activity are determined. The interfering ion is then added to an equal reference solution until achieving the same potential changes. All selectivity coefficients are much less than 1.0,

indicating the higher selectivity of the developed suggested electrode.

Conclusions
Modified carbon paste electrode was fabricated for Hg^{2+} determination potentiometrically. 1-(4,6-dimethyl pyrimidin-2-yl)-3-phenylthiourea was synthesized and used as a new modifier ligand to preparation of CPE. this ligand showed good tendency to Hg^{2+}. According to the obtained results, the potentiometric modified carbon paste electrode was fabricated by 70% graphite powder, 18% paraffin oil and 12% ligand. The Hg^{2+} selective CPE showed a Nernstian slope of 29.1 mV/decade over the concentration range of 3×10^{-2} to 7×10^{-8} mol/L. the electrode indicated a short response time of about 3-5 s.

References
[1] Ozdemir, S., Kilinc, E., & Oner, E. T. (2019). Preconcentrations and determinations of copper, nickel and lead in baby food samples employing Coprinus silvaticus immobilized multi-walled carbon nanotube as solid phase sorbent. *Food chemistry*, *276*, 174-179. https://doi.org/10.1016/j.foodchem.2018.07.123

[2] Rashvand, H. R., Hajiaghababaei, L., Darvich, M. R., Sarvestani, M. R. J., & Miyandoab, F. J. (2020). A liquid membrane mercury selective electrode based on 2-(N-pipyridino methyl)-1-cyano cyclohexanol as a novel neutral carrier. *Journal of Analytical Chemistry*, *75*, 1340-1347.https://doi.org/10.1134/S106193482010010X

[3] Hajiaghababaei, L., Abutalebyar, B., Darvich, M. R., & Shekoftefar, S. (2013). Synthesis of a New Oxime to the construction of a Mercury Potentiometric Sensor. *Sensor Letters*, *11*(12),2315-2321. https://doi.org/10.1166/sl.2013.3076

[4] Umezawa, Y., Umezawa, K., Bühlmann, P., Hamada, N., Aoki, H., Nakanishi, J., ... & Nishimura, Y. (2002). Potentiometric selectivity coefficients of ion-selective electrodes. Part II. Inorganic anions (IUPAC Technical Report). *Pure and applied chemistry*, *74*(6), 923-994. https://doi.org/10.1351/pac200274060923

22nd Iranian Chemistry Congress (ICC22)
Iranian Research Organization for Science and Technology (IROST)
13-15 May 2024

03231-97589

A comparative DFT study of absorption of amoxicillin drug from wastewater by FAU and ZSM-5 zeolites adsorbents

Mahnaz Sheikhi* [a], Hossein Nourmohamadi [b], Alireza gholipour [a]

Corresponding Author E-mail: sheikhi.m@fs.lu.ac.ir

[a] Physical Chemistry Department, Chemistry Faculty, lorestan University, Khorramabad, Iran.

[b] Mining Engineering (Mineral processing), Iranian Research Organization for Science and Technology, Iran.

Abstract: Zeolites are crystalline aluminosilicates that are used to remove pharmaceutical pollutants from wastewater due to their chemical structure and special surface properties. In this article, using the DFT method, adsorption of one of pharmaceutical pollutants on surfaces of FAU and ZSM-5 zeolites has been investigated, and the difference in the interaction energy of the desired molecule with the surfaces was obtained -66.31 kJ/mol.

Keywords: Adsorption; Amoxicillin; Zeolites

Introduction

Preservation of ground as habitat is one of the most important concerns for people[1-3]. pharmaceutical pollutants are dangerous threats to sweet water resources[4-5]. Since wastewater treatment plants are not effective enough to remove contaminants from wastewater, alternative methods of water treatment are needed [6]. Amoxicillin is not completely eliminated in treatment plants and permeates into groundwaterin plants of conventional water and wastewater treatment and groundwater[7], resulting in altered aquatic ecosystems[8-9]. Fujazite zeolites (x, y) and (zsm-5) and zeolite nanocrystals are among the most important types of zeolites. ZSM-5 zeolite with MFI framework has hydrophobic properties, high porosity, ability to catalyze hydrocarbon cracking reactions. Horizontal and zigzag channels with 10 loops that form vertical channels in the MFI network structure. These channels are a good place to absorb pollutants. The use of molecular simulation can increase our understanding of the surface properties of zeolites.

Calculation Methods

The previous studies have indicated that the DFT is among the most versatile and popular methods to investigate electronic structure of solids [10]. The structure of amoxicillin (AMX) was retrieved from the PubChem website (is the source of the molecular structures of drug contaminants). The molecule was loaded into Biovia Materials Studio 2020 (MS) software. We optimized the geometries of AMX by using the B3LYP method employing a double numerical (DND) basis set of DMol3 module. Models of zeolite adsorbents with ZSM-5 (MFI framework) and FAU topology were taken from the IZA database.

They were then imported into the DS Biovia Materials Studio 2017 (MS) software and then optimized using the GGA method and the Perdewe-Burkee-Ernzerhof (PBE) density functional DMol3 module. The (010) and (110) surfaces were selected as 2 and 3 layers from ZSM-5 and FAU, respectively.

The geometry optimization for the ZSM-5 and FAU were performed with $4 \times 4 \times 2$ and $3 \times 3 \times 1$ k-point mesh respectively in COSMO Code (water solvent). In addition, the adsorption of AMX was studied in these zeolites surfaces frameworks with GGA method and the PBE density functional. After optimizing the adsorption of AMX on ZSM-5 and FAU and ensuring that this represented a minimum energy structure, the total binding energies were computed employing the following equation:

$$E_{abs} = E_{total} - (E_{ZEO} + E_{AMX}) \qquad (1)$$

In which (E_{abs}) from the difference of the compound energy (E_{total}) and the sum of the single energy components, AMX energy (E_{AMX}) and energy of surface zeolites energy (E_{ZEO}) is obtained.

Results and Discussion

The values of Eab(AMX-ZSM_5) and Eab(AMX-FAU) are based on the data obtained from the calculations and replacing them in to equation 1 were obtained -177 and -110.7 kJ/mol, respectively. Examining the partial charges of the corresponding oxygen and silicon atoms before the interaction of the srurface of ZSM-5 and srurface of FAU with the amoxicillin molecule showed that positive charge of the silicon atoms decreased and negative charge of the oxygen atoms increased. The

22nd Iranian Chemistry Congress (ICC22)
Iranian Research Organization for Science and Technology (IROST)
13-15 May 2024

03231-97589

ZSM-5 zeolite surface was more active than FAU surface zeolite surface (Fig.2).

Gap energy (Eg) is an important parameter to determine molecular electrical transport properties, which the electronic properties of the systems were investigated according to equation 2 [10]:

$$E_g = E_{(LUMO)} - E_{(HOMO)} \qquad (2)$$

Where $E_{(HOMO)}$ is the value of the highest occupied molecular orbital (HOMO), $E_{(LUMO)}$ is the value of lowest unoccupied molecular orbital (LUMO) and Eg is the gap energy difference between HOMO and LUMO. The E_g surface ZSM-5 zeolite and srurface FAU zeolite were obtained as 0.002 and 0.007 eV, respectively.
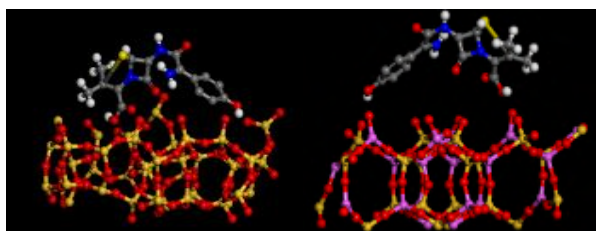
Fig.1: Optimized structures of amoxicillin molecule on the surface of surface ZSM-5 zeolite(a) and srurface FAU zeolite(b).

ZSM-5 zeolite				FAU zeolite			
O		Si		O		Si	
before	after	before	after	before	after	before	after
-0.316	-0.333	0.444	0.407	-0.358	-0.372	0.465	0.454
-0.326	-0.338	0.5	0.492	-0.333	-0.34	0.526	0.521
-0.214	-0.224	0.459	0.438	-0.271	-0.278	0.493	0.485
-0.328	-0.331	0.552	0.531	-0.324	-0.337	0.522	0.514
-0.219	-0.225	0.444	0.407	-0.323	-0.325	0.486	0.472

Fig.2: Charge of oxygen and silicon atoms (near the AMX) calculated in ZSM-5 zeolite and FAU zeolite before and after interaction with amoxicillin molecule.

Conclusions

In the current research, the amount of absorption of amoxicillin by zeolites ZSM-5 and FAU was measured using methods DFT. Studing partial charges of surface atoms zeolite ZSM-5 and zeolite FAU showed that the interaction of amoxicillin molecule with zeolite ZSM-5 is stronger and has more absorption than zeolite FAUAlso, the comparison of Eg value showed that the electrostatic properties of ZSM-5 zeolite are higher than FAU zeolite. Therefore, ZSM-5 zeolite is a more effective adsorbent for the absorption of amoxicillin than FAU zeolite from pharmaceutical wastewater.

References

[1] Barker, Kezia. "Biosecure citizenship: politicising symbiotic associations and the construction of biological threat." Transactions of the Institute of British geographers 35.3 (2010): 350-363.

[2] Biermann, Christine, and Robert M. Anderson. "Conservation, biopolitics, and the governance of life and death." Geography Compass 11.10 (2017): e12329.

[3] Dempsey, Jessica. Enterprising nature: Economics, markets, and finance in global biodiversity politics. John Wiley & Sons, 2016.

[4] Bunke, D., Moritz, S., Brack, W., Herráez, D. L., Posthuma, L., & Nuss, M. (2019). Developments in society and implications for emerging pollutants in the aquatic environment. Environmental Sciences Europe, 31(1), 1-17.

[5] Tang, Y., Yin, M., Yang, W., Li, H., Zhong, Y., Mo, L., & Sun, X. (2019). Emerging pollutants in water environment: Occurrence, monitoring, fate, and risk assessment. Water Environment Research, 91(10), 984-991.

[6] Orata, Francis. "Chemicals of emerging concern in surface and wastewater: a perspective of their fate within the lake victoria catchment area of Kenya." Effects of Emerging Chemical Contaminants on Water Resources and Environmental Health. IGI Global, 2020. 1-16.

[7] Ghauch, Antoine, Almuthanna Tuqan, and Hala Abou Assi. "Antibiotic removal from water: elimination of amoxicillin and ampicillin by microscale and nanoscale iron particles. Environmental pollution157.5 (2009): 1626-1635.

[8] Gholami, M., Mirzaei, R., Kalantary, R. R., Sabzali, A., & Gatei, F. (2012). Performance evaluation of reverse osmosis technology for selected antibiotics removal from synthetic pharmaceutical wastewater. Iranian Journal of Environmental Health Science & Engineering, 9, 1-10..

[9] Al Aukidy, M., Verlicchi, P., Jelic, A., Petrovic, M., & Barcelò, D. (2012). Monitoring release of pharmaceutical compounds: occurrence and environmental risk assessment of two WWTP effluents and their receiving bodies in the Po Valley, Italy. Science of the Total Environment, 438, 15-25.

[10] Nourmohamadi, H., Esrafili, M.D., Aghazadeh, V.,2022. A DFT investigation into the effects of As-doping on the electronic structure and electrochemical activity of pyrite (FeS2). Journal of Molecular Graphics and Modelling 110, 108040.

Development of 1-(1,3-benzothiazole-2-yl)-3-phenylthiourea Modified Carbon Paste Electrode for Sensitive Detection of Cu^{2+}

Elahe Sadat Mousavi Kherad[a*], Leila Hajiaghababaei[a], Jamshid Najafpour[a], Ashraf Sadat Shahvelayati [a], Shiva Dehghan Abkenar[b]

Corresponding Author E-mail: elahe.mousavi69@gmail.com

[a] Department of Chemistry, Yadegar-e-Imam Khomeini (RAH) Shahre Rey Branch, Islamic Azad University, Tehran, Iran.
[b] Department of Chemistry, Islamic Azad University, Savadkooh Branch, Savadkooh, Iran.

Abstract: This article presents a modified carbon paste electrode for detecting Cu^{2+} ions using 1-(1,3-benzothiazole-2-yl)-3-phenylthiourea. The electrode has a good selectivity to Cu^{2+} with a Nernstian slope of 30.4 mV decade^{-1} and a stable potential response over a pH range of 3-6. The detection limit of the method was 1.0×10^{-6} M and the response time of carbon paste electrode was 5-8 seconds.

Keywords: 1-(1,3-benzothiazole-2-yl)-3-phenylthiourea; Carbon Paste Electrode; Potentiometry; Cu^{2+}

Introduction

The release of toxic heavy metals into the environment poses a serious threat to humanity. Heavy metals do not decompose and instead accumulate in soil and human bodies over time[1]. Among various heavy metals, copper (Cu^{2+}) is a significant global concern. Therefore, it is crucial to monitor and control the trace copper content in water and food daily. Advanced analytical techniques are necessary to address this issue. This study aims to enhance the sensitivity and selectivity of copper ion detection by preparation of modified carbon paste electrodes by utilizing synthesized 1-(1,3-benzothiazole-2-yl)-3-phenylthiourea (ABT-NCS) as a modifier ligand [2, 3].

Experimental Section

i. Synthesis of 1-(1,3-benzothiazole-2-yl)-3-phenylthiourea

The synthesis of 1-(1,3-benzothiazole-2-yl)-3phenylthiourea involves a stepwise reaction between 2-amino benzo thiazole and phenyl isothiocyanate in Ethyl Pyridinium iodide [EPy] as a green solvent (Scheme 1). The best yielding was obtained at 40°C for 12 hours.
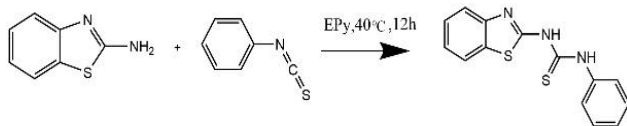
Scheme 1. Reaction of 2-amino benzothiazole with phenyl isothiocyanate

ii. Electrode preparation and potential measurements

Chemically modified CPE was synthesized by incorporating 1-(1,3-benzothiazole-2-yl)-3-phenylthiourea (ABT-NCS) into the graphite-paraffin oil matrix to enhance the electrode's performance. Different compositions of the mixture were used to prepare the modified CPEs, as given in (Table 1). To avoid possible air gaps that could enhance electrode resistance, the paste was packed carefully into the tube tip. A copper wire was inserted into the opposite end to establish electrical contact.

Table 1. Different compositions of Cu^{2+} CPE

Electrode	Compositions(%)			Slope (mV/decade)
	ABT-NCS	Graphite powder	Paraffin oil	
CPE1	5.0	73.0	22.0	25.4
CPE2	7.0	72.0	21.0	26.2
CPE3	10.0	70.0	20.0	26.6
CPE4	**12.0**	**70.0**	**18.0**	**30.4**
CPE5	14.0	69.0	17.0	26.5

Results and Discussion

i. The calibration curve

The electrode showed a linear response in the range of 1.0×10^{-6} to 7.0×10^{-2} mol.L^{-1} Cu^{2+}. The equation of the calibration curve was $y = -30.424x + 353.06$ with a correlation coefficient of $R^2 = 0.9909$. The slope of the CPE calibration curve was 30.4 mV decade^{-1} (Fig. 1). Also, the detection limit of the proposed electrode was 1×10^{-6} mol/L.
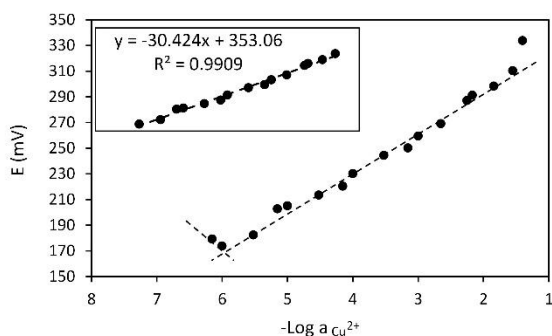
Fig.1: The calibration curve for Cu^{2+} modified CPE (CPE٤)

ii. Effect of pH

The effect of pH on the potential response of copper electrode was studied. Figure 2 shows the effect of pH on the potential response of the CPE in 1.0×10^{-3} mol.L^{-1} Cu^{2+} solution. The potential remained constant in the pH range of 3-6, which is considered the working pH range of the electrode (Fig. 2). However, outside this range, the electrode responses changed significantly. The potential change at pH lower than 3 could be due to the competition of protons with copper ions in the interaction with the ligand on the electrode surface.
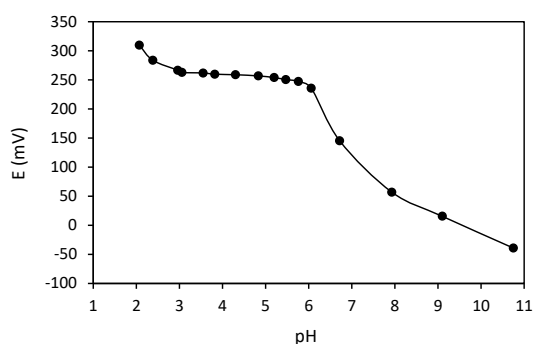
Fig.2: Effect of pH on the potential response of Cu^{2+} CPE

iii. Interference

The selectivity coefficients of the suggested electrode were assessed by the well-known Matched Potential Method (MPM). In MPM, first, the changes in the potentials by altering the primary ion activity are determined. The interfering ion is then added to an equal reference solution until achieving the same potential changes. The selectivity coefficient K_{MPM} is obtained as:

$$K_{MPM} = \Delta a_A/a_B$$

where $\Delta a_A = a'_A - a_A$, a_A represents the initial primary ion activity and a'_A the activity of A, while existing the interfering ion (i.e., a_B). A K_{MPM} value of 1.0 represents the

sensor with similar responses to both interfering and primary ions, with the smaller values denoting its higher selectivity. All selectivity coefficients are much less than 1.0, indicating the higher selectivity of the developed electrodes for the analytes.

iv. Response time

For the successful development of ion-selective electrode, sensitivity, and rapid response are important factors. In this experiment, The average response time of Cu^{2+} selective CPE was about 5-8 s in changing the concentration from low to high.

Conclusions

In this research, 1-(1,3-benzothiazole-2-yl)-3-phenylthiourea was synthesized and a new modified carbon paste electrode has been developed for detecting Cu^{2+} ions by using it as a modifier. The experiments conducted indicate that this new electrode has a wide working concentration range, from 1.0×10^{-6} to 7.0×10^{-2} molL^{-1}, a low detection limit of 1.0×10^{-6} molL^{-1}, and an average response time of 5-8 s. Additionally, the electrode has been found to possess acceptable levels of selectivity.

References

[1] Xhanari, K.; Finšgar, M. Recent advances in the modification of electrodes for trace metal analysis: a review. *Analyst* **2023**, *148* (23), 5805-5821, Review. DOI: 10.1039/d3an01252b Scopus.

[2] Divsar, F.; Isapour, N.; Kefayati, H.; Badiei, A.; Nezhadali, A.; Easapour, S.; Yadavi, M. Fluorene functionalized nanoporous SBA-15 incorporated into carbon paste electrode for trace copper determination. *Journal of Porous Materials* **2015**, *22* (6), 1655-1661. DOI: 10.1007/s10934-015-0049-z.

[3] Abd-Elsabur, K. M.; Abd-Elsabour, M.; Assaf, F. H.; Hasan, I. M. A. Electrochemical Estimation of Cd and Cu Ions Simultaneously Using a Modified MgO/Fe2O3 Nanocomposite/Carbon Paste Electrode. *Electrocatalysis* **2023**, *14* (6), 875-890. DOI: 10.1007/s12678-023-00843-w.

The role of electron-donating and electron-withdrawing groups in tuning the optoelectronic properties of heteroleptic dithiolene complexes

Soheyla Hajivand, Sepideh Samiee*
Corresponding Author E-mail: s.samiee@scu.ac.ir
Department of Chemistry, Faculty of Science, Shahid Chamran University of Ahvaz, Ahvaz, Iran.

Abstract: In this study, the effect of structural modifications on the optoelectronic properties of heteroleptic dithiolene complexes $[Pd(dmio)(dithiolate)]^{2-}$ {dmio = 2-oxo-1,3-dithiole-4,5-dithiolate; dithiolate = 1,2-benzenedithiolate (bdt^{2-}), 4-methylbenzene-1,2-dithiolate (tdt^{2-}) and 4-cyanobenzene-1,2-dithiolate ($cbdt^{2-}$)} have been examined using density functional theory (DFT) and time-dependent density functional theory (TD-DFT) calculation. This theoretical investigation can be practical guide to the molecular engineering of alternative sensitizers used in DSSC devices.

Keywords: DFT; TD-DFT; Dithiolene complex; DSSC.

Introduction
The interest in metal dithiolene chemistry in various fields of materials chemistry has been expanded by the growing attention to heteroleptic derivatives with potential application in dye-sensitized solar cells (DSSCs), superconductor and nonlinear optical (NLO) materials [1]. This wide range of applications derives from unusual magnetic properties and the unique electronic structures, and also their reversible redox behavior [2].

Computational Details
All the calculations in this study were performed with Gaussian 09 package. The geometric structures of the heteroleptic palladium(II) dithiolene complex (see Fig. 1) were optimized using DFT and TD-DFT methods in gas and solvent (dichloromethane) phases. The 6–31g*(d,p) basis set and the Los Alamos effective core potential (Lanl2DZ) were used for the lighter (H, C, N, O, and S) and heavier (Pd) elements, respectively.

Results and Discussion
In the present work, the $[Pd(dmio)(bdt)]^{2-}$ complex is chosen as the starting point and the two hydrogen atoms of the bdt ligand are symmetrically replaced by electron-donating (-CH₃) and electron-withdrawing (-CN) groups (Fig. 1).
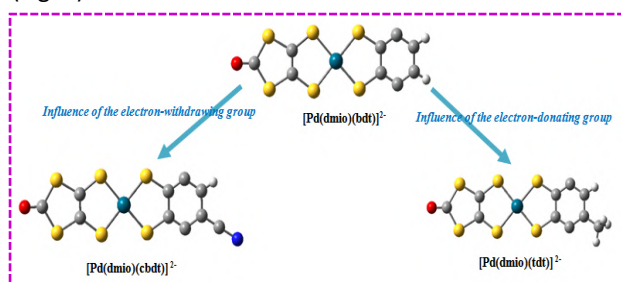
Fig.1: Optimized geometry structures of the considered complexes in this study.

The results indicated that structural modifications by electron-withdrawing group decreases the energy gap of the $[Pd(dmio)(bdt)]^{2-}$ complex in comparison to the electron-donating group. Moreover, the cyanide substitution at bdt position can increase the molar extinction coefficients and red-shift the overall absorption spectrum. The light harvesting efficiency (LHE), as an indicator of incident sunlight-to-electricity conversion efficiency, is correlated with the ability of dyes to harvest light. In this regard, the values of LHE have calculated and compared with each other. It is clearly found that LHE values for $[Pd(dmio)(cbdt)]^{2-}$ are higher than the other complexes.

Conclusions
The results suggest that the substitution of cyanide group on the bdt ligand of heteroleptic palladium(II) complexes using electron-withdrawing groups can finely tune their electronic structures and optical properties.

References
[1] Attar, S.S., Pilia, L., Espa, D,. Artizzu, F., Serpe, A., & P. Deplano, (2021). Insight into the properties of heteroleptic metal dithiolenes: multistimuli responsive luminescence, chromism, and nonlinear optics, Inorganic Chemistry, 60(13), 9332–9344. https://doi.org/10.1021/acs.inorgchem.1c00023.
[2] Kusamoto, T., & Nishihara, H. (2019). Zero-, one- and two-dimensional bis(dithiolato)metal complexes with unique physical and chemical properties, Coordination Chemistry Reviews , 419–439. https://doi.org/10.1016/j.ccr.2018.09.012.

A comparative theoretical study on the structural, electronic and optical properties of palladium(II) dithiolene complexes

Soheyla Hajivand, Sepideh Samiee*

Corresponding Author E-mail: s.samiee@scu.ac.ir
Department of Chemistry, Faculty of Science, Shahid Chamran University of Ahvaz, Ahvaz, Iran.

Abstract: The goal of this investigation is to analyze the geometrical, electronic, and photophysical properties of [Pd(dmio)(dithiolate)]$^{2-}$ derivatives for their use in dye-sensitized solar cells (DSSCs), by employing density functional theory (DFT) and time-dependent density functional theory (TD-DFT) calculations. Thus, our results may give a useful guidance for the molecular design of the metal complex sensitizers used in DSSCs.
Keywords: Theoretical study, Palladium, Dithiolene complex, DSSC.

Introduction

Over the last three decades bis(1,2-dithiolene) metal complexes of group VIII metals have attracted the interest of numerous experimental and theoretical researchers due to their unique properties, which include solution luminescence, large molecular hyperolarizabilities, solvatochromism, and large excited-state oxidation potentials [1].

Computational Details

Gaussian 09 package was used to perform the computational calculations. A series of palladium(II) dithiolene complexes [Pd(dmio)(dithiolate)]$^{2-}$ {dmio = 2-oxo-1,3-dithiole-4,5-dithiolate; dithiolate = 5,6-dihydro-1,4-dithiin-2,3dithiolate (dddt^{2-}), maleonitrildithiolate (mnt^{2-}), 1-phenyl-1,2-ethylenedithiolate (phedt^{2-}), and pyrazine-2,3-dithiolate (pdt^{2-})} have been designed and investigated by DFT and TD-DFT methods in two phases. The geometries of these complexes in their ground states (S$_0$) were fully optimized at B3LYP exchange correlation functional using 6-31G(d) for C, H, O, S and N atoms, and LANL2DZ basis set for Pd atom.

Results and Discussion

The optimized ground state geometry structure of all complexes is displayed in Fig. 1. The calculated geometrical parameters of complexes are in good agreement with available experimental data [2].
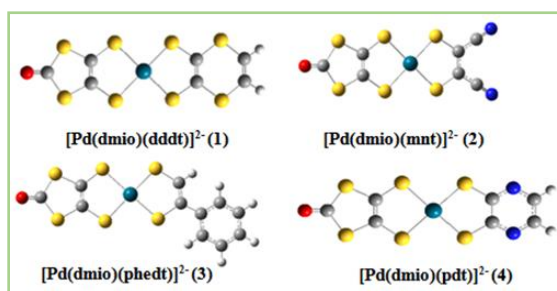
Fig.1: Optimized geometry structures of the considered in this study.

According to natural bond orbital (NBO) analysis, the HOMO–LUMO gaps decrease in the following order **4 > 3 > 2 > 1**, which implies that the complex **1** has the lowest value of gap energy among the studied complexes. It is noteworthy that the LUMO energy levels of all dithiolene complexes (1-4) are higher than that of the conduction band of TiO$_2$ (–4.00 eV), and their HOMO energy levels are lower than that of the redox potential of the electrolyte I$^-$/I$_3^-$ (–4.60 eV). Thus, these complexes are suitable for DSSC applications in terms of energy level matching. The results of TD-DFT calculation indicate that the complex **1** has maximum molar extinction coefficients, and the overall absorption spectrum is red-shifted significantly into visible and near-infrared in comparison to other complexes. Meantime, the value of light harvesting efficiency (LHE) for **2** is higher than the other complexes

Conclusions

Overall, it seems that these palladium(II) dithiolene complexes could be introduced as promising new electro-optical materials.

References

[1] Yang, Y.C., & Lin, J.S., & Ni, J.-S. (2023), Neutral d^8 metal complexes with intervalence charge-transfer transition trigger an effective NIR-II photothermal conversion for solar-driven desalination, Journal of Materials Chemistry A, 11, 26164-26172. https://doi.org/10.1039/D3TA05474H.

[2] Eranda, P., & Basu, P. (2009), Synthesis, characterization and structure of a low coordinate desoxomolybdenum cluster stabilized by a dithione ligand, Dalton Transactions, 25, 5023-5028. https://doi.org/10.1039/B904113C.

22nd Iranian Chemistry Congress (ICC22)
Iranian Research Organization for Science and Technology (IROST)
13-15 May 2024

03231-97589

IROST

Predicting suitable ligands as drug candidates for Amyloid Precursor Protein (APP) target in the treatment of Alzheimer's Disease

Elham Bastani

Corresponding Author E-mail: ebastani97@gmail.com

Chemistry faculty, Iran University of Science and Technology (IUST), Tehran, Iran.

Abstract: Alzheimer's Disease (AD) is characterized by deposition of Amyloid-Beta Peptide (Aβ), which is produced from post-translational processing of Amyloid Precursor Protein (APP) so biochemical and genetic studies of APP processing will be crucial to the development of therapeutic targets to treat AD. The goal of this research is to predict suitable ligands as drug candidates for APP target in the treatment of Alzheimer's disease.

Keywords: Alzheimer's Disease (AD); APP target; drug discovery.

Introduction

Despite many potential therapeutic approaches having been tested for AD the search for effective disease-modifying therapies remains elusive [1]. APP is a transmembrane protein, which has been linked to neurogenesis and the regulation of neural differentiation. There is a high level of expression of APP during brain development although APP has also been shown to be expressed in most tissues [2]. Increased expression of APP leads to Alzheimer's disease, where Aβ directly contributes to pathologies. In this study some ligands as drug candidates were predicted by multiple methods.

Experimental Section

First, a molecular library consisting of 457 molecules was formed, of which 200 molecules were selected from Binding DB and 257 molecules from zink15 base. Then, for modeling, 200 selected molecules from BD were entered into Schrodigner software. In the following, QSAR and docking methods were also used to suggest suitable ligands as drug candidates.

Results and Discussion

Table1: The results obtained from the stage Pharmacophore Hypothesis in Schrodigner software

	Minimum match percentage	Number of features	Minimum number of features	Number of models made	Selected model	Survival score
1	70	4to5	4	11	AAHHR	6.26
2	85	4to5	5	18	AHHHR	6.48
3	90	4to6	6	22	AAAHHR	6.67
4	95	5to7	6	9	AAAHHR	6.67

Table2: The results obtained from the stage Ligand and Database Screening

	Number of ligands matched with the model	Number of features matched with the model	maximum value phaseScreenScore
1	88	4 of 6	1.8
2	70	4 of 6	1.63
3	115	4 of 6	1.75
	18	6 of 6	1.54
4	18	4 of 6	1.54

According to the values obtained from PhaseScreenScore in the step of Ligand and Database Screening and minimum percentage in the step of Develop Pharmacophore Hypothesis,115 ligands obtained from the third processing of the AAAHHR model were selected. To check the hERG parameter,ADMETlab database was used.106 molecules blockers and 9 molecules Non_blockers were reported.

Table3: Docking results

ZINC_ID	Binding affinity	RMSD lower bound	RMSD upper bound
ZINC13808801	-5.4	0	0
ZINC4343325	-6.5	0	0
ZINC13808799	-6.1	0	0
ZINC4343323	-6.1	0	0
ZINC36143495	-5.7	0	0
ZINC45337578	-5.6	0	0
ZINC29544241	-5.9	0	0
ZINC35050569	-5.4	0	0
ZINC35050561	-6.1	0	0

Fortunately, the results obtained from docking all ligands with the receptor are acceptable.

The diagram is based on Chemoface modeling that -logIC50 ligands taken from ZINK15 were predicted:

22nd Iranian Chemistry Congress (ICC22)
Iranian Research Organization for Science and Technology (IROST)
13-15 May 2024

03231-97589

IROST
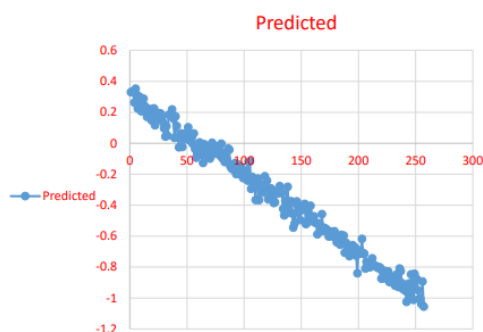
Fig 1: Diagram based on QSAR

The molecule was considered as a drug candidate if -logIC50> -0.9

Table 4: Results obtained from all methods performed

ZINC_ID	Binding affinity	-logIC50 predicted based on QSAR	TPSA	Water solubility	logP$_{O/w}$	GI absorbtion	Liver enzyme inhibitor	BBB permeant	lipinski
ZINC13808801	-5.4	-0.92	82.79	Moderately soluble	3.26	High	Yes 3 enzyme	No	Yes
ZINC4343325	-6.5	-0.87	54.55	Moderately soluble	3.51	High	Yes 2 enzyme	Yes	Yes
ZINC13808799	-6.1	-1.05	54.55	Moderately soluble	3.81	High	Yes 2 enzyme	Yes	Yes
ZINC4343323	-6.1	-0.9	54.55	Moderately soluble	3.51	High	Yes 2 enzyme	Yes	Yes
ZINC36143495	-5.7	0.102	294.12	Soluble	-2.4	Low	No	No	No
ZINC45337578	-5.6	-0.89	58.69	Soluble	2.65	High	Yes 1 enzyme	Yes	Yes
ZINC29544241	-5.9	-1.02	58.69	Moderately soluble	1.89	High	No	Yes	Yes
ZINC35050569	-5.4	-0.6	35.53	Soluble	2.76	High	Yes 2 enzyme	Yes	Yes
ZINC35050561	-6.1	-0.74	35.53	Moderately soluble	3.11	High	Yes 2 enzyme	Yes	Yes
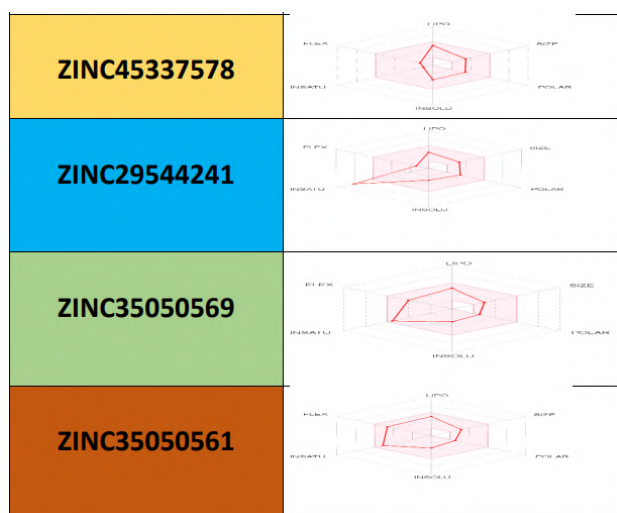
Fig 2: Radar plot

Conclusions

Based on the results and considering that the entry of the drug into the brain cells and its passage through the blood-brain barrier (BBB permeant) were considered important parameters in the final selection, the following compounds were selected as drug candidates.
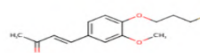
1) ZINC35050561   3) ZINC29544241
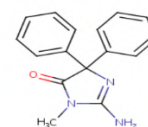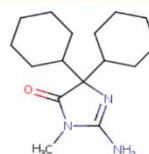
2) ZINC45337578   4) ZINC35050569
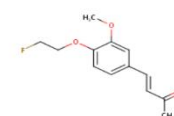
References

[1] Gabriele, R. M., Abel, E., Fox, N. C., Wray, S., & Arber, C. (2022). Knockdown of amyloid precursor protein: biological consequences and clinical opportunities. *Frontiers in Neuroscience*, *16*, 835645.

[2] Bonner, A. B. Amyloid Precursor Protein (APP) processing and potential targets for Alzheimer's Disease. *gene*, *8*, 14.

22nd Iranian Chemistry Congress (ICC22)
Iranian Research Organization for Science and Technology (IROST)
13-15 May 2024

03231-97589

Fabrication of polyamide thin film nanocomposite membrane with enhanced antibacterial properties

M. Arash[a], Y. Mansourpanah[a*], S. Rostamnia[b]

mansourpanah.y@lu.ac.ir

[a] Membrane Research Laboratory, Lorestan University, Khorramabad, Iran.

[b] Iran University of Science and Technology.

Abstract: A polyamide nanofiltration membrane was fabricated via interfacial polymerization with the assistance of a Ag/Cu-BTC-NH2 nanocomposite interlayer to enhance antibacterial performances. The efficacy performance of the developed TFN membranes were compared with TFC membrane and found that TFN membranes showed excellent water flux. Besides, Ag/Cu-BTC-NH2 membranes showed noteworthy antibacterial properties.
Keywords: Bi-metal-organic frameworks; Thin-film nanocomposite; Interfacial polymerization (IP); Antibacterial.

Introduction

Membrane biofouling leads to a reduction in permeation, selectivity change, increase in energy cost and decline in membrane lifespan during operation. There is currently a continued need to look into strategies to mitigate against membrane biofouling. significant research has been carried out to date on developing mitigation strategies against membrane biofouling [1]. The metal core in the framework of the MOFs can be considered as the reservoir of metal ions and its gradual release results in antibacterial activity. The main objectives of this study are (i) The synthesis of bi metal-organic framework to increase antibacterial properties. (ii) promoting interaction and compatibility between the bi-MOF and the polyamide matrix to improve its incorporation within the TFN membranes.

Experimental Section

All materials were purchased from Merck.

MOF preparation $Cu_3(BTC)_2$

H_3BTC was dissolved in mixture solution of DMF and ethanol, and then mixed with an aqueous solution of cupric acetate in a test tube. After the ultrasonic irradiation, the products were isolated by the centrifugation, and then dried at 130 $^\circ$C for 12 h .

Preparation Ag/Cu-BTC

$AgNO_3$ was dissolved in the mixture of deionized water and ethanol in stainless steel autoclave with a polytetrafluoroethylene liner. prepared Cu–BTC was added into and the autoclave was put in a 85 $^\circ$C oven. Finally, the product was dried under vacuum at 100 $^\circ$C over the night.

Preparation Ag/Cu-BTC-NH₂

Ag/Cu-BTC was suspended in toluene. To this suspension, ethylenediamine was added and the mixture was stirred under reflux for 12 h. The products were dried under vacuum.

Fabrication of TFC and TFN membrane

Thin film polyamide layer of NF membranes was made via interfacial polymerization (IP) process on the PES substrates [2]. The membranes were then covered with 25 ml of a Cu/Ag-BTC-NH2 at different concentrations dispersion in ethanol. Then, an aqueous solution of 1wt% CAS, 2 wt% PIP, 2 wt% TEA were strewn on top of UF membrane and was left for 10 min. The aqueous phase was drained off. The organic phase con taining 0.15 wt% TMC in n-hexane was poured into the frame. After about 3 min, n-hexane solution containing TMC was discarded and the membranes were immediately transferred to a steam bath for 15 minutes. The TFN membranes were designated as M0, M1, M2 and M3 TFN membranes, respectively.

Filtration performance

We measured the water permeability of each fabricated thin film membrane at an operating pressure of 0.4 MPa. Water flux, J, (L/m²h) of the TFN membranes was obtained following Eqs. (1):

$$J = m/ A\Delta t \qquad (1)$$

where m is the total mass of water permeated the surface A during the time Δt.

Antibacterial activity of the membranes

The antibacterial activity of the membranes was established using a modified disc-diffusion method described by Pokhrel et al. [3].

Results and Discussion

XRD patterns

The sharp peaks at 2θ of 5.8°, 6.7°, 9.4°, 11.6°, 13.4°, 17.4°, and 19.0° confirm the ordered crystalline structure of Cu-BTC, Ag/Cu-BTC and Ag/Cu-BTC-NH2 (Fig.1).
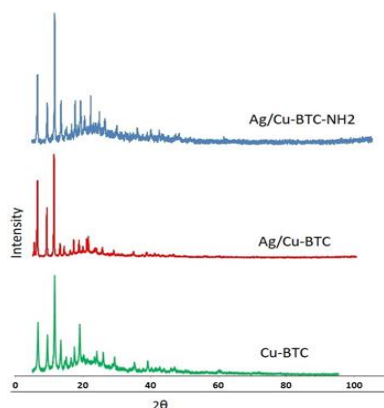
Fig.1: The XRD patterns of Cu-BTC, Ag/Cu-BTC and Ag/Cu-BTC-NH2

TFN membrane performance

Fig. 2 shows the effect of Ag/Cu-BTC-NH$_2$ on the water flux of the prepared membranes. Water flux of TFN membranes increased slightly from 11.8 l/m^2.h to 10.8 l/m^2.h respectively, with an increase in Ag/Cu-BTC-NH$_2$ concentration from 0 to 0.4%wt.
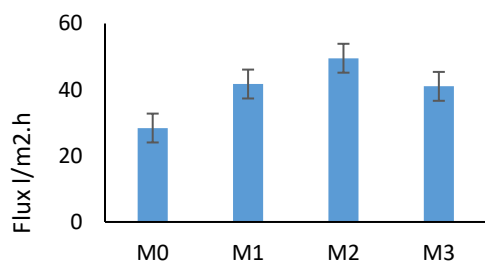
Fig.2: Comparison of water flux of the membranes

Antibacterial Properties of the Membranes

Bacterial inhibition zones of membranes are presented in Fig.3. The inhibition zone thicknesses listed in Table 1 show that higher concentrations of Ag/Cu-BTC-NH$_2$ led to increased antibacterial activities. There are mainly two mechanisms for antibacterial properties of nanometals which is widely considered as the main reason of bacterial elimination. First, ion toxicity released from the surface of metal particles causes serious damage to DNA structure of bacterium cell. Second, the generated reactive oxygen species on the metal surface inhibit the bacterial growth on the membrane.

Table 1: Mean thickness of inhibition zones of TFC and TFN membranes

Membrane	S. aureus	E. coli
M$_0$	0.0mm	0.0mm
M$_1$	21mm	19mm
M$_2$	23mm	21mm
M$_3$	25mm	23mm
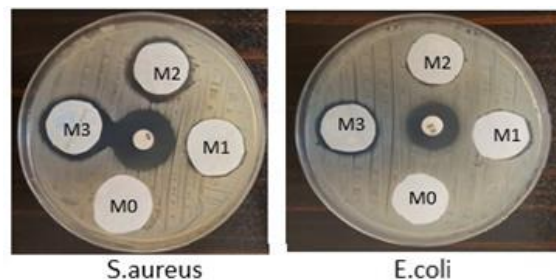
Fig.3: Anti-bacterial test of M$_0$, M$_1$, M$_2$ and M$_3$ membranes

Conclusions

This work reports the use of Ag/Cu-BTC-NH$_2$ nanoparticle as additives for reducing antimicrobial in polyamide TFC membranes. Ag/Cu-BTC-NH$_2$ incorporation improved the properties of TFN membranes in terms of their biocidal properties, thereby leading to enhanced bacterial resistance against S. aureus and E. coli without adversely affecting membrane selectivity.

References

[1] Nguyen, T., Roddick, F. A., & Fan, L. (2012). Biofouling of water treatment membranes: a review of the underlying causes, monitoring techniques and control measures. Membranes, 2(4), 804-840. https://doi.org/10.3390/membranes2040804.

[2] Mansourpanah, Y., Madaeni, S., & Rahimpour, A. (2009). Fabrication and development of interfacial polymerized thin-film composite nanofiltration membrane using different surfactants in organic phase; study of morphology and performance. Journal of Membrane Science, 343(1-2), 219-228. https://doi.org/10.1016/j.memsci.2009.07.033.

[3] Pokhrel, H., Baishya, S., Phukan, B., Pillai, D., & Rather, M. A. (2018). Occurrence and distribution of multiple antibiotic resistance bacteria of public health significance in backwaters and aquaculture farm. Int. J. Curr. Microbiol. Appl. Sci, 7, 975-987. https://doi.org/10.20546/ijcmas.2018.702.121.

The dopamine detection using of the boronic acid-modified magnetic CQD nanoparticles

Fatemeh Rafiee * [a], Niloofar Tajfar [a], Masoumeh Mohammadnejad [b]

Corresponding Author E-mail: f.rafiee@alzahra.ac.ir

[a] Department of Organic Chemistry, Faculty of Chemistry, Alzahra University, Tehran.

[b] Department of Analytical Chemistry, Faculty of Chemistry, Alzahra University, Tehran.

Abstract: The magnetic carbon quantum dots were prepared through the hydrothermal carbonization of chitosan and magnetization with Fe_3O_4 NPs. The surface of CQD NPs was functionalized with $-B(OH)_2$ groups via the condensation of amine functions with 4-acetylphenylboronic acid. The prepared $Fe_3O_4@CQD@AP-B(OH)_2$ sorbent exhibited a high adsorption capacity for detection of dopamine.

Keywords: Chitosan based-carbon quantum dot; Magnetic CQD; Boronic-acid modified CQD; Dopamine detection

Introduction

Dopamine (DA) as one of the main catecholamine neurotransmitters in the hypothalamus and pituitary gland has critical roles in biological procedures in the central nervous, hormonal and cardiovascular systems. Conventional analytical approaches including mass spectrometry, chromatography, electrochemistry, chemiluminescence and enzymatic methods have been used for dopamine detection. The mentioned methods typically suffer from several disadvantages such as high requirements for testers, time consuming detection, low accuracy, the prerequisite of expensive analytic instruments, complicated sample pretreatments, the cost of organic solvents and so on.

By contrast, the fluorescent-based sensors have more advantages containing low cost, high sensitivity, simple operation and fast testing in detection of various target analytic samples [1, 2].

Among of natural polysaccharides, chitosan biopolymer is available, biodegradable and biocompatible with many amine and hydroxyl groups that makes it as an interesting C and N rich source for the preparation of functionalized CQDs [3]. In other to modify the fluorescence properties and adjust effectively the intrinsic structure and optical performance of CQDs, different functional groups doping has been proposed [4]. The boronic acid segment could covalently interacted with the cis-diols and formed five- or six- membered cyclic esters and thus it used in the extraction of cis-diol biomolecules especially neurotransmitter catecholamines such as dopamine molecules [5]. Experimental Section $Fe_3O_4@CQD@AP-B(OH)_2$ NPs were synthesized according to our pervious published work [6].

Experimental Section

$Fe_3O_4@CQD@AP-B(OH)_2$ NPs were synthesized according to our pervious published work [6].

Results and Discussion

The study of the efficiency of $Fe_3O_4@CQD@AP-B(OH)_2$ NPs as a luminescent sensor in dopamine determination

As the synthetic compound is based on quantum dot and show fluorescence property, we investigated the fluorescent changes of N-doped CQD NPs in various concentration of dopamine solution. With this purpose, the mixture of $Fe_3O_4@CQD@AP-B(OH)_2$ (0.003 g) in distillated water (100 ml) was dispersed under ultrasonic conditions for 15 minutes. After this time, to 2 ml of dispersed mixture was added distillated water (2 ml) and the fluorescence emission spectra was recorded under excitation at 390 nm. The maximum emission spectrum was obtained at 540 nm.

To investigation of the efficiency of sensor ($Fe_3O_4@CQD@AP-B(OH)_2$) in detection of DA and also obtain a calibration curve, to 2 ml of dispersed solution of the magnetic boronic acid functionalized CQD NPs was added 2 ml of various concentrations of DA solution (10, 15, 20 and 30 μM) and stirred for 30 minutes. The fluorescent intensity of each sample was measured. The fluorescence intensity of $Fe_3O_4@CQD@AP-B(OH)_2$ NPs sensor was quenched in the presence of different concentration of DA (Fig. 3). There is a linear dependence between fluorescence quenching of sensor with concentration of DA (10-30 μM).

We proposed that dopamine led to the gradual accumulation of CQDs through interaction of OH groups of $B(OH)_2$ segment with DA target and resulted in the quenching of the CQDs fluorescence. The fluorescence intensity of unmodified CQD NPs ($Fe_3O_4@CQD$) and $-B(OH)_2$ modified sensor are shown in Fig. 4.
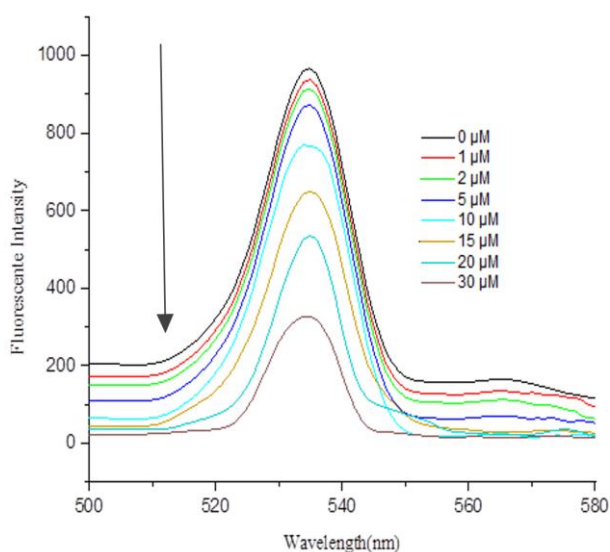
Fig.1: The fluorescence quenching of Fe$_3$O$_4$@CQD@AP-B(OH)$_2$ in the presence of different concentration of DA

Conclusions

In conclusion, the efficiency of a boronic-acid modified magnetic CQD was investigated. The hydroxyl functional of −B(OH)$_2$ segment in the CQD NPs surface were bonded to the vicinal OH groups of DA molecules. For detection of dopamine, the fluorescence quenching of Fe3O4@CQD@AP-B(OH)$_2$ was considered as signal that have a linear relation with concentration of dopamine.

References

[1] An, J., Chen, M., Hu, N., Hu, Y., Chen, R., Lyu, Y., ... & Liu, Y. (2020). Carbon dots-based dual-emission ratiometric fluorescence sensor for dopamine detection. Spectrochimica Acta Part A: Molecular and Biomolecular Spectroscopy,243,118804.
https://doi.org/10.1016/j.saa.2020.118804

[2] Wang, Y., Kang, K., Wang, S., Ma, L., Kang, W., Liu, X. H., ... & Guo, Z. (2020). A novel resonance Rayleigh scattering aptasensor for dopamine detection based on an Exonuclease III assisted signal amplification by G-quadruplex nanowires formation. Arabian Journal of Chemistry, 13(8), 6598-6605.

https://doi.org/10.1016/j.arabjc.2020.06.016.

[3] Wan, J., Gu, J., Zhao, Q., & Liu, Y. (2016). COD capture: a feasible option towards energy self-sufficient domestic wastewater treatment. *Scientific reports*, *6*(1), 25054.

https://doi.org/10.1038/srep25054

[4] Zhou, J., Zhou, H., Tang, J., Deng, S., Yan, F., Li, W., & Qu, M. (2017). Carbon dots doped with heteroatoms for fluorescent bioimaging:a review. *Microchimica Acta*, *184*, 343-368.

https://doi.org/10.1007/s00604-016-2043-9

[5] Bie, Z., Chen, Y., Li, H., Wu, R., & Liu, Z. (2014). Off-line hyphenation of boronate affinity monolith-based extraction with matrix-assisted laser desorption/ionization time-of-flight mass spectrometry for efficient analysis of glycoproteins/glycopeptides. *Analytica chimica acta*, *834*, 1-8. https://doi.org/10.1016/j.aca.2014.04.035

[6] Rafiee, F., Tajfar, N., & Mohammadnejad, M. (2021). The synthesis and efficiency investigation of a boronic acid-modified magnetic chitosan quantum dot nanocomposite in the detection of Cu2+ ions. *International Journal of Biological Macromolecules*, *189*, 477-482. https://doi.org/10.1016/j.ijbiomac.2021.08.158

In-situ forming ZnAl layered doubled hydroxide in the presence of Zeolitic Imidazolate Framework as an efficient system for antibacterial drug delivery

Arash Vahdatkhah, Siamak Javanbakht, Reza Mohammadi*

Corresponding Author E-mail: r.mohammadi@tabrizu.ac.ir

Polymer Research Laboratory, Faculty of Chemistry, University of Tabriz, Tabriz, Iran.

Abstract: Drug delivery applications have demonstrated significant potential with the combination of metal-organic frameworks (MOFs) and layered double hydroxides (LDHs). Whereas MOFs are porous materials with a three-dimensional network of metal ions or clusters connected by organic linkers, LDHs are a class of layered materials with a positively charged brucite-like structure. In this procedure, the ZIF-8 compound was synthesized in situ while the Zn Al-LDH compound was first produced using the co-precipitation method. High porosity, high portability, and antibacterial qualities characterize the resultant nanocomposite.

Keywords: antibacterial, layered double hydroxide, nanocomposite, metal-organic frameworks

Introduction

In recent years, the controlled drug release system has gained more attention due to its effectiveness as a pharmacy technique. The primary benefits of controlled drug delivery systems include biocompatibility, inertia, strong mechanical properties, and the capacity to achieve high drug loading. In addition to being safe and simple to prepare, the optimal drug delivery system should prevent burst release by keeping the drug dose at a specific target level for a prolonged amount of time[1]. Porous materials are attractive options for biomedical applications because of their large pore volume, high specific surface area, and adjustable pore size. Research on nanomaterials has gradually included porous materials. Recently, MOFs—a wonderful and novel class of porous materials—have drawn a lot of attention. MOFs are sometimes referred to as porous coordination networks or coordinated polymers. It is possible to produce crystalline solid MOFs by using organic ligands as a bridge or a flat pack of metal connecting points[2]. Several industries have expressed a great deal of interest in these materials, including luminescence sensors, drug delivery systems, gas storage and separation, and catalysis. Because of their innate characteristics, which include their increased biocompatibility, biodegradability, and ability to hold medication, MOFs have become serious candidates for use as drug carriers. LDHs have shown appetitive properties due to their high drug-loading capacity, pH-dependent drug release pattern, low toxicity, and enhanced cellular internalization[3].

Experimental Section

2-Methylimidazole (Molecular weight 82,11 g/mol, 2-MIM, 99%), zinc nitrate hexahydrate (Zn(NO3)2•6H2O), aluminum nitrate nonahydrate (Al(NO3)3•9H2O) and ethanol (AR) were all purchased from Merck Co.

To generate ZIF-8-MOF/ZnAl-LDH, first ZIF-8-MOF was set up using the coprecipitation method under the following conditions: 1.22 g of zinc nitrate hexahydrate and 3.125 g of aluminum nitrate nonahydrate was combined in water (95 °C) and at a pH of 10 for a full day. After that, we added 1.29 g of 2-methylimidazole and 0.58 g of zinc nitrate hexahydrate to the ZnAl-LDH and ethanol (AR) solution at room temperature.
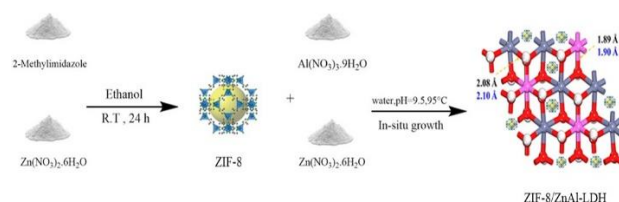
Results and Discussion

To gain a better understanding of the interactions between various substances, in-situ synthesis of ZnAl-LDH/ZIF-8 and FT-IR analysis were considered. The stretching vibrations of the -C-H and -C- -N-, as well as the in-plane bending vibration of the imidazole ring, are responsible for the characteristic absorption peaks for ZIF-8, which are located at 2930 cm-1 and 1576 cm-1, respectively[4]. This supports the in situ forming of ZnAl-LDH/ZIF-8 (Fig 1). The diffraction peaks of LDH-affected samples, which have reflections of 003, 006,009, 110, and 113, represent the typical layered double hydroxide structure, as seen in Fig 2. On the Zn-Al LDH surface, new emerging peaks at 7.3, 12.5, and 18.1, which correspond to the 001, 112, and 220 planes of ZIF-8, [5]are found subsequent to in-situ ZIF-8 growth (Fig 2). The Ceftriaxone (CFX) cumulative release profile from the ZnAl-LDH/ZIF-8 loaded with CFX in PBS at pH 7 point 4 is displayed in Fig 3. The release profile, i.e., shows low initial burst release.

22nd Iranian Chemistry Congress (ICC22)
Iranian Research Organization for Science and
Technology (IROST)
13-15 May 2024

03231-97589

IROST

E. E[1]. Twenty-three points one percent is released after twelve hours, followed by a long-lasting release of sixty-three points one percent for up to 120 hours[6]. ZIF-8 particles have a distinct rhombic crystalline structure, and the synthesized Zn–Al LDH has a flake-like morphology with a smooth surface, as demonstrated by the SEM images (Fig. 4)[7].
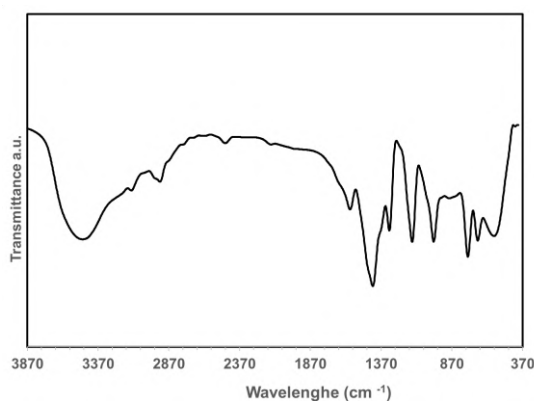
Fig. 1. FT-IR spectra for the ZIF-8-MOF/ZnAl-LDH.
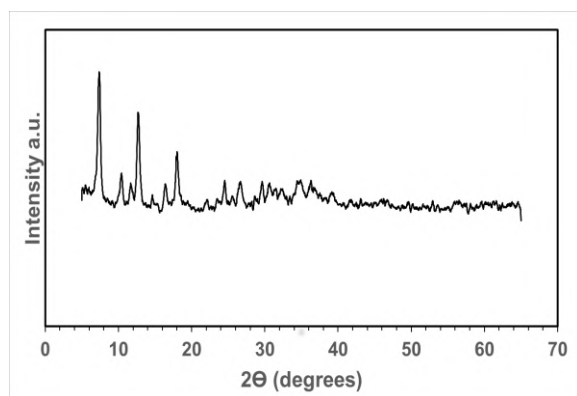
Fig. 2. The XRD pattern of ZIF-8-MOF/ZnAl-LDH.
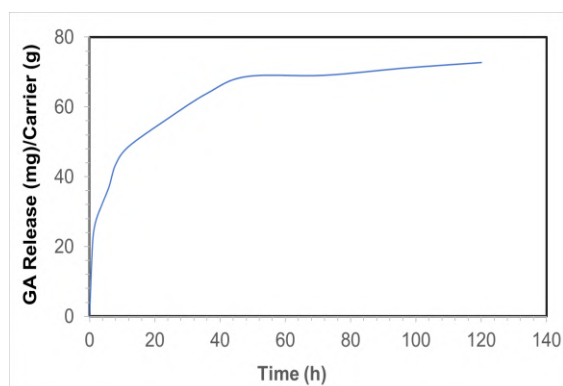
Fig. 3. CFX release behavior of ZIF-8-MOF/ZnAl-LDH.
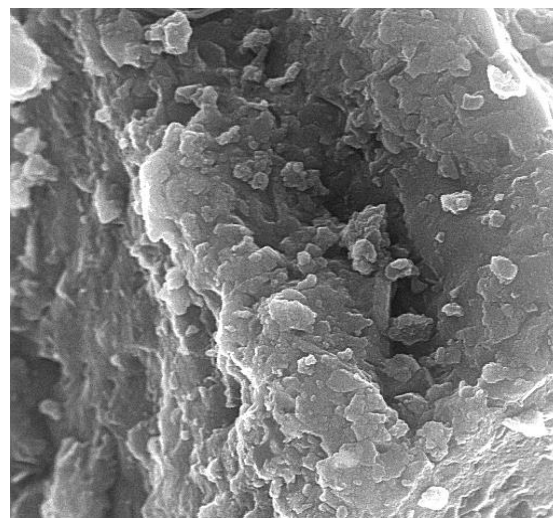
Fig. 4. SEM image of the ZIF-8-MOF/ZnAl-LDH.

Conclusions

The in-situ growth method is used to produce LDH/ZIF-8 nanocontainers. MOFs, a fascinating and relatively new class of porous materials, have attracted a lot of attention. Because of their high drug-loading capacity, pH-dependent drug release pattern, low toxicity, and enhanced cellular internalization, lipoprotein dispersants (LDHs) have demonstrated promising potential in the field of drug delivery. In this study, a layered double hydroxide was present, and a metal-organic framework was created using the co-precipitation technique. Numerous features were present in the ZnAl-LDH/ZIF-8 composite, such as increased porosity, better drug loading and releasing quantity, and enhanced antibacterial qualities.

References

[1]   Ran, F., et al., *Boosting the charge storage of layered double hydroxides derived from carbon nanotube-tailored metal organic frameworks.* Electrochimica Acta, 2019. **301**: p. 117-125.

[2]   Pooresmaeil, M. and H. Namazi, *D-mannose functionalized MgAl-LDH/Fe-MOF nanocomposite as a new intelligent nanoplatform for MTX and DOX co-drug delivery.* International Journal of Pharmaceutics, 2022. **625**: p. 122112.

[3]   Karimi, S., H. Rasuli, and R. Mohammadi, *Facile preparation of pH-sensitive biocompatible alginate beads havening layered double hydroxide supported metal-organic framework for controlled release from doxorubicin to breast cancer cells.* International Journal of Biological Macromolecules, 2023. **234**: p. 123538.

[4]   Zhou, C., et al., *Smart waterborne composite coating with passive/active protective performances using nanocontainers based on metal organic frameworks derived layered double hydroxides.* Journal of Colloid and Interface Science, 2022. **619**: p. 132-147.

[5]   Darvishi, S., et al., *Ultrasound-assisted synthesis of MIL-88 (Fe) coordinated to carboxymethyl cellulose fibers: A safe carrier for highly sustained release of tetracycline.* International Journal of Biological Macromolecules, 2021. **181**: p. 937-944.

[6]   Cánepa, C., et al., *Development of a drug delivery system based on chitosan nanoparticles for oral administration of interferon-α.* Biomacromolecules, 2017. **18**(10): p. 3302-3309.

[7]   Qu, F., et al., *Metal-organic frameworks-derived porous ZnO/Ni0. 9Zn0. 1O double-shelled nanocages as gas sensing material for selective detection of xylene.* Sensors and Actuators B: Chemical, 2017. **252**: p. 649-656.

Modifying Chitosan with Arginine Peptides to Prepare Novel Nanocomposites for Biomedical Applications

Sara Torkaman, Seyed Heydar Mahmoudi Najafi, Alireza Ashori

Corresponding Author E-mail: storkaman91@yahoo.com

Department of Chemical Technologies, Iranian Research Organization for Science and Technology (IROST), Tehran, Iran.

Abstract: In this work, chitosan was chemically modified via selective reactions with arginine to synthesize novel nanocomposites. Protection, activation, and coupling steps resulted in peptide bonds formation between the components. Spectroscopic characterization verified successful derivatization. Decreasing crosslinker density enhanced nanocomposite hydrophilicity and swelling capacity, tailoring properties for potential usage as antibacterial wound dressings.

Keywords: Chitosan; Arginine; Coupling reaction; Nanocomposite

Introduction

Chitosan, a positively charged biopolymer, has attracted growing scientific interest for its potential multifunctional applications. Through chemical and physical modifications, researchers have aimed to enhance chitosan's utility by altering its intrinsic properties [1]. One promising approach involves grafting monomers or polymers onto the chitosan backbone to generate derivatives with tailored attributes [2].

Various monomers and polymers have been grafted onto chitosan, including acrylic acid , vinyl alcohol, methyl methacrylate, polystyrene, and epichlorohydrin. Additionally, grafting chitosan with amino acids and peptides has been explored. Arginine, known for its antibacterial guanidine group [3], has been incorporated into chitosan derivatives. For example, Antunes *et al.* developed chitosan/arginine nanofibers with promising hydrophilicity, porosity and bacteriostatic activity as potential wound dressing materials [4].

This work focuses on the synthesis of a novel chitosan-arginine composite via selective formation of peptide bonds between the nitrogen of chitosan and carbon of arginine. This covalent modification aims to generate an improved biomaterial by integrating the beneficial features of both chitosan and arginine.

Experimental Section

The experimental was carried out first by acetylated chitosan using acetic acid followed by protection of arginine functional groups. Degree of acetylation of chitosan was obtained through titration method. Then coupling reaction performed using DCC (Dicyclohexyl carbodiimide) as a coupling agent at room temperature. Solution casting method were used to prepare nanocomposites with deferent ratio of crosslinkers. TLC (Thin-Layer Chromatography), FT-IR (Fourier Transform Infrared) and NMR (Nuclear Magnetic Resonance) spectroscopeis were used for chemical characterization. Also, after preparing composites swelling water tests were performed. The swelling ratio was calculated using the following equation:

Swelling (%) = $(W_s - W_d)/W_d \times 100$

where W_s is the swollen weight of the nanocomposite film and W_d is the dry weight.

Results and Discussion

Table 1 compares the key infrared (FT-IR) absorption peaks observed for chitosan, protected chitosan, and coupled chitosan-arginine derivatives. As seen, for unmodified chitosan, broad absorption bands at 3200-3500 cm^{-1} correspond to O-H and N-H stretching vibrations. The peak at 1640 cm^{-1} represents the C=O stretching of the amide bond.

After protection, new peaks appear indicating successful functional group modification. A peak at 1740 cm^{-1} corresponds to the C=O stretch of a newly formed ester bond. The amide C=O shifts from 1640 to 1660 cm^{-1} due to the electronic changes around the bond.

For the coupled chitosan-arginine product, a peak emerges at 1656 cm^{-1} representing the C=O stretch of a new carbamate bond formed between chitosan and arginine.

Table1: FT-IR Analysis summarizing key spectral changes during chitosan modification and arginine coupling.

Chitosan	Protected chitosan	Coupled chitosan
N-H, O-H 3200-3500 (broad)	Ester C=O 1740	Carbamate 1656
Amide C=O 1640	Amide C=O 1660	Amide C=O 1600

22nd Iranian Chemistry Congress (ICC22)
Iranian Research Organization for Science and Technology (IROST)
13-15 May 2024

03231-97589

Additionally, the amide C=O shifts again to around 1600 cm^{-1}, verifying peptide bond formation between the two components. The progressive infrared spectral changes confirm the stepwise chemical modifications from chitosan to the final coupled derivative. The shifts in amide C=O peaks demonstrate the electronic variations resulting from protection and coupling reactions. The emergence of new ester and carbamate peaks also verifies the incorporation of new functional groups. Overall, the infrared data supports the successful synthesis of the chitosan-arginine nanocomposites via the selective coupling approach.

Figure 1 shows the swelling ratio of chitosan-arginine nanocomposites prepared with different crosslinker ratios. The swelling ratio increased as the crosslinker ratio decreased. The nanocomposite with a crosslinker ratio of 1:2 showed the highest swelling of around 850%. In contrast, the swelling ratio of the nanocomposite with a 1:8 crosslinker ratio was only around 300%. This trend can be explained by the increased hydrophilicity of the nanocomposites with lower crosslinker ratios. The crosslinker contains hydrophobic groups that reduce the overall hydrophilicity of the nanocomposites. At higher crosslinker ratios, there are more hydrophobic groups, resulting in decreased swelling capacity. Conversely, reducing the crosslinker ratio increases the relative number of hydrophilic groups from chitosan and arginine.
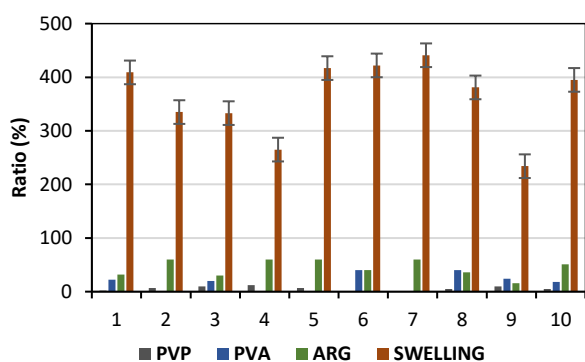
Fig. 1: Swelling ratio of chitosan-arginine nanocomposites as a function of crosslinker ratio.

The amine and hydroxyl groups on chitosan alongside the guanidinium groups on arginine promote water absorption and swelling. Therefore, decreasing the crosslinker density enhances the hydrophilicity and swelling ability of the nanocomposites.

Conclusions

This work demonstrated the successful synthesis of novel chitosan-arginine nanocomposites via selective coupling reactions. The stepwise chemical modifications were verified through characterization techniques like FT-IR and NMR spectroscopies. The data confirmed the incorporation of new functional groups and formation of peptide bonds between chitosan and arginine. Tailoring of the crosslinker ratio allowed modulation of hydrophilicity and swelling capacity of the nanocomposites. Lower crosslinker densities increased the relative content of hydrophilic groups, enhancing water absorption and swelling properties. The chitosan-arginine nanocomposites exhibited promising features like antibacterial activity, biocompatibility, and tunable hydrophilicity that make them suitable for biomedical applications. In particular, these materials show potential for use as antibacterial wound dressings. The versatility of the coupling approach also enables attachment of other beneficial biomolecules to further customize the properties.

References

[1] Negm, N. A., Hefni, H. H. H., Abd-Elaal, A. A. A., Badr, E. A., & Abou Kana, M. T. H. (2020). Advancement on modification of chitosan biopolymer and its potential applications. *International Journal of Biological Macromolecules, 152*, 681-702.

https://doi.org/10.1016/j.ijbiomac.2020.02.196

[2] Tang, W., Wang, J., Hou, H., Li, Y., Wang, J., Fu, J., Lu, L., Gao, D., Liu, Z., Zhao, F., Gao, X., Ling, P., Wang, F., Sun, F., & Tan, H. (2023). Review: Application of chitosan and its derivatives in medical materials. *International Journal of Biological Macromolecules, 240*, 124398. https://doi.org/10.1016/j.ijbiomac.2023.124398

[3] Bijle, M. N., Ekambaram, M., Lo, E. C. M., & Yiu, C. K. Y. (2020). Antibacterial and mechanical properties of arginine-containing glass ionomer cements. *Dental Materials, 36*(9), 1226-1240.

https://doi.org/10.1016/j.dental.2020.05.012

[4] Antunes, B. P., Moreira, A. F., Gaspar, V. M., & Correia, I. J. (2015). Chitosan/arginine-chitosan polymer blends for assembly of nanofibrous membranes for wound regeneration. *Carbohydrate Polymers, 130*, 104-112. https://doi.org/10.1016/j.carbpol.2015.04.072

22nd Iranian Chemistry Congress (ICC22)
Iranian Research Organization for Science and Technology (IROST)
13-15 May 2024

03231-97589

IROST

Optimizing Tensile Strength and Flexibility in Eco-friendly Chitosan Biocomposites Using Glutamic Acid as Crosslinking Agent

Sara Torkaman, Alireza Ashori, Seyd Heydar Mahmoudi Najafi

Corresponding Author E-mail: storkaman91@yahoo.com

Department of Chemical Technologies, Iranian Research Organization for Science and Technology (IROST), Tehran, Iran.

Abstract: Eco-friendly glutamic acid crosslinked chitosan biocomposites with poly(vinyl alcohol)/poly(vinyl pyrrolidone) were synthesized and tested to optimize the tensile strength and flexibility through composition tuning. Varying the ratios of modified chitosan, PVA/PVP, and benign crosslinker allowed custom tailoring of mechanical properties for the diverse applications.
Keywords: Chitosan-based composite; Crosslinking; Mechanical properties

Introduction

Chitosan is a versatile biopolymer used widely in scientific research and industrial applications due to properties like biocompatibility, biodegradability, and nontoxicity. However, the intrinsic mechanical properties of chitosan are poor, limiting its usage. Numerous chemical and physical methods can reinforce chitosan's mechanical performance [1]. One approach involves utilizing crosslinking agents like glutaraldehyde and genipin to form rigid structural networks. However, toxicity concerns arise when applying certain crosslinkers in biomedical contexts [2]. An alternative strategy entails compositing chitosan with polymers having superior mechanical attributes to produce synergistic effects [3].

This work focuses specifically on augmenting the mechanical properties of chitosan composites through an eco-friendly crosslinking approach. Glutamic acid is employed as a nontoxic crosslinking agent for chemical modification of the composite matrix. The goal is developing reinforced green composites with the biocompatibility necessary for applications in wound healing, drug delivery, and beyond. The mechanical effects of the green crosslinker on the ultimate tensile strength and flexibility of the synthesized chitosan composites is investigated.

Experimental Section

The chitosan composites were prepared using a solvent casting technique. First, chitosan was chemically modified to improve its solubility and reactivity. This modified chitosan was then dissolved at 2 wt% in a 1% acetic acid solution. Separately, poly(vinyl alcohol) (PVA) and poly(vinyl pyrrolidone) (PVP) were co-dissolved at varying PVA/PVP ratios into deionized water. Glutamic acid as a crosslinking agent was added to the PVA/PVP solution at prescribed concentrations between 0 - 0.04 wt%. The chitosan and PVA/PVP solutions were combined under vigorous stirring for 30 minutes to ensure thorough mixing. The resulting homogeneous solutions were poured into polytetrafluorethylene molds and dried for 48 hours at 40°C to obtain solid composite films. Eight unique formulations were produced by varying the ratios of modified chitosan (30-90%), PVA/PVP (0.25-10%), and glutamic acid (0-0.04%) as shown in Table 1. This enabled systematic investigation on how composition influences the tensile properties. The composite films were cut into rectangular specimens of 5 mm wide by 50 mm long for tensile testing. The tests were conducted on a universal testing machine per ASTM D638 at a crosshead speed of 5 mm/min. The stress-strain data was collected until specimen failure to determine the ultimate tensile strength as well as flexibility from the strain-to-failure. Five samples were tested for each formulation and the results averaged.

Results and Discussion

Figure 1 shows stress-strain curves for various formulations of crosslinked chitosan composites. The different curves represent composites with varying ratios of modified chitosan, PVA/PVP, and the crosslinking agent glutamic acid, as outlined in Table 1. Overall, the figure demonstrates that both the tensile strength and flexibility of the composites are significantly impacted by changes in formulation.

Table1: Component ratios for glutamic crosslinked chitosan/PVA/PVA composite formulations.

NO.	Modified chitosan (%)	PVA: PVP	Cross linking agent (%)
1	60	1	0.04
2	80	0.25	0
3	90	1	0.02
4	50	1.5	0.02

22nd Iranian Chemistry Congress (ICC22)
Iranian Research Organization for Science and Technology (IROST)
13-15 May 2024

03231-97589

NO.	Modified chitosan (%)	PVA: PVP	Cross linking agent (%)
5	40	5	0.04
6	60	2	0.03
7	60	10	0
8	30	3	0.01

Specifically, the composite with 90% modified chitosan, PVA:PVP ratio of 1, and 0.02% crosslinker (row 3) exhibited the highest ultimate tensile strength of approximately 65 MPa. This suggests that a high chitosan ratio along with minimal crosslinking allows for rigid network formation, transferring load efficiently. In contrast, the formulation with just 30% chitosan and 0.01% crosslinker (row 8) displayed low strength around 10 MPa but maintained integrity up to over 35% strain, indicating flexibility and deformability. Between these extremes, tunable mechanical properties are achieved, with composite 6 balancing strength near 45 MPa and ductility up to 20% strain.

In summary, the stress-strain profiles provide quantifiable confirmation that both strength and flexibility of green crosslinked chitosan composites can be optimized through careful control of composition and crosslink density. Specifically, high chitosan and low crosslinker favors rigidity and brittle fracture, while the inverse distribution improves ductility at the expense of tensile performance. These structure-processing-property relationships offer guidance in tailoring the materials for diverse applications from wound dressings to tissue scaffolds.
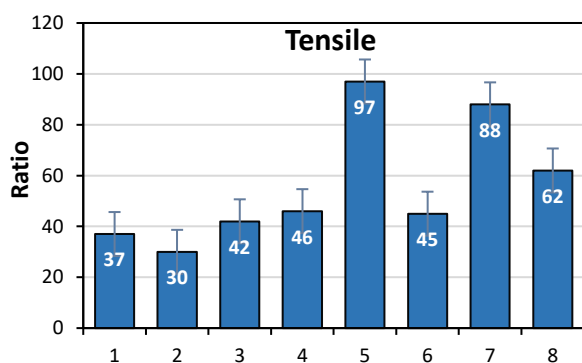

Fig.1: Stress-strain curves for crosslinked chitosan composites with varying formulations.

Conclusions

In this work, eco-friendly glutamic acid crosslinked chitosan composites were fabricated and their tensile properties thoroughly examined as a function of composition. The stress-strain profiles demonstrate that mechanical performance can be tuned based on the ratios of modified chitosan, PVA/PVP, and crosslinking agent.

Specifically, increasing chitosan content to 90% with minimal 0.02% crosslinker produces rigid yet brittle films with enhanced strength near 65 MPa. In contrast, higher proportions of PVA/PVP plasticizer and minimal 0.01% crosslinks improve composite flexibility and ductility, albeit with reduced strength around 10 MPa. Balanced formulations are able to achieve intermediate properties, combining tensile strength exceeding 45 MPa and extensibility over 20% strain.

These composition-processing-property relationships confirm that glutamic acid is an effective crosslinker for reinforcing chitosan green composite matrices. The level of crosslinking and resulting network density plays a key role in determining the mechanical characteristics. By optimizing the formulation, custom chitosan composites can be designed to meet application needs from biomedical scaffolds to food packaging films. Further analyses of additional performance metrics like impact resistance, degradation rate, and cytotoxicity will help widen the usage of these eco-friendly materials. Nonetheless, this initial investigation of engineering tensile strength and flexibility via tuning composition establishes a strong foundation for enabling sustainable chitosan composite technologies through benign crosslinking strategies.

References

[1] Qin, Y., Chen, X., Li, B., Guo, Y., Niu, Z., Xia, T., Meng, W., & Zhou, M. (2021). Study on the mechanical properties and microstructure of chitosan reinforced metakaolin-based geopolymer. *Construction and Building Materials, 271*, 121522. https://doi.org/10.1016/j.conbuildmat.2020.121522

[2] Sanchez-Salvador, J. L., Balea, A., Monte, M. C., Negro, C., & Blanco, A. (2021). Chitosan grafted/cross-linked with biodegradable polymers: A review. *International Journal of Biological Macromolecules, 178*, 325–343. https://doi.org/10.1016/j.ijbiomac.2021.02.200

[3] Liu, X. Q., Zhao, X. X., Liu, Y., & Zhang, T. A. (2022). Review on preparation and adsorption properties of chitosan and chitosan composites. *Polymer Bulletin, 79*(4), 2633–2665. https://doi.org/10.1007/s00289-021-03626-9

22nd Iranian Chemistry Congress (ICC22)
Iranian Research Organization for Science and Technology (IROST)
13-15 May 2024

03231-97589

Thiocyanate coordination mode in a cycloplatinated(II) complex: a fraction of whole

Fatemeh Abdolvand, Mahshid Nikravesh, Hamid R. Shahsavari*

Corresponding Author E-mail: shahsavari@iasbs.ac.ir

Department of Chemistry, Institute for Advanced Studies in Basic Sciences (IASBS), Zanjan 45137-66731, Iran.

Abstract: A cycloplatinated(II) complex with a thiocyanate ligand was prepared, and its coordination mode with the Pt centre was studied using experimental and computational methods. Calculations were performed on the transition state of the title complex in order to demonstrate the isomerization reaction pathway for it.

Keywords: Cycloplatinated complex; Thiocyanate; Theoretical calculations.

Introduction

In recent years, cycloplatinated(II) complexes have received significant attention due to their photophysical characteristics [1]. These complexes can be modified by altering the auxiliary ligands, allowing for versatile applications in various fields [2]. The chalcogenocyanate complexes of Pt(II), particularly those with an oxygen group, have drawn attention [3]. These complexes feature a C^N cyclometalated ligand occupying two coordination sites and forcing pseudohalide ligands to adopt *cis* positions. Previous research on highly emissive cycloplatinated(II) phosphine complexes resulted in the discovery of thiocyanate and cyanide-containing compounds [3].

Experimental Section

To a solution of **A** (200 mg, 0.31 mmol) in CH_2Cl_2 (20 mL) was added 1.3 equivalent of AgSCN (67 mg, 0.41 mmol). The reaction mixture was stirred for a day in the dark at room temperature before being filtered through cotton/Celite in a glass Pasteur pipette to remove AgCl. The resultant green solution was concentrated to a small volume (1 mL), and *n*-hexane (5 mL) was added to precipitate **1** as green solid.

Results and Discussion

The previously reported complex [PtCl(ppy)(PPh₃)], **A** [4], where ppy = 2-phenylpyridine, is treated with silver thiocyanate under an inert atmosphere at room temperature to yield [Pt(NCS-κN)(ppy)(PPh₃)], **1**, as a pure and stable solid. The successful synthesis of **1** has been confirmed by mass spectrometry and NMR spectroscopy, although these methods are insufficient to identify the coordination mode of the thiocyanate ligand. Because of this, we performed density functional theory (DFT) to gain a better understanding of how this ligand can be bound to the platinum centre. We optimized two proposed isomers, in which the SCN ligand is bound to the Pt atom once through the N atom, Pt–NCS-κN (*i.e.* **1**), and the secondly through its S atom, Pt–SCN-κS ([Pt(SCN-κS)(ppy)(PPh₃)], **1'**), in solution and gas phase (Scheme 1).
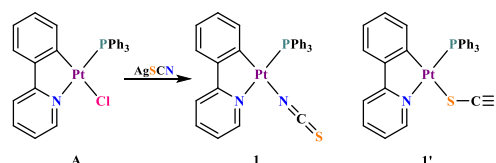
Scheme 1: Synthetic pathway for the preparation of thiocyanate cycloplatinated(II) complex. Both proposed isomers and the ligand numbering are depicted.
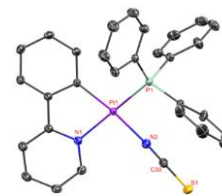
Fig.1: The crystal structure of **1**, with the hydrogens omitted for clarity.

To ascertain the molecular structure of **1**, single-crystal XRD was performed (Fig. 1). It indicates that the thiocyanate moiety is bound preferentially in a side-on coordination mode *via* the N terminal and is *trans* to the ligating carbon of ppy.

Conclusions

In summary, the coordination mode of the thiocyanate ligand was determined using computational methods and X-ray structure determination. The stability of the complex's two isomers was calculated, *i.e.* **1** and **1'**, and the more stable structure, **1**, was investigated. A transition state for the isomerization reaction of SCN was also presented and confirmed through calculations.

References

[1] Berenguer, J. R.; Lalinde, E.; Moreno, M. T., *Coord. Chem. Rev.* 2018, *366*, 69-90.

[2] Chan, A. K.-W.; Ng, M.; Wong, Y.-C.; Chan, M.-Y.; Wong, W.-T.; Yam, V. W.-W., *J. Am. Chem. Soc.* 2017, *139*, 10750-10761.

[3] Sivchik, V.; Sarker, R. K.; Liu, Z. Y.; Chung, K. Y.; Grachova, E. V.; Karttunen, A. J.; Chou, P. T.; Koshevoy, I. O., *Chem. Eur. J.* 2018, *24*, 11475-11484.

[4] Shahsavari, H. R.; Babadi Aghakhanpour, R.; Nikravesh, M.; Ozdemir, J.; Golbon Haghighi, M.; Notash, B.; Beyzavi, M. H., *Organometallics* 2018, *37*, 2890-2900.

Preparation of eco-friendly nanocomposites based on immobilization of magnetic activated carbon with citric acid: Application for catalytic activity in C-N coupling reaction

Seyede Sara Mousavifard, Reza Ranjbarkarimi*, Vajihe Nejadshafee

Corresponding Author E-mail: mikamousavifard@gmail.com ,r.ranjbarkarimi@vru.ac.ir

Abstract: A novel catalyst based on activated carbon merged with magnetic nanoparticles was prepared and its surface was modified with citric acid derivative (Cit@MAC NCs). Then with loading of Pd NPs onto the nanocomposite, the Pd-Cit@MAC NCs catalyst was synthesized and was studied for the C-N and carbon-hetero atom coupling reaction of benzothiazol and phenyl boronic acid under green condition. The nanocomposites exhibited good reusability and was separated easily from an aqueous solution with an external magnet.

Keywords: nanoparticle; Pd-Cit@MAC NCs; magnetic activated carbon.

Introduction

The formation of carbon-carbon bonds is a fundamental reaction in organic synthesis due to its many applications in the field of bioactive compounds and natural products with high efficiency [1]. N-aryl heterocyclic compounds are important organic structures in various natural products and drugs, and also as precursors [2]. Activated carbons are excellent performance materials with their highly porous and surface area that have great potential as adsorbents for cleaning and purification of wastewater and, also as catalyst for organic reaction [3,4]. Recently, the production of activated carbon using agricultural wastes has increased remarkably due to their low production cost, environmentally friendly and large supply [5,6]. Magnetic activated carbon (MAC) composites are combination of AC and magnetic oxides [7–10]. Which, with loading metal complex onto MAC structure as heterogeneous catalysis have a high application in organic reaction due to the large surface area, high catalytic active sites, chemical stability, efficient and easy separation of the catalysts from a reaction mixture with an external magnet and high reusability [11]. In this study, the Pd-Cit@MAC NCs as catalyst was applied for C-N coupling reaction of benzothiazoles with phenylboronic acid in mild conditions and in high yields and short reaction times.

Experimental Section

Materials Raw pistachio shells were obtained from pistachio trees in Rafsanjan city. Ferric chloride hexahydrate, 1,4-butane sultone were purchased from Merck company. Pb (OAC) $_2$, HNO$_3$, CH$_3$CN, and ammonium (25%) were purchased from Sigma-Aldrich.

Preparation of Pd-Cit@MAC NCs

The preparation of Pd-Cit@MAC NCs: consists of three steps; 1) for the synthesis of activated carbon (AC), the raw pistachio shells were used from pistachio trees in Rafsanjan city. The shells were washed thrice with deionized water and dried at 358 K for 24 h in an oven and were crushed using a ball mill into dimensions 1–2 mm, then were carbonized by heating the sample in a muffle furnace at 750 ºC for 1 h. Subsequently, the obtained product was activated at 900 °C under steam using the bench furnace for 12 h duration. The granulated activated carbon was soaked in 50% HNO$_3$ solutions (69% HNO 3) at 50 °C for 10 h and then thoroughly washed with deionized water, and dried in an oven at 70 ºC for 12 h.

2) Loading of AC with Fe$_3$O$_4$ NPs (MAC); an appropriate amount of FeCl$_3$ .6H$_2$O (50 mL, 0.3 M) was added to HCl (0.5 mL, 0.2 M) and the reaction beaker was sonicated under irradiation of 85 kHz for 5 min. Then a solution of Na$_2$SO$_3$ (20 mL, 0.3 M) was added into 40 mL of the above solution and was sonicated, while the yellow color of the solution was obtained again. In the following, the AC powdered (1 g) was added to the mixture and the resulting solution was poured into 400 mL of water containing of ammonium (60 mL, 25%) and the reaction was followed by sonication for 30 min. The obtained MAC was collected by an external magnet, washed with water and dried under vacuum at 50 ºC for 24 h.

3) Immobilization of MAC with citric acid derivate (Cit@MAC NCs); initially, citric acid (0.006 mol) was added thiosemicarbazide (0.003 mol), then the reaction mixture was stirred for 24 h. After this time, the solid was washed with chloroform solvent. The MAC (0.4 g) was dispersed in 10 mL EtOH for 15 min, then citric acid derivate (0.40 g) was added to the dispersed MAC and the reaction mixture was stirred at 60 ºC for 12 h. The magnetic nanocomposites (Cit@MAC NCs) was separated by an external magnet and washed with deionized water/EtOH and dried overnight in a vacuum oven at 60 º C. Finally, the Cit@MAC NPs (0.5 g) was added to a mixture of palladium (II) chloride (0.035 g) and 20 mL solvent (H$_2$ O/MeOH 1:1). The mixture was continuously stirred and refluxed for 24 h at 70 o C. The

magnetic nanocomposite was separated by an external magnet and washed thoroughly with distilled water and dried under vacuum at 70 °C for 5 h to give the catalyst Pd-Cit@MAC NPs.

Typical procedure for the C-N coupling reaction

A mixture of iodobenzene (1.2 mmol), Pd-Cit@MAC NCs catalyst (8 mol %, 0.01 g) and K_2CO_3 (2 mmol) was stirred in $EtOH:H_2O$ (1:1 mL) for 5 minutes. Phenylboronic acid (1mmol) was added to the above mixture and the mixture was vigorously stirred at room temperature for 30 min. The reaction was monitored through Thin Layer Chromatography (TLC). Then, the reaction mixture was diluted with water, and the catalyst was separated by magnetically. The mixture was extracted with CH_2Cl_2 (2×10 ml), and the combined organic layer was dried over $MgSO_4$. The solvent was removed by evaporation in vacuum. The residue was purified by crystallization or, if necessary, silica gel column chromatography.

Results and Discussion

Nanocomposites characterization FTIR (Brucker, TENSOR 27 spectrophotometer) was performed to analyze the chemical functional groups on the Pd-Cit@MAC NCs. Comparison of the FTIR spectra of AC and MAC shows that the peak at 571 cm^{-1} is related to the Fe-O bond (Figure. 1a), which indicates the loading of magnetic nanoparticles onto the AC structure. In Figure. 1b, the main peaks at 1391 and 1578 cm^{-1}, belong to the stretching vibration of C-O; and C=O; of tartaric acid group. Also the peak intensity of Fe-O in Cit@MAC NCs has decreased compared to the MAC structure which confirms the immobilization of the tartaric acid group onto Cit@MAC NCs. The IR spectrum of Pd-Cit@MAC NCs exhibited that all bands of Cit@MAC NCs were retained after loading Pd NPs on the surface of Cit@MAC NCs (Figure. 1c).
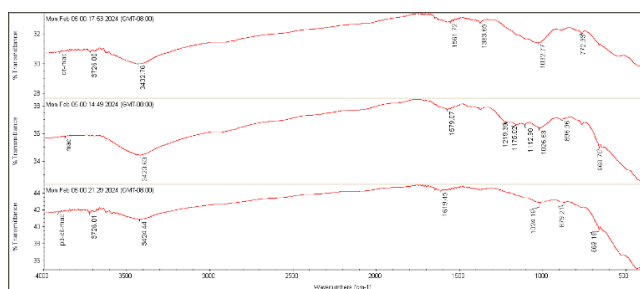
Fig.1: FT-IR spectra of (a) MAC, (b) Cit@MAC NCs and (c) Pd-Cit@MACNCs.

Conclusions

In this research, the preparation of novel nanocomposites was successfully performed using pistachio nut shell as a natural and low-cost precursor. In order to increase the active sites and easy magnetic separation of the nanocomposites from the reaction environment of aqueous contaminants, the nanocomposites surface was immobilized with Fe_3O_4 NPs and citric acid derivate. The prepared Pd-TAR@MAC NCs were applied as nanocatalyst for C–N coupling reaction under mild condition. One of the advantages of this catalyst for the C–N coupling reaction, it was that the reaction was done in accordance with the principles of green chemistry and with a short reaction time and high yields.

References

[1] V, Nejadshafiee And Mohammad Reza Islami, Materials Science & Engineering C. 101 (2019).

[2] F, Maghsoodi Goushki, M, R, Islami, V, Nejadshafiee, Materials Science & Engineering B. 277 (2022) 36–48.

[3] A.G.M. Shoaib, A. El-Sikaily, A. El Nemr, A.E.D.A. Mohamed, A.A. Hassan, Biomass Conversion and Biorefinery. (2020).

[5] A.A. Ahmad, A.T.M. Din, N.K.E. Yahaya, A. Khasri, M.A. Ahmad, Arabian Journal of Chemistry. 13 (2020) 6887–6903.

[6] J.A. Villamil, E. Diaz, M.A. de la Rubia, A.F. Mohedano, Molecules. 25 (2020).

[7] L. Spessato, A.L. Cazetta, S. Melo, O. Pezoti, J. Tami, A. Ronix, et al., Journal of Molecular Liquids. 300 (2020) 112282.

[8] Y. Jiang, Q. Xie, Y. Zhang, C. Geng, B. Yu, J. Chi, Int J Min Sci Technol. 29 (2019) 513–519.

[9] Y. Liu, Z. Huo, Z. Song, C. Zhang, D. Ren, H. Zhong, et al., J Taiwan Inst Chem Eng. 96 (2019) 575–587.

[10] I.S.K. S. Ullah, M. Hashmi, N. Hussain, A. Ullah, M.N. Sarwar, Y. Saito, S.H. Kim, Journal of Water Process Engineering. 33 (2020) 101111.

[11] M. Iwanow, T. Gärtner, V. Sieber, K. Burkhard, Beilstein J Org Chem. 16 (2020) 1188–1202.

22nd Iranian Chemistry Congress (ICC22)
Iranian Research Organization for Science and Technology (IROST)
13-15 May 2024

03231-97589

IROST

The synthesis of a catalytic composite comprising MOF@POM@IL compounds using novel methods for application in the oxidative desulfurization process

Aliakbar Feyzi [a], Seyed Reza Shabanian*[b]

Corresponding Author E-mail: r_shabanian@yahoo.com

[a] PhD student in chemical engineering, Babol Noshirvani University of Technology, Babol, Mazandaran, Iran.

[b] Associate Professor, Faculty of Chemical Engineering, Babol Noshirvani University of Technology, Babol, Mazandaran, Iran.

Abstract: To enhance the reaction rate of oxidative desulfurization (ODS) process, a binary composite of MOF@POM was synthesized as a catalyst via the bottle-assisted ship (BAS) method. Additionally, for the separation of sulfones, an amphiphilic ionic liquid was utilized as an extraction solvent through the ship-in-bottle (SIB) method and characteristic analyses of this composite were conducted.

Keywords: oxidative desulfurization; Catalyst; Polyoxometalates; Metal organic Frameworks; Ionic Liquis;

Introduction

Considering the necessity of environmental preservation, various methods such as hydrogenation, biological, extraction-based, adsorptive, oxidative, etc., are employed for sulfur removal from fossil fuels, among which the ODS method stands out as one of the most sustainable approaches, either complementing conventional and traditional methods or serving as their alternative [1]. This method generally involves a chemical reaction between an oxidizing agent and sulfur, comprising two distinct stages of sulfur oxidation and separation of sulfoxides and sulfones from the fuel [2]. To enhance the oxidation reaction rate, heterogeneous composite catalysts with high selectivity can be utilized, where composites of polyoxometalate compounds with metal-organic frameworks serve as a useful and effective catalyst for the ODS process [3]. (Figure 1)

Amphiphilic ionic liquids, possessing emulsifying properties and dual selectivity, also serve as suitable options for separating sulfoxides and sulfones converted from fuels [4]. However, in conventional synthesis methods such as wet impregnation and co-precipitation, due to the formation of unstable composites, the catalyst and ionic liquid washing off the support occurs. Yet, in the new bottle-assisted ship (BAS) method, a porous structure (bottle) forms around a large molecule (ship), and in the ship-in-bottle (SIB) method, the anions of the ionic liquid (small components) are dispersed in a preformed porous structure (called bottle), while the cations of the ionic liquid (large molecules) form inside a porous framework (ship) [5], thus washing off the POMs or ILs from the MOFs does not occur.
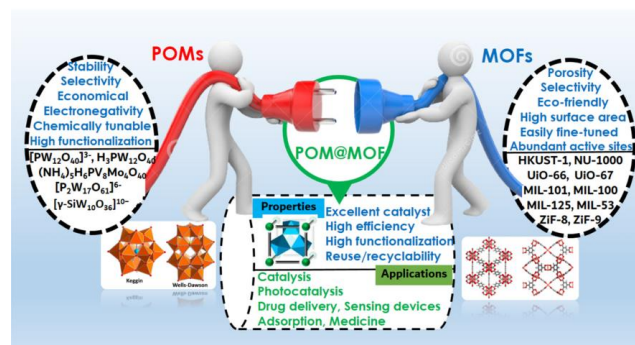
Fig.1: General properties and applications of POMs, MOFs and POMOF-based composites [3]

However, in conventional synthesis methods such as wet impregnation and co-precipitation, due to the formation of unstable composites, the washing off of the catalyst and ionic liquid from the support will occur. Yet, in the new bottle-assisted ship (BAS) method, a porous structure (bottle) forms around a large molecule (ship), and in the ship-in-bottle (SIB) method, the anions of the ionic liquid (small components) are dispersed in a preformed porous structure (referred to as bottle), while the cations of the ionic liquid (large molecules) form inside a porous framework (ship) [3-5], thus, washing off of POMs or ILs from the MOFs does not occur.

Experimental Section

In the process laboratory of the Center of Excellence at Nooshirvani University of Technology (Babol, Iran) initially, ZIF-8, as a compound from the family of MOFs, was synthesized using the conventional synthesis method [4]. Subsequently, employing the BAS strategy, phosphomolybdic acid, as a member of the Keggin-type POM family, was synthesized on it. In the second phase of catalyst composite synthesis using the SIB method, firstly,

22nd Iranian Chemistry Congress (ICC22)
Iranian Research Organization for Science and Technology (IROST)
**13-15 May 2024**

03231-97589

1-methylimidazole as the anion and then 1-bromobutane as the cation of the ionic liquid were deposited on the binary composite ZIF8@HPMO, and characterization analyses were performed on it.

Results and Discussion

Comparison of the XRD and FTIR analyses of the binary composite ZIF8@HPMO with the results of reputable articles [5] in figure 2 indicates that the synthesis of the ZIF8@HPMO binary catalyst has been properly conducted using the BAS method. Furthermore, the comparison of the XRD analysis response of the synthesized composite ZIF8@HPMO@IL with the results of reputable article [55] in figure 3 demonstrates that, in addition to the possibility of synthesizing the catalyst using SIB and BAS methods, the synthesis of this ternary catalyst composite with the BAS method has been properly executed.
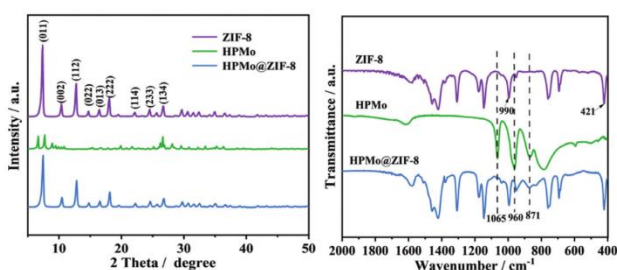
Fig.2: The results of XRD and FTIR tests on two synthesized ZIF8@HPMO and ZIF8 catalysts
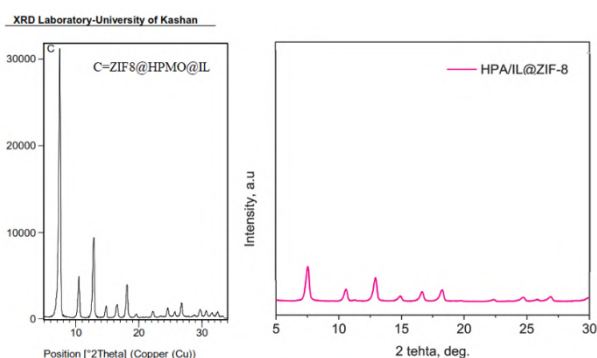
Fig.3: The results of XRD test on the synthesized ZIF8@HPMO@IL catalyst

Conclusions

By utilizing the SIB and BAS methods in the synthesis of catalytic composites, the selectivity and stability of the catalyst and solvent in their deposition onto a material from the metal-organic framework family are preserved. Therefore, to leverage the positive attributes of compounds such as ionic liquids, metal-organic frameworks, and polyoxometalates in processes like ODS, these methods can be employed as simple and acceptable

approaches in the synthesis of composite catalysts in subsequent research and investigations.

References

[1] Jafarinasab, M., Akbari, A., Omidkhah, M., Shakeri, M. (2020). An efficient co-based metal-organic framework nanocrystal (Co-ZIF-67) for adsorptive desulfurization of dibenzothiophene: impact of the preparation approach on structure tuning. Energy Fuels, 34, 12779–12791.

[2] Wei, P., Yang, Y., Li, W., Li, G. (2020). Keggin-POM@rht-MOF-1 composite as heterogeneous catalysts towards ultra-deep oxidative fuel desulfurization. Fuel, 274, 117834.

[3] Abdurrashid, H., Zulkifli, M. A. M., Suleiman, G. M. (2022). Recent advances catalytic oxidative desulfurization of fuel oil- A review. J. of industrial and Engineering Chemistry. 112, 20-36.

[4] Ning, Y. et.al. (2022). Phosphomolybdic acid encapsulated in ZIF-8 based porous ionic liquids for reactive extraction desulfurization of fuels. Inorg. Chem. Front., 9, 165–178.

[5] Nazmul, A. K., Biswa, N. B., Sung, H. J. (2018). Heteropoly acid-loaded ionic liquid @ metal-organic frameworks: Effective and reusable adsorbents for the desulfurization of a liquid model fuel. Chemical Engineering Journal, 334, 2215–2221.

Synthesis, characterization, and anticancer activity of a Ru(II) complex bearing a fluorinated cyclometalated ligand

Yeganeh Abedi[a], Negin Kowsari[a], Sana Yarahmadi[a], Mohammad Seyedhamzeh[b], Aziz Maleki*[b], Hamid R. Shahsavari*[a]

Corresponding Author E-mail: shahsavari@iasbs.ac.ir

[a] Department of Chemistry, Institute for Advanced Studies in Basic Sciences (IASBS), Zanjan 45137-66731, Iran.

[b] Zanjan Pharmaceutical, Nanotechnology Research Center (ZPNRC), and Department of Pharmaceutical Nanotechnology, School of Pharmacy, Zanjan University of Medical Sciences, Zanjan 45139-56184 Iran.

Abstract: A new Ru(II)-arene complex [(*p*-cymene)Ru(dfppy)(OAc)], **1**, bearing 2-(2,4-difluorophenyl)pyridine (dfppy), as a cyclometalated ligand, was prepared by reaction of [(*p*-cymene)RuCl(μ-Cl)]$_2$, **A**, and dfppy in presence of sodium acetate, NaOAc. The complex **1** was characterized by means of various spectroscopic and analytical techniques. On several different human cancer cell lines, and a normal cell, the cytotoxic activities of these compounds were tested. Complex **1** demonstrated good to moderate anti-cancer activity.

Keywords: Cyclometalated ruthenium complex; Piano-stool; Anticancer.

Introduction

As the global incidence of cancer increases, more treatments are needed to overcome the disease [1]. Many efforts have been made to overcome cancer [2], and various methods have been used to treat it, among which we can mention chemotherapy, a pioneering and old method. In this approach, the destruction of cancer cells is accompanied by the appearance of various adverse effects. Consequently, designing an anti-cancer drug with high selectivity and the least amount of side effects is a challenge when dealing with cancer cells nowadays [3]. Ruthenium-based compounds can be mentioned as one of the best candidates for chemotherapy and clinical development [4]. In the framework of our ongoing investigation on the bioactive non-platinum complexes [5], herein we report the preparation of a ruthenium(II) complex bearing a cyclometalated ligand, its characterization, and their biological activities, as well as potential anti-cancer mechanisms.

Experimental Section

[Cp*IrCl(dfppy)], 1, A solution of [(*p*-cymene)RuCl(μ-Cl)]$_2$, **A**, (100 mg, 0.16 mmol), 2-(2,4-difluorophenyl)pyridine (50 µL, 0.32 mmol), and excess of sodium acetate in CH$_2$Cl$_2$ was stirred for 24 h at ambient temperature. The solution was filtered through Celite. The filtrate was evaporated to dryness on a rotary evaporator and washed with cold n-pentane. The product was recrystallized from CH$_2$Cl$_2$/pentane.
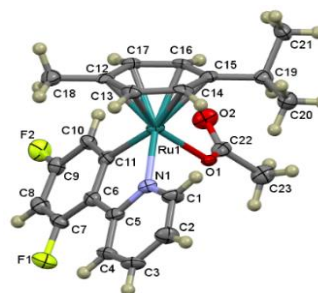
Results and Discussion

Scheme 1 depicts the reaction of [(*p*-cymene)RuCl(μ-Cl)]$_2$, **A**, with 2-(2,4-difluorophenyl)pyridine (dfppy), at room temperature afforded a new Ru(II) complex [(p-cymene)Ru(dfppy)(OAc)], **1**. The arene complex **1** is a green solid that has good solubility organic solvents such

as acetonitrile and dimethyl sulfoxide (dmso). In order to demonstrate that the preparation of the target complex **1** was carried out without any problem, it was subjected to 1D and 2D NMR characterization, during which the diagnostic *p*-cymene and dfppy signals were detected. Elemental analysis, HR ESI-Mass, and X-ray crystal structures, which were all done on **1**, provided additional validation (Fig. 1).
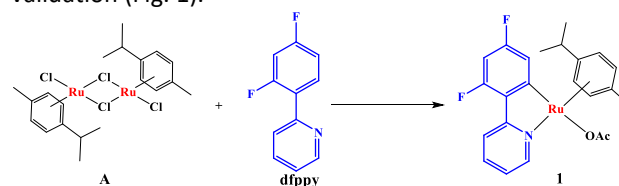
Scheme 1. Synthetic pathway for the iridium complexes.

The X-ray crystallography method defines the optimal single crystal form as **1**. Fig. 1 shows the crystal structure of **1**. The *p*-cymene ring occupies one face of **1** in a half-sandwich arrangement to the Ru metal center in a η^6 fashion. The coordination sphere of Ru is completed by a single oxygen atom of acetate, and the dfppy ligand forms a bidentate coordination mode with the carbon and nitrogen atoms of the dfppy ring. The geometry of the ruthenium center is a pseudo-octahedral.

Fig. 1: ORTEP plot of **1**.

22nd Iranian Chemistry Congress (ICC22)
Iranian Research Organization for Science and Technology (IROST)
13-15 May 2024

03231-97589

Prior to *in vitro* tests, the stability of Ru(II) complexes, **A**, and **1**, was evaluated with the aid of NMR and UV-vis spectroscopies. As an example, the stability of **1** in dmso solution was validated by UV-vis spectroscopy, and ^{1}H NMR monitoring in dmso-d_6, D_2O, and a mixture of dmso-d_6/D_2O showed that this complex was stable for 96 h.

Through the use of the MTT assay, the cytotoxic potential of all these Ru(II) compounds (**A**, and **1**), was assessed against lung (A549), breast (MCF7), and cervical (HeLa) cells, in addition to lung fibroblast (MRC5) cells. The Ru(II) complex **1** was shown to have the most effective cytotoxic activity and the highest inhibition (%) activity against the cancer cells that were investigated (Table 1). The cytotoxic activity found for **1** against A549 lung cancer cells was the highest, with an IC$_{50}$ of 3.1 µM, whereas the cytotoxic activity obtained for cisplatin was 9.8 µM. The results of a statistical test using the one-way analysis of variance revealed that this difference is statistically significant. In comparison to cisplatin's IC$_{50}$s of 16.7 µM and 10.2 µM, respectively, **1** displayed good cytotoxic effects against MCF7, and HeLa cancer cells with IC$_{50}$s of 9.7 µM. However, statistical analysis with a one-way analysis of variance revealed that there is no statistically significant difference between the IC$_{50}$s of cisplatin and **1** when used against MCF7 and HeLa cells. As can be shown in Table 1, all of the compounds that were investigated had significantly higher IC$_{50}$ values when tested against MRC5 than cisplatin. In comparison to the other compounds, **1** showed higher selectivity index (SI = 3.7).

Table 1. Cytotoxicity of the ruthenium(II) complexes against both cancerous and noncancerous cell lines when tested *in vitro*.

Comp.	(IC$_{50}$ ± SD) µM[a]				
	A549	MCF7	HeLa	MRC5	Selectivity Index[b]
A	93.1 ± 1.5	>100	97.3 ± 2.2	>100	-
1	3.1 ± 1.3	10.2 ± 0.3	9.7 ± 1.5	11.4 ± 1.2	3.7
Cisplatin	9.8 ± 1.9	16.7 ± 1.5	18.4 ± 1.2	15.7 ± 2.1	1.6

[a] The MTT assay was performed for 72 h.

[b] IC$_{50}$ for MRC-5 cell line/IC$_{50}$ for A549 cell line.

Conclusions
The compounds containing ruthenium have been considered one of the most favorable metal-based candidates for anti-cancer treatment. The organometallic Ru(II) complex [(*p*-cymene)Ru(dfppy)(OAc)], **1**, containing a C^N donor ligand (dfppy) was prepared and characterized by different spectroscopic methods. The X-ray crystallography data showed that this complex has a piano-stool type structure. Besides, the stability of all compounds in biological environments was examined by UV-vis spectroscopy. The cytotoxic activity of the compounds was evaluated *in vitro* against different cancer cell lines, such as lung (A549), breast (MCF7), and cervix (HeLa), as well as lung fibroblast (MRC5), using the MTT assay. The IC$_{50}$ contents revealed that **1** indicated higher cytotoxic activities against MCF7, and HeLa cancer cells in comparison with **A** and cisplatin. It is worth noting that the selectivity index parameter for our Ru(II) complex, **1**, was better relative to cisplatin. A flow cytometric analysis of **1**'s apoptotic effect on MCF-7 cells exhibited that increasing the concentrations of this complex causes cell death in late-phase apoptosis. Complex **1** was able to control the cleavage of DNA on its own, but it has a strong tendency to intercalate. According to this study, the new Ru(II) complex can be used as a protentional candidate for biomedical research and drug development. We are currently working on ruthenium(II) and its heterobimetallic complexes.

References
[1] Yang, G. W.; Zhang, X.; Li, G. M.; Yang, J.; Shen, L.; Chen, D. Y.; Li, Q. Y.; Zou, D. F., Photochemical property of a Ru(II) compound based on 3-(2-pyridyl) pyrazole and 2,2'-bipyridine for ablation of cancer cells. *New J. Chem.* **2018**, *42*, 5395-5402.

[2] oldevila-Barreda, J. J.; Metzler-Nolte, N., Intracellular Catalysis with Selected Metal Complexes and Metallic Nanoparticles: Advances toward the Development of Catalytic Metallodrugs. *Chem. Rev.* **2019**, *119*, 829-869.

[3] Hartinger, C. G.; Metzler-Nolte, N.; Dyson, P. J., Challenges and opportunities in the development of organometallic anticancer drugs. *Organometallics* **2012**, *31*, 5677-5685.

[4] Rafols, L.; Josa, D.; Aguilà, D.; Barrios, L. A.; Roubeau, O.; Cirera, J.; Soto-Cerrato, V.; Pérez-Tomás, R.; Martínez, M.; Grabulosa, A.; Gamez, P., Piano-Stool Ruthenium(II) Complexes with Delayed Cytotoxic Activity: Origin of the Lag Time. *Inorg. Chem.* **2021**, *60*, 7974-7990.

[5] Nahaei, A.; Mandegani, Z.; Chamyani, S.; Fereidoonnezhad, M.; Shahsavari, H. R.; Kuznetsov, N. Y.; Nabavizadeh, S. M., Half-Sandwich Cyclometalated Rh^{III} Complexes Bearing Thiolate Ligands: Biomolecular Interactions and In Vitro and In Vivo Evaluations. *Inorg. Chem.* **2022**, *61*, 2039-2056.

Enhancing Photocatalytic Decomposition of Rhodamine B Using Mo Nanoparticle-Enhanced CdS Nanorods for Effective Wastewater Treatment

Hamidreza Rahmani, Alireza Mahjoub[*]

Corresponding Author E-mail : mahjouba@modares.ac.ir

Department of Chemistry, Faculty of Basic Sciences, Tarbiat Modares University, Tehran, Iran.

Abstract: In this study, we explored a method to enhance the photocatalytic degradation of rhodamine B, a persistent pollutant in wastewater. We achieved this by depositing molybdenum (Mo) nanoparticles onto cadmium sulfide (CdS) nanorods. This composite material exhibited significantly improved photocatalytic activity towards rhodamine B degradation under light irradiation. This enhancement can be attributed to the formation of interfaces between Mo and CdS, which promote efficient separation of photogenerated electron-hole pairs, leading to a more effective photocatalytic process.

Keywords: Photocatalysis; CdS nanorods; Nanoparticles.

Introduction

Cadmium sulfide nanorods are promising for wastewater treatment due to their photocatalytic properties, but their efficiency can be limited. Recent research suggests incorporating molybdenum nanoparticles into these nanorods can significantly improve their performance by accelerating the transfer of electrons and boosting the production of free radicals that break down pollutants [1].

Secondly, Mo nanoparticles introduce additional redox sites within the nanocomposite, further enhancing the generation of ROS. This increased ROS production translates into a more potent photocatalytic activity, enabling the degradation of a broader range of organic pollutants [2]. Combining molybdenum nanoparticles with cadmium sulfide nanorods significantly enhances their ability to degrade organic pollutants in wastewater treatment. This improvement is due to accelerated electron transfer and increased production of free radicals. The composite material effectively degrades a wide range of contaminants, including dyes, pharmaceuticals, pesticides, and industrial effluents, and utilizes visible light for efficient operation [3].

Mo nanoparticles significantly improve the performance of CdS nanorods in degrading pollutants for wastewater treatment. This is due to faster electron transfer, increased production of free radicals, and the ability to tackle a wider range of contaminants. With further research, Mo-enhanced CdS nanorods have the potential to revolutionize wastewater treatment technologies for a cleaner future [4].

Experimental Section

Synthesis of CdS nanorods: The synthesis of CdS nanorods involves a multi-step process that includes dissolving cadmium nitrate precursor in ethylenediamine, adding thiourea, followed by hydrothermal treatment at 160°C for 20 hours. The resulting product is then washed and dried to remove impurities and solvents [5].

Synthesis of CdS/Mo nanocomposite: We created CdS/Mo nanocomposites in two steps. First, we dispersed CdS nanoparticles in water. Then, we mixed a solution with molybdenum precursor and reducing agent to the CdS dispersion [6]. After stirring, the CdS/Mo composite was separated, washed, dried, and characterized by Figure 1 in the article, revealing a well-defined structure.
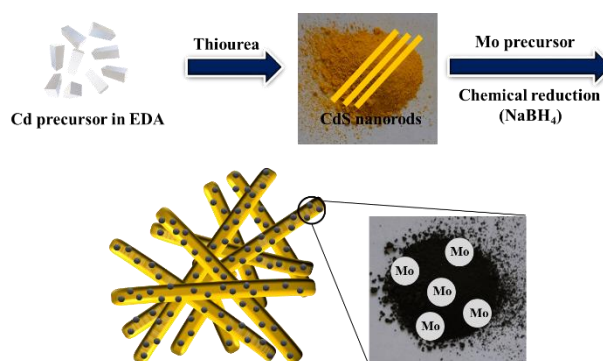
Fig.1: illustration of the synthesis method for CdS/Mo nanocomposite.

Characterization

The morphological and structural properties of the CdS/Mo nanocomposites were characterized by employing various techniques.

X-ray diffraction (XRD) revealed the crystalline phases, while field emission scanning electron microscopy (FESEM) depicted the morphology and size of the nanorods. Transmission electron microscopy (TEM) provided high-resolution images of the arrangement of nanoparticles on the nanorod surfaces. Finally, Fourier

22nd Iranian Chemistry Congress (ICC22)
Iranian Research Organization for Science and Technology (IROST)
13-15 May 2024

03231-97589

IROST

Transform Infrared (FTIR) spectroscopy confirmed the chemical composition of the material.

Results and Discussion
Structural investigation
The crystal structures of the fabricated CdS and CdS/Mo nanocomposites were investigated using X-ray diffraction (XRD) analysis. Figure 2 shows the XRD patterns for both samples.
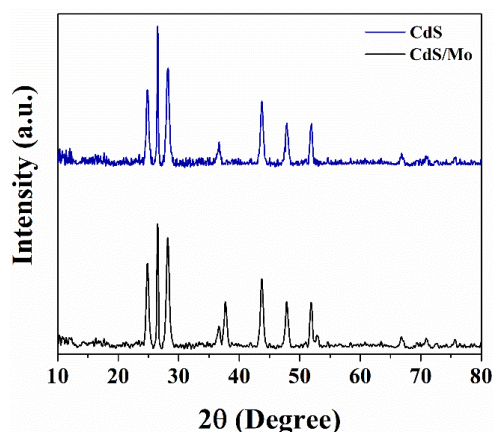
Fig.2: XRD patterns of the pure CdS nanorods and CdS/Mo nanocomposites.

The morphological and microscopic structures of CdS nanorods and CdS/Mo nanocomposites were further investigated using field emission scanning electron microscopy (FESEM) and transmission electron microscopy (TEM).
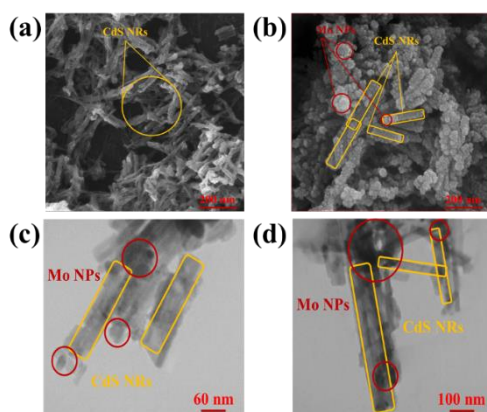
Fig.3: (a) FE-SEM images of the CdS nanorods, (b) CdS/Mo nanocomposite, and (c, d) TEM images of the CdS/Mo nanocomposite.

Conclusions
This study fabricated CdS/Mo nanocomposites by depositing Mo nanoparticles onto CdS nanorods. Characterization with XRD, FESEM, TEM, FTIR, and UV-Vis

DRS confirmed their structure and properties. The nanocomposites showed successful synthesis of CdS/Mo nanocomposites and enhanced photocatalytic activity compared to pure CdS nanorods due to Mo-S-Cd bridges facilitating charge transfer and generation of reactive oxygen species, demonstrating their potential as efficient photocatalysts for wastewater treatment.

References
[1] Bie, C., Zhu, B., Wang, L., Yu, H., Jiang, C., Chen, T., & Yu, J. (2022). A bifunctional CdS/MoO2/MoS2 catalyst enhances photocatalytic H2 evolution and pyruvic acid synthesis. Angewandte Chemie International Edition, 61(44), e202212045.

[2] Tian, L., Yue, L., Wang, F., Min, S., & Zhang, Z. (2020). CdS/Metallic Mo hybrid photocatalysts with highly active interfacial Mo–O–S active sites for efficient photocatalytic hydrogen evolution under visible light. The Journal of Physical Chemistry C, 124(35), 18911-18919.

[3] Xia, J., Ren, X., Zhao, L., Tang, M., Tan, L., Fu, C., ... & Meng, X. (2022). Synthesis of MoS2 nanoflowers on CdS nanorods with a simple route and their application in removal of dyes. Journal of Nanoparticle Research, 24(3), 57.

[4] Ullah, H., Viglašová, E., & Galamboš, M. (2021). Visible light-driven photocatalytic rhodamine B degradation using CdS nanorods. Processes, 9(2), 263.

[5] Yang, J., Zeng, J. H., Yu, S. H., Yang, L., Zhou, G. E., & Qian, Y. T. (2000). Formation process of CdS nanorods via solvothermal route. Chemistry of materials, 12(11), 3259-3263.

[6] Khavar, A. H. C., Mahjoub, A. R., & Khazaee, Z. (2022). MoCu bimetallic nanoalloy-modified copper molybdenum oxide with strong SPR properties; a 2D–0D system for enhanced degradation of antibiotics. Colloids and Surfaces A: Physicochemical and Engineering Aspects, 653, 130032.